Andreas Schörghofer-Queiroz, Dipl.-Ing. BSc

Fatigue behaviour of steel and composite bridges in high-speed railway lines

Doctoral Thesis

to achieve the university degree of

Doctor of Engineering Science

Doctoral programme: Civil Engineering Sciences

submitted to

Graz University of Technology

Supervisor

Univ.-Prof. Dipl-Ing. Dr.techn. Harald Unterweger
Institute of Steel Structures, Graz University of Technology

Univ.-Prof. Dr.-Ing. Karsten Geißler
Conceptual and Structural Design — Steel Construction, Technische Universität Berlin

Graz, January 2021

Affidavit

I declare that I have authored this thesis independently, that I have not used other than the declared sources/resources, and that I have explicitly indicated all material which has been quoted either literally or by content from the sources used.

Date	Signature

Acknowledgements

This thesis would not have been possible without the support of my supervisor Univ.-Prof. Dipl.-Ing. Dr.techn. Harald Unterweger. I am very grateful for his advice and the opportunity to write my thesis during my four and a half years as a university assistant at the Institute of Steel Structures at the Graz University of Technology.
Additionally, I would like to express my gratitude to Univ.-Prof. Dr.-Ing. Karsten Geißler from Technical University of Berlin for reviewing my thesis.
Further on, I would like to thank Prof. Hermes Carvalho for receiving me at the Universidade Federal de Minas Gerais (UFMG) and the fruitful discussions on my thesis and structural engineering.
I gratefully acknowledge Dipl.-Ing. Dr.tech. Zoran Bruschetini-Ambro (ÖBB) and Dipl.-Ing. Dr.-Ing Grunert Günther (DB) for providing me with data.
A special thank you to my colleagues at the Institute of Steel Structures for the pleasant time and fruitful discussions.
I would like to thank my parents who enabled me my education and motivated me throughout my entire life to pursuit the paths I chose.
Finally, I would like to thank my beloved wife Valéria for the mental support and patience, especially throughout the last year of my PhD endeavour.

Abstract

This thesis is concerned with the fatigue behaviour of steel and composite bridges in high-speed railway lines. In general, fatigue is caused by repeated stress cycles, which e.g. occur due to the dynamic problem of a high-speed train crossing a bridge structure. However, the current fatigue design verification is based on a static approach, which considers dynamic effects by the 'dynamic' factor Φ.

However, this factor does not consider resonance scenarios. Therefore, this thesis clarifies, based on a parameter study, whether or not the common static approach for the fatigue design verification of single-span steel and composite railway structures is sufficient to account for the effects of high-speed trains due to a dynamic simulation. Additionally, it defines design requirements in case the above-mentioned static approach is not appropriate. Therefore, a new computational approach, based on the non-dimensional response representation, is developed, which allows to perform more efficiently the above-mentioned parameter study – covering more than 94000 different trains, different train speeds, different wheel load distributions and different damping ratios of the structure. Furthermore, this thesis also clarifies whether or not simplified train models (moving load model) are sufficient and accurate, with respect to the fatigue problem, in comparison to a more detailed approach (2D multi-body model).

Further on, the main structural members (main girders and arches) of a representative arch bridge, with respect to the crossing of more than 94000 different train types, is investigated concerning their fatigue behaviour.

In order to avoid the dynamic calculation and determination of the precise stress range spectra at the critical point of the high-speed bridge structure, the design codes in Austria allow to simply enhance the static fatigue load by an additional factor. This thesis investigates the accuracy of the additional factor as well.

The conclusion of this thesis shows that single-span steel and composite bridges in high-speed railway lines are not prone to fatigue due to the crossing of high-speed railway trains, if they fulfil the vertical bridge deck acceleration criterion due to the crossing of the HSLM-A trains. Besides that, it is also concluded that the additional factor included in the design codes in Austria proves not to be sufficiently accurate.

Kurzfassung

Diese Arbeit befasst sich mit dem Ermüdungsverhalten von Stahl- und Verbundbrücken in Hochgeschwindigkeitseisenbahnstrecken. Im Allgemeinen wird Ermüdung durch wiederholte Spannungszyklen verursacht, welche unter anderem beim dynamischen Problem einer Hochgeschwindigkeitszugsüberfahrt über ein Brückentragwerk resultieren.
Der aktuelle Ermüdungsnachweis basiert jedoch auf einem statischen Ansatz, bei dem dynamische Effekte durch den 'dynamischen' Faktor Φ berücksichtigt werden, wodurch Resonanzszenarien unberücksichtigt bleiben. In dieser Arbeit wird daher anhand einer umfassenden Parameterstudie geklärt, ob der übliche statische Ansatz für den Ermüdungsnachweis von einfeldrigen Stahl- und Verbundtragwerken ausreicht, um die Auswirkungen von Hochgeschwindigkeitszugsüberfahrten zu berücksichtigen. Weiters werden Entwurfsanforderungen definiert, falls der oben genannte statische Ansatz nicht geeignet ist. Zusätzlich wird ein neuer Berechnungsansatz entwickelt, der auf der nichtdimensionalen Darstellung basiert und es somit ermöglicht, die oben genannte Parameterstudie effizienter durchzuführen - mit mehr als 94000 verschiedenen Zügen, verschiedenen Zuggeschwindigkeiten, verschiedenen Radlastverteilungen und verschiedenen Dämpfungsannahmen der Brückenstruktur. Darüber hinaus wird in dieser Arbeit auch geklärt, ob vereinfachte Zugmodelle (Einzellastmodell) im Vergleich zu einem detaillierteren Ansatz (2D-Mehrkörpermodell) in Bezug auf das Ermüdungsproblem ausreichend und genau genug sind.
Weiters werden die Haupttragelemente (Hauptträger und Bögen) einer repräsentativen Bogenbrücke hinsichtlich der Überquerung von mehr als 94000 verschiedenen Zugstypen auf ihr Ermüdungsverhalten untersucht.
Um die dynamische Berechnung und Bestimmung der genauen Spannungskollektive am kritischen Punkt der Hochgeschwindigkeitsbrückenstruktur zu vermeiden, ermöglichen es die Bemessungsnormen in Österreich, die statische Ermüdungsbelastung vereinfacht um einen zusätzlichen Faktor zu erhöhen. Diese Arbeit untersucht weiters die Genauigkeit dieses zusätzlichen Faktors.
Die Schlussfolgerungen dieser Arbeit zeigen unter anderem, dass einfeldrige Stahl- und Verbundeisenbahnbrücken in Hochgeschwindigkeitsstrecken zufolge der Überfahrt von Hochgeschwindigkeitszügen nicht ermüdungsanfällig sind, insofern diese das Kriterium der vertikalen Brückendeckbeschleunigung aufgrund der Überquerung der HSLM-A Züge erfüllen. Weiters kann gezeigt werden, dass sich der zusätzliche Faktor, welcher in den Bemessungsnormen in Österreich enthalten ist, als nicht treffsicher erweist.

Contents

1. Introduction

1.1. Motivation and objectives

The increase in personal mobility in everyday life leads, among other things, to the expansion of high-speed railway lines. These high-speed railway lines and the development of new high-speed trains confront engineers with new challenges. In the last decades great effort has been made in order to understand the behaviour of railway bridges in such high-speed railway lines better. The main focus was thereby on the vertical bridge deck acceleration and, as a consequence, the possibly resulting ballast bed destabilisation.
Long term effects due to the high-speed traffic, such as fatigue damage, were not primary the main emphases of this research. Nevertheless in the literature on the fatigue behaviour a large number of individually and in detail investigated high-speed railway bridge structures exist. These individual results are only valid for the particularly studied structure. Therefore, this thesis aims to generate a more general conclusion by performing a comprehensive parameter study for single-span steel and composite structures.
Furthermore, the amount of considered train types in literature is, due to the various reasons (e.g. computational effort, lack of train data), limited to a rather low number of trains. In this thesis, due to the information provided by the *Österreichische Bundesbahnen (ÖBB)*, it is possible to consider about 95000 different train types.
In order to avoid the dynamic calculation and determination of the precise stress range spectra at the critical point of the high-speed bridge structure, the design codes in Austria allow to simply enhance the static fatigue load by an additional factor — subsequently called 'adjusted' dynamic factor.
Moreover, the *Deutsche Bahn (DB)* provided data of a representative arch bridge, which is in this thesis subject to an exemplary fatigue behaviour investigation.

Therefore, the following points are defined as *objectives* in this thesis:

- clarify whether the common static approach for the fatigue design verification of single-span steel and composite railway bridges (load model LM71 with damage equivalent factor λ) is sufficient to account for resonance effects due to dynamic simulation or not;
- define additional design requirements, in case the above mentioned approach is not sufficient;
- develop a new computational approach, which allows to perform the parameter study more efficiently;
- clarify whether the simplified and generally used train model (*moving load model*) is sufficient and accurate in comparison to a more detailed approach (*2D multi-body model*) or not;
- investigate the influence of different train speeds, different wheel load distributions due to the rail and different damping ratios of the structures on the fatigue behaviour;

- determine the accuracy and necessity of the 'adjusted' dynamic factor;
- investigate the main structural members (main girders and arches) of a representative arch bridge, with respect to the fatigue behaviour due to the crossing of about 95000 different train types.

1.2. Organization

Chapter 2 provides an overview of the current valid design codes in Austria of common and high-speed railway bridges, with respect to the fatigue design. Additionally, a short overview of the state of the art is provided.

Chapter 3 describes the dynamic simulation of a train crossing a bridge structure. The computational approaches are derived for simple beams and complex structures, considering two train models (*moving load model* and *2D multi-body model*). Additionally, a *non-dimensional response representation* for simple beams and the *moving load model*, which allows to reduce the necessary number of dynamic calculations in the context of a parameter study substantially, is presented.

Chapter 4 introduces the five different traffic mixes considered in this doctoral thesis. Additionally, the corresponding train speeds for each traffic mix are defined.

Chapter 5 covers the single-span steel and composite bridges in high-speed railway lines, which carry one track and which are studied with respect to their fatigue and traffic safety behaviour. First, an overview regarding the considered structures, traffic mixes and the computational method itself is presented. Subsequently, preliminary studies and the traffic safety design check (limited vertical acceleration of the bridge deck) for the single-span bridges are performed. Finally, a parameter study is conducted, which combines the traffic safety and fatigue criteria. Additionally, the accuracy of the 'adjusted' dynamic factor, which was introduced in Chapter 2, is studied.

Chapter 6 investigates the main girders and arches of a representative arch bridge with respect to their fatigue behaviour.

2. Background — design of railway bridges

2.1. Code based design according to Eurocode

The semi-probabilistic concept, according to the ÖNORM EN 1990 [41], generally distinguishes characteristic values of the effects of actions E_k and characteristic values of the resistance R_k. These values multiplied and divided respectively by the partial safety factors γ_F and γ_M result into design values, which form the principal design verification format

$$\begin{aligned} E_d &\leq R_d \\ \gamma_F \, E_k &\leq \frac{R_k}{\gamma_M} \end{aligned} \tag{2.1}$$

The expression above classifies the state of a given structure for specific limit states. In case the inequality is fulfilled, the state may be termed satisfactory (safe, serviceable), in all other cases the state may be called unsatisfactory (failed, unserviceable). Consequently, the *limit states* separate the satisfactory from the unsatisfactory conditions.
In general, the ÖNORM EN 1990 [41] defines two categorically different types of limit states. The *ultimate limit state (ULS)* refers to states regarding collapse or to similar forms of structural failure and is related to the safety of people/ structure. The *serviceability limit state (SLS)* covers the conditions of normal use (deflections, vibrations, etc.), the comfort of people and the appearance of the construction works.
However, some undesirable situations may be assigned with difficulty to the one and right limit state. For example, the deformation of a railway bridge deck, which basically is a service ability limit state, may cause a derailment situation of the train. This endangers human life and, therefore, needs to be considered as an ultimate limit state as well. ([7] p.33 et sqq.)

Fatigue failures, which result due to fluctuating or repetitive loading cycles and the emerging crack growth phenomena, may occur at load levels much lower than usually expected for ultimate limit loads. The ÖNORM EN 1990 [41] separates the *fatigue limit state (FLS)* from the ultimate limit state and the serviceability limit state for a number of reasons [7] (p.37 et sqq.):

- The fatigue problem is time dependent, as the magnitude and the number of cycles under service loads needs to be considered.
- The crack growth, which is a local deterioration of material, may stop when restraints are reduced, or continue and accelerate when cracks lead to more critical loading conditions.
- Regular inspections may enable one, under particular circumstances (e.g. tough material), to detect crack growth before it leads to failure.
- Additionally, regarding the fatigue limit state, a safety system has been developed, which considers the possibility of pre-warning and the consequences of failure.

In general, the train crossing on a bridge structure is a dynamic problem, which might lead, especially in case of resonance, to excessive vibrations. However, the three limit states mentioned above are checked with a quasistatic concept according to the ÖNORM EN 1991-2 [43] for common railway bridges. Therefore, the statically calculated deformations and stresses are increased by using dynamic amplification factors (Φ for the LM71 and φ for real trains), which do not consider the resonance scenario. For high-speed railway bridges, the findings after the opening of the first high-speed lines in France and the occurred damages due to exorbitant vibrations, resulting in the deterioration of the ballasted track, led to the necessity of checking and limiting the vertical bridge deck acceleration. ([66], [55] p.10) Hence, the static amplification factors do not sufficiently cover the stresses and deformations in case of resonance, and, consequently, additional dynamic verification is required. ([55] p.10)

Therefore, the actual design code ÖNORM EN 1991-2 [43] clarifies in which cases a static analysis with dynamic amplification factors is sufficient and when an additional dynamic analysis is necessary. The following chapters summarize the basic concepts of the static and dynamic analysis according to the ÖNORM EN 1991-2 [43] and the situation in Austria, including an emphasis on the fatigue limit state (FLS).

2.1.1. Static analysis

The static analysis of bridges due to train crossing is carried out using load models, which represent the vertical real train loads. Therefore, the ÖNORM EN 1991-2 [43] provides the following load models:

- Load model 71 (UIC 71 or LM71) for normal rail traffic — see Figure 2.1
- SW/0 for normal rail traffic on continuous beams — see Figure 2.2
- SW/2 for heavy rail traffic — see Figure 2.4
- "unloaded train" — consists of a vertical uniformly distributed load with a characteristic value of 10.0 kN/m.

In engineering practise, the first three load models are the main ones. These models need to be multiplied by the so called 'dynamic'[1] factor Φ. Additionally, the two load models LM71 and SW/0, representing normal rail traffic, need to be multiplied by the classification factor α in order to consider heavier or lighter rail traffic. Each European country chooses this factor from the pool of the following numbers:

$$0.75 - 0.83 - 0.91 - 1.00 - 1.10 - 1.21 - 1.33 - 1.46$$

In Austria α is set to 1.21 for normal-gauge lines.

[1] The factor Φ is also required to adapt the simple load model LM71 to real train configurations and is consequently not a pure dynamic factor as demonstrated by Equation (2.15).

Historical background of the current valid load models in the ÖNORM EN 1991-2 [43]

The load model LM71 was developed about 50 years ago with the goal to cover the real trains at that time including a prediction of the axle load development for the near future. However, it did not include heavy haul and was only calibrated for single-span beam bridges. Therefore, it neglected more sophisticated structural systems as the computing power was limited. The obvious lack of accuracy, especially regarding continuous beams and heavy haul, of the load model LM71 led to the development and introduction of the load models SW/0 and SW/2. The increasing axle loads and traffic volume has been a challenge ever since. Therefore, in 1991 the ERRI[1] expert group D192 started a research project to estimate future loads on railway bridges. The different railway administrations throughout Europe predicted axle loads up to 30 t and mass per length up to 15 t/m. ([6] p.152) In order to comply with the increasing loads, the ERRI expert group D192 suggested to either introduce a new load model (LM 2000) or to multiply the loads of the existing load model LM71 with the classification factor $\alpha = 1.4$. Additionally, the ERRI expert group D192 carried out a profitability study, which predicted that the overall cost of bridges due to higher axle loads would increase insignificantly (1.4 LM71 versus LM71 leads to 4% cost increase). ([6] p.153) However, the results of the ERRI expert group D192 did not find their way into the Eurocodes developed later, although the UIC Code 702 [28] recommends since 2003 the use of the load model LM 2000 for future rail freight networks. Therefore, in order to implement an interoperable European railway network, a classification factor of $\alpha = 1.33$ is recommended in [6]. The future goal is clearly to define one classification factor for all member countries, which is unfortunately not a fact until now. ([6] p.153)

Consequently, the load models LM71, SW/0 and SW/2, which are explained more in detail in the following chapters, need to be considered according to the ÖNORM EN 1991-2 [43].

Load models for normal rail traffic - Load model 71 and SW/0

The load model LM71, which represents the static effect of vertical loads regarding the normal railway traffic, consists of four single loads and a uniformly distributed load. The characteristic values are 250 kN and of 80 kN/m, as illustrated in Figure 2.1.

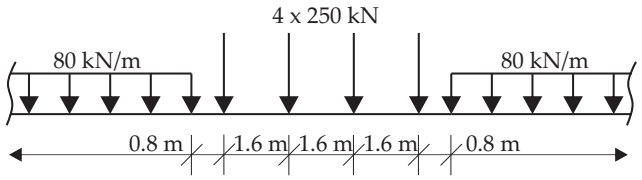

Figure 2.1.: Load model LM71 and characteristic values for vertical loads — according to the ÖNORM EN 1991-2 [43]

Additionally, the load model SW/0 covers the static effect of vertical loads due to normal railway traffic on continuous bridges. It is represented by two 15 m long, 5.3 m separated from each other and 133 kN/m big uniformly distributed loads — see Figure 2.2

[1] European Rail Research Institute of the international union of railways UIC (Union Internationale des Chemins de fer)

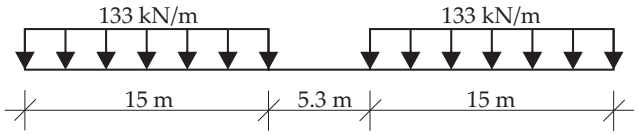

Figure 2.2.: Load model SW/0 and characteristic values for vertical loads — according to the ÖNORM EN 1991-2 [43]

In order to determine the most adverse load effects from the application of load model LM71, the length of the uniformly distributed load (80kN/m) shall be considered as infinite. Furthermore, the areas which lead do a decreasing load effect, due to the load model LM71, shall be neglected — see Figure 2.3.

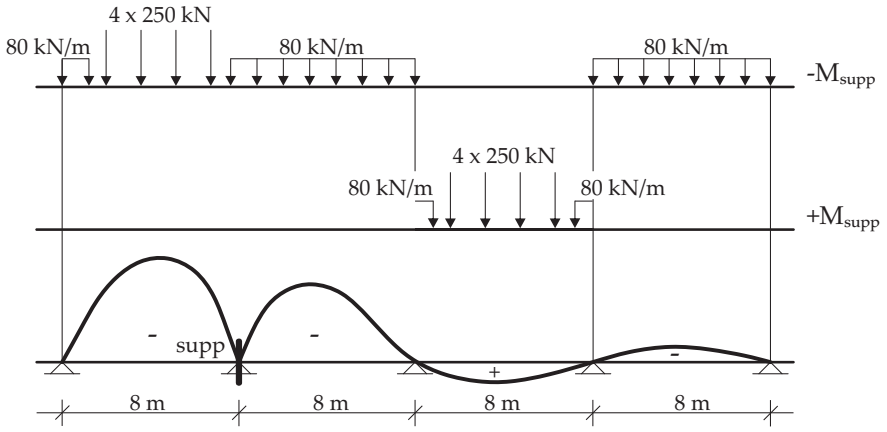

Figure 2.3.: Rules for application of load model LM71 in section supp — according to the ÖNORM B 1991-2 [38]

Load models for heavy rail traffic - SW/2

Equally to the load model SW/0 mentioned above, the load model SW/2 consists of two uniformly distributed loads, whereas the load and the dimensions are defined as shown in Figure 2.4. The load model SW/2 represents the static effect of the vertical loading with respect to heavy rail traffic.

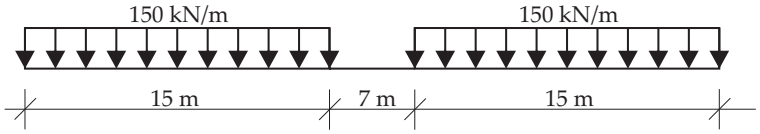

Figure 2.4.: Load model SW/2 and characteristic values for vertical loads — according to the ÖNORM EN 1991-2 [43]

Considering dynamic effects in the static analysis

Trains crossing a bridge structure lead to dynamic load effects, which need to be considered in the quasistatic analysis. Therefore, the ÖNORM EN 1991-2 [43] defines dynamic factors, which shall be multiplied by the specified static loads of either the actual real trains or load models:

- $1+\varphi$ — is the physically determined dynamic factor for **real trains** and serves as a basis for the following factor Φ
- Φ — the 'dynamic factor' for the **load models** LM71, SW/0 and SW/2, which is more an adjustment factor than a pure dynamic factor, as shown in Equation (2.15)

Dynamic factor $1+\varphi$ for real trains

The modern dynamic factors we know today have their origin in 1955. In order to standardise design rules of the European railways, the expert group D23 of the UIC's research and development institute ORE[1] performed measurements on 37 straight railway structures, of all construction types, during the crossing of representative trains of that time. The findings led to the dynamic factors $(1+\varphi)$ for the speed range $0 < v \leq 240$ km/h, being independent of the construction type. However, the formulas were developed with respect to the first bending frequency due to permanent loads and traffic (!) loads. Unfortunately, at that time, it was not possible to find dimensionless values for all bridge members. Due to the mentioned limitations, in the 1970s the task force 7/J/8 of the UIC developed the dynamic factors we know today, using the measurements done by the expert group D23. The improved dynamic factors, depending on the first bending frequency due to permanent loads only (no traffic loads anymore), are valid for speeds $0 < v \leq 300$ km/h and are split into two parts with φ', considering dynamic effects due to ideal rail conditions and φ'' considering vertical track defects and vehicle imperfections. [65] The above mentioned laws were derived from simply supported beams, which cover most of the effects in continuous girders and other structures. Where this is not the case, the effects are considered by the so called determinant length L_Φ. ([6] p.157)

The following equations are implemented in the current ÖNORM EN 1991-2, Annex C [43]. Therefore, the effects of the static loads due to a real train shall be multiplied by:

$$\text{For track with standard maintenance:} \quad 1+\varphi = 1+\varphi'+\varphi'' \tag{2.2}$$

$$\text{For carefully maintained track:} \quad 1+\varphi = 1+\varphi'+0.5\,\varphi'' \tag{2.3}$$

For the perfect level track ($\varphi'' = 0$), the following Equations need to be considered:

$$\varphi' = \frac{K}{(1-K+K^4)} \quad \text{for } K < 0.76 \tag{2.4}$$

$$\varphi' = 1.325 \quad \text{for } K \geq 0.76 \tag{2.5}$$

$$K = \frac{v}{2\,L_\Phi\,n_0} \tag{2.6}$$

[1] Office de Recherches et d'Essais, predecessor of ERRI

Input parameters are the first natural bending frequency of the bridge loaded by permanent actions n_0 in [Hz], the maximum permitted vehicle speed v in [m/s] and the determinant length L_Φ in [m]. The latter is defined in the ÖNORM EN 1991-2 [43]. In case no value for L_Φ is specified in ÖNORM EN 1991-2 [43], the length of the influence line for deflection of the structural element may be used. ([43] 6.4.5.3 (2)) According to [49], Equation (2.4) represents the 95% quantile values of the measured dynamic factors examined by the expert group D23. Unlike in Equation (2.5), there was no plateau value of 1.325 defined for $K > 0.76$ in the original version of the dynamic factor φ' — see Figure 2.5. [65]

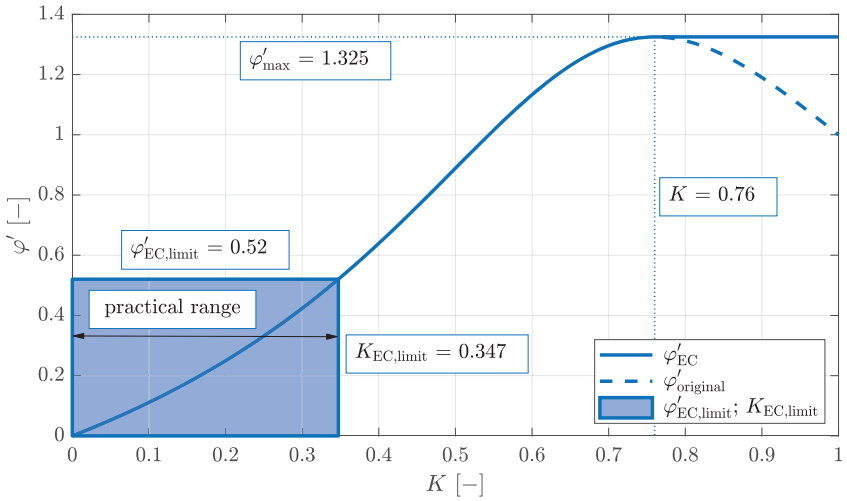

Figure 2.5.: Dynamic factor φ' plotted versus determinant length L_Φ for v = 200 km/h and n_0 according to Equation (2.9), leading to $K_{EC,limit}$

The vertical track imperfections and vehicle imperfections are considered by φ''. Equation (2.7) is the product of parameter studies via computer simulations performed by the British Rail (BR). Therefore, a "model-dip" with 1000mm in length and 2mm in depth was placed in the center of the rail. Additionally, the results were verified by selective in-situ measurements. [65] Equation (2.7) may be exceeded by up to 30% in special cases (high-speed trains with long wheelbase vehicles), while in other cases (e.g. special vehicles with closely spaced axles) only half of these values are reached. ([29] p.42)

$$\varphi'' = \frac{\alpha}{100}\left[56e^{-(\frac{L_\Phi}{10})^2} + 50\left(\frac{L_\Phi\, n_0}{80} - 1\right)e^{-(\frac{L_\Phi}{20})^2}\right] \tag{2.7}$$
$$\varphi'' \geq 0$$

$$\text{with:} \quad \alpha = \frac{v}{22} \quad \text{for} \quad v \leq 22\text{m/s} \tag{2.8}$$
$$\alpha = 1 \quad \text{for} \quad v > 22\text{m/s}$$

In Figure 2.6 the dynamic factor φ'' according to Equation (2.7) is plotted.

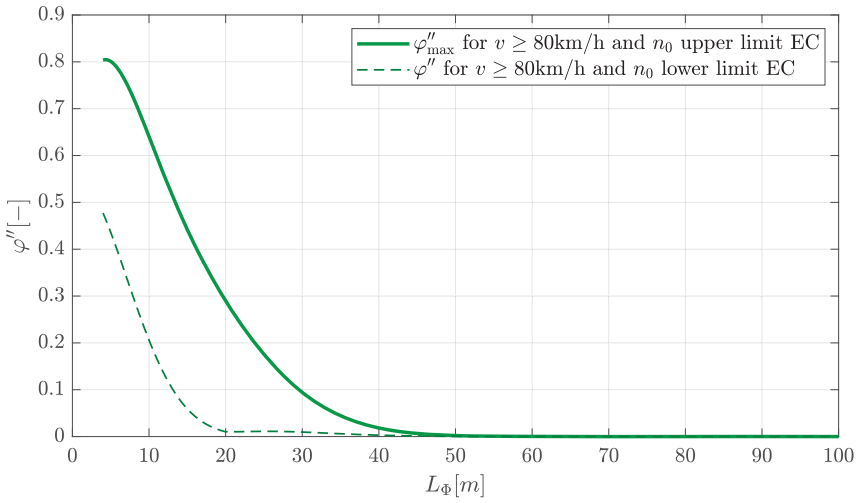

Figure 2.6.: Dynamic factor φ'' plotted versus determinant length L_Φ for $v > 80$ km/h and n_0 according to Equations (2.9), (2.10) and (2.11)

Furthermore, the task force 7/J/8 provided estimations for the upper and lower boundaries of n_0. [65] These boundaries are implemented in the ÖNORM EN 1991-2 [43] — see Figure 2.7 — and the relationships to the dynamic factors are clarified:

- The lower limit of n_0 at 200 km/h — see Equations (2.10), (2.11) and line (2) in Figure 2.7 — is the limit of validity for φ' as well. For all other cases φ' should be determined by a dynamic analysis, according to [43].
- On the other hand, the dynamic factor φ'' is limited by the upper limit of n_0 — see Equation (2.9) and line (1) in Figure 2.7. Again, in all other cases — n_0 above line (1) in Figure 2.7 — φ'' should be calculated by a dynamic analysis, taking into account mass interaction between the unsprung axle masses and the bridge. Notice that for φ'' a speed limit according to [43] does not exist .

$$\text{upper limit:} \quad n_0 = 94.76\, L_\Phi^{-0.748} \tag{2.9}$$

$$\text{lower limit:} \quad n_0 = \frac{80}{L_\Phi} \qquad \text{for} \quad 4m \leq L_\Phi \leq 20m \tag{2.10}$$

$$n_0 = 23.58\, L_\Phi^{-0.592} \quad \text{for} \quad 20m < L_\Phi \leq 100m \tag{2.11}$$

In Figure 2.8 the two dynamic factors φ' and φ'', with their maximum possible values, according to Equations (2.4), (2.5) and (2.7), are plotted versus the determinant length L_Φ. The maximum value $\varphi'_{\max}$ is reached if the maximum speed $v = 200$ km/h, the lowest first natural bending frequencies n_0 and the lowest determinant length L_Φ are inserted for K in Equation (2.6). Keep in mind that the bending frequency n_0 and determinant length L_Φ are linked here through Equations (2.10) and (2.11). Considering this, the blue area in Figure 2.5 results. It describes the possible values for φ' regarding the boundaries defined in [43] and the maximum value $\varphi' = 0.52$ is illustrated as plateau in Figure 2.8. Additionally, the dynamic factor φ' for $v = 200$ km/h and the upper boundary of the first natural bending frequencies n_0 — according to Equation (2.9) — is plotted in Figure 2.7.

The maximum value φ''_{max} is reached if the travel speed v is above 80 km/h and the highest first bending frequency n_0 for a given determinant length L_Φ is assumed according to Equation (2.9) — see the green solid line in Figure 2.8. The maximum possible value for φ''_{max} is about 0.8 and furthermore negligible for determinant lengths $L_\Phi \geq 45$ m. Additionally, the dynamic factor φ'' for $v > 80$ km/h and the lower limit of the first natural bending frequencies n_0 — according to Equations (2.10) and (2.11) — is illustrated in Figure 2.7 by the green dashed line.

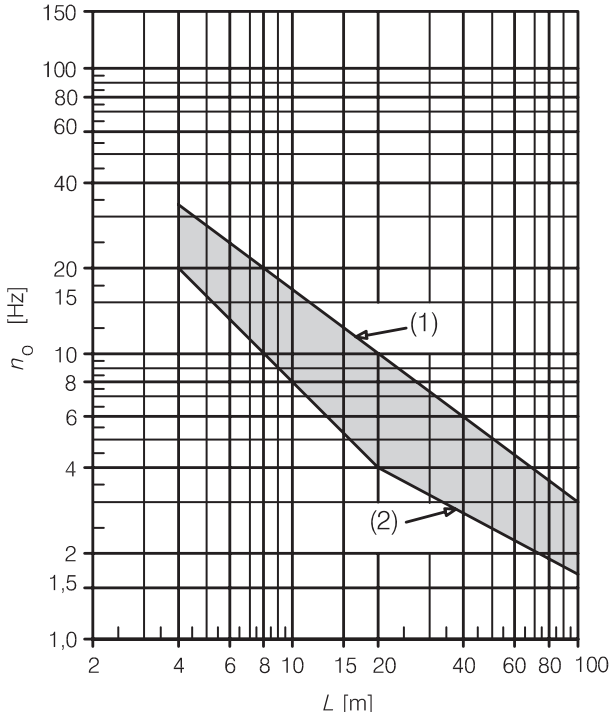

Figure 2.7.: Limits of bridge natural frequency n_0 as a function of L — Figure 6.10 from ÖNORM EN 1991-2 [43]

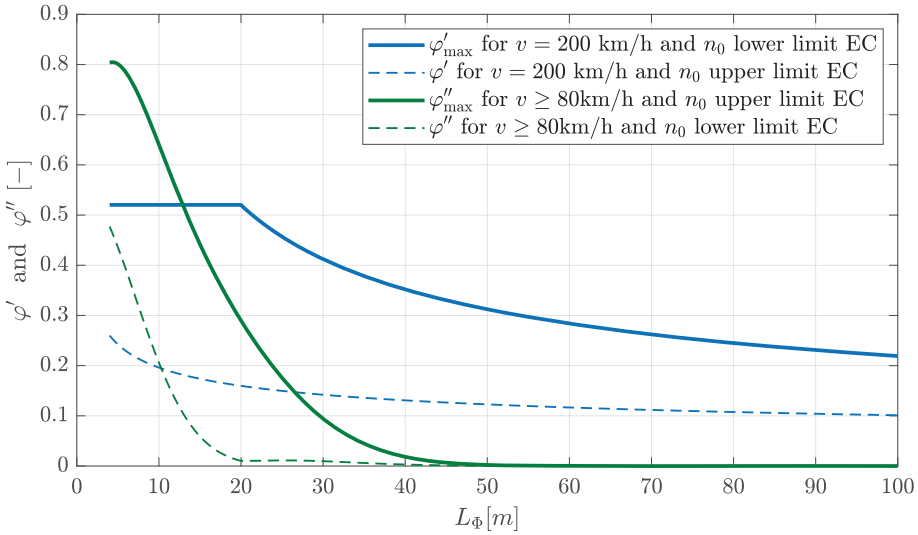

Figure 2.8.: Dynamic factors φ' and φ'' plotted versus determinant length L_Φ — according to the ÖNORM EN 1991-2, Annex C [43]

Furthermore, the ÖNORM EN 1991-2 [43] provides in Annex D, especially for the fatigue assessment, simplified forms of the before discussed dynamic factors φ' and φ''. In order to take account of the average effect over the assumed 100 years of design life, the dynamic enhancement for real trains is reduced to ([43] D.1):

$$(1+\varphi)_D = 1 + 0.5\ (\varphi'_{\mathrm{D}} + 0.5\ \varphi''_{\mathrm{D}}) \tag{2.12}$$

The following Equation (2.13) and (2.14) are simplifications of Equations (2.4) and (2.7) and valid for maximum permitted vehicle speeds up to 200 km/h:

$$\varphi'_{\mathrm{D}} = \frac{K}{(1 - K + K^4)} \tag{2.13}$$

$$\text{with:} \quad K = \frac{v}{160} \qquad \text{for } L_\Phi \leq 20m$$

$$K = \frac{v}{47,16\ L_\Phi^{0.408}} \qquad \text{for } L_\Phi > 20m$$

$$\varphi''_{\mathrm{D}} = \frac{1}{100}\left[56e^{-(\frac{L_\Phi}{10})^2}\right] \tag{2.14}$$

Equation (2.13) for φ'_{D} results, if the lower boundaries for n_0 — see Equations (2.10) and (2.11) — are inserted into Equation (2.6). Furthermore, Equation (2.14) for φ''_{D} results, if the lower boundaries for n_0 according to Equation (2.10) are inserted into Equation (2.7).

In Figure 2.9 the dynamic factors φ'_{D} and φ''_{D} according to Annex D of ÖNORM EN 1991-2 [43] are compared to φ' and φ'' of Annex C. Hence, φ'_{D} represents the maximum possible value of φ'_{max}, whereas φ''_{D} describes more a lower bound value of φ''.

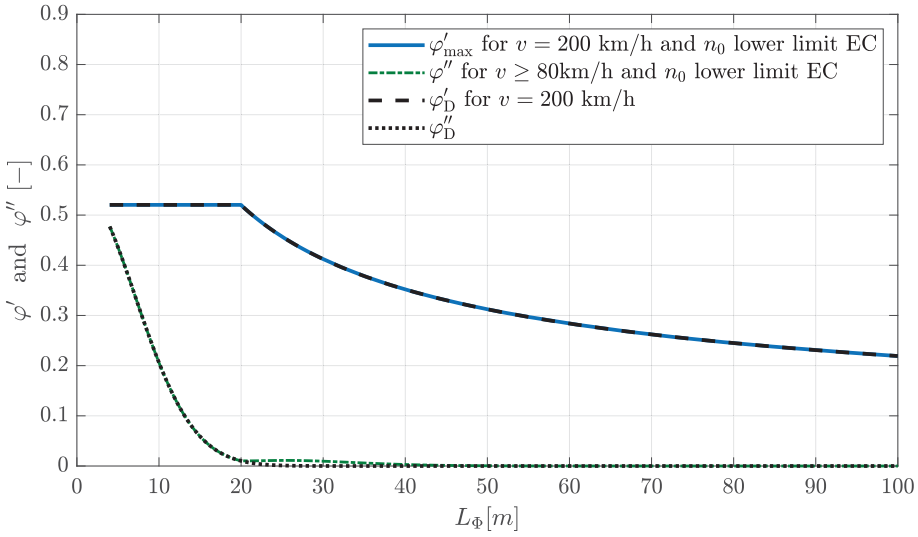

Figure 2.9.: Dynamic factors φ' & φ'' and φ'_{D} & φ''_{D} plotted versus determinant length L_Φ — according to the ÖNORM EN 1991-2, Annex C and D [43]

'Dynamic' factor Φ for load models LM71, SW/0 and SW/2

After establishing the dynamic factors $(1+\varphi)$, the task force 7/J/8 tried to merge all the different load models of the European railway administrations into one standardized concept, which finally led to the previously mentioned load model LM71. Therefore, the load model LM71 had to cover the effects caused by the real trains, at that time common, and additionally include a margin for future developments. The real trains were idealized considering the six types presented in Figure 2.10. ([59] p.18)

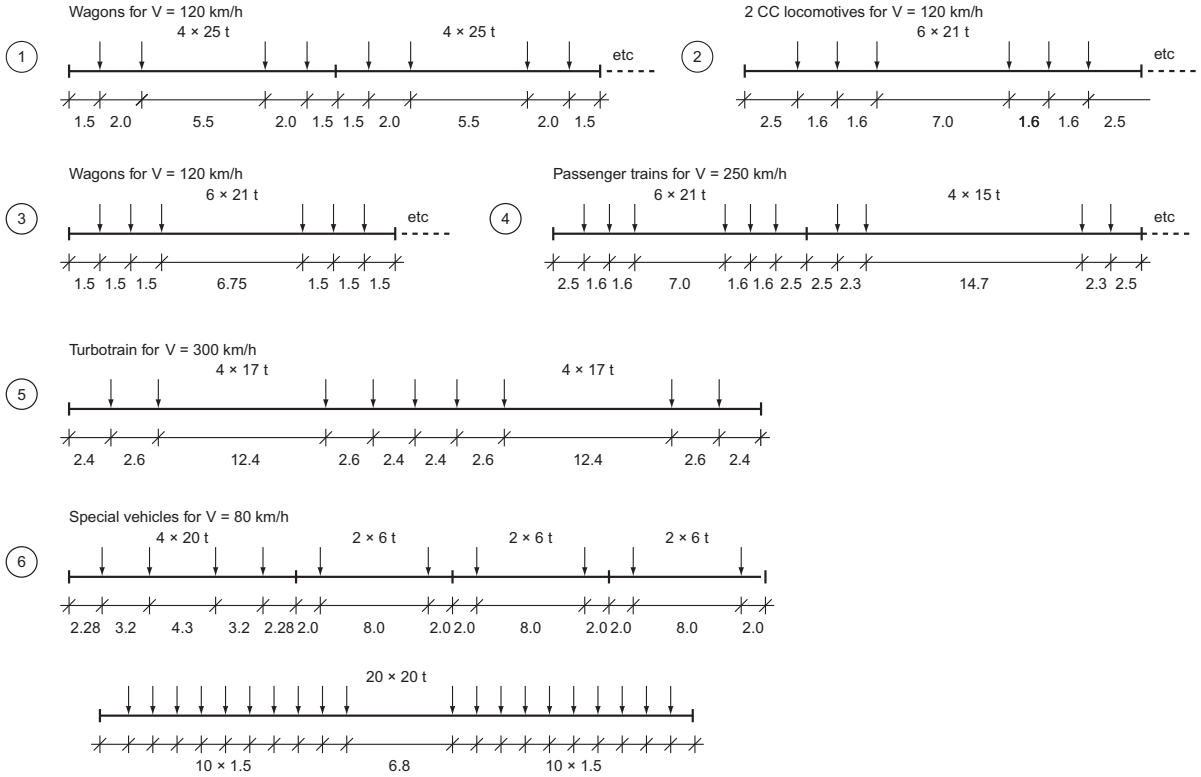

Figure 2.10.: Idealized real standard trains (types 1 to 6) — according to UIC Code 776-1 [29]

However, the load model LM71 was not directly derived from these six idealized trains, but was rather based on the line class C4, which was the highest at that time. ([59] p.18)
The 'dynamic' factor Φ was determined according the following inequality:

$$\sum_{i=1}^{6} (1+\varphi_i)\ S_{\text{ideal train},i} \leq \Phi\ S_{LM71} \tag{2.15}$$

whereas S represents an elastomechanical action effect for M (moment), Q (shear force), z (deflection), σ (normal stress), τ (shear stress), ϵ (strain) and γ (shear deformation) at a point of the structural component.
Hence, the term 'dynamic factor' for Φ is clearly misleading, as it covers, besides dynamic effects, also static loads of the six idealized trains. ([6] p.156 et sqq.) The procedure to determine the 'dynamic' factor Φ regarding the bending moment of the single-span beam is illustrated in Figure 2.11.

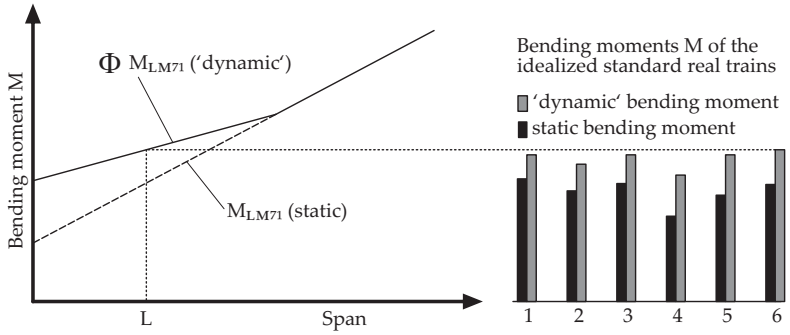

Figure 2.11.: Procedure to determine the 'dynamic' factor Φ regarding the dynamic bending moment — according to ([59] p.20) and [49]

The resulting 'dynamic' factor Φ enhances the static load effects and needs to be applied on the load models LM71, SW/0 and SW/2. It considers the dynamic magnification of stresses and vibration effects, but does not take into account resonance effects. Depending on the quality of the track maintenance, either Φ_2 or Φ_3 shall be applied — both are plotted int Figure 2.12. [43]

For carefully maintained track:

$$\Phi_2 = \frac{1.44}{\sqrt{L_\Phi} - 0.2} + 0.82 \qquad (2.16)$$

$$\text{with} \quad 1.00 \leq \Phi_2 \leq 1.67$$

For track with standard maintenance:

$$\Phi_3 = \frac{2.16}{\sqrt{L_\Phi} - 0.2} + 0.73 \qquad (2.17)$$

$$\text{with} \quad 1.00 \leq \Phi_3 \leq 2.00$$

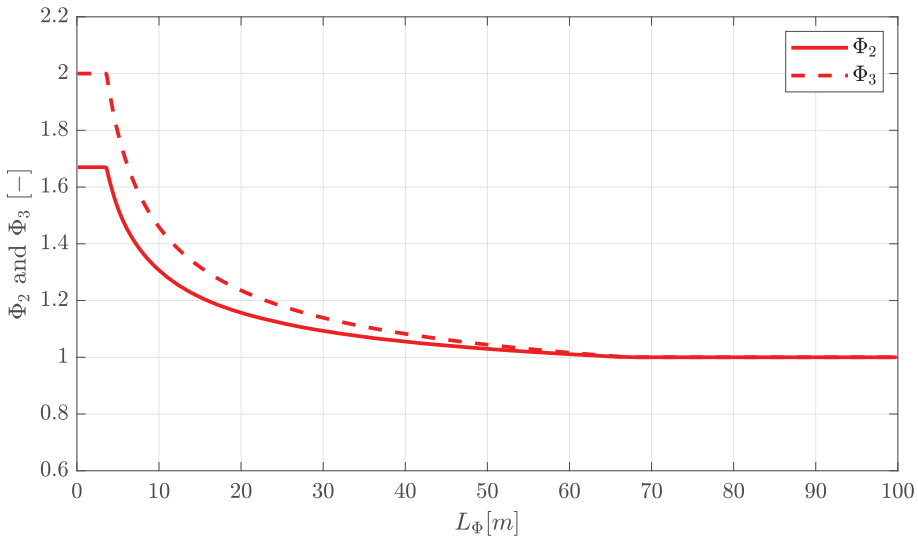

Figure 2.12.: 'Dynamic' factors Φ_2 and Φ_3 — according to the ÖNORM EN 1991-2 [43]

In Austria, generally Φ_2 shall be used. However, Φ_3 shall be used for cross girders at the beginning/ end of a structure and when designing the open deck of steel structures. ([39] 10.3.2) Hereinafter, the previously mentioned dynamic factors $(1+\varphi)$ (for real trains) according to Annex C in ÖNORM EN 1991-2 [43] and Φ (for load models) are compared to each other, whereas the quality of track maintenance is distinguished, and plotted versus the determinant length L_Φ — see Figures 2.13 and 2.14.

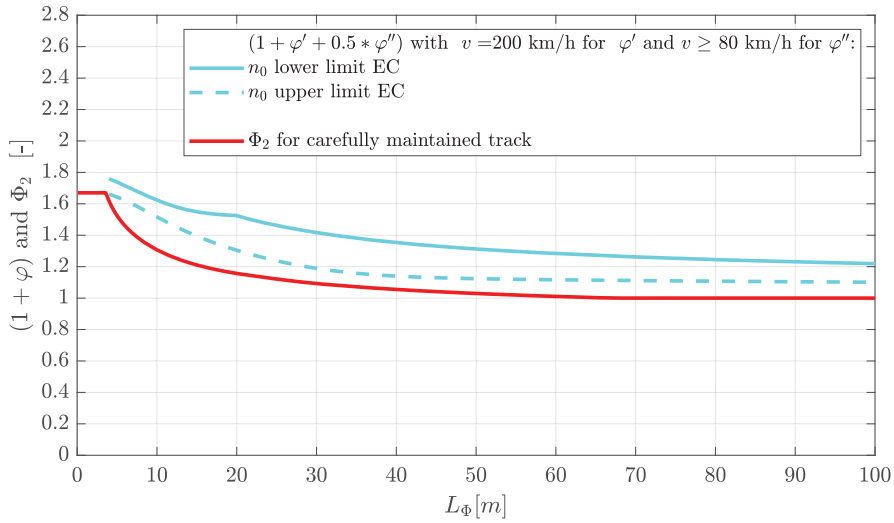

Figure 2.13.: Comparison of dynamic factors for carefully maintained track — according to the ÖNORM EN 1991-2 [43]

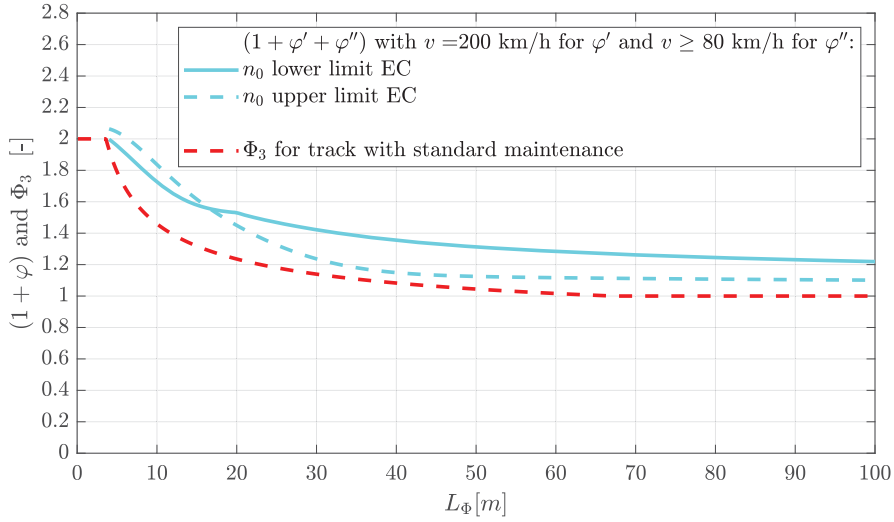

Figure 2.14.: Comparison of dynamic factors for track with standard maintenance — according to the ÖNORM EN 1991-2 [43]

Fatigue design

Fatigue is caused by repeated stress cycles $\Delta\sigma$. Especially prone to fatigue are points with high stress concentration, which arise due to discontinuities in the cross section (bolt holes, undercuts, ends of welds, etc.). If sufficient stress cycles act on these discontinuities, damage occurs, leading first to microscopic cracks, which may continue growing until the failure of the structure results. In general, notches at non-welded details are less pronounced than the ones at welded details. Additionally, stress cycles in tension are more critical regarding fatigue than stress cycles in compression. However, due to the residual stresses in welded details, it is often difficult to determine the real fatigue stresses. ([21] p.863) Therefore, the beneficial effect of stress cycles in compression must be neglected.
For these metal physical complicated damage processes, only phenomenological concepts are relevant for the engineering practice. Hence, the nominal stress concept, the structural stress concept, the notch stress concept or fracture mechanics might be applied. The first three ones also consider the phase of crack initiation, whereas fracture mechanics already requires an existing crack and therefore only covers the crack propagation phase. ([21] p.864) In the case of steel bridge structures, usually the nominal stress concept is applied. In this concept, the nominal elastic stresses are calculated at the expected location of a possible crack, without consideration of the local stress concentration effects. ([21] p.864 et seqq.) The latter are therefore considered in the so called S-N curves, which represent the fatigue strength.
These S-N curves are the results of intense experimental testing programs, performed for various details — e.g. see Figure 2.15 — in the 1970s and 1980s and can be described by the following equation, representing the region above the constant amplitude fatigue limit $\Delta\sigma_D$ — see Figure 2.16: ([21] p.871)

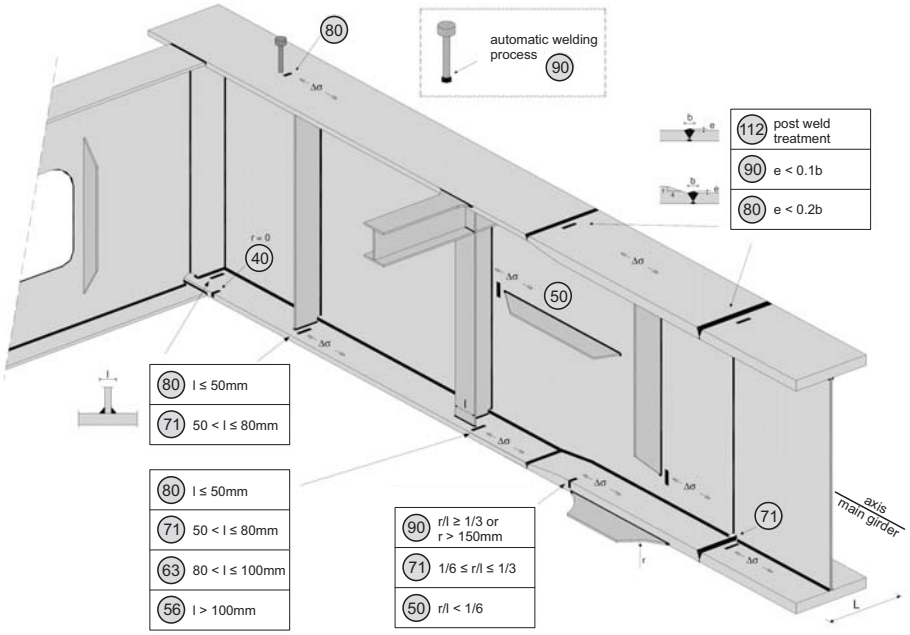

Figure 2.15.: Overview of detail categories — from [58], based on ÖNORM EN 1993-1-9 [45]

$$N_i = N_C \left(\frac{\Delta\sigma_C}{\Delta\sigma_i} \right)^m \tag{2.18}$$
$$\text{with:} \qquad N_C = 2\ 10^6$$

As the tests for the S-N curves were conducted using constant amplitude stress ranges, they are theoretically only valid for such as well. ([21] p.865) However, most stress range spectra in reality do not have a constant amplitude. The crossing of different trains produce various different stress cycles with different stress ranges. The stress histories are evaluated using cycling counting methods, such as the *Rainflow* or the *Reservoir* method and provide the stress ranges $\Delta\sigma_i$, which occur n_i times, finally leading to the stress range spectrum, as illustrated in Figure 2.16.
Subsequently, the *Palmgren-Miner linear damage hypothesis (Miner's rule)* is applied — see Figure 2.16 — to calculate the fatigue damage D:

$$D = \sum_i D_i = \sum_i \frac{n_i}{N_i} \tag{2.19}$$

Note that stress ranges $\Delta\sigma_i$ below the constant amplitude fatigue limit $\Delta\sigma_D$ (at $N_D = 2\ 10^6$) do not produce any damage ($N_3 = \infty$ in Figure 2.16). This leads to unsafe results. Therefore, a modification for stress cycles $\Delta\sigma_i < \Delta\sigma_D$ is necessary — see Figure 2.17. However, if the calculated fatigue damage D exceeds 1.0, the fatigue design check is not fulfilled, consequently if $D \leq 1.0$ the fatigue design check is fulfilled. Another option to perform the design check from above is to transform the stress range spectrum into an equivalent constant amplitude stress range related to two million cycles $\Delta\sigma_{E,2}$. ([21] p.866 et seqq.) Therefore, the Equation (2.18) of the S-N curve is substituted into *Miner's rule* of Equation (2.19)

$$D = \sum_i \frac{n_i}{N_i} = \sum_i \frac{n_i\ \Delta\sigma_i^m}{N_C\ \Delta\sigma_C^m} \tag{2.20}$$

The damage D of Equation (2.20) is set equal to the damage due to the equivalent constant amplitude stress range related to two million cycles $\Delta\sigma_{E,2}$

$$D = \frac{\Delta\sigma_{E,2}^m}{\Delta\sigma_C^m} \tag{2.21}$$

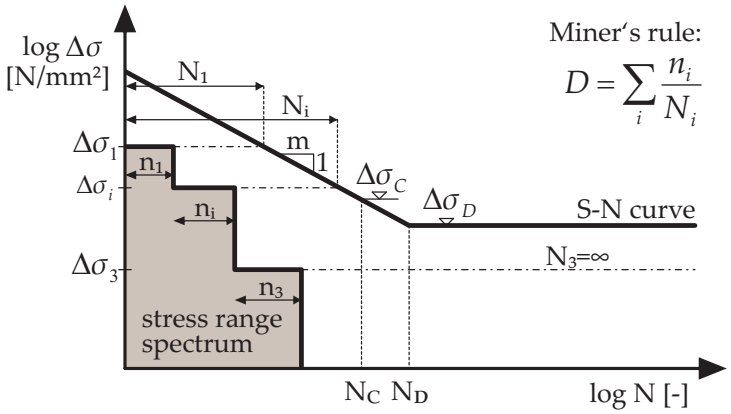

Figure 2.16.: S-N curve and stress range spectrum, based on ÖNORM EN 1993-1-9 [45]

which leads to

$$D = \frac{\Delta\sigma_{E,2}^m}{\Delta\sigma_C^m} = \sum_i \frac{n_i \, \Delta\sigma_i^m}{N_C \, \Delta\sigma_C^m} \tag{2.22}$$

and, as the detail category $\Delta\sigma_C$ is defined for two million cycles ($N_C = 2\ 10^6$), $\Delta\sigma_{E,2}$ becomes

$$\Delta\sigma_{E,2} = \sqrt[m]{\frac{\sum_i \, n_i \, \Delta\sigma_i^m}{2\ 10^6}} \tag{2.23}$$

Consequently, as the equivalent constant amplitude stress rang $\Delta\sigma_{E,2}$ and the detail category $\Delta\sigma_C$ are defined for two million cycles, the fatigue design check may be written, considering partial safety factors, as follows:

$$\gamma_{Ff} \, \Delta\sigma_{E,2} \leq \frac{\Delta\sigma_C}{\gamma_{Mf}} \tag{2.24}$$

In engineering practice, $\Delta\sigma_{E,2}$ is obtained in a simplified way by ([21] p.867)

- defining a load model to calculate a reference stress range $\Delta\sigma_p$ and
- adjusting the reference stress range $\Delta\sigma_p$ using damage equivalent factors λ_i

which are calibrated on the before mentioned damage calculations.

For example, for the single span steel and composite railway bridges, the load model LM71 was selected. The damage equivalent factor λ_1, according to the EC mix in the ÖNORM EN 1993-2, Table 9.3 [43], was consequently calibrated on the damage produced by the train types 1 to 8, under consideration of the traffic mix in Table D.1, according to the ÖNORM EN 1991-2, Annex D [43].

The S-N curve presented in Figure 2.16 is valid for undamaged details which are loaded by constant amplitude stress ranges. The fact that a damaged sample has a lower constant amplitude fatigue limit $\Delta\sigma_D$ is considered in the ÖNORM EN 1991-2 [43] by introducing a bilinear S-N curve with a cut-off limit $\Delta\sigma_L$, according to [22]. ([21] p.875) Figure 2.17 illustrates the S-N curves for various fatigue details, which have all the same shape, but different levels regarding the detail category $\Delta\sigma_C$. Consequently, stress cycles $\Delta\sigma_i < \Delta\sigma_D$ lead now to a reduced fatigue damage, whereas the fatigue damage due to stress cycles $\Delta\sigma_i < \Delta\sigma_L$ can be neglected.

In the following sections the general fatigue design of steel railway bridges, according to the Eurocode and the situation in Austria, is described. In general, there are the two above mentioned verification formats available, in order to perform the fatigue design check. ([45] A.6) The first one — usually applied — is based on stress range, and uses the equivalent constant amplitude stress range related to two million cycles $\Delta\sigma_{E,2}$, which is compared to the detail category $\Delta\sigma_C$, considering partial safety factors:

$$\gamma_{Ff} \, \Delta\sigma_{E,2} \leq \frac{\Delta\sigma_C}{\gamma_{Mf}} \tag{2.25}$$

whereas the second one is based on damage accumulation, using *Miner's rule* for a certain S-N curve (defined by the detail category $\Delta\sigma_C$ and divided by the partial safety factor γ_{Mf}) in order

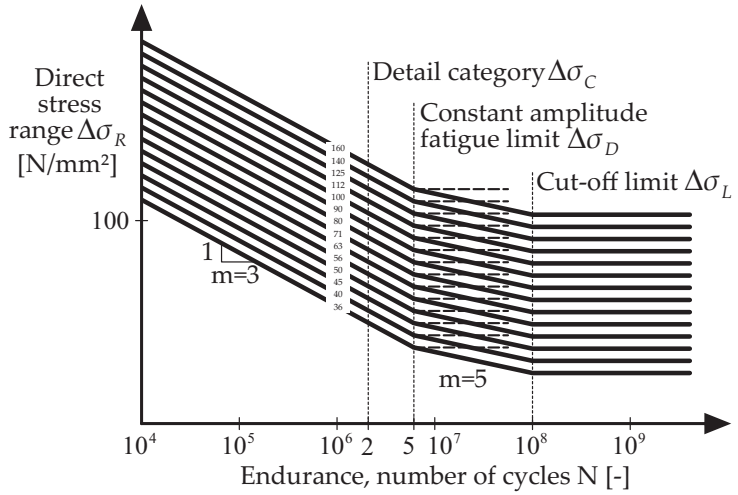

Figure 2.17.: S-N curves for direct stress ranges according to the ÖNORM EN 1993-1-9 [45]

to determine the damage D_d of a certain stress range spectrum (stress ranges $\Delta\sigma_i$ multiplied by γ_{Ff}):

$$D_d = \sum_i \frac{n_i}{N_i} \leq 1.0 \tag{2.26}$$

However, the fatigue load must be multiplied by γ_{Ff}, which is recommended to be set to 1.0 ([43] 9.3 (1)), and the fatigue strength divided by γ_{Mf}. Regarding the latter partial factor, the ÖNORM EN 1993-1-9 [45] distinguishes two design concepts. The *damage tolerance* concept is recommended for the fatigue check of steel components, which have a regular maintenance/ inspection program. On the other hand, the *safe life* concept is used for steel components, which can not be inspected (e.g. shear studs) or in case no inspection is planned within the design life. Depending on the consequence of failure (*low* for redundancy components/ *high* if severe damage or collapse results), the partial safety factors according to Table 2.1 may be applied. ([24] p.287)

Assessment concept	Consequence of failure	
	Low consequence	High consequence
Damage tolerance	1.00	1.15
Safe life	1.15	1.35

Table 2.1.: Values for partial factors γ_{Mf} for fatigue strength — according to the ÖNORM EN 1993-1-9, Table 3.1 [45]

Fatigue verification based on load model LM71 and stress range

The fatigue design check, based on stress range, using the load model LM71, is represented by the following Equation (2.27):

$$\gamma_{Ff} \underbrace{\lambda\ \Phi\ \Delta\sigma_{LM71}}_{\Delta\sigma_{E,2}} \leq \frac{\Delta\sigma_C}{\gamma_{Mf}} \tag{2.27}$$

First, due to the crossing of the load model LM71, a reference stress range $\Delta\sigma_{LM71}$ times the 'dynamic' factor Φ is calculated. Subsequently, this expression is adjusted, using the damage

equivalent factor λ, which yields to the equivalent constant amplitude stress range related to two million cycles $\Delta\sigma_{E,2}$. Finally, the latter is compared to the detail category $\Delta\sigma_C$, considering the partial factors γ_{Ff} and γ_{Mf}.
The classification factor α is set to 1.0 for the FLS design check. ([39] 10.2.2) Furthermore, for structures with multiple tracks, the load model LM71 shall be applied to a maximum of two tracks in the most unfavourable position. ([43] 6.9 (5)) The load model LM71 is presented in Figure 2.1 and the 'dynamic' factor Φ_2 is calculated according to Equation (2.16). The damage equivalent factor λ consists of four parts,

$$\lambda = \lambda_1 \, \lambda_2 \, \lambda_3 \, \lambda_4 \leq \lambda_{max} \tag{2.28}$$

which are described in more detail as follows:

- λ_1 — Accounts for the structural member type and for the chosen service traffic (e.g EC mix, rail traffic with 25 t axles). Members with a short influence line get more stress cycles than members with long influence lines. Consequently, λ_1 is a function of the influence line, which depends on the type of internal force and, as already mentioned, on the type of member (e.g. single span beam, continuous spans in midspan section, etc.). ([21] p.892)

L [m]	λ_1	L [m]	λ_1	L [m]	λ_1	L [m]	λ_1	L [m]	λ_1
0.5	1.60	3.5	1.17	8.0	0.92	20.0	0.67	50.0	0.63
1.0	1.60	4.0	1.07	9.0	0.88	25.0	0.66	60.0	0.63
1.5	1.60	4.5	1.02	10.0	0.85	30.0	0.65	70.0	0.62
2.0	1.46	5.0	1.03	12.5	0.82	35.0	0.64	80.0	0.61
2.5	1.38	6.0	1.03	15.0	0.76	40.0	0.64	90.0	0.61
3.0	1.35	7.0	0.97	17.5	0.70	45.0	0.64	100.0	0.60

Table 2.2.: Factor λ_1 for standard rail traffic (EC mix) — according to the ÖNORM EN 1993-2 Table 9.3 [46]

- λ_2 — Accounts for the annual traffic volume and, in case of steel bridges, is defined by $t/track/year$ with a reference value of 25 10^6 $t/track/year$. Due to the change of the annual traffic volume from 25 10^6 t to the value of x, only the number of cycles change, hence with an average slope of the fatigue strength curve m = 5[1], yields: ([21] p.896)

$$\lambda_2 = \sqrt[5]{\frac{x \; 10^6 t/track/year}{25 \; 10^6 t/track/year}} \tag{2.29}$$

- λ_3 — Accounts for the planned design life of the member. Here, Equation (2.29) results as well, but with a reference value of 100 years in the denominator and the planned years in service in the numerator.
- λ_4 — Accounts for the loading of more than one track. The bridge is statically calculated considering the load model LM71 on two tracks in the most unfavourable positions. Therefore, the factor λ_4 considers the "positive" effect of a second track, as the probability of two trains crossing at the same time on the bridge is very low. The given values of λ_4 in the ÖNORM EN 1991-2 [43] assume that 12% (very high value) of the total traffic crosses the bridges while there is traffic on the other track. However, if the percentage of traffic

[1]The slope m = 5 was chosen because the majority of the stress cycles $\Delta\sigma_i$ is usually smaller than $\Delta\sigma_D$.

crossing at the same time on different tracks is known better, the following Equation might be used: ([21] p.897)

$$\lambda_4 = \sqrt[5]{n + [1-n][a^5 + (1-a)^5]} \tag{2.30}$$

with: $a = \frac{\Delta\sigma_1}{\Delta\sigma_{1+2}}$

n ... percentage of traffic on both tracks simultaneously (e.g. for 15 % $\rightarrow n = 0.15$)

$\Delta\sigma_1$ ... stress range due to load model LM71 on one track

$\Delta\sigma_{1+2}$ ... stress range due to load model LM71 on any two tracks

- λ_{max} — With the equivalent constant fatigue limit $\Delta\sigma_D$, one can determine the maximum possible damage equivalent factor $\lambda_{max} = 1.4$ for steel railway bridges. ([21] p.868)

Fatigue verification based on service trains type 1 to 8 and damage accumulation

The second procedure is to calculate the static train crossings of real trains and determine the internal force/ stress history diagrams. Subsequently, one obtains the stress ranges per train crossing, using cycle counting methods, such as the *Rainflow* or the *Reservoir* method. According to a certain traffic mix, which indicates the number of crossings per train type and year, one can sum up these stress ranges to a stress range spectrum for the whole service life (in general 100 years). Furthermore, the S-N curve defines the fatigue resistance for each detail, which may be divided by the partial safety factor γ_{Mf}. Multiplying the previously determined stress range spectrum by the partial safety factor γ_{Ff} and evaluating it on the S-N curve, using *Miner's rule* including the reduced damage effect for stress cycles $\Delta\sigma_i < \Delta\sigma_D$ based on Figure 2.17, leads to a certain damage D_d. As mentioned before, if the value of D_d is below or equal to 1.0 the fatigue design check is fulfilled, otherwise not. Table 2.3 and Figure 2.18 illustrate the train types and the traffic mix for the standard rail traffic (EC mix) as in the ÖNORM EN 1991-2 [43], which lead for single span steel and composite bridges to the same results[1] as the fatigue design check, based on stress range due to load model LM71 and using λ_1 factor according to the standard rail traffic (EC mix) in Table 2.3.

Train type	Number of trains/ day	Mass of train [t]	Traffic volume [10^6 t/ year]
1	12	663	2.90
2	12	530	2.32
3	5	940	1.72
4	5	510	0.93
5	7	2160	5.52
6	12	1431	6.27
7	8	1035	3.02
8	6	1035	2.27
	67		24.95

Table 2.3.: Standard rail traffic (EC mix) with axles $\leq$ 22.5 t — according to the ÖNORM EN 1991-2 Table D.1 [43] — with 1 year = 365 days

[1] Only if the utilisation factor of the fatigue verification is equal to 1.0.

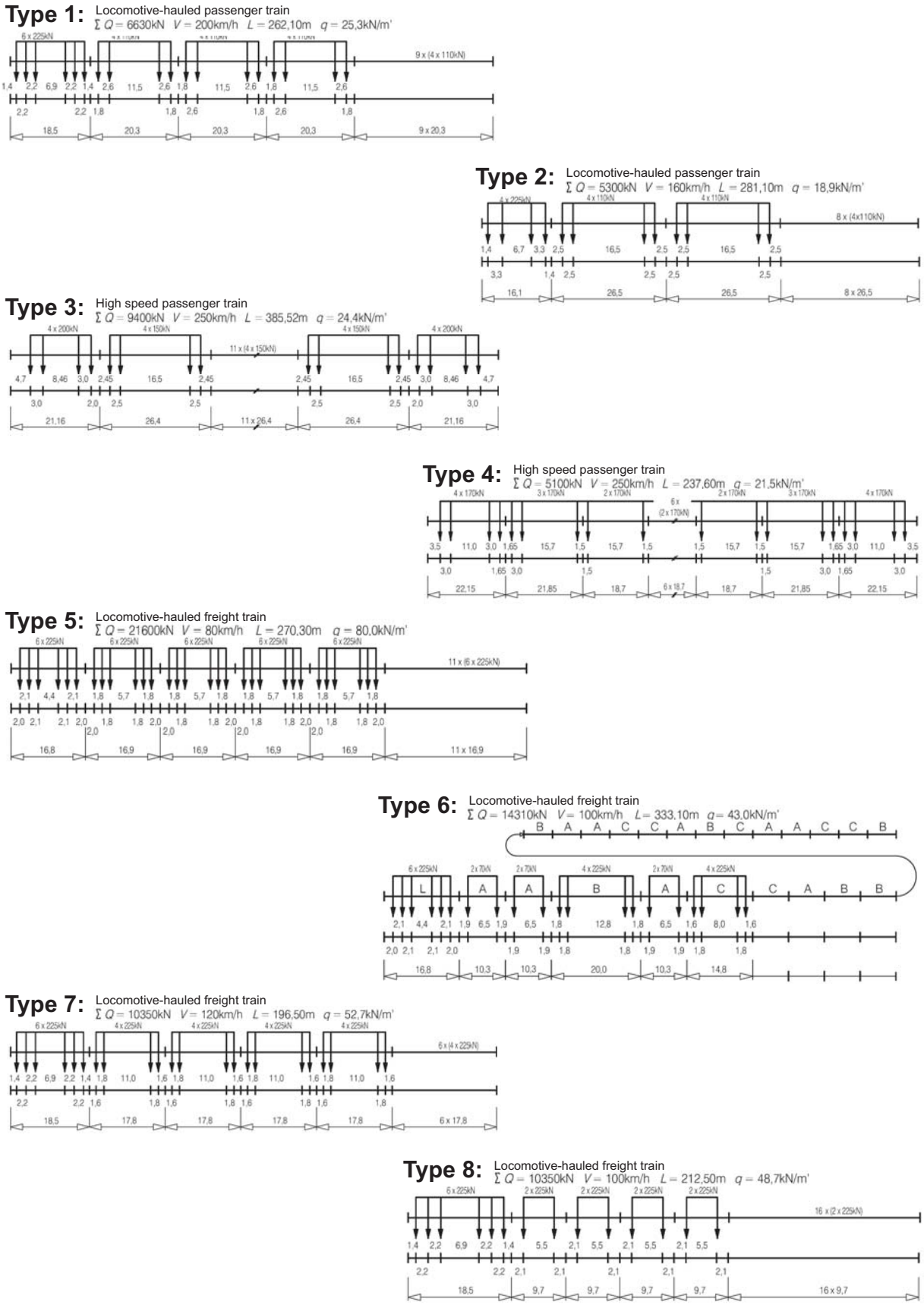

Figure 2.18.: Standard traffic mix Type 1 to 8 — according to the ÖNORM EN 1991-2 [43]

2.1.2. Dynamic analysis

The introduction of high-speed trains from Paris-Lyon led to resonance problems on some (mostly short span) structures. Bridge deck accelerations up to 9.81 m/s^2 caused rapid deterioration of the track quality and even some damages to the structure. [66] Therefore, in 1996 the ERRI expert committee D214 was installed in order to investigate the effects on railway bridges for train speeds exceeding 200 km/h. ([59] p.21) The expert group D214 mentioned and criticised the very limited background information leading to the development of the dynamic load factors Φ, φ' and φ''. However, the available information showed that the effects due to the crossing of repeated groups of axles, hence resonance, was underestimated. The probable reasons might be: ([13] p.12)

- High values for structural damping were used in comparison to lower damping values found in more modern structures.
- The considered high-speed trains were much shorter than modern high-speed trains
- Possibly, only the dynamic increment of deflection and bending, but not the effect of the maximum bridge deck acceleration, were considered.

The results of the final report D214-RP9 confirmed that the quasistatic concept with the load model LM71 and the 'dynamic' factors Φ are not sufficient in order to guarantee the safety of structures in case of resonance. [13] Among other things, the expert committee D214 identified safety related design criteria for bridges subjected to high-speed traffic, suggested methods that allow to predict the dynamic load effects, provided values for key parameters (bridge stiffness and structural damping) and proposed a flow chart to determine whether a dynamic calculation is necessary. These findings were embedded in the ÖNORM EN 1991-2 [43] and will be described, considering the national annex for Austria, as follows.

Requirement of additional dynamic analysis

As mentioned above, the ÖNORM EN 1991-2 [43] provides a flow chart, which determines, together with the upper and lower limits for n_0 according to Figure 2.7 and Equations (2.9), (2.10) and (2.11) whether a dynamic analysis is necessary or not — see Figure 2.19. Consequently, if the first bending frequency n_0 is within the limits of Figure 2.7 and an additional of the following requirements is met, no dynamic calculation is necessary: ([59] p.21)

- maximum line speed at site $v \leq 200$ km/h
- the structure is a single-span bridge with only longitudinal line beams and a span length L $\geq$ 40m

However, in Austria the use of the flow chart in Figure 2.19 is not allowed. The national annex ÖNORM B 1991-2 ([39] 10.3.1) obligates to use the ÖBB guideline [37]. The latter states in section 3.1 under which circumstances a dynamic calculation is not necessary:

- If the maximum nominal speed or the maximum line speed at site is less than 120 km/h.
- If the maximum nominal speed or the maximum line speed at site exceeds 120 km/h:

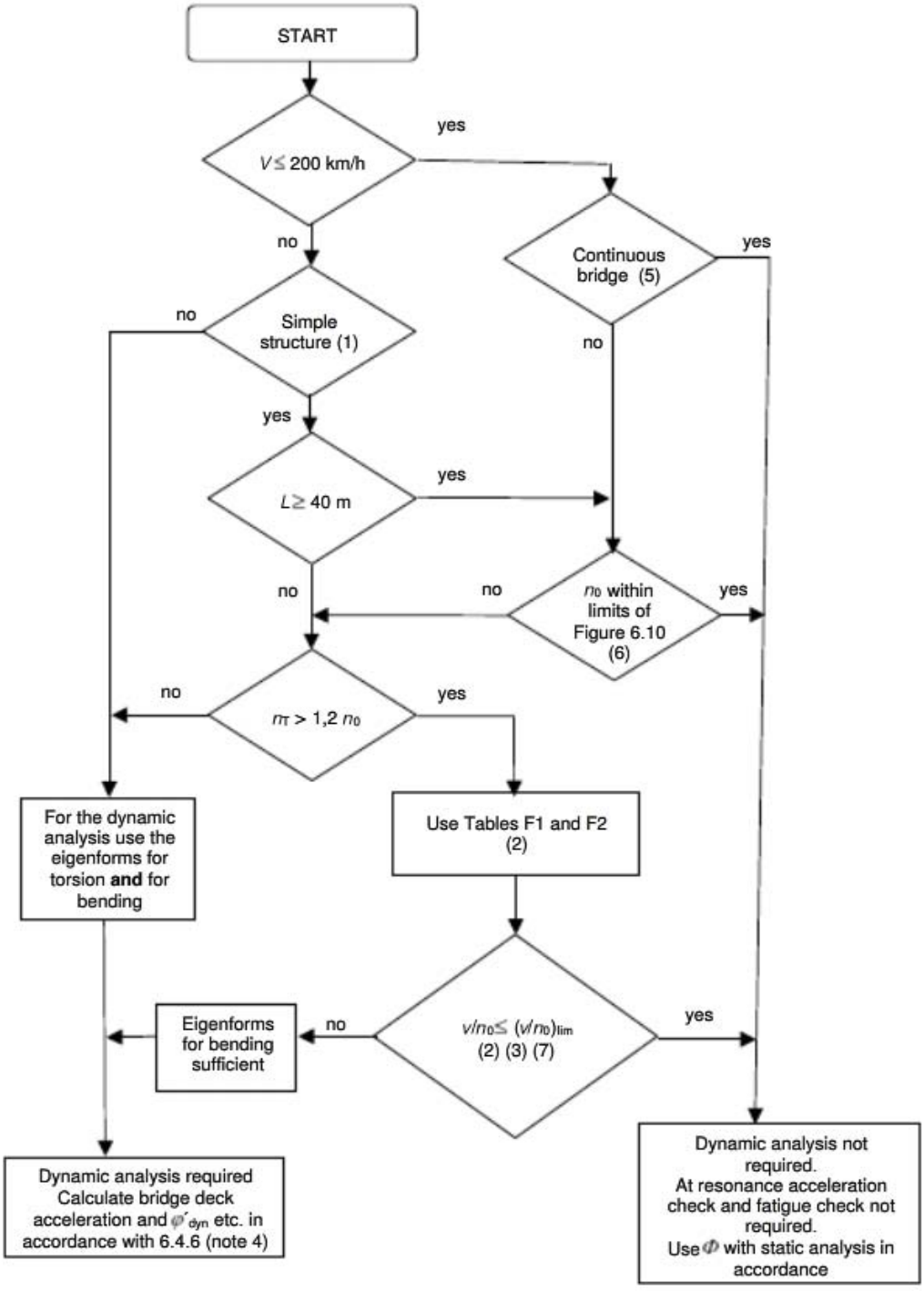

Figure 2.19.: Flow chart for determining whether a dynamic analysis is required — according to the ÖNORM EN 1991-2 [43]

  - According to the ÖBB guideline [37], for the following single-track structures, parameter studies[1] were performed and summarized in [36]. If the new structure fulfils a specific span length cirteria or a certain slenderness requirement (λ = span length L / construction height d) for a given maximum train speed limit (160 to 250 km/h), consequently no dynamic calculation is necessary:
    * platelike structures for span lengths L = 5.0 to 15m
    * framelike structures for span lengths L = 2.5 to 10m
    * filler beam structures for span lengths L = 5.0 to 29.5m
  - For covered structures with a minimum distance track to structure of 1.5 m.
  - For small objects with a span length L $\leq$ 2.0 m, which additionally fulfil a length dependent construction height d criteria.
  - For new structures, which may be compared to existing reference structures. The latter needs to fulfil all criteria according to the ÖBB guideline [37], whereas dynamic measurements need to exist as well. All parameters of the new structure, which might influence the dynamic behaviour, need to be identical to or more favourable than the reference structure.

In all other cases, which do not fulfil the requirements mentioned above, a dynamic calculation is necessary. Therefore, in the next chapter a short overview of the requirements for a dynamic calculation, according to the situation in Austria [37], is presented.

Requirements for additional dynamic analysis

- *Loading and load combinations:* The dynamic analysis shall be performed using, on the one hand, the characteristic values of real trains travelling faster than 200 km/h, but, on the other, the load model HSLM. The latter consists of two load models, the load model HSLM-A and the HSLM-B. As the load model HSLM-B is only applied on very short (L<7m) simply supported spans, the load model HSLM-A is more important in engineering practice. The load model HSLM-A consists of 10 different trains and is illustrated in Figure 2.20. Additionally, limits of validity of the load model HSLM, regarding axle distances, axle loads, maximum train lengths and train masses, are stated in Annex E of the ÖNORM EN 1991-2 [43]. Hence, if a real train complies with these limits of validity, the effects due to the load model HSLM supposingly exceed the ones of the real train. Studies in [57], [62] and [63] have shown that this is, especially for conventional and regular trains regarding simple span structures, not the case. However, in the ÖBB guideline [37] is stated to consider, additionally to the load model HSLM, the following real trains:

  - Types 1 to 12 according to the ÖNORM EN 1991-2, Annex D [43]
  - Five Railjet trains and four other real trains according to the ÖNORM B 1991-2 [39]
  - Two ICE-high-speed trains (ICE BR 401 and ICE-T1 411)
  - After consultation with the railway administration (ÖBB), other additional real trains may have to be considered.

  The load combination of vertical traffic loads, in case of multiple tracks, is regulated in the ÖBB guideline [37] as follows. If the dynamic calculation is simply compared to the

[1] The parameter studies are valid for certain traffic mixes.

quasistatic calculation, only one track (the most critical one) needs to be loaded. If the total effects of the traffic loads need to be calculated, the dynamic simulation shall be performed on the most critical track and the other tracks shall be loaded with the load model LM71, according to the ÖNORM EN 1991-2 6.8.1 (4), whereas the load model HSLM and the real trains shall not be reduced to 75%. ([37] 5.7.2) If the vertical bridge deck acceleration is determined, only one track shall be loaded with the load model HSLM and the real trains. ([37] 6.3.2) However, horizontal forces (centrifugal forces and nosing forces) only need to be applied in case the total effects due to traffic loads, hence the dynamic effects exceed the static effects, need to be calculated. ([37] 5.7.3)

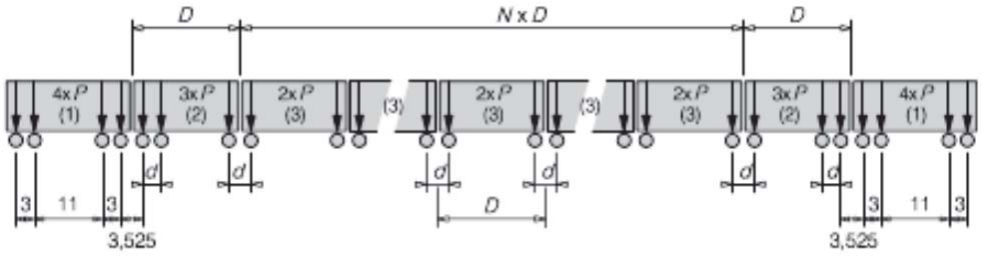

Key
(1) Power car (leading and trailing power cars identical)
(2) End coach (leading and trailing end coaches identical)
(3) Intermediate coach

Universal Train	Number of intermediate coaches N	Coach length D [m]	Bogie axle spacing d [m]	Point force P [kN]
A1	18	18	2,0	170
A2	17	19	3,5	200
A3	16	20	2,0	180
A4	15	21	3,0	190
A5	14	22	2,0	170
A6	13	23	2,0	180
A7	13	24	2,0	190
A8	12	25	2,5	190
A9	11	26	2,0	210
A10	11	27	2,0	210

Figure 2.20.: HSLM-A — according to the ÖNORM EN 1991-2 [43]

- *Speeds to be considered:* in general, the operator of the high-speed line (ÖBB) specifies the maximum nominal speed. Furthermore, a speed range and its upper and lower limits need to be defined: ([37] 4.2.1)
  - upper limit
    - 1.2 times the maximum nominal speed
    - 1.2 times the maximum line speed at site, only in special cases and after consulting the operator
  - lower limit
    - 0.5 times the upper limit, but less than 144 km/h
    - 0.6 times the maximum permitted vehicle speed of the slowest real train
    - speeds below 80 km/h can be neglected

For the load model HSLM the whole (above described) speed range needs to be considered, whereas for real trains the dynamic analysis needs to be performed starting from the lower limit to 1.2 times the maximum permitted vehicle speed of the real train. Regarding the speed steps, in general, a Δv of 5 km/h is sufficient, except close to the resonant speed. In this case, speed steps Δv of 2 km/h are necessary. ([37] 4.2.2)

- *Bridge parameters:*
  - Stiffness of the bridge: the ÖNORM EN 1991-2 ([43] 6.5.6.3.3) suggests to use a lower bound estimation of the stiffness, in order to avoid an overestimation of the resonance speed. Consequently, only members contributing through force-fitting connections (e.g. composite structures) shall be considered with respect to the system stiffness. ([37] 5.3)
  - Mass of the bridge: equally to the stiffness, the mass of the bridge has a big influence on the dynamic behaviour of the structure. Therefore, in the ÖBB guideline [37], a differentiation between the mass of the structure itself and the mass of the train is made. First, the mass of the structure shall be applied as close to reality as possible (e.g. acting on secondary members and not in a simplified way directly applied on main girders), whereas only one variation of mass regarding the ballast track needs to be considered (in contradiction to the ÖNORM EN 1991-2 [43], where upper and lower bound variations of density and thickness need to be considered). Second, the mass of the train shall be considered for big (smallest single span L is at least 20 m), but not for small structures (biggest single span L is $\leq$ 7 m and the lowest bending frequency is above 1.5 Hz). For medium sized structures (between big and small structures) two calculations are necessary, one with and one without the mass of the train. As all trains have different masses, which would lead to a vast computational effort, 20 kN/m per track shall be considered for all load models and real trains and added to the bridge mass. ([37] 5.6)
  - Structural damping: in general, the rules according to the ÖNORM EN 1991-2 [43] need to be followed. Hence, the damping ratios ζ, according to Table 2.4, are obligatory unless no other damping ratios due to measurements, performed at the particular structure of interest, are available. In case the traffic load is modelled using the moving load model, the beneficial vehicle/bridge interaction may be considered for span lengths up to 30m, with an increase of the damping ratio $\Delta\zeta$ according to Figure 2.21. Furthermore, the ÖBB guideline [37] covers modal and Rayleigh-like damping — see section 3.4 — and requires the factors α and β to be based on the frequencies of the first vertical bending mode and a bending mode of second order, as these usually contribute substantially to the total response.

Bridge type	ζ lower limit of percentage of critical damping [%]	
	Span L $<$ 20 m	Span L $\geq$ 20 m
Steel and composite	$\zeta = 0.5 + 0.125(20 - L)$	$\zeta = 0.5$
Prestressed concrete	$\zeta = 1.0 + 0.07(20 - L)$	$\zeta = 1.0$
Filler beam and reinforced concrete	$\zeta = 1.5 + 0.07(20 - L)$	$\zeta = 1.5$

Table 2.4.: Damping ratios ζ [%] to be assumed for design purposes — according to the ÖNORM EN 1991-2, Table 6.6 [43]

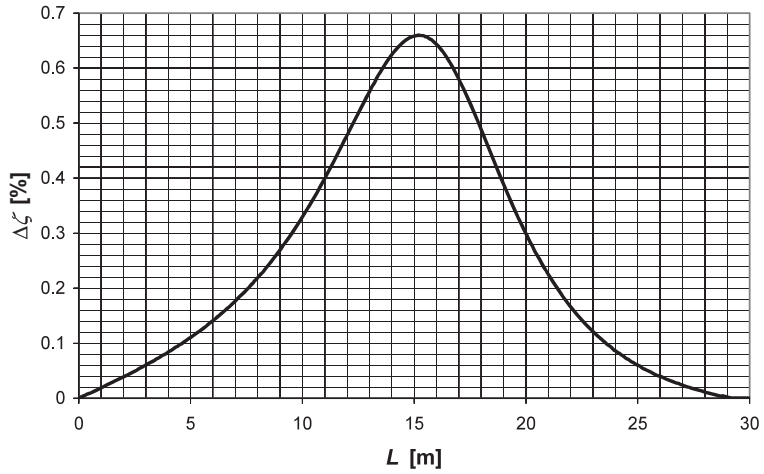

Figure 2.21.: Additional damping $\Delta\zeta$ [%] as a function of the span length L [m] — according to the ÖNORM EN 1991-2 [43] Figure 6.15

- *Modelling the excitation and the dynamic behaviour of the structure:* in order to guarantee a certain level of quality, rules for the modelling of bridge systems using frame or FEM analysis programs are provided. Additionally, the choices of calculation methods — modal analysis, direct stiffness approach — are presented and discussed. Regarding the modal analysis, mode shapes and related frequencies up to the greater of
  - 30 Hz
  - 1.5 times the frequency of the fundamental mode of vibration
  - the highest frequency of all third modes of vibration

  shall be considered. ([37] 5.2.4) Furthermore, track imperfections and vehicle imperfections may be considered according to Equation (2.7), whereas, in case the upper limit of n_0 is exceeded, this Equation is still valid. In Austria, carefully maintained tracks can be assumed, hence Equation (2.3) is applied and consequently all results of the dynamic calculation are multiplied by $(1 + 0.5\ \varphi'')$. ([37] 6.2) The load application is realized using the moving force (axle loads represented as moving forces), whereas the distribution of the forces may be performed according to the ÖNORM EN 1991-2 [43]. ([37] 5.7)

- *Verification of limit states:* regarding the following statements, one can suppose that the deformation criteria regarding the traffic safety, according to [42], are fulfilled by the new structure for the quasistatic analysis. ([37] 6.3.1)
  - Ultimate limit state (ULS): for the ULS design, more unfavourable stresses need to be considered, due to the quasistatic concept, including Φ, and due to the dynamic calculation, regarding the relevant load models and real trains including $(1 + 0.5\ \varphi'')$. ([37] 6.3.8)
  - Servicability limit state (SLS): the passenger comfort criteria requires a dynamic vehicle-bridge-interaction analysis in order to directly calculate the resulting vertical acceleration inside the train car. These analysis need information about the masses of the train car's parts, respectively the springs and dashpots connecting them, which the load model HSLM does not provide. Therefore, a quasistatic deflection criteria

for checking the passenger comfort was introduced, which additionally may be seen as fulfilled in case the dynamic internal forces are lower than the static ones in the ULS design for the most relevant bridge members. ([37] 6.3.7)

– Traffic safety[1] (TS): the structure needs to fulfil design criteria regarding the deck twist, vertical deformation of the deck, the transverse deformation/ vibration of the deck and the longitudinal displacement of the deck. The latter two can be considered as fulfilled insofar the dynamic internal forces are lower than the static ones in the ULS design. ([37] 6.3)
  However, in practise usually the acceleration criterion will be the decisive one. ([6] p.177) In order to prevent ballast instability and guarantee a safe rail wheel contact, the vertical acceleration of the bridge deck, checked at the SLS level, shall not exceed the following design values for new bridge structures: ([37] 6.3.2)
  * 3.5 m/s^2 for ballasted track
  * 5.0 m/s^2 for direct fastened tracks

  and increased design values for existing bridge structures:
  * 6.0 m/s^2 for ballasted track
  * 8.0 m/s^2 for direct fastened tracks

  The values for new bridge structures are the result of research done by the ERRI expert group D214, according to which an adverse behaviour of the ballast track begins with deck accelerations of the order 0.7 to 0.8 g. Therefore, considering a factor of safety of two, the permitted maximum bridge deck acceleration of 3.5 m/s^2 for ballasted track results. The permitted maximum bridge deck acceleration for direct fastening decks becomes 5.0 m/s^2, again with a safety factor of two for avoiding a lift of the deck plate. ([59] p.32) These thresholds shall meet at the ballast bed area, but might be exceeded in other areas (cantilever beam, etc.). Additionally, single events leading to an exceeding of these thresholds do not consequently lead to a destabilisation of the ballasted track. Therefore, the ÖBB guideline [37] allows to consider the fifth highest acceleration value, instead of the maximum acceleration value, due to the train crossing. ([37] 6.3.2)
– Fatigue (FLS): Under certain circumstances, additional fatigue design checks are necessary, which will be discussed in detail in the following chapter.

Fatigue design

In this chapter, the general valid design rules according to the ÖNORM EN 1991-2 [43] and, afterwards, in particular for the situation in Austria, will be described.

The ÖNORM EN 1991-2 [43] names in section 6.9 the general traffic loads for fatigue. Under point (8) the following, regarding the dynamic analysis and fatigue assessment, is stated:

"6.9 Traffic loads for fatigue

[...]

[1] Some servicability limit states (SLS) for the deck need to be considered as ultimate limit states (ULS) for the track. ([7] p.34)

(8) Additional requirements for the fatigue assessment of bridges where a dynamic analysis is required in accordance with 6.4.4 when dynmaic effects are likely to be excessive are given in 6.4.6.6." ([43] p.122)

Hence, if a dynamic analysis according to section 6.4.4 in [43] (described in Chapter 2.1.2) is required, the section 6.4.6.6 in [43] needs to be considered.

"6.4.6.6 Additional verification for fatigue where dynamic analysis is required

(1)P The fatigue check of the structure shall allow for the stress range resulting from elements of the structure oscillating above and below the corresponding permanent load deflection due to:

- *additional free vibrations set up by impact effects from axle loads travelling at high speed,*
- *the magnitude of dynamic live loading effects at resonance,*
- *the additional cycles of stress caused by the dynamic loading at resonance.*

(2)P Where the frequent operating speed of a real train at a structure is near to a resonant speed the design shall allow for the additional fatigue loading due to resonance effects.

NOTE The individual project may specify the fatigue loading, e.g. details, annual tonnage and mix of real trains and associated frequent operating speeds at the site to be taken into account in the design.

(3) Where the bridge is designed for load model HSLM accordance with 6.4.6.1.1(2) the fatigue loading should be specified taking into account the best estimate of current and future traffic.

NOTE The individual project may specify the fatigue loading, e.g. details, annual tonnage and mix of real trains and associated frequent operating speeds at the site to be taken into account in the design.

(4) For structures that satisfy annex F the resonant speed may be estimated using equations 6.9 and 6.10.

(5) For the verification for fatigue a series of speeds up to the maximum nominal speed should be considered.

NOTE It is recommended that the individual project specify an increased maximum nominal speed at the site to take into account potential modifications to the infrastructure and future rolling stock." ([43] p.92)

The regulations in the ÖNORM EN 1991-2 [43] provide general information, therefore the Austrian national specifications in the ÖNORM B 1991-2 [39] state additionally:

"9.3.16 Ergänzung zu ÖNORM EN 1991-2:2012, Abschnitt 6.4.6.6(3)

Überschreiten die Jahresbruttotonnen der Züge, die mit mehr als 200 km/h verkehren, 5 Mio. Jahresbruttotonnen je Gleis, so ist ein zusätzlicher Ermüdungsnachweis erforderlich. In diesem Fall ist die ermüdungswirksame Last um den Prozentsatz zu erhöhen, um den die maximalen Schnittkräfte aus der dynamischen Berechnung mit HSLM die Werte der statischen Berechnung mit dynamischem Beiwert überschreiten, falls keine genaue Untersuchung erfolgt." ([39] p.21)

Furthermore, the ÖBB guideline [37] clarifies precisely:

> *"6.3.9 Nachweis der Ermüdung*
>
> *Im Falle der Nachweisführung der Tragsicherheit über Schnittgrößenvergleiche (siehe Pkt. 6.3.8) kann der Ermüdungsnachweis auch für die dynamischen Lastmodelle als erbracht angesehen werden, sofern die Beanspruchungen gemäß Pkt. 6.3.8 durch die statischen Vergleichslasten abgedeckt sind.*
>
> *Sofern der Nachweis der Tragsicherheit über direkte Bemessungen mit den aus der dynamischen Berechnung gewonnenen Maximalschnittgrößen erfolgt und diese größer sind als jene aus den statischen Vergleichslasten, so ist hinsichtlich der Ermüdung ein gesonderter Nachweis dann erforderlich, wenn gemäß ÖNORM B 1991-2, Pkt. 9.3.16 die Jahresbruttotonnen aller Betriebszüge mit einer Geschwindigkeit über 200 km/h den Wert von 5 Mio. Jahresbruttotonnen je Gleis überschreiten. Die ermüdungswirksame Last ist dabei um jenen Prozentsatz zu erhöhen, um den die maximalen Schnittgrößen aus der dynamischen Berechnung jener der statischen Vergleichslasten überschreiten."* ([37] p.46)

In conclusion, the following assumptions can be made for the situation in Austria:

- The fatigue design check can be seen as fulfilled, if the ultimate limit state design (ULS) is performed using the internal forces due to the quasistatic analysis (static load models including Φ), which exceed the internal forces due to the dynamic analysis (high speed load models and real trains, both including $(1 + 0.5\ \varphi'')$).
- In case the ultimate limit state design (ULS) of the structure is performed directly, using the dynamic internal forces, as these exceed the static internal force, an additional fatigue design is necessary, if real trains with speeds > 200 km/h make up more than 5 million tons per year and track. If the above conditions are met, the fatigue load must be increased by the percentage the internal forces of the dynamic calculation exceed the ones of the static calculation ('adjusted' dynamic factor).

Consequently, even if the ultimate limit state design (ULS) is performed using the internal forces due to a dynamic calculation, the fatigue limit state design (FLS) is performed in a static way, considering an 'adjusted' dynamic factor, for the situation in Austria.

Note that in the ÖNORM B 1991-2 [43] for the dynamic analysis regarding the FLS and the increasing factor φ_{FAT} according to Equation (2.31), only the load models HSLM are mentioned, whereas in the ÖBB guideline [37] no such reference is made. As the ÖBB guideline [37] defines precisely, which high-speed load models and real trains regarding the dynamic analysis need to be considered, the 'adjusted' dynamic factor φ_{FAT} shall be determined according to the ÖBB guideline [37].

$$\varphi_{FAT} = \max \frac{E_{dyn}}{E_{stat,LM}} \tag{2.31}$$

with: E_{dyn} ... maximum dynamic internal forces due to
load model HSLM and real trains, all including $(1 + 0.5\ \varphi'')$

$E_{stat,LM}$ ... maximum static internal forces due to
load models LM71, SW/0 and SW/2,
all including Φ_2 and the first two $\alpha = 1.21$

Subsequently, the 'adjusted' dynamic factor φ_{FAT} is applied on the fatigue load and the fatigue limit state design check performed:

$$\gamma_{Ff} \; \lambda \; \Phi_2 \; \Delta\sigma_{LM71} \; \varphi_{FAT} \leq \frac{\Delta\sigma_c}{\gamma_{Mf}} \tag{2.32}$$

Independently of the stated above, one could design the structure in such a way that the maximum stress range $\Delta\sigma_{max}$ due to the dynamic calculation of all considered real trains, is smaller than the constant amplitude fatigue limit $\Delta\sigma_D/\gamma_{Mf}$ of a given detail and consequently no damage occurs. ([21] p.1067) In this case, the bridge should be designed for the additional fatigue effects at resonance, considering real trains on any one track. ([43] 6.4.6.1.2 (7)) Furthermore, speeds up to the maximum nominal speed should be considered, hence the factor 1.2 can be neglected. ([43] 6.4.6.6 (5))

2.2. State of the art

In the field of research regarding train and bridge dynamics a lot of literature is available. Therefore, the following paragraphs are meant to give a short overview — making no claim to be exhaustive.

A good overview and state of the art review regarding the train-track-bridge dynamic interaction may be found in [67]. However, the bridge structure may be modelled using simple beam models (for preliminary studies) or more sophisticated finite element models (FEM). Regarding the train model, either moving load models or complex 2D and 3D multi-body models are available. The moving load model represents each axle load as constant forces and thus neglects inertia effects of the train masses. On the other hand, the multi-body model considers the vehicle-bridge interaction and allows additionally to model track irregularities. For both, the train and bridge structure models, various levels of refinement are available and hence almost no limits exist in modelling the physical details. ([55] p.14 et seqq.)

As the focus of this doctoral thesis is on the fatigue behaviour, regarding the dynamic excitation of bridge structures due to train crossing, the following literature gives a short insight on this specific research area.
In [18] the general procedure, leading from the dynamic calculated stresses acting on railway bridges to their effects on the fatigue design, are discussed. Hence, the modelling options, as described previously, are introduced and subsequently the fatigue design, including the *Rainflow* counting method, *Miner's rule* and fracture mechanics are covered. Finally, in an exemplary manner, an estimation of inspection intervals of a stringer for a specific crack length and certain traffic loads is proposed. However, [18] illustrates in the year 1998 the general procedure of combining dynamic calculations/ fatigue analysis and makes aware of the future possibilities due to increasing computational power.
In [52] a simple arch bridge model was subjected to train crossings, considering the moving load model. Besides real high-speed trains also fatigue trains were calculated. Regarding the fatigue assessment on the bridge deck, the S-N approach ($\Delta\sigma_C$ = 80 N/mm^2, γ_{Mf} = 1.35) was selected. It was possible to show that the damage due to real high speed trains in case of resonance exceeds the one caused by most adverse freight trains.

In [2] the dynamic analysis is combined with fracture mechanics. Using the sub-modelling technique and modal analysis, a new and fast method is established and demonstrated at the simple beam.
Consequently, the before mentioned method is applied in [3] on a composite bowstring bridge, whereas the detail of interest is located on the diaphragm. Furthermore, a monitoring system of the real bridge is available, which allows to compare the measured and calculated strains due to 565 real trains (freight and passenger trains). Considering an initial crack length of 15 mm leads for the current traffic volume at site ($3.1\ 10^6$ t/year) to a hypothetical failure in approximately 95 years. However, the method was further developed and published in [25] and [26] .
In [31] an approach is proposed, which uses a probabilistic dynamic stress analysis of a 3D coupled train-bridge system. Therefore, train speed and track irregularities were considered as random variables. With sets of these two random variables, train crossings were simulated and stress time histories of local members were calculated. Subsequently, for each train crossing, equivalent stress ranges and number of stress cycles were calculated, which followed certain probability distributions. Finally, the limit-state function (LSF), using the S-N approach, was established, which yields to a certain failure probability P_F.
In [68] a composite railway bridge (Sesia viaduct) designed for high speed trains is analysed. The FEM model of the structure is thereby validated by field measurements and six details for the fatigue assessment are identified. The stress ranges produced by the one considered high speed train ETR500Y are evaluated using the S-N curve approach in combination with Miner's damage rule. In [69], which is the continuation of the before mentioned literature, three different load model variants are discussed — static analysis with dynamic amplification factor, dynamic analysis with moving load model and dynamic analysis with multi-body model. In conclusion, the fatigue damage is governed more by the stress range rather than by the maximum stress. Hence, a dynamic amplification factor may not predict a conservative fatigue damage of the bridge. In general, the moving load model covers in a conservative way the fatigue damage produced by the multi-body model. In [70] the before mentioned Sesia viaduct is analysed again, here using a fracture mechanics concept instead of the S-N approach.

As the examples above show, there is no lack in modelling the bridge-train interaction or the fatigue process itself in sufficient detail. Usually the focus is on a particular structure with the goal to model reality as good as possible. Furthermore, due to the insufficient data regarding real traffic mixes, only few train types are considered. Consequently, in this doctoral thesis the main focus is on simplified, but therefore many bridge structures, which allows to consider the crossing of a vast number of trains. Hence, the interest is not directed to the small details but to the bigger picture of the fatigue problem itself.

3. Dynamic analysis

This chapter describes the dynamic simulation of a train crossing over a bridge structure.
First, the general *equation of motion* for a Bernoulli-Euler beam under transversal loading, varying with time, is formulated. Afterwards the *natural frequencies* and *eigenfunctions* for the simple beam are derived.
Subsequently, two different load models representing the train crossing are discussed. The *moving load model* is the most simple one, as it considers static axle loads only. The more complex *2D multi-body model* takes the individual rigid parts of a train car (car body, bogies and wheel-sets) and their masses, interconnected through springs and dampers, into account. Thus, the latter train model considers the interaction of the train and the bridge structure.
However, a discretization is necessary in order to solve the resulting partial differential equation. Therefore, the *Ritz-Galerkin approximation method* for simple structures and the *finite element method (FEM)* for more complex structures are introduced.
The resulting coupled systems of equations may be either solved directly using numerical approximation methods (e.g. *direct numerical integration*) or initially be decoupled with the *modal analysis* and afterwards solved either numerically or, if possible, analytically. Solving the systems of equations, after applying the modal analysis, is covered for both load models more in detail.
Finally, a *non-dimensional response representation* for the simple Euler-Bernoulli beam, subjected to the moving load model, is presented. This approach allows to reduce the necessary number of dynamic calculations in the context of a parameter study substantially.

3.1. Equation of motion

3.1.1. Formulation

In the following section the partial differential equation of motion for the Bernoulli-Euler beam under transversal loading will be derived according to [8] p.366, [32], [71] p.358. The physical characteristics of the beam are represented by the bending stiffness $EI(x)$, the mass per unit length $\mu(x)$ and an external damping force per unit length $c(x)$, which are all varying along the x-axis. The transverse loading $p_z(x,t)$ and the transverse displacement response $w(x,t)$ are assumed to be functions of place and time — see Figure 3.1(a). The equation of motion can be derived by formulating the equilibrium of forces on a differential element as illustrated in Figure 3.1(b).

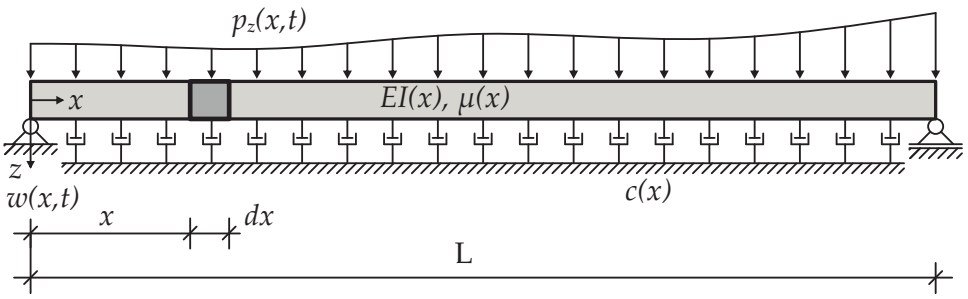

(a) Overview

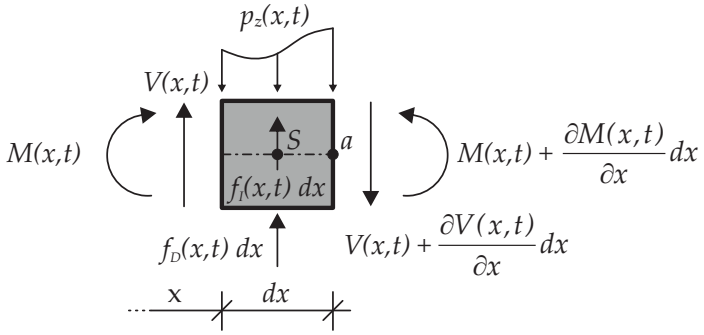

(b) Differential element

Figure 3.1.: Bernoulli-Euler beam with dynamic loading — according to [8]

The equilibrium in vertical direction leads to

$$V(x,t) + f_D(x,t)\ dx + f_I(x,t)\ dx - p_z(x,t)\ dx - \left(V(x,t) + \frac{\partial V(x,t)}{\partial x}\ dx \right) = 0 \tag{3.1}$$

whereas $f_I(x,t)$ describes the inertia force which is equal to the mass of the element multiplied by the transverse acceleration acting on the element

$$f_I(x,t)\ dx = \mu(x)\ dx\ \frac{\partial^2 w(x,t)}{\partial t^2} \tag{3.2}$$

and $f_D(x,t)$ representing the external damping force which opposes velocity

$$f_D(x,t)\ dx = c(x)\ dx\ \frac{\partial w(x,t)}{\partial t} \tag{3.3}$$

Substituting Equations (3.2) and (3.3) into (3.1) and dividing by dx yields

$$c(x)\ \frac{\partial w(x,t)}{\partial t} + \mu(x)\ \frac{\partial^2 w(x,t)}{\partial t^2} - p_z(x,t) - \frac{\partial V(x,t)}{\partial x} = 0 \tag{3.4}$$

The following equilibrium is found by summing up the moments about point a as presented in Figure 3.1(b).

$$\begin{aligned} M(x,t) + V(x,t)\ dx + f_D(x,t)\ \frac{dx^2}{2} + f_I(x,t)\ \frac{dx^2}{2} - \\ p_z(x,t)\ \frac{dx^2}{2} - \left(M(x,t) + \frac{\partial M(x,t)}{\partial x}\ dx \right) = 0 \end{aligned} \tag{3.5}$$

After dropping all terms including dx^2, the well known relationship between bending and shear results

$$V(x,t) = \frac{\partial M(x,t)}{\partial x} \tag{3.6}$$

Introducing additionally the bending-curvature relationship for the Bernoulli-Euler beam

$$M(x,t) = -EI\ \frac{\partial^2 w(x,t)}{\partial x^2} \tag{3.7}$$

and inserting (3.6) and (3.7) into (3.5) finally the partial differential equation of motion in terms of $w(x,t)$ results

$$\frac{\partial^2}{\partial x^2} \left[EI(x)\ \frac{\partial^2 w(x,t)}{\partial x^2} \right] + \mu(x)\ \frac{\partial^2 w(x,t)}{\partial t^2} + c(x)\ \frac{\partial w(x,t)}{\partial t} = p_z(x,t) \tag{3.8}$$

Assuming constant bending stiffness EI, mass per unit length μ and damping force c along the x-axis of the beam and introducing the superscripts i to iv representing derivatives with respect to location and dots above the variable represent derivatives with respect to time, Equation (3.8) becomes

$$EI\ w^{iv}(x,t) + \mu\ \ddot{w}(x,t) + c\ \dot{w}(x,t) = p_z(x,t) \tag{3.9}$$

3.1.2. Natural frequencies and eigenfunctions

The natural frequencies and eigenfunctions are derived for the unloaded and undamped Bernoulli-Euler beam [64], [8]. Therefore, the Equation (3.9) reduces to

$$EI\ w^{iv}(x,t) + \mu\ \ddot{w}(x,t) = 0 \tag{3.10}$$

which can be reordered to

$$w^{iv}(x,t) = -\frac{1}{a^2}\ \ddot{w}(x,t) \tag{3.11}$$

$$\text{with:} \quad a = \sqrt{\frac{EI}{\mu}}$$

In order to solve the free-vibration equation, the separation of variables is used

$$w(x,t) = \phi(x)\ q(t) \tag{3.12}$$

which indicates that the solution is of shape $\phi(x)$ oscillating with the time depending amplitude $q(t)$. Inserting Equation (3.12) into (3.11) leads to

$$q(t)\ \phi^{iv}(x) = -\frac{1}{a^2}\ \phi(x)\ \ddot{q}(t) \tag{3.13}$$

Dividing by $-\phi(x)\ q(t)$, the variables can be ordered as follows

$$-\frac{\phi^{iv}(x)}{\phi(x)} = \frac{1}{a^2}\ \frac{\ddot{q}(t)}{q(t)} = -k_j^4 \tag{3.14}$$

The equality of functions, which depend only on x and those which only depend on t is only satisfied if the functions are constant ([27] p.508). As a result it is possible to introduce the constant $-k_j^4$ for later mathematical convenience.

The time-dependent part of (3.14) yields

$$\ddot{q}(t) + \omega_j^2\ q(t) = 0 \tag{3.15}$$

$$\text{with:} \quad \omega_j^2 = a^2\ k_j^4 = \frac{EI}{\mu}\ k_j^4$$

which represents the free-vibration of an undamped single degree of freedom system with the solution ([8] p.378)

$$q(t) = A_1 \cos\left(\omega_j t\right) + A_2 \sin\left(\omega_j t\right) \tag{3.16}$$

The constants A_1 and A_2 depend on the initial conditions of displacement and velocity.

The location-dependent part of (3.14) yields

$$\phi^{iv}(x) = k_j^4 \, \phi(x) \tag{3.17}$$

and can be solved by assuming the solution of the form

$$\phi(x) = C \, e^{\lambda x} \tag{3.18}$$

which leads after substituting (3.18) into (3.17) to

$$\lambda^4 = k_j^4 \tag{3.19}$$

and further

$$\lambda_{1,2} = \pm i k_j \qquad \lambda_{3,4} = \pm k_j \tag{3.20}$$

The complete solution is obtained by inserting the solutions of (3.20) into Equation (3.18) and adding up the four terms

$$\phi(x) = C_1 \, e^{ik_j x} + C_2 \, e^{-ik_j x} + C_3 \, e^{k_j x} + C_4 \, e^{-k_j x} \tag{3.21}$$

The solution above can be expressed in trigonometric and hyperbolic equivalents as shown as follows

$$\phi(x) = B_1 \cos\left(k_j x\right) + B_2 \sin\left(k_j x\right) + B_3 \cosh\left(k_j x\right) + B_4 \sinh\left(k_j x\right) \tag{3.22}$$

The real constants B_1, B_2, B_3 and B_4 must be evaluated in a way in order to fulfil the boundary conditions at the end of the beam (slope, displacement, moment and shear). Considering this, three of the four constants can be expressed in terms of the fourth. Furthermore, the so called frequency equation can be formulated and the frequency parameter k_j determined. In a free-vibration problem it is not possible to directly obtain the fourth constant as it represents an arbitrary amplitude of the shape function $\phi(x)$ ([8] p.379).

$$\phi'(x) = k_j \left[-B_1 \sin(k_j x) + B_2 \cos(k_j x) + B_3 \sinh(k_j x) + B_4 \cosh(k_j x)\right] \tag{3.23}$$

$$\phi''(x) = k_j^2 \left[-B_1 \cos(k_j x) - B_2 \sin(k_j x) + B_3 \cosh(k_j x) + B_4 \sinh(k_j x)\right] \tag{3.24}$$

$$\phi'''(x) = k_j^3 \left[\ B_1 \sin(k_j x) - B_2 \cos(k_j x) + B_3 \sinh(k_j x) + B_4 \cosh(k_j x)\right] \tag{3.25}$$

$$\phi^{IV}(x) = k_j^4 \left[\ B_1 \cos(k_j x) + B_2 \sin(k_j x) + B_3 \cosh(k_j x) + B_4 \sinh(k_j x)\right] \tag{3.26}$$

Regarding the *uniform simple beam* the following four boundary conditions can be formulated:

$$\phi(0) = 0 \qquad M(0) = -EI \, \phi''(0) = 0 \tag{3.27}$$

$$\phi(L) = 0 \qquad M(L) = -EI \, \phi''(L) = 0 \tag{3.28}$$

Applying (3.27) on (3.22) and (3.24) leads to

$$\phi(0) = B_1 \cos(k_j 0) + B_2 \sin(k_j 0) + B_3 \cosh(k_j 0) + B_4 \sinh(k_j 0) = 0 \tag{3.29}$$

$$\phi''(0) = k_j^2 \left[-B_1 \cos(k_j 0) - B_2 \sin(k_j 0) + B_3 \cosh(k_j 0) + B_4 \sinh(k_j 0)\right] = 0 \tag{3.30}$$

which results in

$$\begin{aligned} B_1 + B_3 &= 0 \\ -B_1 + B_3 &= 0 \\ B_1 = B_3 &= 0 \end{aligned} \tag{3.31}$$

Equally, (3.28) can be used and after setting B_1 and B_3 to zero

$$\phi(L) = B_2 \sin(k_j L) + B_4 \sinh(k_j L) = 0 \tag{3.32}$$

$$\phi''(L) = k_j^2 \left[- B_2 \sin(k_j L) + B_4 \sinh(k_j L) \right] = 0 \tag{3.33}$$

results, which added up (after cancelling k_j^2) leads to

$$2\ B_4 \sinh(k_j L) = 0 \tag{3.34}$$

Since $\sinh k_j L \neq 0$ results $B_4 = 0$. Therefore, with the only nonzero constant B_2 remaining, the eigenfunction is described by

$$\phi(x) = B_2 \sin(k_j x) \tag{3.35}$$

Considering the boundary condition $\phi(L) = 0$, Equation (3.35) can only be satisfied (excluding the trivial solution $B_2 = 0$) if

$$\sin(k_j L) = 0 \tag{3.36}$$

which represents the system frequency equation and demands that

$$k_j = j\pi / L \qquad j = 0, 1, 2, \ldots \tag{3.37}$$

Inserting Equation (3.37) into (3.15) one obtains the frequency expression of the *uniform simple beam*

$$\omega_j = \frac{j^2 \pi^2}{L^2} \sqrt{\frac{EI}{\mu}} \tag{3.38}$$

Substituting Equation (3.37) into (3.35) the corresponding eigenfunctions (again neglecting the trivial case $j = 0$) of the *uniform simple beam* can be written as

$$\phi_j(x) = B_2 \sin\left(\frac{j\pi}{L} x\right) \qquad j = 1, 2, 3, \ldots \tag{3.39}$$

with B_2 being the arbitrary amplitude of the eigenfunctions.

For multi-member structures the Equations (3.22) to (3.26) can be used equally. However, the boundary conditions need to be adapted according to the stated problem. E.g. in case of a two-span uniform beam, 8 equations for the 8 unknown constants are available. After organizing these equations in matrix from, the determinant of this 8x8 matrix can be set to zero. Hence, one gets the frequency equation which only contains the single variable k_j. After finding the roots of the frequency equation, those can be substituted individually into the matrix equation

which allows to represent 7 of the constants (degrees of freedom) in terms of the 8th and therefore identify the corresponding eigenfunction. The last coefficient allows to scale the eigenfunction by an arbitrary amplitude. The natural frequencies can be found by inserting the roots into Equation (3.15) ([8] p.386, [27] p.314). The mentioned simple example of the two-span beam shows that the free-vibration analysis of the distributed parameter procedure rather fast produces big computational problems. Therefore, discrete-parameter (e.g. finite element methode (FEM)) forms are used nowadays to solve more complex systems.

Orthogonal characteristics of the eigenfunction

The orthogonality relationships of the eigenfunctions are key characteristics in the dynamic analysis ([27] p.236) — as later shown in section 3.3.2. In the following section the procedure for the uniform simple beam is shown, although the discussion is true for arbitrary bending stiffness and mass distribution along the beam's length, as well as arbitrary boundary conditions ([8] p.389).

$$\int_0^L \phi_j(x)\ \phi_k(x)\ dx = \int_0^L \sin\left(\frac{j\pi}{L}x\right)\ \sin\left(\frac{k\pi}{L}x\right)\ dx = \begin{cases} 0 & \text{if } j \neq k \\ \frac{L}{2} & \text{if } j = k \end{cases} \tag{3.40}$$

3.1.3. Load functions

In the following section two models to describe the loading due to the train crossing on a structure are presented. Single forces represent the axle loads in the first model, whereas multibody-systems describe the behaviour of the train cars in the second model. For both options, the load functions $p_z(x,t)$ in Equation (3.8) are formulated according to [19], [32].

Moving load model

The simplest way to model a train crossing is done by assuming the axle loads P_i ($i = 1...m$) as forces which move at constant speed v, from left to right, across the structure — see Figure 3.2. An implicit assumption in this model is that the mass of the beam is relatively big compared to the the mass of the load. Therefore, only gravitational effects of the load shall be considered ([19] p.13).

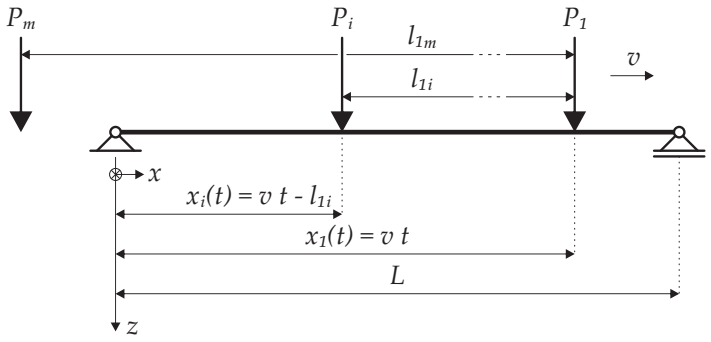

Figure 3.2.: Single force model — according to [32]

The distances of the single forces P_i to the force P_1, which passes the beam first, is described by l_{1i}. The variable $x_i(t)$ then represents the current position of the single force P_i regarding the first bridge's support. The transverse load function $p_z(x,t)$ for the moving load model can be formulated as

$$p_z(x,t) = \sum_{i=1}^{n} P_i\ \Gamma(x_i)\ \delta(x - x_i) \tag{3.41}$$

Here, $\Gamma(x_i)$ is a window function which comprises two Heaviside functions $H(x_i)$ ([47] p.561)

$$\Gamma(x_i) = H(x_i) - H(x_i - L) = \begin{cases} 1 & \text{if } 0 < x_i < L \\ 0 & \text{if } 0 > x_i > L \end{cases} \tag{3.42}$$

and considers whether or not the single force is currently on the structure. The dirac delta function $\delta(x - x_i)$ expresses the axle loads as unit concentrated forces. Additionally, considering

a and b as constants and $f(x)$ as a continuous function the dirac delta function $\delta(x - x_i)$ holds the following characteristics ([47] p.567)

$$\delta(x - x_i) = \begin{cases} \infty & \text{if } x - x_i = 0 \\ 0 & \text{if } x - x_i \neq 0 \end{cases} \tag{3.43}$$

$$\int_{-\infty}^{\infty} \delta(x) = 1 \tag{3.44}$$

$$\int_{-\infty}^{\infty} \delta(x - x_i)\, f(x) = f(x_i) \tag{3.45}$$

$$\int_{a}^{b} \delta(x - x_i)\, f(x) = \begin{cases} f(x_i) & \text{if } a \leq x_i \leq b \\ 0 & \text{all other } x_i \end{cases} \tag{3.46}$$

2D multi-body model

A detailed description of the 2D multi-body model may be found in [32], [30], [19] or [55].
In general, the following additional assumptions, in comparison to the single-force model, are made — see [30], [55]:

a.) All vehicle elements are rigid and interconnected by linear springs and dashpot dampers.
b.) All vehicles can move independently from each other within the train. However, the horizontal distance (x-direction) in between the single vehicles is held constant.
c.) The kinematic relationships may be linearised regarding a reference point.
d.) In vertical direction the contact between rail and wheel-sets is intact at all times.
e.) The wheels roll without friction or slip on the rail.

The subsequent procedure is based on [32], who followed the detailed approach of [30] to establish the equations of motion for a 2D multi-body vehicle. In this doctoral thesis, the 2D multi-body modelling is only performed for so-called conventional high-speed trains with a front and rear bogie, each holding two wheel-sets — see Figure 3.3 and Table 3.1.

The 2D multi-body model of the vehicle, with its 10 degrees of freedom (DOF), is described by a set of equations of motion. Furthermore, the bridge structure and the 2D multi-body model interact with each other via contact forces. In the following paragraphs the equations of motion for one vehicle are derived. Therefore, they are formulated, using the *D'Alembert's principle* and the *principle of virtual work*, for the free system (all DOF of the vehicle system are free — subscript f) and afterwards for the constrained system (the DOF regarding the wheel-sets are equal to the deflection of the bridge structure — due to assumption d.) above).

The *D'Alembert's principle* is based on the *principle of virtual work* and its extension to dynamics. For some point in time t, virtual displacements are applied to the instant configuration of the moving body. In total, the sum of the virtual work, due to internal and external forces, δW and the virtual work due to inertia forces δW_m vanish — see [71] p.438.

$$\delta W + \delta W_m = 0 \tag{3.47}$$

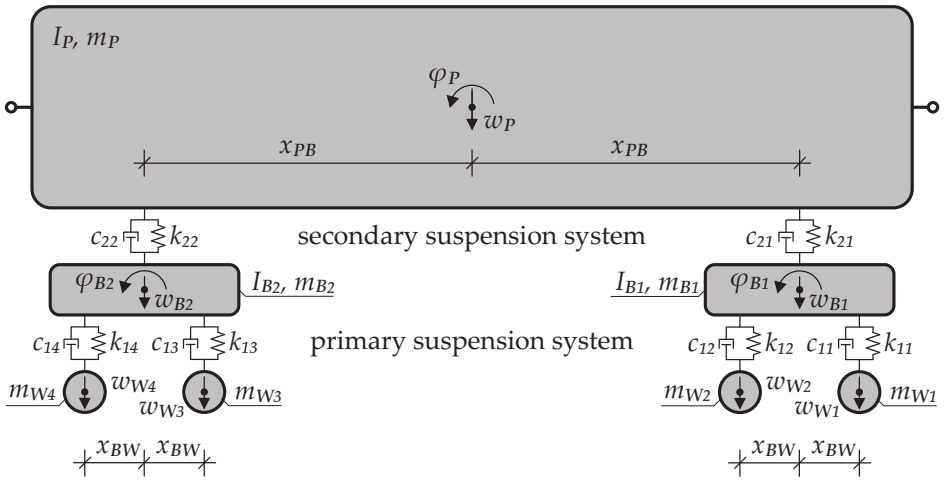

Figure 3.3.: 2D multi-body model — overview — according to [32]

Geometry		
x_{PB}	...	distance of the car body's center of gravity to the connection of the secondary suspension system [m]
x_{BW}	...	distance of the bogie's center of gravity to the connection of the primary suspension system [m]

Masses and moments of inertia		
m_P	...	mass of the car body [kg]
I_P	...	mass moment of inertia of the car body [kgm^2]
m_{B1}, m_{B2}	...	masses of the bogies 1 and 2 [kg]
I_{B1}, I_{B2}	...	mass moments of inertia of the bogies 1 and 2 [kgm^2]
m_{W1}, m_{W2}, m_{W3}, m_{W4}	...	masses of the wheel-sets 1 to 4 [kg]

Spring and damping constants		
k_{11}, k_{12}, k_{13}, k_{14}	...	primary suspension stiffness [kN/m]
c_{11}, c_{12}, c_{13}, c_{14}	...	primary suspension damping [kNs/m]
k_{21}, k_{22}	...	secondary suspension stiffness [kN/m]
c_{21}, c_{22}	...	secondary suspension damping [kNs/m]

10 degrees of freedom		
w_P	...	displacement in z-direction of the car body
φ_P	...	rotation of the car body
w_{B1}, w_{B2},	...	displacement in z-direction of the bogies 1 and 2
φ_{B1}, φ_{B2}	...	rotation of the bogies 1 and 2
w_{W1}, w_{W2}, w_{W3}, w_{W4}	...	displacement in z-direction of wheel-sets 1 to 4

Table 3.1.: 2D multi-body model — overview — according to [32]

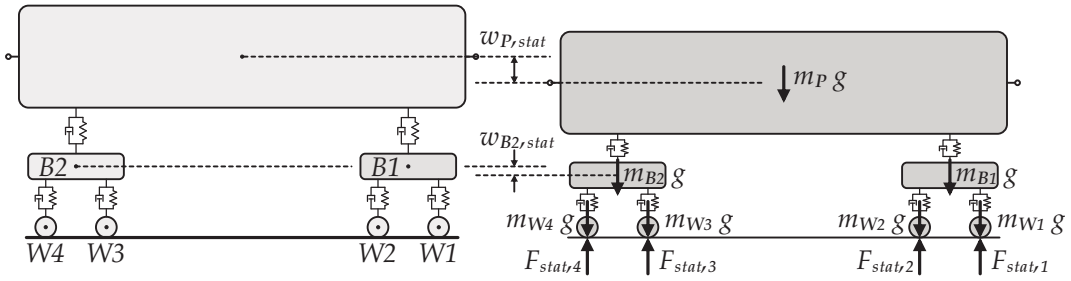

Figure 3.4.: 2D multi-body model — initial condition and static equivalent position

In Figure 3.4 on the left side, the initial condition, before applying any loads on the 2D multi-body system, is shown. After considering the gravity loads — of the vehicle car, the two bogies and the four wheels-sets — the static equivalent position is found (Figure 3.4 on the right side). From this position on, the degrees of freedom (DOF) are measured. Hence, the spring forces due to the gravity loads and the gravity loads themselves are not considered in order to describe the dynamic behaviour of the 2D multi-body system.

Consequently, the internal and external forces, acting on each body of the vehicle, are illustrated in their positive effective direction in Figure 3.5. One can distinguish spring forces F_k, dashpot forces F_c and contact force P_R. Spring and dashpot forces are positive for increasing displacements and velocities.

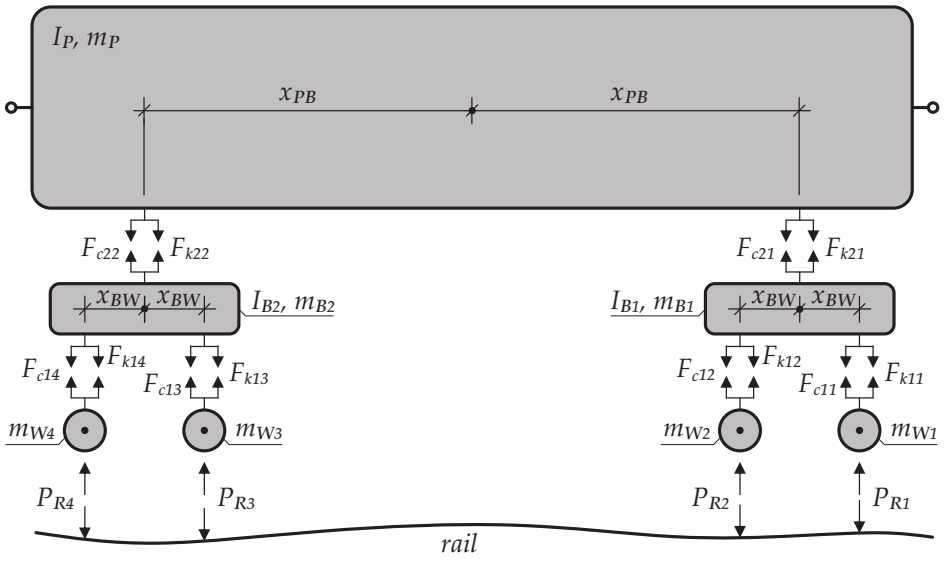

Figure 3.5.: 2D multi-body model — free body diagram — according to [32]

Vector with degrees of freedom (DOF)

The vector $\mathbf{u}_f$ contains the 10 DOF of the vehicle — see Figure 3.3 — which are measured from the static equilibrium position of the individual parts — see Figure 3.4 on the right side:

$$\mathbf{u}_f^T = \{w_P,\ \varphi_P,\ w_{B1},\ \varphi_{B1},\ w_{B2},\ \varphi_{B2},\ w_{W1},\ w_{W2},\ w_{W3},\ w_{W4}\} \tag{3.48}$$

Relationship between spring and system displacement

The vector $\mathbf{v}$ holds the displacement entries of the 6 springs,

$$\mathbf{v}^T = \{v_{z11},\ v_{z12},\ v_{z13},\ v_{z14},\ v_{z21},\ v_{z22},\} \tag{3.49}$$

whereas $\dot{\mathbf{v}}$ encloses the velocity entries regarding the 6 dashpots.

$$\dot{\mathbf{v}}^T = \{\dot{v}_{z11},\ \dot{v}_{z12},\ \dot{v}_{z13},\ \dot{v}_{z14},\ \dot{v}_{z21},\ \dot{v}_{z22},\} \tag{3.50}$$

As the displacements in the springs $\mathbf{v}$ result due to the displacements of the 10 DOF in $\mathbf{u}_f$, the relationship may be formulated, according to the *principle of superposition*, using the matrix $\mathbf{T}_v$. The procedure therefore is as follows: Each of the 10 DOF in $\mathbf{u}_f$ is applied with the value of '1' individually on the vehicle system. The resulting displacements in the springs are subsequently calculated and finally superposed for all 10 DOF. Figure 3.6 illustrates the process for the rotation $\varphi_{B1} = 1$ in bogie 1, which leads to the following spring displacements:

$$\begin{aligned} v_{z11} &= x_{BW} \\ v_{z12} &= -x_{BW} \\ v_{z13} &= 0 \\ v_{z14} &= 0 \\ v_{z21} &= 0 \\ v_{z22} &= 0 \end{aligned} \tag{3.51}$$

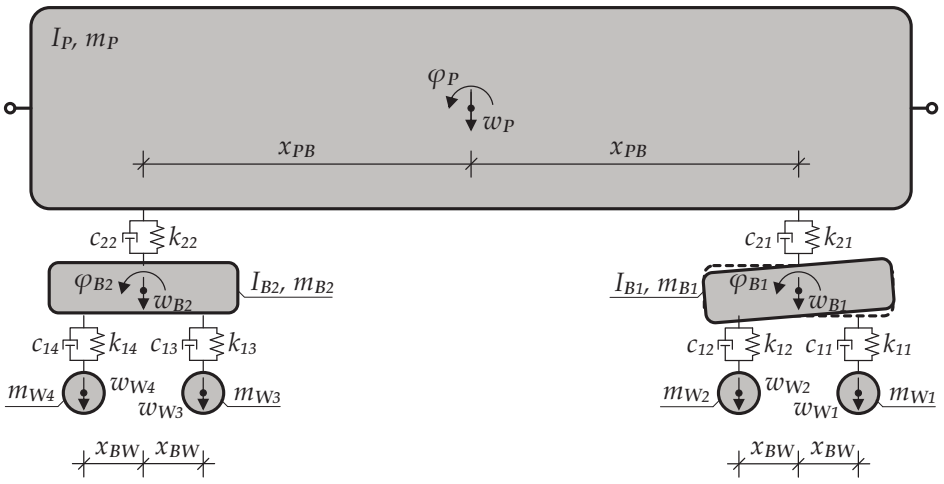

Figure 3.6.: 2D multi-body model — relationship between spring and system displacement — rotation in bogie 1 φ_{B1}

The matrix $\mathbf{T}_v$ represents the results, as mentioned above, for all 10 DOF and contains Equation (3.51) in column four.

$$\mathbf{T}_v = \begin{bmatrix} 0 & 0 & -1 & x_{BW} & 0 & 0 & 1 & 0 & 0 & 0 \\ 0 & 0 & -1 & -x_{BW} & 0 & 0 & 0 & 1 & 0 & 0 \\ 0 & 0 & 0 & 0 & -1 & x_{BW} & 0 & 0 & 1 & 0 \\ 0 & 0 & 0 & 0 & -1 & -x_{BW} & 0 & 0 & 0 & 1 \\ -1 & x_{PB} & 1 & 0 & 0 & 0 & 0 & 0 & 0 & 0 \\ -1 & -x_{PB} & 0 & 0 & 1 & 0 & 0 & 0 & 0 & 0 \end{bmatrix} \tag{3.52}$$

The relationships for the displacements in the springs and the velocities in the dashpots yield to:

$$\begin{aligned} \mathbf{v} &= \mathbf{T}_v \, \mathbf{u}_f \\ \dot{\mathbf{v}} &= \mathbf{T}_v \, \dot{\mathbf{u}}_f \end{aligned} \tag{3.53}$$

Virtual work of spring and dashpot forces

The spring forces can be calculated assuming a linear relationship with the spring displacements:

$$\begin{pmatrix} F_{k11} \\ F_{k12} \\ F_{k13} \\ F_{k14} \\ F_{k21} \\ F_{k22} \end{pmatrix} = \begin{bmatrix} k_{11} & 0 & \cdots & & & 0 \\ 0 & k_{12} & & & & \vdots \\ \vdots & & k_{13} & & & \\ & & & k_{14} & & \\ & & & & k_{21} & 0 \\ 0 & \cdots & & & 0 & k_{22} \end{bmatrix} \begin{pmatrix} v_{z11} \\ v_{z12} \\ v_{z13} \\ v_{z14} \\ v_{z21} \\ v_{z22} \end{pmatrix} \tag{3.54}$$

Using index notation, Equation (3.54) becomes:

$$\mathbf{f}_k = \mathbf{S}_k \, \mathbf{v} \tag{3.55}$$

Furthermore, for the parallel arranged dashpods

$$\mathbf{f}_c = \mathbf{S}_c \, \dot{\mathbf{v}} \tag{3.56}$$

is valid. The diagonal matrix $\mathbf{S}_c$ contains the damping coefficients $c_{11}, c_{12}, \ldots, c_{22}$.

In the following step, the virtual work done by the spring and dashpot forces is calculated. Therefore, the virtual displacements $\delta\mathbf{u}_f$ are applied on the free body diagram. The virtual displacements $\delta\mathbf{v}$, in accordance with Equation (3.53), become:

$$\delta\mathbf{v} = \mathbf{T}_v \, \delta\mathbf{u}_f \tag{3.57}$$

Considering Equations (3.53) and (3.55) to (3.57) the virtual work due to spring and dashpot forces leads to:

$$\delta W_{kc,f} = -\delta\mathbf{u}_f^T \underbrace{\mathbf{T}_v^T \, \mathbf{S}_k \, \mathbf{T}_v}_{\mathbf{K}_f} \, \mathbf{u}_f - \delta\mathbf{u}_f^T \underbrace{\mathbf{T}_v^T \, \mathbf{S}_c \, \mathbf{T}_v}_{\mathbf{C}_f} \, \dot{\mathbf{u}}_f \tag{3.58}$$

Furthermore, as shown in Equation (3.58) the stiffness matrix $\mathbf{K}_f$ and the damping matrix $\mathbf{C}_f$ for the free system can be defined.

Mass matrix — virtual work of inertia forces

Combining the masses and mass moments of inertia to the mass matrix $\mathbf{M}_f$ of the free system

$$\mathbf{M}_f = \begin{bmatrix} m_P & 0 & & & \cdots & & & & 0 \\ 0 & I_p & & & & & & & \\ & & m_{B1} & & & & & & \\ & & & I_{B1} & & & 0 & & \\ & & & & m_{B2} & & & & \vdots \\ \vdots & & & & & I_{B1} & & & \\ & & 0 & & & & m_{W1} & & \\ & & & & & & & m_{W2} & \\ & & & & & & & & m_{W3} \quad 0 \\ 0 & & & & \cdots & & & 0 & m_{W4} \end{bmatrix} \tag{3.59}$$

enables one to formulate the virtual work due to inertia forces in index notation:

$$\delta W_{m,f} = -\delta \mathbf{u}_f^T \, \mathbf{M}_f \, \ddot{\mathbf{u}}_f \tag{3.60}$$

Virtual work of external forces

As the DOF are measured from the static equivalent position, only the contact forces are considered as external forces.

$$\mathbf{p}_{C,f}^T = \{0,\ 0,\ 0,\ 0,\ 0,\ 0,\ -P_{R1},\ -P_{R2},\ -P_{R3},\ -P_{R4}\} \tag{3.61}$$

The virtual work done by the external forces result to:

$$\delta W_{ext,f} = \delta \mathbf{u}_f^T \, \mathbf{p}_{C,f} \tag{3.62}$$

Equations of motion for the free system

The sum of the virtual work done due to virtual displacements needs to vanish, which leads to

$$\delta W_{kc,f} + \delta W_{ext,f} + \delta W_{m,f} = 0 \tag{3.63}$$

$$-\delta \mathbf{u}_f^T \, \mathbf{K}_f \, \mathbf{u}_f - \delta \mathbf{u}_f^T \, \mathbf{C}_f \, \dot{\mathbf{u}}_f + \delta \mathbf{u}_f^T \, \mathbf{p}_{C,f} - \delta \mathbf{u}_f^T \, \mathbf{M}_f \, \ddot{\mathbf{u}}_f = 0 \tag{3.64}$$

The virtual displacements are arbitrary, therefore the equations of motion for the free system result to:

$$\mathbf{M}_f \, \ddot{\mathbf{u}}_f + \mathbf{C}_f \, \dot{\mathbf{u}}_f + \mathbf{K}_f \, \mathbf{u}_f = \mathbf{p}_{C,f} \tag{3.65}$$

Equations of motion for the constrained system

However, the 2D multi-body model of a vehicle crossing a bridge structure represents a constrained system as the DOF of the wheel-sets can not move independently. These 4 DOF are, by definition due to assumption d.) for the 2D multi-body model (see p.41), equal to the deflection of the bridge structure :

$$\begin{aligned} w_{W1} &= w(x_1) \\ w_{W2} &= w(x_2) \\ w_{W3} &= w(x_3) \\ w_{W4} &= w(x_4) \end{aligned} \tag{3.66}$$

The Equations (3.66) modify the displacements of the free system $\mathbf{u}_f$ as follows

$$\underbrace{\begin{pmatrix} w_P \\ \varphi_P \\ w_{B1} \\ \varphi_{B1} \\ w_{B2} \\ \varphi_{B2} \\ w_{W1} \\ w_{W2} \\ w_{W3} \\ w_{W4} \end{pmatrix}}_{\mathbf{u}_f} = \underbrace{\begin{bmatrix} 1 & 0 & 0 & 0 & 0 & 0 \\ 0 & 1 & 0 & 0 & 0 & 0 \\ 0 & 0 & 1 & 0 & 0 & 0 \\ 0 & 0 & 0 & 1 & 0 & 0 \\ 0 & 0 & 0 & 0 & 1 & 0 \\ 0 & 0 & 0 & 0 & 0 & 1 \\ 0 & \cdots & & & & 0 \\ \vdots & \ddots & & & & \vdots \\ & & & & & \\ 0 & \cdots & & & & 0 \end{bmatrix}}_{\mathbf{T}_{kin}} \underbrace{\begin{pmatrix} w_P \\ \varphi_P \\ w_{B1} \\ \varphi_{B1} \\ w_{B2} \\ \varphi_{B2} \end{pmatrix}}_{\mathbf{u}} + \underbrace{\begin{bmatrix} 0 & \cdots & & 0 \\ \vdots & \ddots & & \vdots \\ & & & \\ & & & \\ & & & \\ 0 & \cdots & & 0 \\ 1 & 0 & 0 & 0 \\ 0 & 1 & 0 & 0 \\ 0 & 0 & 1 & 0 \\ 0 & 0 & 0 & 1 \end{bmatrix}}_{\mathbf{T}_C} \underbrace{\begin{pmatrix} w(x_1) \\ w(x_2) \\ w(x_3) \\ w(x_4) \end{pmatrix}}_{\mathbf{w}_{x_i}} \tag{3.67}$$

and can be written in index notation

$$\mathbf{u}_f = \mathbf{T}_{kin}\ \mathbf{u} + \mathbf{T}_C\ \mathbf{w}_{x_i} \tag{3.68}$$

For the virtual displacements holds

$$\delta\mathbf{u}_f = \mathbf{T}_{kin}\ \delta\mathbf{u} \tag{3.69}$$

Inserting of Equations (3.68) and (3.69) into (3.64) yields

$$\begin{aligned} &- \delta\mathbf{u}^T\ \mathbf{T}_{kin}^T\ \mathbf{K}_f\ \mathbf{T}_{kin}\ \mathbf{u} - \delta\mathbf{u}^T\ \mathbf{T}_{kin}^T\ \mathbf{K}_f\ \mathbf{T}_C\ \mathbf{w}_{x_i} \ldots \\ &- \delta\mathbf{u}^T\ \mathbf{T}_{kin}^T\ \mathbf{C}_f\ \mathbf{T}_{kin}\ \dot{\mathbf{u}} - \delta\mathbf{u}^T\ \mathbf{T}_{kin}^T\ \mathbf{C}_f\ \mathbf{T}_C\ \dot{\mathbf{w}}_{x_i} \ldots \\ &\qquad + \delta\mathbf{u}^T\ \mathbf{T}_{kin}^T\ \mathbf{p}_{C,f} \ldots \end{aligned} \tag{3.70}$$

$$- \delta\mathbf{u}^T\ \mathbf{T}_{kin}^T\ \mathbf{M}_f\ \mathbf{T}_{kin}\ \ddot{\mathbf{u}} - \delta\mathbf{u}^T\ \mathbf{T}_{kin}^T\ \mathbf{M}_f\ \mathbf{T}_C\ \ddot{\mathbf{w}}_{x_i} = 0 \tag{3.71}$$

Introducing the abbreviations

$$\begin{aligned} \mathbf{M} &= \mathbf{T}_{kin}^T\ \mathbf{M}_f\ \mathbf{T}_{kin} & \mathbf{F}_w &= \mathbf{T}_{kin}^T\ \mathbf{K}_f\ \mathbf{T}_C\ \mathbf{w}_{x_i} & \mathbf{p}_C &= \mathbf{T}_{kin}^T\ \mathbf{p}_{C,f} = 0 \\ \mathbf{C} &= \mathbf{T}_{kin}^T\ \mathbf{C}_f\ \mathbf{T}_{kin} & \mathbf{F}_{\dot{w}} &= \mathbf{T}_{kin}^T\ \mathbf{C}_f\ \mathbf{T}_C\ \dot{\mathbf{w}}_{x_i} & & \\ \mathbf{K} &= \mathbf{T}_{kin}^T\ \mathbf{K}_f\ \mathbf{T}_{kin} & \mathbf{F}_{\ddot{w}} &= \mathbf{T}_{kin}^T\ \mathbf{M}_f\ \mathbf{T}_C\ \ddot{\mathbf{w}}_{x_i} = 0 & & \end{aligned} \tag{3.72}$$

and considering the arbitrary characteristics of the virtual displacements $\delta\mathbf{u}$, leads to the equations of motions for the constraint system valid for one vehicle car

$$\mathbf{M}\,\ddot{\mathbf{u}} + \mathbf{C}\,\dot{\mathbf{u}} + \mathbf{K}\,\mathbf{u} = -\mathbf{F}_w - \mathbf{F}_{\dot{w}} \tag{3.73}$$

$$\mathbf{M} = \begin{bmatrix} m_P & 0 & \cdots & & 0 \\ 0 & I_p & & & \\ & & m_{B1} & & \vdots \\ \vdots & & & I_{B1} & \\ & & & & m_{B2} \quad 0 \\ 0 & & \cdots & & 0 \quad I_{B1} \end{bmatrix} \tag{3.74}$$

$$\mathbf{C} = \begin{bmatrix} c_{21}+c_{22} & (c_{22}-c_{21})\,x_{PB} & -c_{21} & 0 & -c_{22} & 0 \\ & (c_{22}+c_{21})\,x_{PB}^2 & c_{21}\,x_{PB} & 0 & -c_{22}\,x_{PB} & 0 \\ & & c_{11}+c_{12}+c_{21} & (c_{12}-c_{11})\,x_{BW} & 0 & 0 \\ & & & (c_{12}+c_{11})\,x_{BW}^2 & 0 & 0 \\ & & & & c_{13}+c_{14}+c_{22} & (c_{14}-c_{13})\,x_{BW} \\ \textit{sym.} & & & & & (c_{14}+c_{13})\,x_{BW}^2 \end{bmatrix} \tag{3.75}$$

$$\mathbf{K} = \begin{bmatrix} k_{21}+k_{22} & (k_{22}-k_{21})\,x_{PB} & -k_{21} & 0 & -k_{22} & 0 \\ & (k_{22}+k_{21})\,x_{PB}^2 & k_{21}\,x_{PB} & 0 & -k_{22}\,x_{PB} & 0 \\ & & k_{11}+k_{12}+k_{21} & (k_{12}-k_{11})\,x_{BW} & 0 & 0 \\ & & & (k_{12}+k_{11})\,x_{BW}^2 & 0 & 0 \\ & & & & k_{13}+k_{14}+k_{22} & (k_{14}-k_{13})\,x_{BW} \\ \textit{sym.} & & & & & (k_{14}+k_{13})\,x_{BW}^2 \end{bmatrix} \tag{3.76}$$

$$\mathbf{F}_w = \begin{pmatrix} 0 \\ 0 \\ -k_{11}\,w(x_1) - k_{12}\,w(x_2) \\ \{k_{11}\,w(x_1) - k_{12}\,w(x_2)\}\;x_{BW} \\ -k_{13}\,w(x_3) - k_{14}\,w(x_4) \\ \{k_{13}\,w(x_3) - k_{14}\,w(x_4)\}\;x_{BW} \end{pmatrix} \qquad \mathbf{F}_{\dot{w}} = \begin{pmatrix} 0 \\ 0 \\ -c_{11}\,\dot{w}(x_1) - c_{12}\,\dot{w}(x_2) \\ \{c_{11}\,\dot{w}(x_1) - c_{12}\,\dot{w}(x_2)\}\;x_{BW} \\ -c_{13}\,\dot{w}(x_3) - c_{14}\,\dot{w}(x_4) \\ \{c_{13}\,\dot{w}(x_3) - c_{14}\,\dot{w}(x_4)\}\;x_{BW} \end{pmatrix} \tag{3.77}$$

$$\mathbf{u} = \begin{pmatrix} w_P \\ \varphi_P \\ w_{B1} \\ \varphi_{B1} \\ w_{B2} \\ \varphi_{B2} \end{pmatrix} \tag{3.78}$$

After solving the equations of motion in Equation (3.73) one is able to calculate the spring displacements by inserting Equation (3.68) into Equation (3.53):

$$\mathbf{v} = \mathbf{T}_v \ (\mathbf{T}_{kin}\ \mathbf{u} + \mathbf{T}_C\ \mathbf{w}_{x_i}) \tag{3.79}$$

Considering Equations (3.55) and (3.56), the spring forces

$$\mathbf{f}_k = \mathbf{S}_k\ \mathbf{T}_v \ (\mathbf{T}_{kin}\ \mathbf{u} + \mathbf{T}_C\ \mathbf{w}_{x_i}) \tag{3.80}$$

and dashpot forces

$$\mathbf{f}_c = \mathbf{S}_k\ \mathbf{T}_v \ (\mathbf{T}_{kin}\ \dot{\mathbf{u}} + \mathbf{T}_C\ \dot{\mathbf{w}}_{x_i}) \tag{3.81}$$

result.

Contact forces and load function

In accordance with [32] p.79 the wheel-sets of the vehicle are modelled as concentrated masses crossing with constant speed the bridge structure. As mentioned above, no uplift of the wheel-set is possible, the displacement of the wheel-set is equal to the deflection of the beam (constrained system). The resulting location-dependent contact forces P_{Ri} are calculated using the free body diagram. In Figure 3.7 the situation is illustrated for the first wheel-set of bogie 1. The gravitational load $F_{stat,1}$ therefore consequently considers the associated masses of the vehicle body, the bogie and the wheel-set.

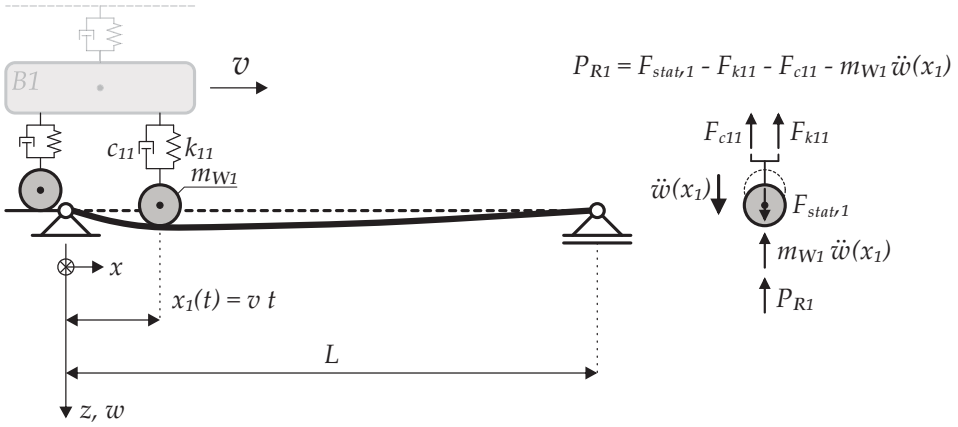

Figure 3.7.: 2D multi-body model — according to [32]

Regarding all four contact forces of the vehicle, one obtains

$$P_{Ri}(x_i) = F_{stat,i} - F_{k1i} - F_{c1i} - m_{Wi}\ \ddot{w}(x_i) \tag{3.82}$$

Inserting Equation (3.82) into (3.41) leads to the transverse load function $p_z(x,t)$ of the 2D multi-body model, considering one train car

$$p_z(x,t) = \sum_{i=1}^{4} \{F_{stat,i} - F_{k1i} - F_{c1i} - m_{Wi}\ \ddot{w}(x_i)\}\ \Gamma(x_i)\ \delta(x - x_i) \tag{3.83}$$

3.2. Discretization

The equation of motion for the Bernoulli-Euler beam with constant bending stiffness EI and mass per unit length μ results according Equation (3.9) to a partial differential equation of 4th order:

$$EI\ w^{iv}(x,t) + \mu\ \ddot{w}(x,t) + c(x)\ \dot{w}(x,t) = p_z(x,t) \tag{3.84}$$

In general, it is rather difficult to solve the above mentioned equation of motion for the uniform beam, with its infinite number of degrees of freedom (DOF) ([8] p.365). Therefore, a discretization is necessary in order to obtain an ordinary differential equation ([32] p.8). In the following section two options of discretization will be presented.

3.2.1. The Ritz-Galerkin approximation method

In [32] and [5] good overviews are presented which base on [71]. The general idea is to approximate the displacement $w(x,t)$ of the whole structure, which is a function of the axial coordinate x and time t, by a finite series of functions separated in x and t, the *Ritz* approximation ([71] p.455 et sqq.)

$$w(x,t) \approx \widetilde{w}(x,t) = \sum_{j=1}^{m} \phi_j(x)\ q_j(t) \tag{3.85}$$

where $q_j(t)$ may be interpreted as the weighting function (called generalized coordinate) of the shape function $\phi_j(x)$ — see Figure3.8

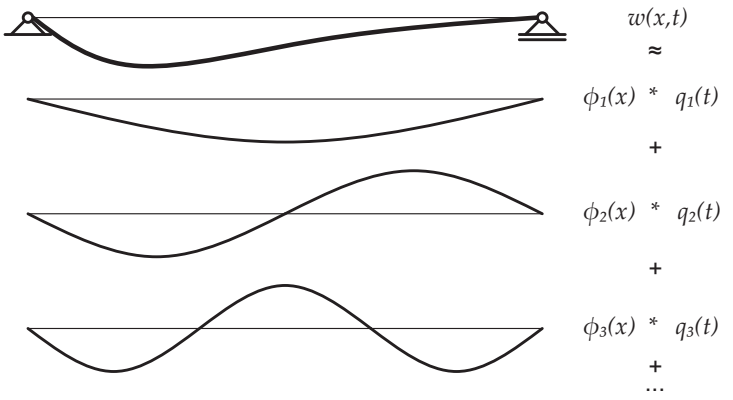

Figure 3.8.: *Ritz* approximation of a simple beam

In the *Galerkin procedure* the partial differential equations of the distributed parameter system are summarized using the partial differential operator $D\{w\}$

$$D\{w\} = 0 \tag{3.86}$$

Applying virtual displacements δw on the instant configuration and integrating over the domain of definition B, the virtual work needs to vanish

$$\int_B D\{w\}\,\delta w\,dB = 0 \tag{3.87}$$

Substituting the *Ritz* approximation produces the error $\widetilde{p}$

$$D\{\widetilde{w}\} = \widetilde{p} \tag{3.88}$$

which can be interpreted as fictitious loading. In case the *Ritz* approximation fulfils the kinematic (related to deformations w and w') as well as the dynamic boundary conditions (related to internal forces and hence w'' and w'''), those fictitious loadings form a self-equilibrium, which requires the virtual work to vanish again

$$\int_B \widetilde{p}\,\delta\widetilde{w}\,dB = 0 \tag{3.89}$$

Substituting the variation of the *Ritz* approximation

$$\delta\widetilde{w} = \sum_{j=1}^{m} \phi_j\,\delta q_j \qquad\qquad j = 1,2,\dots\ k,m \tag{3.90}$$

and demanding the integral

$$\int_B \widetilde{p}\,\phi_k\,\delta q_k\,dB = 0 \tag{3.91}$$

to vanish independently of the variation of δq_k yields to *Galerkin's* rule (m equations to calculate the q_j)

$$\int_B \widetilde{p}\,\phi_k\,dB = 0 \tag{3.92}$$

which is equivalent to

$$\int_B D\{\widetilde{w}\}\,\phi_k\,dB = 0 \tag{3.93}$$

Inserting the *Ritz* approximation of Equation (3.85) into (3.84), multiplying all terms according to *Galerkin's* rule with ϕ_k and after integrating with respect to L, one obtains ([5] p.8):

$$\int_L \sum_{j=1}^{m} \left\{ EI\,q_j\,\phi_j^{iv} + \mu\,\ddot{q}_j\,\phi_j + c\,\dot{q}_j\,\phi_j \right\} \phi_k\,dx = \int_L p_z\,\phi_k\,dx \tag{3.94}$$

Introducing the following abbreviations according to [32] p.49

$$\begin{aligned} &\int_L \phi_j\,\phi_k\,dx = \Phi_{1,jk} \\ &\int_L \phi_j^{iv}\,\phi_k\,dx = \Phi_{4,jk} = \frac{\omega_i^2\,\mu}{EI}\,\Phi_{1,jk} \quad \text{with Eq. (3.17) and (3.15)} \\ &\int_L p_z\,\phi_k\,dx = p_k \end{aligned} \tag{3.95}$$

$$\boldsymbol{\Phi}_1 = \begin{bmatrix} \Phi_{1,11} & \cdots & \Phi_{1,1k} & \Phi_{1,1m} \\ \vdots & \ddots & & \vdots \\ \Phi_{1,j1} & & \Phi_{1,jk} & \Phi_{1,jm} \\ \Phi_{1,m1} & \cdots & \Phi_{1,mk} & \Phi_{1,mm} \end{bmatrix} \quad \boldsymbol{\Phi}_4 = \begin{bmatrix} \Phi_{4,11} & \cdots & \Phi_{4,1k} & \Phi_{4,1m} \\ \vdots & \ddots & & \vdots \\ \Phi_{4,j1} & & \Phi_{4,jk} & \Phi_{4,jm} \\ \Phi_{4,m1} & \cdots & \Phi_{4,mk} & \Phi_{4,mm} \end{bmatrix} \quad \boldsymbol{p} = \begin{pmatrix} p_1 \\ \vdots \\ p_k \\ p_m \end{pmatrix}$$

the generalized matrices become [32] p.49

$$\begin{aligned} \mathbf{M} &= \mu\ \boldsymbol{\Phi}_1 \\ \mathbf{K} &= EI\ \boldsymbol{\Phi}_4 \\ \mathbf{C} &= c\ \boldsymbol{\Phi}_1 \end{aligned} \tag{3.96}$$

which leads to Equation (3.94) in index notation — see Equation (3.97) [32] p.49

$$\mathbf{M}\,\ddot{\mathbf{q}} + \mathbf{C}\,\dot{\mathbf{q}} + \mathbf{K}\,\mathbf{q} = \mathbf{p} \tag{3.97}$$

Due to the discretization process, Equation (3.84) was reduced from a partial differential equation of 4th order to a second order, ordinary differential equation, which is much easier to solve ([32] p.9). In general, the chosen shape functions in the *Ritz* approximation according to Equation (3.85) need to meet certain requirements. As mentioned before, they have to fulfil the kinematic and dynamic boundary conditions in order to use *Galerkin's* rule as described above. Additionally, the shape functions need to be linearly independent and have derivations of the order the method of solution requires. Furthermore, if the eigenfunctions are used as shape function, the *Modal Analysis* results. If additionally, an infinite number of eigenfunctions (m = ∞) is considered the solution $\widetilde{w}(x,t)$ of Equation (3.85) becomes the exact solution $w(x,t)$ ([5] p.8).

3.2.2. Finite element method

The *finite element method (FEM)* may be seen as the further development of the *Ritz-Galerkin* approximation method as the latter has some serious drawbacks [9] p.418

- The chosen shape functions ϕ_j (see Equation (3.85)) have to describe the deflected shape of the entire structure, which is very difficult for complex structures.
- The resulting equations are usually highly coupled, which requires very much computer time and memory.
- For each new geometry, a different set of shape functions ϕ_j must be selected — there is little carryover from one problem to another.

The FEM overcomes these difficulties as the structure is divided into a finite number of smaller, simple parts (finite elements). These finite elements are joined together at nodes, where displacement compatibility is enforced ([9] p.419) — see Figure 3.9 (a). Therefore, the shape functions ψ_j do not need to be formulated for the entire structure (*Ritz* approximation) but only for the finite element itself — see Figure 3.9 (b).

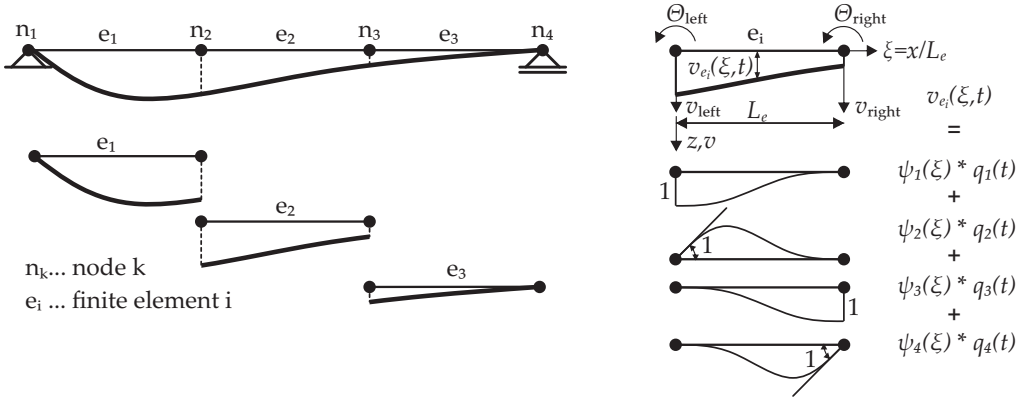

(a) Discretization of a simple beam

(b) Finite Bernoulli-Euler element e_i

Figure 3.9.: FEM principle procedure

The displacement $v_{e_i}(x,t)$ within the finite element e_i is calculated using linear interpolation between the displacement at the two ends (nodes) of the element ([9] p.421)

$$v_{e_i}(\xi,t) = \sum_{j=1}^{2*n_{DOF}} \psi_j(\xi)\ q_j(t) \qquad \text{with:} \quad \xi = \frac{x}{L_e} \tag{3.98}$$

where the shape functions $\psi_j(\xi)$ are weighted by the node displacement $q_j(t)$.

In case of a finite Bernoulli-Euler element e_i each node got $n_{DOF} = 2$ degrees of freedom (DOF), one vertical displacement v and one rotation Θ — see Figure 3.9 (b). The four shape functions for transverse deflection are ([9] p.422)

$$\begin{aligned}
\psi_1(x) &= 1 - 3\xi^2 + 2\xi^3 \\
\psi_2(x) &= -\xi(1-\xi)^2\ L_e \\
\psi_3(x) &= 3\xi^2 - 2\xi^3 \\
\psi_4(x) &= \xi^2(1-\xi)\ L_e
\end{aligned} \tag{3.99}$$

Using the *principle of virtual work* and the shape functions of Equation (3.99) the element stiffness, element mass matrix and element force vector are obtained, which are then assembled to the global system ([20] p.490 et sqq.).
Therefore, if the structure got discretized by k nodes, consequently $N = n_{DOF} * k = 2 * k$ degrees of freedom (DOF) q_j for the global system result. After assembling the single finite elements to a global model the following linear system of ordinary differential equations of second order arises ([5] p.10)

$$\mathbf{M}\,\ddot{\mathbf{q}} + \mathbf{C}\,\dot{\mathbf{q}} + \mathbf{K}\,\mathbf{q} = \mathbf{p} \tag{3.100}$$

with $\mathbf{M}$ representing the mass matrix, $\mathbf{C}$ the damping matrix and $\mathbf{K}$ the stiffness matrix of the global system. The nodal forces are summarized within the vector $\mathbf{p}$, whereas the N node displacements q_j and their derivatives are represented by $\mathbf{q}$, $\dot{\mathbf{q}}$ and, $\ddot{\mathbf{q}}$ ([5] p.10).

3.3. Solution of the equation of motion

In the following section common approaches to solve the equations of motion are presented. The first one uses step-by-step procedure methods which solve the entire coupled system of equations directly. One big group of these methods uses numerical integration techniques in order to approximately satisfy the equations of motion and is therefore called *direct numerical integration*. The second approach, called *modal analysis*, decouples in a first step the system of equations, hence each line of the system of equations can be solved independently. Therefore, the effort to solve the equations of motion, either using analytical or numerical (step-by-step procedure) methods, is considerably reduced.

3.3.1. Direct numerical integration

On this subject a lot of literature has been written in the recent years and therefore the following remarks, which may be found in [48], [8], shall be seen as a short introduction. All the different step-by-step methods have in common to divide the loading and response history in time intervals or so called steps. The initial conditions (displacement and velocity) at the beginning of one step and the history of loading during the step are then used to compute the response at the end of the step. These approaches allow to consider non-linear behaviour as the structural properties are assumed to stay constant within one step and change from one step to another. Furthermore, any desired degree of refinement is possible by shorting the time steps adequately. ([8] p.112)
The numerical approximation step-by-step methods — using either numerical integration or numerical differentiation — can be distinguished in explicit or implicit types. The first method makes it possible to calculate the response values at the end of a step only depending on the quantities at the beginning of the step. On the other hand, for implicit methods the expression calculating the response at the end of the step includes one or more quantities of the pertaining end of the step. Therefore, trial values for these quantities must be assumed which then are refined by iterations. The best step-by-step method choice for a given problem must be efficient, which means a certain level of accuracy needs to be met within a certain range of computational effort. ([8] p.116)

In the following, the concept of the numerical integration is presented

$$\dot{q}_1 = \dot{q}_0 + \int_0^{\Delta t} \ddot{q}(\tau)\, dx \tag{3.101}$$

$$q_1 = q_0 + \int_0^{\Delta t} \dot{q}(\tau)\, dx \tag{3.102}$$

which describes the velocity and displacement at the end of the step (subscript 1) in terms of the initial values at the beginning of the step (subscript 0) plus an integral expression. Hence, the change of velocity is proportional to the integral of the acceleration history within the interval Δt of the current step — see Equation (3.101). Equally, the change of displacement depends on the integral of the velocity history — see Equation (3.102). For this type of step-to-step method it is necessary to make an assumption regarding the acceleration curve within the time step,

which consequently controls the variation of velocity as well and therefore makes it possible to succeed to the next time step. ([8] p.120)

Figure 3.10 shows the assumptions of the *Euler-Gauss* method (for one degree of freedom), which considers the acceleration to be constant within the time step of the duration Δt. Consequently, the velocity and displacement behaviour must be linear and quadratic. The value of the constant acceleration is assumed to be the average of the initial and final acceleration.
In order to start this calculation, the initial accelerations $\ddot{\mathbf{q}}_0$ are obtained by solving the equations of motion (see Equation (3.100)) at the time $t = t_0$.

$$\ddot{\mathbf{q}}_0 = \mathbf{M}^{-1}[\mathbf{p}_0 - \mathbf{C}\,\dot{\mathbf{q}}_0 - \mathbf{K}\,\mathbf{q}_0] \tag{3.103}$$

Additionally, for this implicit procedure the accelerations $\ddot{\mathbf{q}}_1$ at the end of the step are necessary, which are arbitrary assumed. Subsequently, with Formulas (a) and (b) of Figure 3.10 it is possible to calculate the values of $\dot{\mathbf{q}}_1$ and $\mathbf{q}_1$ at the end of this step. Inserting $\dot{\mathbf{q}}_1$ and $\mathbf{q}_1$ in an expression like Equation (3.100)) for the point in time t_1 yields to an improved value of $\ddot{\mathbf{q}}_1$, which afterwards leads to improved values of $\dot{\mathbf{q}}_1$ and $\mathbf{q}_1$. If the iteration converges to a specified value of $\ddot{\mathbf{q}}_1$ for this time step, the following time step may be calculated. ([8] p.121)

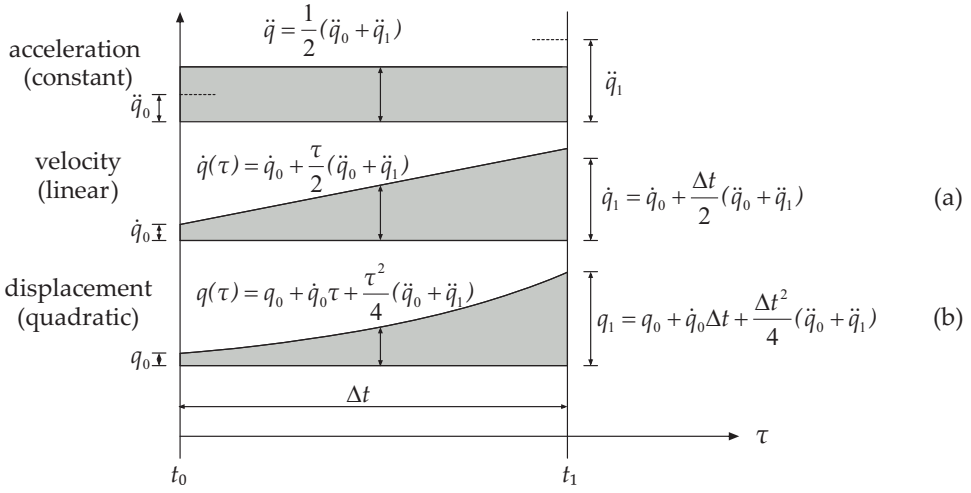

Figure 3.10.: Acceleration, velocity and displacement for the constant average acceleration method for one degree of freedom — according to [8]

The *Newmark* formulation is more general and includes the *Euler-Gauss* method as a special case with $\gamma = \frac{1}{2}$ and $\beta = \frac{1}{4}$.

$$\dot{q}_1 = \dot{q}_0 + (1-\gamma)\;\Delta t\;\ddot{q}_0 + \gamma\;\Delta t\;\ddot{q}_1 \tag{3.104}$$

$$q_1 = q_0 + \Delta t\;\dot{q}_0 + (\frac{1}{2} - \beta)\;\Delta t^2\;\ddot{q}_0 + \beta\;\Delta t^2\;\ddot{q}_1 \tag{3.105}$$

The *Newmark* method assumes the acceleration curve to be linear within a time step and is therefore also known as linear acceleration method. However, the *Euler-Gauss* method is unconditionally stable, whereas the Newmark method will be unstable unless $\frac{\Delta t}{T} \leq \frac{\sqrt{3}}{\pi} = 0.55$. ([8] p.122) The methods above were presented as implicit procedures, whereas the conversion to explicit formulation is possible (see e.g. ([8] p.123, [48] p.16), as the iteration within a step may be prohibitive.

3.3.2. Modal Analysis

The goal of the modal analysis is to decouple the equations of vibrations (Equations (3.97) and (3.100)) from Chapter 3.2. This means, the system matrices (**M**, **C**, **K**) become diagonal matrices and each equation is represented by a single-degree-of-freedom system (SDOF). For the decoupling process, the orthogonal characteristics of the eigenfunctions/ mode shapes[1] are necessary. However, there are some limitations to the modal analysis. For example, it is not possible to consider non-linear material behaviour and additionally certain requirements regarding the damping need to be met ([5] p.6). Furthermore, even if the decoupling of the system matrices (**M**, **C** and **K** become diagonal matrices) is successful, the equations of motion of the SDOF system still might be coupled due to the load vector **p**, respectively due to the selected load model — see section 3.5.3.

In general, the modal analysis is applicable on both, distributed-parameter (infinite number of DOF) and lumped-parameter systems (finite number of DOF) ([27] p.556). The latter refers to systems which are discretized using FEM and therefore have a finite number of DOF — in most cases more than one DOF, what makes them multiple-degree-of-freedom system (MDOF) as well.

Lumped-parameter system (MDOF system) $\Rightarrow$ SDOF system

In case the system was discretized using the FEM, the transformation from physical (coupled) into modal (uncoupled) coordinates is performed considering ([27] p.336 et. sqq.)

$$\mathbf{q} = \mathbf{S}\,\mathbf{r} \tag{3.106}$$
$$\boldsymbol{q}^T = \left(\; q_1, \;\; \cdots, \;\; q_j, \;\; q_N \; \right)$$
$$\boldsymbol{S} = \left(\; \boldsymbol{\phi}_1, \;\; \cdots, \;\; \boldsymbol{\phi}_j, \;\; \boldsymbol{\phi}_N \; \right)$$
$$\boldsymbol{r}^T = \left(\; r_1, \;\; \cdots, \;\; r_j, \;\; r_N \; \right)$$

where **q** holds the DOF in physical, **r** the DOF in modal coordinates and **S** contains the mode shapes $\boldsymbol{\phi}_j$ of the system.

However, the main task in dynamic analysis is to obtain the natural frequencies ω_j and mode shapes $\boldsymbol{\phi}_j$ of the undamped and unloaded structure. Therefore, the following paragraphs present a quick overview of the procedure, regarding the lumped-parameter systems, which connects the undamped vibration problem to the mathematics of the eigenvalue problem ([27] p.318).

[1] Precisely, the eigenvectors, which are related to the mode shapes by a factor of the mass matrix, decouple the system of equations ([27] p.332).

The first step is to neglect the damping matrix $\mathbf{C}$ and force vector $\mathbf{p}$ of Equation (3.100) which leads to the undamped vibration problem

$$\mathbf{M}\,\ddot{\mathbf{q}} + \mathbf{K}\,\mathbf{q} = 0 \tag{3.107}$$

Subsequently, the *generalized eigenvalue problem results*[1] by substituting $\mathbf{q} = e^{j\omega t}\,\boldsymbol{\phi}$

$$\begin{aligned} \mathbf{K}\,\boldsymbol{\phi} &= \lambda\,\mathbf{M}\,\boldsymbol{\phi} \\ \lambda &= \omega^2 \end{aligned} \tag{3.108}$$

with $j = \sqrt{-1}$, λ as eigenvalues, ω as natural frequencies and $\boldsymbol{\phi}$ representing the mode shapes. Rewriting Equation (3.108) yields

$$[\mathbf{K} - \lambda\,\mathbf{M}]\;\boldsymbol{\phi} = 0 \tag{3.109}$$

Neglecting the trivial solution $\boldsymbol{\phi} = 0$ forces the inverse of the coefficient matrix $[\mathbf{K} - \lambda\,\mathbf{M}]$ to not exist. Hence, the coefficient matrix needs to be singular and therefore its determinant has to be zero ([27] p.310)

$$\det[\mathbf{K} - \lambda\,\mathbf{M}] = 0 \tag{3.110}$$

which leads to the *characteristic equation*. From this equation the eigenvalues λ_j, natural frequencies ω_j and mode shapes $\boldsymbol{\phi}_j$ for all number of DOF ($j = 1 \ldots N$) are obtained ([27] p.324). Afterwards, the individual mode shapes $\boldsymbol{\phi}_j$ are organized in matrix $\mathbf{S}$ — see Equation (3.106).

Substituting Equation (3.106) into (3.100) and multiplying the result by $\mathbf{S}^T$ yields

$$\underbrace{\mathbf{S}^T\,\mathbf{M}\,\mathbf{S}}_{\mathbf{M}^*}\,\ddot{\mathbf{r}} + \underbrace{\mathbf{S}^T\,\mathbf{C}\,\mathbf{S}}_{\mathbf{C}^*}\,\dot{\mathbf{r}} + \underbrace{\mathbf{S}^T\,\mathbf{K}\,\mathbf{S}}_{\mathbf{K}^*}\,\mathbf{r} = \underbrace{\mathbf{S}^T\,\mathbf{p}}_{\mathbf{p}^*} \tag{3.111}$$

with $\mathbf{M}^*$ as modal mass matrix, $\mathbf{C}^*$ as modal damping matrix, $\mathbf{K}^*$ as modal stiffness matrix and $\mathbf{p}^*$ as modal force vector one obtains

$$\mathbf{M}^*\,\ddot{\mathbf{r}} + \mathbf{C}^*\,\dot{\mathbf{r}} + \mathbf{K}^*\,\mathbf{r} = \mathbf{p}^* \tag{3.112}$$

Due to the orthogonal characteristics for $j \neq k$

$$\begin{aligned} \boldsymbol{\phi}_j^T\,\mathbf{M}\,\boldsymbol{\phi}_k &= 0 & \boldsymbol{\phi}_j^T\,\mathbf{M}\,\boldsymbol{\phi}_j &= m_j^* \\ \boldsymbol{\phi}_j^T\,\mathbf{C}\,\boldsymbol{\phi}_k &= 0 & \boldsymbol{\phi}_j^T\,\mathbf{C}\,\boldsymbol{\phi}_j &= c_j^* \\ \boldsymbol{\phi}_j^T\,\mathbf{K}\,\boldsymbol{\phi}_k &= 0 & \boldsymbol{\phi}_j^T\,\mathbf{K}\,\boldsymbol{\phi}_j &= k_j^* \end{aligned} \tag{3.113}$$

the system matrices ($\mathbf{M}$, $\mathbf{C}$, $\mathbf{K}$) decouple. Hence, the modal matrices are diagonal matrices

$$\begin{aligned} \mathbf{M}^* &= \mathbf{diag}(m_j^*) \\ \mathbf{C}^* &= \mathbf{diag}(c_j^*) \\ \mathbf{K}^* &= \mathbf{diag}(k_j^*) \end{aligned} \tag{3.114}$$

[1] The generalized eigenvalue problem is the worst type of eigenvalue problem in terms of computational effort, but therefore leads directly to the mode shapes $\boldsymbol{\phi}$. In general, the *symmetric eigenvalue problem* should be used ([27] p.400).

and for the j^{th} SDOF system (represents the j^{th} row in Equation (3.112)) results

$$m_j^* \ \ddot{r}_j + c_j^* \ \dot{r}_j + k_j^* \ r_j = p_j^* \tag{3.115}$$

which then can be solved.[1]. Subsequently, the solutions are transformed back into the physical coordinate system using Equation (3.106).

Distributed-parameter systems ⇒ SDOF system

For distributed-parameter systems the *Ritz-Galerkin* approximation method, according to Equation (3.85), is used.

$$w(x,t) \approx \widetilde{w}(x,t) = \sum_{j=1}^{m} \phi_j(x) \ q_j(t)$$

The difference here is that for the shape functions $\phi_j(x)$ the exact eigenfunctions are substituted. Due to the orthogonal characteristics of the eigenfunctions ([5] p.13) — see section 3.1.2

$$\int_L \phi_j(x) \ \phi_k(x) \ dx = 0 \qquad \int_L \phi_j(x) \ \phi_j(x) \ dx = \Phi_{1,jj} \quad \text{for } j \neq k \tag{3.116}$$

the abbreviations

$$\mathbf{\Phi}_1 = \begin{bmatrix} \Phi_{1,11} & \cdots & 0 & 0 \\ \vdots & \ddots & & \vdots \\ 0 & & \Phi_{1,jj} & 0 \\ 0 & \cdots & 0 & \Phi_{1,mm} \end{bmatrix} \qquad \mathbf{\Phi}_4 = \begin{bmatrix} \Phi_{4,11} & \cdots & 0 & 0 \\ \vdots & \ddots & & \vdots \\ 0 & & \Phi_{4,jj} & 0 \\ 0 & \cdots & 0 & \Phi_{4,mm} \end{bmatrix}$$

and hence the system matrices of Equation (3.96) become diagonal modal matrices

$$\begin{aligned} \mathbf{M}^* &= \mu \ \mathbf{\Phi}_1 = \mathbf{diag}(m_j^*) \\ \mathbf{K}^* &= EI \ \mathbf{\Phi}_4 = \mathbf{diag}(k_j^*) \\ \mathbf{C}^* &= c \ \mathbf{\Phi}_1 = \mathbf{diag}(c_j^*) \end{aligned} \tag{3.117}$$

Considering the load function p_z according to Equation (3.95)

$$\int_L p_z \ \phi_j(x) \ dx = p_j^* \tag{3.118}$$

the modal force vector $\mathbf{p}^*$ becomes

$$\mathbf{p}^* = \begin{pmatrix} p_1^* \\ \vdots \\ p_j^* \\ p_m^* \end{pmatrix} \tag{3.119}$$

[1] Independently of the other SDOF systems if p_j^* is decoupled as well.

which leads to

$$\mathbf{M}^* \ \ddot{\mathbf{q}} + \mathbf{C}^* \ \dot{\mathbf{q}} + \mathbf{K}^* \ \mathbf{q} = \mathbf{p}^* \tag{3.120}$$

For the j^{th} SDOF system (represents the j^{th} row in Equation (3.120)) results

$$m_j^* \ \ddot{q}_j + c_j^* \ \dot{q}_j + k_j^* \ q_j = p_j^* \tag{3.121}$$

which then can be solved.[1]. Subsequently, the solutions are transformed back into the physical coordinate system using Equation (3.85).

3.4. Damping

In the following chapters the considered options of viscous damping are discussed. In general, the viscous damping of the form

$$f_D = c \ \dot{x}(t) \tag{3.122}$$

with f_D being the damping force, proportionally related by the *damping coefficient* c to the velocity $\dot{x}(t)$, is used due to physical observations and mathematical convenience ([27] p.21).

3.4.1. Modal damping

The most common approach is to decouple the undamped system of equations and add the damping term afterwards to the decoupled SDOF system equations ([64] p.90) — see Equation Equation (3.121)

$$c_j^* = 2 \ m_j^* \ \zeta_j \ \omega_j \tag{3.123}$$

Therefore, the *damping ratio* ζ_j is used which is introduced in Chapter 3.5.1 with Equation (3.135).

3.4.2. Rayleigh damping — proportional damping

Another common approach is to write the damping matrix $\mathbf{C}$ as linear combination of the mass and stiffness matrix ([64] p.91)

$$\mathbf{C} = \alpha \ \mathbf{M} + \beta \ \mathbf{K} \tag{3.124}$$

Since the mass and stiffness matrices become diagonal matrices applying the modal analysis, the above defined damping matrix becomes diagonal as well. Hence, one can write for the j^{th} SDOF system

$$2 \ m_j^* \ \zeta_j \ \omega_j = \alpha \ m_j^* + \beta \ k_j^* \tag{3.125}$$

[1] Independently of the other SDOF systems if p_j^* is decoupled as well.

which yields the damping ratio for the j^{th} mode

$$\zeta_j = \frac{\alpha}{2\omega_j} + \frac{\beta\omega_j}{2} \tag{3.126}$$

The two parameters α and β can be specified for two selected natural frequencies ω_1 and ω_2 with the corresponding damping ratios ζ_1 and ζ_2. Assuming $\zeta_1 = \zeta_2$ leads to

$$\alpha = \zeta_1 \frac{2\,\omega_1\,\omega_2}{\omega_1 + \omega_2} \qquad \beta = \zeta_1 \frac{2}{\omega_1 + \omega_2} \tag{3.127}$$

The other damping ratios ζ_j result with Equation (3.126) automatically. The proportional damping is often used as well in case the system is solved with the direct numerical integration approach ([64] p.91).

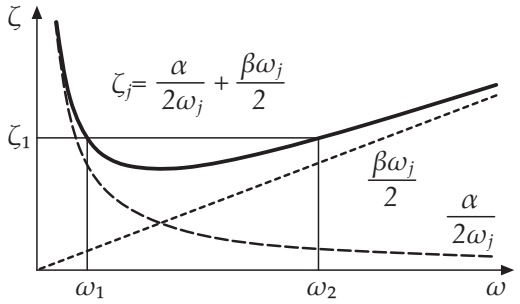

Figure 3.11.: Rayleigh (proportional) damping due to ω_1, ω_2 and ζ_1

3.5. Solution of the SDOF system

The previous chapters demonstrated how to reduce a distributed-parameter system or a MDOF system to a set of equivalent SDOF systems using the modal analysis. Therefore, in this chapter we place the focus on SDOF systems.
First, the basic equations for the

- undamped and unforced SDOF system,
- the damped but unforced SDOF system,
- the damped SDOF system with harmonic excitation and
- the dameped SDOF system with linear excitation

are discussed.
Second, the SDOF systems, which result due to different load models (moving load model, 2D multi-body load model) representing the train crossing and the consequences regarding the coupling of theses SDOF systems are investigated. Finally, the numerical and, if existing, the analytical solutions for the above mentioned SDOF systems are presented.

3.5.1. SDOF system — basic equations

In the following chapters the well known basic equations for the SDOF system are presented, as they are essential for the further discussion.

Spring-mass model

In Figure 3.12 the spring-mass model, which connects the mass m with a linear spring k to a fixed object, is illustrated ([27] p.5 et sqq.).

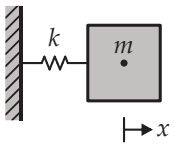

Figure 3.12.: SDOF — spring-mass model

Summing the forces due to a motion in x-direction leads to the equation of motion

$$m\ \ddot{x}(t) + k\ x(t) = 0 \tag{3.128}$$

With the solution approach $x(t) = A_1\ cos(\omega t) + A_2\ sin(\omega t)$ results

$$\omega = \sqrt{\frac{k}{m}} \tag{3.129}$$

Considering the initial conditions $x(t = 0) = x_0$ and $v(t = 0) = \dot{x}(t = 0) = v_0$ the solution of the equation of motion for the mass-spring model becomes

$$x(t) = x_0\ cos(\omega t) + \frac{v_0}{\omega}\ sin(\omega t) \tag{3.130}$$

Spring-mass-damper model

If *viscous damping* is added, in the form of the dashpot c, the spring-mass-damper model — see Figure 3.13 — results ([27] p.21 et sqq.).

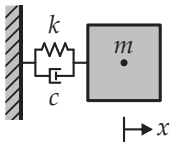

Figure 3.13.: SDOF — spring-mass-damper model

The term $c\ \dot{x}(t)$ in Equation (3.131), which describes the decay of the oscillating SDOF system, is chosen partly due to physical and mathematical convenience.

$$m\ \ddot{x}(t) + c\ \dot{x}(t) + k\ x(t) = 0 \tag{3.131}$$

However, substituting the solution approach $x_h(t) = a\ e^{\lambda t}$ into Equation (3.131 leads to the *characteristic equation*

$$m\ \lambda^2 + c\ \lambda + k = 0 \tag{3.132}$$

Using the quadratic formula yields the solution

$$\lambda_{1,2} = -\frac{c}{2\ m} \pm \frac{c}{2\ m}\ \sqrt{c^2 - 4\ k\ m} \tag{3.133}$$

Depending on the value of the discriminant $c^2 - 4\ k\ m$, three different solutions for λ and hence $x(t)$ are obtained:

- $c^2 - 4\ k\ m > 0$: Two real solutions exist and a non-oscillatory response results — the movement is called *overdamped motion*.
- $c^2 - 4\ k\ m = 0$: Two equal real solutions exist and a non-oscillatory response results as well — the movement is called *critically damped motion*.
- $c^2 - 4\ k\ m < 0$: Two complex solutions exist and a oscillatory response results — the movement is called *underdamped motion*.

It is useful to introduce the *critical damping coefficient* c_{cr}

$$c_{cr} = 2\sqrt{k\ m} = 2\ m\ \omega \tag{3.134}$$

and the non-dimensional *damping ratio* ζ

$$\zeta = \frac{c}{c_{cr}} = \frac{c}{2\sqrt{k\ m}} = \frac{c}{2\ m\ \omega} \tag{3.135}$$

Substituting Equations (3.129) and (3.135) into (3.131) and dividing by m yields

$$\ddot{x}(t) + 2\ \zeta\ \omega\ \dot{x}(t) + \omega^2\ x(t) = 0 \tag{3.136}$$

Furthermore, Equation (3.133) is rewritten to

$$\lambda_{1,2} = -\zeta\ \omega \pm \omega\ \sqrt{\zeta^2 - 1} \tag{3.137}$$

Here only the common case of the *underdamped motion* $\zeta < 1$ is discussed, which leads to

$$\sqrt{\zeta^2 - 1} = \sqrt{(1 - \zeta^2)(-1)} = \sqrt{1 - \zeta^2}\ j \tag{3.138}$$

where $j = \sqrt{-1}$ and subsequently the two roots become

$$\begin{aligned} \lambda_1 &= -\zeta\ \omega + \omega\ \sqrt{1 - \zeta^2}\ j \\ \lambda_2 &= -\zeta\ \omega - \omega\ \sqrt{1 - \zeta^2}\ j \end{aligned} \tag{3.139}$$

Introducing the *damped natural frequency* ω_d yields

$$\omega_d = \omega\ \sqrt{1 - \zeta^2} \tag{3.140}$$

Due to the two roots there are two solutions

$$x_h(t) = a_1\ e^{\lambda_1 t} \qquad \text{and} \qquad x_h(t) = a_2\ e^{\lambda_2 t} \tag{3.141}$$

additionally, since Equation (3.131) is linear, the sum of two solutions is also a solution, hence the response $x_h(t)$ is ([27] p.18)

$$x_h(t) = a_1\ e^{\lambda_1 t} + a_2\ e^{\lambda_2 t} \tag{3.142}$$
$$x_h(t) = e^{-\zeta\omega t}\left(a_1\ e^{j\omega_d t} + a_2\ e^{-j\omega_d t}\right)$$

Using the *Euler relations*, this can be written as

$$x_h(t) = e^{-\zeta\omega t}\left[A\cos(\omega_d t) + B\sin(\omega_d t)\right] \tag{3.143}$$

The constants A and B, as the constants a_1 and a_2, are obtained considering the initial condition like in the case of the mass-spring system.

Spring-mass-damper model and harmonic excitation

If a harmonic excitation is applied on the spring-mass-damper model, the situation presented in Figure 3.14 results ([48] p.43 et sqq.).

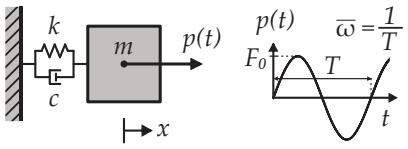

Figure 3.14.: SDOF — spring-mass-damper model and harmonic excitation

The harmonic excitation is considered in form of the term $F_0\ \sin(\overline{\omega}t)$ in the equation of motion

$$m\ \ddot{x}(t) + c\ \dot{x}(t) + k\ x(t) = p(t) = F_0\ \sin(\overline{\omega}t) \tag{3.144}$$

Dividing by the mass m and considering Equations (3.129) and (3.135) leads to

$$\ddot{x}(t) + 2\ \zeta\ \omega\ \dot{x}(t) + \omega^2\ x(t) = \frac{F_0}{m}\ \sin(\overline{\omega}t) \tag{3.145}$$

Equation (3.145) is a linear non-homogeneous differential equation with a solution consisting of a homogeneous and a particular solution

$$x(t) = x_h(t) + x_p(t) \tag{3.146}$$

The latter can be found assuming it has the same shape as the forcing function ([27] p.119) but with a different amplitude and phase. The phase shift is argued due to the influence of the damping force. Therefore, the particular solution is expected to be of the form

$$x_p(t) = C\cos(\overline{\omega}t) + D\sin(\overline{\omega}t) \tag{3.147}$$

Substituting Equation (3.147) and its derivatives $\dot{x}_p(t)$ and $\ddot{x}_p(t)$ into the equation of motion (3.145) and grouping the terms as coefficients of $\cos(\overline{\omega}t)$ and $\sin(\overline{\omega}t)$ leads to

$$\left(-\overline{\omega}^2\ D + 2\ \zeta\ \omega\ \overline{\omega}\ C + \omega^2\ D - \frac{F_0}{m}\right)\sin(\overline{\omega}t)$$
$$+\left(-\overline{\omega}^2\ C - 2\ \zeta\ \omega\ \overline{\omega}\ D + \omega^2\ C\right) \qquad \cos(\overline{\omega}t) = 0 \tag{3.148}$$

Equation (3.148) must hold for all time, therefore the coefficients of $\cos(\overline{\omega}t)$ and $\sin(\overline{\omega}t)$ must vanish. This yields to two equations for the two coefficients C and D which result for

$$\beta = \frac{\overline{\omega}}{\omega} \tag{3.149}$$

to

$$\begin{aligned} C &= \frac{F_0}{k}\left[\frac{-2\,\zeta\,\beta}{(1-\beta^2)^2+(2\,\zeta\,\beta)^2}\right] \\ D &= \frac{F_0}{k}\left[\frac{1-\beta^2}{(1-\beta^2)^2+(2\,\zeta\,\beta)^2}\right] \end{aligned} \tag{3.150}$$

Hence, the particular solution is described completely. However, neither the displacement $x_p(t)$ nor the velocity $\dot{x}_p(t)$ provide for the point in time $t = 0$ the value zero. In combination with the homogeneous solution — see Equation (3.143) — these initial conditions need to be fulfilled

$$\begin{aligned} x(t=0) &= x_h(t=0) + x_p(t=0) = 0 \\ \dot{x}(t=0) &= \dot{x}_h(t=0) + \dot{x}_p(t=0) = 0 \end{aligned} \tag{3.151}$$

which leads to

$$A = -C \qquad B = \frac{-\zeta\,\omega\,C - \overline{\omega}\,D}{\omega_d} \tag{3.152}$$

The complete solution for the harmonic excitation of the spring-mass-damper system is consequently

$$\begin{aligned} x(t) &= x_h(t) + x_p(t) \\ &= e^{-\zeta\omega t}\left[A\cos(\omega_d t) + B\sin(\omega_d t)\right] + \left[C\cos(\overline{\omega}t) + D\sin(\overline{\omega}t)\right] \end{aligned} \tag{3.153}$$

and regarding the acceleraton $\ddot{x}(t)$

$$\begin{aligned} \ddot{x}(t) = e^{-\zeta\omega t}\Big\{ &\left[(-\zeta\omega)^2 - \omega_d^2\right]\left[A\cos(\omega_d t) + B\sin(\omega_d t)\right]\ldots \\ &\cdots + 2\,(-\zeta\omega)^2\,\omega_d\left[-A\sin(\omega_d t) + B\cos(\omega_d t)\right]\Big\}\ldots \\ &\cdots - \overline{\omega}^2\left[C\cos(\overline{\omega}t) + D\sin(\overline{\omega}t)\right] \end{aligned} \tag{3.154}$$

Spring-mass-damper model and linear excitation

In case of a linear excitation, as shown in Figure 3.15, the following equation of motion results ([48] p.41 et sqq.)

$$m\,\ddot{x}(t) + c\,\dot{x}(t) + k\,x(t) = p(t) = F_0 + \Delta F\,t \tag{3.155}$$

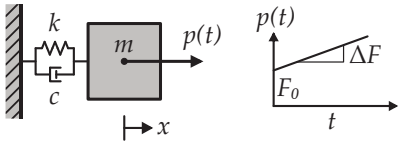

Figure 3.15.: SDOF — spring-mass-damper model and linear excitation

Like for the harmonic excitation, the solution again consists of a homogeneous and particular solution. The latter is assumed to be of the form

$$x_p(t) = \frac{\Delta F}{k}\, t - \frac{c\ \Delta F}{k^2} + \frac{F_0}{k} \tag{3.156}$$

Within the particular solution a linear time behaviour means a linear increase of the displacement and hence of the spring force. Furthermore, the constant velocity causes a constant restraining force of the damper ([48] p.41).

The contradiction regarding the required initial conditions for the point in time $t = 0$

$$x(t=0) = 0 \qquad \dot{x}(t=0) = 0 \tag{3.157}$$

and the actual initial values of the particular solution

$$x_p(t=0) = -\frac{c\ \Delta F}{k^2} + \frac{F_0}{k} \qquad \dot{x}_p(t=0) = \frac{\Delta F}{k} \tag{3.158}$$

is again correct by considering the homogeneous $x_h(t)$ solution (Equation (3.143)) like for the harmonic excitation — see Equation (3.151) — which leads to the constant coefficients of the harmonic solution

$$A = \frac{c\ \Delta F}{k^2} - \frac{F_0}{k} \qquad B = \left[\frac{c\ \Delta F}{k^2} - \frac{F_0}{k}\right] \frac{\zeta\ \omega}{\omega_d} - \frac{\Delta F}{k\ \omega_d} \tag{3.159}$$

The complete solution for the linear excitation of the spring-mass-damper system results to

$$\begin{aligned} x(t) &= x_h(t) + x_p(t) \\ &= e^{-\zeta\omega t}\left[A\cos(\omega_d t) + B\sin(\omega_d t)\right] + \left[\frac{\Delta F}{k}\, t - \frac{c\ \Delta F}{k^2} + \frac{F_0}{k}\right] \end{aligned} \tag{3.160}$$

and regarding the acceleraton $\ddot{x}(t)$

$$\begin{aligned} \ddot{x}(t) = e^{-\zeta\omega t}\Big\{ &\left[(-\zeta\omega)^2 - \omega_d^2\right]\left[A\cos(\omega_d t) + B\sin(\omega_d t)\right] \ldots \\ &\cdots + 2\,(-\zeta\omega)^2\,\omega_d\left[-A\sin(\omega_d t) + B\cos(\omega_d t)\right]\Big\} \end{aligned} \tag{3.161}$$

3.5.2. SDOF system — moving load model

The differential equation for the Bernoulli-Euler beam — see Equation (3.9) — including the load function of the moving load model — see Equation (3.41) — yields

$$EI\ w^{iv}(x,t) + \mu\ \ddot{w}(x,t) + c(x)\ \dot{w}(x,t) = p_z(x,t) = \sum_{i=1}^{n} P_i\ \Gamma(x_i)\ \delta(x - x_i) \tag{3.162}$$

Applying the *Ritz-Galerkin* approximation with the eigenfunctions as shape functions, hence the *modal analysis*, on Equation (3.162) reduces it to the modal equations like demonstrated in Equation (3.120)

$$\mathbf{M}^*\ \ddot{\mathbf{q}} + \mathbf{C}^*\ \dot{\mathbf{q}} + \mathbf{K}^*\ \mathbf{q} = \mathbf{p}^* \tag{3.163}$$

The modal force vector $\mathbf{p}^*$is calculated according to Equation (3.118) with

$$\mathbf{p}^* = \begin{pmatrix} \int_L p_z\ \phi_1(x)\ dx \\ \vdots \\ \int_L p_z\ \phi_j(x)\ dx \\ \int_L p_z\ \phi_m(x)\ dx \end{pmatrix} = \begin{pmatrix} p_1^* \\ \vdots \\ p_j^* \\ p_m^* \end{pmatrix} \tag{3.164}$$

Hence, for the j^{th} modal force yields

$$p_j^* = \int_L p_z\ \phi_j(x)\ dx = \int_L \sum_{i=1}^{n} P_i\ \Gamma(x_i)\ \delta(x - x_i)\ \phi_j(x)\ dx \tag{3.165}$$

and due to the characteristics of the dirac delta function — see Equation (3.46) — becomes, after solving the integral, to

$$p_j^* = \sum_{i=1}^{n} P_i\ \Gamma(x_i)\ \phi_j(x_i) \tag{3.166}$$

Therefore, one can write the modal equations like ([32] p.87)

$$\mathbf{M}^*\ \ddot{\mathbf{q}} + \mathbf{C}^*\ \dot{\mathbf{q}} + \mathbf{K}^*\ \mathbf{q} = \sum_{i=1}^{n} P_i\ \Gamma(x_i)\ \boldsymbol{\phi}(x_i) \tag{3.167}$$

with $\boldsymbol{\phi}(x_i)$ holding the eigenfunctions $\phi_j(x_i)$ of each SDOF system

$$\boldsymbol{\phi}^T(x_i) = \left(\ \phi_1(x_i),\ \ \cdots,\ \ \phi_j(x_i),\ \ \phi_m(x_i)\ \right) \tag{3.168}$$

Each SDOF system (represented by each line) of Equation (3.167) is decoupled and linear. Therefore, it is possible to solve the system of equations for one single load of e.g. '1 kN'. The answer for a whole train crossing (various consecutive single loads) is then obtained via superposition of the the '1 kN' results under weighting regarding the real axle set loads ([32] p.87). In [56] analytical solutions with various boundary conditions (simply supported, clamped-clamped, clamped-hinged, cantilever beam) for the Bernoulli-Euler beam subjected to single loads moving at constant speed are presented. However, in the following chapter the analytical solution for the simply supported case is presented which may be found in e.g. [32] as well.

Analytical solution — simply supported Bernoulli-Euler beam

As mentioned above, the system of equations in Equation (3.167) are decoupled and linear. Hence, in the following chapter the j^{th} SDOF system is examined in detail. Furthermore, the crossing of one single load is considered, as the results for an entire train are obtained by simple superposition, considering the shift between the individual axle loads — see Figure 3.2.

With the eigenfunctions for the simple beam based on Equation (3.39) (B_2 is set to 1)

$$\phi_j(x) = \sin\left(\frac{j\pi}{L}x\right) \qquad j = 1, 2, 3, \ldots \tag{3.169}$$

the equation of motion for the j^th SDOF system subjected to one single load (see Equation (3.166) with $n = 1$) becomes

$$m_j^*\ \ddot{q}_j(t) + c_j^*\ \dot{q}_j(t) + k_j^*\ q_j(t) = p_j^*(t) = P_1\ \Gamma(x_1)\ \sin\left(\frac{j\pi}{L}x_1\right) \tag{3.170}$$

Furthermore, as $x_1 = v\ t$ (see Figure 3.2) Equation (3.170) yields to

$$m_j^*\ \ddot{q}_j(t) + c_j^*\ \dot{q}_j(t) + k_j^*\ q_j(t) = P_1\ \Gamma(x_1)\ \sin(\overline{\omega}_j t) \qquad \text{with: } \overline{\omega}_j = \frac{j\pi v}{L} \tag{3.171}$$

One can see that Equation (3.171) represents the equation of motion for a *spring-mass-damper model under harmonic excitation* according to Equation (3.144).

The modal mass m_j^*, the modal damping c_j^* and the modal stiffness k_j^* are determined with Equations (3.95), (3.116) and (3.117) and become for the simple beam to

$$\begin{aligned} m_j^* &= \int_L \mu\ \phi_j^2(x)\ dx = \mu\ \frac{L}{2} \\ c_j^* &= \int_L c\ \phi_j^2(x)\ dx = c\ \frac{L}{2} \\ k_j^* &= \int_L EI\ \phi_j^{iv}(x)\ \phi_j(x)\ dx = EI\ \frac{j^4\pi^4}{2L^3} \end{aligned} \tag{3.172}$$

However, after considering Equations (3.129) and (3.135)

$$\omega_j = \sqrt{\frac{k_j^*}{m_j^*}} \qquad c_j^* = \zeta_j\ 2\ m_j^*\ \omega_j \tag{3.173}$$

and dividing Equation (3.171) by m_j^* yields Equation (3.145) in modal coordinates

$$\ddot{q}_j(t) + 2\ \zeta_j\ \omega_j\ \dot{q}_j(t) + \omega_j^2\ q_j(t) = \frac{P_1\ \Gamma(x_1)}{m_j^*}\ \sin(\overline{\omega}_j t) \tag{3.174}$$

with the solution according to Equation (3.153), here specified for the j^{th} SDOF system

$$q_j(t) = e^{-\zeta_j\omega_j t}\left[A_j\cos(\omega_{d,j}t) + B_j\sin(\omega_{d,j}t)\right] + \left[C_j\cos(\overline{\omega}_j t) + D_j\sin(\overline{\omega}_j t)\right] \tag{3.175}$$

$$\ddot{q}_j(t) = e^{-\zeta_j \omega_j t} \Big\{ \left[\left(-\zeta_j \omega_j\right)^2 - \omega_{d,j}^2 \right] \left[A \cos(\omega_{d,j} t) + B \sin(\omega_{d,j} t) \right] \dots$$

$$\dots + \; 2 \left(-\zeta_j \omega_j\right)^2 \omega_{d,j} \left[- A \sin(\omega_{d,j} t) + B \cos(\omega_{d,j} t) \right] \Big\} \dots$$

$$\dots - \; \overline{\omega}_j^2 \left[C \cos(\overline{\omega}_j t) + D \sin(\overline{\omega}_j t) \right] \tag{3.176}$$

$$\beta_j = \frac{\overline{\omega}_j}{\omega_j} \qquad \omega_{d,j} = \omega_j \sqrt{1 - \zeta_j^2}$$

$$A_j = -C_j \qquad B_j = \frac{-\zeta_j \; \omega_j \; C_j - \overline{\omega}_j \; D_j}{\omega_{d,j}}$$

$$C_j = \frac{P_1 \; \Gamma(x_1)}{k_j^*} \left[\frac{-2 \; \zeta_j \; \beta_j}{(1 - \beta_j^2)^2 + (2 \; \zeta_j \; \beta_j)^2} \right] \qquad D_j = \frac{P_1 \; \Gamma(x_1)}{k_j^*} \left[\frac{1 - \beta_j^2}{(1 - \beta_j^2)^2 + (2 \; \zeta_j \; \beta_j)^2} \right]$$

However, Equation (3.175) describes the so called 'phase 1' which represents the single axle crossing the beam. In order to consider the so called 'phase 2', after the single force left the beam, one uses the conditions (displacement and velocity) at the end of phase 1 as initial conditions for the free motion of the damped SDOF system according to Equation (3.143). With the analytical solution, considering phase 1 and phase 2, one can calculate the deflection of the beam regarding the j^{th} SDOF system in physical coordinates $\widetilde{w}_j(x,t)$ using Equation (3.85)

$$\widetilde{w}_j(x,t) = \phi_j(x) \; q_j(t) \tag{3.177}$$

After solving each SDOF system ($j = 1 \dots m$) analytically and independently from each other, these can be summed up to the approximate solution of the beam's deflection $\widetilde{w}(x,t)$, again according to Equation (3.85)

$$w(x,t) \approx \widetilde{w}(x,t) = \sum_{j=1}^{m} \phi_j(x) \; q_j(t) \tag{3.178}$$

Theoretically, if an infinite number of eigenfunctions ($m = \infty$) is considered, then one obtains the exact solution, hence $w(x,t) = \widetilde{w}(x,t)$. After calculating the crossing of a '1 kN' single load, the result for a train is obtained by considering the actual axle-set loads and the time difference with which the axle-sets approach the structure.

Analytical solution — general structure

The following approach was developed by [48] leading to a powerful and for engineers easy to implement software tool which allows to simulate high-speed train crossings on complex bridge structures in an analytical way. The general idea is to use the analytical solutions for SDOF system under harmonic and linear excitation, which were presented in the previous chapters. Therefore, the bridge structure is first modelled in a commercial FEM program. In order to be able to reduce the problem from a MDOF system to a set of SDOF systems, the second step is to solve the eigenvalue problem of the bridge structure using the FEM software as well. One obtains for all modes of interest ($j = 1 \dots N$) the natural frequencies ω_j, modal masses m_j^* and the mode shapes $\boldsymbol{\phi}_{rail,j,FEM}$ along the centerline of the rail where the single force crossing is simulated as presented in Figure 3.16.

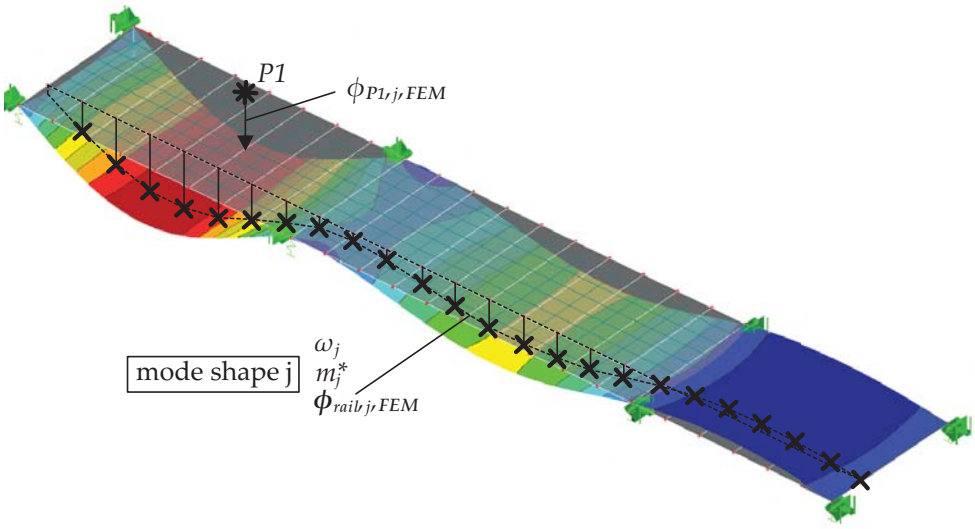

Figure 3.16.: 3-span-plate structure modelled with FEM — total length L=24m — mode shape j — mode shape along centerline of rail axis $\boldsymbol{\phi}_{rail,j,FEM}$

In the next step the mode shape $\boldsymbol{\phi}_{rail,j,FEM}$ is approximated by $l = 1 \ldots h$ sin-functions and one linear function using the *least squares method* [48]. The approximated mode shape $\phi_{rail,j,app}(x)$ is then calculated according to Equation (3.179) with $a_{j,l}$ being the amplitudes of the sin-functions and $b_{j,h+1}$ and $b_{j,h+2}$ defining the linear function.

$$\boldsymbol{\phi}_{rail,j,FEM} \approx \phi_{rail,j,app}(x) = \sum_{l=1}^{h} a_{j,l} \ \sin\left(\frac{x}{L}\ l\pi\right) + \left(b_{j,h+1} + \frac{\left(b_{j,h+2} - b_{j,h+1}\right)}{L}\ x\right) \tag{3.179}$$

Figure 3.17 illustrates the general approach with eight ($h = 8$) sin-functions (first four are plotted) and the linear function yielding to $\phi_{rail,j,app}(x)$ for the 3-span-plate structure of Figure 3.16.
Reviewing the definition of the modal force p_j^* according to Equation (3.166) provides for the crossing of one single load P_1

$$p_j^* = P_1\ \Gamma(x_1)\ \phi_j(x_1) \qquad \text{with: } x_1 = v\ t \tag{3.180}$$

and inserting the approximated mode shape along the centerline of the rail $\phi_{rail,j,app}(x)$ for $\phi_j(x_1)$ leads with $x = x_1$ to

$$p_j^* = P_1\ \Gamma(x_1)\ \phi_{rail,j,app}(x_1) \qquad \text{with: } x_1 = v\ t \tag{3.181}$$

$$p_j^* = P_1\ \Gamma(x_1)\ \left[\sum_{l=1}^{h} a_{j,l}\ \sin\left(\overline{\omega}_l\ t\right) + \left(b_{j,h+1} + \frac{\left(b_{j,h+2} - b_{j,h+1}\right)\ v}{L}\ t\right)\right] \qquad \text{with: } \overline{\omega}_l = \frac{v\ \pi\ l}{L}$$

As the MDOF system in the FEM program was already decoupled by solving the eigenvalue problem, one can solve each line of the system of equations (each SDOF) independently of the other.

Therefore, the equation of motion for the j^{th} SDOF system becomes, regarding the crossing of

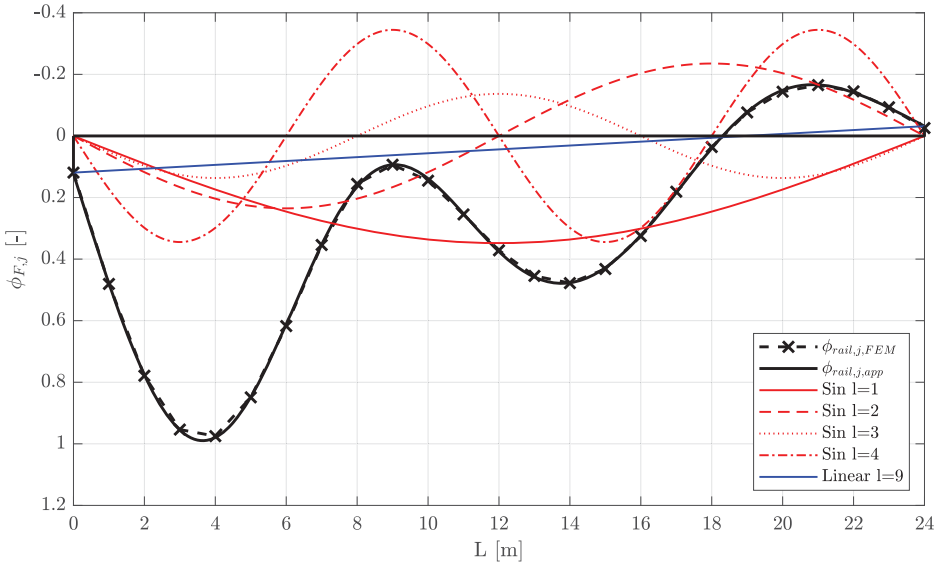

Figure 3.17.: Mode shape along centerline of rail axis $\boldsymbol{\phi}_{rail,j,FEM}$ — approximation with sin-functions and linear-functions by $\phi_{rail,j,app}(x)$

one single load along the centerline of the rail, to

$$m_j^* \ \ddot{q}_j(t) + c_j^* \ \dot{q}_j(t) + k_j^* \ q_j(t) = \ldots \tag{3.182}$$
$$\ldots \ P_1 \ \Gamma(x_1) \left[\sum_{l=1}^{h} a_{j,l} \ \sin\left(\overline{\omega}_l \ t\right) + \left(b_{j,h+1} + \frac{\left(b_{j,h+2} - b_{j,h+1}\right) \ v}{L} \ t \right) \right] \qquad \text{with: } \overline{\omega}_l = \frac{v \ \pi \ l}{L}$$

Figure 3.18 illustrates the meaning of Equation (3.182). The given modal force $p_j^*(t)$ is split up into h harmonic excitation terms $p_{j,l}^*(t)$ and one linear excitation term $p_{j,h+1}^*(t)$, which can be solved independently and analytically.

The modal mass m_j^*, modal damping c_j^* and modal stiffness k_j^* stay for each excitation within a SDOF system the same. However, for each harmonic excitation the solution according to Equation (3.153) is used, considering

$$F_0 = a_{j,l} \qquad \text{and} \qquad \overline{\omega} = \overline{\omega}_l = \frac{v \ \pi \ l}{L} \tag{3.183}$$

For the linear excitation the solution according to Equation (3.160) is used equally, considering

$$F_0 = b_{j,h+1} \qquad \text{and} \qquad \Delta F = \frac{\left(b_{j,h+2} - b_{j,h+1}\right) \ v}{L} \tag{3.184}$$

After evaluating the analytical solutions for each excitation, the SDOF system's total response $q_j(t)$ is obtained with

$$q_j(t) = \sum_{l=1}^{h} q_{j,l}(t) + q_{j,h+1}(t) \tag{3.185}$$

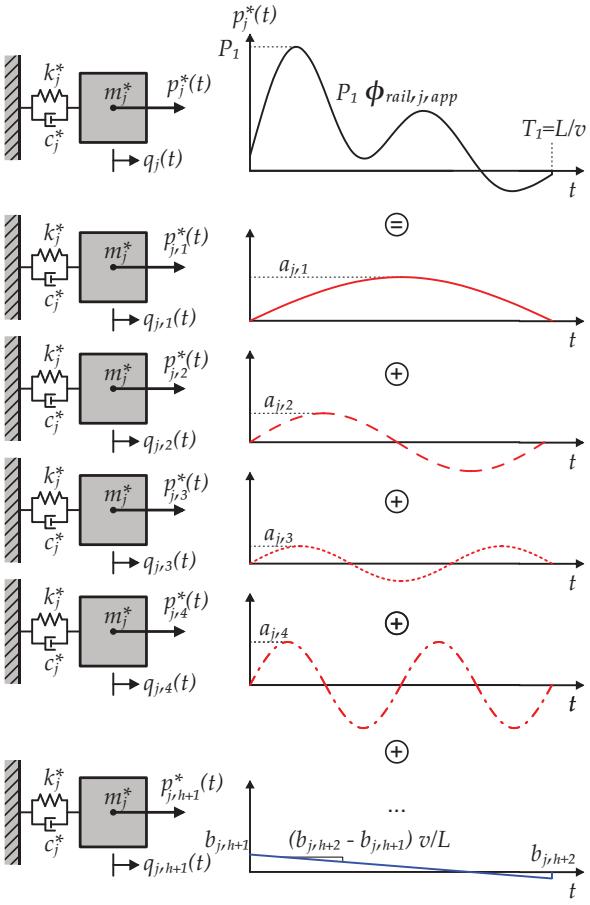

Figure 3.18.: SDOF system for the j^{th} mode — modal force $p_j^*(t)$ approximated by harmonic and linear excitation

This procedure is repeated for all considered mode shapes ($j = 1 \dots m$) and afterwards transformed back to the physical coordinate system according to Equation (3.85) yielding to the deflection along the centerline of the rail

$$w_{rail}(x,t) \approx \widetilde{w}_{rail}(x,t) = \sum_{j=1}^{m} \phi_{rail,j,app}(x)\ q_j(t) \tag{3.186}$$

In case one would like to obtain the deflections on another point of the structure, e.g. at point P1 in Figure 3.16, the to point P1 associated values of the mode shapes $\phi_{P1,j,FEM}$ need to be considered

$$w_{P1}(t) \approx \widetilde{w}_{P1}(t) = \sum_{j=1}^{m} \phi_{P1,j,FEM}\ q_j(t) \tag{3.187}$$

The same approach is applied in case one would like to calculate internal forces, e.g. the bending moment $\widetilde{M}_{P1}(t)$ at point P1, due to the crossing of a single load along the centerline of the rail. Here, the bending moments at point P1 $M_{P1,j,FEM}$ associated to the individual mode shapes j need to be considered

$$M_{P1}(t) \approx \widetilde{M}_{P1}(t) = \sum_{j=1}^{m} M_{P1,j,FEM}\ q_j(t) \tag{3.188}$$

Numerical solution — general structure

Another approach is to solve the equations of motion of the SDOF system numerically. As presented in the previous chapters this is for the linear problem, due to the moving load model, not necessary. In case of coupled modal equations (e.g. for the 2D multi-body load model) the numerical solution can not be avoided anymore. However, here the numerical approach will be presented and implemented according to [32]. The programming is done by using the software *Matlab*, in particular *Simulink*. This software package allows to use block diagrams, which makes an intuitive programming possible. The first step is to rearrange the modal equation of motion in a way so that $\ddot{\mathbf{q}}$ is on one side of the equation. Hence, Equation (3.167) becomes

$$\ddot{\mathbf{q}} = [\mathbf{M}^*]^{-1} \left[\sum_{i=1}^{n} P_i\ \Gamma(x_i)\ \boldsymbol{\phi}(x_i) - \mathbf{C}^*\ \dot{\mathbf{q}} - \mathbf{K}^*\ \mathbf{q} \right] \tag{3.189}$$

Figure 3.19 illustrates the block diagram for the modal system of equations due to the moving load model. The modal mass matrix $\mathbf{M}^*$, modal damping matrix $\mathbf{C}^*$, modal stiffness matrix $\mathbf{K}^*$ and the modal force vector $\mathbf{p}^*$ are represented as blocks and interact via the modal coordinates $\ddot{\mathbf{q}}$, $\dot{\mathbf{q}}$ and $\mathbf{q}$ with each other. The block 'product' combines the inverse of the modal mass matrix $\mathbf{M}^*$ and the sum of $-\mathbf{C}^*\ \dot{\mathbf{q}} - \mathbf{K}^*\ \mathbf{q}$ and the modal force vector $\mathbf{p}^*$ which needs to be equal to the start signal $\ddot{\mathbf{q}}$ ([32] p.91).
After solving the modal system of equations, *Simulink* returns the following results:

- time vector $\mathbf{t}$ for $l = 1 \dots h$ time steps
- matrix $\mathbf{ML\_q}$ with results for the modal coordinate $\mathbf{q}$

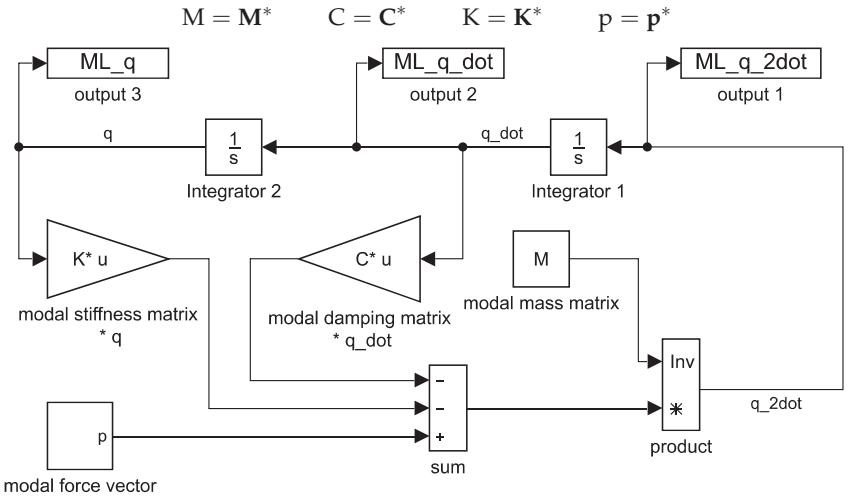

Figure 3.19.: *Simulink* block diagram for the modal system of equations and the moving load model

- matrix **ML_q_dot** with results for the modal coordinate $\dot{\mathbf{q}}$
- matrix **ML_q_2dot** with results for the modal coordinate $\ddot{\mathbf{q}}$

The structures of the time vector **t** and the matrix **ML_q** (with $j = 1 \dots m$ considered mode shapes; equivalent for **ML_q_dot** and **ML_q_2dot**) are

$$\mathbf{t} = \begin{pmatrix} t_1 \\ \vdots \\ t_l \\ t_h \end{pmatrix} \qquad \mathbf{ML\_q} = \begin{pmatrix} q_{11} & \cdots & q_{j1} & q_{m1} \\ \vdots & \ddots & & \\ q_{1l} & & q_{jl} & q_{ml} \\ q_{1h} & & q_{jh} & q_{mh} \end{pmatrix} \tag{3.190}$$

The numerical integration was performed using the from *Matlab* provided solver *113*, according to [32].

3.5.3. SDOF system — 2D multi-body model

The load function for the 2D multi-body model of one car is according to Equation (3.83)

$$p_z(x,t) = \sum_{i=1}^{4} \{F_{stat,i} - F_{k1i} - F_{c1i} - m_{Wi}\, \ddot{w}(x_i)\}\ \Gamma(x_i)\ \delta(x - x_i) \tag{3.191}$$

In order to apply the *modal analysis* on the above stated load function, the acceleration $\ddot{w}(x_i)$ needs to be substituted by the *Ritz* approximation ([32] p.69 et sqq.)

$$w(x,t) \approx w^*(x,t) = \sum_{j=1}^{m} \phi_j(x)\ q_j(t) \qquad x = x_i(t) \tag{3.192}$$

and subsequently, considering the variable x_i being a function of time as well, its second derivative with respect to time yields

$$\ddot{w}^*(x_i,t) = \sum_{j=1}^{m} \left(\ddot{q}_j\ \phi_j(x_i) + 2\ \dot{q}_j\ \dot{\phi}_j(x_i) + q_j\ \ddot{\phi}_j(x_i)\right) \tag{3.193}$$

The j^{th} eigenfunction for the Bernoulli-Euler beam, according to Equation (3.22) and considering $x = x_i(t) = v\ t - l_{1,i}$ according to Figure 3.2, is

$$\phi_j(x_i) = B_{1,j}\cos(k_j x_i) + B_{2,j}\sin(k_j x_i) + B_{3,j}\cosh(k_j x_i) + B_{4,j}\sinh(k_j x_i) \tag{3.194}$$

and its first derivative with respect to time, considering Equation (3.23) leads to

$$\begin{aligned}\dot{\phi}_j(x_i) &= v\ k_j\ \left[-B_{1,j}\ \sin(k_j x_i) + B_{2,j}\ \cos(k_j x_i) + B_{3,j}\ \sinh(k_j x_i) + B_{4,j}\ \cosh(k_j x_i)\right] \\ \dot{\phi}_j(x_i) &= v\ \phi_j'(x_i)\end{aligned} \tag{3.195}$$

respectively its second derivative with respect to time, considering Equation (3.24) yields to

$$\begin{aligned}\ddot{\phi}_j(x_i) &= v^2\ k_j^2\ \left[-B_{1,j}\ \cos(k_j x_i) - B_{2,j}\ \sin(k_j x_i) + B_{3,j}\ \cosh(k_j x_i) + B_{4,j}\ \sinh(k_j x_i)\right] \\ \ddot{\phi}_j(x_i) &= v^2\ \phi_j''(x_i)\end{aligned} \tag{3.196}$$

Substituting Equations (3.195) and (3.196) into (3.193) yields

$$\ddot{w}(x,t) \approx \ddot{w}^*(x_i,t) = \sum_{j=1}^{m}(\underbrace{\ddot{q}_j\ \phi_j(x_i)}_{(a)} + \underbrace{2\ v\ \dot{q}_j\ \phi_j'(x_i)}_{(b)} + \underbrace{v^2\ q_j\ \phi_j''(x_i)}_{(c)}) \tag{3.197}$$

The three terms in Equation (3.197) one can interpret as follows ([17] p.65)

(a) Vertical acceleration of the beam
(b) Coriolis acceleration due to the rotation velocity of the cross section
(c) Influence of the beam curvature

Substituting Equation (3.197) into (3.191) and applying the modal analysis, like in Chapter 3.5.2, on the resulting load function yields the following modal load vector for the 2D multi-body model of one car

$$\mathbf{p}^* = \sum_{i=1}^{4}\left\{F_{stat,i} - F_{k1i} - F_{c1i} - m_{Wi}\ \sum_{j=1}^{m}\left[\ddot{q}_j\ \phi_j(x_i) + 2\ v\ \dot{q}_j\ \phi_j'(x_i) + v^2\ q_j\ \phi_j''(x_i)\right]\right\}\ \Gamma(x_i)\ \boldsymbol{\phi}(x_i) \tag{3.198}$$

and subsequently the system of equations for the bridge structure — superscripts b stands for 'bridge' on the system matrices — results to

$$\begin{aligned}\mathbf{M}^{*,b}\ \ddot{\mathbf{q}} + \mathbf{C}^{*,b}\ \dot{\mathbf{q}} + \mathbf{K}^{*,b}\ \mathbf{q} = \sum_{i=1}^{4}\Bigg\{F_{stat,i} - F_{k1i} - F_{c1i} - m_{Wi}\ \sum_{j=1}^{m}\Big[\ddot{q}_j\ \phi_j(x_i) + 2\ v\ \dot{q}_j\ \phi_j'(x_i) + \dots \\ \cdots + v^2\ q_j\ \phi_j''(x_i)\Big]\Bigg\}\ \Gamma(x_i)\ \boldsymbol{\phi}(x_i)\end{aligned} \tag{3.199}$$

Simultaneously, the equations of motion of the car — see Equation (3.73), superscript c stand for 'car' on the system matrices — need to be solved

$$\mathbf{M}^c\ \ddot{\mathbf{u}} + \mathbf{C}^c\ \dot{\mathbf{u}} + \mathbf{K}^c\ \mathbf{u} = -\mathbf{F}_w - \mathbf{F}_{\dot{w}} \tag{3.200}$$

Equations (3.199) are coupled with Equations (3.200) via the spring and damper forces. These are represented regarding the beam (Equations (3.199)) by F_{k1i} and F_{c1i} and regarding the train car by $\mathbf{F}_w$ and $\mathbf{F}_{\dot{w}}$. Furthermore, the 2D multi-body model of the train car is split up and distributed on both equations. The wheels with their mass m_{Wi} are part of the Equations for the beam (3.199) and constrained to the movement of the beam. The modelling of the wheels on the beam is performed as presented in Chapter 3.1.3 by using the moving mass model. On the other hand, the dynamic behaviour of the car body and the two bogies is described by the Equations (3.200) ([32] p.111).

Numerical solution — general structure

The differential equations mentioned in the chapter above (Equation (3.199) and (3.200)) can only be solved using numerical solutions, which is realized again with the software *Simulink*. Therefore, Equation (3.199) needs to be transformed in a way so that $\ddot{q}$ is on the left side of the equation. Subsequently, the algebraic loop of Equation (3.199) — term $\ddot{q}$ is part of the right and left side of the equation — will be resolved as follows considering only one wheel mass m_{Wi} (i=1) and two eigenfunctions $\phi_j(x_i)$ (j=2) ([32] p.112). Hence, Equation (3.199) becomes

$$\begin{bmatrix} m_1 & 0 \\ 0 & m_2 \end{bmatrix} \begin{pmatrix} \ddot{q}_1 \\ \ddot{q}_2 \end{pmatrix} + \begin{bmatrix} c_1 & 0 \\ 0 & c_2 \end{bmatrix} \begin{pmatrix} \dot{q}_1 \\ \dot{q}_2 \end{pmatrix} + \begin{bmatrix} k_1 & 0 \\ 0 & k_2 \end{bmatrix} \begin{pmatrix} q_1 \\ q_2 \end{pmatrix} = \dots \tag{3.201}$$

$$\left\{ F_{stat,1} - F_{k11} - F_{c11} - m_{W1} \left[\ddot{q}_1\, \phi_1(x_1) + 2\, v\, \dot{q}_1\, \phi_1'(x_1) + v^2\, q_1\, \phi_1''(x_1) \dots \right.\right.$$

$$\left.\left. \dots + \ddot{q}_2\, \phi_2(x_1) + 2\, v\, \dot{q}_2\, \phi_2'(x_1) + v^2\, q_2\, \phi_2''(x_1) \right] \right\} \Gamma(x_1) \begin{pmatrix} \phi_1(x_1) \\ \phi_2(x_1) \end{pmatrix}$$

which yields

$$\begin{bmatrix} m_1 & 0 \\ 0 & m_2 \end{bmatrix} \begin{pmatrix} \ddot{q}_1 \\ \ddot{q}_2 \end{pmatrix} + \begin{bmatrix} c_1 & 0 \\ 0 & c_2 \end{bmatrix} \begin{pmatrix} \dot{q}_1 \\ \dot{q}_2 \end{pmatrix} + \begin{bmatrix} k_1 & 0 \\ 0 & k_2 \end{bmatrix} \begin{pmatrix} q_1 \\ q_2 \end{pmatrix} = \dots \tag{3.202}$$

$$\left\{ F_{stat,1} \begin{pmatrix} \phi_1(x_1) \\ \phi_2(x_1) \end{pmatrix} - F_{k11} \begin{pmatrix} \phi_1(x_1) \\ \phi_2(x_1) \end{pmatrix} - F_{c11} \begin{pmatrix} \phi_1(x_1) \\ \phi_2(x_1) \end{pmatrix} \dots \right.$$

$$\dots - m_{W1} \left[\begin{bmatrix} \phi_1\phi_1 & \phi_2\phi_1 \\ \phi_1\phi_2 & \phi_2\phi_2 \end{bmatrix}_{x=x_1} \begin{pmatrix} \ddot{q}_1 \\ \ddot{q}_2 \end{pmatrix} + 2\, v \begin{bmatrix} \phi_1'\phi_1 & \phi_2'\phi_1 \\ \phi_1'\phi_2 & \phi_2'\phi_2 \end{bmatrix}_{x=x_1} \begin{pmatrix} \dot{q}_1 \\ \dot{q}_2 \end{pmatrix} \dots \right.$$

$$\left.\left. \dots + v^2 \begin{bmatrix} \phi_1''\phi_1 & \phi_2''\phi_1 \\ \phi_1''\phi_2 & \phi_2''\phi_2 \end{bmatrix}_{x=x_1} \begin{pmatrix} q_1 \\ q_2 \end{pmatrix} \right] \right\} \Gamma(x_1)$$

For m considered mode shapes, Equation (3.202) is in index notation

$$\mathbf{M}^{*,b}\, \ddot{\mathbf{q}} + \mathbf{C}^{*,b}\, \dot{\mathbf{q}} + \mathbf{K}^{*,b}\, \mathbf{q} = \sum_{i=1}^{4} \left\{ F_{stat,i}\, \boldsymbol{\phi}(x_i) - F_{k1i}\, \boldsymbol{\phi}(x_i) - F_{c1i}\, \boldsymbol{\phi}(x_i) \dots \right. \tag{3.203}$$

$$\left. \dots - m_{Wi} \left[\boldsymbol{\phi}(x_i)\, \boldsymbol{\phi}^T(x_i)\, \ddot{\mathbf{q}} + 2\, v\, \boldsymbol{\phi}(x_i)\, \boldsymbol{\phi}'^T(x_i)\, \dot{\mathbf{q}} + v^2\, \boldsymbol{\phi}(x_i)\, \boldsymbol{\phi}''^T(x_i)\, \mathbf{q} \right] \right\} \Gamma(x_i)$$

In order to eliminate the algebraic loop, all terms including $\ddot{\mathbf{q}}$ are put on the left side of the equation

$$\mathbf{M}^{*,b}\,\ddot{\mathbf{q}} + \sum_{i=1}^{4}\left\{m_{Wi}\,\boldsymbol{\phi}(x_i)\,\boldsymbol{\phi}^T(x_i)\,\Gamma(x_i)\right\}\,\ddot{\mathbf{q}} = \sum_{i=1}^{4}\left\{F_{stat,i}\,\boldsymbol{\phi}(x_i) - F_{k1i}\,\boldsymbol{\phi}(x_i) - F_{c1i}\,\boldsymbol{\phi}(x_i)\ldots\right.$$
$$\left.\cdots - \; m_{Wi}\left[2\,v\,\boldsymbol{\phi}(x_i)\,\boldsymbol{\phi}'^T(x_i)\,\dot{\mathbf{q}} + v^2\,\boldsymbol{\phi}(x_i)\,\boldsymbol{\phi}''^T(x_i)\,\mathbf{q}\right]\right\}\Gamma(x_i) - \mathbf{C}^{*,b}\,\dot{\mathbf{q}} - \mathbf{K}^{*,b}\,\mathbf{q} \tag{3.204}$$

Introducing the abbreviations for the modal mass matrix $\mathbf{M}^{*,b}_{nal}$ and the force vector $\mathbf{p}^{*,b}_{nal}$ avoiding the algebraic loop (subscript *nal* = no algebraic loop)

$$\mathbf{M}^{*,b}_{nal} = \mathbf{M}^{*,b} + \sum_{i=1}^{4}\left\{m_{Wi}\,\boldsymbol{\phi}(x_i)\,\boldsymbol{\phi}^T(x_i)\,\Gamma(x_i)\right\} \tag{3.205}$$

$$\mathbf{p}^{*,b}_{nal} = \sum_{i=1}^{4}\left\{F_{stat,i}\,\boldsymbol{\phi}(x_i) - F_{k1i}\,\boldsymbol{\phi}(x_i) - F_{c1i}\,\boldsymbol{\phi}(x_i)\ldots\right.$$
$$\left.\cdots - \; m_{Wi}\left[2\,v\,\boldsymbol{\phi}(x_i)\,\boldsymbol{\phi}'^T(x_i)\,\dot{\mathbf{q}} + v^2\,\boldsymbol{\phi}(x_i)\,\boldsymbol{\phi}''^T(x_i)\,\mathbf{q}\right]\right\}\Gamma(x_i) \tag{3.206}$$

finally yields

$$\ddot{\mathbf{q}} = \left[\mathbf{M}^{*,b}_{nal}\right]^{-1}\,\left\{\mathbf{p}^{*,b}_{nal} - \mathbf{C}^{*,b}\,\dot{\mathbf{q}} - \mathbf{K}^{*,b}\,\mathbf{q}\right\} \tag{3.207}$$

Figure 3.20 illustrates the block diagram for the modal system of equations presented in Equation (3.207). Like for the moving load model in Equation (3.189) the solver *ode113* was used here as well.

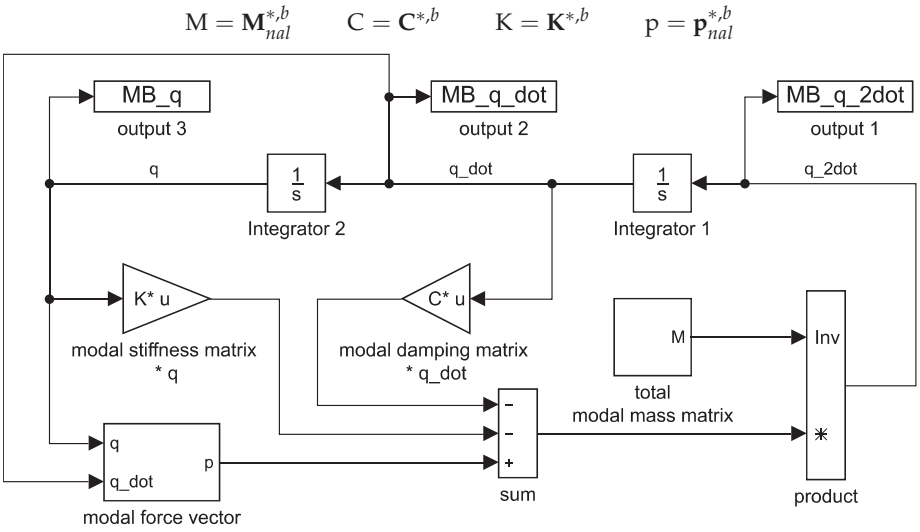

Figure 3.20.: *Simulink* block diagram for the modal system of equations and the 2D multi-body load model — according to Equation (3.207)

The block diagram for the modal force vector $\mathbf{p}_{nal}^{*,b}$ from Figure 3.20 is shown in detail in Figure 3.21 for three train cars.

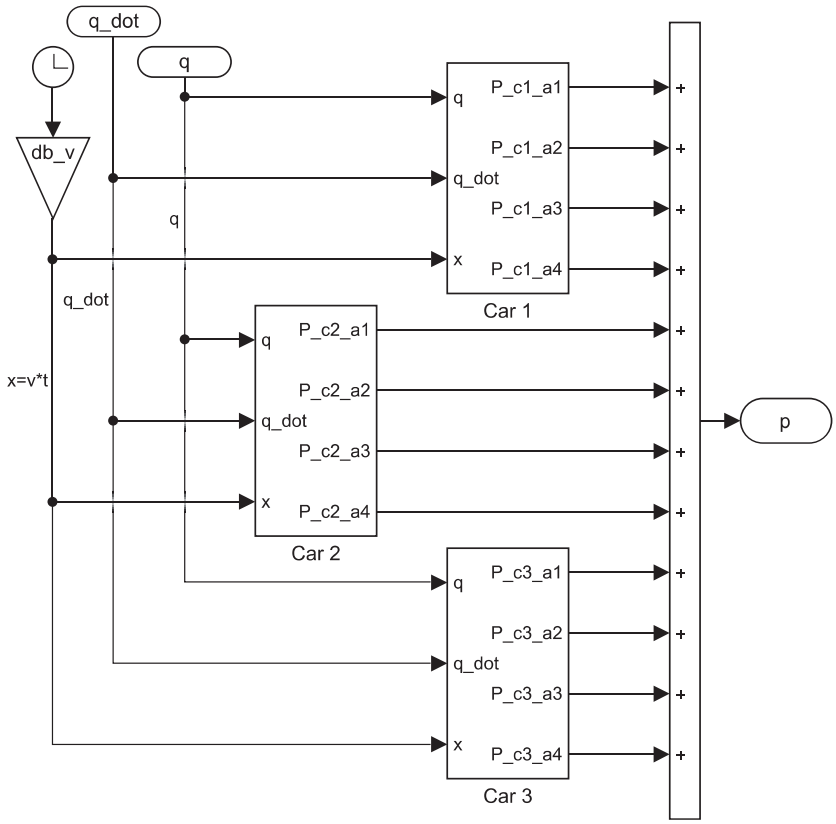

Figure 3.21.: *Simulink* block diagram for the modal force vector $\mathbf{p}_{nal}^{*,b}$ of the 2D multi-body load model due to three train cars — according to Equation (3.206)

In Figure 3.22 one can see the block diagram of the system of equations, according to Equation (3.200), for the train car number one (Car 1) illustrated in Figure 3.21.

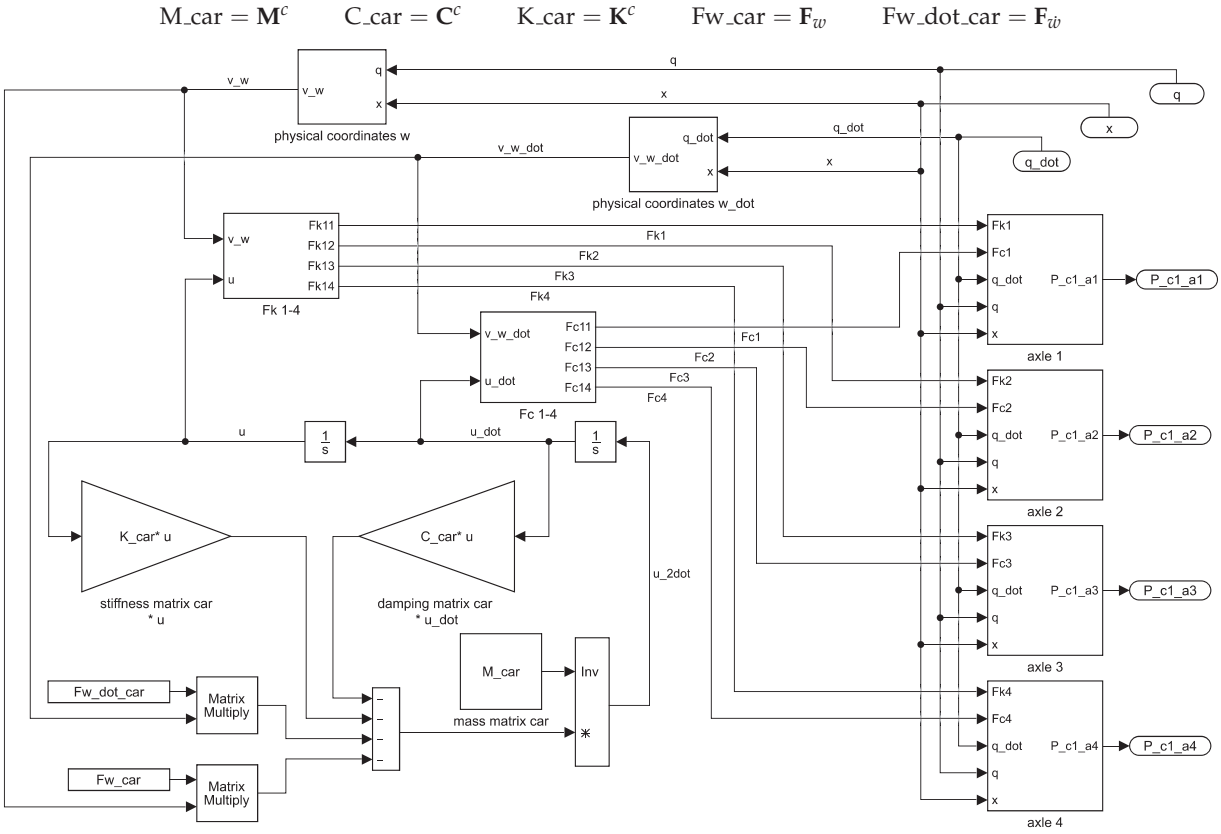

Figure 3.22.: *Simulink* block diagram for the system of equations of train car number one — according to Equation (3.200)

3.6. Non-dimensional response representation

The dynamic simulation of a train crossing, represented by the moving load model, on a bridge structure, represented by a Bernoulli-Euler beam, is a computationally demanding task. Therefore, simple methods were developed, which enable the practising engineer, without performing complex time history analysis, to quickly check whether a design criteria (e.g. maximum bridge deck acceleration $\ddot{w}(x,t)$), according to the relevant design code, is fulfilled or not. One methodology is the *non-dimensional response representation*, which according to [1] was developed simultaneously by [23] and [15]. The idea was to create diagrams, which are valid for a chosen bridge type (e.g. steel bridges) and a set of trains (e.g. the ten HSLM-A trains), only depending on the bridge span L and a frequency ratio β_1. With these two values, the practising engineer is able to determine first the non-dimensional result (e.g. the non-dimensional maximum bridge deck acceleration $\ddot{w}_{non-dim}(x,t)$) by evaluating the diagram. In the second step, the dimensional result (e.g. dimensional maximum bridge deck acceleration $\ddot{w}(x,t)$) for the given bridge structure, characterised by EI and μ, is calculated.

In the following paragraphs a quick overview of the mathematical and mechanical background will be given, which may be found in more detail in [16], [32], [33], [23], [1], [55], [54] and [53]. Additionally, an illustrative example explains the application of these non-dimensional response diagrams.

Equation (3.175), which is the solution of the j^{th} SDOF system representing the crossing of one single load P_1, may be written as

$$q_j(t) = \frac{P_1\,\Gamma(x_1)}{k_j^*}\left\{e^{-\zeta_j\omega_j t}\left[\hat{A}_j\cos(\omega_{d,j}t)+\hat{B}_j\sin(\omega_{d,j}t)\right]\ldots \right.$$
$$\left.\ldots+\left[\hat{C}_j\cos(\overline{\omega}_j t)+\hat{D}_j\sin(\overline{\omega}_j t)\right]\right\} \tag{3.208}$$

$$\beta_j = \frac{\overline{\omega}_j}{\omega_j} \qquad \omega_{d,j} = \omega_j\sqrt{1-\zeta_j^2}$$
$$\hat{A}_j = -\hat{C}_j \qquad \hat{B}_j = \frac{-\zeta_j\,\omega_j\,\hat{C}_j - \overline{\omega}_j\,\hat{D}_j}{\omega_{d,j}}$$
$$\hat{C}_j = \frac{-2\,\zeta_j\,\beta_j}{(1-\beta_j^2)^2+(2\,\zeta_j\,\beta_j)^2} \qquad \hat{D}_j = \frac{1-\beta_j^2}{(1-\beta_j^2)^2+(2\,\zeta_j\,\beta_j)^2}$$

Furthermore, considering an entire train, hence $i = 1\ldots n$ single loads, and the time difference Δt_{1i} of the first to the i_{th} single load (axle-set), results

$$q_j(t) = \frac{\sum_{i=1}^{n} P_i\,\Gamma(x_i)}{k_j^*}\left\{e^{-\zeta_j\omega_j(t-\Delta t_{1i})}\left[\hat{A}_j\cos(\omega_{d,j}(t-\Delta t_{1i}))+\hat{B}_j\sin(\omega_{d,j}(t-\Delta t_{1i}))\right]\ldots \right.$$
$$\left.\ldots+\left[\hat{C}_j\cos(\overline{\omega}_j(t-\Delta t_{1i}))+\hat{D}_j\sin(\overline{\omega}_j(t-\Delta t_{1i}))\right]\right\} \tag{3.209}$$

Substituting the modal stiffness k_j^* for the simple beam according to Equation (3.172) yields

$$q_j(t) = \frac{2L^3}{EI\ j^4\pi^4} \sum_{i=1}^{n} P_i\ \Gamma(x_i) \left\{ e^{-\zeta_j\omega_j(t-\Delta t_{1i})} \left[\hat{A}_j \cos(\omega_{d,j}(t-\Delta t_{1i})) + \hat{B}_j \sin(\omega_{d,j}(t-\Delta t_{1i})) \right] \dots \right.$$
$$\left. \dots + \left[\hat{C}_j \cos(\overline{\omega}_j(t-\Delta t_{1i})) + \hat{D}_j \sin(\overline{\omega}_j(t-\Delta t_{1i})) \right] \right\} \tag{3.210}$$

and expressing the main part of the resulting equation by $\lambda_{non-dim,j}$ leads to

$$q_j(t) = \frac{2L^3}{EI\ j^4\pi^4}\ \lambda_{non-dim,j} \tag{3.211}$$

$$\text{with: } \lambda_{non-dim,j} = \sum_{i=1}^{n} P_i\ \Gamma(x_i) \left\{ e^{-\zeta_j\omega_j(t-\Delta t_{1i})} \left[\hat{A}_j \cos(\omega_{d,j}(t-\Delta t_{1i})) + \hat{B}_j \sin(\omega_{d,j}(t-\Delta t_{1i})) \right] \dots \right.$$
$$\left. \dots + \left[\hat{C}_j \cos(\overline{\omega}_j(t-\Delta t_{1i})) + \hat{D}_j \sin(\overline{\omega}_j(t-\Delta t_{1i})) \right] \right\} \tag{3.212}$$

Equation (3.212) is formulated independently of the bending stiffness EI and the mass per unit length μ. This fact, is the basic idea of the non-dimensional representation. The bending stiffness EI and the mass per unit length μ are only represented in indirect form by ω_j ([32] p.125). In general, Equation (3.212) depends on the following variables[1]:

- Damping ratio ζ_j
- Ratio β_j of the forcing frequency $\overline{\omega}_j$ and natural frequency ω_j
- Loading term $\sum_{i=1}^{n} P_i\ \Gamma(x_i)$

Therefore, $\lambda_{non-dim,j}$ is a function of ζ_j, β_j and P_i. Hence, Equation (3.211) becomes

$$q_j(t) = \frac{2L^3}{EI\ j^4\pi^4}\ \lambda_{non-dim,j}(\zeta_j, \beta_j, P_i) \tag{3.213}$$

Substituting $q_j(t)$ from above together with the eigenfunction for the simple beam — see Equation (3.169) — into the *Ritz* approximation of Equation (3.85) yields

$$w(x,t) \approx \widetilde{w}(x,t) = \sum_{j=1}^{m} q_j(t)\ \phi_j(x)$$
$$\widetilde{w}(x,t) = \sum_{j=1}^{m} \frac{2L^3}{EI\ j^4\pi^4}\ \lambda_{non-dim,j}(\zeta_j, \beta_j, P_i)\ \sin\left(\frac{j\pi}{L}x\right) \tag{3.214}$$

[1] Neglecting the variable of time t.

Multiplying Equation (3.214) by $\frac{EI}{L^3}$ and dividing it by the trains maximum axle-set load P_{max}[1] yields

$$\widetilde{w}(x,t)\ \frac{EI}{P_{max}\ L^3} = \underbrace{\frac{1}{P_{max}}\ \sum_{j=1}^{m} \frac{2}{j^4\pi^4}\ \lambda_{non-dim,j}(\zeta_j,\beta_j,P_i)\ \sin\left(\frac{j\pi}{L}x\right)}_{f(\zeta_j,\beta_j,P_i,L)} \tag{3.215}$$

The resulting Equation (3.215) is now dimensionless and a function of ζ_j, β_j, P_i and L. Furthermore, for the simple beam, the ratios β_j can be expressed in the form ([32] p.126)

$$\beta_j = \frac{\overline{\omega}_j}{\omega_j} = \frac{\beta_1}{j} \tag{3.216}$$

meaning that all β_j can be expressed by β_1. Additionally, the damping ratios ζ_j usually depend on one defined ζ ([32] p.128). These assumptions lead to the non-dimensional deflection of the Bernoulli-Euler beam due to the crossing of a set of single loads ([32] p.126)

$$\widetilde{w}_{non-dim}(x,t) = \widetilde{w}(x,t)\ \frac{EI}{P_{max}\ L^3} = f(\zeta,\beta_1,P_i,L) \tag{3.217}$$

Consequently, the non-dimensional deflection $\widetilde{w}_{non-dim}(x,t)$ is the same for systems only differing in the bending stiffnesses EI and masses per unit lengths μ, as long as the resulting natural frequencies $\omega_{n,1}$ and hence the ratios β_1 are the same. Furthermore, it is possible to illustrate the non-dimensional deflections for a given train P_i and damping ratio ζ in dependence of the frequency ratio β_1 and beam length L ([32] p.128).

Equally, it is possible to find the non-dimensional bending Moment $\widetilde{M}_{y,non-dim}(x,t)$

$$\begin{aligned}
M_y(x,t) \approx \widetilde{M}_y(x,t) &= \sum_{j=1}^{m} q_j(t)\ \phi_j''(x)(-EI) \\
\widetilde{M}_y(x,t) &= \sum_{j=1}^{m} \frac{2L^3}{EI\ j^4\pi^4}\ \lambda_{non-dim,j}(\zeta_j,\beta_j,P_i)\ \frac{j^2\pi^2}{L^2}\ \sin\left(\frac{j\pi}{L}x\right)\ EI \\
\widetilde{M}_y(x,t) &= \sum_{j=1}^{m} \frac{2L}{j^2\pi^2}\ \lambda_{non-dim,j}(\zeta_j,\beta_j,P_i)\ \sin\left(\frac{j\pi}{L}x\right) \\
\widetilde{M}_{y,non-dim}(x,t) = \widetilde{M}_y(x,t)\ \frac{1}{P_{max}\ L} &= \underbrace{\frac{1}{P_{max}} \sum_{j=1}^{m} \frac{2}{j^2\pi^2}\ \lambda_{non-dim,j}(\zeta_j,\beta_j,P_i)\ \sin\left(\frac{j\pi}{L}x\right)}_{f(\zeta,\beta_1,P_i,L)}
\end{aligned} \tag{3.218}$$

[1] Since the equations are linear, the results are scaled down to a '1 kN' load regarding the maximum axle-set load P_{max}.

The similar approach regarding the acceleration leads with Equation (3.176) to

$$\begin{aligned}
\ddot{w}(x,t) \approx \widetilde{\ddot{w}}(x,t) &= \sum_{j=1}^{m} \ddot{q}_j(t)\ \phi_j(x) \\
\widetilde{\ddot{w}}(x,t) &= \sum_{j=1}^{m} \frac{1}{m_j^*}\ \ddot{\lambda}_{non-dim,j}(\zeta_j,\beta_j,P_i)\ \sin\left(\frac{j\pi}{L}x\right) \\
\widetilde{\ddot{w}}(x,t) &= \sum_{j=1}^{m} \frac{2}{\mu\ L}\ \ddot{\lambda}_{non-dim,j}(\zeta_j,\beta_j,P_i)\ \sin\left(\frac{j\pi}{L}x\right) \\
\widetilde{\ddot{w}}_{non-dim}(x,t) = \widetilde{\ddot{w}}(x,t)\ \frac{\mu\ L}{P_{max}} &= \underbrace{\frac{1}{P_{max}} \sum_{j=1}^{m} 2\ \ddot{\lambda}_{non-dim,j}(\zeta_j,\beta_j,P_i)\ \sin\left(\frac{j\pi}{L}x\right)}_{f(\zeta,\beta_1,P_i,L)}
\end{aligned} \tag{3.219}$$

In conclusion, the following relationships regarding the dimensional and non-dimensional expressions — see Equations (3.217), (3.218) and (3.219), here for an infinite number of considered eigenfunctions ($m = \infty$) — are summarized[1]

$$w_{non-dim}(x,t) = w(x,t)\ \frac{EI}{P_{max}\ L^3} \tag{3.220}$$

$$M_{y,non-dim}(x,t) = \frac{M_y(x,t)}{P_{max}\ L} \tag{3.221}$$

$$\ddot{w}_{non-dim}(x,t) = \ddot{w}(x,t)\ \frac{\mu\ L}{P_{max}} \tag{3.222}$$

The variable β_1 according to Equation (3.216) in [32] is equal to the variable S which is used in [1] and in this doctoral thesis.

$$\beta_1 = \frac{\overline{\omega}_1}{\omega_1} = \frac{\frac{\pi v}{L}}{n_1\ 2\ \pi} = S = \frac{v}{2\ L\ n_1} \tag{3.223}$$

In the following paragraphs, a short example, regarding the bridge deck acceleration due to the crossing of the HSLM-A3 train on three different bridge structures, will illustrate the general procedure. In practice, the time history for the acceleration is not of interest, but the absolute maximum acceleration $|a_{max}|$ along the x-axis of the bridge structure is essential as it is compared to a limit value of the relevant design code. In Figure 3.23 these absolute maximum accelerations $|a_{max}|$ due to the HSLM-A3 train for three different structures are plotted against the train speed.

On the other hand, Figure 3.24 shows the non-dimensional response spectra in black

$$|\bar{a}_{max}| = \max \ddot{w}_{non-dim}(x,t) = \max \ddot{w}(x,t)\ \frac{\mu\ L}{P_{max}} = |a_{max}|\ \frac{\mu\ L}{P_{max}} \tag{3.224}$$

which also includes the responses of the three different bridges. Hence, one needs to calculate once the non-dimensional response spectra $|\bar{a}_{max}|$, which is valid for a certain damping ratio ζ, bridge length L and train model, and is afterwards able to determine the dimensional results

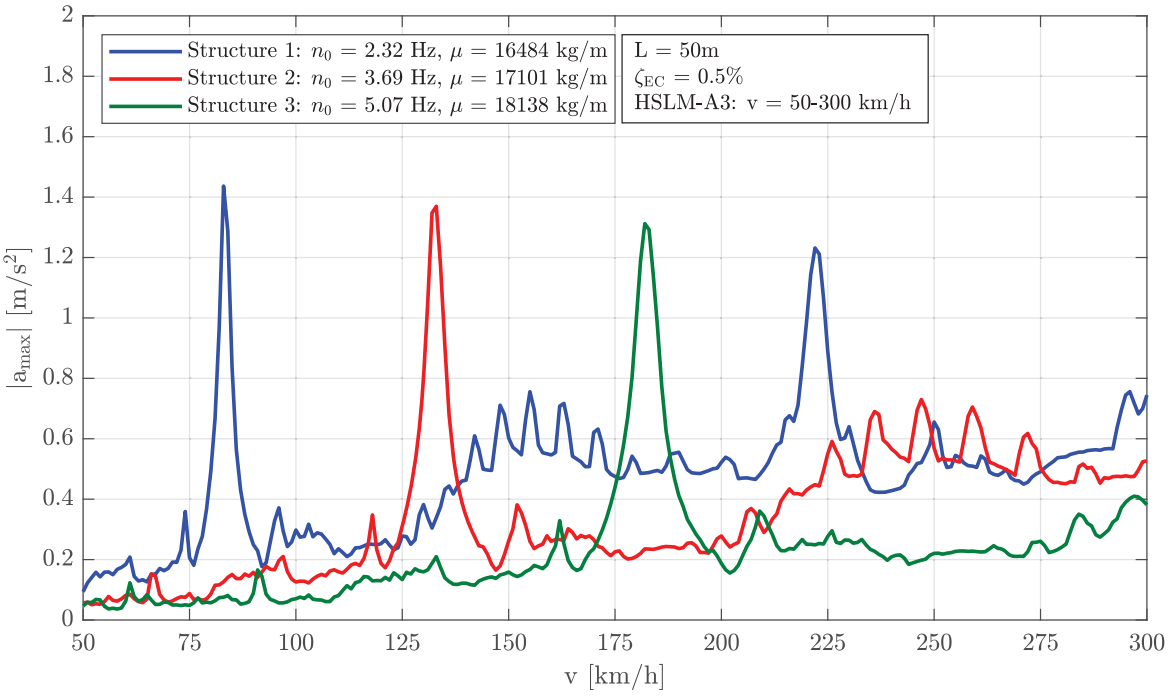

Figure 3.23.: Dimensional results $|a_{max}|$ due to HSLM-A3 train — for structures 1 to 3 — all L = 50m and ζ_{EC} = 0.5% Rayleigh like damping

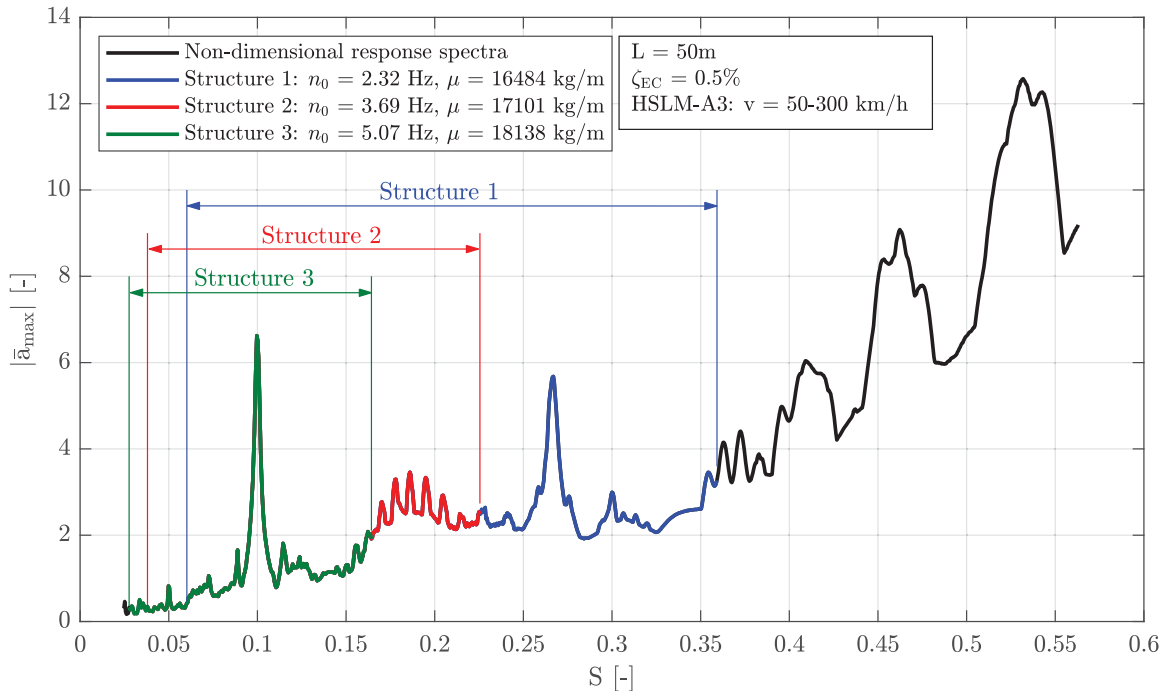

Figure 3.24.: Non-dimensional results $|\bar{a}_{max}|$ due to HSLM-A3 train — for structures 1 to 3 — all L = 50m and ζ_{EC} = 0.5% Rayleigh like damping

$|a_{max}|$ for a certain velocity range (here 50 to 300 km/h) and for all bridges differing in μ — see Equation (3.223) and Equation (3.224).

The procedure described above was demonstrated for a simple-span beam bridge with a total length of $L = 50m$. Calculating the non-dimensional response spectra for the range of lengths starting from 7m to 80m with a $\Delta L = 0.5m$ leads to Figure 3.25. The black line represents the non-dimensional response spectra of Figure 3.24.

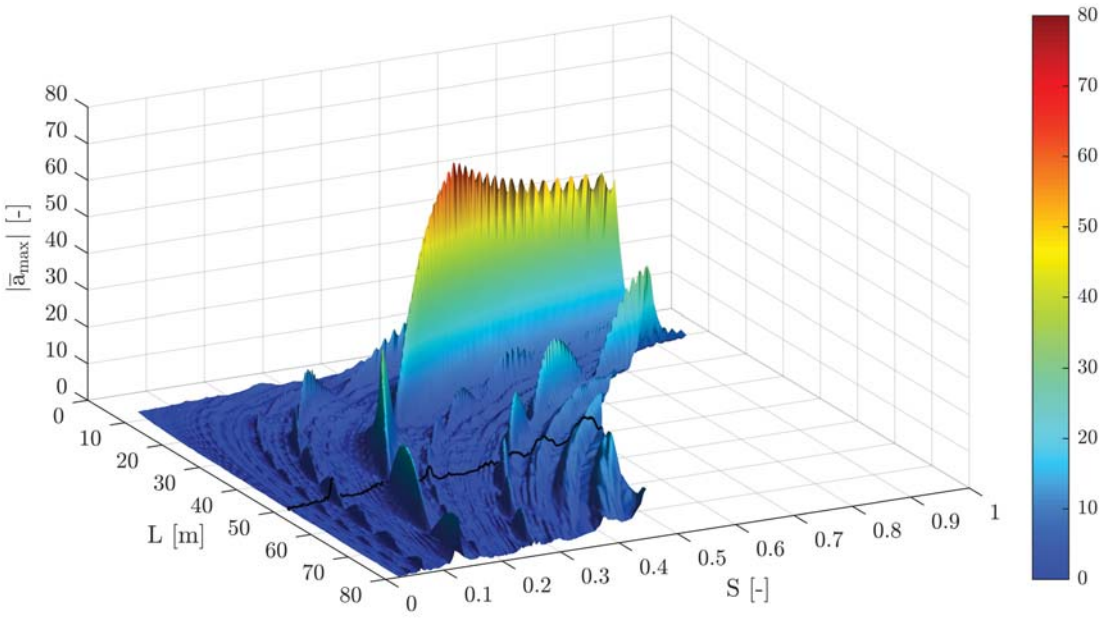

Figure 3.25.: Non-dimensional results $|\bar{a}_{max}|$ due to HSLM-A3 train — for structures 1 to 3 — all L = 50m and $\zeta_{EC} = 0.5\%$ Rayleigh like damping

[1]The relationships of Equations (3.220) to (3.222) comply with the ones presented in [1].

4. Traffic mixes

In this chapter, the five different traffic mixes, which are used in this doctoral thesis, are introduced. All five traffic mixes are based on a traffic volume of 24.95 10^6 t/year/track and a design life of 100 years. The first traffic mix — traffic mix 1 — contains the first eight service trains of ÖNORM EN 1991-2 [43] Annex D. This traffic mix 1 is also the basis for the fatigue design of new railway bridges, based on the load model LM71 and the damage equivalent factor λ — see Equation (2.28). The traffic mixes 2 and 3 consider measured trains along the high-speed line *Westbahn*, which connects the cities of Vienna and Salzburg via Linz. Within two years about 94602 real trains were measured. The procedure to identify and group these real trains is described as follows. The traffic mixes 4 and 5 are theoretical, and supposed to cover a pure high-speed traffic mix and a mixed traffic mix (high-speed trains and freight trains). Additionally, the considered train speeds for each traffic mix are defined.

4.1. Traffic mix 1

The traffic mix 1 considers the eight trains according to ÖNORM EN 1991-2 [43] Annex D, which are illustrated in Figure 2.18 and Annex A.1. In the following, these trains are labelled according to [37], hence e.g. *Type 1* becomes *TypeC1*. Consequently, these eight trains are combined according to ÖNORM EN 1991-2 Table D.1 [43], leading to traffic mix 1 — see Table 4.1.

	Train type	Mass of train [t]	Nr. of trains/day	Traffic volume [10^3 t/year]	Nr. of trains /100years	Traffic volume [10^3 t /100years]
1	TypeC1	663	12	2903.9	438000	290390
2	TypeC2	530	12	2321.4	438000	232140
3	TypeC3	940	5	1715.5	182500	171550
4	TypeC4	510	5	930.8	182500	93080
5	TypeC5	2160	7	5518.8	255500	551880
6	TypeC6	1431	12	6267.8	438000	626780
7	TypeC7	1035	8	3022.2	292000	302220
8	TypeC8	1035	6	2266.7	219000	226670
			67	$\approx$ **24950.0**	**2445500**	$\approx$ **2495000**

Table 4.1.: Traffic mix 1 — according to standard rail traffic (EC mix) with axles $\leq$ 22.5t in ÖNORM EN 1991-2 Table D.1 [43]

The produced damage D_{dyn} of a train crossing strongly depends, besides many other factors, on the train speed. Therefore, three different variations in train speeds were considered for the dynamic calculation, as illustrated in Table 4.2.

Variant	**TM1***	**TM1****	**TM1*****
Train type	Speed v_{EC} [km/h]	Speed range 50 - 1.2 v_{EC} [km/h]	Speed range 50 - 1.2 v_{EC} [km/h]
TypeC1	200	50-240	50-240
TypeC2	160	50-192	50-192
TypeC3	250	50-300	50-300
TypeC4	250	50-300	50-300
TypeC5	80	50-96	50-96
TypeC6	100	50-120	50-120
TypeC7	120	50-144	50-144
TypeC8	100	50-120	50-120
Train speed — used for D_{dyn} calculation	$\mathbf{v_{EC}}$	$\mathbf{v_{D_{max}}}$	$\mathbf{v_{a_{max}}}$

Table 4.2.: Traffic mix 1 — considered variants of train speeds

The first variant — TM1* — considers the trains speeds v_{EC} according to ÖNORM EN 1991-2 [43] in Annex D. Hence, only one train speed per train type is stated in Table 4.2.
The second variant — TM1** — considers for each train type, a speed range starting from 50 km/h up to 1.2 times v_{EC}. Within this defined speed range, for each train type on each structure, the speed $v_{D_{max}}$ is looked for. This speed is defined as the one, at which the particular train produces the maximum damage D_{dyn} on a particular structure. Consequently, all eight train types cross all structures, for the design life of 100 years, with the speed causing the maximum damage D_{dyn}. Hence, variant TM1** can be seen as the most conservative approach possible.
The last variant — TM1*** — considers the before mentioned speed ranges as well, but it is looked for the speed $v_{a_{max}}$, which produces the maximum absolute vertical bridge deck acceleration $|a_{max}|$. This speed is then used for the damage calculation and should give an answer to the question whether or not one can simply use the bending moment ranges at resonant speed, regarding the bridge deck acceleration $|a_{max}|$, in order to obtain the maximum damage D_{dyn}.

4.2. Traffic mix 2 and traffic mix 3

This chapter covers the analysis of the measured train axle loads, which was provided by the ÖBB. First, the location of the monitoring station and the raw-data itself are briefly discussed. Subsequently, the method to identify train-types and train-classes using the measured train axle loads raw-data and the consequential results are presented. Finally, the traffic mixes 2 and 3 are specified and introduced.

4.2.1. Monitoring Station

The raw-data represents measured train axle loads from the monitoring point *Enns*, which is located on the high-speed line *Westbahn* between the two cities of *Linz* and *Vienna* — see Figure 4.1.

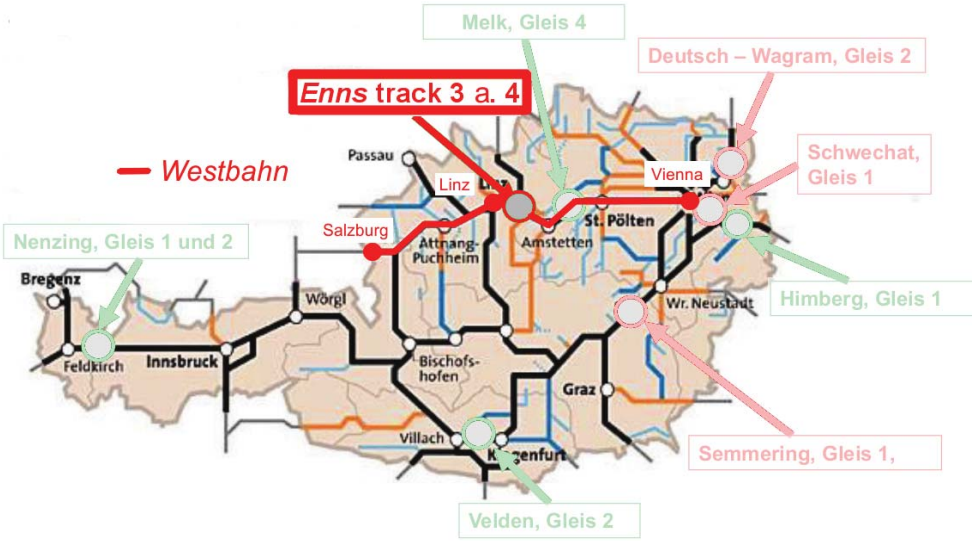

Figure 4.1.: High-speed line *Westbahn* between cities of Salzburg and Vienna — monitoring station *Enns* between the cities of Linz and Vienna

4.2.2. Raw-data of the measured axle loads

At the monitoring point *Enns* the system was installed on two tracks. Track 3 leads towards the city of *Vienna*, whereas track 4 leads to the city of *Linz*. In Table 4.3 the number of measured train axles per track is illustrated for the two considered years 2014 and 2015.

Year \ Track	3 (Vienna)	4 (Linz)
2014	1251724	940569
2015	1147879	921346

Table 4.3.: Number of measured train axles per track and year

The monitoring system collected the following information for each passed train axle:

- Date
- Time
- Train number
- Direction
- Number of cars within train
- Number of axles within car
- Average speed [km/h]
- Monitoring point number
- Total number of axles within train
- Axle mass [t]
- Train mass [t]
- Train length [m]
- Distance to the subsequent axle [m]

In Figure 4.2 the distribution of the axle masses combined for both tracks and the years 2014 & 2015 are illustrated. One can see that the vast majority is beneath 22.5 t[1], as from the ÖBB demanded. Furthermore, about 46% of all axle masses are between 11.5 t and 13.5 t, as the cumulative distribution function (CDF) shows in Figure 4.2.

[1]See in Figure 4.2 class 22t, which covers axle masses $>$ 21.5t to $\leq$ 22.5t.

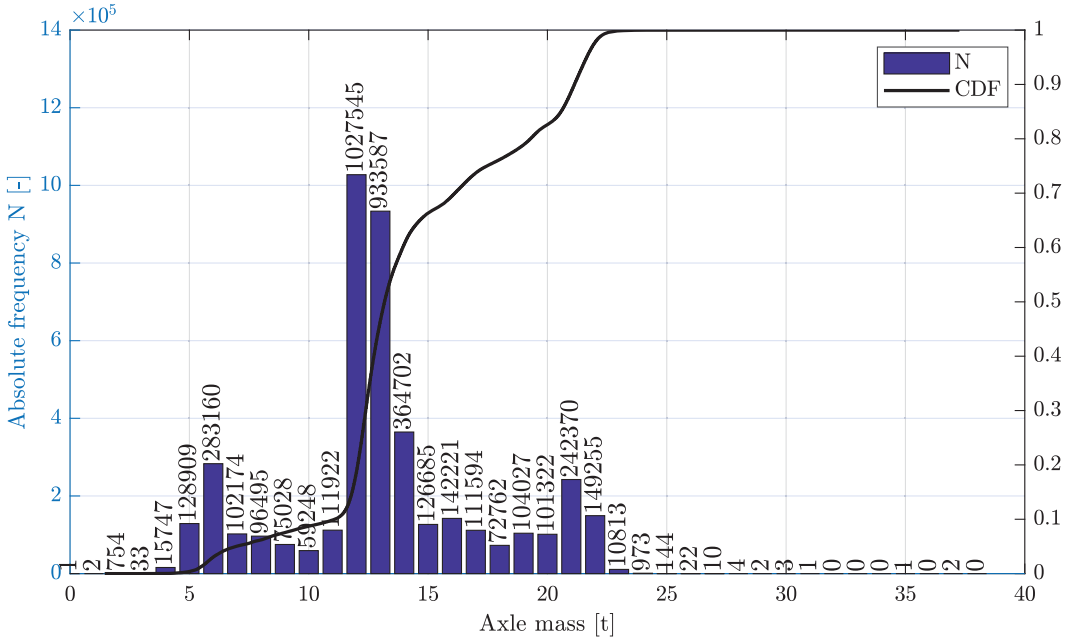

Figure 4.2.: Axle mass distribution — years 2014 & 2015 and tracks 3 & 4

4.2.3. Method to identify different train classes and train types

In general, the goal was to identify train-types — such as ICE, Railjet, etc. — and train-classes — such as passenger train (PT), freight train (FT) and special train (ST) — using the train axle loads raw-data from Chapter 4.2.2. As the list above states, the different train axle loads were already grouped into trains. Nevertheless, neither the train-type nor the train-class is known. However, this information is necessary in order to develop simplified real traffic mixes, which cover the damage induced by all real trains — see Chapter 5. The applied method to identify train-type and train-class of each single train is described as follows in this section.

First, an identification via the train number — see list on page 87 — was performed. This approach did not turn out to be successful as the train number led to contradictory results. The same train numbers identified different train-types. Therefore, an identification scheme using the axle distance geometries was developed. The procedure shown in Figure 4.3 was realized with the software MATLAB [34].

Initially, the trains were identified using the information *Number of axle within car*, *Date* and *Time* from the list on page 87. These trains were sorted into groups with the same number of axles, hence *train axle groups* result. Within these groups, the trains were compared, regarding the axle distances, to each other. If trains matched with no less than 3% divergence, they were put into a common *train group*. This procedure was repeated until each *train* within a *train axle group* was assigned to a *train group*.

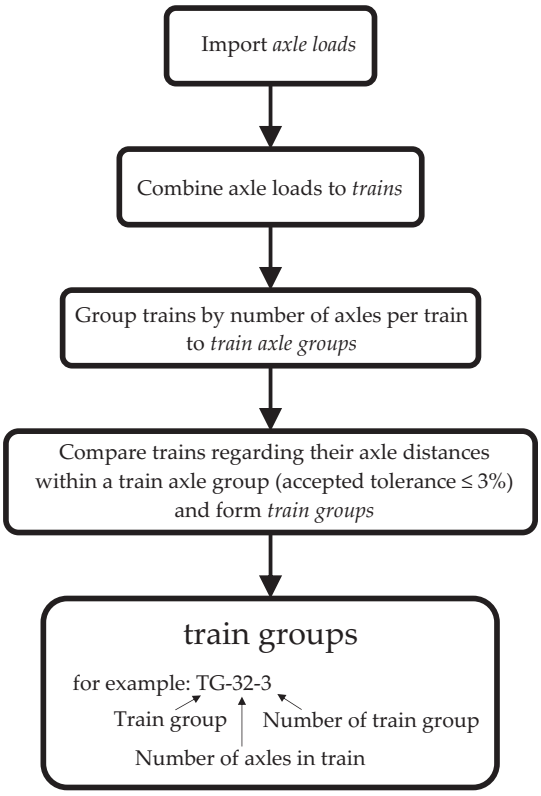

Figure 4.3.: Flowchart diagram for train identification

Next, these train groups were allocated to train types, hence real trains, if possible. Consequently, the average axle distances of the train groups were compared to the ones of known passenger trains (PT), which are listed here:

- Railjet (TypeC19)
- ICE-T1 411 (TypeC14)
- DOSTO
- Talent 4023
- Talent 4024

The names in brackets refer to the terms according to the ÖBB guideline [37].

In the last step, the remaining train groups were assigned to train classes — passenger trains (PT), freight trains (FT) and special trains (ST). Therefore, the following characteristics were used consecutively:

- Freight trains (FT)
  - *Bogie axle distance = 1800mm*: The bogie types Y25 and WU83 are the most used ones for freight trains in Europe. For both, various versions exist, but all of them are characterized by a wheelbase of 1800mm ([4] p.164).
  - *Wheelbases for two-axle cars*: The wheelbases for the in Austria used two-axle cars is either 6000mm, 8000mm or 9000mm. [50]

  - *Speed 120 km/h*: According to the Rail Cargo Austrian AG the maximum speed for freight cars can not exceed 120 km/h [50].

- Passenger trains (PT)
  The well known train *Railjet* was used as basis to identify passenger cars. The *Railjet*'s axle distances 2500mm (bogie) and 16500mm (innermost axle distance) were identified in many other trains with speeds > 160 km/h as well. These trains featured another common type of PT with axle distances of 2500mm and 15800mm, respectively. Consequently, the following axle distances were used to identify PT:

  - *Bogie axle distance = 2500mm*
  - *Axle distance between the innermost axles of a four-axle passenger car = 15800mm, 16500mm*

  Additionally, the axle loads of PT vary little in comparison to FT, which makes it easier to identify the first ones.

- Special trains (ST)
  - *Power cars*: Sometimes exclusively locomotives were put together in line. In general, the power car *Taurus* was detected easily due to the unique axle distances and the very little varying axle loads.
  - *Other trains*: In this category all track construction trains, test trains, trains with less than 8 axles and unknown trains were considered.

4.2.4. Results

In the following chapter, the results of the analysed monitoring station raw-data is presented. It was possible to group the identified trains into train classes — passenger trains (PT), freight trains (FT) and special trains (ST).
First, the train class PT is discussed, which is split into two parts — the labelled passenger trains PT_L and the not labelled passenger trains PT_{nL}. The first ones passed the monitoring station at least 75 times within the two considered years, the latter ones less. Regarding the PT_L the overall result is presented in Table 4.4. In total 73 train types were identified and labelled — their detailed measured axle loads and axle geometry may be found in Annex A.3. Regarding the first sixteen PT_L in Table 4.4 it was possible to allocate the actual train name (e.g. DOSTO, Railjet, etc.). The remaining 57 PT_L have all in common to be hauled by a Taurus locomotive (four axles) followed by a variable number of four-axle passenger cars. Consequently, e.g. train number 17 — PT-24-1 — consists of one Taurus locomotive and 5 passenger cars. In general, only a few train types contribute to the PT_L's total traffic volume. The labelled passenger trains *DOSTO*, *ICE-T1 411* and the different configurations of the *Railjet* make about 79% of the PT_L's total traffic volume (32383.1 10^3 t/2years).

	Train type	Av. mass [t]	Nr. trains 2014		Nr. trains 2015		Total Nr. trains	Traffic volume [10^3 t/2years]
			Track 3 (Vienna)	Track 4 (Linz)	Track 3 (Vienna)	Track 4 (Linz)		
1	DOSTO	326.6	5538	4182	4867	3967	18554	6059.9
2	2xDOSTO	630.6	26	224	242	173	665	419.3
3	TypeC14 (ICE-T1 411)	390.2	2130	1735	2643	2075	8583	3348.7
4	TypeC19 Taurus-front (Railjet)	887.3	44	3122	24	3499	6689	5934.9
5	TypeC19 Taurus-back (Railjet)	887.3	3400	28	3961	13	7402	6567.4
6	TypeC19* Taurus-front (Railjet)	443.4	149	1502	267	742	2660	1179.5
7	TypeC19* Taurus-back (Railjet)	443.4	2343	36	1418	14	3811	1689.8
8	TypeC19** (Railjet)	476.8	232	129	204	125	690	329.0
9	Talent 4023	94.4	3	1	2	1	7	0.7
10	Talent 4024	115.5	23	15	22	25	85	9.8
11	2xTalent4024	241	5	7	34	27	73	17.6
12	3xTalent4024	346.8	0	0	1	0	1	0.3
13	Train 4020	143.8	0	0	28	19	47	6.8
14	2xTrain 4020	285.1	0	0	33	28	61	17.4
15	3xTrain 4020	422.7	0	0	9	0	9	3.8
16	4xTrain 4020	571.4	0	0	23	22	45	25.7
17	PT-24-1	332.6	7	584	2	115	708	235.5
18	PT-24-2	331.2	158	139	34	31	362	119.9
19	PT-24-3	333.6	4	181	3	1	189	63.0
20	PT-24-4	345.8	9	154	0	0	163	56.4
21	PT-24-5	351.5	0	77	1	0	78	27.4
22	PT-24-6	330.6	551	0	129	0	680	224.8
23	PT-24-7	331.6	163	0	1	3	167	55.4
24	PT-24-8	347	187	0	0	0	187	64.9
25	PT-24-9	351.8	79	0	0	0	79	27.8
26	PT-24-10	337.1	0	0	1	357	358	120.7
27	PT-24-11	330.6	0	0	615	0	615	203.3
28	PT-24-12	329.6	0	0	141	0	141	46.5
29	PT-24-13	344	0	0	80	0	80	27.5
30	PT-28-1	383	3	296	4	664	967	370.4
31	PT-28-2	385.1	3	199	2	163	367	141.3
32	PT-28-3	381.5	215	0	243	186	644	245.7
33	PT-28-4	380.3	76	0	1	0	77	29.3

Continued on next page

Table 4.4 – continued from previous page

	Train	Av. mass [t]	Nr. trains 2014		Nr. trains 2015		Total Nr. trains	Traffic volume [10^3 t/2years]
			Track 3 (Vienna)	Track 4 (Linz)	Track 3 (Vienna)	Track 4 (Linz)		
34	PT-28-5	381	105	0	78	8	191	72.8
35	PT-28-6	381.1	354	0	225	1	580	221.0
36	PT-28-7	380.8	450	0	853	4	1307	497.7
37	PT-28-8	390.3	0	0	9	354	363	141.7
38	PT-28-9	383.4	0	0	181	118	299	114.6
39	PT-28-10	381.3	0	0	1	95	96	36.6
40	PT-28-11	379.3	0	0	0	107	107	40.6
41	PT-28-12	383.1	0	0	622	0	622	238.3
42	PT-28-13	378.8	0	0	111	0	111	42.0
43	PT-28-14	379.7	0	0	103	0	103	39.1
44	PT-32-1	425.5	213	135	216	309	873	371.5
45	PT-32-2	436.4	7	91	2	139	239	104.3
46	PT-32-3	430.1	227	0	180	0	407	175.0
47	PT-32-4	441.4	135	0	129	0	264	116.5
48	PT-32-5	429.7	129	0	88	1	218	93.7
49	PT-32-6	429.3	105	0	19	44	168	72.1
50	PT-32-7	428	103	0	26	1	130	55.6
51	PT-32-8	432.7	0	0	0	223	223	96.5
52	PT-32-9	430.5	0	0	186	137	323	139.0
53	PT-36-1	485.1	5	144	0	54	203	98.5
54	PT-36-2	477.9	26	86	49	16	177	84.6
55	PT-36-3	471.4	153	0	14	14	181	85.3
56	PT-36-4	478.2	138	0	81	0	219	104.7
57	PT-36-5	487.7	101	0	0	0	101	49.3
58	PT-36-6	517.3	0	0	140	94	234	121.0
59	PT-36-7	469	0	0	274	0	274	128.5
60	PT-40-1	521.6	68	181	134	102	485	253.0
61	PT-40-2	527.5	1	77	0	17	95	50.1
62	PT-40-3	526.5	0	0	0	112	112	59.0
63	PT-48-1	682.6	10	199	0	0	209	142.7
64	PT-48-2	630.7	166	99	28	19	312	196.8
65	PT-48-3	622.3	0	78	0	0	78	48.5
66	PT-48-4	668.3	231	0	0	0	231	154.4
67	PT-48-5	628	0	0	0	129	129	81.0
68	PT-52-1	632.1	3	79	0	0	82	51.8
69	PT-52-2	615.9	85	0	0	0	85	52.4
70	PT-52-3	676.9	76	0	6	9	91	61.6
71	PT-56-1	732	80	0	0	2	82	60.0
72	PT-56-2	794.8	0	0	9	82	91	72.3
73	PT-56-3	790.9	0	0	112	0	112	88.6
		Σ	**18319**	**13780**	**18911**	**14441**	**65451**	**32383.1**

Table 4.4.: Labelled passenger trains PT_L

In Table 4.5 the overall results regarding the train classes are summarized. The large majority with 81.6% of all trains are passenger trains (PT). This number includes the labeled (PT_L) and not labeled passenger trains PT_{nL}. In the latter category, the train types were monitored, as described above, less than 75 times during the considered time range. However, all passenger trains together are only responsible for 68.8% of the total traffic volume. The second most frequent train class (16.1%) represents the *freight trains* (FT) and covers almost a third (30.9%) of the total traffic volume. The last and with 0.3% of the traffic volume neglectable train class is the one regarding the *special trains* (ST).

Train class	**Track 3 and Track 4** 2014 & 2015	
	Nr. of trains/ 2years	Traffic volume [10^3 t/2years]
Passenger trains - labeled (PT_L) - Table 4.4	65451	32383.1
Passenger trains - not labeled (PT_{nL})	11766	6152.8
Total passenger trains (PT)	**77217** (81.6%)	**38535.9** (68.8%)
Freight trains (FT)	**15178** (16.1%)	**17294.9** (30.9%)
Special trains (ST)	2207 (2.3%)	198.3 (0.3%)
Total trains (RT)	**94602** (100%)	**56029.1** (100%)

Table 4.5.: Train classes - overall result of years 2014 & 2015 for track 3 and 4 combined

The above presented results combined the train data of track 3 and track 4. In Table 4.6 the results are stated separately for both tracks.

Train class	**Track 3** (Vienna) 2014 & 2015		**Track 4** (Linz) 2014 & 2015	
	Nr. of trains/ 2years	Traffic volume [10^3 t/2years]	Nr. of trains/ 2years	Traffic volume [10^3 t/2years]
Passenger trains - labeled (PT_L)	37230	17992.3	28221	14390.8
Passenger trains - not labeled (PT_{nL})	6072	3173.1	5694	2979.7
Total passenger trains (PT)	**43302** (80.7%)	**21165.4** (69.5%)	**33915** (82.8%)	**17370.5** (68.0%)
Freight trains (FT)	**8768** (16.3%)	**9167.3** (30.1%)	**6410** (15.7%)	**8127.6** (31.8%)
Special trains (ST)	1598 (3.0%)	139.0 (0.4%)	609 (1.5%)	59.3 (0.2%)
Total trains (RT)	**53668** (100.0%)	**30471.7** (100.0%)	**40934** (100.0%)	**25557.4** (100.0%)

Table 4.6.: Train classes - overall result of years 2014 & 2015 for track 3 and 4 separately

In Figure 4.4 the characteristics of the identified PT and FT are compared to each other. The cumulative distribution function (CDF) of the train lengths in Figure 4.4(a) already indicates the difficulties one faces if trying to categorize FT — almost all variations of lengths appear equally, hence the CDF is almost linear. On the other hand, the PT's lengths vary much less

and certain train types may be identified with less difficulties. The same is true regarding the axle mass of PT and FT — see Figure 4.4(b). Again, the axle masses of FT vary much more than the ones of PT. In the latter category e.g. the passenger cars with axle masses ranging from 12t to 14t can clearly be distinguished from the 21t axle masses of the Taurus locomotive. On the other hand, regarding the train speeds in Figure 4.4(c), the FT vary much less than the PT. The majority of the FT speeds is about 100 km/h. Comparing the train lengths to the corresponding train masses leads to Figure 4.4(d). Due to the different loading conditions, the FTs cover a big area of the train length/ mass diagram. Then again, the PT are concentrated in a much smaller range, as the passenger car and locomotive masses do not vary that much. In Figure 4.4(e) the train length is plotted against the train speed showing that PT of almost all lengths reach about 200 km/h and on the other hand, FT of almost all lengths reach 100 km/h.

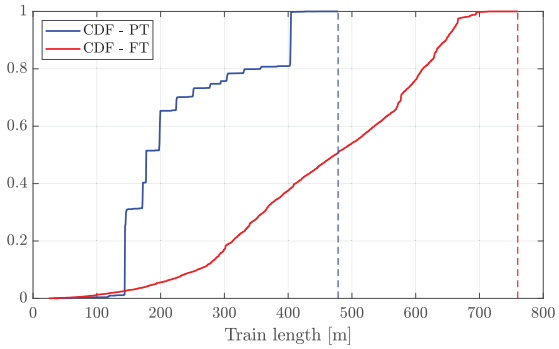

(a) CDF for train length

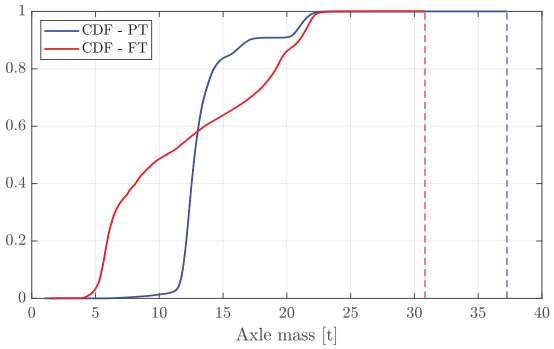

(b) CDF for axle mass

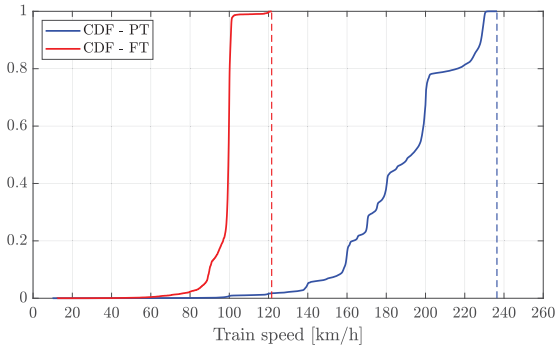

(c) CDF for train speed

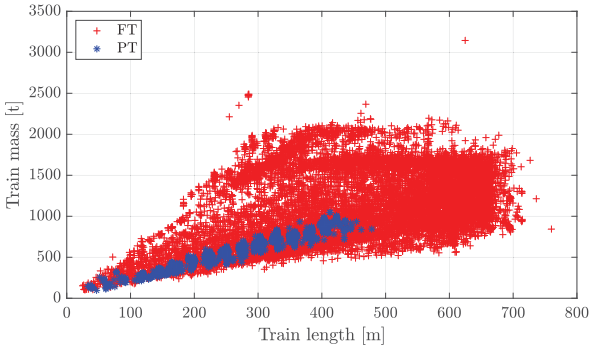

(d) Train lengths vs. train mass

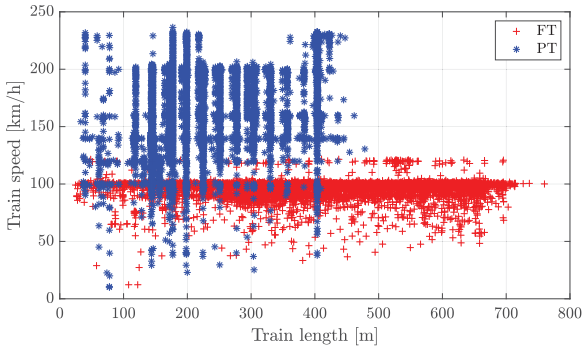

(e) Train lengths vs. train speeds

Figure 4.4.: Cumulative distribution functions (CDF) and comparison of train lengths/masses and train lengths/speeds — passenger trains (PT) and freight trains (FT) — years 2014 & 2015 and track 3 & 4 combined

Traffic mix 2

The traffic mix 2 considers all measured trains, hence all 94602 real trains (RT) — see e.g. Table 4.5 — are used. However, in order to be able to compare the results to the ones of other traffic mixes, the traffic volume is scaled to $m_{ECmix} = 24.95\ 10^6$ t/year/track. This leads for single track structures, with the factor $f_{TM2-st,Track3\&4,100years}$ according to Equation (4.1), to the traffic mix as shown in Table 4.7.

$$f_{TM2-st,Track3\&4,100years} = \frac{m_{ECmix}}{m_{RT,Track3\&4}}\ 100\ \text{years} = \frac{24950 * 10^3}{56029.1 * 10^3}\ 100 = 44.5304 \tag{4.1}$$

Track	Train class	**2014** & **2015** (2 years)		**TM2-st** (100 years)	
		Nr. of trains/ 2years	Traffic volume [10^3t/2years]	Nr. of trains/ 100years	Traffic volume [10^3t/100years]
3 & 4	**PT**	77217 (81.6%)	38535.9 (68.8%)	**3438504** (81.6%)	**1716020** (68.8%)
	FT	15178 (16.1%)	17294.9 (30.9%)	**675882** (16.1%)	**770150** (30.9%)
	ST	2207 (2.3%)	198.3 (0.3%)	98279 (2.3%)	8830 (0.3%)
	RT	94602 (100%)	56029.1 (100%)	**4212665** (100%)	**2495000** (100%)

Table 4.7.: Traffic mix 2 - single track structures

For structures with two tracks, the traffic mix according to Table 4.8 results using Equations (4.2) and (4.3).

$$f_{TM2-dt,Track3,100years} = \frac{m_{ECmix}}{m_{RT,Track3}}\ 100\ \text{years} = \frac{24950 * 10^3}{30471.7 * 10^3}\ 100 = 81.8793 \tag{4.2}$$

$$f_{TM2-dt,Track4,100years} = \frac{m_{ECmix}}{m_{RT,Track4}}\ 100\ \text{years} = \frac{24950 * 10^3}{25557.4 * 10^3}\ 100 = 97.6234 \tag{4.3}$$

Track	Train class	**2014** & **2015** (2 years)		**TM2-dt** (100 years)	
		Nr. of trains/ 2years	Traffic volume [10^3t/2years]	Nr. of trains/ 100years	Traffic volume [10^3t/100years]
3	**PT**	43302 (80.7%)	21165.4 (69.5%)	**3545537** (80.7%)	**1733008** (69.5%)
	FT	8768 (16.3%)	9167.3 (30.1%)	**717918** (16.3%)	**750612** (30.1%)
	ST	1598 (3.0%)	139.0 (0.4%)	130843 (3.0%)	11380 (0.4%)
	RT	53668 (100%)	30471.7 (100%)	**4394298** (100%)	**2495000** (100%)
4	**PT**	33915 (82.8%)	17370.5 (68.0%)	**3310898** (82.8%)	**1695767** (68.0%)
	FT	6410 (15.7%)	8127.6 (31.8%)	**625766** (15.7%)	**793444** (31.8%)
	ST	609 (1.5%)	59.3 (0.2%)	59453 (1.5%)	5789 (0.2%)
	RT	40934 (100%)	25557.4 (100%)	**3996116** (100.0%)	**2495000** (100%)

Table 4.8.: Traffic mix 2 - for double track structures

Regarding the train speeds in traffic mix 2, always the real measured train speeds of all 94602 real trains (RT) are used. Hence, there are no different speed variants like e.g. in traffic mix 1 and consequently only two names — **TM2-st** for single track structures and **TM2-dt** for double track structures — are necessary.

Traffic mix 3

Traffic mix 3 considers, like traffic mix 2, the measured trains of the monitoring station *Enns*, but neglects FT and ST. Consequently, only PT are considered, which are like in traffic mix 2 scaled to 24.95 10^6 t/year/track. Subsequently, the results for single and double track structures are stated.

$$f_{\mathrm{TM3-st,Track3\&4,100years}} = \frac{\mathrm{m_{ECmix}}}{\mathrm{m_{PT,Track3\&4}}}\ 100\ \mathrm{years} = \frac{24950 * 10^3}{38535.9 * 10^3}\ 100 = 64.7448 \tag{4.4}$$

Track	Train class	**2014** & **2015** (2 years)		**TM3-st** (100 years)	
		Nr. of trains/ 2years	Traffic volume [10^3t/2years]	Nr. of trains/ 100years	Traffic volume [10^3t/100years]
3 & 4	**PT**	77217	38535.9	**4999399**	**2495000**

Table 4.9.: Traffic mix 3 - single track structure

$$f_{\mathrm{TM3-dt,Track3,100years}} = \frac{\mathrm{m_{ECmix}}}{\mathrm{m_{PT,Track3}}}\ 100\ \mathrm{years} = \frac{24950 * 10^3}{21165.4 * 10^3}\ 100 = 117.8811 \tag{4.5}$$

$$f_{\mathrm{TM3-dt,Track4,100years}} = \frac{\mathrm{m_{ECmix}}}{\mathrm{m_{PT,Track4}}}\ 100\ \mathrm{years} = \frac{24950 * 10^3}{17370.5 * 10^3}\ 100 = 143.6343 \tag{4.6}$$

Track	Train class	**2014** & **2015** (2 years)		**TM3-dt** (100 years)	
		Nr. of trains/ 2years	Traffic volume [10^3t/2years]	Nr. of trains/ 100years	Traffic volume [10^3t/100years]
3	**PT**	43302	21165.4	**5104487**	**2495000**
4	**PT**	33915	17370.5	**4871357**	**2495000**

Table 4.10.: Traffic mix 3 - double track structure

Regarding the train speeds in traffic mix 3, the same as for traffic mix 2 is valid. Hence, always the real measured train speeds of the 77217 PT are used. Again, there are no different speed variants considered and consequently only two names — **TM3-st** for single track structures and **TM3-dt** for double track structures — are necessary.

4.3. Traffic mix 4

Traffic mix 4 represents a pure high-speed traffic mix, which theoretically could be possible in Austria. The first four train types are very common on the high-speed line *Westbahn* — see Table 4.4. Therefore, in traffic mix 4, the traffic volume of these four trains is assumed to increase by 50% in comparison to the measured traffic volume.[1] On the other hand, the new high-speed passenger trains (PT) *ICE4-K3-12cars* and *EC250-Brutto18* are assumed to have about the same traffic volume ($\approx 3182\ 10^3$ t/year) in order to cause a total traffic volume, for the traffic mix 4, of $24.95\ 10^6$ t/year/track — see Table 4.11. All here considered trains are conventional trains, except *EC250-Brutto18*, which is an articulated train.

	Train type	Mass of train [t]	Nr. of trains/year	Traffic volume [10^3t/year]	Nr. of trains /100years	Traffic volume [10^3t /100years]
1	DOSTO (Westbahn)	326.6	13917	4545.4	1391700	454540
2	TypeC14 (ICE-T1 411)	390.2	6437	2511.5	643700	251150
3	TypeC19 Taurus-front (Railjet)	887.3	10568	9376.5	1056800	937650
4	TypeC19* Taurus-front (Railjet)	443.4	4853	2151.9	485300	215190
5	ICE4-K3-12cars	905.3	3515	3182.3	351500	318230
6	EC250-Brutto18	437.6	7273	3182.5	727300	318250
			46563.0	24950.0	**4656300**	**2495000**

Table 4.11.: Traffic mix 4

Regarding the train speeds, three different variants — like for traffic mix 1 — are considered according to Table 4.12.

[1] In traffic mix 4, the traffic volume of train type *TypeC19 Taurus-front* is the by 1.5 multiplied annual sum of the train types *TypeC19 Taurus-front* and *TypeC19 Taurus-back* of Table 4.4. The same is valid for train type *TypeC19* Taurus-front*.

Variant	**TM4***	**TM4****	**TM4*****
Train type	Speed v_{train} [km/h]	Speed range 50 - 1.2 v_{train} [km/h]	Speed range 50 - 1.2 v_{train} [km/h]
DOSTO (Westbahn)	200	50-240	50-240
TypeC14 (ICE-T1 411)	230	50-276	50-276
TypeC19 Taurus-front (Railjet)	230	50-276	50-276
TypeC19* Taurus-front (Railjet)	230	50-276	50-276
ICE4-K3-12cars	250	50-300	50-300
EC250-Brutto18	250	50-300	50-300
Train speed — used for D_{dyn} calculation	$\mathbf{v_{train}}$	$\mathbf{v_{D_{max}}}$	$\mathbf{v_{a_{max}}}$

Table 4.12.: Traffic mix 4 — considered variants of train speeds

4.4. Traffic mix 5

Traffic mix 5 was established to represent both, high-speed and freight traffic. Therefore, the traffic volume distributions according to the monitoring station *Enns* was used — see Table 4.5. Hence, the train types number one to four of traffic mix 5, which serve as high-speed trains, represent together 68.8% of the overall traffic volume (24.95 10^6 t/year/track) — see Table 4.13. Consequently, the remaining 31.2% are covered by freight trains for which the train types TypeC5 to TypeC8 were selected.

	Train type	Mass of train [t]	Nr. of trains/year	Traffic volume [10^3t/year]		Nr. of trains /100years	Traffic volume [10^3t /100years]	
1	DOSTO (Westbahn)	326.6	12850	4196.8		1285000	419680	
2	TypeC14 (ICE-T1 411)	390.2	5944	2319.3		594400	231930	
3	TypeC19 Taurus-front (Railjet)	887.3	9758	8658.2	68.8%	975800	865820	68.8%
4	TypeC19* Taurus-front (Railjet)	443.4	4481	1986.8		448100	198680	
5	TypeC5	2160.0	1166	2518.5		116600	251850	
6	TypeC6	1431.0	1998	2859.0	31.2%	199800	285900	31.2%
7	TypeC7	1035.0	1332	1378.6		133200	137860	
8	TypeC8	1035.0	998	1032.8		99800	103280	
			38527	24950.0	100%	**3852700**	**2495000**	**100%**

Table 4.13.: Traffic mix 5

Regarding the train speeds, three different variants — like for traffic mixes 1 and 4 — are considered according to Table 4.14.

Variant	**TM5***	**TM5****	**TM5*****
Train type	Speed v_{train} [km/h]	Speed range 50 - 1.2 v_{train} [km/h]	Speed range 50 - 1.2 v_{train} [km/h]
DOSTO (Westbahn)	200	50-240	50-240
TypeC14 (ICE-T1 411)	230	50-276	50-276
TypeC19 Taurus-front (Railjet)	230	50-276	50-276
TypeC19* Taurus-front (Railjet)	230	50-276	50-276
TypeC5	80	50-96	50-96
TypeC6	100	50-120	50-120
TypeC7	120	50-144	50-144
TypeC8	100	50-120	50-120
Train speed — used for D_{dyn} calculation	$\mathbf{v_{train}}$	$\mathbf{v_{D_{max}}}$	$\mathbf{v_{a_{max}}}$

Table 4.14.: Traffic mix 5 — considered variants of train speeds

5. Single-span bridges

In this chapter, single-span steel and composite bridges in high-speed railway lines, carrying one track, are studied with respect to their fatigue and traffic safety behaviour. Therefore, first an overview regarding the considered structures, traffic mixes and the computational method itself is presented. Subsequently, preliminary studies and the traffic safety design check for the single-span bridges are performed. Finally, a parameter study is conducted, which combines the traffic safety and fatigue criteria. Additionally, the accuracy of the 'adjusted' dynamic factor, which was introduced in Chapter 2.1.2, is studied.

5.1. Overview of studied single-span bridges

In this chapter, an overview of the subsequently performed parameter study regarding single-span beam bridges, carrying one track, is presented. Therefore, first the selected single-span steel and composite bridges with the related damping assumptions are introduced. Second, the here considered traffic mixes are briefly discussed and finally an overview of the method, regarding the fatigue design parameter study, is covered.

This doctoral thesis assumes that the vast majority of real single-span steel and compsite bridges is within the limits of ÖNORM EN 1991-2, Figure 6.10 [43] in terms of their length L and first bending frequency n_0 — see Figure 5.1. This hypothesis is e.g. supported in [5], which is based on [17], [14], [12], [51] and additional measurements of 235 ÖBB structures along a high-speed line in Austria. Hence, the parameter study is based on a total of 126 single-span structures (63 as steel, 63 as composite construction, L = 7 to 80 m), which cover the area of the before mentioned n_0 limits and a range of 25% above and below these limits — according to Figure 5.1. Therefore, in Chapters 5.1.1 to 5.1.3 these single-span steel and composite structures are defined and pre-designed.

Furthermore, this doctoral thesis differentiates between new and existing structures based on the different acceleration traffic safety (TS) criteria according to Chapter 2.1.2. In principal, only new structures with ballasted track are allowed in Austria and consequently only such are subsequently covered.
Therefore, the following TS criteria are applied:

- $|a_{HSLM-A,max}| \leq 3.5$ m/s^2 for new bridge structures
- $|a_{HSLM-A,max}| \leq 6.0$ m/s^2 for existing bridge structures

These acceleration criteria are checked at 99 equidistant points along the longitudinal axes of the single-span structures. On the other hand, as a constant fatigue resistance along the longitudinal axes is assumed (e.g. vertical stiffener welded to the main girder, which is repeated at each cross girder/ main girder connection and defines the fatigue resistance of the main

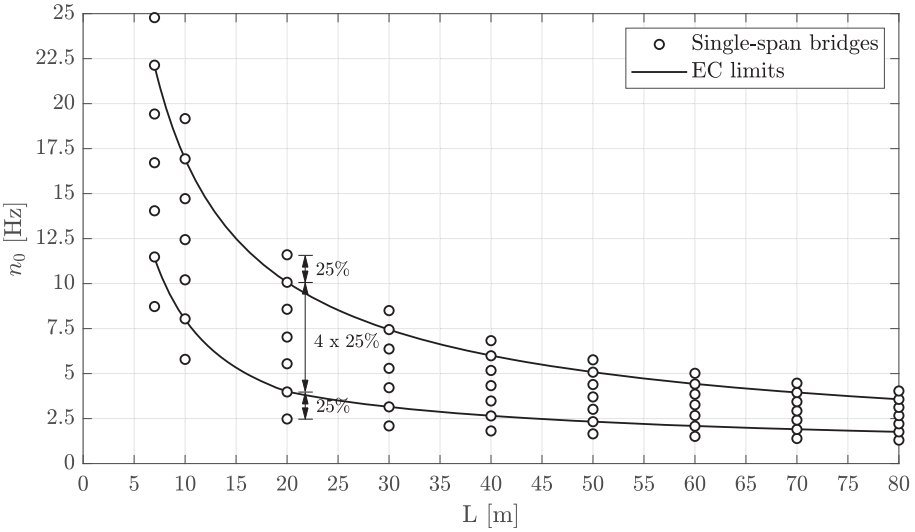

Figure 5.1.: Overview of pre-designed single-span structures as basis for the parameter study

girder), only the midspan cross section is checked regarding the FLS criterion. Subsequently, these assumptions are justified in Chapter 5.2.
Furthermore, the longitudinal load distribution of each axle load, according to ÖNORM EN 1991-2 [43], is considered as a variant in the parameter study — see Figure 5.2.

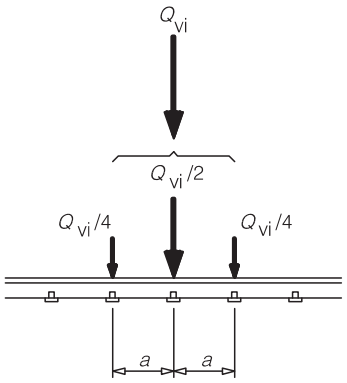

Figure 5.2.: Longitudinal distribution of a point force or wheel load by the rail — from ÖNORM EN 1991-2, Figure 6.4 [43]

5.1.1. Single-span steel bridges

A total of 63 single-span steel beam bridges, which form the basis of the parameter study, were pre-designed. All considered single-span steel beam bridges carry one track and are based on the cross section type featured in Figure 5.3. The structure's width of 4.5 m, the thickness of the web with 18 mm, the geometry and number of longitudinal ribs and the ballast bed are kept, in a simplified way, constant for all 63 cross sections. In order to consider only plausible single-span steel bridges, a base section for each bridge length L was established. Therefore, the

height of the main girder h_{MG} was set to $\approx L/12$. Consequently, the deck plate thickness t_{DP} and the geometry of the lower chord (w_{LC} and t_{LC}) were designed so that the global normal design stresses $\sigma_{global,ULS}$ due to the loads in the ULS reach about 60 % of the yield strength f_{yd} (S355). Subsequently, the design values for actions on the structure, for the ULS, are described by Equation (5.1), according to [41], [42] and [35]. In general, the load models LM71 and SW/2 — see Figures 2.1 and 2.4 — and the design rules for the effective width for elastic shear lag ([44] 3.2.1) were considered.

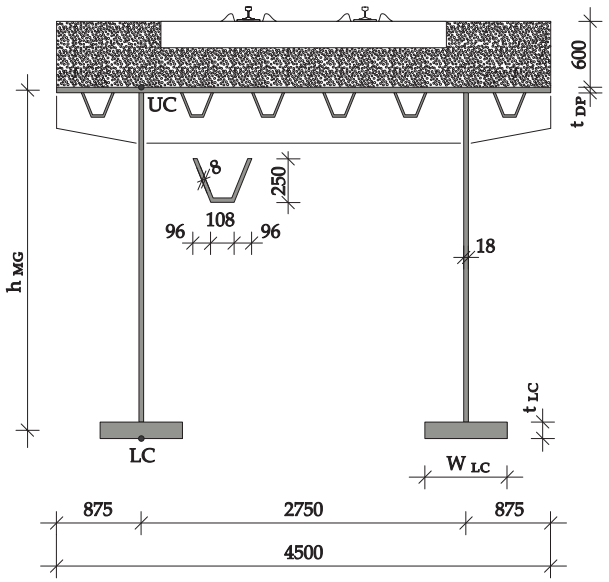

Figure 5.3.: Single-span steel bridges — geometry overview — material S355

$$E_d = \gamma_{G,j,sup} * G_{k,j,sup} + \gamma_{Q,i} * Q_{k,i} \tag{5.1}$$

with: $\gamma_{G,j,sup} = 1.35$ $\quad$ $Q_{k,i}$ due to:

$\gamma_{Q,LM71} = 1.45$ $\quad$ $Q_{LM71} = M_{y,LM71,k} * \alpha * \Phi_2$

$\gamma_{Q,SW/2} = 1.20$ $\quad$ $Q_{SW/2} = M_{y,SW/2,k} * \Phi_2$

$$\Phi_2 = \frac{1.44}{\sqrt{L_\Phi} - 0.2} + 0.82 \qquad \alpha = 1.21 \quad L_\Phi = L$$

$G_{k,j,sup}$ due to: $\mu = \gamma_a * A_a + \gamma_{bb} * A_{bb}$

$\gamma_a = 7850\ kg/m^3$ $\quad$ $\gamma_{bb} = 2000\ kg/m^3$

$A_{bb} = 4.5 * 0.6 = 2.7\ m^2$

After defining the geometry of the base section for each bridge length L, the geometries of these base sections were varied in order to define steel bridges with different first bending frequencies n_0 — see Equation (5.2).

$$n_0 = \frac{\pi}{2 * L} * \sqrt{\frac{EI_y}{\mu}} \tag{5.2}$$

The resulting 63 single-span steel bridges are illustrated in Figure 5.4(a) and Table B.1 provides additional information. Furthermore, the ULS design checks were performed for the 63 single-span steel bridges, leading to the results displayed in Figure 5.4(b). Hence, only structures with a first bending frequency n_0 beneath the lower EC limit do not fulfil the ULS criterion — the utilisation factors may be found in Table B.2. Additionally, dynamic analysis for all structures, applying the load model HSLM-A from 50-300 km/h, were performed, whereas the damping ratio according to ÖNORM EN 1991-2 [43] for steel structures, including the additional damping $\Delta\zeta$, was considered — see ζ_{EC} in Figure 5.9. Figure 5.4(c) shows the results regarding the TS criterion $|a_{HSLM-A,max}| \leq 3.5$ m/s^2, which applies for new structures with ballasted track, in combination with the ULS design results. Only very long and stiff structures are able to fulfil the acceleration criterion. In Figure 5.4(d) the results for existing structures and ballasted track ($|a_{HSLM-A,max}| \leq 6.0$ m/s^2) are presented in combination with the ULS criterion. In this case, also medium sized but still very stiff structures fulfil the acceleration criterion. The detailed acceleration results may be found in Table B.3.

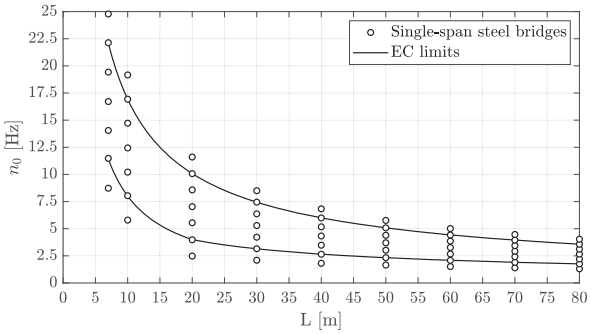

(a) L and n_0 distribution — 63 single-span steel bridges

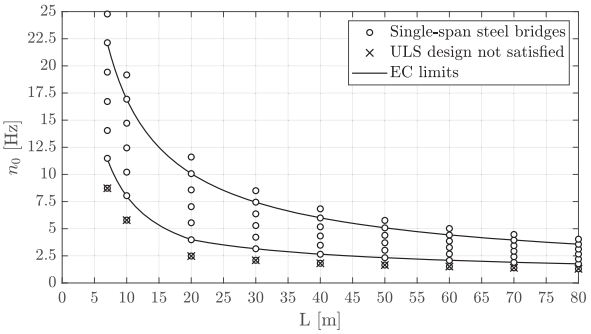

(b) ULS design check

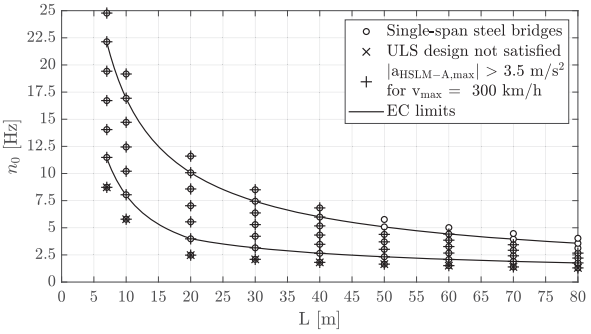

(c) ULS design & TS $|a_{HSLM-A,max} > 3.5$ m/s$^2|$ check

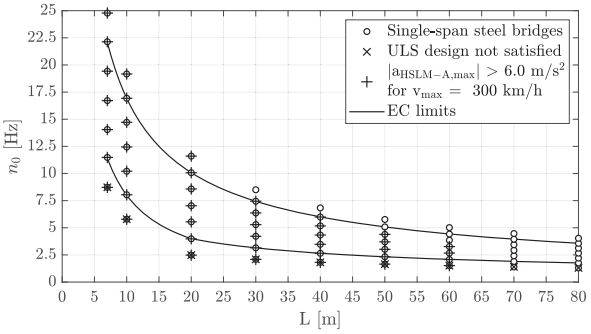

(d) ULS design & TS $|a_{HSLM-A,max} > 6.0$ m/s$^2|$ check

Figure 5.4.: Defined and pre-designed single-span steel bridges

Figure 5.5 illustrates the mass distribution μ_{SSB} for the 63 pre-designed reference structures (red dots) and the interpolated surface. This information is later needed for the non-dimensional representation in Chapter 5.3.

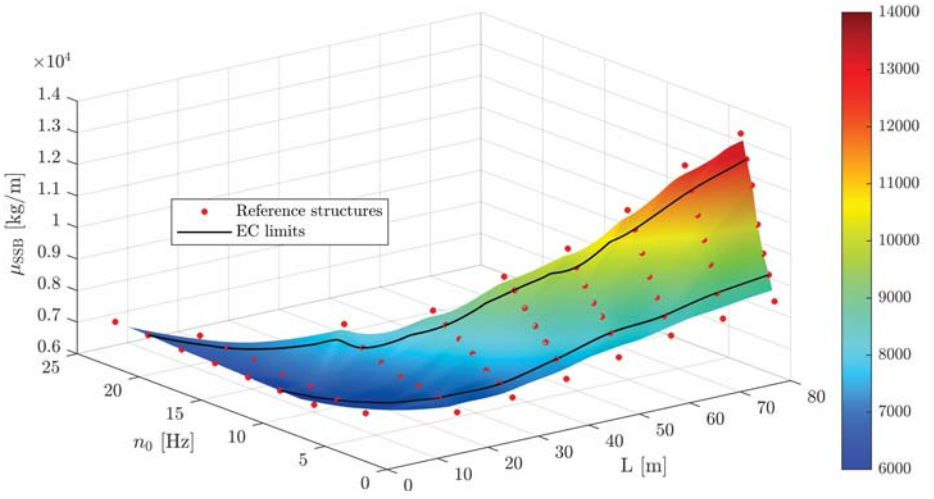

Figure 5.5.: Mass distribution μ_{SSB} for 63 single-span steel bridges (reference structures) and enveloping surface

5.1.2. Single-span composite bridges

The procedure to pre-design the 63 single-span composite bridges was performed similar to the one for the steel bridges in the previous Chapter 5.1.1. Consequently, all composite structures are based on the cross section illustrated in Figure 5.6. The edge beams, the ballast bed, the concrete upper chord and the steel web are kept, in a simplified way, constant for all 63 considered cross sections. Hence, in order to determine the geometry of the base section for each bridge length L, the height of the steel girder $h_{MG,a}$ was set to $\approx L/12$. Furthermore the loads were distinguished into loads acting on the steel cross section only and on the composite cross section. In the first step, the required areas of the steel chords were estimated using Equations (5.3) and (5.4) [60] for the ULS, which is represented by Equation (5.5). Afterwards, the base section geometry was varied in order to create single-span composite structures with different first bending frequencies n_0 — see Figure 5.7(a). In the final step, the global normal design stresses $\sigma_{global,ULS}$ due to the loads in the ULS at the points UC-c, UC-a and LC-a — see Figure 5.6 — were calculated and the utilization ratios summarized in Table C.2 and illustrated in Figure 5.7(b). Like in case of the single-span steel bridges, dynamic calculations were performed for the single-span composite bridges according to the damping ratios of the ÖNORM EN 1991-2 [43] — see damping variant ζ_{EC} in Figure 5.9. Subsequently, the TS results, in combination with the ULS results, are illustrated in Figure 5.7(c) for new and in Figure 5.7(d) for existing single-span composite bridges. In comparison to the single-span steel bridges, also shorter single-span composite bridges, due to the bigger mass, are able to fulfil the TS criterion.
In Figure 5.8 the mass distribution μ_{SCB} for the 63 pre-designed reference structures (red dots) and the interpolated surface are illustrated.

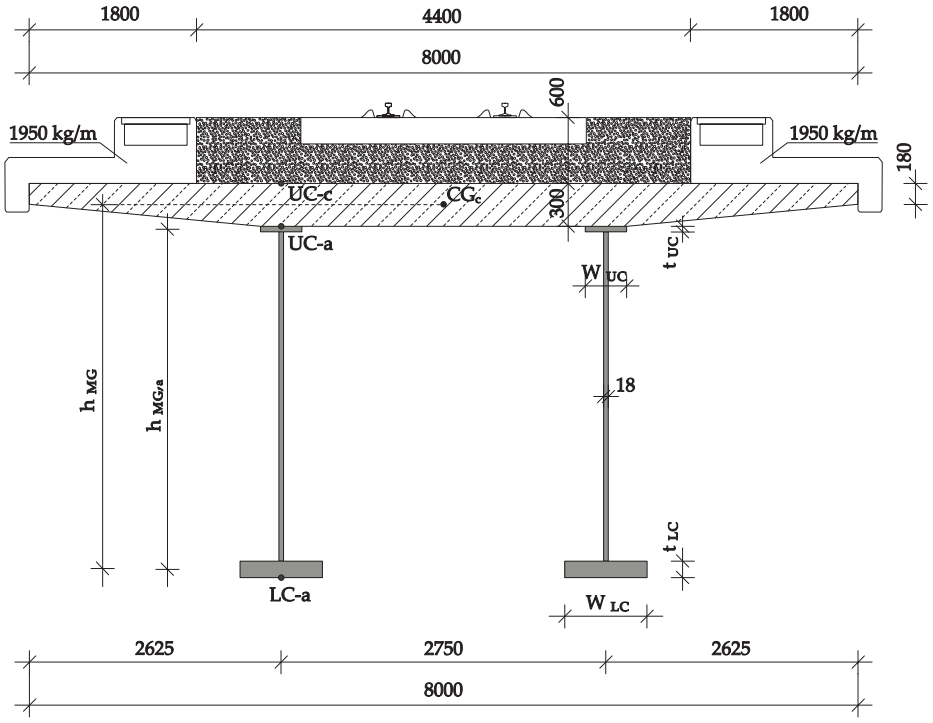

Figure 5.6.: Composite bridges — geometry overview — material S355, C35/45

$$A_{LC,a,requ} = \frac{\frac{M_1}{h_{MG,a}} + \frac{M_2}{h_{MG}}}{f_{yd}} - \frac{A_{web}}{6} \tag{5.3}$$

$$A_{UC,a,requ} = \frac{\frac{M_1}{h_{MG,a}} + \frac{M_2}{h_{MG}} * 0.25}{f_{yd}} - \frac{A_{web}}{6} \tag{5.4}$$

with: $M_1 = f(q_a, q_c) \ldots$ due to loads on steel cross section only (permanent weight of steel q_a and concrete q_c)

$M_2 = f(q_{bb}, q_{eb}, LM71, SW/2) \ldots$ due to loads on composite cross section

$$E_d = \gamma_{G,j,sup} * G_{k,j,sup} + \gamma_{Q,i} * Q_{k,i} \tag{5.5}$$

with: $\gamma_{G,j,sup} = 1.35$ $\quad$ $Q_{k,i}$ due to:

$\gamma_{Q,LM71} = 1.45$ $\quad$ $Q_{LM71} = M_{LM71,k} * \alpha * \Phi_2$

$\gamma_{Q,SW/2} = 1.20$ $\quad$ $Q_{SW/2} = M_{SW/2,k} * \Phi_2$

$$\Phi_2 = \frac{1.44}{\sqrt{L_\Phi} - 0.2} + 0.82 \qquad \alpha = 1.21 \quad L_\Phi = L$$

$$q_a = \gamma_a * A_a \qquad \gamma_a = 7850\ \mathrm{kg/m^3}$$
$$q_c = \gamma_c * A_c \qquad \gamma_c = 2500\ \mathrm{kg/m^3}$$
$$q_{bb} = \gamma_{bb} * A_{bb} \qquad \gamma_{bb} = 2000\ \mathrm{kg/m^3} \qquad A_{bb} = 4.4 * 0.6 = 2.64\ \mathrm{m^2}$$
$$q_{eb} = 1950\ \mathrm{kg/m} \qquad \ldots\text{weight of one end beam}$$

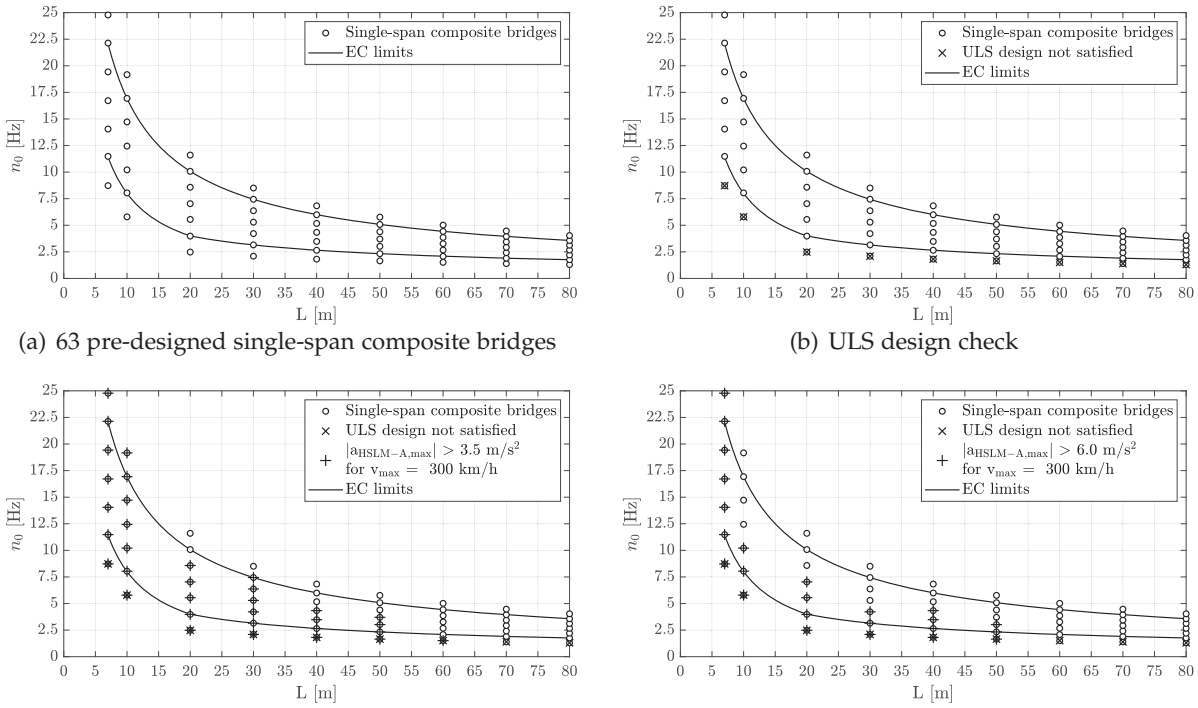

(a) 63 pre-designed single-span composite bridges

(b) ULS design check

(c) ULS design & TS $|a_{HSLM-A,max} > 3.5\ m/s^2|$ check

(d) ULS design & TS $|a_{HSLM-A,max} > 6.0\ m/s^2|$ check

Figure 5.7.: Single-span composite bridges

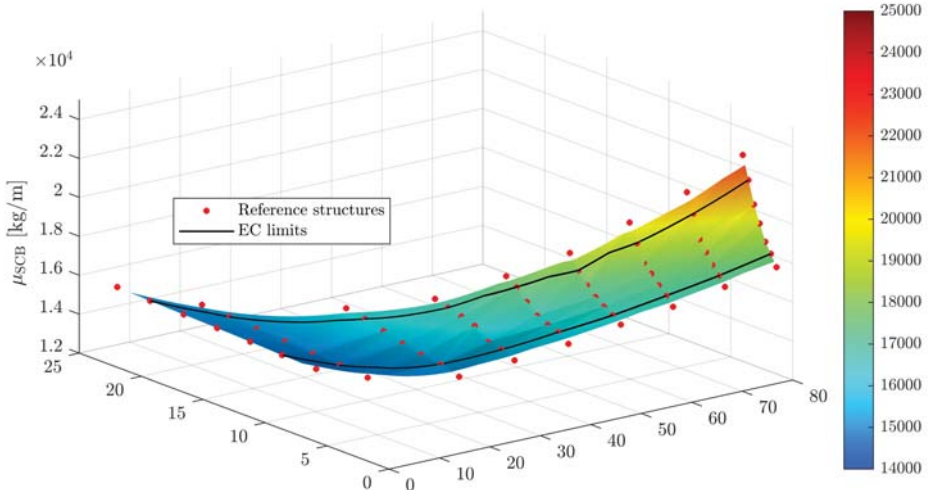

Figure 5.8.: Mass distribution μ_{SCB} for 63 single-span composite bridges (reference structures) and enveloping surface

5.1.3. Damping variants

Subsequently, Figure 5.9 illustrates the four considered damping variants. The first option, ζ_{EC}, represents the damping ratios according to ÖNORM EN 1991-2 [43] for steel and composite structures — see Equation (5.6) — inculding the additional damping $\Delta\zeta$ according to Equation (5.7). The latter considers for lengths up to 30 m the vehicle/ bridge mass interaction. The damping variants ζ_{V1} and ζ_{V2} are based on ζ_{EC}, but have damping ratios ≥ 1.0 % and ≥ 1.5 %, respectively, throughout the entire length range. The last damping variant ζ_{V3} considers a constant damping ratio of 3 % for all bridge lengths L.

$$\begin{aligned} \zeta_{\mathrm{steel/composite}} &= 0.5 + 0.125(20 - L)\ [\%] \qquad \text{for L} < 20\text{m} \\ \zeta_{\mathrm{steel/composite}} &= 0.5\ \% \qquad\qquad\qquad\qquad\ \ \text{for L} \geq 20\text{m} \end{aligned} \tag{5.6}$$

$$\Delta\zeta = \frac{0.0187\ \mathrm{L} - 0.00064\ \mathrm{L}^2}{1 - 0.0441\ \mathrm{L} - 0.0044\ \mathrm{L}^2 + 0.000255\ \mathrm{L}^3}\ [\%] \qquad \text{for } 0 \leq \mathrm{L} \leq 30\ \mathrm{m} \tag{5.7}$$

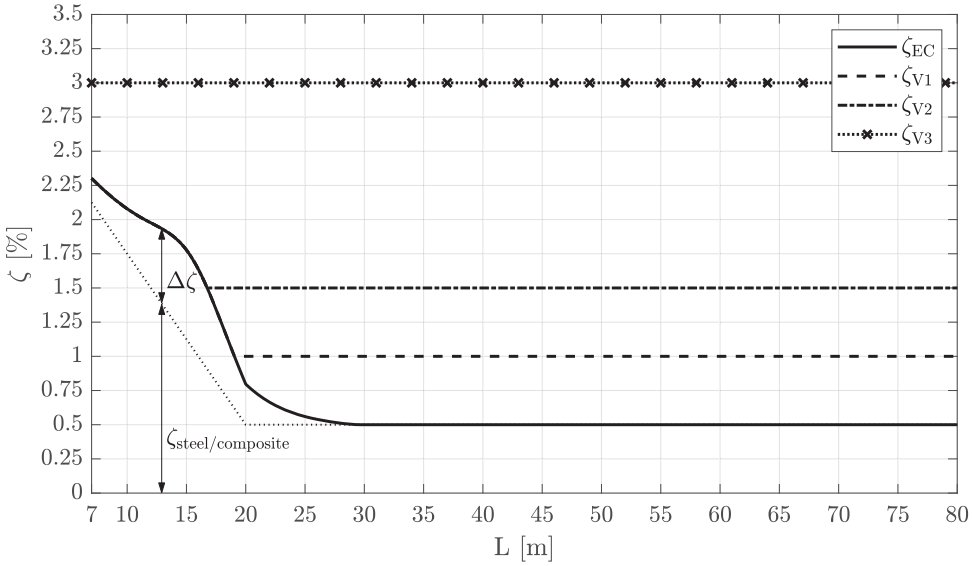

Figure 5.9.: Overview of damping variants for steel and composite structures

5.1.4. Analysed traffic mixes

All five traffic mixes according to Chapter 4 are used here for the single track, single-span steel and composite bridges. Consequently, on each structure a traffic volume of 24.95 10^6 t/year is applied for the considered design life of 100 years. The traffic mixes **TM1** (EC trains TypeC1 to TypeC8), **TM4** (high-speed trains only) and **TM5** (high-speed and freight trains) can be applied as already described in Chapter 4. On the other hand, the traffic mixes **TM2-st** and **TM3-st**, which resulted due to measurements of real trains at the monitoring point *Enns*, are additionally simplified, as described subsequently.

Traffic mix 2 for single track structures — TM2-st

Table 5.1 summarizes the measured trains at the monitoring point *Enns* for the two years 2014 & 2015. In total, 94602 real trains (RT) with a traffic volume of 56029.1 10^3 t passed the monitoring station.

Train class	**2014** & **2015** (2 years)		**TM2-st** (100 years)	
	Nr. of trains/ 2years	Traffic volume [10^3t/2years]	Nr. of trains/ 100years	Traffic volume [10^3t/100years]
PT_L	**65451** (69.2%)	**32383.1** (57.8%)	2914559 (69.2%)	1442033 (57.8%)
PT_{nL}	11766 (12.4%)	6152.8 (11.0%)	523945 (12.4%)	273987 (11.0%)
PT	77217 (81.6%)	38535.9 (68.8%)	3438504 (81.6%)	1716020 (68.8%)
FT	**15178** (16.1%)	**17294.9** (30.9%)	675882 (16.1%)	770150 (30.9%)
ST	2207 (2.3%)	198.3 (0.3%)	98279 (2.3%)	8830 (0.3%)
RT	94602 (100%)	56029.1 (100%)	4212665 (100%)	**2495000** (100%)

Table 5.1.: Traffic mix 2 - single track structures

Consequently, the factor $f_{\mathrm{TM2-st,100years}}$, according to Equation (5.8), is applied to consider a traffic volume of 24.95 10^6 t/year for the 100 years of design life

$$f_{\mathrm{TM2-st,100years}} = \frac{\mathrm{m_{ECmix}}}{\mathrm{m_{RT}}}\ 100\ \text{years} = \frac{24950 * 10^3}{56029.1 * 10^3}\ 100 = 44.5304 \tag{5.8}$$

Furthermore, it was possible to group these RT into passenger trains (PT), freight trains (FT) and special trains (ST) — see Table 5.1 and Chapter 4.2.4. The PT were additionally separated into labeled passenger trains (PT_L) and not labeled passenger trains PT_{nL}. Each train of the 65451 PT_L passed the monitoring station at least 75 times in the years 2014 & 2015 and all together represent about 69.2 % of all RT. Furthermore, the PT_L are grouped into 73 average trains as illustrated in Table 4.4 and Chapter A.3. Consequently, 73 average labeled passenger trains are able to cover the effects of 65451 PT_L. However, the remaining 11766 PT_{nL} are not directly considered in the calculations here, but their traffic volume by the factor

$$f_{PT} = 1 + \frac{\mathrm{m_{PT_{nL}}}}{\mathrm{m_{PT_L}}} = 1 + \frac{6152.8 * 10^3}{32383.1 * 10^3} = 1.1900 \tag{5.9}$$

which is applied on the results of the 73 average PT_L.
Furthermore, the ST are not directly calculated either, but their effects considered by applying the factor

$$f_{ST} = 1 + \frac{\mathrm{m_{ST}}}{\mathrm{m_{FT}}} = 1 + \frac{198.3 * 10^3}{17294.9 * 10^3} = 1.0115 \tag{5.10}$$

on the results of the FT. Finally, the damage $\mathrm{D_{TM2-st}}$ due to traffic mix **TM2-st** is obtained according to Equation (5.11)

$$\mathrm{D_{TM2-st}} = (\mathrm{D_{PT_L}} * f_{PT} + \mathrm{D_{FT}} * f_{ST}) * f_{\mathrm{TM2-st,100years}} \tag{5.11}$$

whereas only 73 average PT_L and 15178 FT need to be calculated directly.

Traffic mix 3 for single track structures — TM3-st

The traffic mix 3 for single track structures **TM3-st** is based on the above discussed traffic mix **TM2-st**, but does not consider FT and ST.
Consequently, the factor

$$f_{\mathrm{TM3-st,100years}} = \frac{\mathrm{m_{ECmix}}}{\mathrm{m_{PT_L}}}\ 100\ \mathrm{years} = \frac{24950 * 10^3}{32381.1 * 10^3}\ 100 = 77.0511 \tag{5.12}$$

is applied on the results of the 73 directly calculated average $\mathrm{PT_L}$. Hence the damage $\mathrm{D_{TM3-st}}$ becomes to

$$\mathrm{D_{TM3-st}} = \mathrm{D_{PT_L}} * f_{\mathrm{TM3-st,100years}} \tag{5.13}$$

5.1.5. Method overview

In this chapter, an overview regarding the method for the fatigue design parameter study of single-span steel and composite bridges is presented. The basis of this overview are two single-span steel (SSB) and two single-span composite bridges (SCB) according to Table 5.2.

Name	L [m]	n_0 [Hz]	$\zeta_{\mathrm{SSB/SCB}}$ [%]	$\mathrm{W_y}$ [$\mathrm{cm^3}$]
SSB50-1	50	2.33	0.50	317456 **
SSB50-5	50	5.08	0.50	1259715 *
SCB50-1	50	2.33	0.50	398741 **
SCB50-5	50	5.08	0.50	1487032 **

The upper chord (*)/ the lower chord (**) is decisive.

Table 5.2.: Definition of single-span steel bridges (SSB) and single-span composite bridges (SCB)

First, on the level of static internal forces, hence for the bending moment M at midspan, the static equivalent constant amplitude bending moment range related to 2 million cycles $\Delta\mathrm{M_{E,2,static}}$ is calculated. This is, as subsequently shown, possible in two ways, which lead to the same result. One option is to use the load model LM71 and the damage equivalent factor λ, whereas the second option uses the service trains TypeC1 to TypeC8 — see traffic mix 1 in Table 4.1 — and damage accumulation. However, after performing this first step, $\Delta\mathrm{M_{E,2,stat}}$ is determined and defines the level of the S-N curve for the next step.
Subsequently, dynamic calculations are performed for the service trains TypeC1 to TypC8 and consequently the dynamic bending moment range spectra result. These are evaluated, using *Miner's rule*, on the before, by $\Delta\mathrm{M_{E,2,static}}$ defined, S-N curve, which leads to the damage $\mathrm{D_{dyn}}$.
Finally, with the calculated damage $\mathrm{D_{dyn}}$ and the static equivalent constant amplitude stress range related to 2 million cycles $\Delta\sigma_{\mathrm{E,2,static}}$, which is simply $\Delta\mathrm{M_{E,2,static}}$ divided by the elastic section modulus of the structure $\mathrm{W_y}$, the dynamic equivalent constant amplitude stress range related to 2 million cycles $\Delta\sigma_{\mathrm{E,2,dyn}}$ is calculated, which may be compared to the decisive detail category.

$\Delta M_{E,2,stat}$ based on static calculation of load model LM71 and stress range

Subsequently, the determination of the static equivalent constant amplitude bending moment range $\Delta M_{E,2,stat}$ using the load model LM71 and the damage equivalent factor λ, as described in Chapter 2, is presented for a 50 m long single-span structure. Therefore, the maximum static bending moment $M_{LM71,max}$ at midspan due to the crossing of the load model LM71 is determined — see Figure 5.10. Considering carefully maintained track with Φ_2 and the *EC mix* — see traffic mix 1 in Table 4.1 — in ÖNORM-EN 1993-2 [46] for λ leads, according to Equation (5.14), to a static equivalent constant amplitude bending moment range $\Delta M_{E,2,LM71}$ of about 19936 kNm.

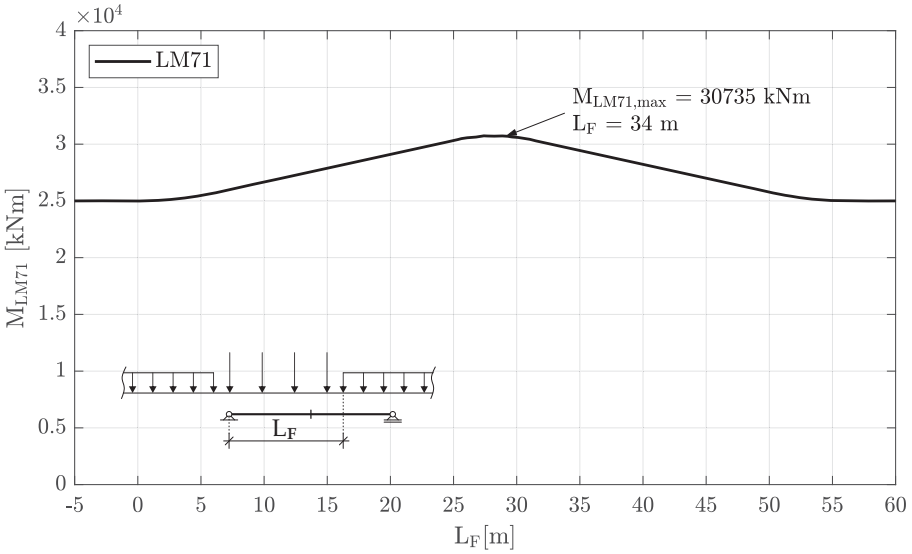

Figure 5.10.: Single-span bridge L = 50 m - SB50 — static — LM71

$$\begin{aligned}\Delta M_{E,2,LM71} &= \lambda_1 * \lambda_2 * \lambda_3 * \lambda_4 * \Delta M_{LM71,max} * \Phi_2 \\ &= 0.63 * 1.00 * 1.00 * 1.00 * 30735 * 1.0296 = 19936 \text{ kNm}\end{aligned} \tag{5.14}$$

$$\begin{aligned}\text{with:}\quad & \lambda_1 = 0.63 \quad \ldots \text{acc. to [46] Tab. 9.3 EC Mix, L = 50 m} \\ & \lambda_2 = 1.00 \quad \lambda_3 = 1.00 \quad \lambda_4 = 1.00 \\ & \Phi_2 = \frac{1.44}{\sqrt{L_\Phi} - 0.2} + 0.82 \\ & \quad = \frac{1.44}{\sqrt{50} - 0.2} + 0.82 = 1.0296 \quad \ldots \text{acc. to [43], Equ. 6.4, } L_\Phi = L = 50\text{m}\end{aligned} \tag{5.15}$$

$\Delta M_{E,2,stat}$ based on static calculation of service trains TypeC1 to TypeC8 and damage accumulation

Furthermore, the static equivalent constant amplitude bending moment range $\Delta M_{E,2,stat}$ may be determined by using the trains TypeC1 to TypeC8 of ÖNORM-EN 1991-2, Annex D [43], which

are represented by traffic mix 1 in this doctoral thesis — see Figure 2.18. Therefore, the crossing of each train type is simulated statically and the resulting bending moment ranges are counted using a cycle counting method (e.g. reservoir method). After obtaining the bending moment range spectrum for one crossing of each of these eight train types, those are combined according to the *standard traffic mix with axles* $\leq$ *22.5 t* — see Table 2.3, or Table 4.1 and ÖNORM-EN 1991-2, Table D.1 [43] — to the bending moment range spectrum for a design life of 100 years.
For the train TypeC7 and a 50 m long single-span bridge the procedure is described in detail as follows. First, the crossing of the train is simulated in a static way, which leads to the bending moment signal M at midspan, as illustrated in Figure 5.11(a), already including the dynamic factor $(1+\varphi)_D$ according to Equation (2.12) and ÖNORM EN 1991-2, Annex D [43]. In the next step, the signal is prepared for the reservoir counting method. Therefore, it is split at its maximum (point B) and reordered according to Figure 5.11(b). As only the local maxima and minima are of interest, the turning point signal is determined — see Figure 5.11(c). Further, the ordinate is split into equidistant segments, hence classes of the classwidth $\Delta M_{step} \leq M_{max}/100$ are introduced as illustrated in the small window of Figure 5.11(c). Consequently, each local maxima and minima is assigned to a specific class M_{up} and the signal is ready for the reservoir counting method. Therefore, the 'reservoir' is theoretically filled with water and the maximum possible distance between the 'water surface' and the 'reservoir bottom' measured — ΔM_1 in Figure 5.11(d). Subsequently, the reservoir is opened at the lowest point of the reservoir bottom, which leads to the new reservoirs illustrated in Figure 5.11(e). The process is repeated until all reservoirs are emptied, hence all remaining bending moment ranges ΔM_2 to ΔM_4 are identified.
The bending moment range spectrum due to one crossing of the train TypeC7, which was calculated according to the procedure in Figure 5.11, is now illustrated in Figure 5.12 by the dashed pink line. On the ordinate, the bending moment ranges ΔM are plotted, whereas on the abscissa the number of cycles N are drawn on a logarithmic scale. In order to obtain the bending moment range spectrum for the design life of 100 years, the information of Table 2.3 is applied. Consequently, the number of cycles of the bending moment range spectrum due to one train crossing is multiplied by the number of trains/ day, 365 days/ year and 100 years, which leads to the bending moment range spectrum for the entire design life — see solid pink line in Figure 5.12.
The above described procedure is then repeated for the remaining seven train types. Hence, their bending moment range spectra due to one train crossing are determined first, including the dynamic factor $(1+\varphi)_D$ according to Equation (2.12). Consequently, the bending moment range spectrum for the entire design life of 100 years is calculated according to Table 2.3, which leads to the black solid line in Figure 5.13. In the next step this bending moment range spectrum for the design life is evaluated at the modified S-N curve — see black dashed line in Figure 5.13 — using *Miner's rule* according to Equation (2.19), which results into a certain value for the damage D_{stat}. The level of the modified S-N curve is changed and the damage calculation repeated until a damage of $D_{stat} = 1.0$ results, hence an iteration is performed. Subsequently, the static equivalent constant amplitude bending moment range $\Delta M_{E,2,TypeC1-C8,stat}$, defined for $2\ 10^6$ cycles, is obtained, which is in this case about 19778 kNm. The error made by the method of the previous chapter, which uses the load model LM71 and the damage equivalent factor λ, leading to a $\Delta M_{E,2,LM71}$ of 19936 kNm, according to Equation (5.14), is only about 0.8 %.

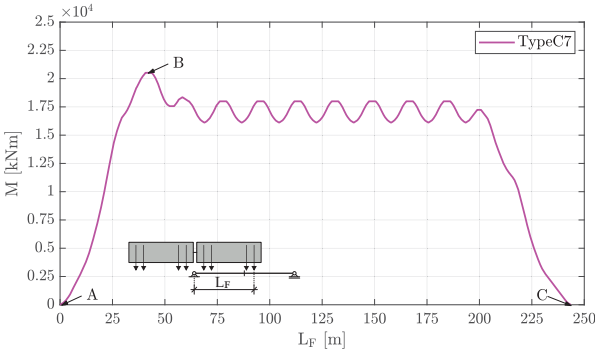

(a) Signal M from static calculation

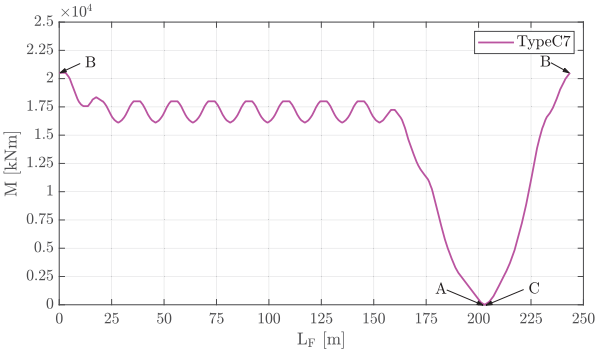

(b) Prepaired input signal M for reservoir method

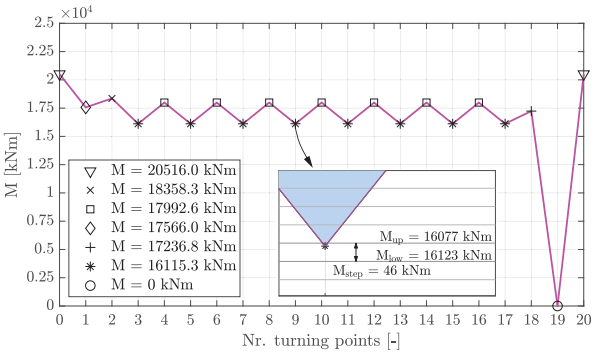

(c) Turning point signal M — classwidth $\Delta M_{step} \leq M_{max}/100$

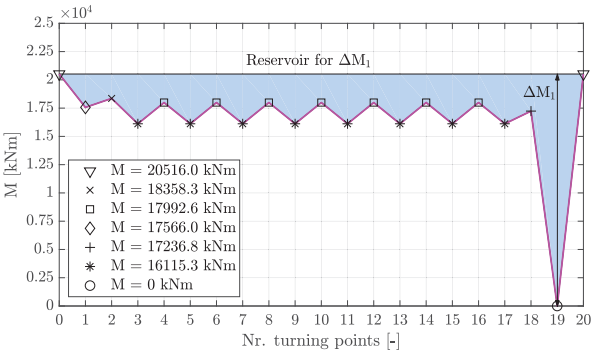

(d) Reservoir for ΔM_1

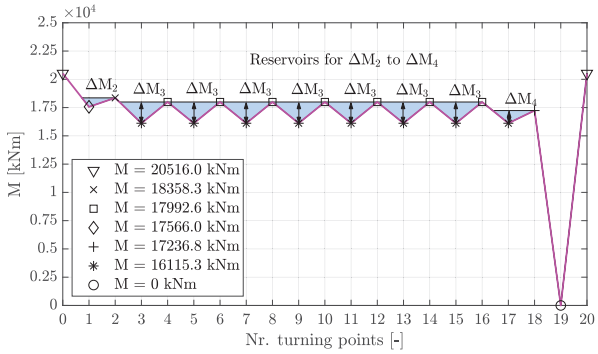

(e) Reservoirs for ΔM_2 to ΔM_4

Figure 5.11.: Procedure for rainflow-analysis — SB50 — TypeC7 static

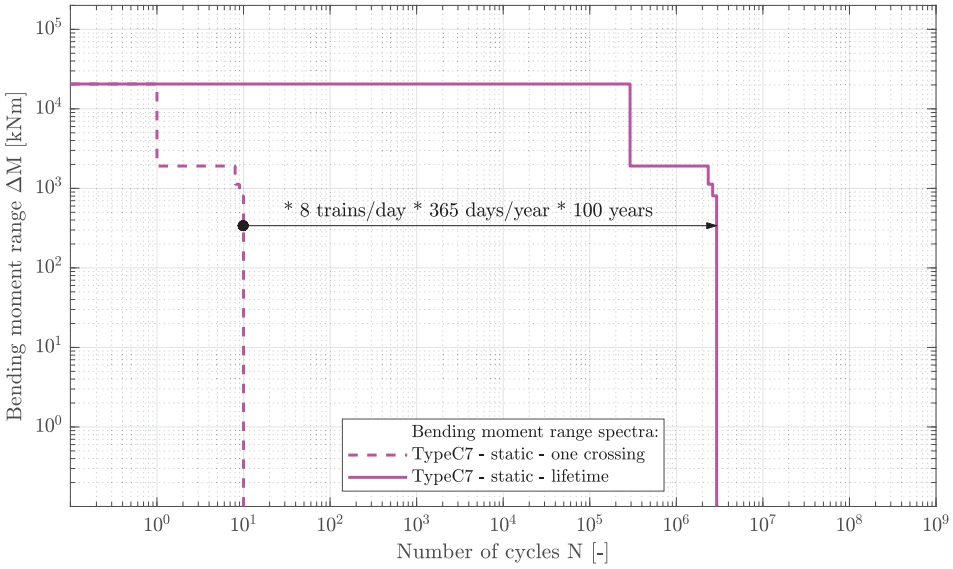

Figure 5.12.: Bending moment ranges for one train crossing and over design life — SB50 — TypeC7 static incl. $(1+\varphi)_D$ according to ÖNORM EN 1991-2, Annex D [43]

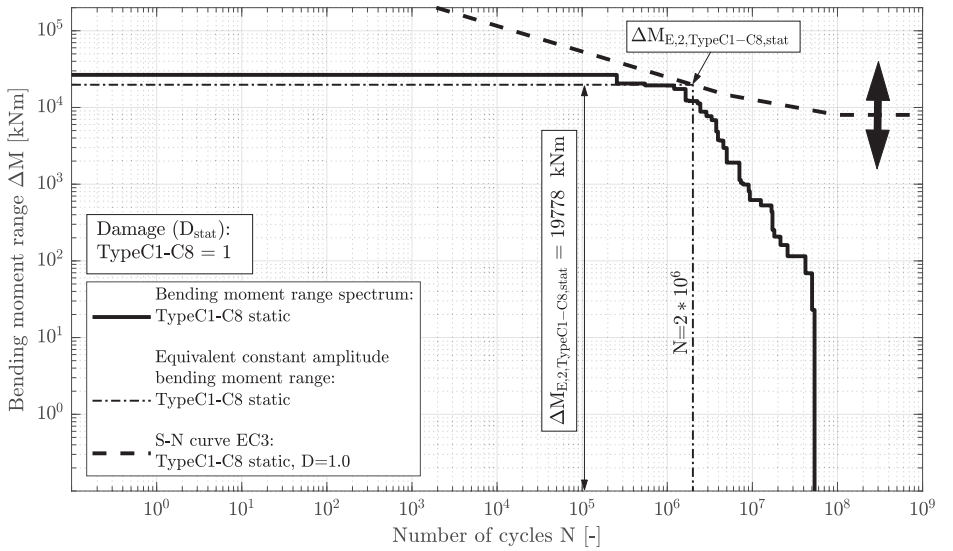

Figure 5.13.: Single-span bridge L = 50 m — SB50 — static — TypeC1-C8 of traffic mix 1

In Figure 5.14 the individual results for the trains TypeC1 to TypeC4, which represent the passenger trains of the traffic mix *EC mix*, are illustrated. Figure 5.14(a) shows the static bending moment signals M at midspan, whereas Figure 5.14(b) presents the related bending moment range spectra for the design life and the damage values D_{stat} calculated using the above in Figure 5.13 determined S-N curve. Furthermore, the same procedure is performed for the trains TypeC5 to TypeC8, which represent the freight trains of the traffic mix *EC mix* — see Figure 5.15. Comparing the damage values D_{stat} of the passenger and freight trains, one can see that the latter are mainly responsible for the damage according to the static calculation.

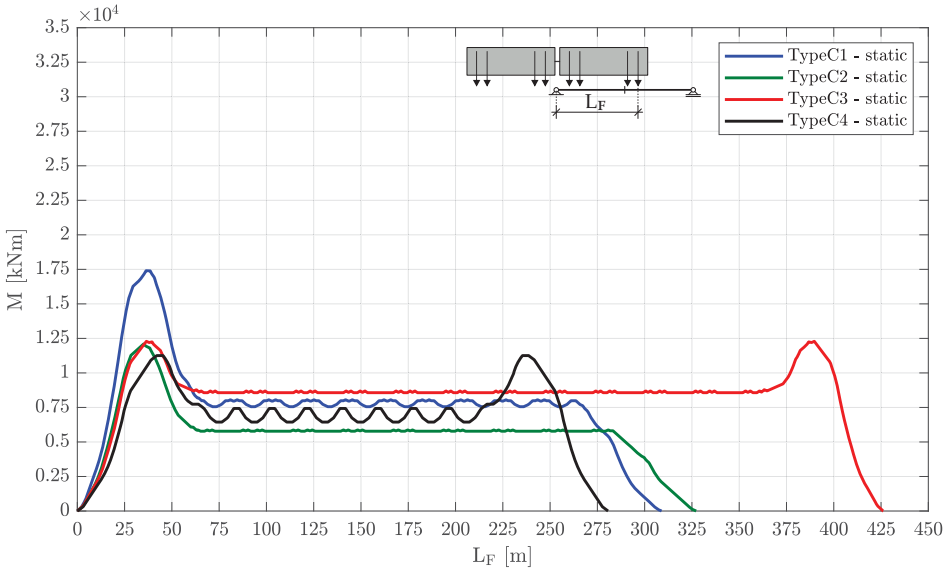

(a) Bending moment M incl. $(1+\varphi)_D$ according to ÖNORM EN 1991-2, Annex D [43]

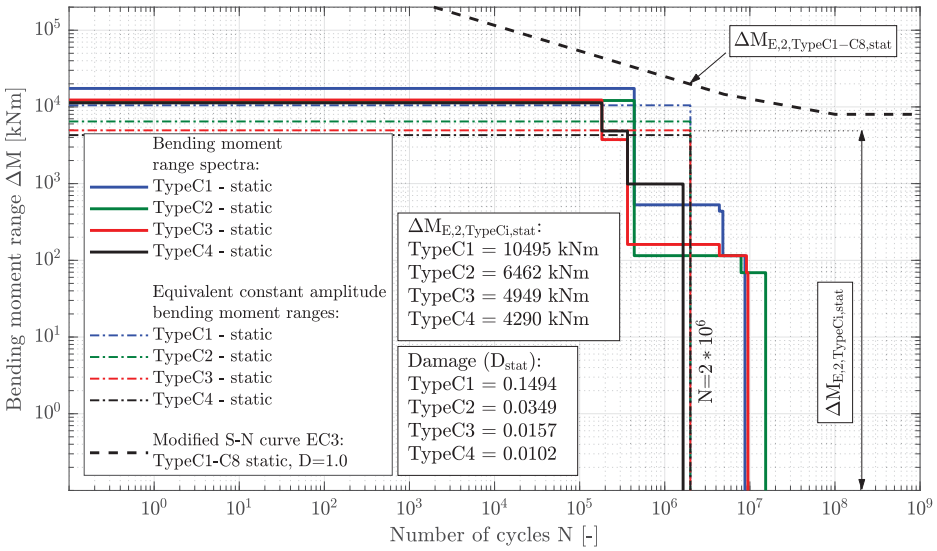

(b) Bending moment range spectra for design life of 100 years

Figure 5.14.: Single-span bridge L = 50 m - SB50 — static — TypeC1-C4

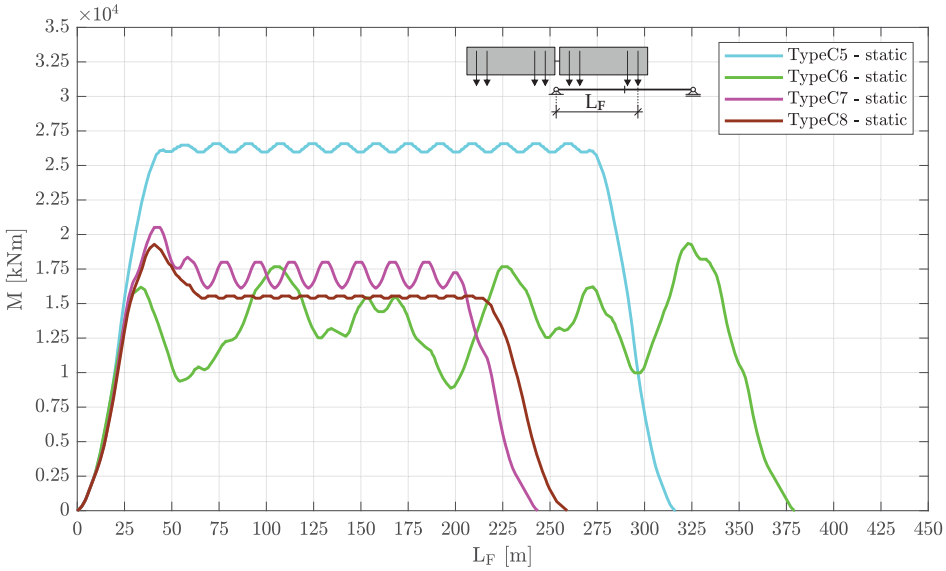

(a) Bending moment M incl. $(1+\varphi)_D$ according to ÖNORM EN 1991-2, Annex D [43]

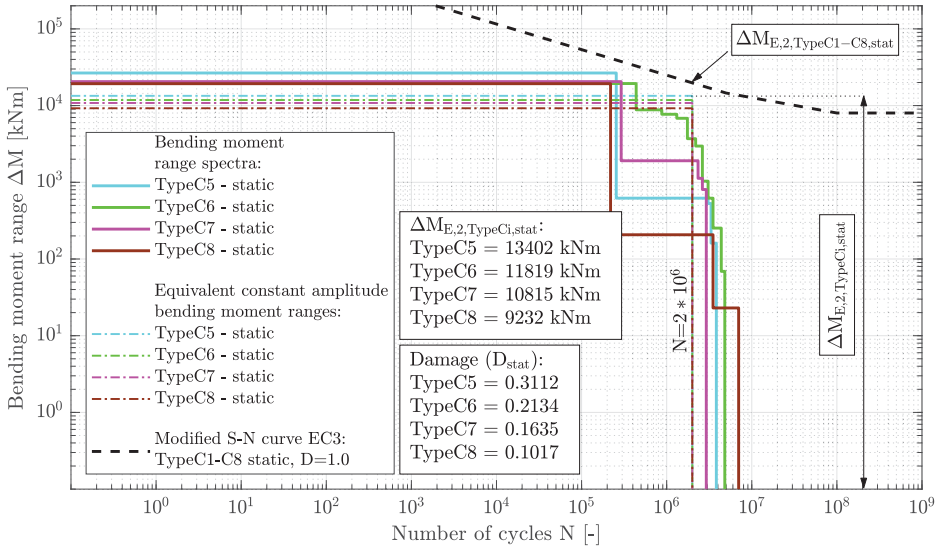

(b) Bending moment range spectra for design life of 100 years

Figure 5.15.: Single-span bridge L = 50 m - SB50 — static — TypeC5-C8

The before described procedure is valid for the static calculation of a 50 m long single-span bridge. Figure 5.16 shows the results for span lengths starting from 7-80 m. Variant A in Figure 5.16 represents the method using the load model LM71 and the damage equivalent factor λ. On the other hand, the variants B and C illustrate the results using the trains TypeC1-C8 and damage accumulation. The dynamic factor $(1+\varphi)_D$ according to ÖNORM EN 1991-2, Annex D [43], which needs to be applied for the latter two variants, only allows to consider trains with speeds up to 200 km/h. However, trains TypeC3 and C4 have a maximum train speed v_{max} of 250 km/h — see Figure 2.18. Therefore, the variant B considers the trains TypeC3 and C4 with a $v_{max} = 250$ km/h and variant C consequently with $v_{max} = 200$ km/h. However, as

the impact of these two trains is very limited — see damage values D_{stat} in Figure 5.14(b) — it is also neglectable in the overall result of Figure 5.16. Subsequently, the variant B, which was already used for all presented results, is used continuously, as its average error in comparison to variant A is with 1.1 % about 0.3 % lower than variant C. Hence, $\Delta M_{E,2,TypeC1-C8,stat}$ of variant B becomes $\Delta M_{E,2,stat}$ and is also used to determine $\Delta\sigma_{E,2,static}$.

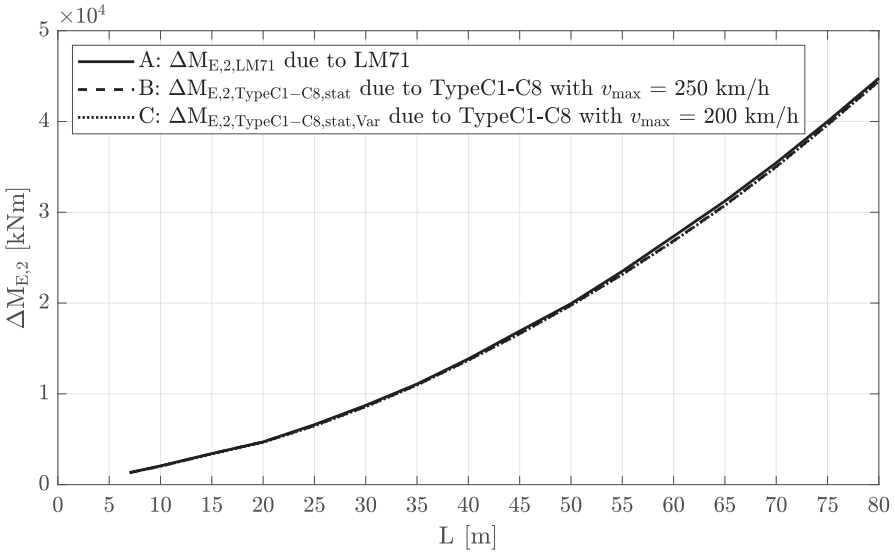

Figure 5.16.: Comparison of $\Delta M_{E,2}$ due to LM71 and TypeC1-C8 — static

Fatigue design based on dynamic calculation of service trains TypeC1 to TypeC8 and damage accumulation

Subsequently, the fatigue design is again based on the trains TypeC1 to TypeC8 of taffic mix 1, using damage accumulation, but the train crossing is here simulated by a dynamic instead of a static calculation. Hence, except the dynamic calculation (moving load model), the same procedure as in the previous chapter is applied. Furthermore, the S-N curve, which is needed to obtain, using *Miner's rule*, the damage D_{dyn} due to the dynamic calculation, is set to the level of the static calculation — see Figure 5.13. The procedure is explained using the four example single-span steel and composite bridges of Table 5.2. Each of the eight trains, crosses the structure with the speed $v_{D_{max}}$, which produces the maximum possible damage within the considered speed range of 50 to 1.2 v_{EC} km/h. Hence, the discussed examples are results of the in Chapter 4.1 defined traffic mix TM1**. Further, all in this chapter performed dynamic calculations base on the moving load model and Rayleigh like damping using the damping variant ζ_{EC} — see Figure 5.9. However, regarding the dynamic calculation, first the dimensional approach — see Chapter 3.5.2 — and afterwards the non-dimensional response representation — see Chapter 3.6 — and its benefits are presented.

Damage accumulation based on dimensional calculation

Figure 5.17 illustrates the results for the passenger trains TypeC1 to TypeC4 acting on the single-span steel bridge SSB50-1 and single-span composite bridge SCB50-1. As the first bending frequencies n_0 and the damping ratios ζ_{EC} of SSB50-1 and SCB50-1 are identical, the resulting bending moments are equivalent as well — see non-dimensional approach and Equations (3.221)

and (3.223). In Figure 5.17(a) the bending moments M at midspan varying with time due to the crossing of trains TypeC1 to TypeC4 are illustrated. Consequently, Figure 5.17(b) shows the corresponding bending moment range spectra for the entire design life of 100 years. The latter are evaluated at the S-N curve, which was defined due to the static calculation as described above — see Figure 5.13, leading to the damage D_{dyn}. Finally, the equivalent constant amplitude bending moment ranges $\Delta M_{E,2,TypeCi,dyn}$ were calculated and plotted.

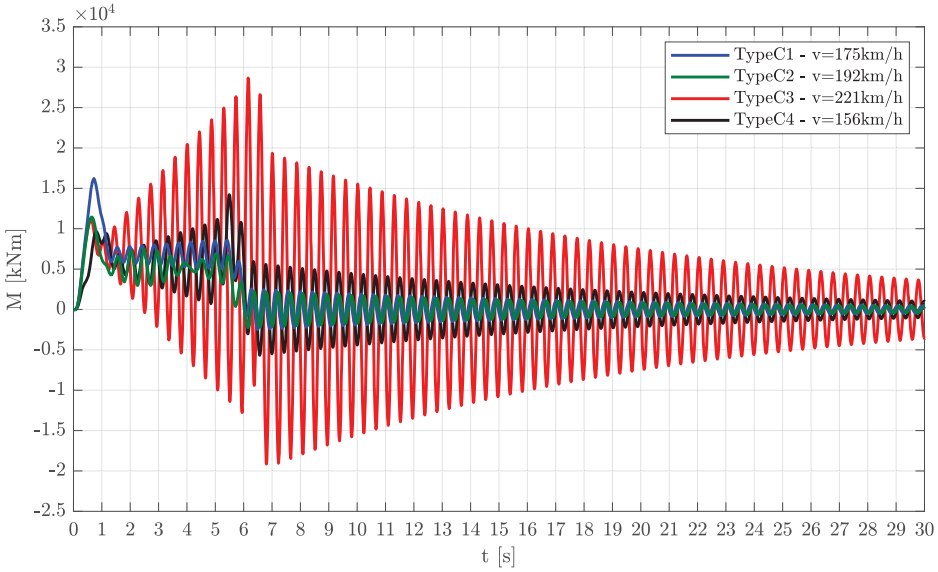

(a) Bending moment M incl. $(1 + 0.25\ \varphi''_D)$ according to ÖNORM EN 1991-2, Annex D [43]

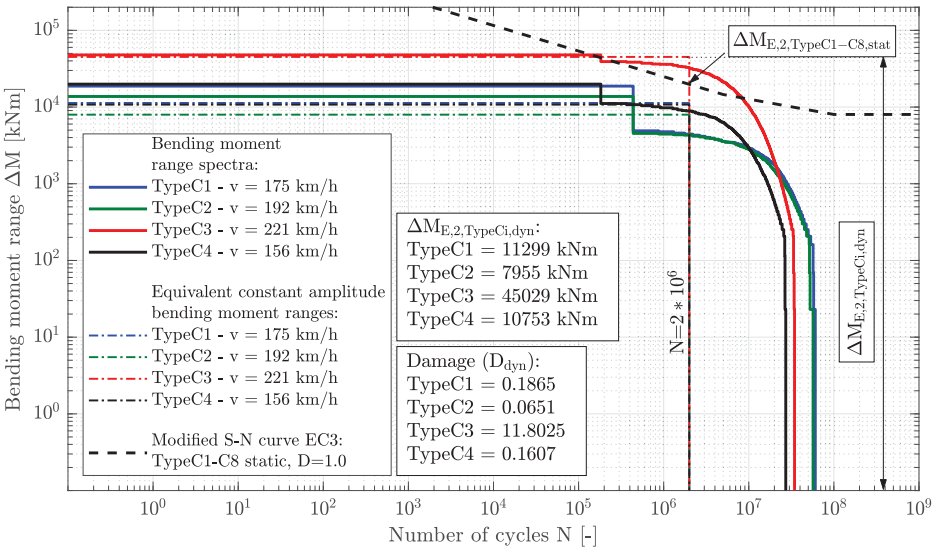

(b) Bending moment range spectra for design life of 100 years

Figure 5.17.: Single-span bridge L = 50 m — SSB50-1 & SCB50-1 — dynamic — $v_{D_{max}}$ — ζ_{EC} — Rayleigh like damping — TypeC1-C4 of traffic mix TM1**

In Figure 5.18 the results for the freight trains TypeC5 to TypeC8 are illustrated.

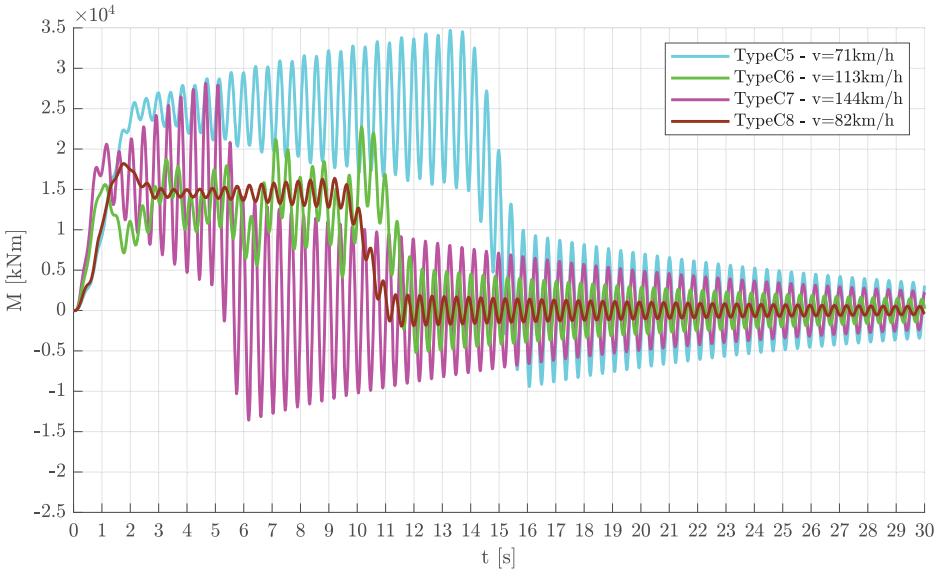

(a) Bending moment M incl. $(1 + 0.25\ \varphi''_{D})$ according to ÖNORM EN 1991-2, Annex D [43]

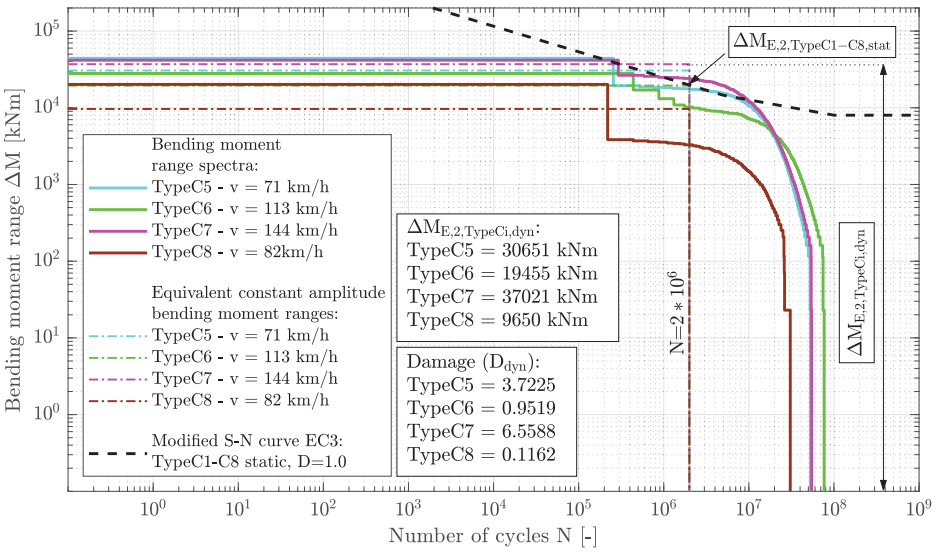

(b) Bending moment range spectra for design life of 100 years

Figure 5.18.: Single-span bridge L = 50 m — SSB50-1 & SCB50-1 — dynamic — $v_{D_{max}}$ — ζ_{EC} — Rayleigh like damping — TypeC5-C8 of traffic mix TM1**

The overall outcome, which compares the static and the dynamic results of the trains TypeC1 to TypeC8 crossing the single-span steel and composite bridges SSB50-1 and SCB50-1 is presented in Figure 5.19. The blue solid line shows the bending moment range spectrum of the dynamic calculation for the entire design life of 100 years, whereas the black solid line illustrates the one for the static calculation. Considering the S-N curve, defined by the static calculation, for the damage accumulation calculation, according *Miner's rule*, leads for the static case, by definition,

to D_{stat} = 1.0. On the other hand, the dynamic bending moment range spectrum evokes a damage of D_{dyn} = 23.5641 and exceeds severely the static calculation.

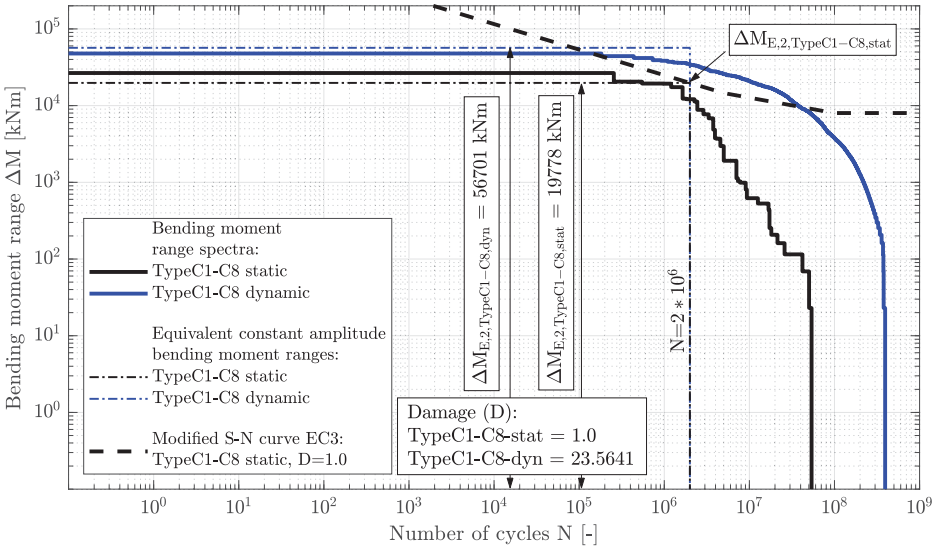

Figure 5.19.: Single-span bridge L = 50 m — SSB50-1 & SCB50-1 — static vs. dynamic — $v_{D_{max}}$ — ζ_{EC} — Rayleigh like damping — TypeC1-C8 of traffic mix TM1**

The following two Figures 5.20 and 5.21 show again the results of the dynamic calculation of the trains TypeC1 to TypeC8, but now acting on the single-span steel and composite bridges SSB50-5 and SCB50-5, with significantly higher first bending frequencies — see Table 5.2. However, the impact of all trains on this structure is substantially lower than on the previously discussed single-span bridge SSB50-1 and SCB50-1 — compare with Figures 5.17 and 5.18.

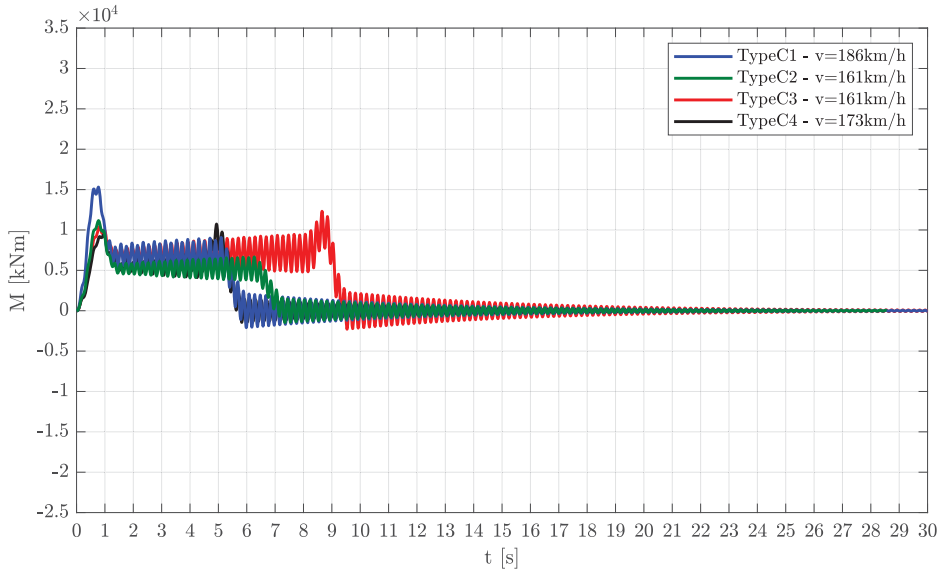

(a) Bending moment M incl. $(1 + 0.25\ \varphi''_{D})$ according to ÖNORM EN 1991-2, Annex D [43]

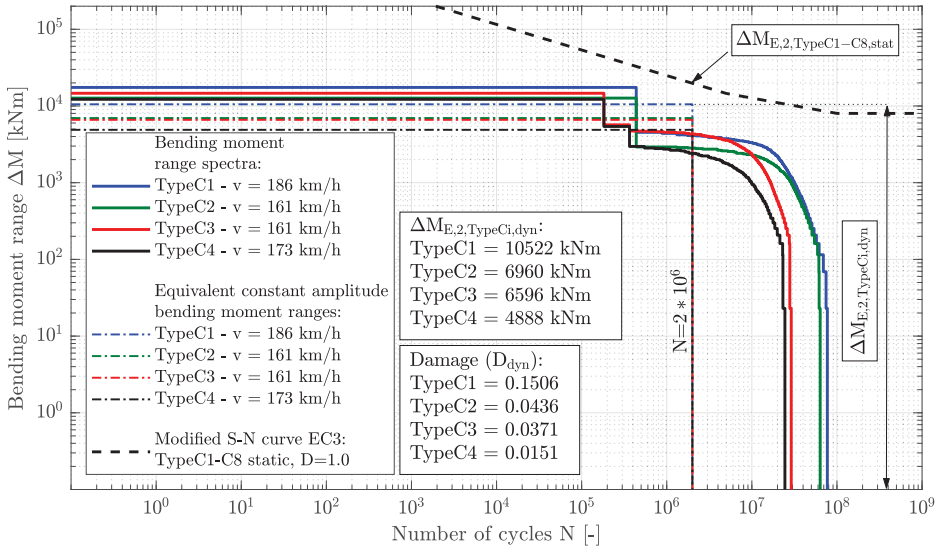

(b) Bending moment range spectra for design life of 100 years

Figure 5.20.: Single-span bridge L = 50 m — SSB50-5 & SCB50-5 — dynamic — $v_{D_{max}}$ — ζ_{EC} — Rayleigh like damping — TypeC1-C4 of traffic mix TM1**

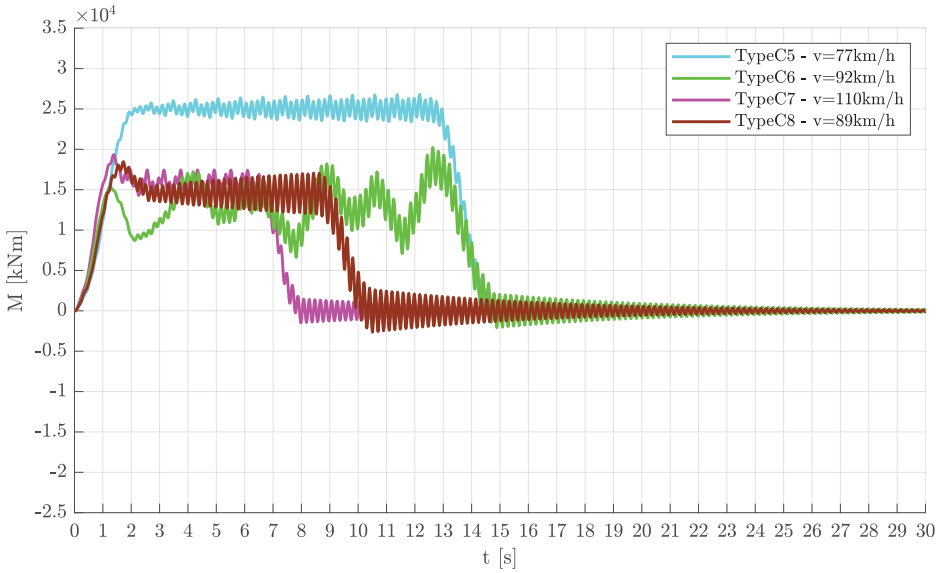

(a) Bending moment M incl. $(1 + 0.25\ \varphi''_D)$ according to ÖNORM EN 1991-2, Annex D [43]

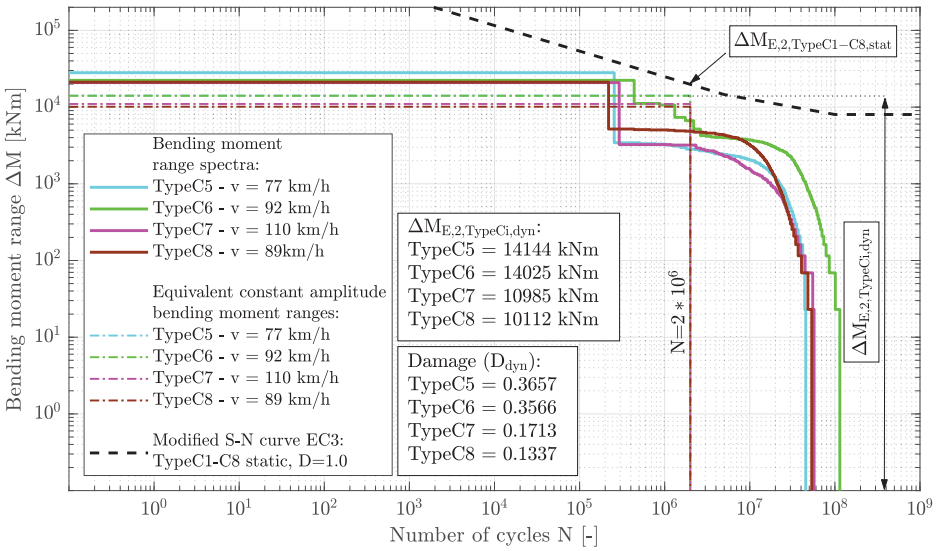

(b) Bending moment range spectra for design life of 100 years

Figure 5.21.: Single-span bridge L = 50 m — SSB50-5 & SCB50-5 — dynamic — $v_{D_{max}}$ — ζ_{EC} — Rayleigh like damping — TypeC5-C8 of traffic mix TM1**

In Figure 5.22 the overall dynamic and static results for the single-span steel and composite structure SSB50-5 and SCB50-5, which are crossed by the trains TypeC1 to TypeC8, are presented. The damage D_{dyn}, due to the dynamic calculation, exceeds with 1.2737 again the static result ($D_{stat} = 1.0$) but is reduced significantly in comparison to the structures SSB50-1 and SCB50-1 — see Figure 5.19.

Here, the dynamic bending moment range spectrum (blue solid line) has again much more cycles than the static bending moment range spectrum (black solid line), but these, however, do not cause any damage D_{dyn} as their amplitude is below the cut-off limit $\Delta\sigma_L$.

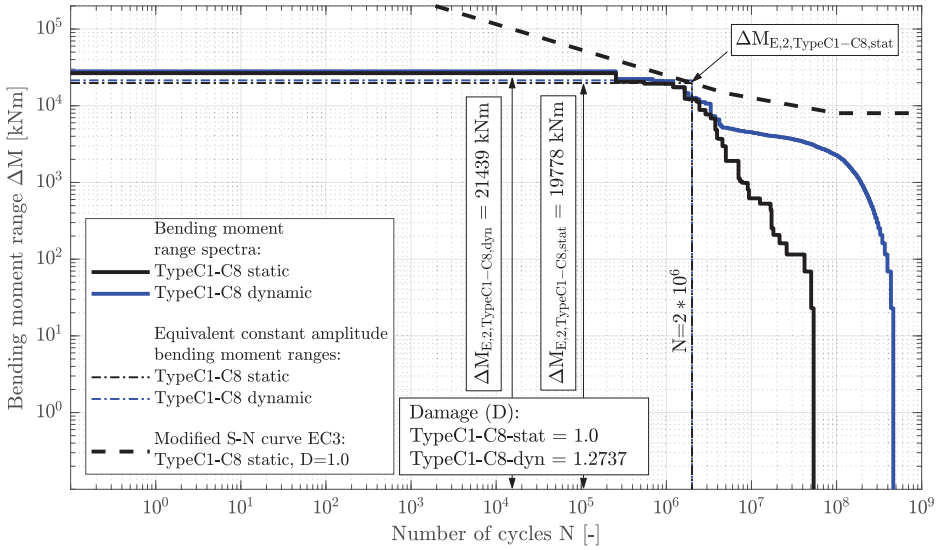

Figure 5.22.: Single-span bridge L = 50 m — SSB50-5 & SCB50-5 — static vs. dynamic — $v_{D_{max}}$ — ζ_{EC} — Rayleigh like damping — TypeC1-C8 of traffic mix TM1**

The trains TypeC3, TypeC5 and TypeC7 have the biggest impact on the damage D_{dyn}, regarding the single-span steel and composite bridges SSB50-1 and SCB50-1 — see Figures 5.17 and 5.18. In Table 5.3 an explanation is presented why these trains produce on structures SSB50-1 and SCB50-1 much more damage than on SSB50-5 and SCB50-5. All trains cross the structures with the individual speed $v_{D_{max}}$, which produces the maximum possible damage D_{dyn} within the speed range of each train. Considering the car length L_D of each train, allows to calculate the excitation frequency n_{L_D}. If the excitation frequency n_{L_D} or an integral multiple $i = \mathbb{N}$ of it, is equal to the structure's first bending frequency n_0, then resonance occurs. Within one excitation period, the first bending mode performs i oscillations. Consequently, the lower i is, the more often the first bending mode is excited, which is throughout the case for the single-span steel and composite bridge SSB50-1 and SCB50-1 in comparison to SSB50-5 and SCB50-5.

Bridge	n_0 [Hz]	Train type	$v_{D_{max}}$ [km/h]	L_D	$n_{L_D} = \frac{v_{D_{max}}}{3.6\ L_D}$ [Hz]	$i = \frac{n_0}{n_{L_D}}$
SSB50-1 SCB50-1	2.33	TypeC3	221	26.4	2.33	1
		TypeC5	71	16.9	1.17	2
		TypeC7	144	17.8	2.25	≈1
SSB50-5 SCB50-5	5.08	TypeC3	161	26.4	1.69	3
		TypeC5	77	16.9	1.27	4
		TypeC7	110	17.8	1.72	3

Table 5.3.: Excitation frequency n_{L_D} of specific EC trains acting on single-span steel (SSB50-1/ SSB50-5) and composite bridges (SCB50-1/ SCB50-5)

Damage accumulation based on non-dimensional response representation

In the following paragraphs, the use of the non-dimensional response representation, which was defined in Chapter 3.6, is presented. Therefore, the additional 50 m long single-span steel structure SSB50-3, whose first bending frequency $n_0 = 3.70$ Hz is between the ones of SSB50-1 and SSB50-5, is introduced.[1] The crossing of all three structures by the train TypeC3 and the resulting damage D_{dyn} for the speed range 50 to 300 km/h is plotted in Figure 5.23. Again, the level of the S-N curve for the damage accumulation calculation (*Miner's rule*) was defined by the static calculation for single-span bridges with lengths of 50 m — see Figure 5.13.

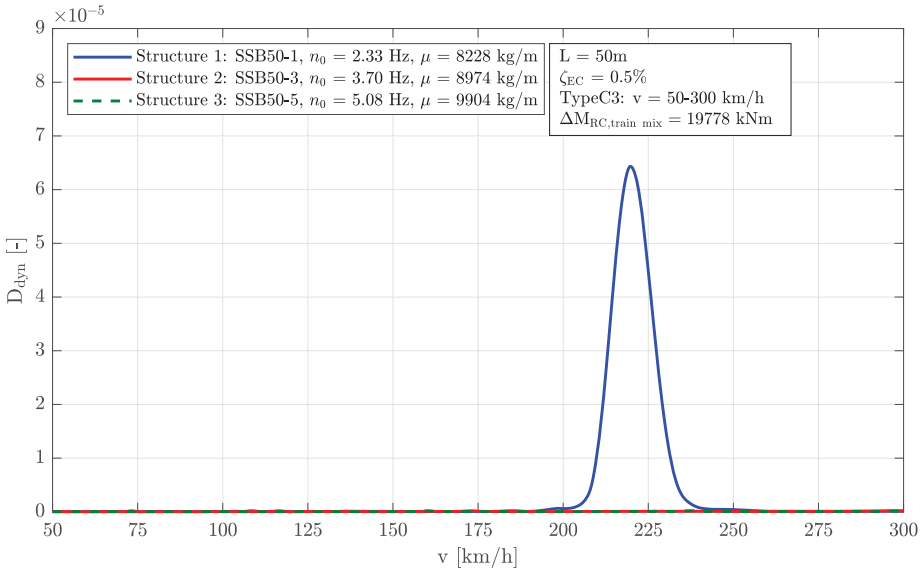

Figure 5.23.: Dimensional results for D_{dyn} — three single-span bridges with L = 50 m (structures 1 to 3) — one crossing of train TypeC3 — v = 50-300km/h — ζ_{EC} — Rayleigh like damping

Rewriting Equations (3.221) and (3.223) illustrates the basic idea of the non-dimensional response representation regarding the bending moment M

$$M_{non-dim} = \frac{M}{P_{max}\ L} \tag{5.16}$$

$$S = \frac{v}{2\ L\ n_0} \tag{5.17}$$

Consequently, the ordinate of the dimensional bending moment representation M needs to be divided by the structure's length L and the train's maximum axle load P_{max} — according to Equation (5.16). Furthermore, the abscissa of the non-dimensional representation becomes with Equation (5.17), the train velocity v and the first bending frequency n_0 to S. However, as the level of the S-N curve is determined by the static calculation, which is valid for all single-span structures of a particular length L, $\Delta M_{E,2,TypeC1-C8,stat}$ stays constant for all single-span structures of this particular length L as well, hence

$$\Delta M_{E,2,TypeC1-C8,stat} = f(L) \tag{5.18}$$

[1] The here described procedure is also valid for the single-span composite bridges SCB50-1, SCB50-3 and SCB50-5 as they have the same first bending frequency n_0 and damping ratio ζ_{EC} like the single-span steel bridges SSB50-1, SSB50-3 and SSB50-5. However, due to reasons for simplicity they are not mentioned here.

as illustrated in Figure 5.16. This consequently allows to write

$$D_{non-dim} = \frac{D}{P_{max}\, L} \tag{5.19}$$

whereas the maximum axle load P_{max} and the length of the structure L stay constant for all structures with a particular length (e.g. all structures in Figure 5.23 have a span length of L = 50 m), which theoretically makes the division in Equation (5.19) unnecessary and therefore is subsequently not performed either. In Figure 5.24 the transformation from the dimensional to the non-dimensional representation, applying Equation (5.17), is shown. The black line illustrates the non-dimensional response solution for a particular S range and simultaneously represents the solutions of all three structures. Hence, one only needs to calculate the non-dimensional solution once and consequently receives the solution for the other three structures as well.

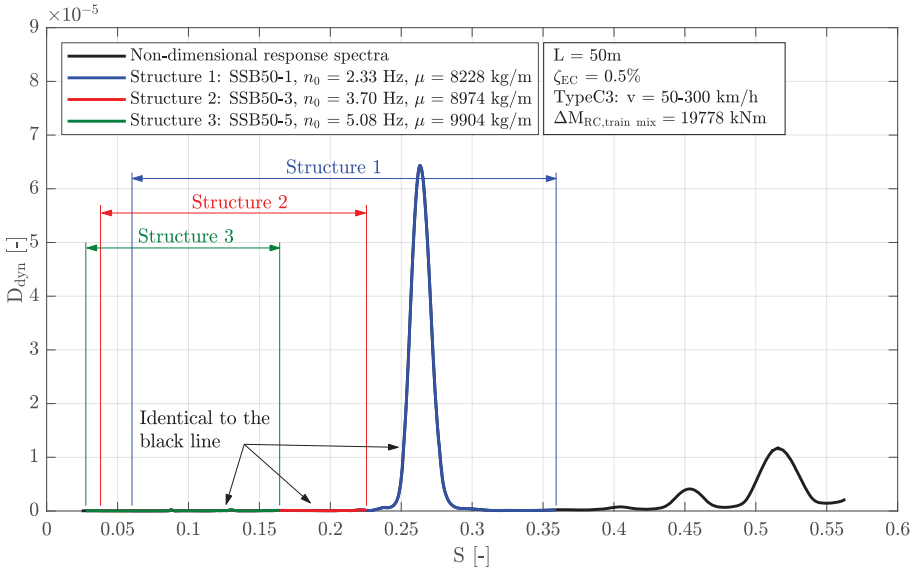

Figure 5.24.: Non-dimensional results for D_{dyn} — three single-span bridges with L=50m (structures 1 to 3) — one crossing of train TypeC3 — ζ_{EC} — Rayleigh like damping

Figure 5.25 shows the damage D_{dyn} results for the crossing of one train TypeC3 on single-span structures with lengths L starting from 7 to 80 m. The non-dimensional solution of Figure 5.24 is plotted in Figure 5.25 at L = 50 m.

The dimensional solutions can be found by simply applying Equation (5.17) and choosing a particular damage D_{dyn} value within a given speed range. This was performed in Figure 5.26 by looking for the maximum damage D_{dyn} value within the speed range v = 50-300 km/h for the single-span structures defined by the upper and lower limits according to ÖNORM EN1991-2, Fig. 6.10 [43] — see Figure 2.7. Consequently, for each bridge in Figure 5.26, defined by the length L and first bending frequency n_0, the maximum possible damage value D_{dyn}, reached by the train speed $v_{D_{max}}$, within the speed range v = 50-300 km/h, was selected.

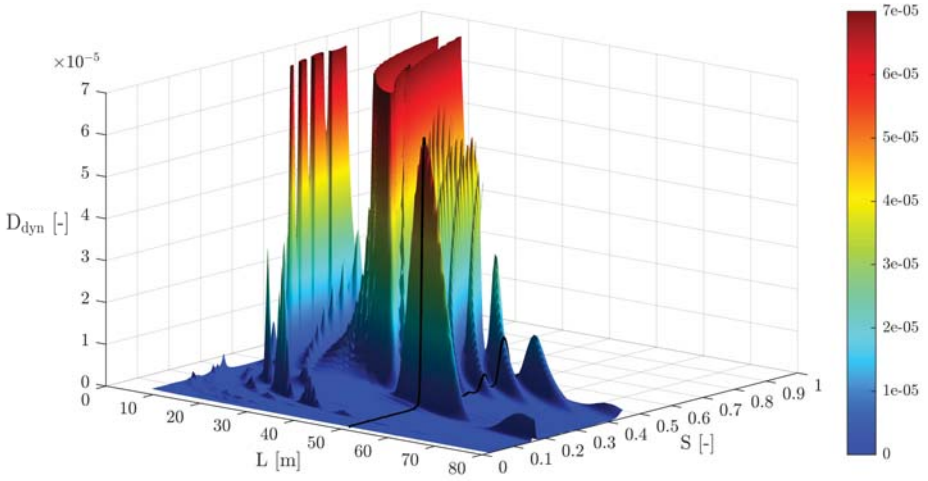

Figure 5.25.: Non-dimensional results for D_{dyn} (3D view) — single-span bridges — one crossing of train TypeC3 — ζ_{EC} — Rayleigh like damping

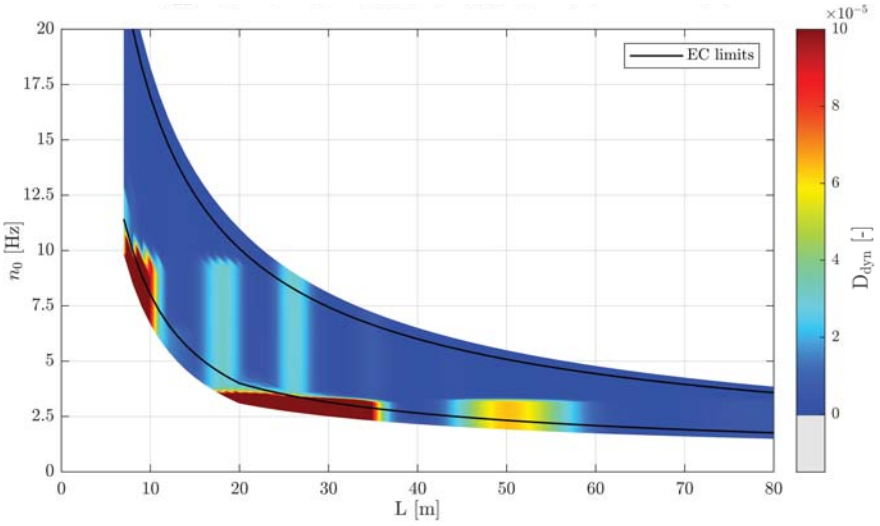

Figure 5.26.: Dimensional results for D_{dyn} (top view) — single-span bridges — one crossing of train TypeC3 — $v_{D_{max}}$ — ζ_{EC} — Rayleigh like damping

The damage D_{dyn} values in Figure 5.26 result due to one crossing of train TypeC3. These need to be multiplied by the number of train crossings within the design life of the structure, which leads for train TypeC3 — considering Table 4.1 — to Figure 5.27.

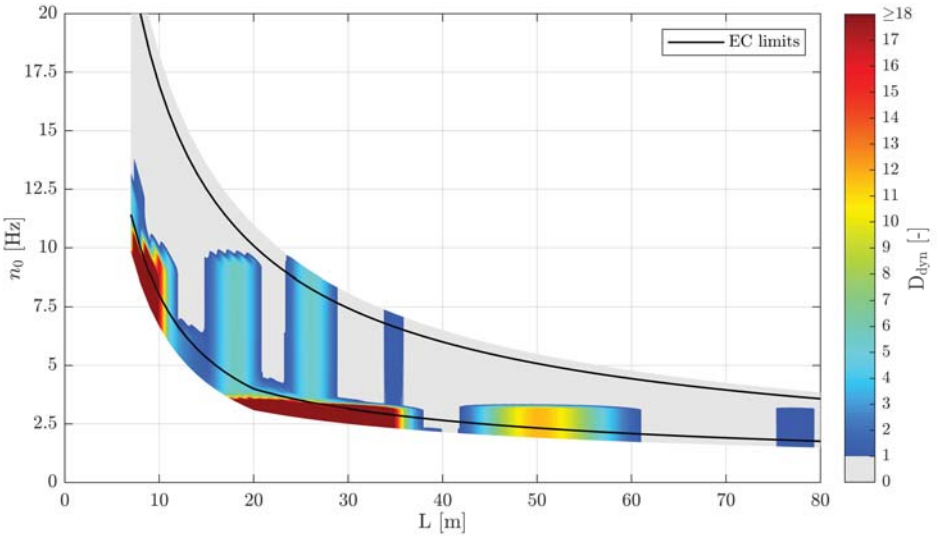

Figure 5.27.: Dimensional results for D_{dyn} (top view) — single-span bridges — all crossings of train TypeC3 for design life (100 years) of bridge (traffic volume 1.72 10^6 t/ year) — $v_{D_{max}}$ — ζ_{EC} — Rayleigh like damping

The above described procedure for train TypeC3 may be repeated for the other seven remaining trains of traffic mix TM1** according to Table 4.1 and Table 4.2. The summarized results for traffic mix TM1** (design life of 100 years and traffic volume of 24.95 10^6 t/ year) is shown in Figure 5.28. The results of the dimensional calculation for structure 1 (SSB50-1) and structure 3 (SSB50-5) — see Figures 5.19 and 5.22 — are plotted in Figure 5.28 as well.

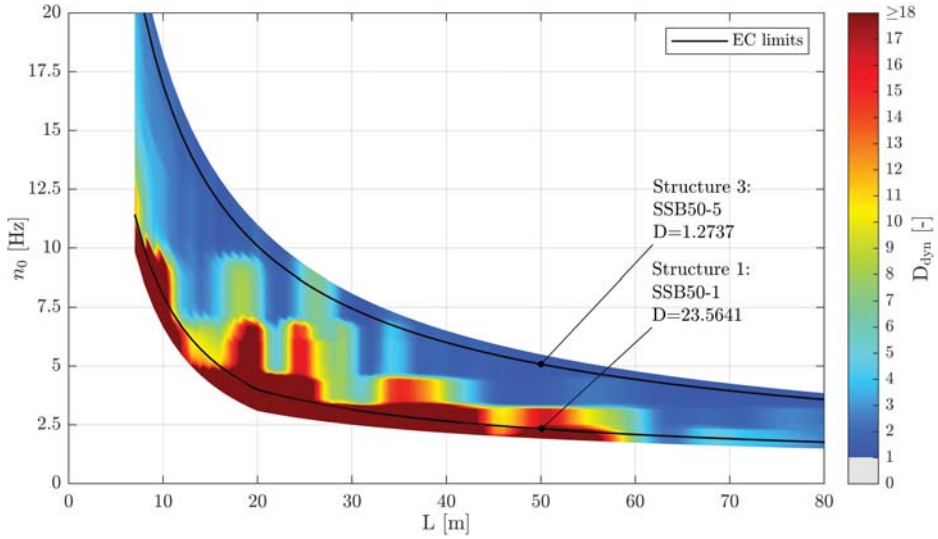

Figure 5.28.: Dimensional results for D_{dyn} (top view) — single-span bridges — traffic mix 1 (TM1**) — $v_{D_{max}}$ — ζ_{EC} — Rayleigh like damping

Calculation of $\Delta\sigma_{E,2,dyn}$ for steel/ composite bridges

In the final step, the equivalent constant amplitude stress range $\Delta\sigma_{E,2,dyn}$ due to the dynamic calculation is determined, which then may be compared to the decisive detail category. Therefore, on the one hand, the before determined damage D_{dyn} is necessary. On the other hand, the equivalent constant amplitude stress range $\Delta\sigma_{E,2,stat}$ due to the static calculation is required as well. The latter is again calculated for the defined single-span steel and composite reference bridges and the area in between is interpolated. Figure 5.29 shows the equivalent constant amplitude stress ranges $\Delta\sigma_{E,2,stat}$ for the single-span steel bridges.

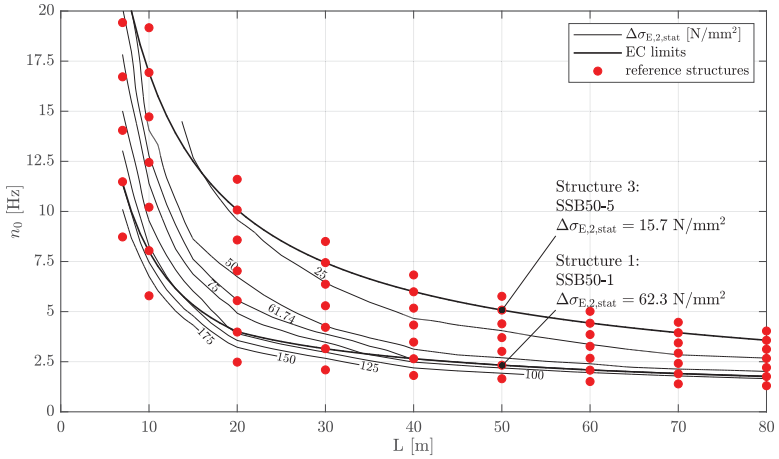

Figure 5.29.: Single-span steel bridges — $\Delta\sigma_{E,2,stat}$ due to trains TypeC1 to TypeC8 — reference structures and interpolated surface — no load distribution

According to Equation (5.20) and using the damage D_{dyn} values of Figure 5.28 the equivalent constant amplitude stress ranges $\Delta\sigma_{E,2,dyn}$, which are illustrated in Figure 5.30, result.[1]

$$\Delta\sigma_{E,2,dyn} = {D_{dyn}}^{1/m}\,\Delta\sigma_{E,2,stat} = {D_{dyn}}^{1/3}\,\Delta\sigma_{E,2,stat} \tag{5.20}$$

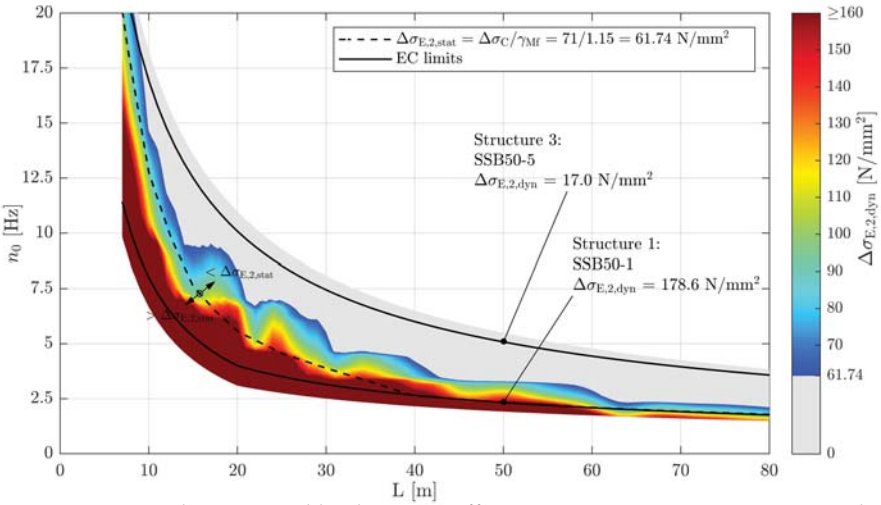

Figure 5.30.: Single-span steel bridges — traffic mix TM1* — $v_{D_{max}}$ — ζ_{EC} — Rayleigh like damping — no load distribution — top view $\Delta\sigma_{E,2,dyn}$ & $\Delta\sigma_{E,2,stat}$

[1] Due to the chosen procedure becomes $D_{stat} = 1.0$ for $\Delta\sigma_{E,2,stat}$.

Figure 5.31 illustrates the equivalent constant amplitude stress ranges $\Delta\sigma_{E,2,stat}$ for the single-span composite bridges.

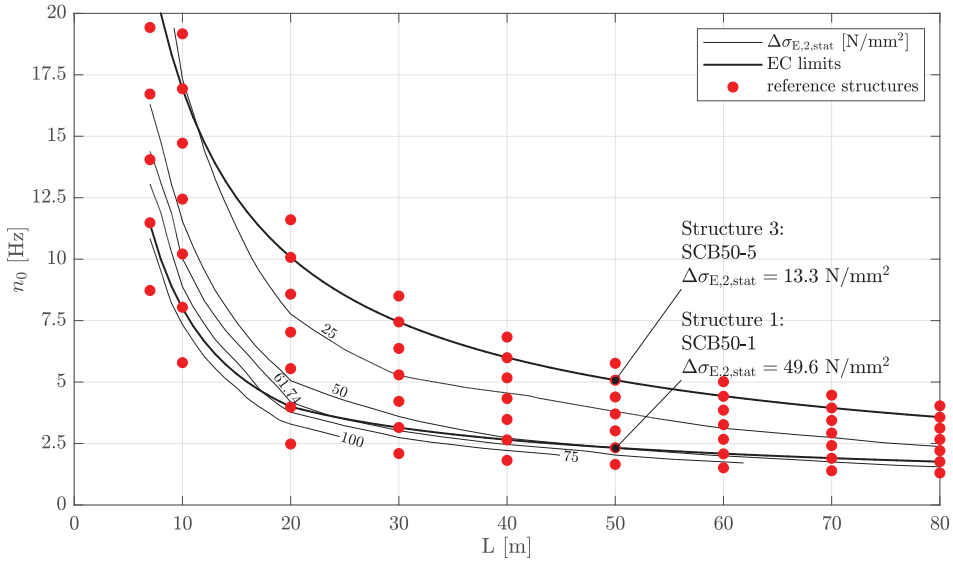

Figure 5.31.: Single-span composite bridges — $\Delta\sigma_{E,2,stat}$ due to trains TypeC1 to TypeC8 — reference structures and interpolated surface — no load distribution

Again, using the damage D_{dyn} values of Figure 5.28 and the relations according to Equation (5.20), the equivalent constant amplitude stress ranges $\Delta\sigma_{E,2,dyn}$ for the single-span composite bridges, as illustrated in Figure 5.32, result.

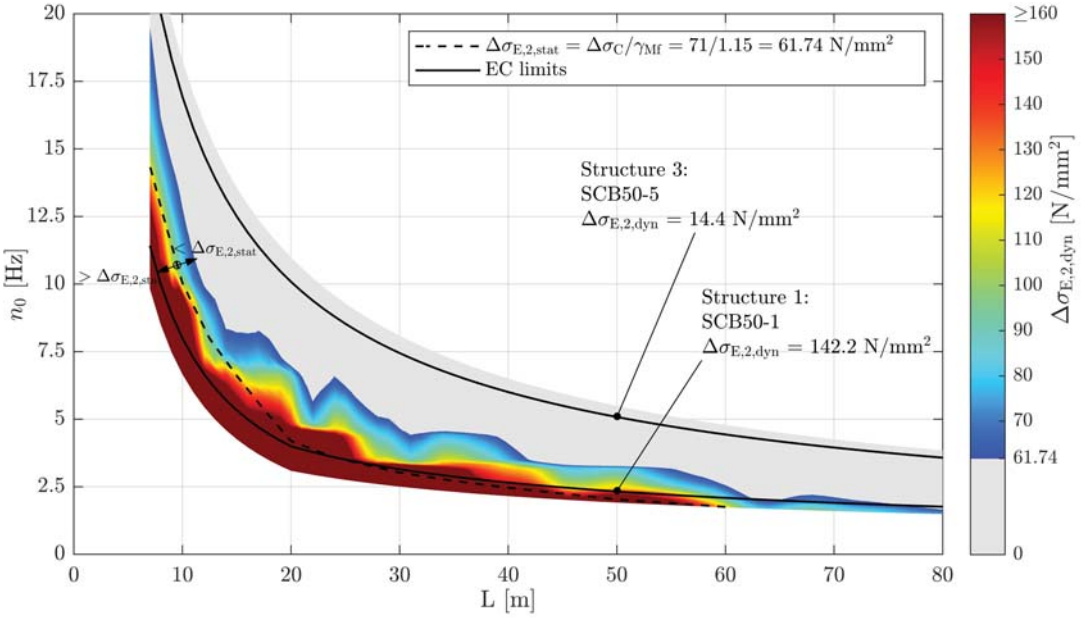

Figure 5.32.: Single-span composite bridges — traffic mix TM1* — $v_{D_{max}}$ — ζ_{EC} — Rayleigh like damping — no load distribution — top view $\Delta\sigma_{E,2,dyn}$ & & $\Delta\sigma_{E,2,stat}$

5.2. Preliminary studies

In this chapter, two preliminary studies are performed to answer the question whether the simple *moving load model* is sufficient enough to model the train crossing and whether all four damping variants introduced in Chapter 5.1.3 need to be considered in the subsequent parameter study.
First, the two different train models explained in Chapter 3 are compared, regarding the absolute maximum vertical bridge deck acceleration $|a_{max}|$, absolute maximum bending moment $|M_{max,dyn}|$ and damage D_{dyn}, to each other. The train TypeC19, which represents one of the common *Railjet* configurations, operating on the high-speed line *Westbahn* in Austria, is modelled using the *moving load model* — see Chapter 3.5.2 — and using the*2D multi-body model* according to Chapter 3.5.3.
In the second part of this chapter, for selected single-span bridges and different damping variants — see Figure 5.9 — the damage D_{dyn} is calculated due to traffic mix TM2-st according to Chapter 4.2.

5.2.1. Comparison of train models

For the comparison of the effects on the structure due to the *moving load model* and the *2D multi-body model*, the following nine single-span steel bridges — see Table 5.4 and also Chapter 5.1.1 and Appendix B — were considered. Therefore, the damping variant ζ_{EC} was selected for all load models and bridge structures, whereas for the *moving load model* the additional damping $\Delta\zeta$ was considered and consequently for the *2D multi-body model* was neglected.
Furthermore, the high-speed train TypeC19, according to Table A.11 and A.12, was used in the following study. The 64 axle conventional train consists of two 32 axle *Railjet* configurations, both hauled by a *Taurus* power car. The measurements at the monitoring point *Enns* of Chapter 4.2.4 indicate that this train configuration is not used for speeds exceeding 240 km/h. However, the following study was performed for a speed range v = 50-300 km/h. The vertical bridge deck accelerations $|a_{max}|$ were all multiplied by the factor $(1 + 0.5\ \varphi'')$ according to ÖNORM EN 1991-2, Annex C [43] and the bending moments $|M_{max,dyn}|$ by the factor $(1 + 0.25\ \varphi''_D)$ according to ÖNORM EN 1991-2, Annex D [43]. For the damage accumulation calculation the S-N- curve was again set to the level of the static calculation according to Figure 5.16. Furthermore, the results were calculated at the midspan cross section — subsequently defined as $CS_{L/2}$ — and additionally the maximum values — subsequently defined as CS_{max} — of 99 points, which were equidistantly positioned along the longitudinal axis, were determined.

Nr.	Name	L [m]	h_{MG} [mm]	t_{DP} [mm]	w_{LC} [mm]	t_{LC} [mm]	EI_y [Nm^2]	μ [kg/m]	n_0 [Hz]	ζ_{EC} [%]
1	SSB10-1	10	675	20	340	25	1.746E+09	6660.8	8.04	2.079 1.750
2	SSB10-3	10	890	20	480	30	4.276E+09	6813.5	12.44	2.079 1.750
3	SSB10-5	10	1050	20	600	40	8.142E+09	7008.0	16.93	2.079 1.750
4	SSB30-1	30	1685	20	600	40	2.344E+10	7187.5	3.15	0.500
5	SSB30-3	30	2435	25	800	50	7.195E+10	7825.1	5.29	0.500
6	SSB30-5	30	3100	25	950	70	1.533E+11	8426.3	7.45	0.500
7	SSB50-1	50	2800	30	800	60	1.129E+11	8228.4	2.33	0.500
8	SSB50-3	50	4115	30	900	80	3.1192E+11	8974.0	3.70	0.500
9	SSB50-5	50	5310	30	1000	110	6.469E+11	9904.1	5.08	0.500

Table 5.4.: Single-span steel bridges — geometry

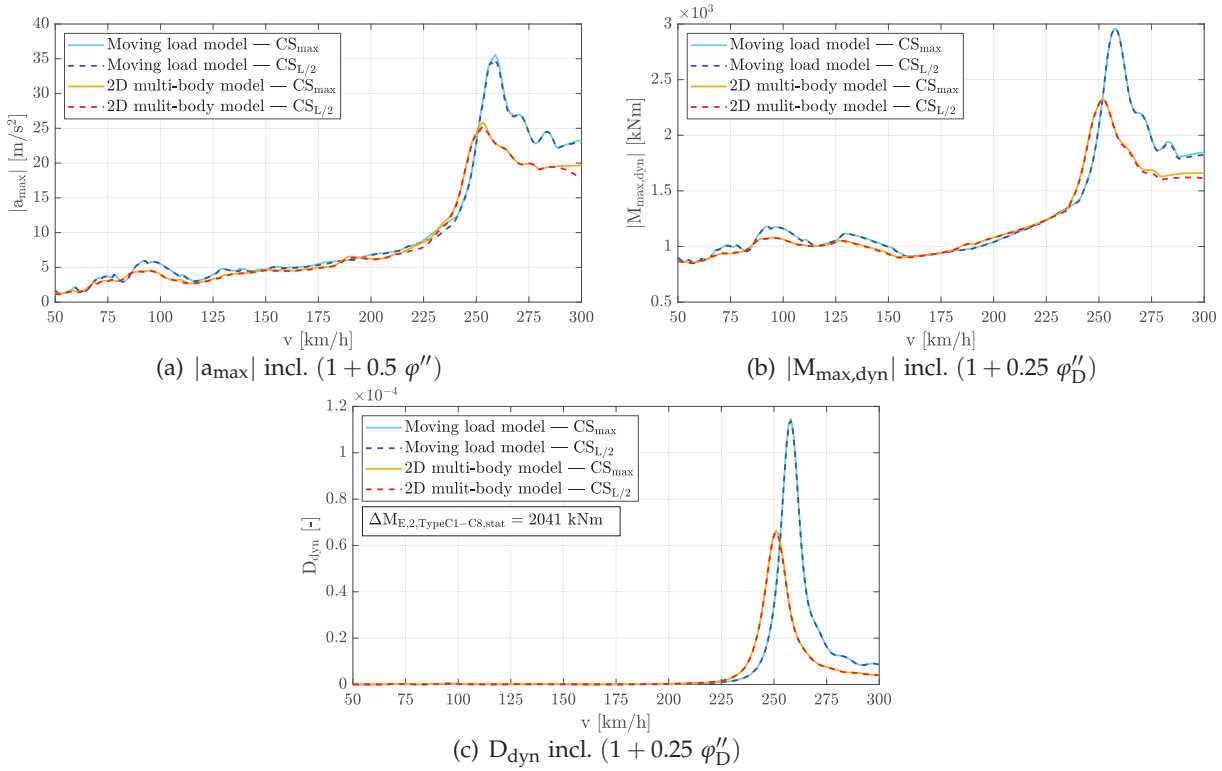

(a) $|a_{max}|$ incl. $(1 + 0.5\ \varphi'')$

(b) $|M_{max,dyn}|$ incl. $(1 + 0.25\ \varphi''_D)$

(c) D_{dyn} incl. $(1 + 0.25\ \varphi''_D)$

Figure 5.33.: Comparison of *moving load model* and *2D multi-body model* — SSB10-1 — one crossing of train TypeC19 — v = 50-300km/h — ζ_{EC} — Rayleigh like damping

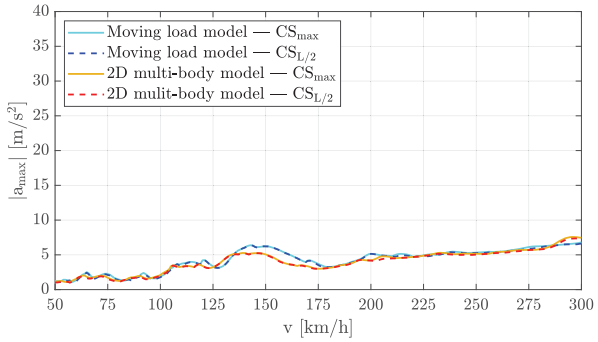

(a) $|a_{max}|$ incl. $(1 + 0.5\ \varphi'')$

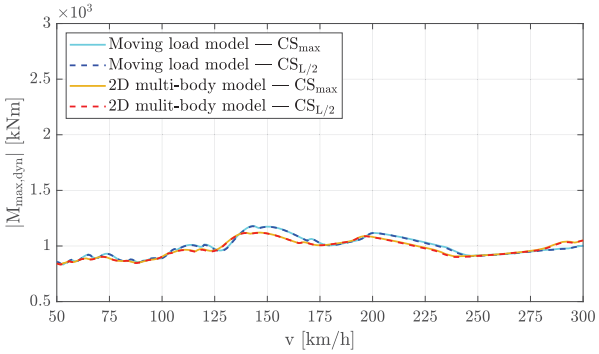

(b) $|M_{max,dyn}|$ incl. $(1 + 0.25\ \varphi''_D)$

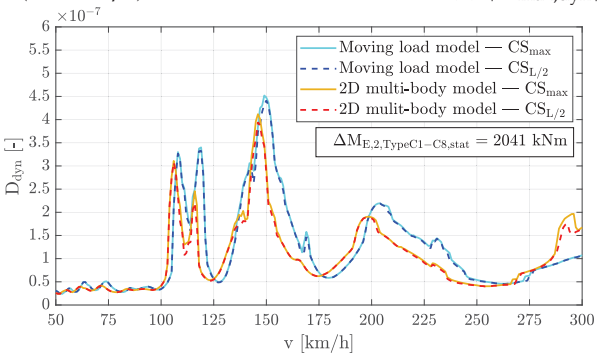

(c) D_{dyn} incl. $(1 + 0.25\ \varphi''_D)$

Figure 5.34.: Comparison of *moving load model* and *2D multi-body model* — SSB10-3 — one crossing of train TypeC19 — v = 50-300km/h — ζ_{EC} — Rayleigh like damping

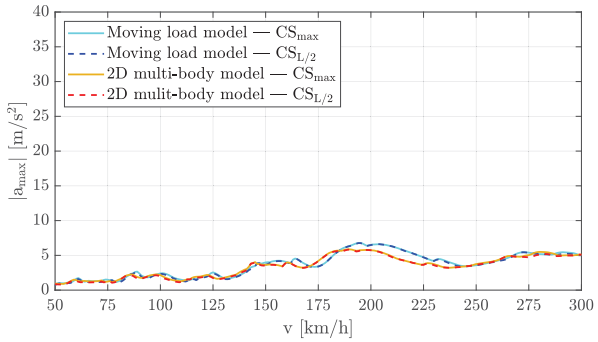

(a) $|a_{max}|$ incl. $(1 + 0.5\ \varphi'')$

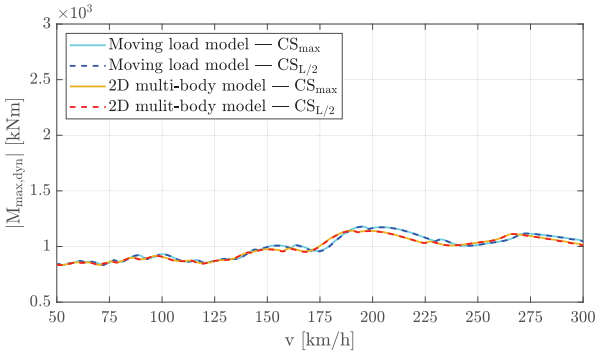

(b) $|M_{max,dyn}|$ incl. $(1 + 0.25\ \varphi''_D)$

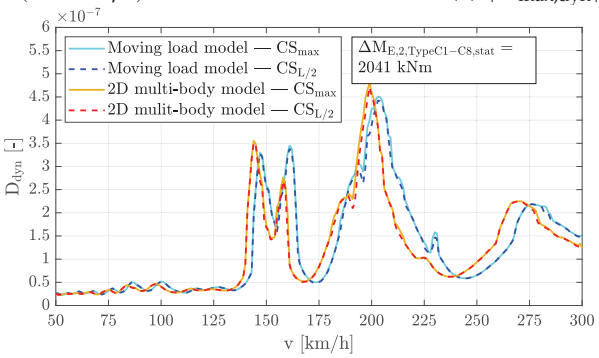

(c) D_{dyn} incl. $(1 + 0.25\ \varphi''_D)$

Figure 5.35.: Comparison of *moving load model* and *2D multi-body model* — SSB10-5 — one crossing of train TypeC19 — v = 50-300km/h — ζ_{EC} — Rayleigh like damping

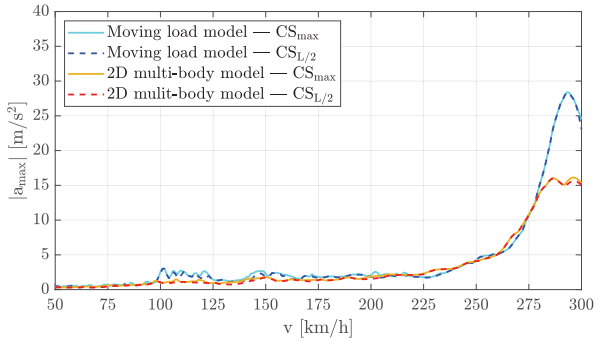

(a) $|a_{max}|$ incl. $(1 + 0.5\ \varphi'')$

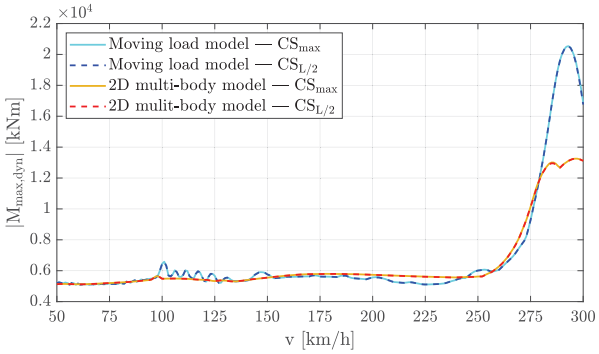

(b) $|M_{max,dyn}|$ incl. $(1 + 0.25\ \varphi''_D)$

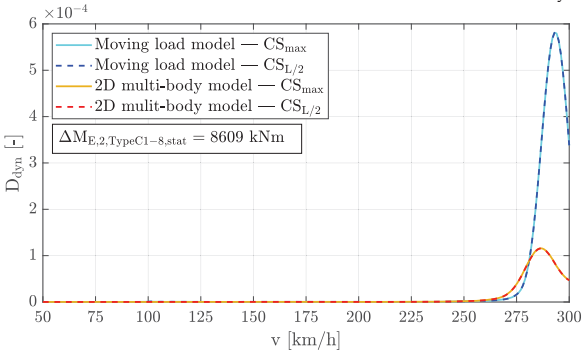

(c) D_{dyn} incl. $(1 + 0.25\ \varphi''_D)$

Figure 5.36.: Comparison of *moving load model* and *2D multi-body model* — SSB30-1 — one crossing of train TypeC19 — v = 50-300km/h — ζ_{EC} — Rayleigh like damping

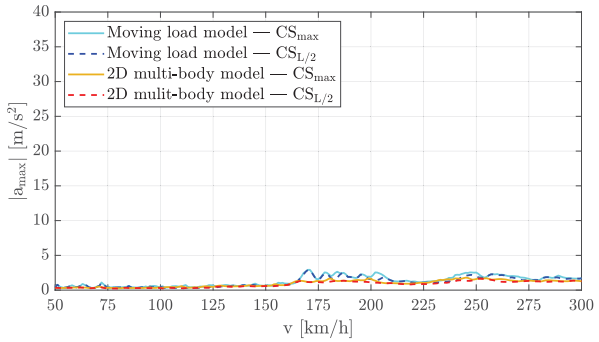

(a) $|a_{max}|$ incl. $(1 + 0.5\ \varphi'')$

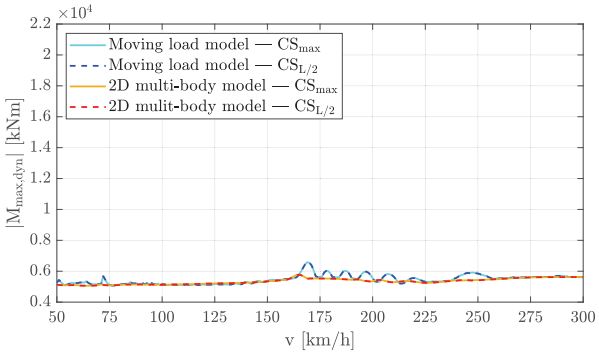

(b) $|M_{max,dyn}|$ incl. $(1 + 0.25\ \varphi''_D)$

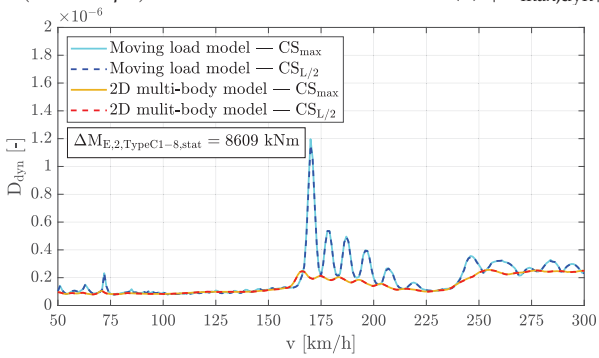

(c) D_{dyn} incl. $(1 + 0.25\ \varphi''_D)$

Figure 5.37.: Comparison of *moving load model* and *2D multi-body model* — SSB30-3 — one crossing of train TypeC19 — v = 50-300km/h — ζ_{EC} — Rayleigh like damping

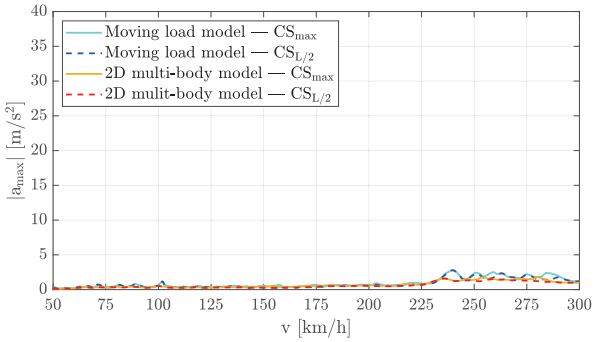

(a) $|a_{max}|$ incl. $(1 + 0.5\ \varphi'')$

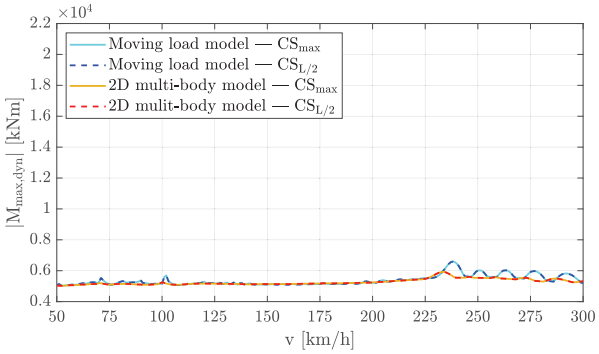

(b) $|M_{max,dyn}|$ incl. $(1 + 0.25\ \varphi''_D)$

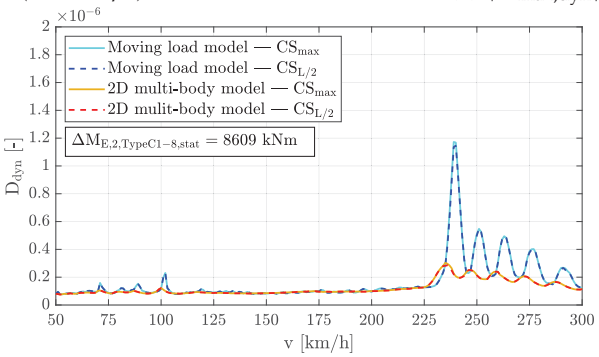

(c) D_{dyn} incl. $(1 + 0.25\ \varphi''_D)$

Figure 5.38.: Comparison of *moving load model* and *2D multi-body model* — SSB30-5 — one crossing of train TypeC19 — v = 50-300km/h — ζ_{EC} — Rayleigh like damping

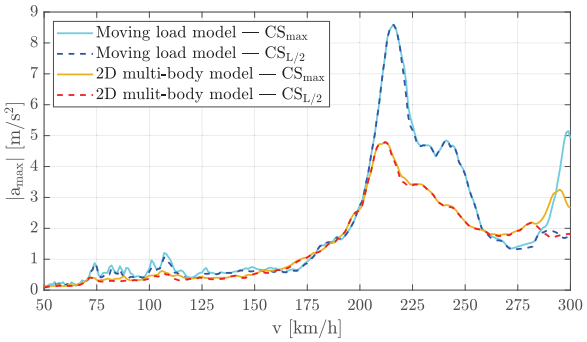

(a) $|a_{max}|$ incl. $(1 + 0.5\ \varphi'')$

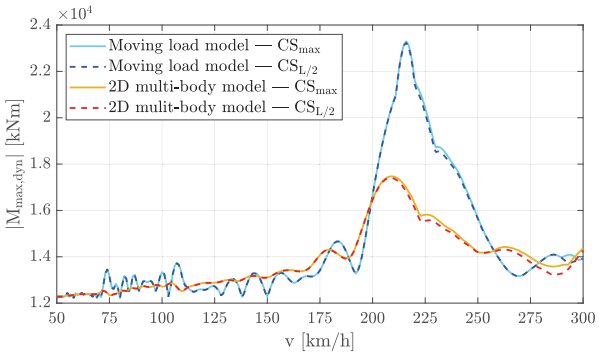

(b) $|M_{max,dyn}|$ incl. $(1 + 0.25\ \varphi''_D)$

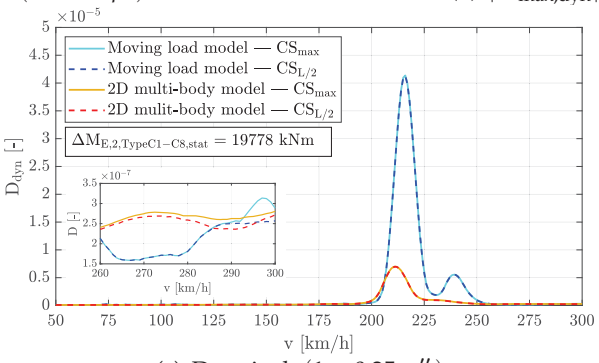

(c) D_{dyn} incl. $(1 + 0.25\ \varphi''_D)$

Figure 5.39.: Comparison of *moving load model* and *2D multi-body model* — SSB50-1 — one crossing of train TypeC19 — v = 50-300km/h — ζ_{EC} — Rayleigh like damping

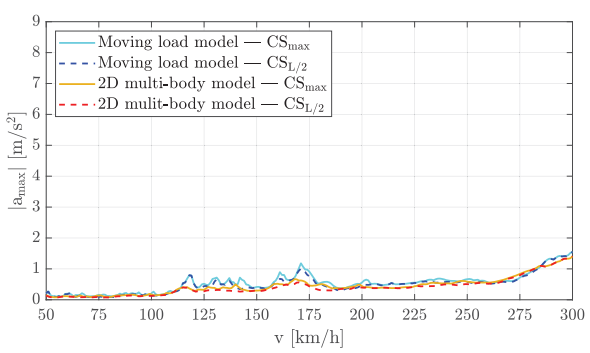

(a) $|a_{max}|$ incl. $(1 + 0.5\ \varphi'')$

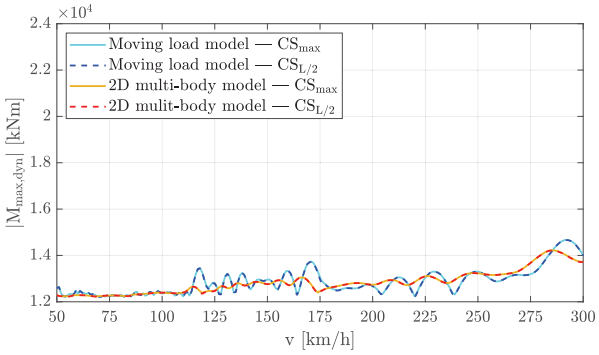

(b) $|M_{max,dyn}|$ incl. $(1 + 0.25\ \varphi''_D)$

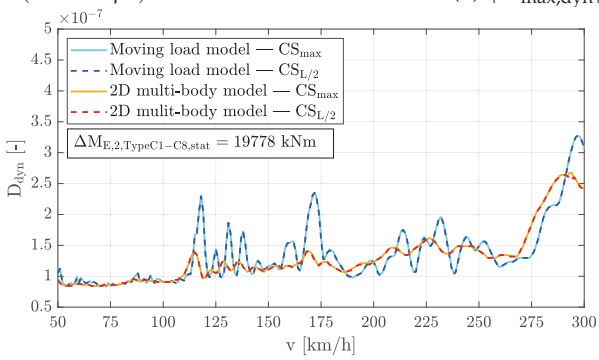

(c) D_{dyn} incl. $(1 + 0.25\ \varphi''_D)$

Figure 5.40.: Comparison of *moving load model* and *2D multi-body model* — SSB50-3 — one crossing of train TypeC19 — v = 50-300km/h — ζ_{EC} — Rayleigh like damping

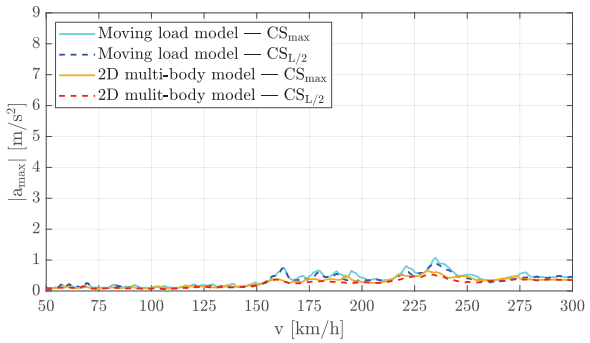

(a) $|a_{max}|$ incl. $(1 + 0.5\ \varphi'')$

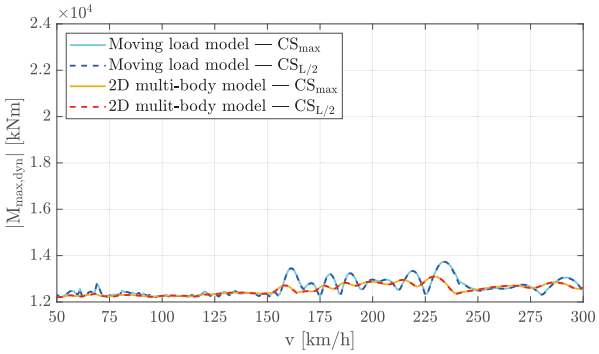

(b) $|M_{max,dyn}|$ incl. $(1 + 0.25\ \varphi''_D)$

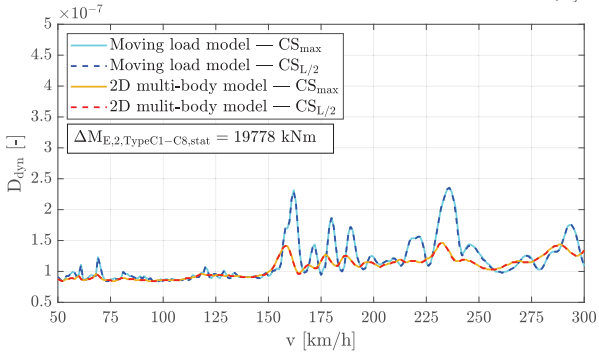

(c) D_{dyn} incl. $(1 + 0.25\ \varphi''_D)$

Figure 5.41.: Comparison of *moving load model* and *2D multi-body model* — SSB50-5 — one crossing of train TypeC19 — v = 50-300km/h — ζ_{EC} — Rayleigh like damping

The following conclusions due to the performed train model comparison may be stated:

- The peak values of all studied variables ($|a_{max}|$, $|M_{max,dyn}|$ and D_{dyn}) using the *moving load model*, usually exceed the ones using the *2D multi-body model* — except for two cases, see Figure 5.34(a) and Figure 5.35(c).
- The studied variables using the *2D multi-body model* are for large areas, within the considered speed range, below the ones due to the *moving load model*.
- The maximum bridge deck acceleration $|a_{max}|$ is not sufficiently captured by considering the midspan cross section only — see Figures 5.37(a), 5.38(a), 5.39(a), 5.40(a) and 5.41(a)
- On the other hand, the maximum bending moment $|M_{max,dyn}|$ is sufficiently determined by the midspan cross section. For the single-span steel bridge SSB50-1 in Figure 5.39(b) this is, within the speed range 260-300 km/h, not the case. However, the consequences for the damage D_{dyn} are of neglectable magnitude as demonstrated in the small box of Figure 5.39(c).

Consequently, only the *moving load model* is used for the parameter study. Furthermore, the maximum bridge deck acceleration $|a_{max}|$ is determined considering 99 points, which are equidistantly positioned along the structure's longitudinal axis. The maximum bending moment $|M_{max,dyn}|$ and the damage D_{dyn} are calculated considering the midspan cross section only.

5.2.2. Preliminary fatigue design check of single-span steel bridges

In this chapter, a preliminary fatigue design check study on 40 single-span steel bridges, regarding traffic mix **TM2-st**, is presented in order to study the effect of different damping variants.
Therefore, the structures illustrated in Figure 5.42, ranging from spans of 10-80 m, were used. Furthermore, for each span length L, five structures with different first bending frequencies n_0 were taken into account. The naming of these, in total, 40 single-span steel bridges is indicated in Figure 5.42 for spans with L = 10 m. Detailed information regarding the single-span steel structures may be found in Appendix B. The subsequently performed calculations are also valid for single-span composite bridges with the same first bending frequency n_0. However, the preliminary study was conducted for the four different damping variants ζ_{EC}, ζ_{V1}, ζ_{V2} and ζ_{V3} considering Rayleigh like damping — see Figure 5.9.

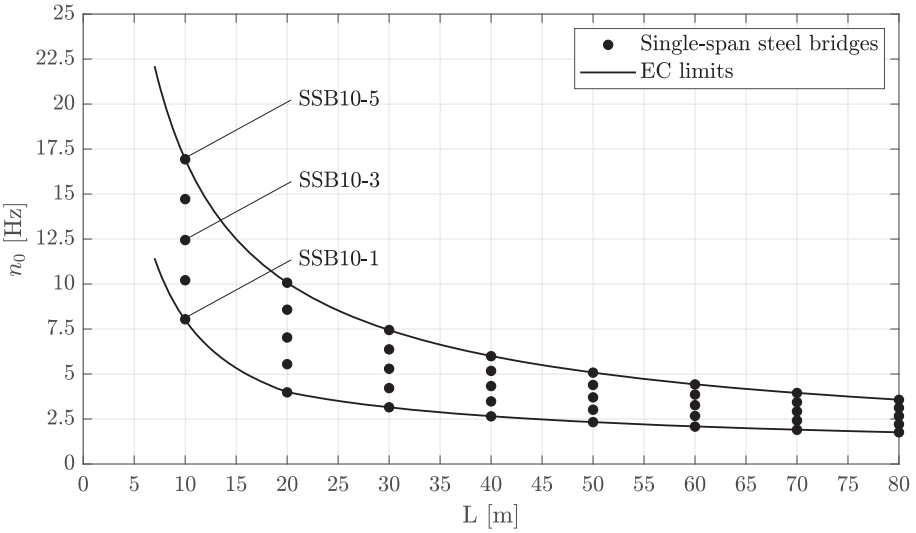

Figure 5.42.: Single-span steel bridges for preliminary study with respect to different damping variants

The 94602 real trains (RT) of traffic mix **TM2-st** — see Table 5.1 — are considered directly in the dimensional dynamical calculation. Hence, the factors f_{PT} and f_{ST} are not needed and consequently only $f_{\mathrm{TM2-st,100years}}$ is used here — see Equations (5.8) to (5.10).
Therefore, the damage $\mathrm{D_{TM2-st}}$ for the entire design life of 100 years becomes to

$$\mathrm{D_{TM2-st}} = \mathrm{D_{RT}} * f_{\mathrm{TM2-st,100years}} \tag{5.21}$$

whereas $\mathrm{D_{RT}}$ represents the damage due to the 94602 RT. Regarding the damage calculation, using *Miner's rule*, the level of the S-N curve was again set to the result of the static calculation $\Delta \mathrm{M_{E,2,TypeC1-C8,stat}}$ — see Figure 5.16. The dynamic calculation is performed, as mentioned above, in dimensional form and all results are multiplied by the factor $(1 + 0.25\ \varphi''_{\mathrm{D}})$ according to ÖNORM EN 1991-2, Annex D [43].

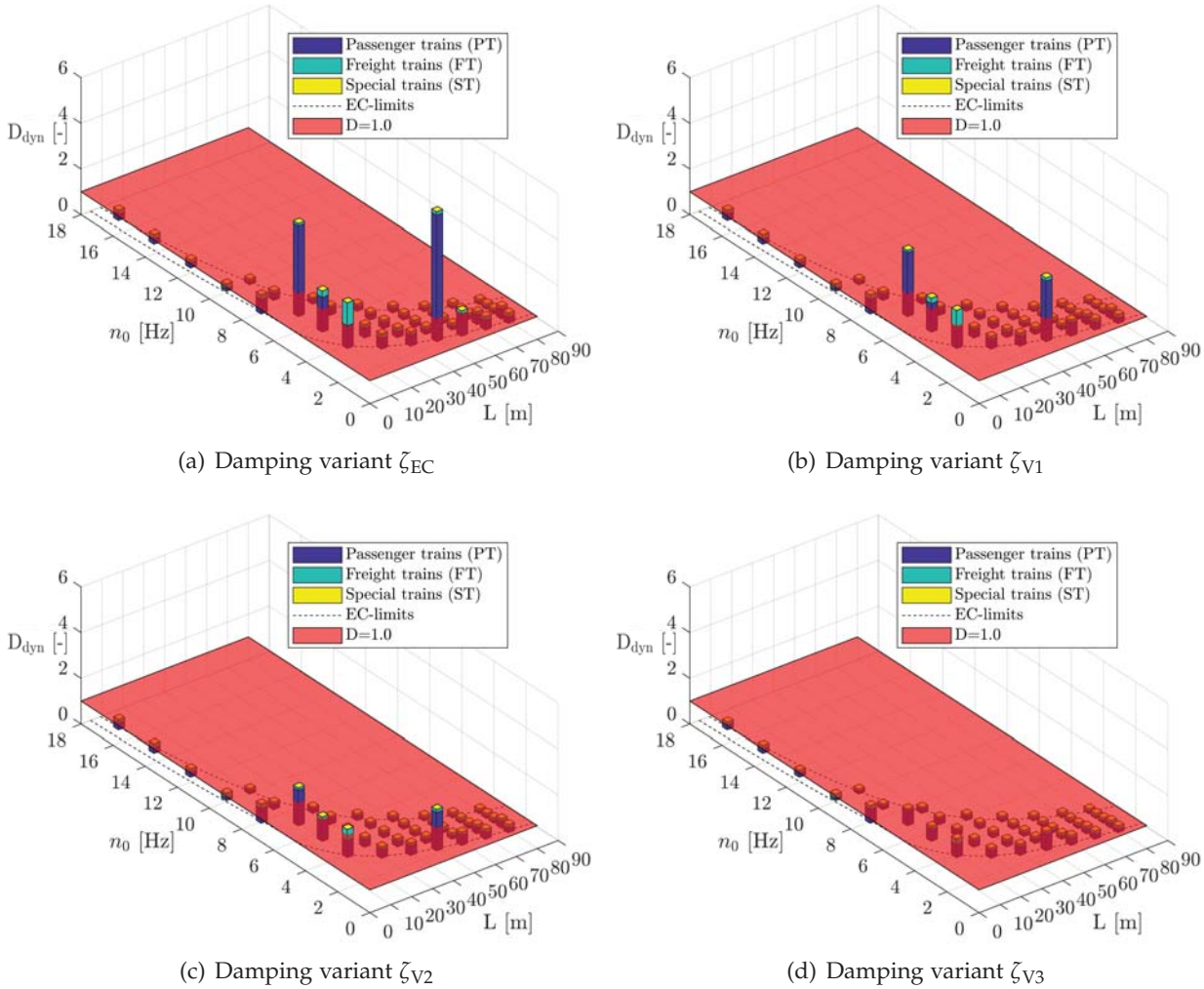

(a) Damping variant ζ_{EC}

(b) Damping variant ζ_{V1}

(c) Damping variant ζ_{V2}

(d) Damping variant ζ_{V3}

Figure 5.43.: Single-span steel bridges — traffic mix 2 (TM2-st) — ζ_{EC} — Rayleigh like damping — no load distribution — top view D_{dyn}

Figure 5.43 presents the results of the preliminary fatigue design check for the four different damping variants. The damage values D_{dyn} are divided into the three parts due to PT, FT, and ST. The influence of the PT is dominant in all structures, the one of the FT is rather constant and the ST are in general neglectable. However, the structures with obvious damage peaks, the single-span steel bridges SSB20-3 and SSB50-1, are driven by the influence of the PT. Increasing the damping ratio from the design code level, represented by ζ_{EC}, up to a damping ratio of 3% (ζ_{V3}) allows to decrease the damage D_{dyn} below 1.0 for all structures.
Consequently, the damping variants ζ_{EC} and ζ_{V1} are considered further on, as the first represent the state of the art rules for new structures and the latter may be interpreted as measured damping values at site for existing structures.

5.3. Traffic safety design check — acceleration criterion

Subsequently, the results of the acceleration criteria, representing the traffic safety (TS) design check, which is performed using the high-speed load model HSLM-A — see Figure 2.20 — are shown. First, the non-dimensional response representation for single-span bridges is applied according to Chapter 3.6. This allows to calculate the non-dimensional bridge deck acceleration, independently of the bridge type (steel, composite). The procedure is repeated for all ten HSLM-A trains and the absolute maximum of the bridge deck acceleration is determined.
Finally, the results for real single-span steel and composite bridges are obtained through transforming the non-dimensional solutions into the dimensional form.

5.3.1. Non-dimensional response representation

The non-dimensional response representation was applied subsequently according to Chapter 3.6 for single-span bridges, considering ten HSLM-A trains. Therefore, Equation (3.224) is here rewritten for the peak acceleration of one HSLM-A train number i

$$|\bar{a}_{\mathrm{HSLM-Ai,max}}| = |a_{\mathrm{HSLM-Ai,max}}| \; \frac{\mu \; L}{P_{\mathrm{HSLM-Ai,max}}} \tag{5.22}$$

As the maximum axle load $P_{\mathrm{HSLM-Ai,max}}$ for each HSLM-A train i (i=1...10) is different, a pure non-dimensional representation for the envelope of the entire HSLM-A train set is not possible anymore. Consequently, the peak acceleration parameter $|\bar{a}_{\mathrm{HSLM-A,max}}| \; P_{\mathrm{max}}$ for ten HSLM-A trains becomes to

$$\begin{aligned} |\bar{a}_{\mathrm{HSLM-A,max}}| \; P_{\mathrm{max}} = \max\left(|\bar{a}_{\mathrm{HSLM-Ai,max}}| \; P_{\mathrm{HSLM-Ai,max}}\right) &= \max\left(|a_{\mathrm{HSLM-Ai,max}}|\right) \; \mu \; L \\ &= |a_{\mathrm{HSLM-A,max}}| \; \mu \; L \end{aligned} \tag{5.23}$$

Additionally, two different damping variants (ζ_{EC} and ζ_{V1}), two different damping types (modal and Rayleigh like damping) and two different types of load application (with and without load distribution) were studied. The influence of track defects and vehicle imperfections was not considered yet, as the factor $(1 + 0.5 \; \varphi'')$ — according to ÖNORM EN 1991-2, Annex C [43] — depends on the maximum permitted vehicle speed v_{max} and the first bending frequency n_0 of the bridge structure. Consequently, this factor is considered later in the dimensional response representation — see Chapters 5.3.2 and 5.3.3. The overall results for the non-dimensional solution $|\bar{a}_{\mathrm{HSLM-A,max}}|$ are illustrated in Figure 5.44 and the corresponding assumptions listed below:

- Span length L: starting from 7 to 80 m with a step size ΔL of 1 m
- Frequency ratio S: range depending on span length L, defined in a way so that in the dimensional representation the n_0 ranges between the EC limits and 10% above/ below are reached; step size ΔS of 0.001
- Number of eigenfunctions ϕ: first five
- Damping ratio ζ: two damping variants ζ_{EC} and ζ_{V1}, according to Figure 5.9
- Damping type: modal and Rayleigh like damping
- Track defects and vehicle imperfections φ'': as $\varphi'' = f(v_{\mathrm{max}}, n_0)$ according to ÖNORM EN 1991-2, Annex C [43], here not considered yet, later in dimensional representation

- Number of considered output points along the longitudinal axis of the bridge: 99 points with a step size Δx of L/100 m
- Load distribution (3 forces per axle load): with and without load-distribution considered according to ÖNORM EN 1991-2, Figure 6.4 [43] — see Figure 5.2.

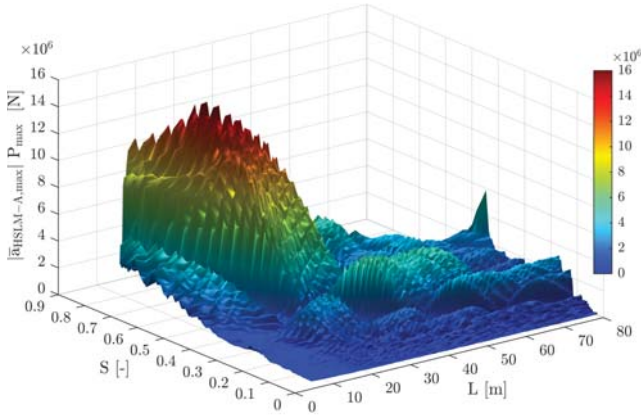

(a) ζ_{EC} — modal damping — no load distribution

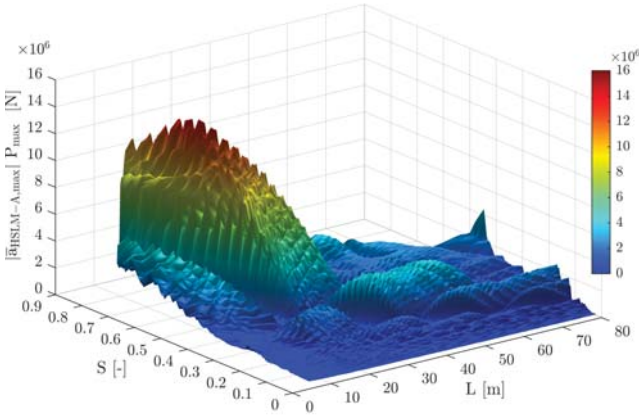

(b) ζ_{V1} — modal damping — no load distribution

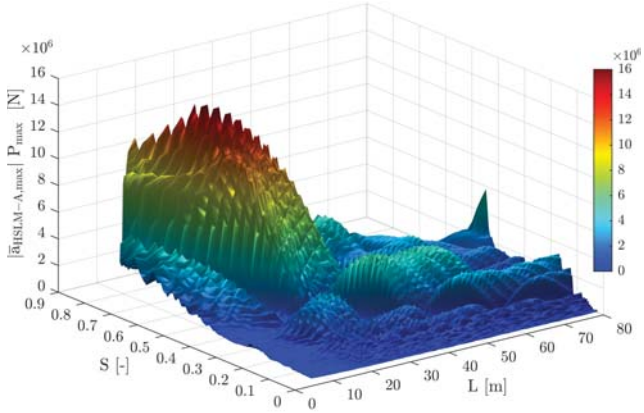

(c) ζ_{EC} — Rayleigh like damping — no load distribution

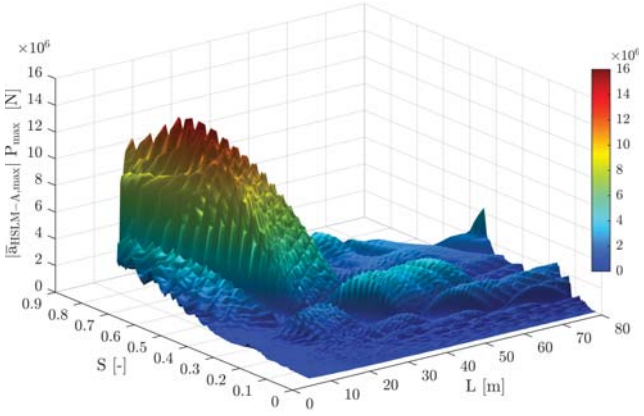

(d) ζ_{V1} — Rayleigh like damping — no load distribution

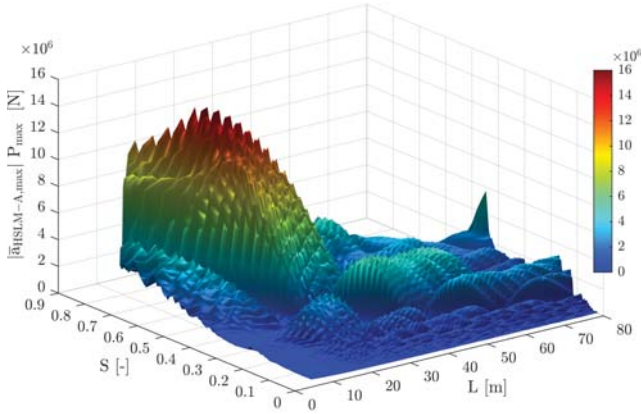

(e) ζ_{EC} — Rayleigh like damping — with load distribution

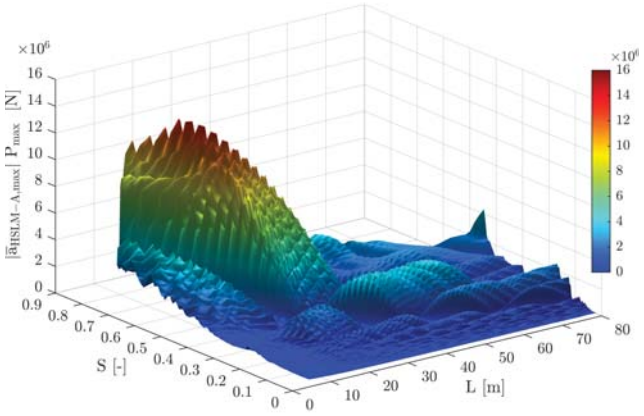

(f) ζ_{V1} — Rayleigh like damping — with load distribution

Figure 5.44.: Single-span bridges — vertical bridge deck acceleration parameter $|\bar{a}_{HSLM-A,max}|\ P_{max}$ due to HSLM-A trains

5.3.2. Dimensional results — single-span steel bridges

Finally, it is possible to determine the peak acceleration for single-span steel bridges (SSB). Therefore, Equation (5.23) is reordered and the mass distribution for single-span steel bridges μ_{SSB} according to Figure 5.5 inserted. As the track defects and the vehicle imperfections were not considered in the non-dimensional approach, the factor $(1 + 0.5\ \varphi'')$ is added to Equation (5.24), which leads to the peak acceleration for single-span steel bridges in dimensional form

$$|a_{HSLM-A,max}| = \frac{|\bar{a}_{HSLM-A,max}|\ P_{max}}{\mu_{SSB}\ L}\ (1 + 0.5\ \varphi'') \tag{5.24}$$

In order to consider a certain speed range v = v_{min}-v_{max} for a given single-span beam bridge with the first bending frequency n_0, Equation (3.223) is applied

$$S = \frac{v}{2\ L\ n_0} \qquad S_{min} = \frac{v_{min}}{2\ L\ n_0} \qquad S_{max} = \frac{v_{max}}{2\ L\ n_0} \tag{5.25}$$

Consequently, the maximum dimensional peak acceleration $|a_{HSLM-A,max}|$ within the range S_{min} and S_{max} is determined for a particular single-span steel bridge. This procedure was performed in Figure 5.45 considering Rayleigh like damping, the damping variant ζ_{EC} and a speed range of v = 50-300 km/h. Hence, for each single-span steel bridge, defined by a span length L and first bending frequency n_0, the maximum dimensional peak acceleration $|a_{HSLM-A,max}|$ due to the ten HSLM-A trains, crossing the structure from 50 to 300 km/h with a speed step Δv = 1 km/h, is plotted. Figures 5.46(a) and 5.46(b) illustrate the top view of Figure 5.45, considering

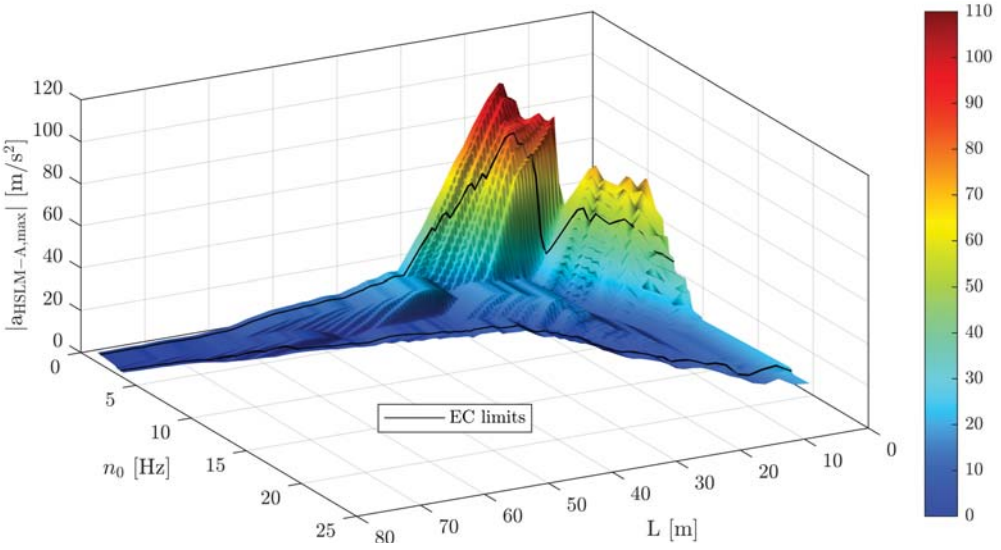

Figure 5.45.: Single-span steel bridges — vertical bridge deck acceleration $|a_{HSLM-A,max}|$ due to HSLM-A trains incl. $(1 + 0.5\ \varphi'')$ — v_{max} = 300 km/h — ζ_{EC} — Rayleigh like damping — no load distribution

the TS criteria $|a_{HSLM-A,max}| \leq 3.5$ m/s² for new structures and $|a_{HSLM-A,max}| \leq 6.0$ m/s² for existing structures. Consequently, the coloured areas represent the structures, which comply with the particular TS criterion. Figures 5.46(c) to 5.46(h) show the results regarding the load distribution (LD) — see Figure 5.2 — and the damping ratio — see Figure 5.9 — variation. However, the modal damping variant was not considered as the difference in respect to the Rayleigh like damping for single-span structures can be neglected — see Appendix B.2.

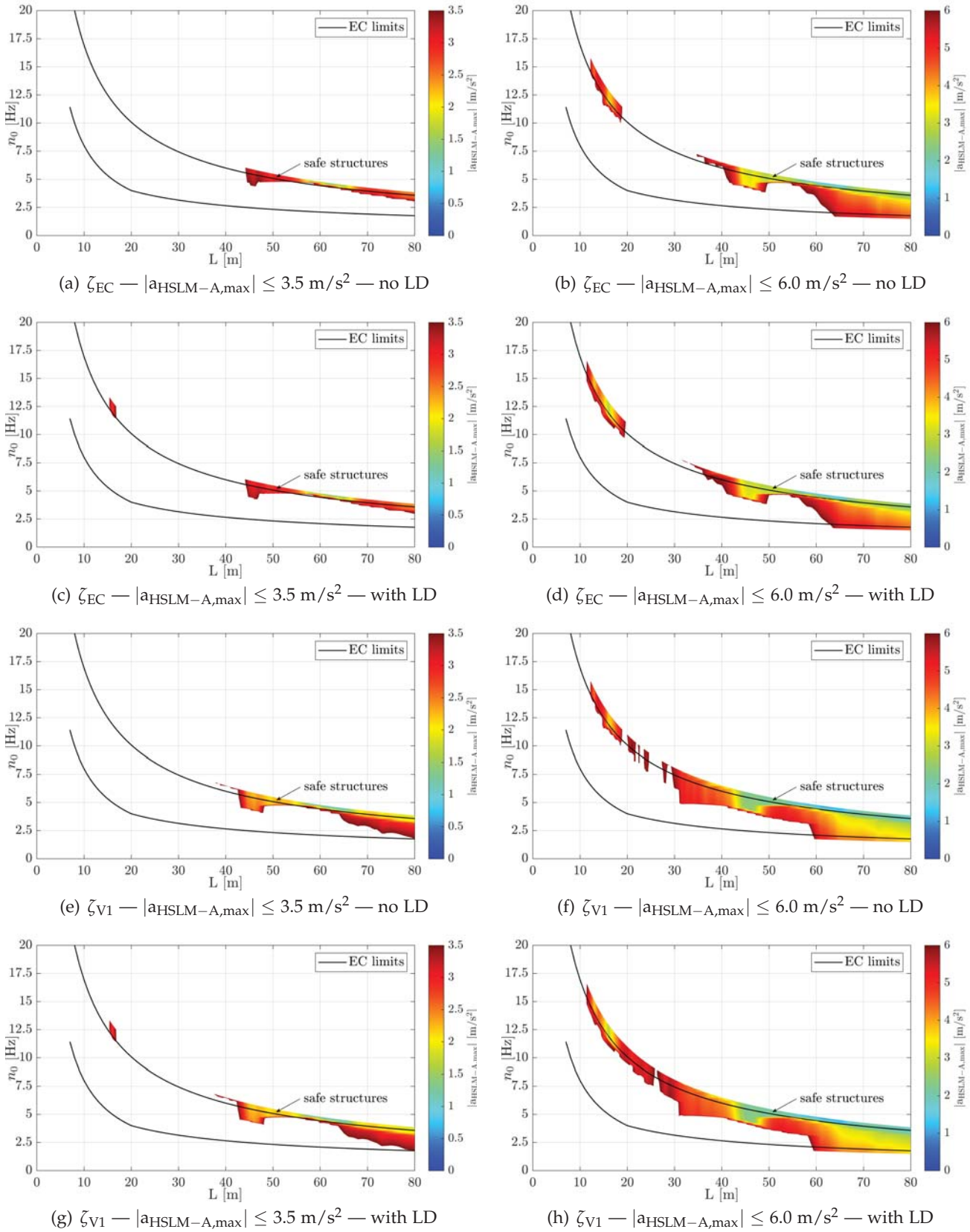

(a) ζ_{EC} — $|a_{HSLM-A,max}| \leq 3.5$ m/s^2 — no LD

(b) ζ_{EC} — $|a_{HSLM-A,max}| \leq 6.0$ m/s^2 — no LD

(c) ζ_{EC} — $|a_{HSLM-A,max}| \leq 3.5$ m/s^2 — with LD

(d) ζ_{EC} — $|a_{HSLM-A,max}| \leq 6.0$ m/s^2 — with LD

(e) ζ_{V1} — $|a_{HSLM-A,max}| \leq 3.5$ m/s^2 — no LD

(f) ζ_{V1} — $|a_{HSLM-A,max}| \leq 6.0$ m/s^2 — no LD

(g) ζ_{V1} — $|a_{HSLM-A,max}| \leq 3.5$ m/s^2 — with LD

(h) ζ_{V1} — $|a_{HSLM-A,max}| \leq 6.0$ m/s^2 — with LD

Figure 5.46.: Single-span steel bridges — vertical bridge deck acceleration $|a_{HSLM-A,max}|$ due to HSLM-A trains incl. $(1 + 0.5\ \varphi'')$ — v_{max} = 300 km/h — Rayleigh like damping

5.3.3. Dimensional results — single-span composite bridges

The dimensional peak acceleration for single-span composite bridges (SCB) due to the crossing of the HSLM-A train set is determined according to the procedure for single-span steel bridges in Chapter 5.3.2. Hence, for the mass distribution μ the values for SCB, according to Figure 5.8, are inserted, which leads to

$$|a_{HSLM-A,max,SCB}| = \frac{|\bar{a}_{HSLM-A,max}| \; P_{max}}{\mu_{SCB} \; L} \; (1 + 0.5 \; \varphi'') \tag{5.26}$$

Figure 5.47 shows again the results for the case of Rayleigh like damping, a damping variant ζ_{EC} and a speed range of v = 50-300 km/h, but here for single-span composite bridges.

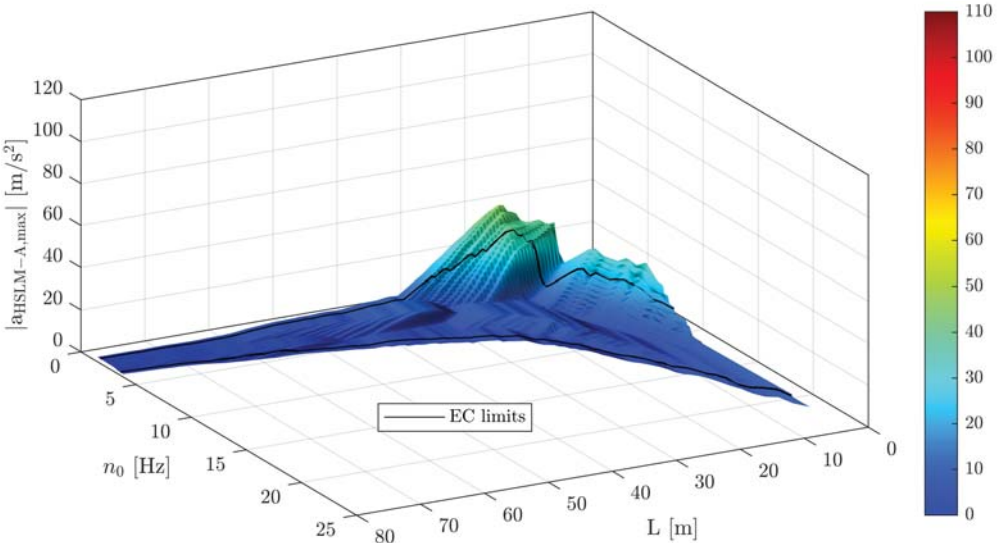

Figure 5.47.: Single-span composite bridges — vertical bridge deck acceleration $|a_{HSLM-A,max}| \leq 3.5$ m/s^2 due to HSLM-A trains — v_{max} = 300 km/h — ζ_{EC} — Rayleigh like damping — no load distribution

In Figure 5.48 again the top view results are presented, considering different damping types, damping variants and load distribution. However, due to the bigger mass of composite structures in comparison to steel bridges — compare the increase of coloured areas in Figure 5.8 to Figure 5.5 — the vertical bridge deck acceleration $|a_{HSLM-A,max}|$ is severely reduced for single-span composite bridges — see linear influence of μ_{SCB} in Equation (5.26).

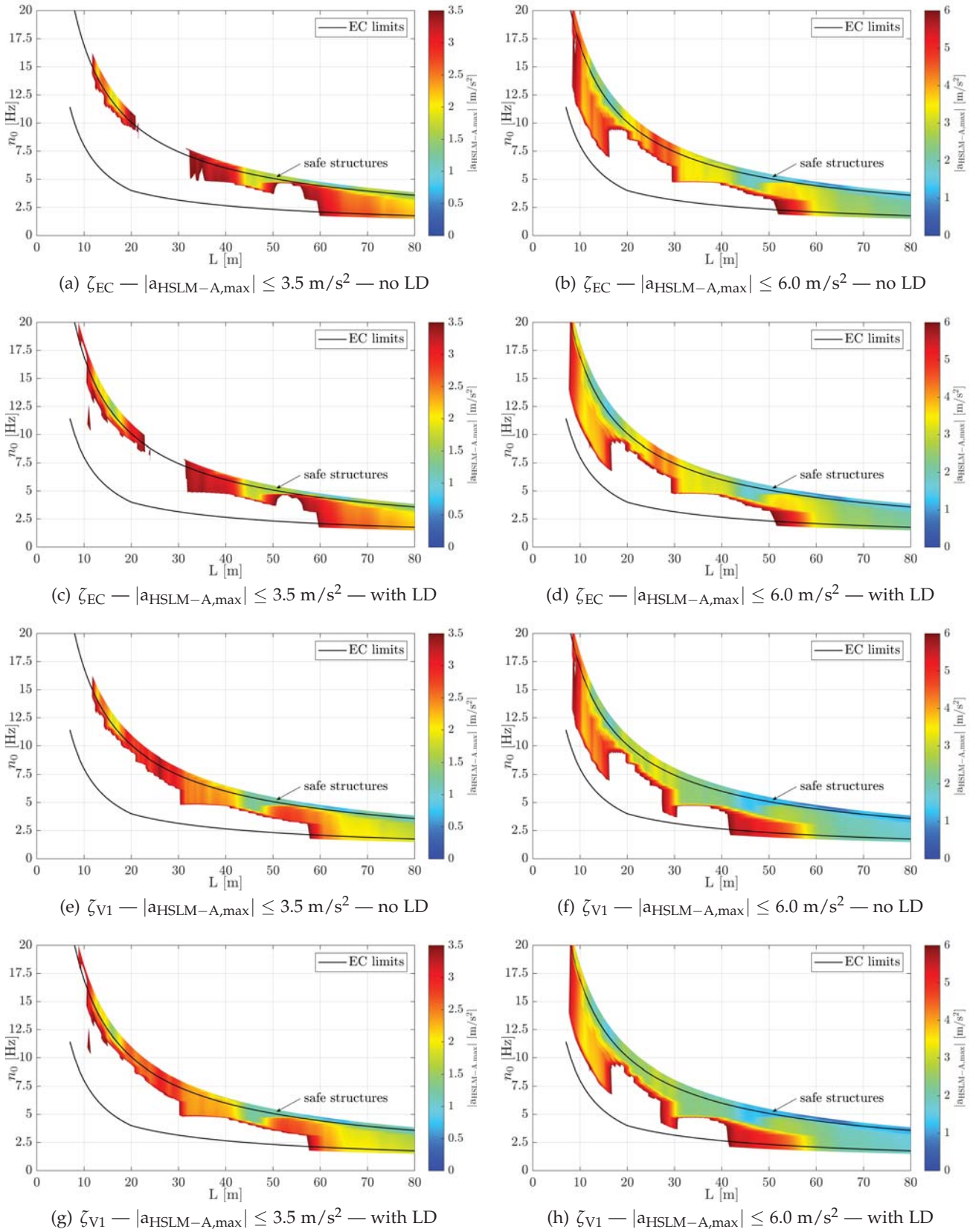

(a) ζ_{EC} — $|a_{HSLM-A,max}| \leq 3.5$ m/s^2 — no LD

(b) ζ_{EC} — $|a_{HSLM-A,max}| \leq 6.0$ m/s^2 — no LD

(c) ζ_{EC} — $|a_{HSLM-A,max}| \leq 3.5$ m/s^2 — with LD

(d) ζ_{EC} — $|a_{HSLM-A,max}| \leq 6.0$ m/s^2 — with LD

(e) ζ_{V1} — $|a_{HSLM-A,max}| \leq 3.5$ m/s^2 — no LD

(f) ζ_{V1} — $|a_{HSLM-A,max}| \leq 6.0$ m/s^2 — no LD

(g) ζ_{V1} — $|a_{HSLM-A,max}| \leq 3.5$ m/s^2 — with LD

(h) ζ_{V1} — $|a_{HSLM-A,max}| \leq 6.0$ m/s^2 — with LD

Figure 5.48.: Single-span composite bridges — vertical bridge deck acceleration $|a_{HSLM-A,max}|$ due to HSLM-A trains — v_{max} = 300 km/h — Rayleigh like damping

5.4. Fatigue design check — FLS — static versus dynamic damage

Subsequently, the fatigue limit state design check (FLS) for single-span steel and composite bridges, as described in Chapter 5.1.5, is performed. In total, the five traffic mixes, according to Chapter 4 and 5.1.4, are considered. For all subsequently presented results, regarding the damage D_{dyn}, the following assumptions for the non-dimensional approach — see Chapter 5.1.5 — were made:

- Span length L: starting from 7 to 80 m with a step size ΔL of 1 m
- Frequency ratio S: range depending on span length L, defined in a way so that in the dimensional representation the n_0 ranges between the EC limits and 10% above/ below are reached; step size ΔS of 0.001
- Number of eigenfunctions ϕ: first five
- Damping ratio ζ: two damping variants ζ_{EC} and ζ_{V1}, according to Figure 5.9
- Damping type: Rayleigh like damping only
- Track defects and vehicle imperfections φ'': factor $(1 + 0.25\varphi''_D)$ according to ÖNORM EN 1991-2, Annex D [43]
- Number of considered output points along the longitudinal axis: cross section at midspan
- Load distribution (3 forces per axle load): with and without load-distribution considered according to ÖNORM EN 1991-2, Figure 6.4 [43] — see Figure 5.2.

All subsequently shown Figures, regarding the FLS criterion, are based on a traffic volume of 24.95 10^6 t/year and on a design life of 100 years, unless stated otherwise.
Additionally, it is possible to compare the dynamic damage D_{dyn}, due to a certain traffic mix, directly the static damage D_{stat}, due to traffic mix 1 (*EC-mix*), as for both damage calculations the same level of the S-N curve is selected. Due to the previously described procedure — see Chapter 5.1.5 — the static damage always becomes to $D_{stat} = 1.0$. Furthermore, the here presented FLS is combined with the traffic safety design check (TS) of Chapter 5.3.

5.4.1. Traffic mix 1

Traffic mix 1 contains the first eight train types according to ÖNORM EN 1991-2, Annex D [43] — see Chapter 4.1. The trains TypeC1 to TypeC4 represent passenger trains and are responsible for about 31.5 % of the traffic volume, whereas the remaining 68.5 % are covered by the freight trains TypeC5 to TypeC8. However, three different variations of train speeds were considered for the dynamic calculation — see Table 4.2:

- v_{EC}: maximum train speed according to ÖNORM EN 1991-2, Annex D [43] — abbreviation for subcategory of traffic mix 1 $\rightarrow$ TM1*
- $v_{D_{max}}$: train speed, which leads to maximum damage D_{dyn} within the speed range v = 50-1.2v_{EC} km/h for each train TypeCi (i=1...8) — abbreviation for subcategory of traffic mix 1 $\rightarrow$ TM1**
- $v_{a_{max}}$: train speed, which leads to maximum vertical bridge deck acceleration $|a_{TypeCi,max}|$ within the speed range v = 50-1.2v_{EC} km/h for each train TypeCi (i=1...8) — abbreviation for subcategory of traffic mix 1 $\rightarrow$ TM1***

Traffic mix TM1* — train speed v_{EC}

Figure 5.49 illustrates the damage D_{dyn} results of the eight trains TypeC1 to TypeC8 individually. All trains crossed the single-span structures with the speed v_{EC} and according to Table 4.1 for the entire design life. Furthermore, the damping variant ζ_{EC} and no load distribution was considered.

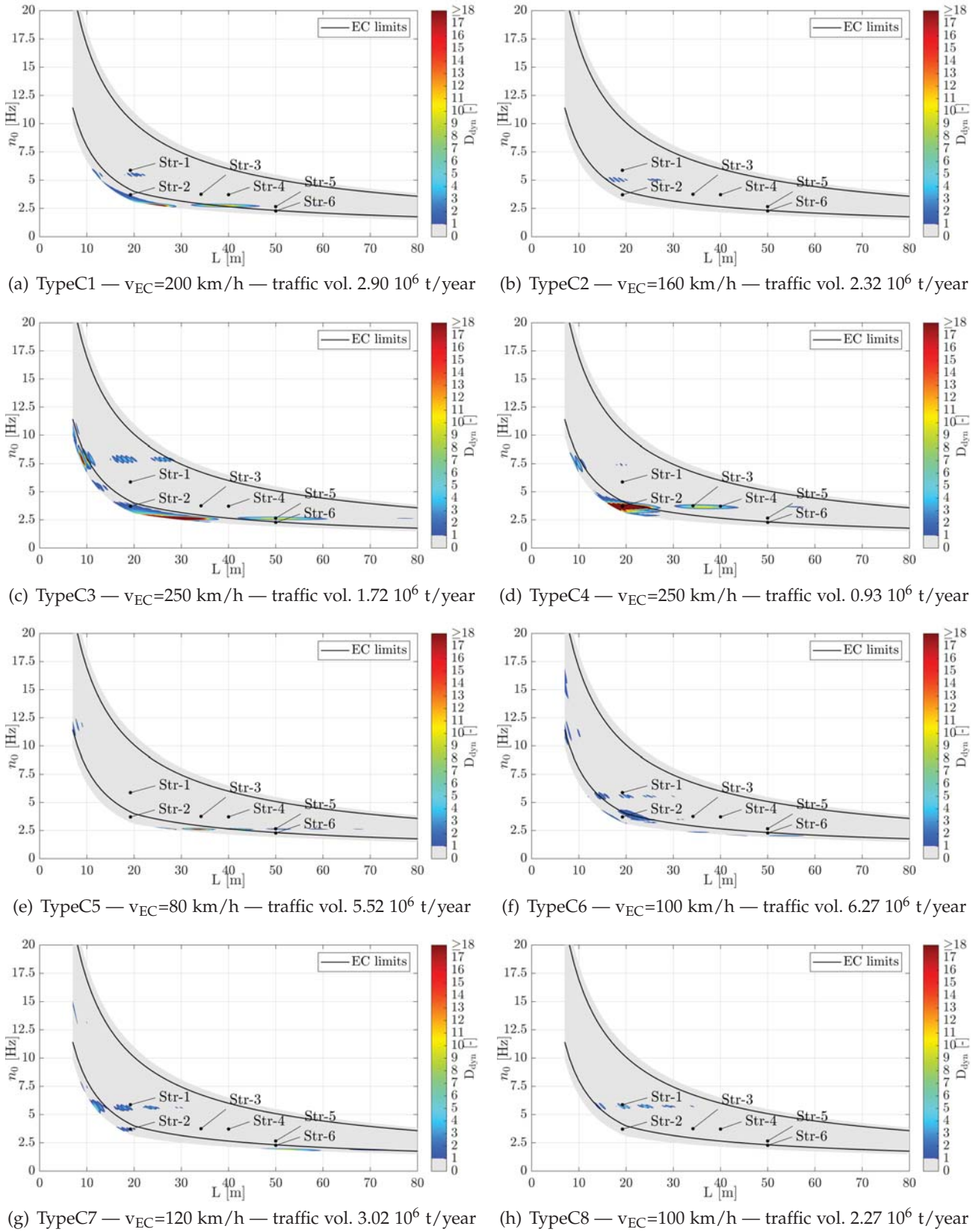

(a) TypeC1 — v_{EC}=200 km/h — traffic vol. 2.90 10^6 t/year

(b) TypeC2 — v_{EC}=160 km/h — traffic vol. 2.32 10^6 t/year

(c) TypeC3 — v_{EC}=250 km/h — traffic vol. 1.72 10^6 t/year

(d) TypeC4 — v_{EC}=250 km/h — traffic vol. 0.93 10^6 t/year

(e) TypeC5 — v_{EC}=80 km/h — traffic vol. 5.52 10^6 t/year

(f) TypeC6 — v_{EC}=100 km/h — traffic vol. 6.27 10^6 t/year

(g) TypeC7 — v_{EC}=120 km/h — traffic vol. 3.02 10^6 t/year

(h) TypeC8 — v_{EC}=100 km/h — traffic vol. 2.27 10^6 t/year

Figure 5.49.: Single-span bridges — trains of traffic mix TM1* — v_{EC} — ζ_{EC} — Rayleigh like damping — no load distribution — top view D_{dyn}

Figure 5.50 shows the total damage D_{dyn} of the individual trains of Figure 5.49. However, the high-speed passenger trains TypeC3 and TypC4 cause the biggest damage values D_{dyn} — compare Figure 5.50 to 5.49(c) and 5.49(d).

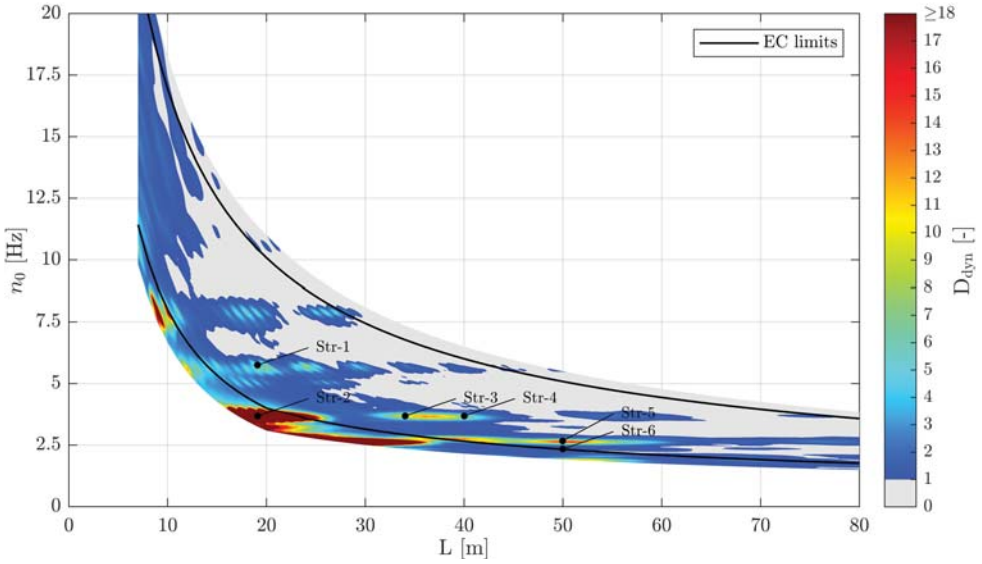

Figure 5.50.: Single-span bridges — traffic mix TM1* — v_{EC} — ζ_{EC} — Rayleigh like damping — no load distribution — top view D_{dyn}

Subsequently, a detailed investigation of the single-span structures Str-1 to Str-6, which are defined in Table 5.5 and shown in Figures 5.49 and 5.50, is presented.

Name	L [m]	n_0 Hz]	$\zeta_{SSB/SCB}$ [%]	$\Delta\sigma_{E,2,stat,SSB}$ [N/mm^2]	$\Delta\sigma_{E,2,stat,SCB}$ [N/mm^2]
Str-1	19	5.714	1.01	65.7	46.9
Str-2	19	3.658	1.01	134.6	90.2
Str-3	34	3.658	0.50	55.0	43.3
Str-4	40	3.658	0.50	39.2	35.8
Str-5	50	2.633	0.50	52.1	43.2
Str-6	50	2.325	0.50	62.3	49.6

Table 5.5.: Definition of single-span bridges Str-1 to Str-6

Damage D_{dyn} versus D_{stat} for structures Str-1 and Str-2

Structures Str-1 and Str-2 have a span length of 19 m. Hence, the static calculation in Figure 5.51 is valid for both equally. Again, the trains TypeC1 to TypeC8 were first simulated statically, including the factor $(1+\varphi)_D$, with respect to the bending moment M in the midspan cross section. Subsequently, using the *reservoir method*, their bending moment range spectra was determined. Considering the traffic volume for these eight trains — according to Table 4.1 — the static bending moment range spectra for the entire design life of 100 years was calculated for each train and the entire traffic mix, as illustrated in Figure 5.51. Again, the damage accumulation calculation, using *Miner's rule*, was performed and the level of the S-N curve iterated, until the damage D_{stat} was set to 1.0, which led to a minimum fatigue resistance of $\Delta\sigma_C = \Delta\sigma_{E,2,stat}$ — see Table 5.5 — and an static equivalent constant amplitude bending moment range $\Delta M_{E,2,TypeC1-C8,stat}$ of 4393.84 kNm.

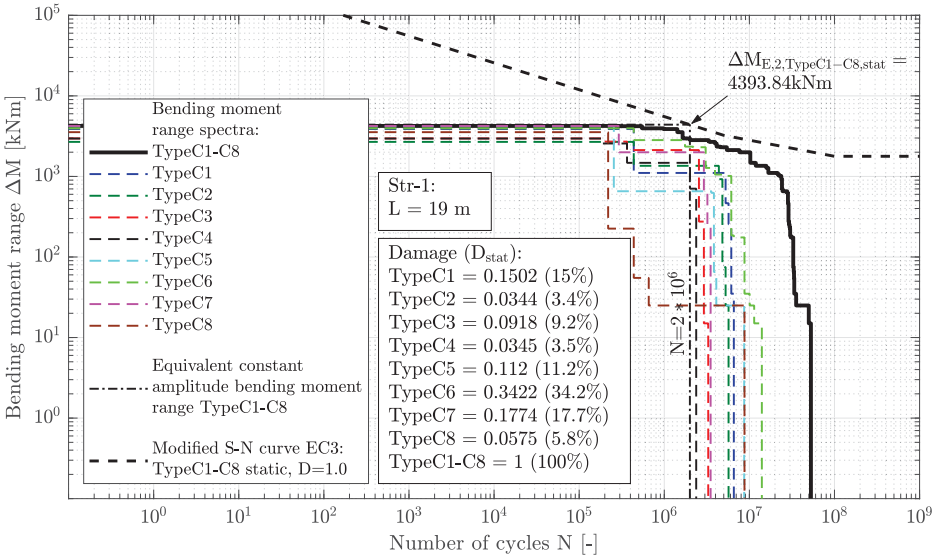

Figure 5.51.: Str-1 — static bending moment ranges — TypeC1-C8 — traffic mix TM1*

In the next step, the dynamic calculation of structure Str-1, additionally defined by the first bending frequency n_0 with 5.714 Hz and a damping ratio $\zeta_{SSB/SCB}$ of 1.01 %, was performed for the crossing of trains TypeC1 to TypeC8. Subsequently, the corresponding bending moment ranges spectra were evaluated, again using *Miner's rule*, at the before iterated S-N curve, defined by $\Delta M_{E,2,TypeC1-C8,stat} = 4393.84$ kNm — as illustrated in Figure 5.52. The total damage D_{dyn} due to the entire traffic mix TM1* results to about $D_{dyn} = 8.42$ and the related dynamic equivalent constant amplitude bending moment range $\Delta M_{E,2,TypeC1-C8,dyn}$ becomes 8939 kNm. The freight train TypeC8 has the greatest impact with a damage D_{dyn} of approximately 6. Due to the regular car length of $L_D = 9.7$ m — see Figure 2.18 — the excitation frequency for a travel speed of 100 km/h becomes to $n_{L_D} = 2.863$ Hz, which is about the half of the structures first bending frequency $n_0 = 5.714$ Hz. Hence, train TypeC8 excites the first bending mode at each second oscillation cycle.

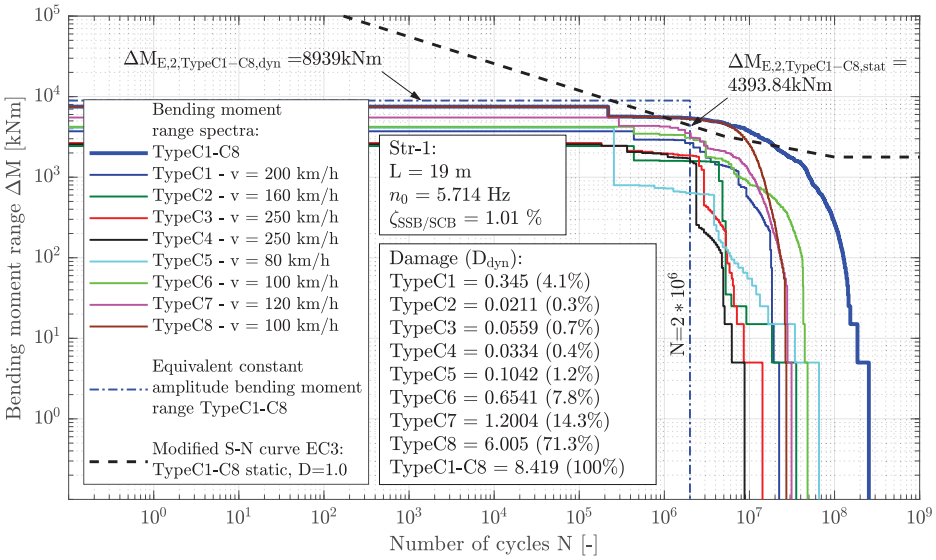

Figure 5.52.: Str-1 — dynamic bending moment ranges — v_{EC} — ζ_{EC} — TypeC1-C8 — traffic mix TM1*

Figure 5.53 compares the bending moment range spectra of the dynamic calculation to the ones of the static calculation. Figures 5.53(a) and 5.53(b) illustrate the results for the passenger trains TypeC1 to TypeC4 and the freight trains TypeC5 to TypeC8 respectively, on the logarithmic scale. Additionally, Figures 5.53(c) and 5.53(d) present the before mentioned bending moment range spectra, using the linear representation.
For Structure Str-2, in comparison to Str-1, only the first bending frequency n_0 was changed from 5.714 Hz to 3.658 Hz. The consequences are illustrated in the final results of Figure 5.54.

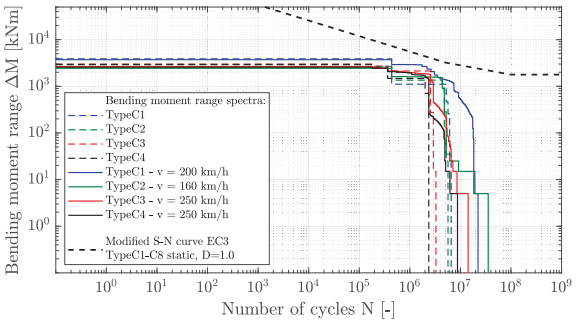

(a) TypeC1-C4 on log-log scale

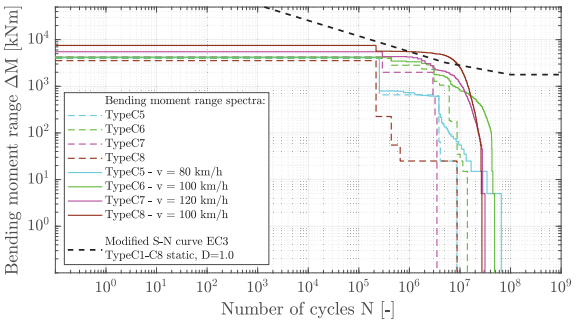

(b) TypeC5-C8 on log-log scale

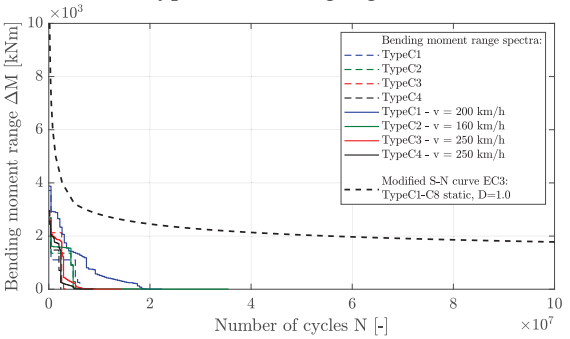

(c) TypeC1-C4 on linear-linear scale

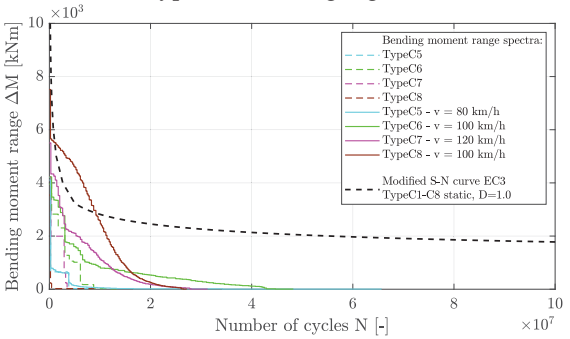

(d) TypeC5-C8 on linear-linear scale

Figure 5.53.: Str-1 — static vs. dynamic bending moment ranges on log-log and linear-linear scale — TypeC1-C8 — traffic mix TM1*

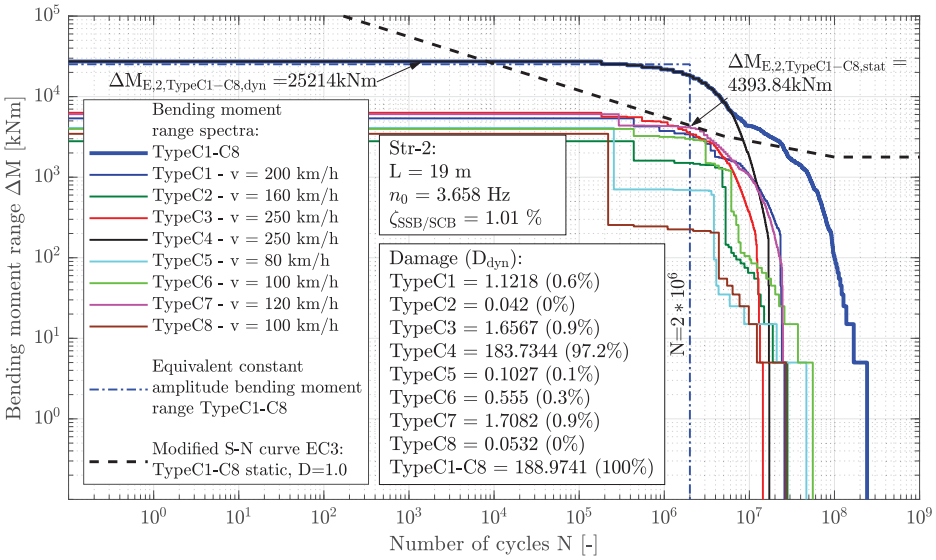

Figure 5.54.: Str-2 — dynamic bending moment ranges — v_{EC} — ζ_{EC} — TypeC1-C8 — traffic mix TM1*

The high-speed passenger train TypeC4 causes with its car length $L_D = 18.7$ m — see Figure 2.18 — at a travelling speed of 250 km/h an excitation frequency of $n_{L_D} = 3.714$ Hz, which is almost equal to the structures first bending frequency $n_0 = 3.658$ Hz and therefore causes resonance. Again, Figure 5.55 illustrates the bending moment range spectra of the static and dynamic calculation with respect to the trains TypeC1-C8, crossing structure Str-2. Especially the differences between static and dynamic calculation for train TypeC4 are very server — see Figures 5.55(a) and 5.55(c).

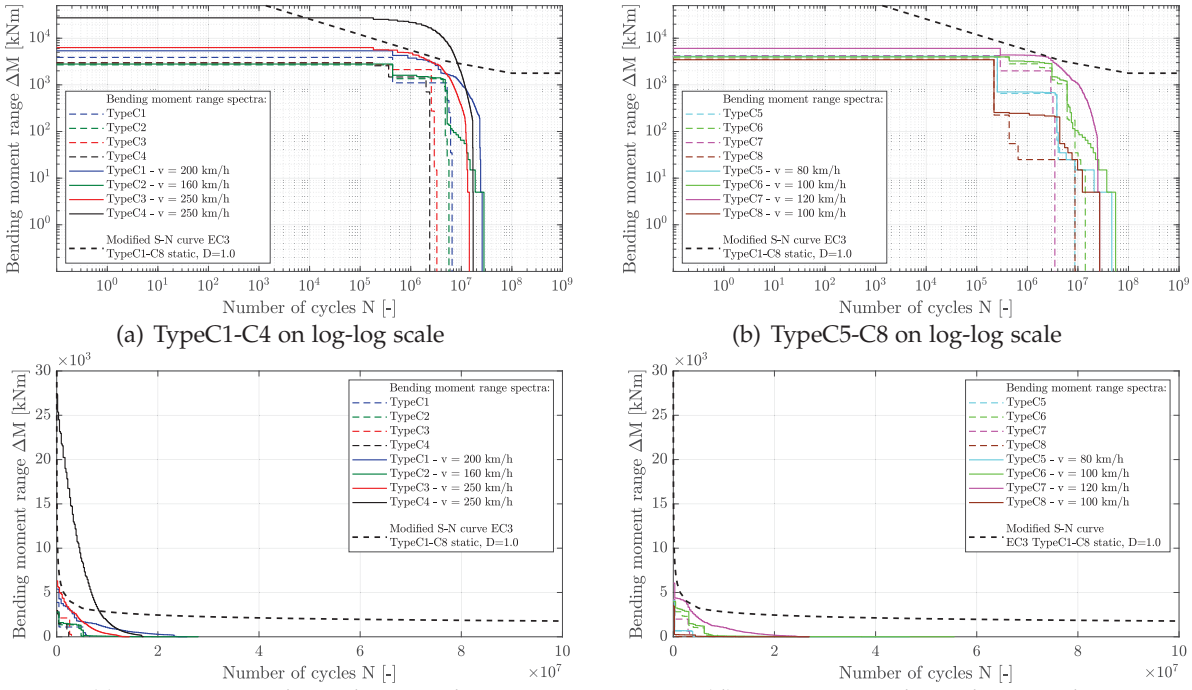

(a) TypeC1-C4 on log-log scale

(b) TypeC5-C8 on log-log scale

(c) TypeC1-C4 on linear-linear scale

(d) TypeC5-C8 on linear-linear scale

Figure 5.55.: Str-2 — static vs. dynamic bending moment ranges on log-log and linear-linear scale — TypeC1-C8 — traffic mix TM1*

Damage D_{dyn} versus D_{stat} for structure Str-3

The static results for structure Str-3, with a span length L of 34 m, are shown in Figure 5.56.

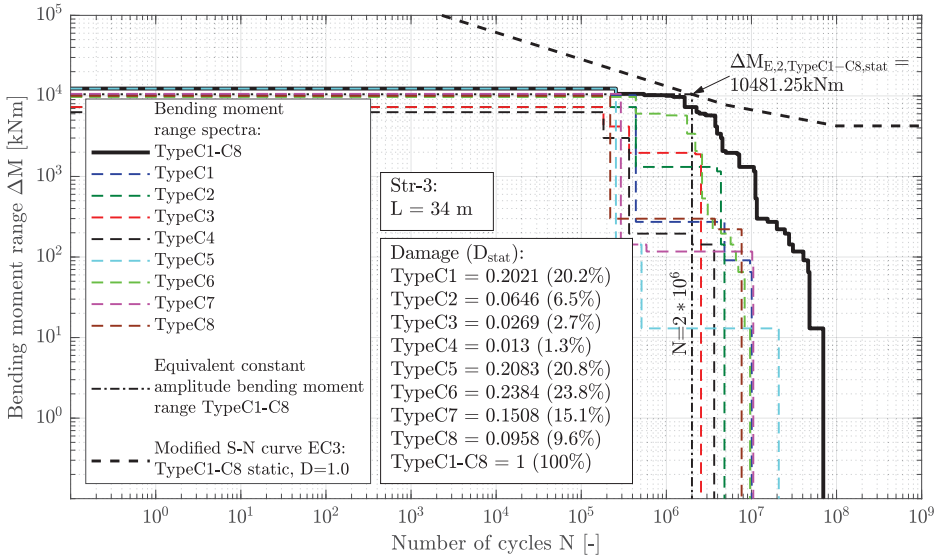

Figure 5.56.: Str-3 — static bending moment ranges — TypeC1-C8 — traffic mix TM1*

As structures Str-2 and Str-3 have both the same first bending frequency $n_0 = 3.658$ Hz, again, high-speed passenger train TypeC4 causes sever damage D_{dyn} due to resonance phenomena — see Figure 5.57. Besides train TypeC4, the freight trains TypeC5 and TypeC7 cause in the dynamic simulation many bending moment range cycles more, than in the static calculation — see Figures 5.58(b) and 5.58(d). However, most of them do not reach the level of the cut-off limit $\Delta\sigma_L$ and consequently do not cause any damage D_{dyn}.

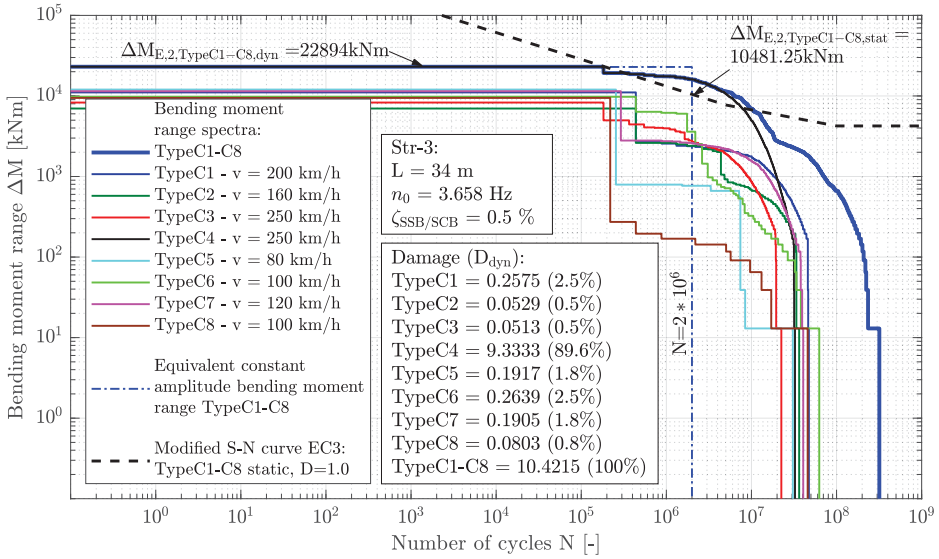

Figure 5.57.: Str-3 — dynamic bending moment ranges — v_{EC} — ζ_{EC} — TypeC1-C8 — traffic mix TM1*

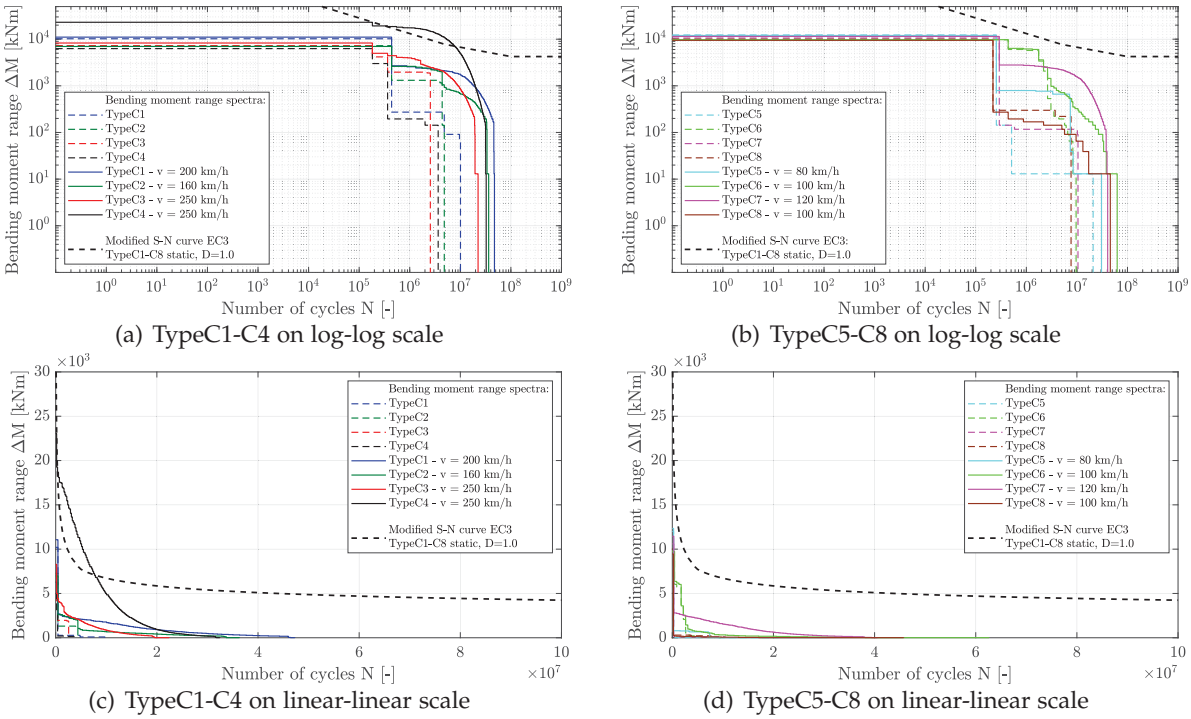

(a) TypeC1-C4 on log-log scale

(b) TypeC5-C8 on log-log scale

(c) TypeC1-C4 on linear-linear scale

(d) TypeC5-C8 on linear-linear scale

Figure 5.58.: Str-3 — static vs. dynamic bending moment ranges on log-log and linear-linear scale — TypeC1-C8 — traffic mix TM1*

Damage D_{dyn} versus D_{stat} for structure Str-4

In Figure 5.59 again the result for the iterated static equivalent constant amplitude bending moment $\Delta M_{E,2,TypeC1-C8,stat}$ due to the static calculation of trains TypeC1 to TypeC8 is shown.

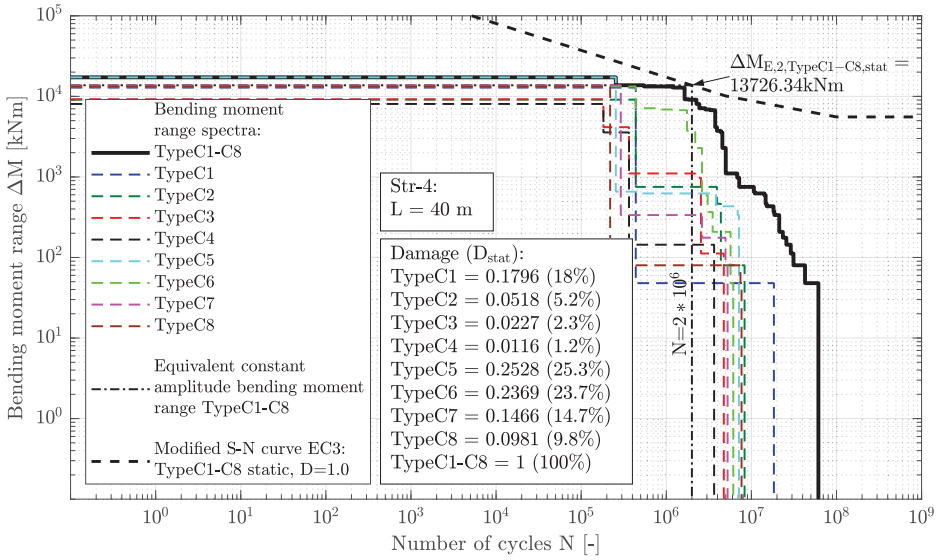

Figure 5.59.: Str-4 — static bending moment ranges — TypeC1-C8 — traffic mix TM1*

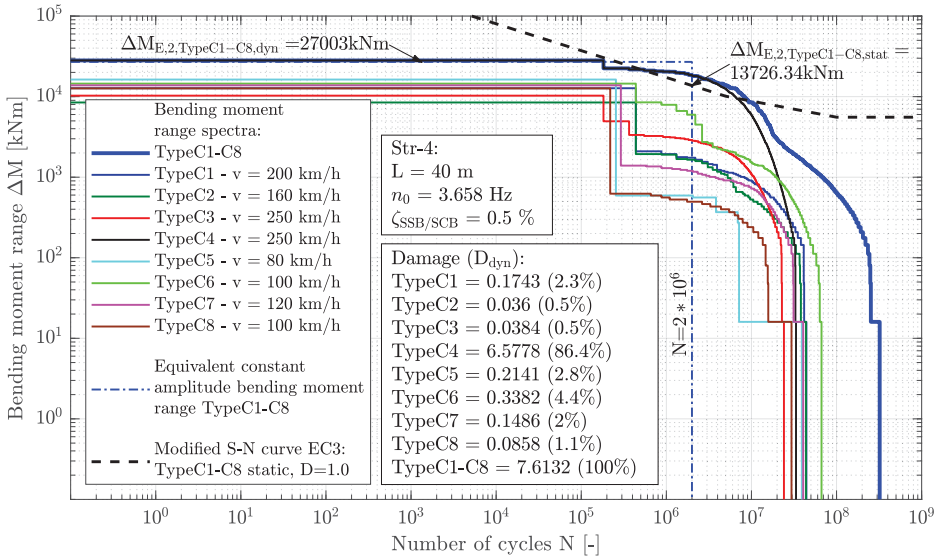

Figure 5.60.: Str-4 — dynamic bending moment ranges — v_{EC} — ζ_{EC} — TypeC1-C8 — traffic mix TM1*

Like structures Str-2 and Str-3, the subsequently discussed structure Str-4 features a first bending frequency of $n_0 = 3.658$ Hz as well. Hence, train TypeC4 has again the biggest influence on the damage D_{dyn} as illustrated in Figure 5.60. The vast differences between the static and dynamic calculation with respect to the resulting bending moment range spectra is once again illustrated in Figure 5.61. The dynamic results of almost all trains lead to a significant increase of bending moment cycles. However, the broad majority of these cycles, except for train TypeC4, has no influence on the damage as they are below the cut-off limit $\Delta\sigma_L$.

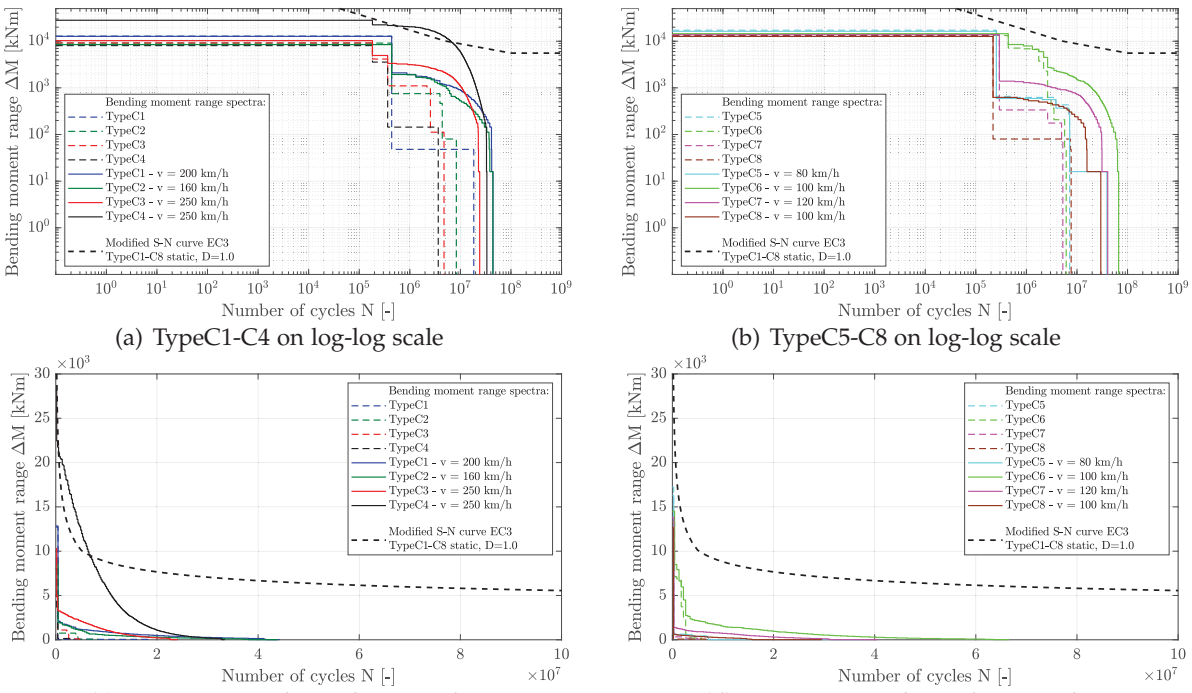

(a) TypeC1-C4 on log-log scale

(b) TypeC5-C8 on log-log scale

(c) TypeC1-C4 on linear-linear scale

(d) TypeC5-C8 on linear-linear scale

Figure 5.61.: Str-4 — static vs. dynamic bending moment ranges on log-log and linear-linear scale — TypeC1-C8 — traffic mix TM1*

Damage D_{dyn} versus D_{stat} for structures Str-5 and Str-6

In Figure 5.62 the static results for a 50 m long single-span beam bridge, which apply for structures Str-5 and Str-6, is presented.

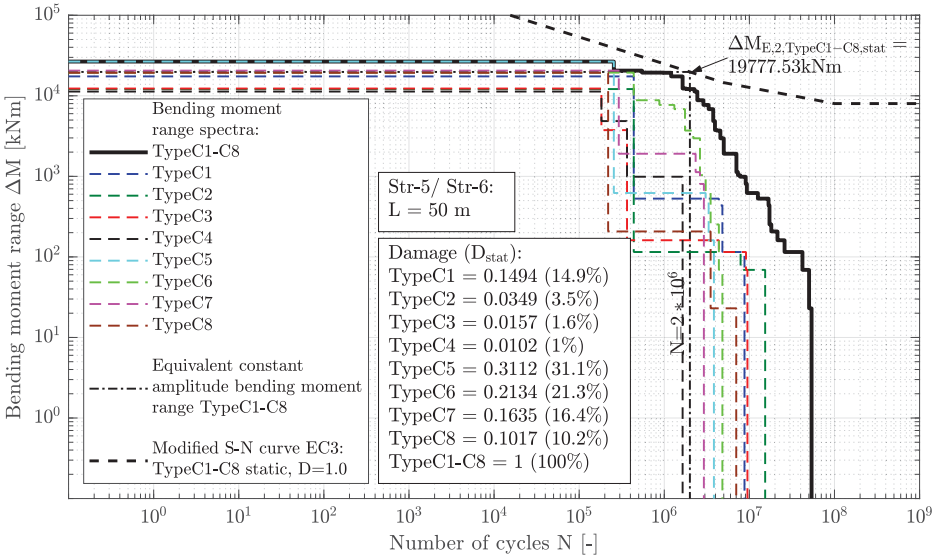

Figure 5.62.: Str-5 — static bending moment ranges — TypeC1-C8 — traffic mix TM1*

The high-speed passenger train TypeC3 and the freight train TypeC5 cause for structure Str-5, which has a first bending frequency of $n_0 = 2.633$ Hz, the most damage D_{dyn}. This is, because train TypeC3 causes due to its car length $L_D = 26.4$ m — see Figure 2.18 — at 250 km/h an excitation frequency of $n_{L_D} = 2.671$ Hz, which is equal to the structures first bending frequency n_0. Equally, the freight train TypeC5 is able to excite, because of its car length of $L_D = 16.9$ m, at 80 km/h each second oscillation cycle of the first bending mode.

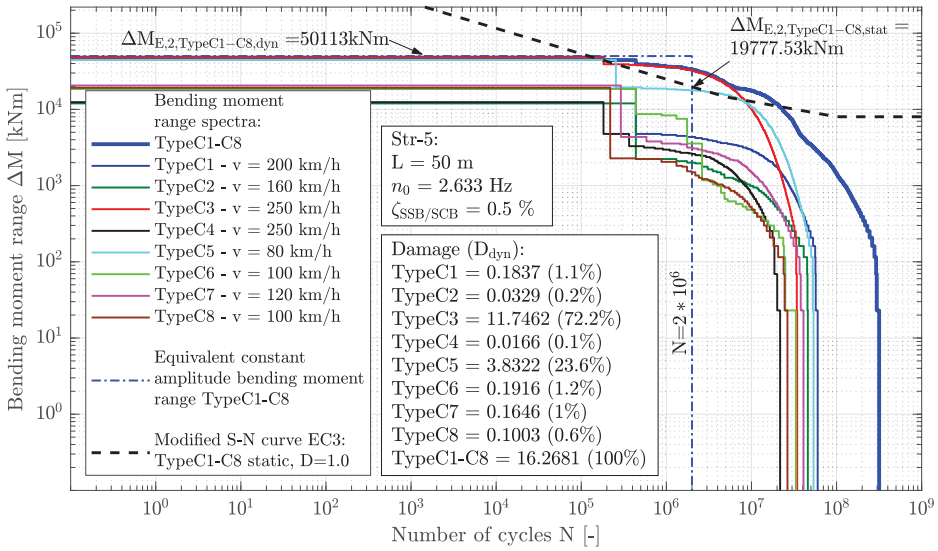

Figure 5.63.: Str-5 — dynamic bending moment ranges — v_{EC} — ζ_{EC} — TypeC1-C8 — traffic mix TM1*

In Figure 5.64 the resulting dynamic and static bending moment range spectra are compared to each other on a linear and logarithmic scale, whereas the impact of trains TypeC3 and TypeC5 due to the dynamic calculation are noteworthy.

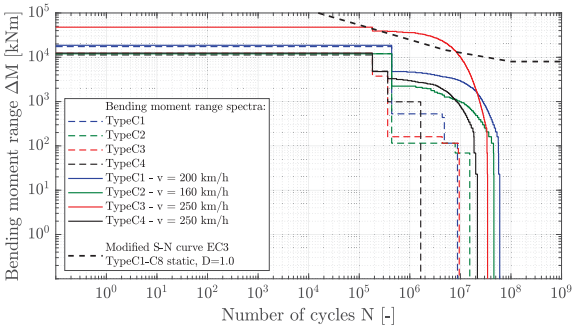

(a) TypeC1-C4 on log-log scale

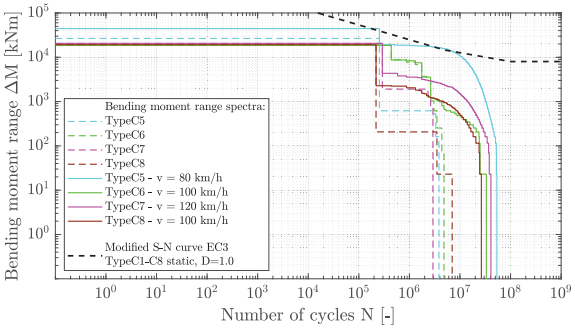

(b) TypeC5-C8 on log-log scale

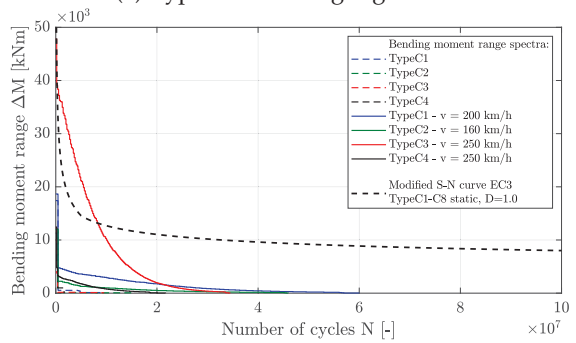

(c) TypeC1-C4 on linear-linear scale

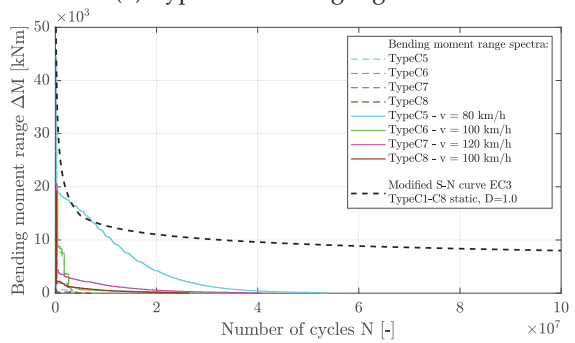

(d) TypeC5-C8 on linear-linear scale

Figure 5.64.: Str-5 — static vs. dynamic bending moment ranges on log-log and linear-linear scale — TypeC1-C8 — traffic mix TM1*

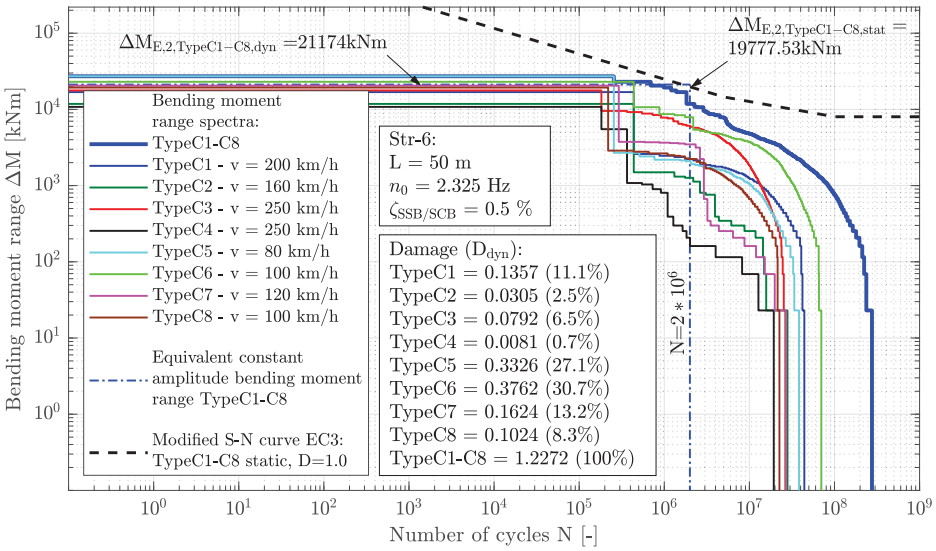

Figure 5.65.: Str-6 — dynamic bending moment ranges — v_{EC} — ζ_{EC} — TypeC1-C8 — traffic mix TM1*

However, structure Str-6 got the same span length of 50 m as Str-5, but an about 12 % lower first bending frequency of $n_0 = 2.325$ Hz. Consequently, trains TypeC3 and TypeC5 are not able to cause resonance effects as on structure Str-5 and the total damage D_{dyn}, due to traffic mix TM1* for the entire design life of 100 years, reduces to about 1.23.

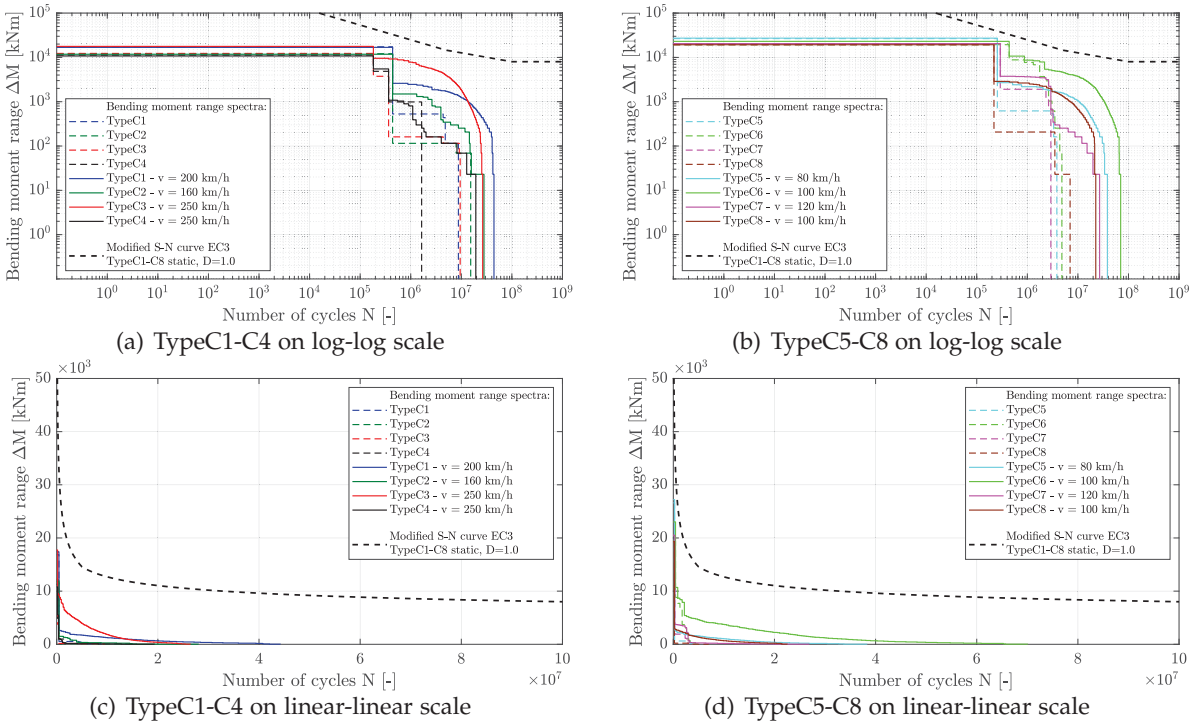

(a) TypeC1-C4 on log-log scale

(b) TypeC5-C8 on log-log scale

(c) TypeC1-C4 on linear-linear scale

(d) TypeC5-C8 on linear-linear scale

Figure 5.66.: Str-6 — static vs. dynamic bending moment ranges on log-log and linear-linear scale — TypeC1-C8 — traffic mix TM1*

In the next and final step, the dynamic equivalent constant amplitude stress range $\Delta\sigma_{E,2,dyn}$ is calculated according to Equation (5.20), which is here rewritten:

$$\Delta\sigma_{E,2,dyn} = D_{dyn}{}^{1/3}\ \Delta\sigma_{E,2,stat} \tag{5.27}$$

In order to apply the above stated Equation, the equivalent constant amplitude stress ranges $\Delta\sigma_{E,2,stat}$ are necessary. Therefore, the 63 single-span steel bridges of Chapter 5.1.1 are used as reference structures according to Figure 5.67. The surface in between these reference structures is interpolated and one can estimate the equivalent constant amplitude stress ranges $\Delta\sigma_{E,2,stat}$ for any other structure. Applying Equation (5.27), under consideration of Figures 5.50 and 5.67,

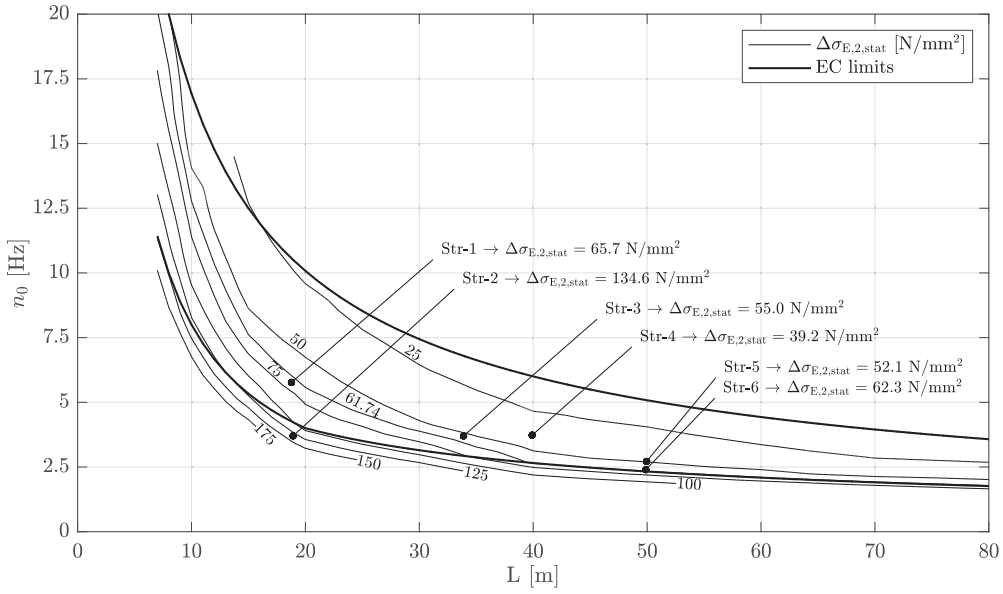

Figure 5.67.: Single-span steel bridges — $\Delta\sigma_{E,2,stat}$ due to TM1 — no load distribution

leads to the results in Figure 5.68 for single-span steel bridges (SSB). The level of the S-N curve, for the damage accumulation calculation (*Miner's rule*) was set to the static result of the trains TypeC1 to TypC8 crossing the structures. Hence, on stress basis this complies with $\Delta\sigma_{E,2,stat}$ of Figure 5.67.

The minimum scale of the color bar in Figure 5.68 is now set to 61.74 N/mm^2, which represents the detail category 71 divided by the safety factor $\gamma_{Mf} = 1.15$ — hereinafter also being referred to as FAT-71[1]. Additionally, the static constant equivalent stress range $\Delta\sigma_{E,2,stat}$ regarding the detail category FAT-71 is also plotted in Figure 5.68 — see black dashed line. Along this line, the level of the S-N curve was exactly at 61.74 N/mm^2, on a stress basis, for the damage accumulation calculation. Considering a detail category FAT-71 as given, structures below this line, towards lower first bending frequencies n_0, can not exist due to the insufficient safety level of the static fatigue design check (FLS). Consequently, only structures above this line, towards higher first bending frequencies n_0, can exist. Furthermore, all coloured areas ($\Delta\sigma_{E,2,dyn}$) above this line, represent conservative results, regarding the detail category FAT-71, as the S-N level, for the damage accumulation calculation, was below 61.74 N/mm^2 — more precisely, exactly at the level according to Figure 5.67. In summary, all $\Delta\sigma_{E,2,dyn}$ values above the black dashed line represent a conservative approach, regarding the detail category FAT-71.

[1] In engineering practice the minimum fatigue strength used for railway bridges.

Additionally, the acceleration criteria of Chapter 5.3.2 are plotted in Figure 5.68 as well. The red solid line represents the criterion for new structures, whereas the red dashed line the one for existing structures. Within the areas defined by these lines, depending on whether the concerned structure is new or already existing, single-span steel bridges are suitable for high-speed railway lines regarding the traffic safety design check (TS), represented by the acceleration criteria. Consequently, if the coloured areas ($\Delta\sigma_{E,2,dyn} > 61.74$ N/mm^2) do not match with the acceleration criteria areas, no potential fatigue problem exists for new/ existing single-span steel structures in high-speed lines. This is the case for traffic mix TM1* on single-span steel bridges (SSB), as illustrated in Figure 5.68. Furthermore, the $\Delta\sigma_{E,2,dyn}$ results for structures Str-1 to Str-6, calculated according to Equation (5.27), are plotted as well.

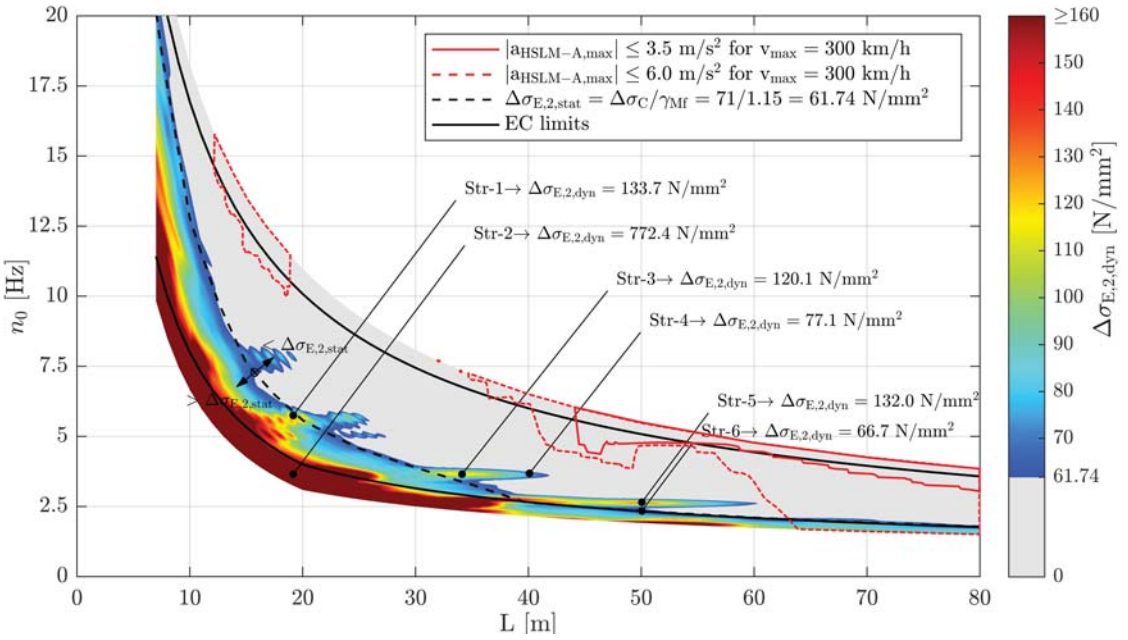

Figure 5.68.: Single-span steel bridges —traffic mix TM1* — v_{EC} — ζ_{EC} — Rayleigh like damping — no load distribution — top view $\Delta\sigma_{E,2,dyn}$ & $|a_{HSLM-A,max}|$ & $\Delta\sigma_{E,2,stat}$

Subsequently, the same procedure is performed for single-span composite bridges (SCB) as well. Therefore, the $\Delta\sigma_{E,2,stat}$ surface, using the 63 reference SCB of Chapter 5.1.2, is interpolated, according to Figure 5.69. Furthermore, Figure 5.70 shows the results for $\Delta\sigma_{E,2,dyn}$, which were obtained using Equation (5.27) in combination with Figures 5.50 and 5.69. Additionally, the TS results of Chapter 5.3.3 are plotted, which allows to perform a combined TS and FLS interpretation.

Again, the vast majority of FLS areas above $\Delta\sigma_{E,2,dyn} = 61.74$ N/mm^2 do not interfere with the TS areas, in which single-span composite structures for high-speed lines would, theoretically, be suitable. An exception represent a few existing SCB with the TS criterion $|a_{HSLM-A,max}| < 6.0$ m/s^2 — see Figure 5.70. Very short structures with a span length of L = 9 m and a first bending frequency of about $n_0 = 12$ Hz and structures with the first bending frequency of Str-5 ($n_0 = 2.633$) and span lengths bigger than 51 m interfere with the TS area for existing structures. One needs to keep in mind that, for existing structures a traffic volume of 24.95 10^6 t/year was considered for the entire design life of 100 years as well.

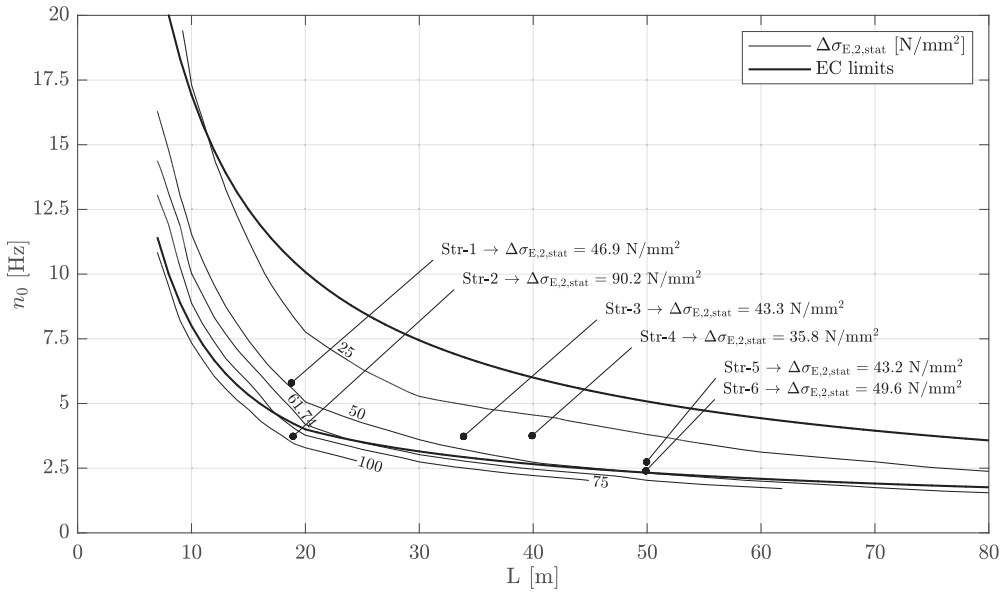

Figure 5.69.: Single-span composite bridges — $\Delta\sigma_{E,2,stat}$ due to TM1 — no load distribution

Furthermore, as explained above, the dynamic FLS results, which are above the static FAT-71 line, are in general conservative regarding the detail category FAT-71. Therefore, for structure Str-5 a damage accumulation calculation with the S-N curve on the level of the discussed detail category FAT-71 was performed in an exemplary manner. Consequently, the S-N curve level was increased, by the factor $61.74/\Delta\sigma_{E,2,stat} = 61.74/43.2 = 1.43$ — see Figure 5.69 — from 19777.53 kNm — see Figure 5.63 — to $\Delta M_{E,2,TypeC1-C8,stat} = 28265.38$ kNm — see Figure 5.71 — leading to a damage of $D_{dyn} = 5.0949$.

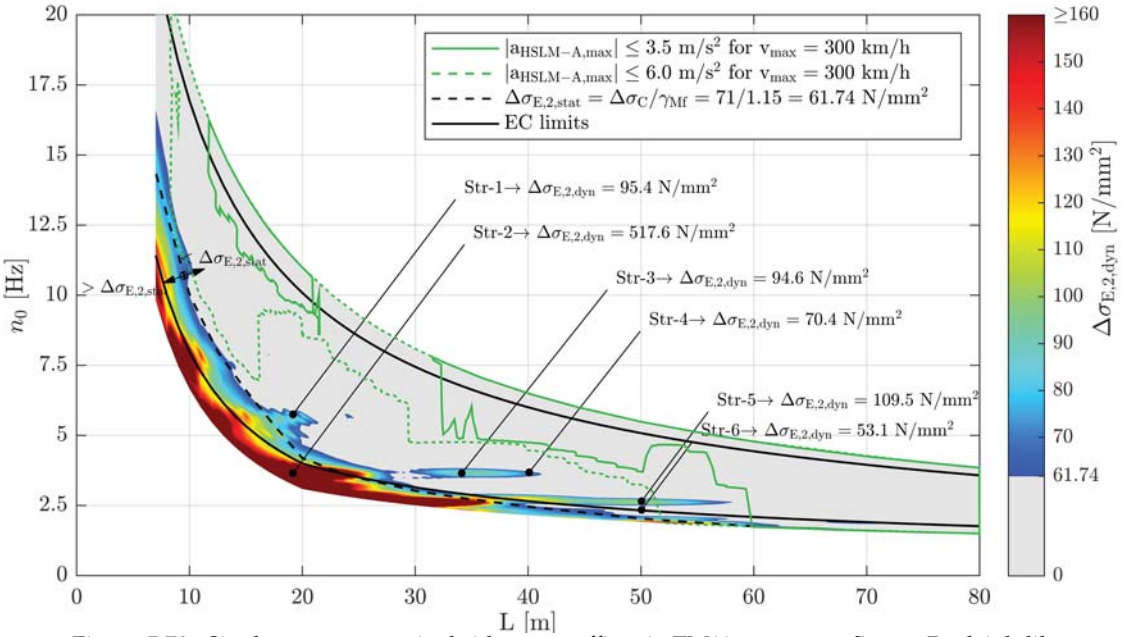

Figure 5.70.: Single-span composite bridges —traffic mix TM1* — v_{EC} — ζ_{EC} — Rayleigh like damping — no load distribution — top view $\Delta\sigma_{E,2,dyn}$ & $|a_{HSLM-A,max}|$ & $\Delta\sigma_{E,2,stat}$

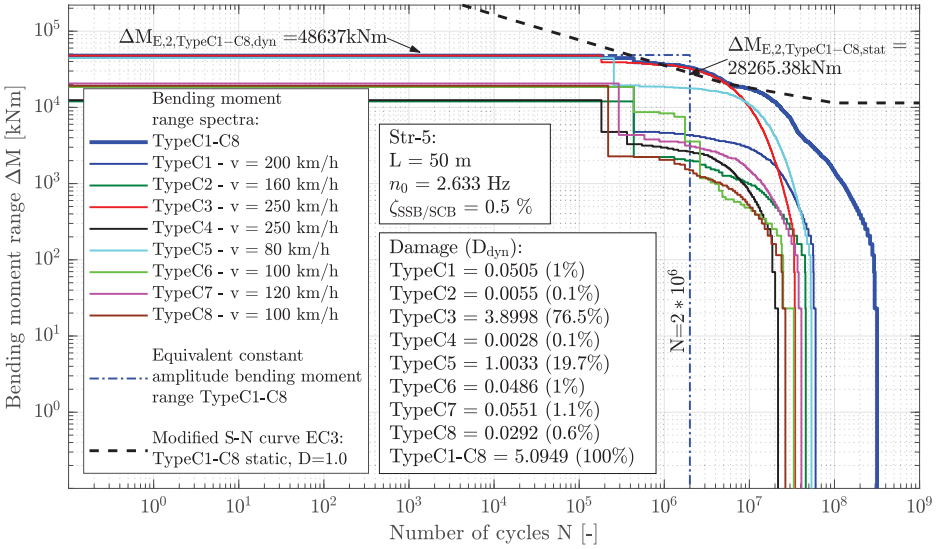

Figure 5.71.: Str-5 — dynamic bending moment ranges — v_{EC} — ζ_{EC} — TypeC1-C8 — traffic mix TM1* — S-N curve set to $\Delta M_{E,2,TypeC1-C8,stat,FAT-71} = 61.74/43.2\ \Delta M_{E,2,TypeC1-C8,stat}$kNm

Applying Equation (5.27) and inserting $\Delta\sigma_{E,2,stat} = 61.74$ N/mm^2, a dynamic equivalent constant amplitude stress range of $\Delta\sigma_{E,2,dyn} = 106.2$ N/mm^2 results. Hence, although the S-N curve was set to the level of the discussed detail category FAT-71, only a minimal reduction of the resulting $\Delta\sigma_{E,2,dyn}$, from 109.5 N/mm^2 to 106.2 N/mm^2 was achieved. The dynamic bending moment range spectra $\Delta\sigma_{E,2,dyn}$ in comparison to the S-N curve, set according to the detail category FAT-71, are illustrated in Figure 5.72.

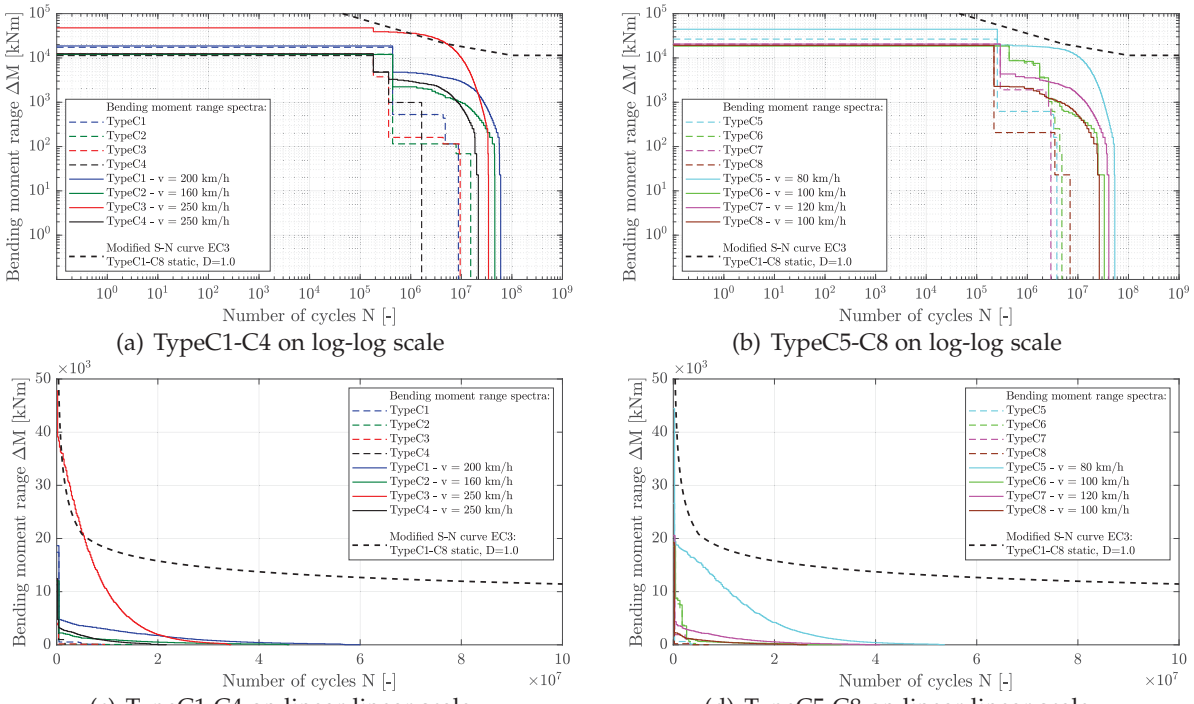

(a) TypeC1-C4 on log-log scale

(b) TypeC5-C8 on log-log scale

(c) TypeC1-C4 on linear-linear scale

(d) TypeC5-C8 on linear-linear scale

Figure 5.72.: Str-5 — static vs. dynamic bending moment ranges on log-log and linear-linear scale — TypeC1-C8 — traffic mix TM1* — S-N curve set to $\Delta M_{E,2,TypeC1-C8,stat,FAT-71} = 61.74/43.2\ \Delta M_{E,2,TypeC1-C8,stat}$kNm

The following Figures 5.73 to 5.75 illustrate the results considering load distribution according to Figure 5.2. Hence, each axle load was divided into three loads, the one in the center being 50 % and the other two lateral ones being 25 % of the original axle load. All other variables, in comparison to the results presented before, were kept unchanged.
The load distribution has especially influence on structures of smaller spans up to L = 15 m — compare Figures 5.50 and 5.73.

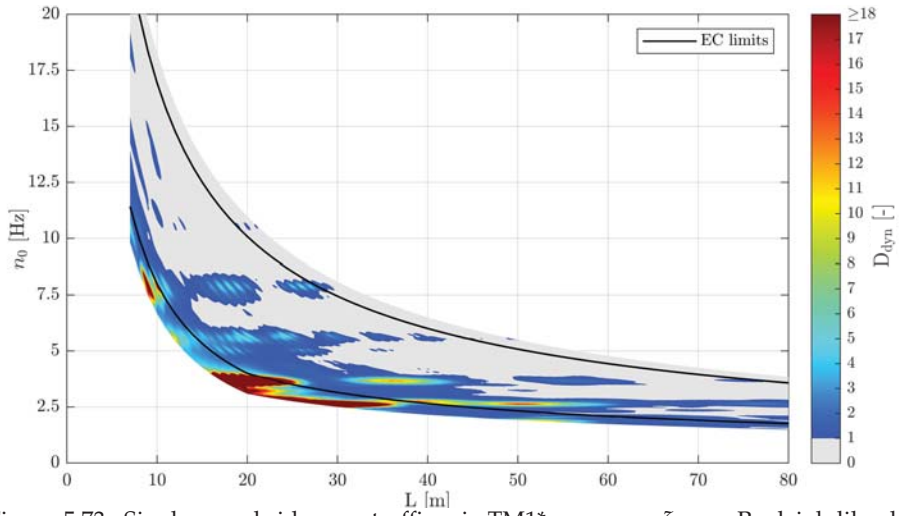

Figure 5.73.: Single-span bridges — traffic mix TM1* — v_{EC} — ζ_{EC} — Rayleigh like damping — load distribution — top view D_{dyn} & $|a_{HSLM-A,max}|$

In Figure 5.74 the FLS and TS results for single-span steel bridges, under consideration of the load distribution, are presented. The load distribution has on both design criteria a positive influence. The areas of the TS criteria increase, hence more structures are suitable for high-speed traffic, whereas the coloured areas ($\Delta\sigma_{E,2,dyn} > 61.74$ N/mm^2) of the FLS design decrease — compare Figure 5.74 to 5.68. Consequently, the conclusion is unchanged, if new/existing single-span steel bridges fulfil the TS criteria, no FLS problem will arise, considering traffic mix TM1*.

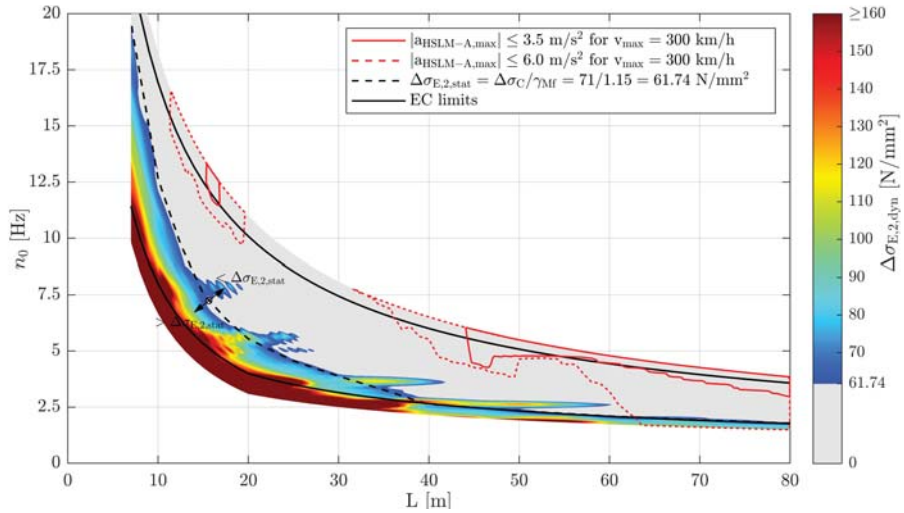

Figure 5.74.: Single-span steel bridges — traffic mix TM1* — v_{EC} — ζ_{EC} — Rayleigh like damping — load distribution — top view $\Delta\sigma_{E,2,dyn}$ & $|a_{HSLM-A,max}|$ & $\Delta\sigma_{E,2,stat}$

The above described phenomena, regarding the load distribution, is also true for single-span composite bridges (SCB). Hence, the statements for the case of no load distribution apply as well. Consequently, if new SCB comply with the TS criterion, no FLS problem will arise with respect to traffic mix TM1*. The same is true for existing SCB, except structures with span lengths L = 51-58 m and a first bending frequency of $n_0 = 2.633$ Hz and spans of about L = 9 m with a first bending frequency $n_0 = 12$ Hz — see Figure 5.75.
Considering the load distribution in this parameter study always led to the same effects like described above. Therefore, subsequently only the results without load distribution are presented, whereas the ones with load distribution may be found in Appendices B and C.

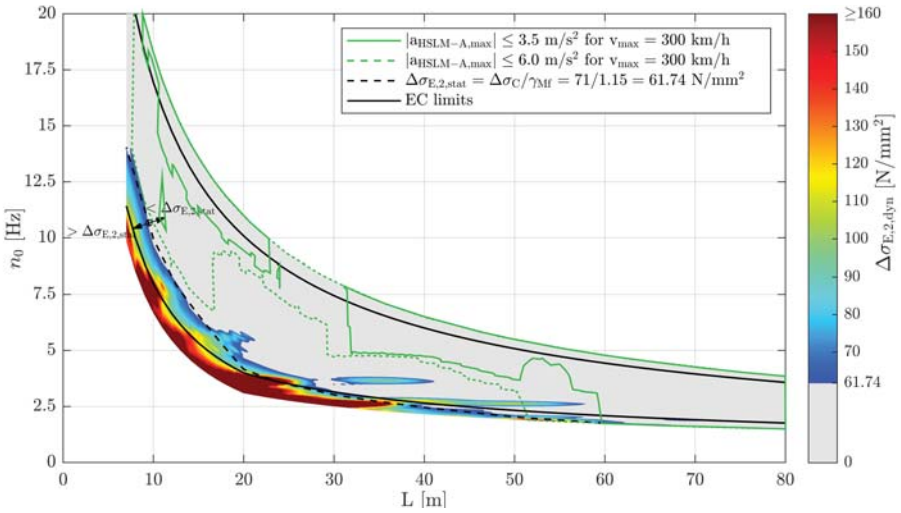

Figure 5.75.: Single-span composite bridges — traffic mix TM1* — v_{EC} — ζ_{EC} — Rayleigh like damping — load distribution — top view $\Delta\sigma_{E,2,dyn}$ & $|a_{HSLM-A,max}|$ & $\Delta\sigma_{E,2,stat}$

The Figures 5.76 to 5.78 show the results considering the damping variant ζ_{V1} without load distribution, consequently the damage D_{dyn} due to traffic mix TM1* is reduced — compare Figures 5.76 and 5.50.

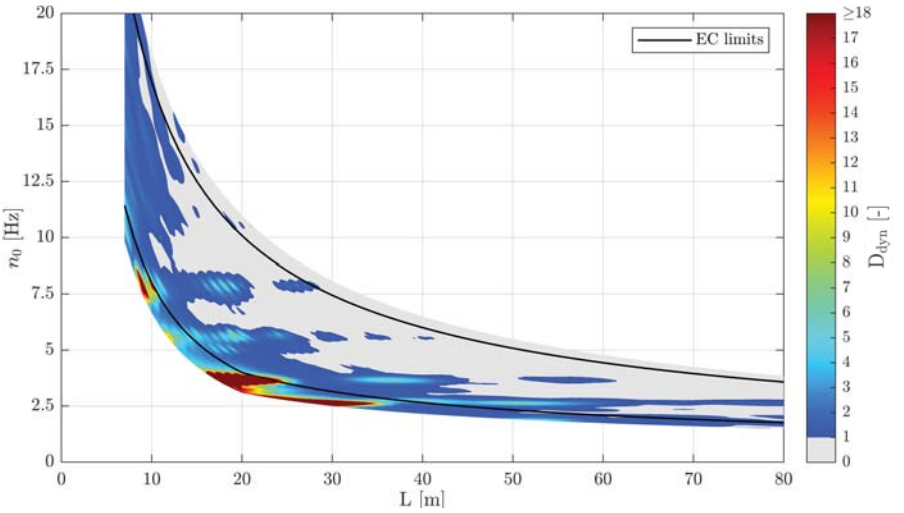

Figure 5.76.: Single-span bridges — traffic mix TM1* — v_{EC} — ζ_{V1} — Rayleigh like damping — no load distribution — top view D_{dyn} & $|a_{HSLM-A,max}|$

The increased damping ratios ζ_{V1} allow for more single-span steel bridges (SSB) to fulfil the TS criterion — see Figure 5.77. Likewise, the FLS areas are diminished, which consequently leads, in this case, for SSB to the same conclusion as for the damping variant ζ_{EC} — as long as the new/ existing SSB fulfil the TS criterion, no FLS problem arises regarding the traffic mix TM1*.

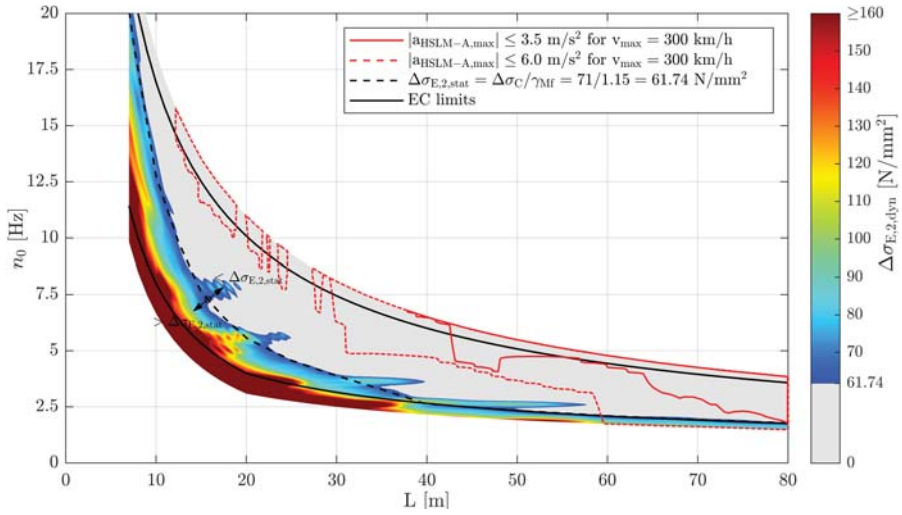

Figure 5.77.: Single-span steel bridges — traffic mix TM1* — v_{EC} — ζ_{V1} — Rayleigh like damping — no load distribution — top view $\Delta\sigma_{E,2,dyn}$ & $|a_{HSLM-A,max}|$ & $\Delta\sigma_{E,2,stat}$

In case of single-span composite bridges (SCB), the same conclusion can be drawn for the damping variants ζ_{V1} and ζ_{EC} as well. Only few existing structures do not fulfil the FLS criteria, while complying with the TS criteria — see Figure 5.78.

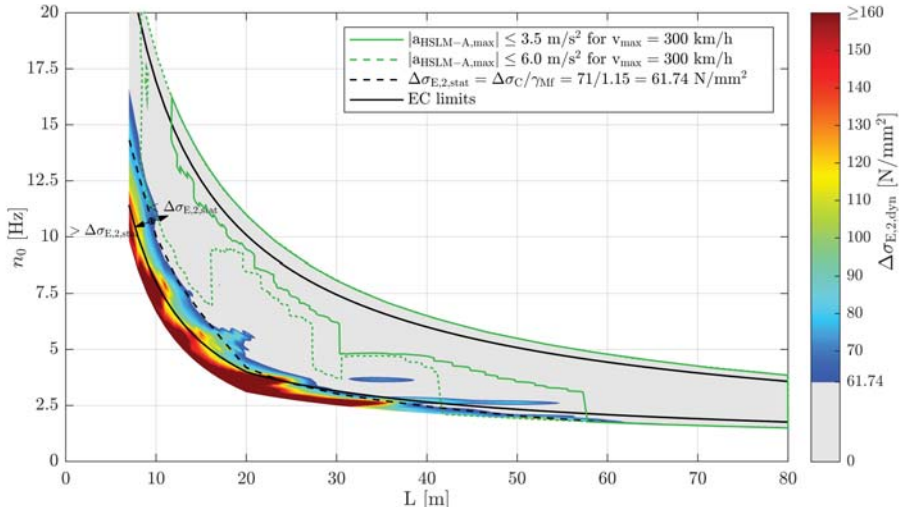

Figure 5.78.: Single-span composite bridges — traffic mix TM1* — v_{EC} — ζ_{V1} — Rayleigh like damping — no load distribution — top view $\Delta\sigma_{E,2,dyn}$ & $|a_{HSLM-A,max}|$ & $\Delta\sigma_{E,2,stat}$

Traffic mix TM1** — train speed $v_{D_{max}}$

Subsequently, the results of traffic mix TM1** are presented, which considers the trains TypeC1 to TypeC8 passing the structures with the speed $v_{D_{max}}$. As described before, $v_{D_{max}}$ represents the speed, within a certain speed range, at which the particular train produces the maximum damage D_{dyn} — see Table 4.2. As illustrated in Figure 5.79, the traffic mix TM1** causes at each single-span structure a damage D_{dyn} above the static level D_{stat} for the case of the damping according to ÖNORM EN 1991-2 [43], hence ζ_{EC}.

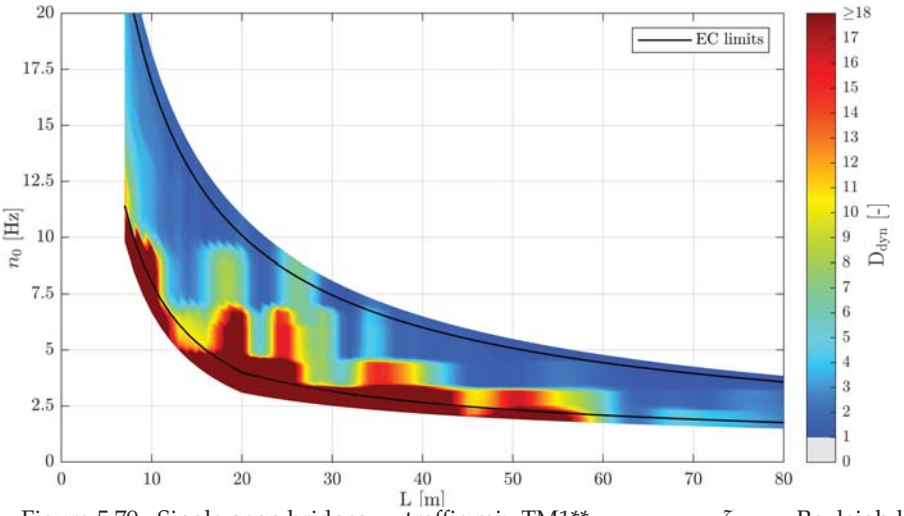

Figure 5.79.: Single-span bridges — traffic mix TM1** — $v_{D_{max}}$ — ζ_{EC} — Rayleigh like damping — no load distribution — top view D_{dyn}

However, transforming the damage D_{dyn} into the dynamic equivalent constant amplitude stress range $\Delta\sigma_{E,2,dyn}$ and neglecting all results below 61.74 N/mm^2, leads for single-span steel structures (SSB) to Figure 5.80. Considering the TS criteria for the SSB, shows that all new structures, which fulfil the TS criteria do not have a FLS problem. This is, again, true for most of the existing SSB as well, except for structures above a span length L = 62 m and a first bending frequency n_0 near the lower EC limit.

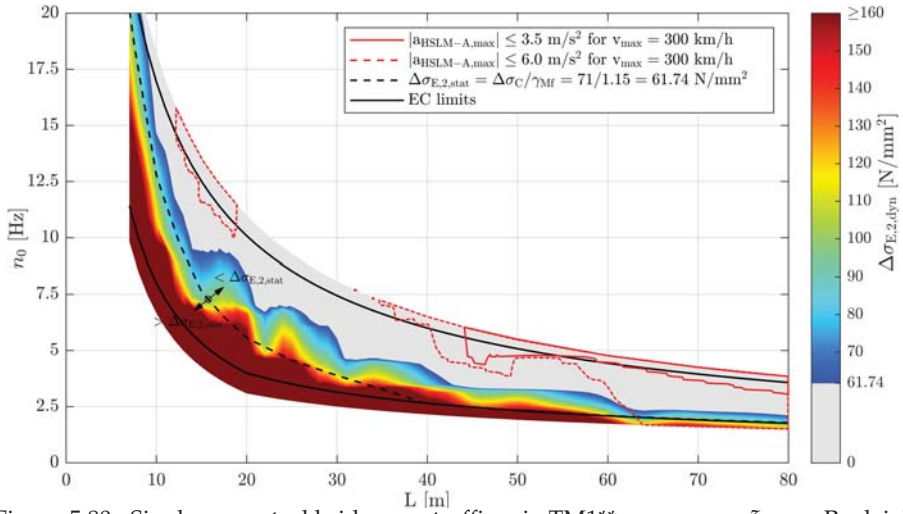

Figure 5.80.: Single-span steel bridges — traffic mix TM1** — $v_{D_{max}}$ — ζ_{EC} — Rayleigh like damping — no load distribution — top view $\Delta\sigma_{E,2,dyn}$ & $|a_{HSLM-A,max}|$ & $\Delta\sigma_{E,2,stat}$

New composite structures, which fulfil the TS criteria, also comply with the FLS criteria, except for structures with spans above L = 60 m and a first bending frequency n_0 close to the lower EC limit — see Figure 5.81. On the other hand, existing structures with spans up to 16 m and spans starting from 51 m do not fulfil the FLS criteria, while complying with the TS criteria. However, one needs to consider that TM1** assumes the trains TypeC1 - TypeC8 to pass each structure for 100 years with the most unfavourable speed.

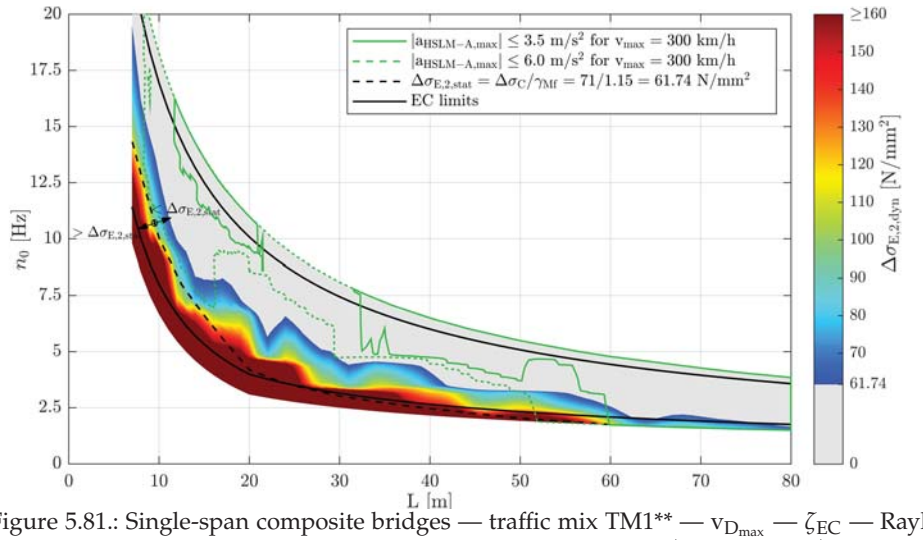

Figure 5.81.: Single-span composite bridges — traffic mix TM1** — $v_{D_{max}}$ — ζ_{EC} — Rayleigh like damping — no load distribution — top view $\Delta\sigma_{E,2,dyn}$ & $|a_{HSLM-A,max}|$ & $\Delta\sigma_{E,2,stat}$

Figures 5.82 to 5.84 show the results for the increased damping variant ζ_{V1}. However, the majority of the structures suffers a dynamic damage D_{dyn} above the static threshold — see Figure 5.82.

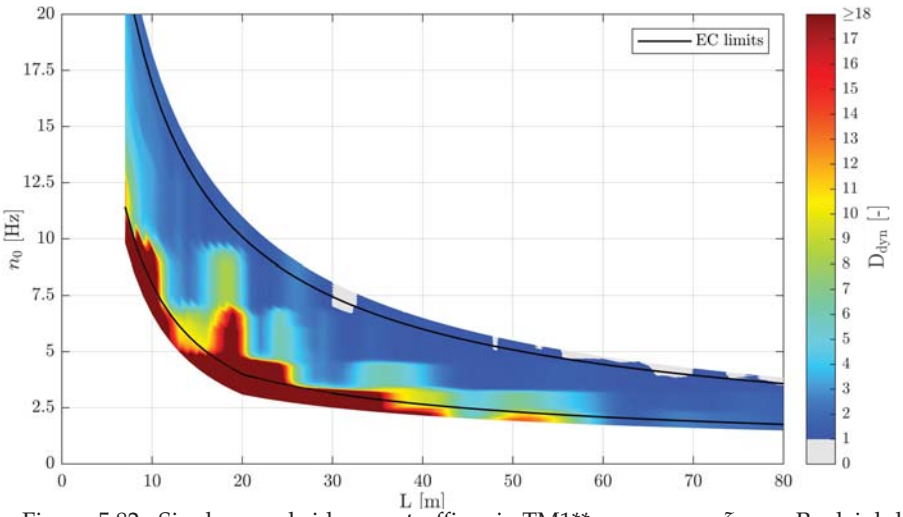

Figure 5.82.: Single-span bridges — traffic mix TM1** — $v_{D_{max}}$ — ζ_{V1} — Rayleigh like damping — no load distribution — top view D_{dyn}

Considering the FLS and TS results for single-span steel bridges, as in Figure 5.83 illustrated, allows to conclude again, that in general new SSB, fulfilling the TS criteria, do not have a FLS

problem. For existing structures this is the case as well, except for SSB with span lengths L beyond 59 m and a first bending frequency n_0 close to the lower EC limit.

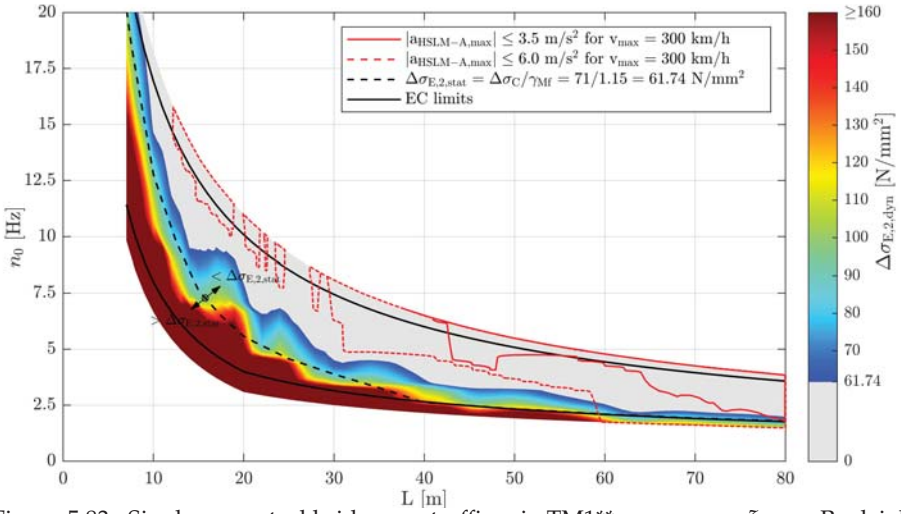

Figure 5.83.: Single-span steel bridges — traffic mix TM1** — $v_{D_{max}}$ — ζ_{V1} — Rayleigh like damping — no load distribution — top view $\Delta\sigma_{E,2,dyn}$ & $|a_{HSLM-A,max}|$ & $\Delta\sigma_{E,2,stat}$

New single-span composite structures, loaded by the traffic mix TM1** for 100 years, do not have a FLS problem, if their span lengths are not above 58 m and their first bending frequency n_0 are above the lower EC limit — see Figure 5.84. Furthermore, existing SCB do have a FLS problem even when complying with the TS criteria, as already mentioned for the damping variant ζ_{EC} before.

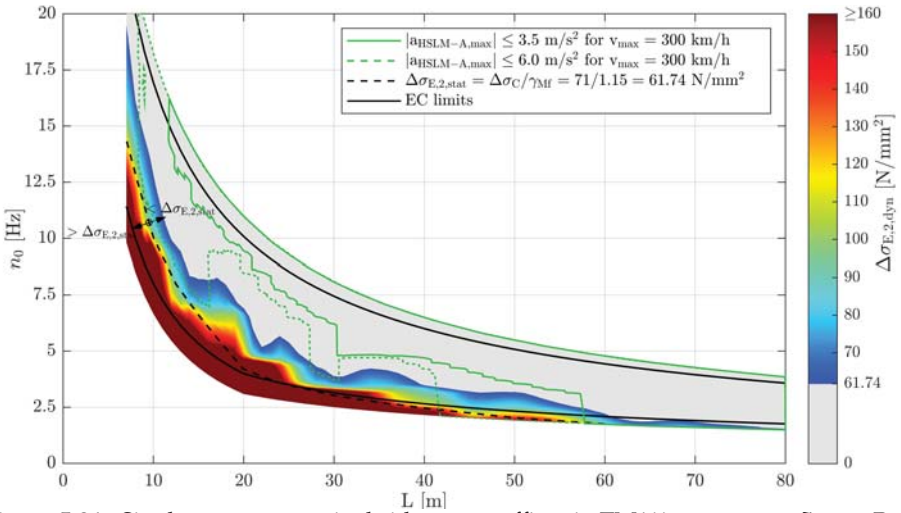

Figure 5.84.: Single-span composite bridges — traffic mix TM1** — $v_{D_{max}}$ — ζ_{V1} — Rayleigh like damping — no load distribution — top view $\Delta\sigma_{E,2,dyn}$ & $|a_{HSLM-A,max}|$ & $\Delta\sigma_{E,2,stat}$

Traffic mix TM1* — train speed $v_{a_{max}}$**

Subsequently, the results regarding traffic mix TM1*** are presented. First, the maximum vertical bridge deck acceleration $|a_{max}|$ and the corresponding train speed $v_{a_{max}}$ for each of the trains TypeC1 to TypeC8, considering the train's speed ranges, was determined for each single structure. In the next step, the dynamic simulation was performed with the train speed $v_{a_{max}}$ and the dynamic damage D_{dyn} was calculated as illustrated in Figure 5.85 for the damping variant ζ_{EC}. Comparing Figure 5.85 to the results due to the train speed $v_{D_{max}}$ of Figure 5.79 shows the similarities of these two outcomes. Consequently, one can estimate the maximum damage D_{dyn} due to a particular train with its speed leading to the maximum bridge deck acceleration $v_{a_{max}}$.

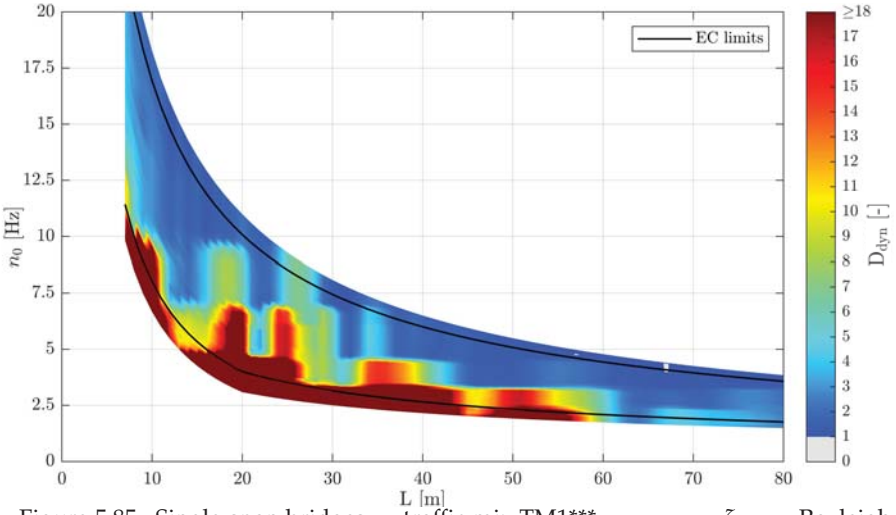

Figure 5.85.: Single-span bridges — traffic mix TM1*** — $v_{a_{max}}$ — ζ_{EC} — Rayleigh like damping — no load distribution — top view D_{dyn}

Hence, the results for SSB and SCB due to the trains crossing the structures with the speed $v_{a_{max}}$ — see Figures 5.86 and 5.87 — are very similar to the ones of the speed $v_{D_{max}}$ — see Figures 5.80 and 5.81.

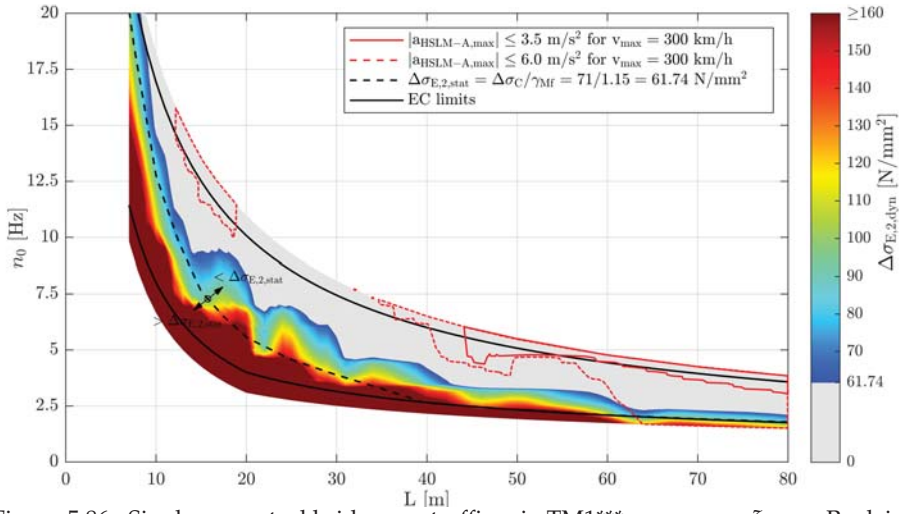

Figure 5.86.: Single-span steel bridges — traffic mix TM1*** — $v_{a_{max}}$ — ζ_{EC} — Rayleigh like damping — no load distribution — top view $\Delta\sigma_{E,2,dyn}$ & $|a_{HSLM-A,max}|$ & $\Delta\sigma_{E,2,stat}$

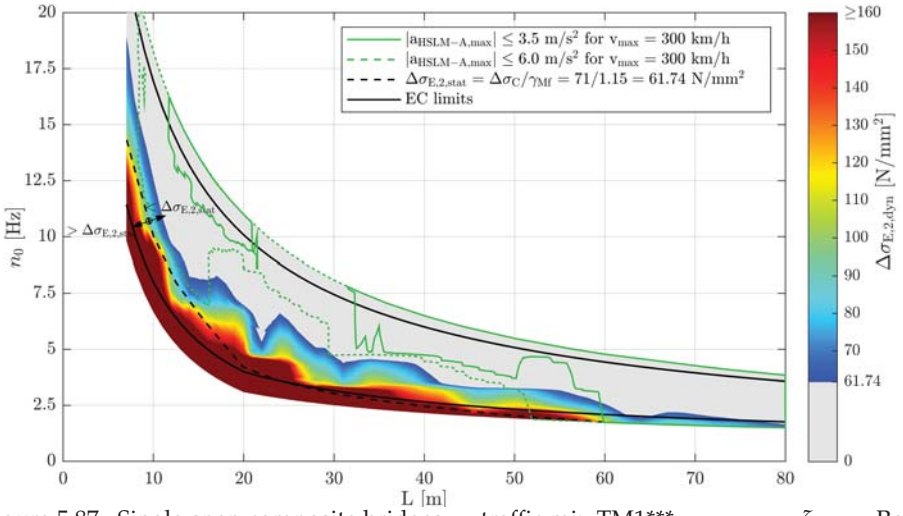

Figure 5.87.: Single-span composite bridges — traffic mix TM1*** — $v_{a_{max}}$ — ζ_{EC} — Rayleigh like damping — no load distribution — top view $\Delta\sigma_{E,2,dyn}$ & $|a_{HSLM-A,max}|$ & $\Delta\sigma_{E,2,stat}$

Increasing the damping ratio to ζ_{V1} does not change the validity of the stated above for single-span steel and composite structures — compare Figures 5.88, 5.89 and 5.90 to Figures 5.82, 5.83 and 5.84.

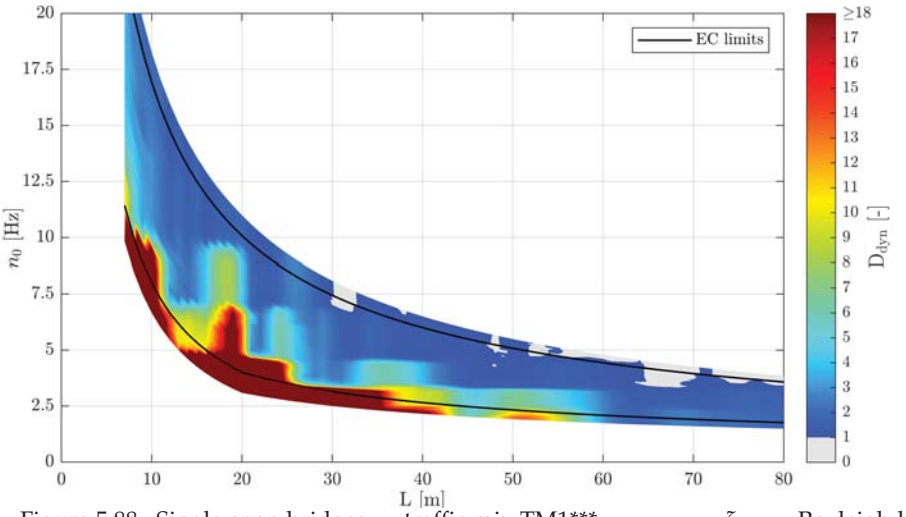

Figure 5.88.: Single-span bridges — traffic mix TM1*** — $v_{a_{max}}$ — ζ_{V1} — Rayleigh like damping — no load distribution — top view D_{dyn}

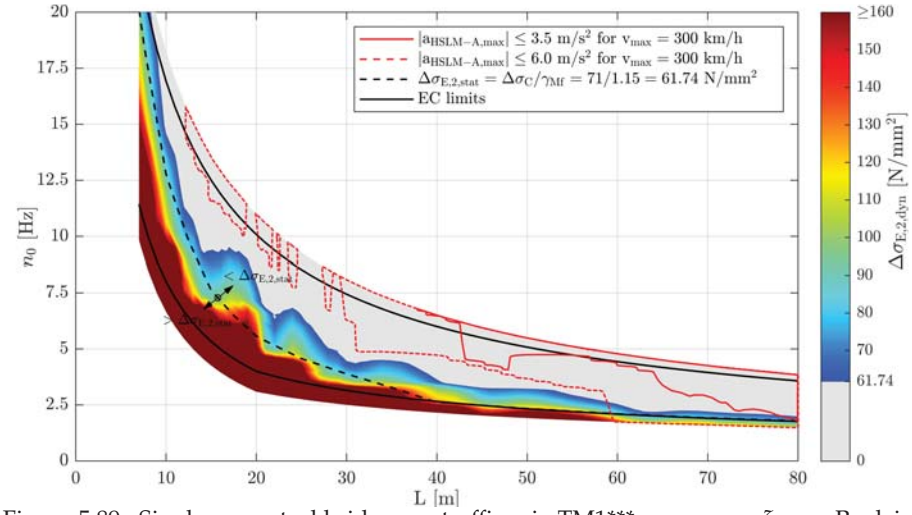

Figure 5.89.: Single-span steel bridges — traffic mix TM1*** — $v_{a_{max}}$ — ζ_{V1} — Rayleigh like damping — no load distribution — top view $\Delta\sigma_{E,2,dyn}$ & $|a_{HSLM-A,max}|$ & $\Delta\sigma_{E,2,stat}$

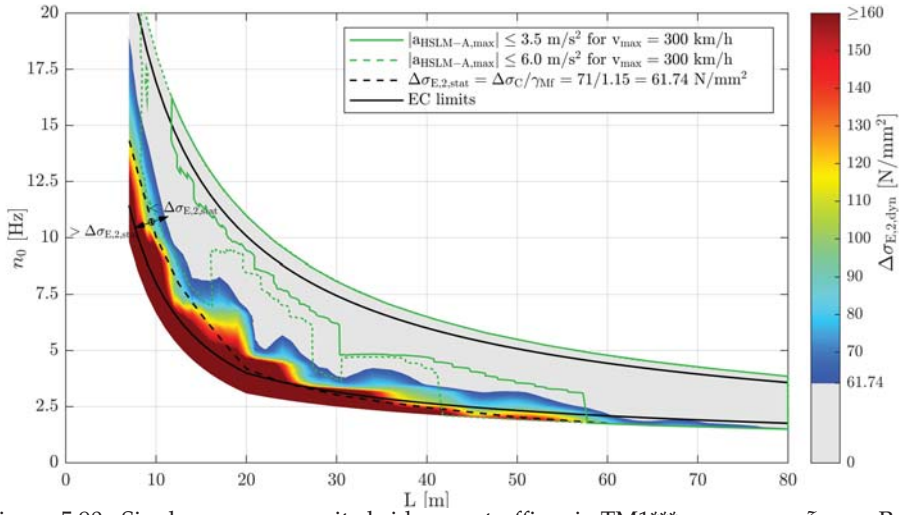

Figure 5.90.: Single-span composite bridges — traffic mix TM1*** — $v_{a_{max}}$ — ζ_{V1} — Rayleigh like damping — no load distribution — top view $\Delta\sigma_{E,2,dyn}$ & $|a_{HSLM-A,max}|$ & $\Delta\sigma_{E,2,stat}$

5.4.2. Traffic mix 2

In the following paragraphs the traffic mix 2 is discussed, in particular traffic mix TM2-st, as only single track single-span railway bridge are covered here. The trains in traffic mix TM2-st and the corresponding train speeds originate from measurements as described in Chapter 4 and precised in Chapter 5.1.4. In total, over two consecutive years, 77217 passenger trains (PT) were counted, of which 65451 were grouped into 73 average trains. These 73 average passenger trains represent the total of 77217 PT, as described subsequently. Additionally, 15178 freight trains (FT) were identified, which due to their big variety of train car combinations were not grouped into average FT. Furthermore, the 2207 registered special trains (SP) are not directly considered, but their traffic volume added to the one of the FT. In summary, the non-dimensional approach is applied on 73 average PT, representing 77217 real PT. Furthermore, the 15178 real FT are calculated, using the dimensional approach, for selected reference structures, whereas the results for other structures are consequently interpolated.
First, the PT are discussed and Figure 5.91 shows the non-dimensional D_{dyn} results of the average passenger train TypeC19 (Taurus power car in front), crossing once the single-span structures with a span length L = 7 to 80 m. For the dynamic calculation the damping variant ζ_{EC}, Rayleigh like damping and no load distribution were considered.

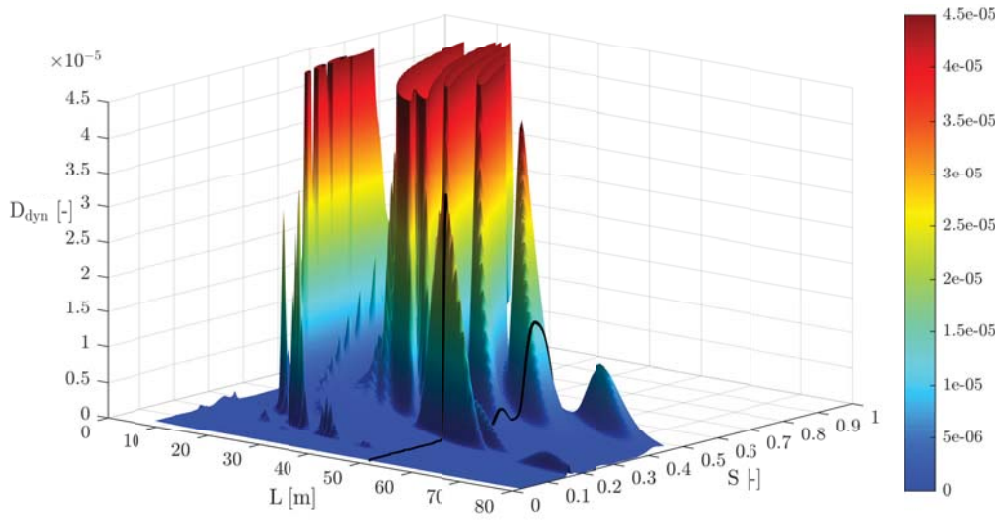

Figure 5.91.: Single-span bridges — non-dimensional representation of D_{dyn} — TypeC19 Taurus-front (average train) — one train crossing — ζ_{EC} — Rayleigh like damping — no load distribution

Figure 5.91 is based on the average train TypeC19, which was determined based on the measurement results due to 6689 real trains TypeC19 — see Table 4.4, line four. Subsequently, Figure 5.92 gives, in an exemplary way, information of the error made due to this simplification in case of the single-span bridge SSB50-1 with a span length L = 50 m and a first bending frequency $n_0 = 2.33$ Hz. Therefore, on the one hand the non-dimensional results of Figure 5.91 — see black line at L = 50 m — are illustrated in Figure 5.92. Additionally, the results of the preliminary FLS calculation of Chapter 5.2.2 for the 6689 real TypeC19 trains are plotted for structure SSB50-1 as well. The transformation was, as explained in Chapter 5.1.5, performed

using Equation (5.17) , which is here rewritten

$$S = \frac{v}{2\ L\ n_0} \tag{5.28}$$

The maximum absolute error $|\Delta D_{dyn,max}|$ made by the average train TypeC19 in comparison to the real 6689 trains is 50 %, whereas the average absolute error $|\Delta D_{dyn,average}|$ is only about 5.3 %.

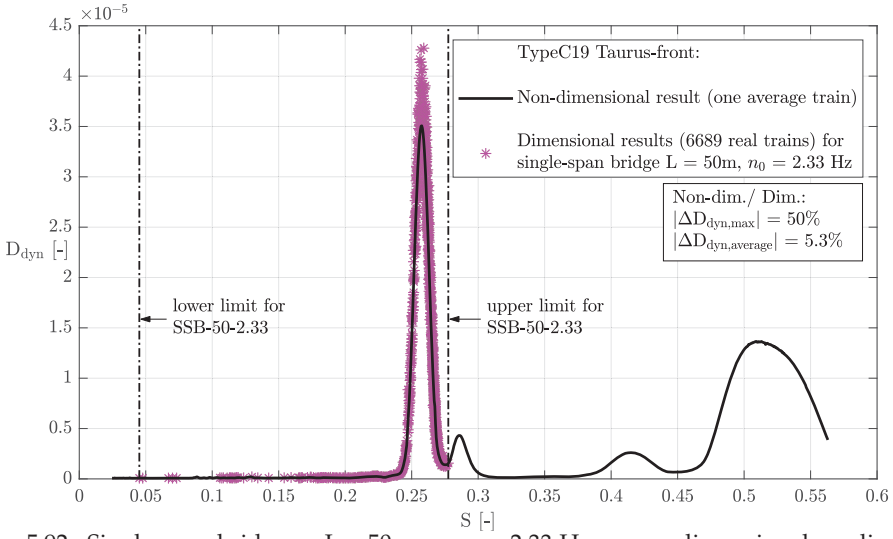

Figure 5.92.: Single-span bridge — L = 50 m — n_0 = 2.33 Hz — non-dimensional vs. dimensional calculation D_{dyn} — TypeC19 Taurus-front (average train) — 6689 train speeds — one train crossing — ζ_{EC} — Rayleigh like damping — no load distribution

Creating for all 73 average PT — see Table 4.4 — the non-dimensional solutions, as described for train TypeC19 in Figure 5.91, and evaluating these, using Equation (5.28), for the single-span structures, defined by the span length L and the first bending frequency n_0, and adding these up, leads for the entire design life of 100 years to the results of Figure 5.93.

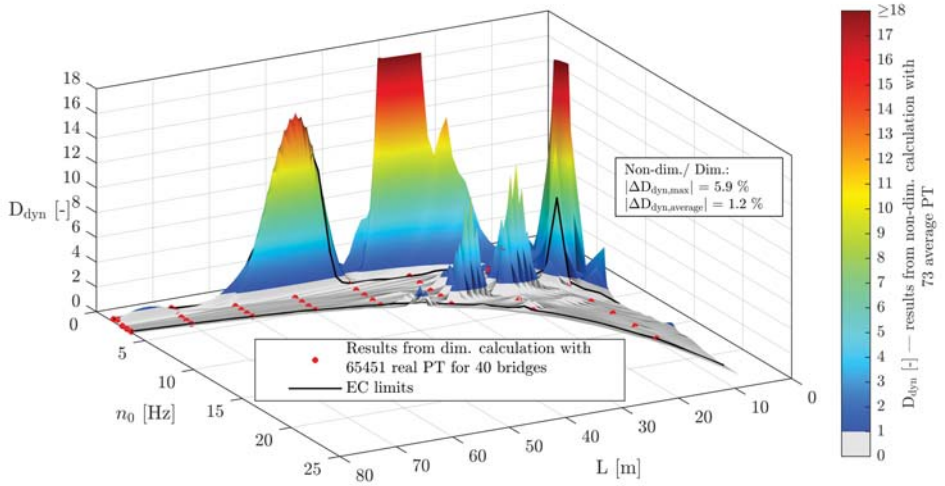

Figure 5.93.: Single-span bridges — non-dimensional vs. dimensional calculation D_{dyn} — 73 average PT vs. 65451 real (labeled) PT — ζ_{EC} — Rayleigh like damping — design life train mass = 32383.1 * $f_{TM2-st,100years}$ [10^3 t] — 3D view

This means, Figure 5.94, which is the top view representation of Figure 5.93, illustrates the D_{dyn} results due to 73 average PT, which cover 65451 real PT. Additionally, the results of the dimensional calculation for 40 reference structures, considering the real 65451 PT for each of those structures — see Chapter 5.2.2 — are compared to the results due to the average 73 PT using the non-dimensional approach. The maximum absolute error $|\Delta D_{dyn,max}|$ of 5.9 % and the average absolute error $|\Delta D_{dyn,average}|$ of 1.2 % in Figure 5.94 consequently compare the 40 red points to the surface.

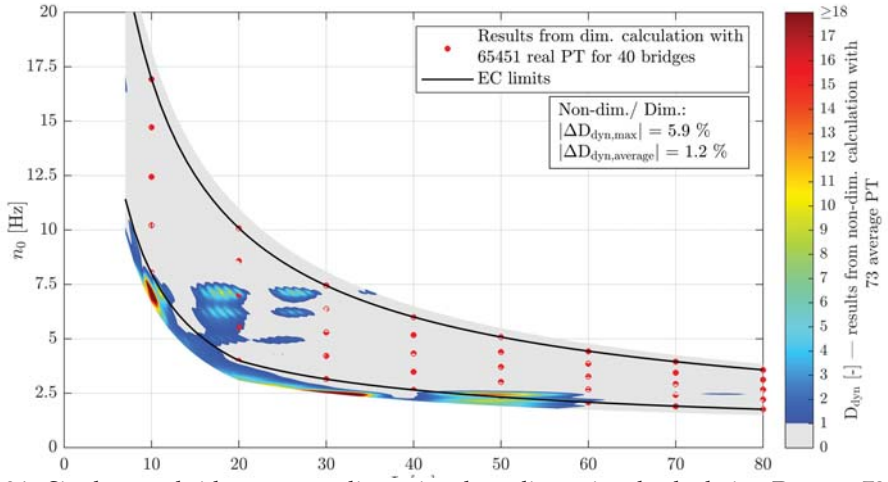

Figure 5.94.: Single-span bridges — non-dimensional vs. dimensional calculation D_{dyn} — 73 average PT vs. 65451 real (labeled) PT — ζ_{EC} — Rayleigh like damping — design life train mass = 32383.1 * $f_{TM2-st,100years}$ [10^3 t] — top view

Up to now, the 73 average PT cover the 65451 real PT on which they were originally based. In order to account for the total 77217 PT — according to Table 5.1 and Equation (5.9) — the results of Figure 5.94 are multiplied by the factor f_{PT} = 1.1900, which leads to Figure 5.95. Consequently, the maximum absolute error $|\Delta D_{dyn,max}|$ rises to 14.3 % and the average absolute error $|\Delta D_{dyn,average}|$ becomes 5.3 %.

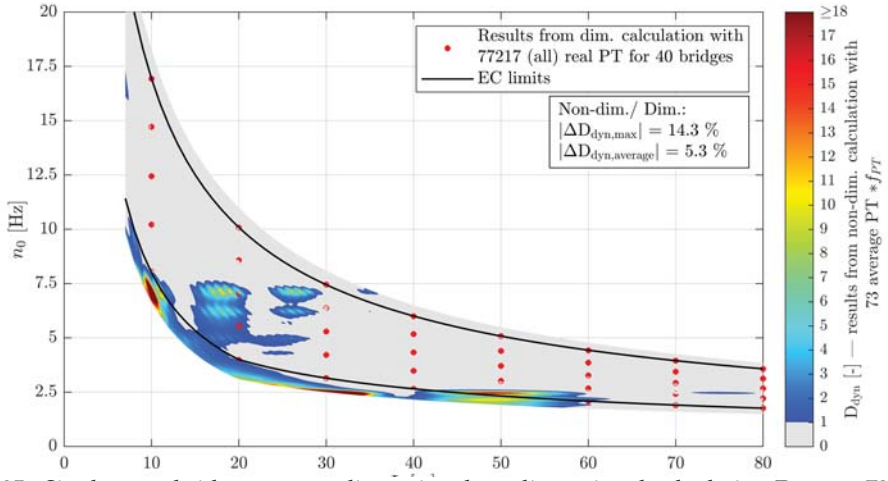

Figure 5.95.: Single-span bridges — non-dimensional vs. dimensional calculation D_{dyn} — 73 average PT $*f_{PT}$ vs. 77217 real (all) PT — ζ_{EC} — Rayleigh like damping — design life train mass = 38535.9 * $f_{TM2-st,100years}$ [10^3 t] — top view

As already mentioned above, the 15178 FT were not simplified to average trains as their train car combinations are too random — see Figure 4.4. Therefore, the dimensional results of reference structures from the preliminary FLS survey — see Chapter 5.2.2 — were used and the areas in between interpolated, as illustrated in Figure 5.96.

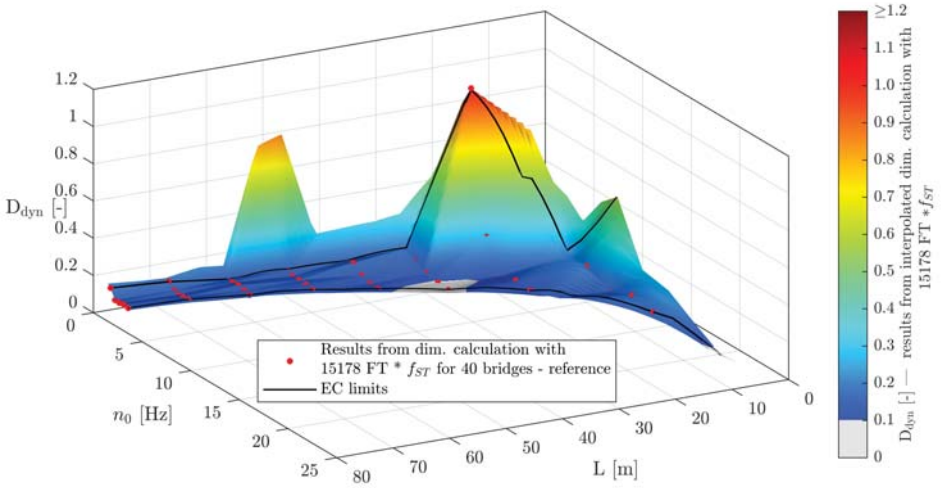

Figure 5.96.: Single-span bridges — dimensional calculation D_{dyn} — 15178 real FT $*f_{ST}$ calculated for 40 reference bridges and interpolated for all other structures — ζ_{EC} — Rayleigh like damping — design life train mass = 17294.9 * $f_{TM2-st,100years}$ [10^3 t] — 3D view

Subsequently, the results of Figure 5.96 were multiplied by the factor f_{ST} = 1.0115, in order to account for the traffic volume of special trains (SP) and added up with the results of the passenger trains (PT) according to Figure 5.95. This finally leads to the D_{dyn} result for the entire traffic mix TM2-st of 100 years with an annual traffic volume of 24.95 10^6 t — see Figure 5.97.

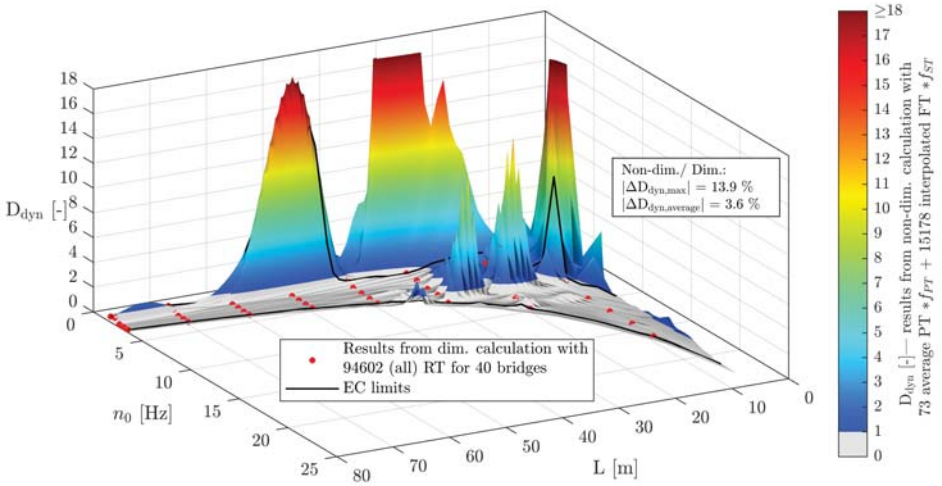

Figure 5.97.: Single-span bridges — non-dimensional vs. dimensional calculation D_{dyn} — traffic mix TM2-st — ζ_{EC} — Rayleigh like damping — design life train mass = 56029.1 * $f_{TM2-st,100years}$ [10^3 t] — 3D view

Figure 5.98 is the top view representation of Figure 5.97. In comparison to the traffic mix TM1* of the previous Chapter 5.4.1 the damage D_{dyn} is reduced severely. Hence, the real traffic mix TM2-st, due to measured data, causes less damage than the eight trains of the EC mix.

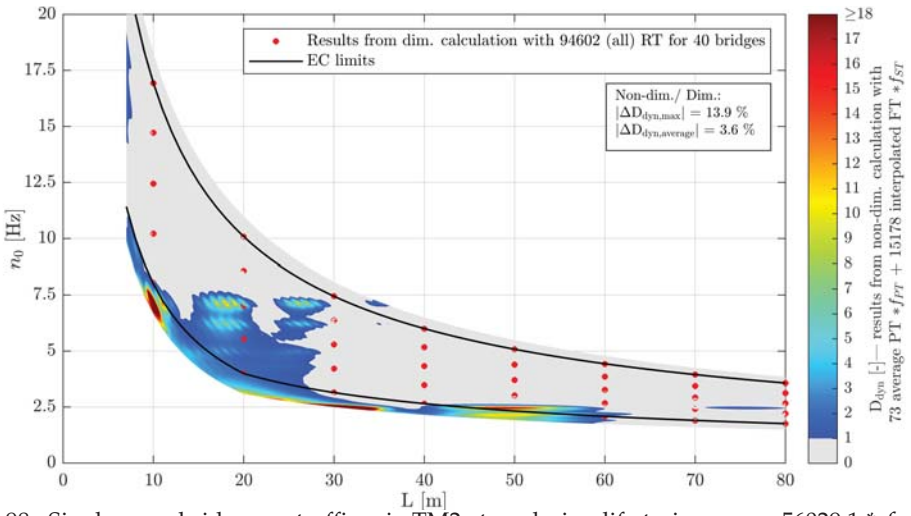

Figure 5.98.: Single-span bridges — traffic mix TM2-st — design life train mass = 56029.1 * $f_{TM2-st,100years}$ [10^3 t] — ζ_{EC} — Rayleigh like damping — no load distribution — top view D_{dyn} & $|a_{HSLM-A,max}|$

Again, applying Equation (5.27) in combination with Figures 5.67 and 5.98 results into the dynamic equivalent constant amplitude stress range $\Delta\sigma_{E,2,dyn}$ for single-span steel bridges (SSB) — see Figure 5.99. Additionally, the TS criteria for new/ existing SSB is plotted as well, which allows again to perform a combined interpretation. Both, new and existing SSB structures, do not have a FLS problem, regarding the traffic mix TM2-st and the damping variant ζ_{EC}, if fulfilling the TS criteria.

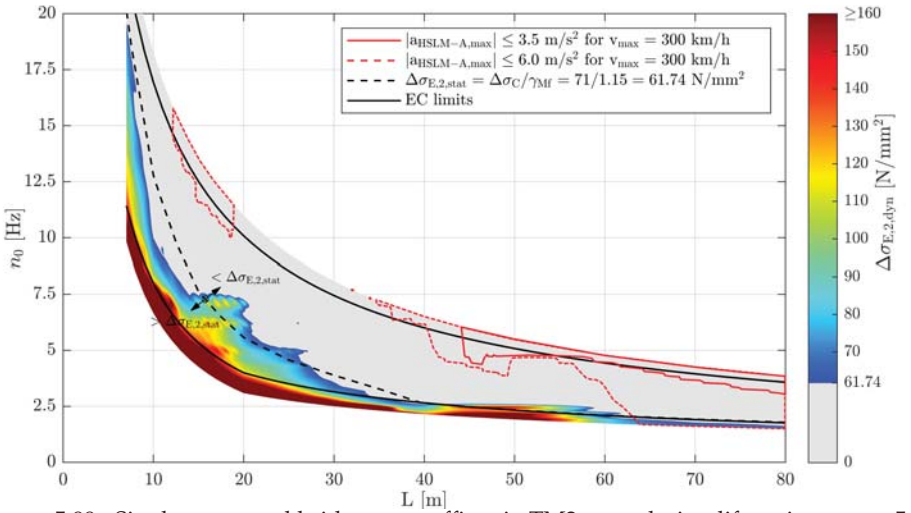

Figure 5.99.: Single-span steel bridges — traffic mix TM2-st — design life train mass = 56029.1 * $f_{TM2-st,100years}$ [10^3 t] — ζ_{EC} — Rayleigh like damping — no load distribution — top view $\Delta\sigma_{E,2,dyn}$ & $|a_{HSLM-A,max}|$ & $\Delta\sigma_{E,2,stat}$

The same is true for single-span composite bridges (SCB), except for existing structures with a span length L = 16 m and a first bending frequency $n_0 = 7.25$ Hz and for existing structures with spans lengths L = 51-58 m and a first bending frequency n_0 close to the lower EC limit — see Figure 5.100.

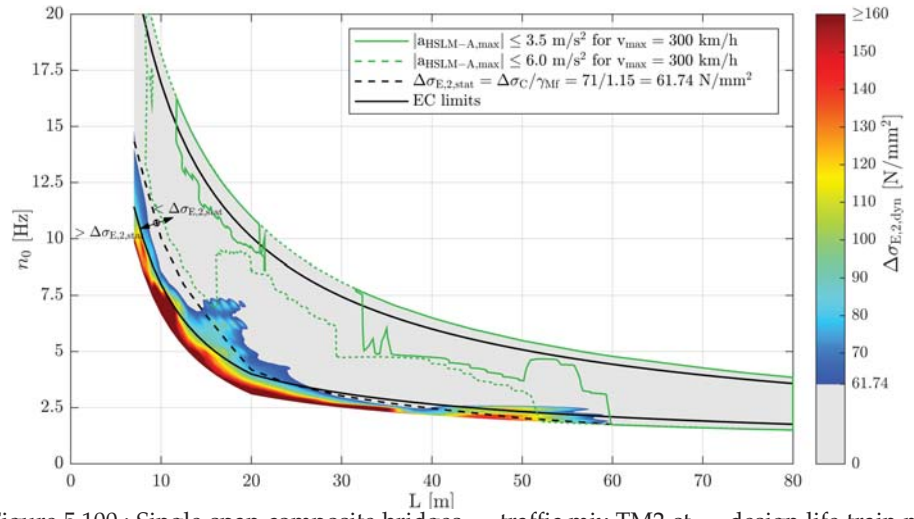

Figure 5.100.: Single-span composite bridges — traffic mix TM2-st — design life train mass = 56029.1 * $f_{TM2-st,100years}$ [10^3 t] — ζ_{EC} — Rayleigh like damping — no load distribution — top view $\Delta\sigma_{E,2,dyn}$ & $|a_{HSLM-A,max}|$ & $\Delta\sigma_{E,2,stat}$

Repeating the before described procedure of TM2-st with the damping variant ζ_{V1}, leads to the Figures 5.101 to 5.103. In general, the conclusions made for the damping variant ζ_{EC} apply here as well, as the resulting damage D_{dyn} is reduced while the areas of the TS criteria are extended due to the increased damping ratios ζ_{V1}. Consequently, only existing SCB with a span length L = 16 m and a first bending frequency $n_0 = 7.25$ Hz and with spans lengths L = 42-56 m and a first bending frequency n_0 close to the lower EC limit do not fulfill the FLS criteria, while complying with the TS criteria — see Figure 5.103.

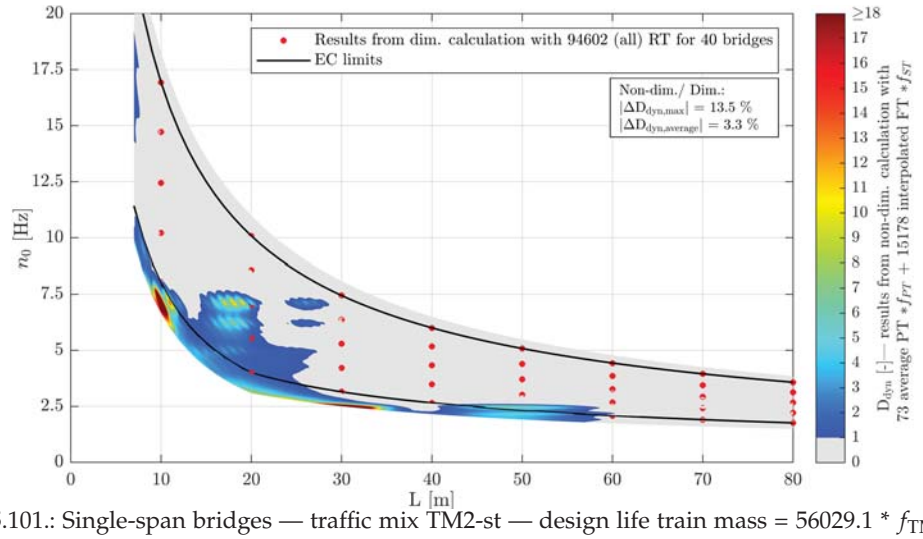

Figure 5.101.: Single-span bridges — traffic mix TM2-st — design life train mass = 56029.1 * $f_{TM2-st,100years}$ [10^3 t] — ζ_{V1} — Rayleigh like damping — no load distribution — top view D_{dyn} & $|a_{HSLM-A,max}|$

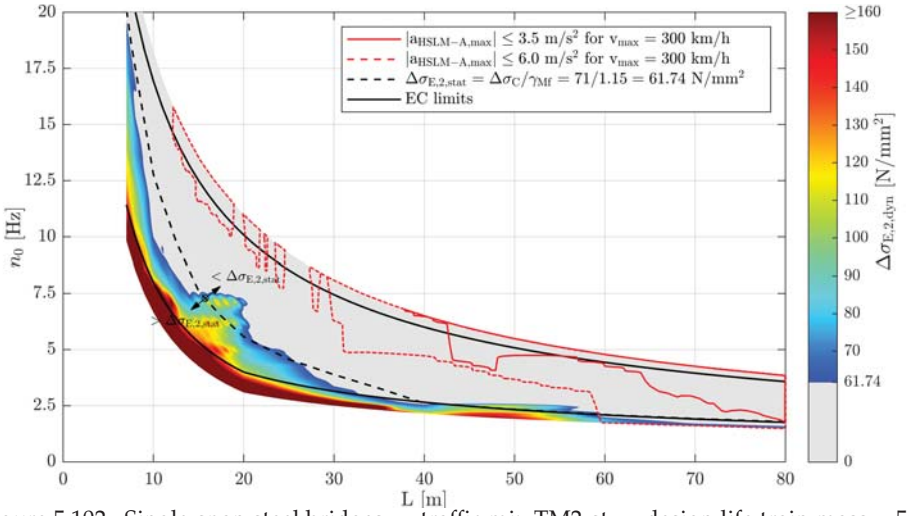

Figure 5.102.: Single-span steel bridges — traffic mix TM2-st — design life train mass = 56029.1 * $f_{TM2-st,100years}$ [10^3 t] — ζ_{V1} — Rayleigh like damping — no load distribution — top view $\Delta\sigma_{E,2,dyn}$ & $|a_{HSLM-A,max}|$ & $\Delta\sigma_{E,2,stat}$

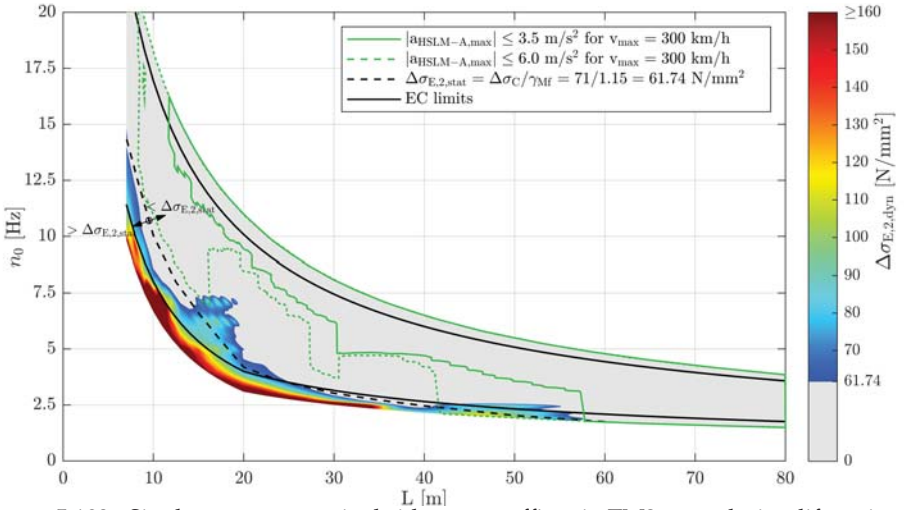

Figure 5.103.: Single-span composite bridges — traffic mix TM2-st — design life train mass = 56029.1 * $f_{TM2-st,100years}$ [10^3 t] — ζ_{V1} — Rayleigh like damping — no load distribution — top view $\Delta\sigma_{E,2,dyn}$ & $|a_{HSLM-A,max}|$ & $\Delta\sigma_{E,2,stat}$

5.4.3. Traffic mix 3

Subsequently, the results for traffic mix TM3-st according to Chapters 4.4 and 5.1.4 are presented. Traffic mix TM3-st considers, in contrast to traffic mix TM2-st of the previous chapter, only passenger trains (PT) and neglects freight trains (FT) and special trains (ST). Consequently, the results of TM2-st for all PT — see Figure 5.94 — are multiplied by the factor f_{RT} = 1.7302 — according to Equation (5.12) — in order to account for an annual traffic volume of 24.95 10^6 over the design life of 100 years.
In Figures 5.104 to 5.106 one finds the results for the damping variant ζ_{EC} according to ÖNORM EN 1991-2 [43]. In comparison to the traffic mix TM2-st, the damage D_{dyn} increases at its peak

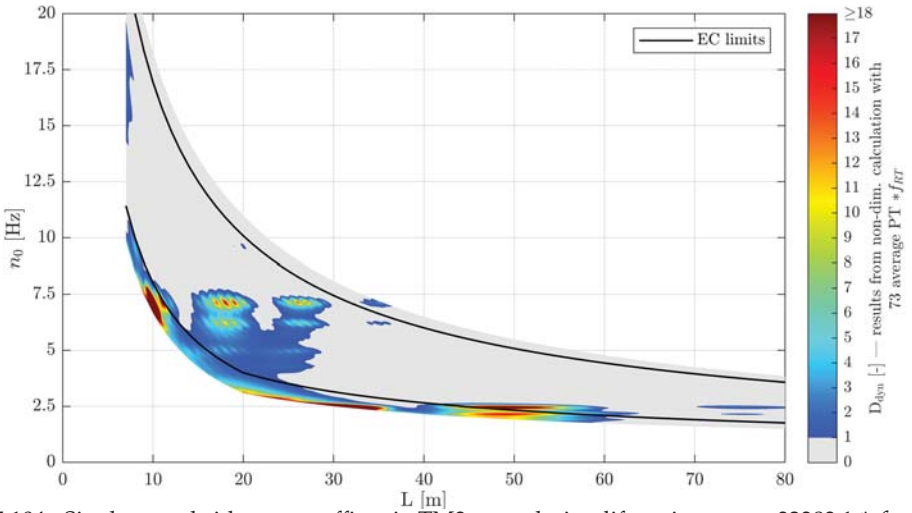

Figure 5.104.: Single-span bridges — traffic mix TM3-st — design life train mass = 32383.1 * $f_{TM3-st,100years}$ [10^3 t] — ζ_{EC} — Rayleigh like damping — no load distribution — top view D_{dyn} & $|a_{HSLM-A,max}|$

values — see Figures 5.104 and 5.98. This is due to the fact that PT, which cause resonance, are considered in TM3-st more than in TM2-st.

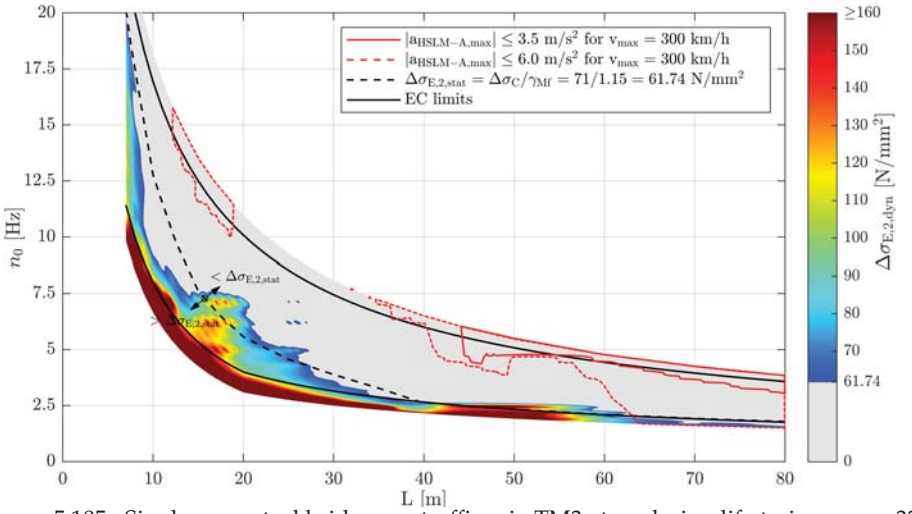

Figure 5.105.: Single-span steel bridges — traffic mix TM3-st — design life train mass = 32383.1 * $f_{TM3-st,100years}$ [10^3 t] — ζ_{EC} — Rayleigh like damping — no load distribution — top view $\Delta\sigma_{E,2,dyn}$ & $|a_{HSLM-A,max}|$ & $\Delta\sigma_{E,2,stat}$

Consequently, the dynamic equivalent constant amplitude stress range $\Delta\sigma_{E,2,dyn}$ for singel-span steel bridges (SSB) is increased as well but in context with the TS criteria, no structure in a high-speed line is affected by the FLS criteria — see Figure 5.105. The same is applicable for single-span composite bridges (SCB), except for existing structures with a span length L = 16 m and a first bending frequency $n_0 = 7.25$ Hz and for existing structures with spans lengths L = 51-58 m and a first bending frequency n_0 close to the lower EC limit — see Figures 5.100 and 5.106.

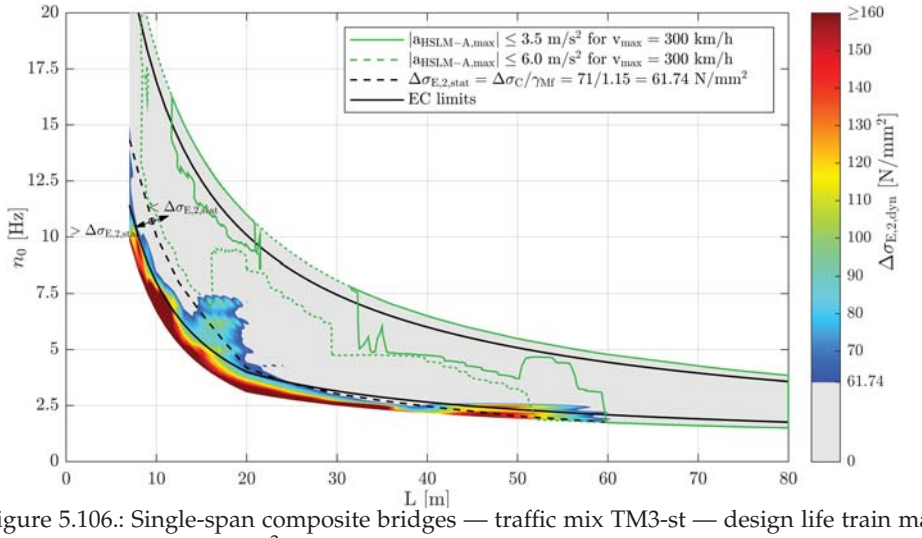

Figure 5.106.: Single-span composite bridges — traffic mix TM3-st — design life train mass = 32383.1 * $f_{TM3-st,100years}$ [10^3 t] — ζ_{EC} — Rayleigh like damping — no load distribution — top view $\Delta\sigma_{E,2,dyn}$ & $|a_{HSLM-A,max}|$ & $\Delta\sigma_{E,2,stat}$

Again, increasing the damping ratio to ζ_{V1} basically does not change the essence of the conclusion. In Figure 5.107 the damage D_{dyn} results are presented, which are diminished in comparison to Figure 5.104.

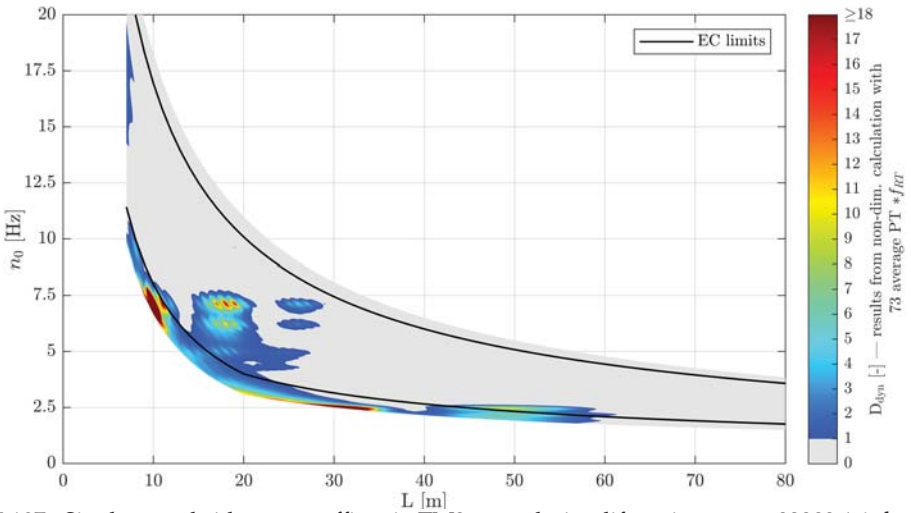

Figure 5.107.: Single-span bridges — traffic mix TM3-st — design life train mass = 32383.1 * $f_{TM3-st,100years}$ [10^3 t] — ζ_{V1} — Rayleigh like damping — no load distribution — top view D_{dyn} & $|a_{HSLM-A,max}|$

Figure 5.108 shows the dynamic equivalent constant amplitude stress ranges $\Delta\sigma_{E,2,dyn}$ in combination with the TS criteria for SSB. In general, all SSB fulfilling the TS criteria, do not have a FLS problem either, except existing SSB with span lengths L = 59-60 m and a first bending frequency n_0 close to the lower EC limit.

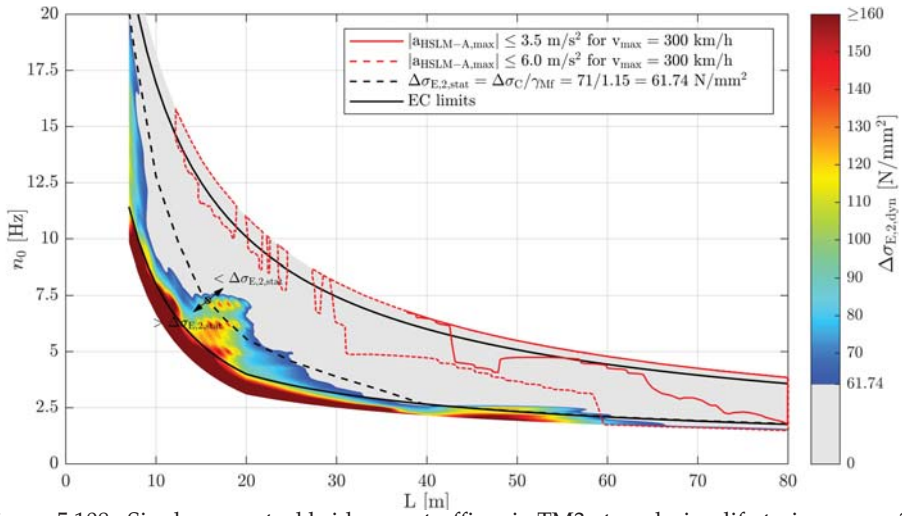

Figure 5.108.: Single-span steel bridges — traffic mix TM3-st — design life train mass = 32383.1 * $f_{TM3-st,100years}$ [10^3 t] — ζ_{V1} — Rayleigh like damping — no load distribution — top view $\Delta\sigma_{E,2,dyn}$ & $|a_{HSLM-A,max}|$ & $\Delta\sigma_{E,2,stat}$

Regarding SCB and the damping variant ζ_{V1} the same is true as for the damping variant ζ_{EC}, except that the length span of existing structures with a first bending frequency n_0 close to the lower EC limit, which fulfil the TS criteria but not the FLS criteria, changes from L = 51-58 m to L = 42-56 m — compare Figures 5.109 and 5.107.

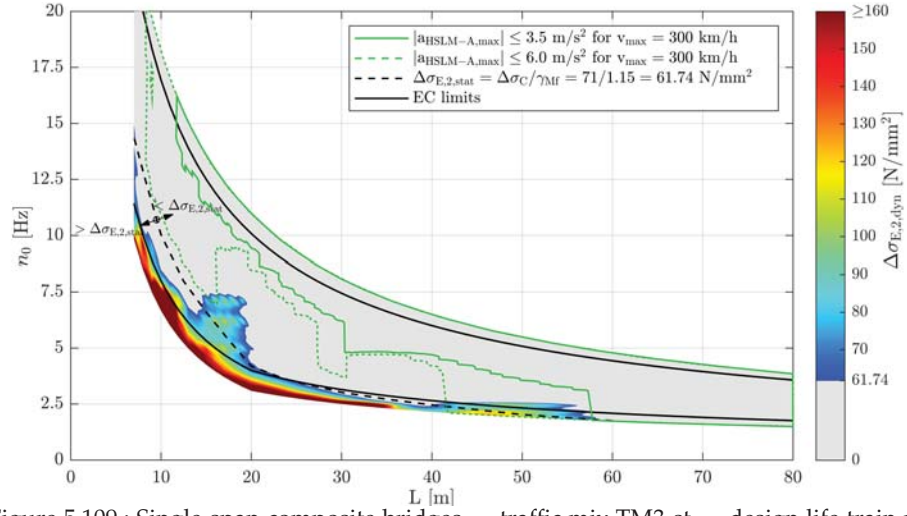

Figure 5.109.: Single-span composite bridges — traffic mix TM3-st — design life train mass = 32383.1 * $f_{TM3-st,100years}$ [10^3 t] — ζ_{V1} — Rayleigh like damping — no load distribution — top view $\Delta\sigma_{E,2,dyn}$ & $|a_{HSLM-A,max}|$ & $\Delta\sigma_{E,2,stat}$

5.4.4. Traffic mix 4

Subsequently, the results regarding traffic mix TM4, which represents a pure high-speed traffic mix for Austria, is presented. It consists of six partly common, partly new in Austria introduced, high speed trains, which are described in Chapter 4.3. As for traffic mix 1, three different speed variants — v_{train}, $v_{D_{max}}$ and $v_{a_{max}}$ — are considered and discussed as follows.

Traffic mix TM4* — train speed v_{train}

In this chapter, the maximum vehicle speed v_{train} of each high-speed train is used for the dynamic calculation — see Table 4.12. Figure 5.110 shows the overall damage D_{dyn} results due to the traffic mix TM4* for the entire design life of 100 years, considering the damping variant ζ_{EC}. In contrast to the results of the traffic mixes TM1*, TM2-st and TM3-st — see Figures 5.50, 5.97 and 5.104 — the peak damage values D_{dyn} of TM4* are very pronounced and well defined.

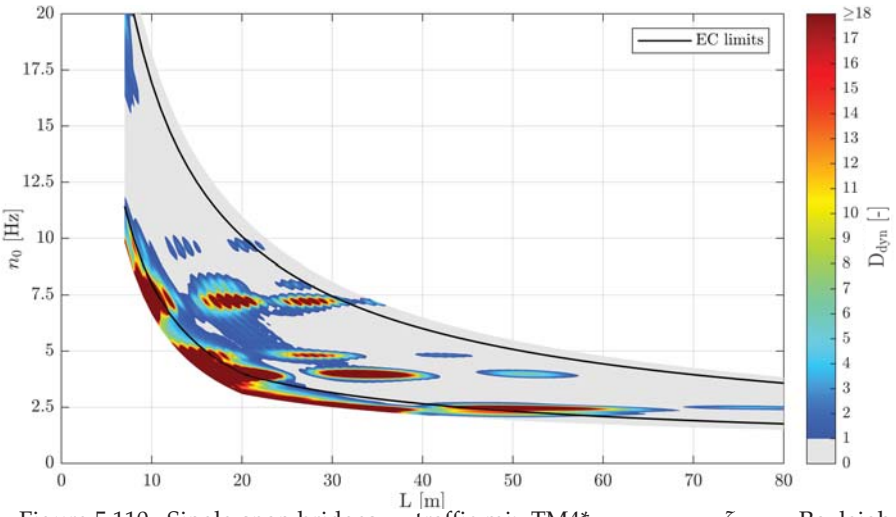

Figure 5.110.: Single-span bridges — traffic mix TM4* — v_{Train} — ζ_{EC} — Rayleigh like damping — no load distribution — top view D_{dyn}

As these six high-speed trains have very regular train car lengths L_D, each of these trains causes with the maximum train speed v_{train} resonance effects for particular structures, as illustrated in Figure 5.111. For example, the train ICE4-K3-12cars got a car length $L_D = 28.9$ m, which causes with the train speed of 250 km/h an excitation frequency $n_{L_D} = 2.40$ Hz. As illustrated in Figure 5.111(e), peaks occur at about 2.5 Hz, 5.0 Hz and 7.5 Hz representing structures, which are excited at each, at each second and each third oscillation cycle. Similar reflections lead to the peaks due to the other trains.

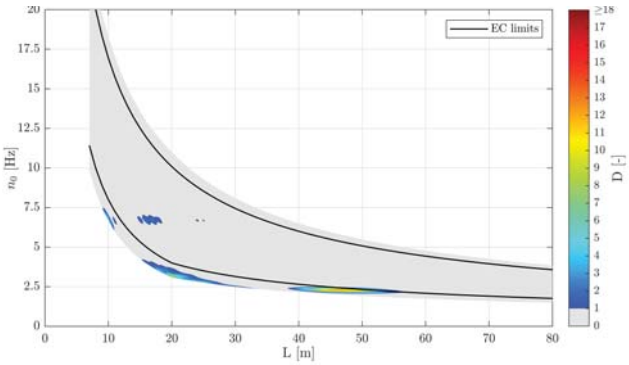

(a) DOSTO (Westbahn) — v_{train}=200 km/h — traffic vol. 4.55 10^6 t/year

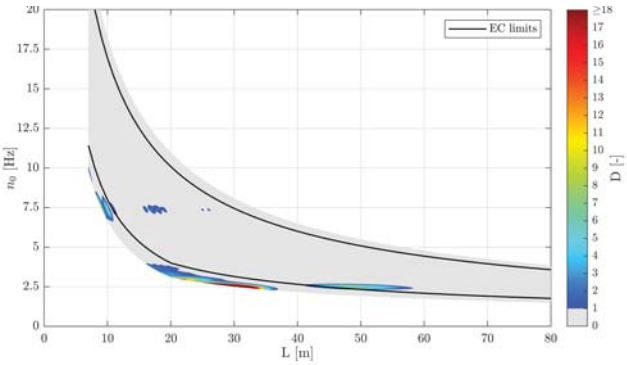

(b) TypeC14 (ICE-T1 411) — v_{train}=230 km/h — traffic vol. 2.51 10^6 t/year

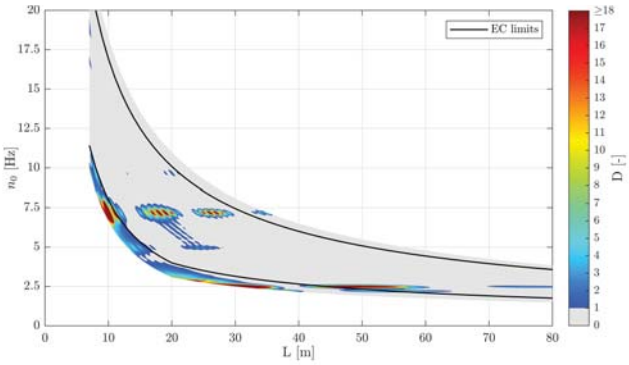

(c) TypeC19 Taurus-front (Railjet) — v_{train}=230 km/h — traffic vol. 9.38 10^6 t/year

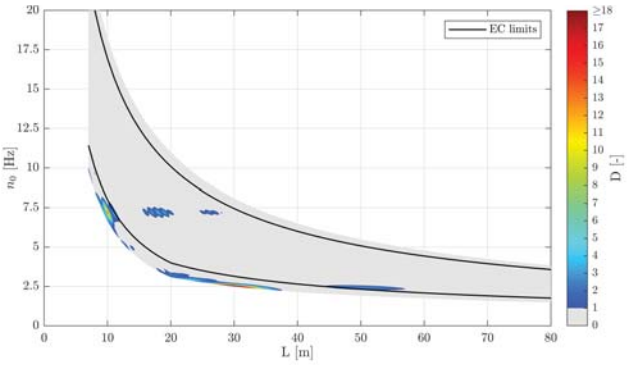

(d) TypeC19* Taurus-front (Railjet) — v_{train}=230 km/h — traffic vol. 2.15 10^6 t/year

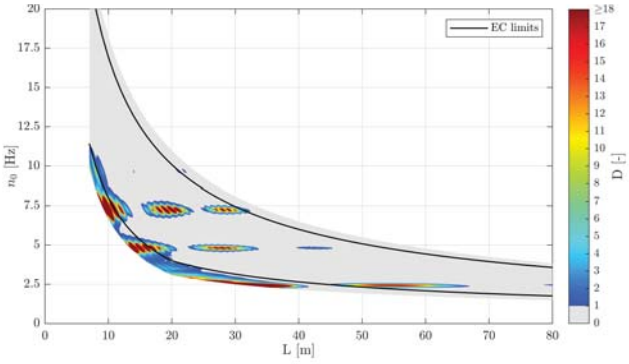

(e) ICE4-K3-12cars — v_{train}=250 km/h — traffic vol. 3.18 10^6 t/year

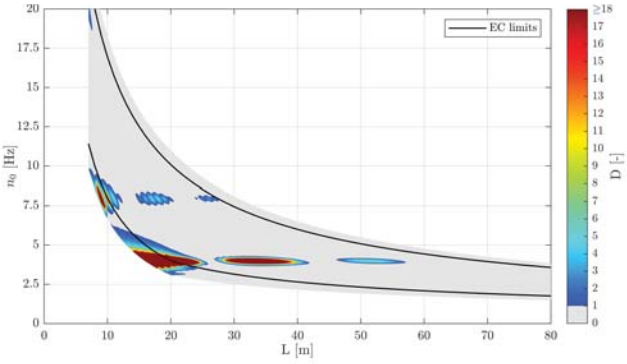

(f) EC250-Brutto18 — v_{train}=250 km/h — traffic vol. 3.18 10^6 t/year

Figure 5.111.: Single-span bridges — trains of traffic mix TM4* — v_{train} — ζ_{EC} — Rayleigh like damping — no load distribution — top view D_{dyn}

Calculating again the dynamic equivalent constant amplitude stress range $\Delta\sigma_{E,2,dyn}$ for single-span steel bridges (SSB) leads to Figure 5.112 for the traffic mix TM4*. Consequently, new SSB, which comply with the TS citeria — $|a_{HSLM-A,max}| \leq 3.5$ m/s^2 — do not have a FLS problem. Regarding existing SSB, the majority, which fulfills the TS criteria — $|a_{HSLM-A,max}| \leq 6.0$ m/s^2 — does not have a FLS problem either, except very long structures of L = 62-65 m with a first bending frequency n_0 close to the lower EC limit.

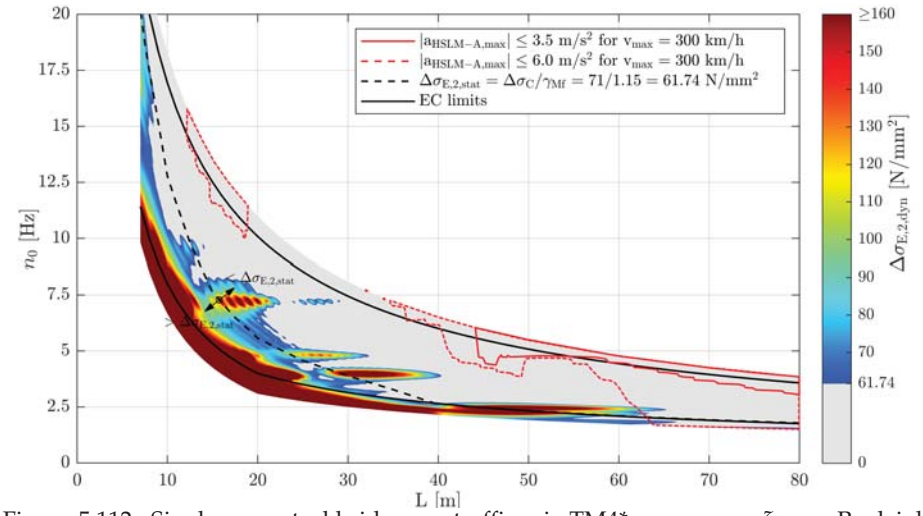

Figure 5.112.: Single-span steel bridges — traffic mix TM4* — v_{Train} — ζ_{EC} — Rayleigh like damping — no load distribution — top view $\Delta\sigma_{E,2,dyn}$ & $|a_{HSLM-A,max}|$ & $\Delta\sigma_{E,2,stat}$

New single-span composite bridges (SCB), fulfilling the TS criteria do not have a FLS problem either, except SCB with spans of L = 60-63 m and a first bending frequency n_0 close to the lower EC limit. On the other hand, existing SCB complying with the TS criteria, do fail in the FLS check for span lengths L = 16 m and $n_0 = 7.5$ Hz, L = 30 m and $n_0 = 5.0$ Hz and additionally L = 51-62 m and n_0 close to the lower EC limit.

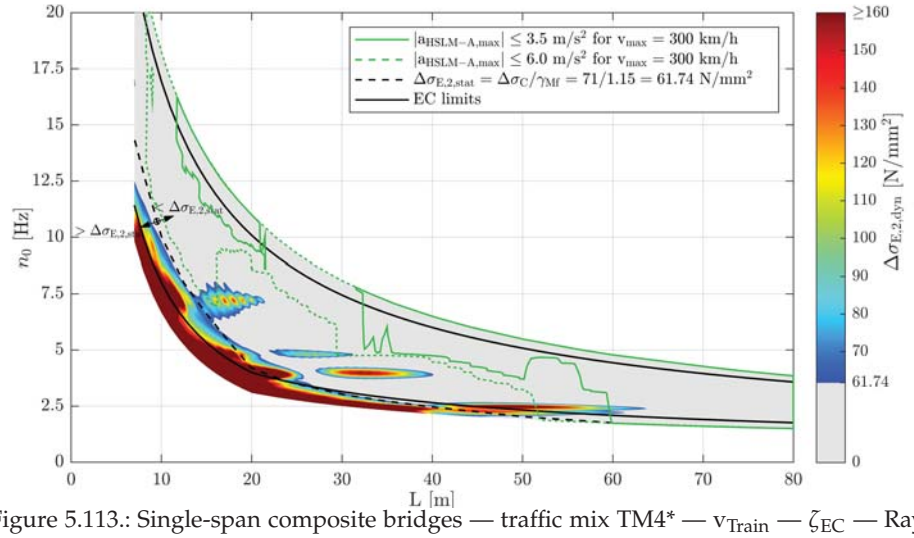

Figure 5.113.: Single-span composite bridges — traffic mix TM4* — v_{Train} — ζ_{EC} — Rayleigh like damping — no load distribution — top view $\Delta\sigma_{E,2,dyn}$ & $|a_{HSLM-A,max}|$ & $\Delta\sigma_{E,2,stat}$

Figures 5.114 to 5.116 show the outcome for the increased damping variant ζ_{V1} regarding the traffic mix TM4*. Although, the damage peaks are still present in Figure 5.114, it was clearly possible to reduced the damage D_{dyn} in comparison to the damping variant ζ_{EC} in Figure 5.110.

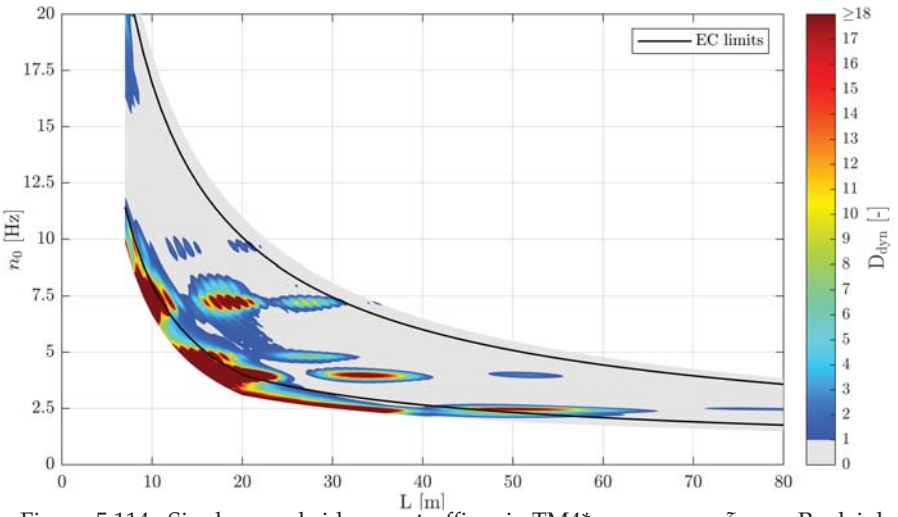

Figure 5.114.: Single-span bridges — traffic mix TM4* — v_{Train} — ζ_{V1} — Rayleigh like damping — no load distribution — top view D_{dyn}

Consequently, the dynamic equivalent constant amplitude stress range $\Delta\sigma_{E,2,dyn}$ for SSB is reduced as well, while the TS areas increase significantly — see Figure 5.115. However, new SSB, which fulfill the TS criteria, are not affected by the FLS criteria. Only very long existing SSB (L = 59-62 m), with first bending frequencies n_0 close to the lower EC limit, meet the TS, but not the FLS criteria.

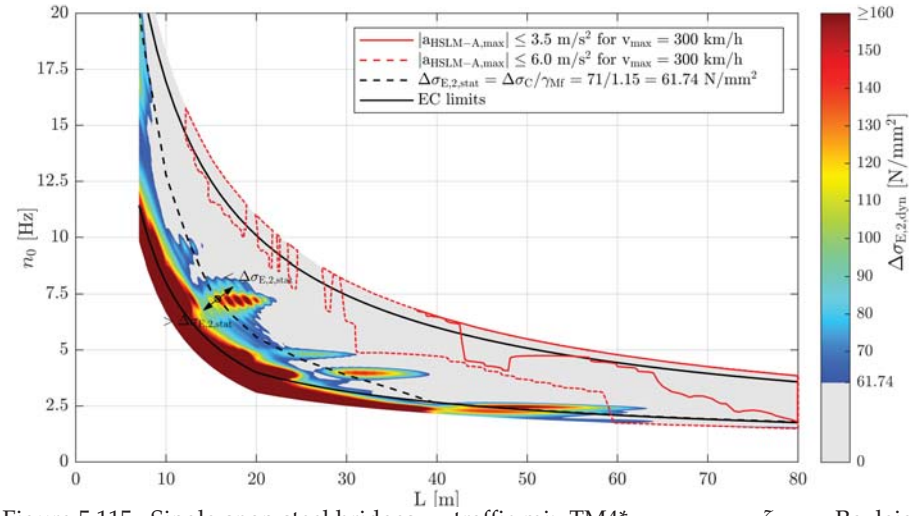

Figure 5.115.: Single-span steel bridges — traffic mix TM4* — v_{Train} — ζ_{V1} — Rayleigh like damping — no load distribution — top view $\Delta\sigma_{E,2,dyn}$ & $|a_{HSLM-A,max}|$ & $\Delta\sigma_{E,2,stat}$

On the other hand, increasing the damping ratios to ζ_{V1} has a negative effect on existing SCB. While more SCB, with first bending frequencies n_0 close to the lower EC limit, do not fulfil the FLS, but the TS criteria (L = 42-60 m), also structures of spans L = 27-30 m and with first

bending frequencies $n_0 = 5 - 4$ Hz are applicable for high-speed lines, but have a FLS problem. For new structures and furthermore existing structures with span lengths L = 16 m and $n_0 =$ 7.5 Hz the situation is unchanged to the damping variant ζ_{EC} — compare Figures 5.113 and 5.116.

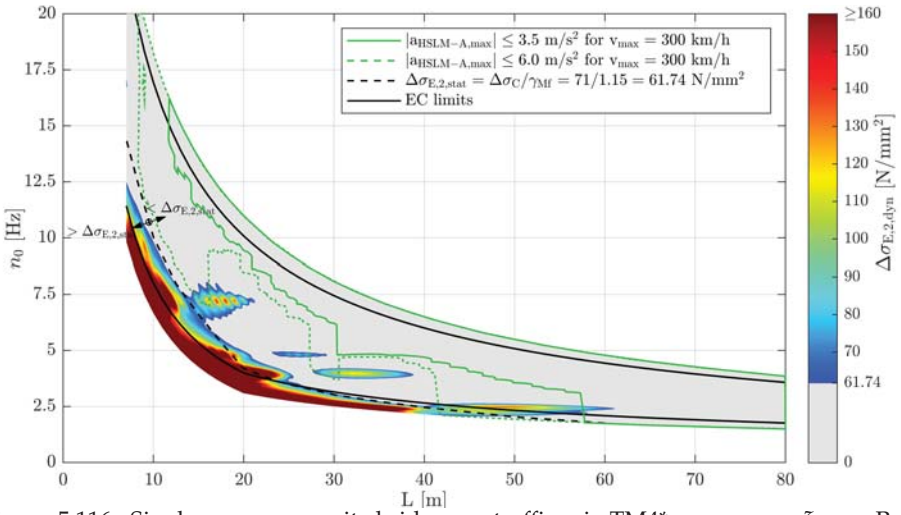

Figure 5.116.: Single-span composite bridges — traffic mix TM4* — v_{Train} — ζ_{V1} — Rayleigh like damping — no load distribution — top view $\Delta\sigma_{E,2,dyn}$ & $|a_{HSLM-A,max}|$ & $\Delta\sigma_{E,2,stat}$

Train speed $v_{D_{max}}$

Subsequently, the traffic mix variant TM4**, which uses the speeds $v_{D_{max}}$ leading to the maximum possible damage D_{dyn}, within the speed ranges of each high-speed train, is covered. Figure 5.117 illustrates the results for traffic mix TM4**, considering the damping variant ζ_{EC}. In comparison to the $v_{D_{max}}$ variant of traffic mix 1, hence TM1** — see Figure 5.79 — the results $D_{dyn} > 1$ in Figure 5.117 do not cover the whole area of investigated structures. However, the resonance effects, as only high-speed trains are considered in TM4**, are more severe.

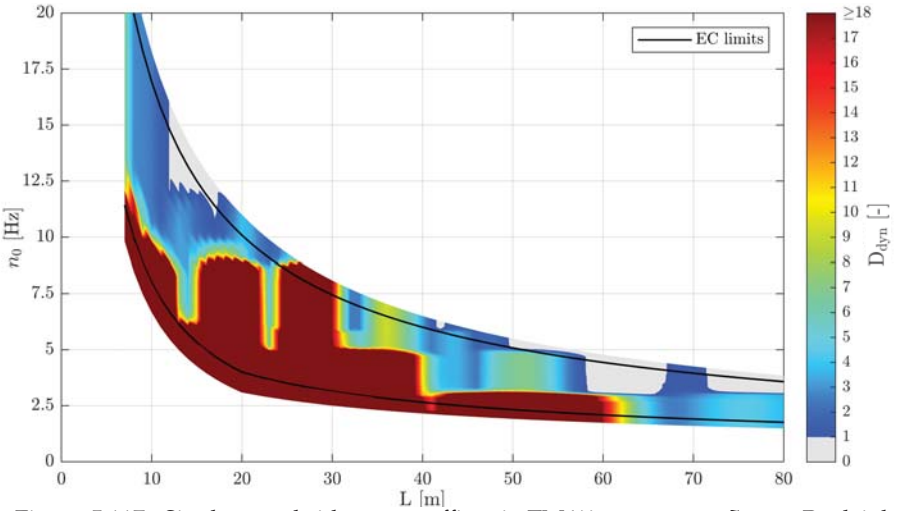

Figure 5.117.: Single-span bridges — traffic mix TM4** — $v_{D_{max}}$ — ζ_{EC} — Rayleigh like damping — no load distribution — top view D_{dyn}

However, considering the dynamic equivalent constant amplitude stess ranges $\Delta\sigma_{E,2,dyn}$ and the TS criteria for SSB, as illustrated in Figure 5.118, shows that new SSB, which fulfill the TS criteria, do not have a FLS problem. Furthermore, existing SSB only do have a FLS problem, while complying with the TS criteria, if their first bending frequency n_0 is close to the lower EC limit and if the span length L exceeds 61 m.

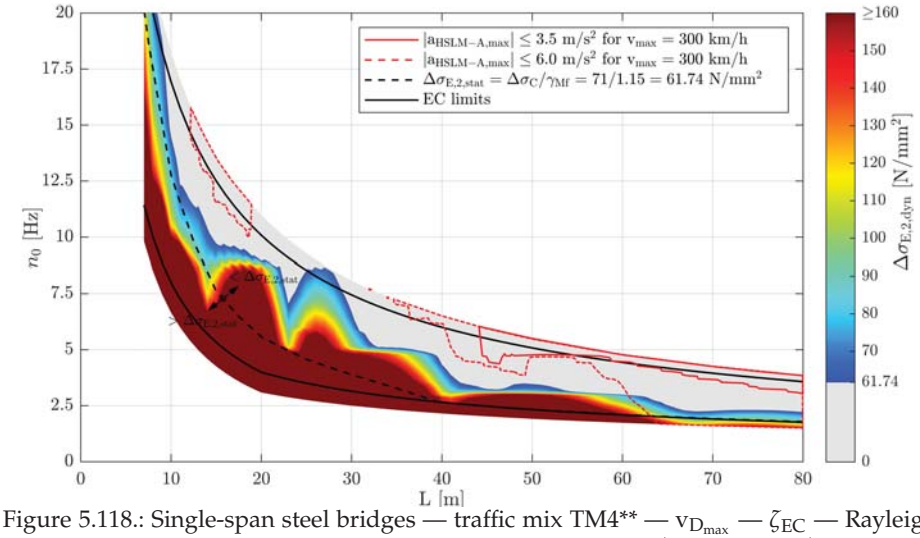

Figure 5.118.: Single-span steel bridges — traffic mix TM4** — $v_{D_{max}}$ — ζ_{EC} — Rayleigh like damping — no load distribution — top view $\Delta\sigma_{E,2,dyn}$ & $|a_{HSLM-A,max}|$ & $\Delta\sigma_{E,2,stat}$

New SCB with a span length L = 32-39 m and a first bending frequency $n_0 = 5.0$ Hz do fulfill the TS criterion and slightly harm the FLS criterion — see Figure 5.119. Furthermore, new SCB with span lengths L > 60 m and a first bending frequency close to the lower EC limit violate the FLS criterion, but fulfill the TS criterion. Existing SCB throughout the whole span range fulfill the TS criterion but do not comply with the FLS criterion.

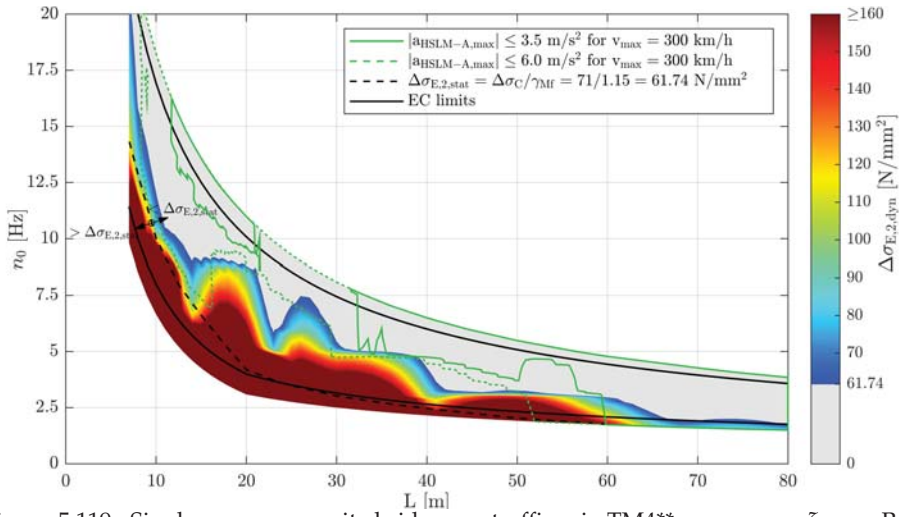

Figure 5.119.: Single-span composite bridges — traffic mix TM4** — $v_{D_{max}}$ — ζ_{EC} — Rayleigh like damping — no load distribution — top view $\Delta\sigma_{E,2,dyn}$ & $|a_{HSLM-A,max}|$ & $\Delta\sigma_{E,2,stat}$

Figures 5.120 to 5.122 show the results with the increased damping variant ζ_{V1}. Again, the damage D_{dyn} was reduced, while the peaks are still present — compare Figures 5.117 and 5.120.

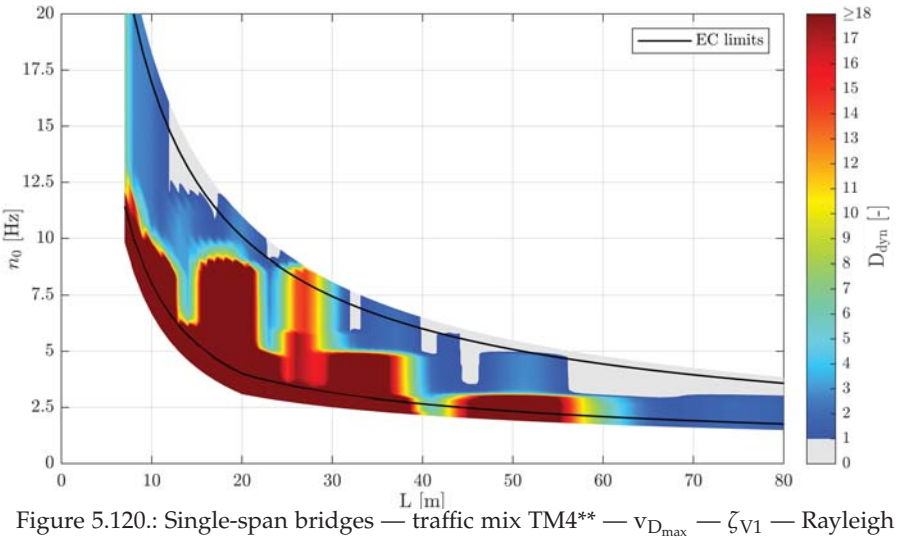

Figure 5.120.: Single-span bridges — traffic mix TM4** — $v_{D_{max}}$ — ζ_{V1} — Rayleigh like damping — no load distribution — top view D_{dyn}

The particular results for SSB in Figure 5.121 do not fundamentally change the conclusion made for the damping variant ζ_{EC} — see Figure 5.118 — as only spans with L = 79-80 m fulfill the TS criterion while violating the FLS criterion. However, regarding existing SSB the increase of the damping ratios to ζ_{V1} led to a worsening of the situation. Existing SSB with spans L = 31-39 m and a first bending frequency $n_0 = 5.0$ Hz do fulfill the TS criterion, but harm the FLS criterion. The same is true for structures with first bending frequencies n_0 close to the lower EC limit and spans L exceeding 59 m.

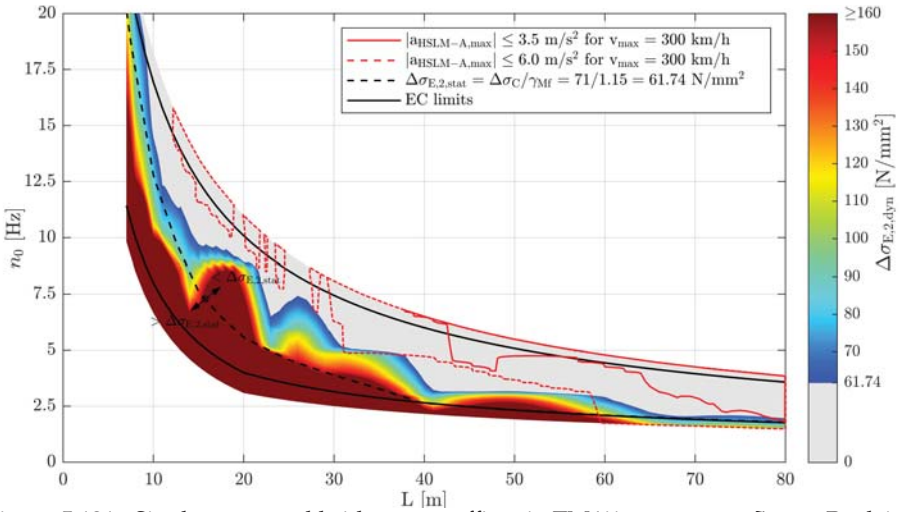

Figure 5.121.: Single-span steel bridges — traffic mix TM4** — $v_{D_{max}}$ — ζ_{V1} — Rayleigh like damping — no load distribution — top view $\Delta\sigma_{E,2,dyn}$ & $|a_{HSLM-A,max}|$ & $\Delta\sigma_{E,2,stat}$

For new SCB the situation got slightly worse, in comparison to the damping variant ζ_{V1}, as well — see Figures 5.119 and 5.122. Structures with spans L = 30-37 m and a first bending frequency $n_0 = 5.0$ Hz and spans with L > 58 m and a bending frquency n_0 close to the lower EC limit do fulfill the TS criterion, but harm the FLS criterion. For existing SCB the same conclusion as for

the damping variant ζ_{EC} is applicable, hence, SCE throughout the whole span range fulfill the TS criterion but do not comply with the FLS criterion.

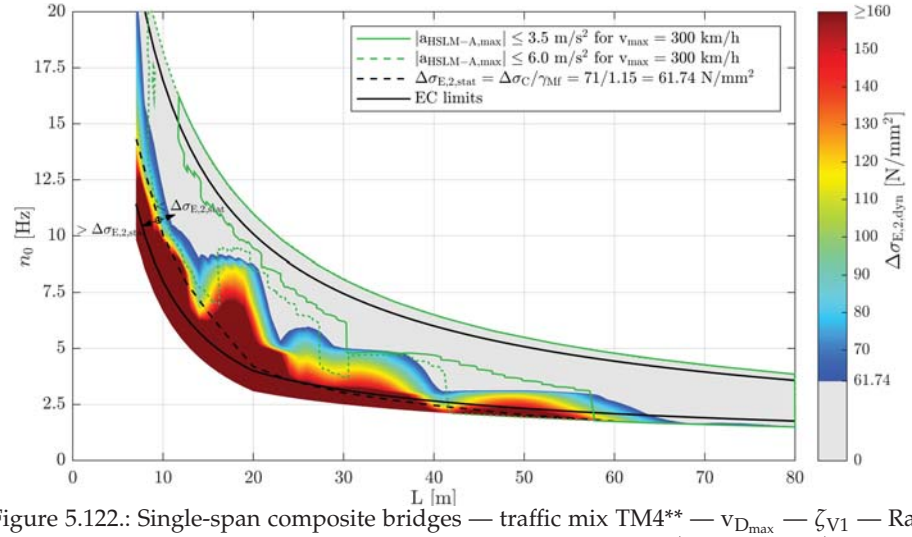

Figure 5.122.: Single-span composite bridges — traffic mix TM4** — $v_{D_{max}}$ — ζ_{V1} — Rayleigh like damping — no load distribution — top view $\Delta\sigma_{E,2,dyn}$ & $|a_{HSLM-A,max}|$ & $\Delta\sigma_{E,2,stat}$

Train speed $v_{a_{max}}$

The traffic mix TM4*** represents the variant, which uses the train speeds $v_{a_{max}}$, leading to the maximum vertical bridge deck acceleration $|a_{max}|$, for the damage D_{dyn} prediction. As already shown for traffic mix TM1***, the same applies here for traffic mix TM4***. Using the train speeds $v_{a_{max}}$, provides for the majority of the single-span structures, a good estimation to predict the maximum damage due to $v_{D_{max}}$ and hence traffic mix TM4** — compare Figures 5.117 and 5.123. This conclusion applies for all considered variations of damping ratios and load distribution within TM4*** and therefore, it is referred to the Appendices B and C.

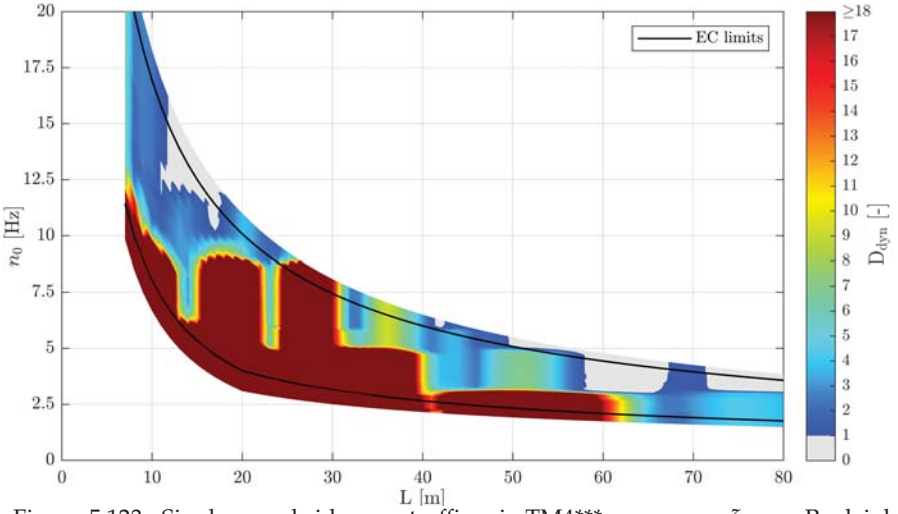

Figure 5.123.: Single-span bridges — traffic mix TM4*** — $v_{a_{max}}$ — ζ_{EC} — Rayleigh like damping — no load distribution — top view D_{dyn}

5.4.5. Traffic mix 5

Subsequently, the results of traffic mix 5, which is a combination of the first four high-speed trains of traffic mix 4 and the four freight trains of traffic mix 1 — see Chapter 4.4 — and consequently represents a mixed traffic mix.

Traffic mix TM5* — train speed v_{train}/ v_{EC}

First, the variant considering the maximum train speed v_{train}/ v_{EC} is presented. Figure 5.124 shows the results for the damping variant ζ_{EC}. In comparison to traffic mix TM4*, which represents a pure high-speed traffic mix, the damage $D_{dyn} > 1.0$ areas are less and the peaks are significantly lower — see Figure 5.110.

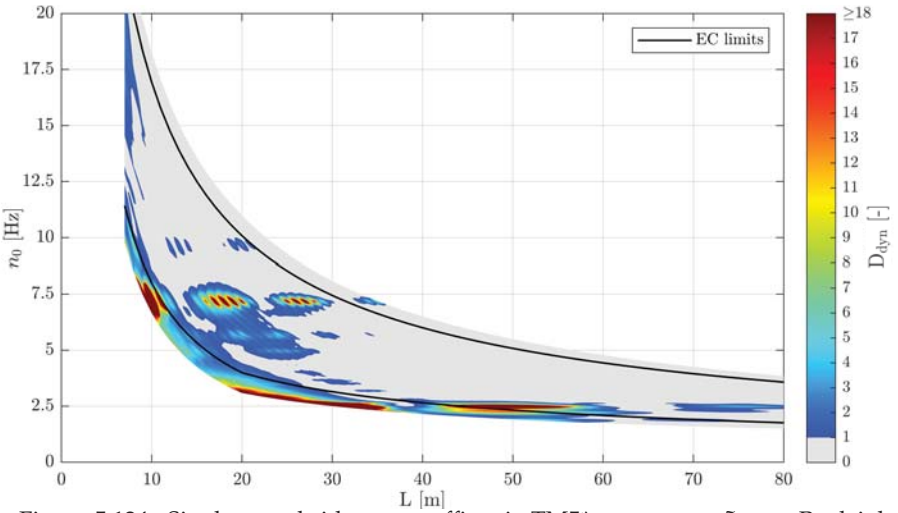

Figure 5.124.: Single-span bridges — traffic mix TM5* — v_{Train} — ζ_{EC} — Rayleigh like damping — no load distribution — top view D_{dyn}

Consequently, new and existing SSB, which fulfill the TS criterion do not have a FLS problem, except for existing structures with a span length L = 63 m and a first bending frequency $n_0 = 2.5$ Hz — see Figure 5.125.

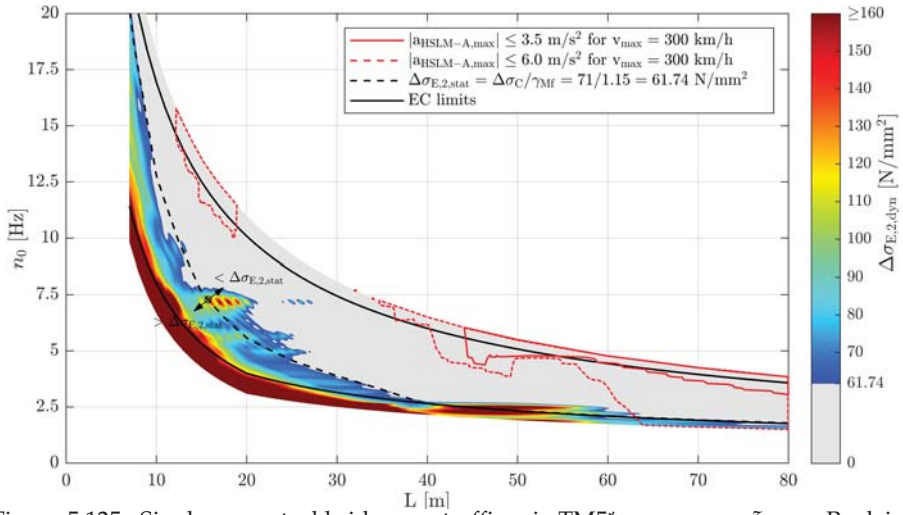

Figure 5.125.: Single-span steel bridges — traffic mix TM5* — v_{Train} — ζ_{EC} — Rayleigh like damping — no load distribution — top view $\Delta\sigma_{E,2,dyn}$ & $|a_{HSLM-A,max}|$ & $\Delta\sigma_{E,2,stat}$

Regarding new SCB structures, the stated above is true as well, except for structures with a span length L = 61 m and a first bending frequency $n_0 = 2.5$ Hz — see Figure 5.126. Existing structures, which do fulfill the TS, but not the FLS criterion, have a span length of L = 16 m and a first bending frequency $n_0 = 7.5$ Hz or span length L = 51-61 m and a first bending frequency n_0 close to the lower EC limit.

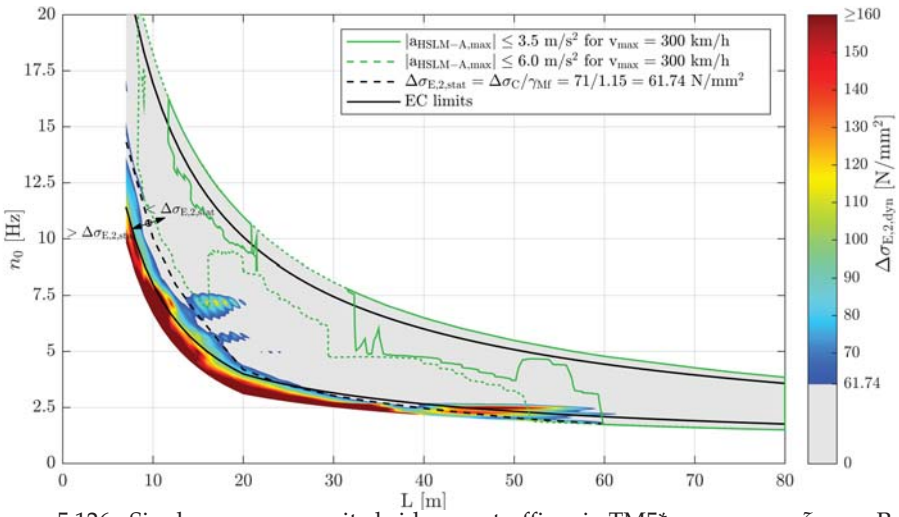

Figure 5.126.: Single-span composite bridges — traffic mix TM5* — v_{Train} — ζ_{EC} — Rayleigh like damping — no load distribution — top view $\Delta\sigma_{E,2,dyn}$ & $|a_{HSLM-A,max}|$ & $\Delta\sigma_{E,2,stat}$

Increasing the damping ratios to ζ_{V1} decreases, as already mentioned before, the produced damage D_{dyn} — see Figures **??** and 5.127.

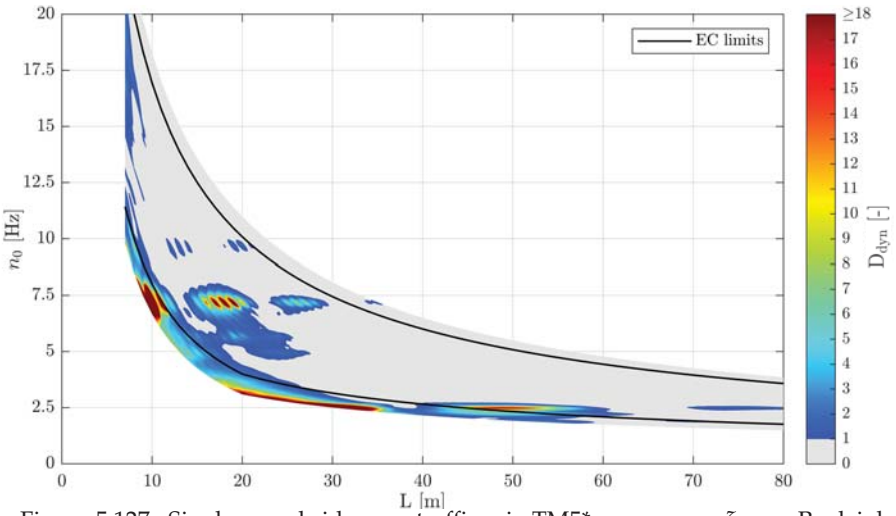

Figure 5.127.: Single-span bridges — traffic mix TM5* — v_{Train} — ζ_{V1} — Rayleigh like damping — no load distribution — top view D_{dyn}

Consequently, the areas of SSB, which are suitable for high speed traffic, increase as well, as shown in Figure 5.128. However, for new structures these do not interfere with the areas of $\Delta\sigma_{E,2,dyn} > 61.74$ N/mm^2. Furthermore, only existing structures of span lengths L = 59 m and a first bending frequency n_0 close to the lower EC limit comply with the TS, but not with the FLS criterion.

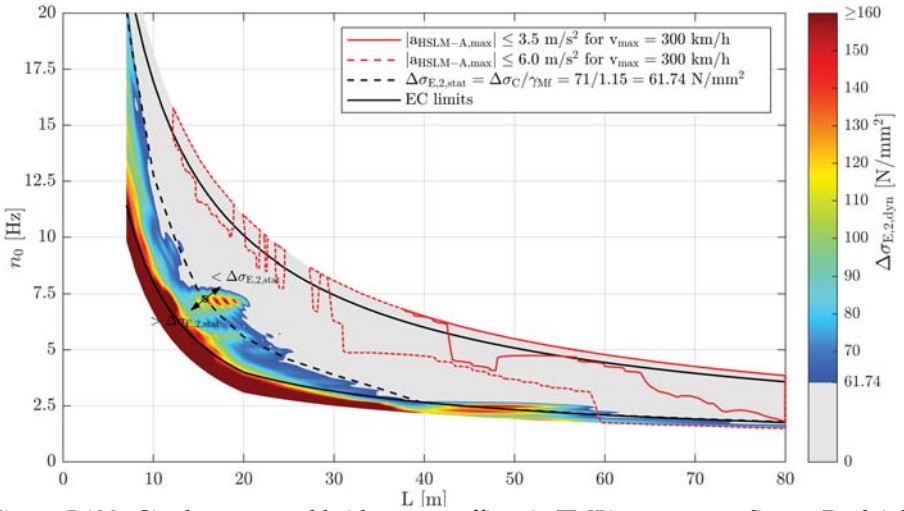

Figure 5.128.: Single-span steel bridges — traffic mix TM5* — v_{Train} — ζ_{V1} — Rayleigh like damping — no load distribution — top view $\Delta\sigma_{E,2,dyn}$ & $|a_{HSLM-A,max}|$ & $\Delta\sigma_{E,2,stat}$

New SCB, which do fulfil the TS criterion, do not have a FLS problem, if the damping variant ζ_{V1} is considered for TM5*. Existing SCB, however, do have a FLS problem, while complying with the TS criterion for span lengths L = 16 m and a fist bending frequency $n_0 = 7.5$ Hz and for span lenghts L = 42-58 m and bending frequencies n_0 close to the lower EC limit.

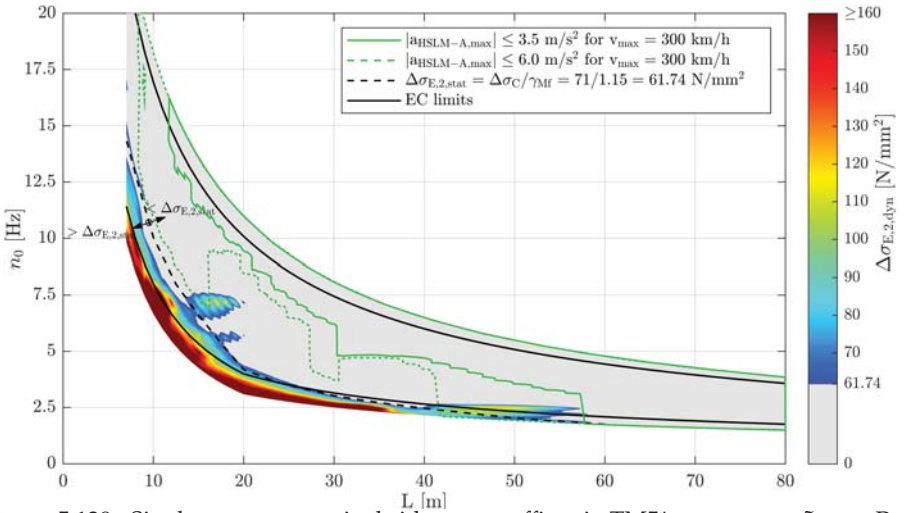

Figure 5.129.: Single-span composite bridges — traffic mix TM5* — v_{Train} — ζ_{V1} — Rayleigh like damping — no load distribution — top view $\Delta\sigma_{E,2,dyn}$ & $|a_{HSLM-A,max}|$ & $\Delta\sigma_{E,2,stat}$

Train speed $v_{D_{max}}$

Considering the train speed $v_{D_{max}}$, which leads to the maximum possible damage D_{dyn}, the results are illustrated for the damping variant ζ_{EC} in Figure 5.130. As the traffic mix versions using $v_{D_{max}}$ are mainly driven by the high-speed trains and their resonance scenarios, the here presented results are very similar to the ones of TM4** — see Figure 5.117.

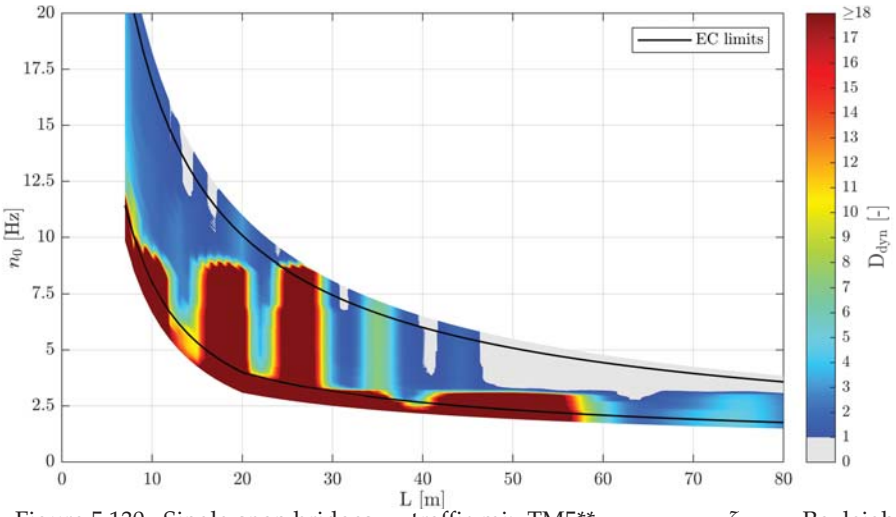

Figure 5.130.: Single-span bridges — traffic mix TM5** — $v_{D_{max}}$ — ζ_{EC} — Rayleigh like damping — no load distribution — top view D_{dyn}

Again, SSB which do fulfill the TS criteria, but still have a FLS problem are limited to existing structures with span lengths L beyond 61 m and a first bending frequency n_0 close to the lower EC limit — see Figure 5.131.

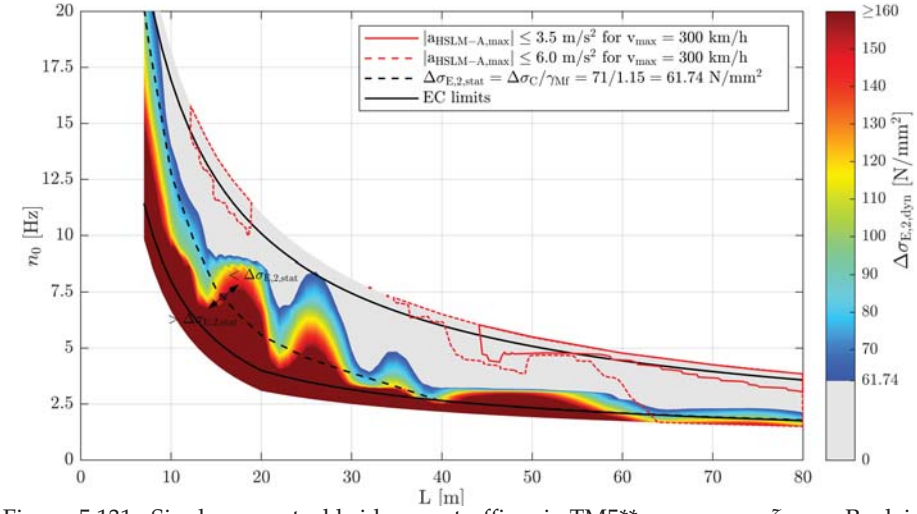

Figure 5.131.: Single-span steel bridges — traffic mix TM5** — $v_{D_{max}}$ — ζ_{EC} — Rayleigh like damping — no load distribution — top view $\Delta\sigma_{E,2,dyn}$ & $|a_{HSLM-A,max}|$ & $\Delta\sigma_{E,2,stat}$

However, unless new SCB do have span lengths L > 60 m and a first bending frequency n_0 close to the lower EC limit, they do not have a FLS problem, if fulfilling the TS criteria — see Figure 5.132. On the other hand, existing SCB with span lengths L = 9-16 m and first bending frequencies $n_0 = 7.4 - 15$ Hz and span lengths L = 51-63 m and first bending frequency n_0 close to the lower EC limit, do have a FLS problem, while complying with the TS criterion.

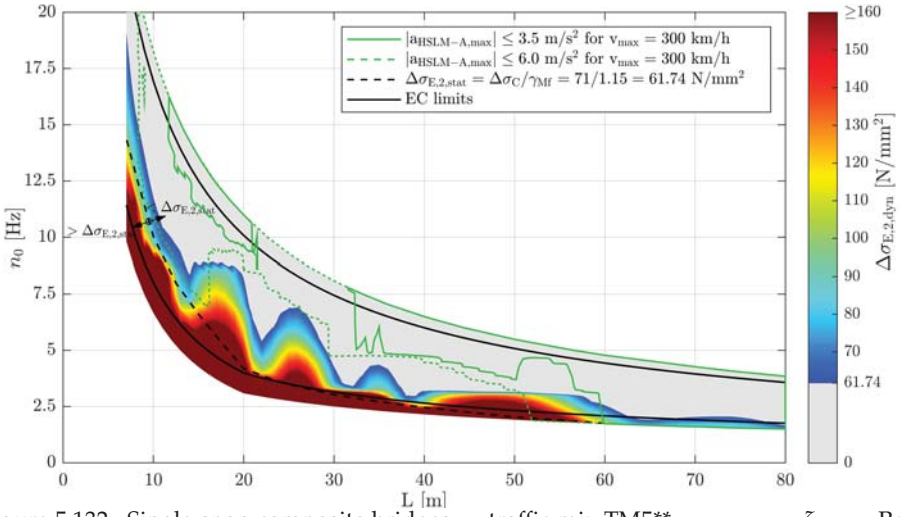

Figure 5.132.: Single-span composite bridges — traffic mix TM5** — $v_{D_{max}}$ — ζ_{EC} — Rayleigh like damping — no load distribution — top view $\Delta\sigma_{E,2,dyn}$ & $|a_{HSLM-A,max}|$ & $\Delta\sigma_{E,2,stat}$

Increasing the damping variant to ζ_{V1} leads, again to a reduction of the damage D_{dyn} — compare 5.130 to 5.133.

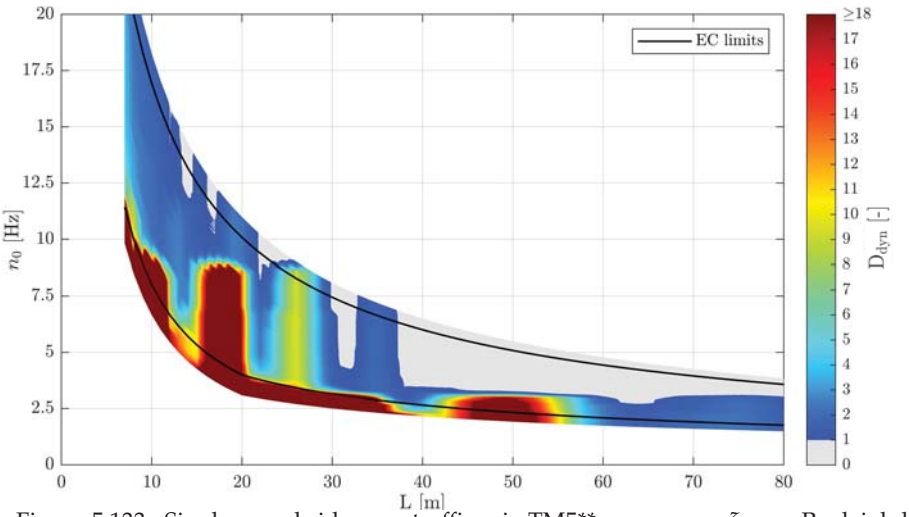

Figure 5.133.: Single-span bridges — traffic mix TM5** — $v_{D_{max}}$ — ζ_{V1} — Rayleigh like damping — no load distribution — top view D_{dyn}

The change of the damping ratios has very little impact on the results for SSB, as illustrated in Figure 5.134. Only structures with very low first bending frequencies $n_0 = 2.5$ Hz and spans L $>$ 59 m (existing SSB) and L $>$ 79 m (new SSB) have a FLS problem, while complying with the TS criteria.

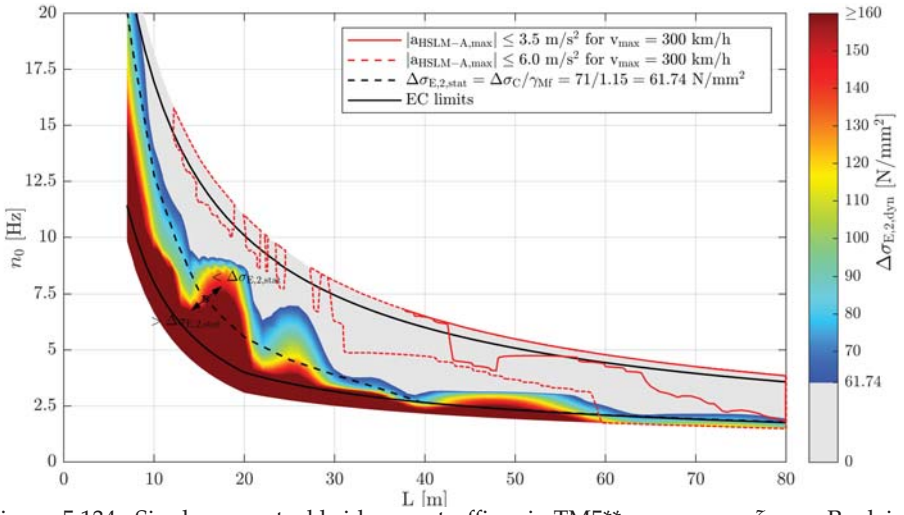

Figure 5.134.: Single-span steel bridges — traffic mix TM5** — $v_{D_{max}}$ — ζ_{V1} — Rayleigh like damping — no load distribution — top view $\Delta\sigma_{E,2,dyn}$ & $|a_{HSLM-A,max}|$ & $\Delta\sigma_{E,2,stat}$

Considering the damping variant ζ_{V1}, allows for the big majority of new SCB to neglect the FLS criterion, while fulfilling the TS criterion — see Figure 5.135. On the other hand, existing SCB which do fulfill the TS criterion, but fail in the FLS design check, have either short span lengths L = 9-16 m, middle span lengths L = 27-29 m or long span lengths L = 42-60 m.

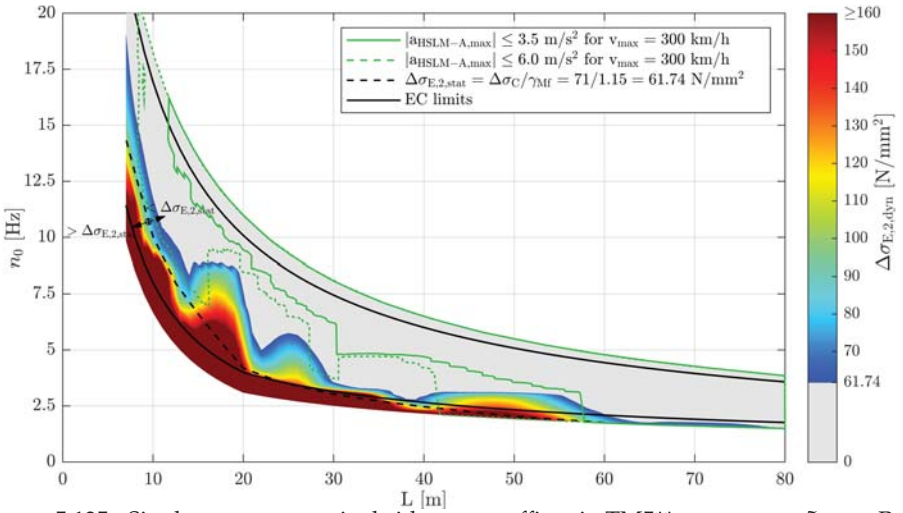

Figure 5.135.: Single-span composite bridges — traffic mix TM5** — $v_{D_{max}}$ — ζ_{V1} — Rayleigh like damping — no load distribution — top view $\Delta\sigma_{E,2,dyn}$ & $|a_{HSLM-A,max}|$ & $\Delta\sigma_{E,2,stat}$

Train speed $v_{a_{max}}$

For the traffic mix variant TM5***, the same is true as for the traffic mix variant TM4***. Using the train speeds $v_{a_{max}}$, provides for the majority of the single-span structures, a good estimation to predict the maximum damage due to $v_{D_{max}}$ and hence traffic mix TM5** — compare Figures 5.130 and 5.136. This conclusion applies for all considered variations of damping ratios and load distribution within TM5*** and therefore, it is referred to the Appendices B and C.

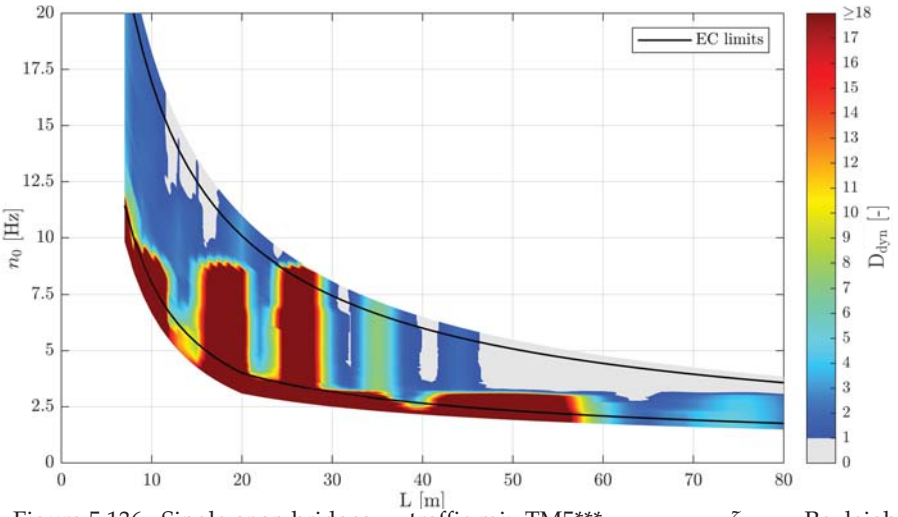

Figure 5.136.: Single-span bridges — traffic mix TM5*** — $v_{a_{max}}$ — ζ_{EC} — Rayleigh like damping — no load distribution — top view D_{dyn} & $|a_{HSLM-A,max}|$

5.4.6. Conclusion

Table 5.6 represents a summary of the before illustrated results, with respect to single-span steel bridges (SSB), and all considered traffic mixes. Hence, Table 5.6 lists the areas, in which the TS criteria, separated for new and exiting structures, are fulfilled, but the FLS criterion, for the detail category FAT-71, is not met.
Consequently, new single-span steel bridges, which comply with the TS criterion $|a_{HSLM-A,max}| \leq 3.5\ m/s^2$, basically, do not have a FLS problem. On the other hand, existing SSB with very long spans (L $>$ 59 m) and a first bending frequency n_0 close to the lower EC-limit, which fulfill the TS criterion $|a_{HSLM-A,max}| \leq 6.0\ m/s^2$, do not comply with the FLS criterion. Furthermore, existing SSB with a span range L = 31-39 m and a first bending frequency of $n_0 = 5.0$ Hz do not meet the just before stated criteria either. However, one needs to consider that TM4** assumes the trains to cross the structures for 100 years and a traffic volume of 24.95 10^6 t/year with the most unfavourable speed possible.
In conclusion, single-span steel bridges, if fulfilling the TS criteria, are not prone to have a FLS problem.

Traffic mix	Damping variant	single-span steel bridges (SSB)		
		$\|a_{HSLM-A,max}\| \leq 3.5\ m/s^2$	$\|a_{HSLM-A,max}\| \leq 6.0\ m/s^2$	Figure
TM1*	ζ_{EC}	-	-	5.68
	ζ_{V1}	-	-	5.77
TM1**	ζ_{EC}	-	L = 62-80 m; n_0 = EC low	5.80
	ζ_{V1}	L = 79-80 m; n_0 = EC low	L = 59-80 m; n_0 = EC low	5.83
TM2-st	ζ_{EC}	-	-	5.99
	ζ_{V1}	-	-	5.102
TM3-st	ζ_{EC}	-	-	5.105
	ζ_{V1}	-	L = 59-60 m; n_0 = EC low	5.108
TM4*	ζ_{EC}	-	L = 62-65 m; n_0 = EC low	5.112
	ζ_{V1}	-	L = 59-62 m; n_0 = EC low	5.115
TM4**	ζ_{EC}	-	L = 61-80 m; n_0 = EC low	5.118
	ζ_{V1}	L = 79-80 m; n_0 = EC low	L = 31-39 m; n_0 = 5 Hz L = 59-80 m; n_0 = EC low	5.121
TM5*	ζ_{EC}	-	L = 63 m; n_0 = EC low	5.125
	ζ_{V1}	-	L = 59 m; n_0 = EC low	5.128
TM5**	ζ_{EC}	-	L = 61-80 m; n_0 = EC low	5.131
	ζ_{V1}	L = 79-80 m; n_0 = EC low	L = 59-80 m; n_0 = EC low	5.134

Table 5.6.: Results FLS parameter study — single-span steel bridges — structures fulfilling TS criteria but do not meet FLS criteria

In Table 5.7 the results, with respect to the single-span composite bridges (SCB), are summarized. In general, new SCB with a smaller span length than L = 58 m, do not have a FLS problem, regarding the detail category FAT-71, as long as the comply with the TS criterion of $|a_{HSLM-A,max}| \leq 3.5\ m/s^2$. For the two exceptions of traffic mix TM4** the same comments, as for the SSB, apply. In case of existing SCB more structures comply with the TS criterion of $|a_{HSLM-A,max}| \leq 6.0\ m/s^2$, while not fulfilling the FLS criterion. Neglecting the traffic mixes TM1**, TM4** and TM5**, as these are very conservative approaches, consequently only the following structures, not distinguishing between the damping variants, do meet the TS criterion but not the FLS limit:

- spans L = 9 m and a first bending frequency of $n_0 = 12$ Hz
- L = 16 m and $n_0 = 7.25$ Hz
- L = 27-30 m and $n_0 = 4 - 5$ Hz
- L = 42-63 m and n_0 equal to the lower EC limit

Traffic mix	Damping variant	single-span composite bridges (SCB)		
		$\lvert a_{HSLM-A,max} \rvert \leq 3.5$ m/s^2	$\lvert a_{HSLM-A,max} \rvert \leq 6.0$ m/s^2	Figure
TM1*	ζ_{EC}	-	L = 9 m; n_0 = 12 Hz L = 51-58 m; n_0 = EC low	5.70
	ζ_{V1}	-	L = 9 m; n_0 = 12 Hz L = 42-54 m; n_0 = 2.63 Hz	5.78
TM1**	ζ_{EC}	L = 60-75 m; n_0 = EC low	L = 7-16 m; n_0 = 7-14 Hz L = 51-75 m; n_0 = EC low	5.81
	ζ_{V1}	L = 58-60 m; n_0 = EC low	L = 7-16 m; n_0 = 7-14 Hz L = 28-30 m; n_0 = 4 Hz L = 42-60 m; n_0 = 2.5-3.5 Hz	5.84
TM2-st	ζ_{EC}	-	L = 16 m; n_0 = 7.25 Hz L = 51-58 m; n_0 = EC low	5.100
	ζ_{V1}	-	L = 16 m; n_0 = 7.25 Hz L = 42-56 m; n_0 = EC low	5.103
TM3-st	ζ_{EC}	-	L = 16 m; n_0 = 7.25 Hz L = 51-58 m; n_0 = EC low	5.106
	ζ_{V1}	-	L = 42-56 m; n_0 = 7-14 Hz	5.109
TM4*	ζ_{EC}	L = 60-63 m; n_0 = EC low	L = 16 m; n_0 = 7.25 Hz L = 30 m; n_0 = 5 Hz L = 51-62 m; n_0 = EC low	5.113
	ζ_{V1}	L = 58-60 m; n_0 = EC low	L = 16 m; n_0 = 7.25 Hz L = 27-30 m; n_0 = 5-4 Hz L = 42-60 m; n_0 = EC low	5.116
TM4**	ζ_{EC}	L = 32-39 m; n_0 = 5 Hz L = 60-66 m; n_0 = EC low	majority of span range	5.119
	ζ_{V1}	L = 30-37 m; n_0 = 5 Hz L = 58-62 m; n_0 = EC low	majority of span range	5.122
TM5*	ζ_{EC}	L = 61 m; n_0 = EC low	L = 16 m; n_0 = 7.25 Hz L = 51-61 m; n_0 = EC low	5.126
	ζ_{V1}	-	L = 16 m; n_0 = 7.25 Hz L = 42-58 m; n_0 = EC low	5.129
TM5**	ζ_{EC}	L = 60-78 m; n_0 = EC low	L = 9-16 m; n_0 = 7.4-15 Hz L = 51-63 m; n_0 = EC low	5.132
	ζ_{V1}	L = 58-60 m; n_0 = EC low	L = 9-16 m; n_0 = 14-7.4 Hz L = 27-16 m; n_0 = 4-5 Hz L = 42-60 m; n_0 = EC low	5.135

Table 5.7.: Results FLS parameter study — single-span composite bridges — structures fulfilling TS criteria but do not meet FLS criteria

5.5. 'Adjusted' dynamic factor φ_{FAT}

Subsequently, the in Chapter 2.1.2 introduced, 'adjusted' dynamic factor φ_{FAT} is discussed. This factor needs to be applied in Austria as summarized on page 30:

> In case the ultimate limit state design (ULS) of the structure is performed directly, using the dynamic internal forces, as these exceed the static internal force, an additional fatigue design is necessary, if real trains with speeds $>$ 200 km/h make up more than 5 million tons per year and track. If the above conditions are met, the fatigue load must be increased by the percentage the internal forces of the dynamic calculation exceed the ones of the static calculation ('adjusted' dynamic factor).

Consequently, the following 'adjusted' dynamic factor φ_{FAT} is calculated for the ULS[1], with respect to the before discussed traffic mixes:

$$\varphi_{FAT} = \max \frac{E_{dyn}}{E_{stat,LM}} \tag{5.29}$$

with: E_{dyn} ... maximum dynamic internal forces due to load model HSLM and real trains, all including $(1 + 0.5\ \varphi'')$

$E_{stat,LM}$ ... maximum static internal forces due to load models LM71, including Φ_2 and $\alpha = 1.21$

In Equation (5.29) no partial safety factors γ_Q are considered, as for both, load models HSLM-A/ real trains and load model LM71, the factor 1.45 according to ÖNORM EN 1990/A1, Table A2.4(B) [42], needs to be applied.
Subsequently, the 'adjusted' dynamic factor φ_{FAT} is applied on the static fatigue load $\Delta\sigma_{\mathrm{E,2,stat}}$ and the fatigue limit state design check is finally performed according to Equation (5.30):

$$\frac{\underbrace{\gamma_{Ff}\ \lambda\ \Phi_2\ \Delta\sigma_{LM71}}\ \varphi_{FAT}}{\Delta\sigma_{\mathrm{E,2,stat}}} \leq \frac{\Delta\sigma_c}{\gamma_{Mf}} \tag{5.30}$$

5.5.1. Traffic mix 1

In this chapter, the 'adjusted' dynamic factor φ_{FAT} for traffic mix 1 is determined. Although, traffic mix 1 does not have a traffic volume exceeding 5.0 10^6 t/year of trains with speeds $>$ 200 km/h, the applicability of the 'adjusted' dynamic factor φ_{FAT} is investigated anyhow. According to Tables 4.1 and 4.2 only TypeC3 and TypeC4 go faster than 200 km/h, hence, the traffic volume for these two high-speed passenger trains together is about 2.85 10^6 t/year. However, passenger train TypeC1 got a maximum train speed of 200 km/h with a traffic volume of 2.9 10^6 t/year, which if considered, would cause traffic mix 1 to exceed the 5.0 10^6 t/year limit.
However, Figure 5.137 shows the general procedure to determine the 'adjusted' dynamic factor φ_{FAT} for traffic mix 1. Figures 5.137(a) and 5.137(b) show the static maximum bending moments at midspan $M_{\mathrm{max,stat}}$ in *3D view* and *top view* due to the load model LM71, considering the

[1]The load model SW/0 is here not considered, as only single-span structures are investigated.

classificaiton factor $\alpha = 1.21$ and the 'dynamic' factor Φ_2 for carefully maintained track. In Figures 5.137(c) and 5.137(d), again in 3D and top view, the dynamic absolute maximum bending moments $|M_{max,dyn}|$ due to the trains TypeC1 to TypeC8, considering the speed ranges of each train (v = 50-1.2v_{EC}) and the dynamic factor $(1 + 0.5\ \varphi'')$ according to ÖNORM EN 1991-2, Annex C [43] are presented. The final two Figures 5.137(e) and 5.137(f) show the 'adjusted' dynamic factor φ_{FAT} for traffic mix 1, which was calculated according to Equation (5.29). Consequently, the trains TypeC1 to TypeC8 cause, due to a dynamic calculation, only on few single-span structures bigger bending moments than the static load model LM71 — see Figure 5.137(f).

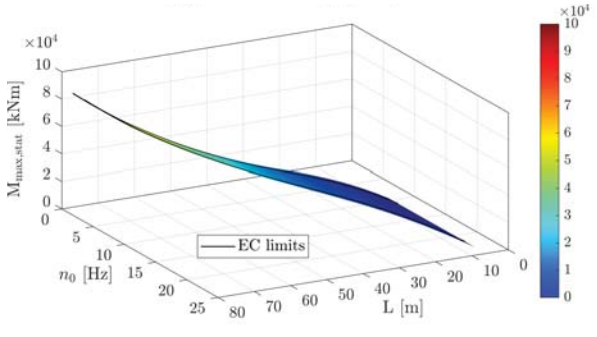

(a) $M_{max,stat}$ — LM71, incl. α and Φ_2 — 3D view

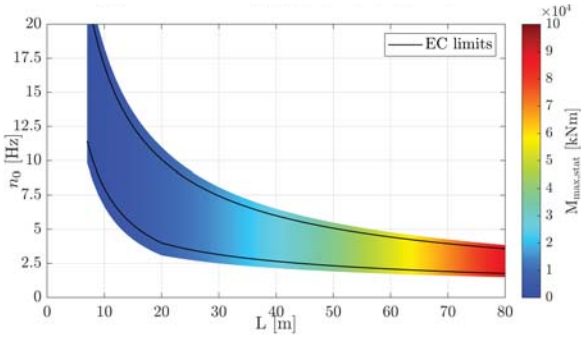

(b) $M_{max,stat}$ — LM71, incl. α and Φ_2 — top view

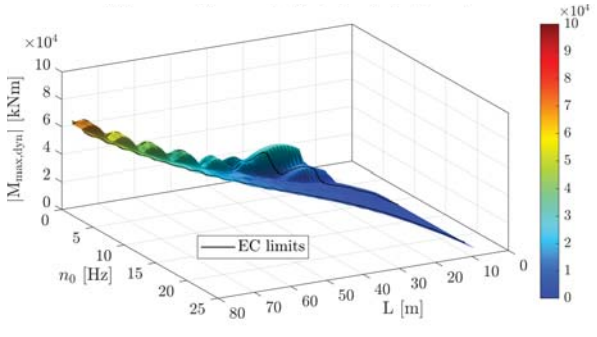

(c) $|M_{max,dyn}|$ — TM1**, incl. $(1 + 0.5\ \varphi'')$ — 3D view

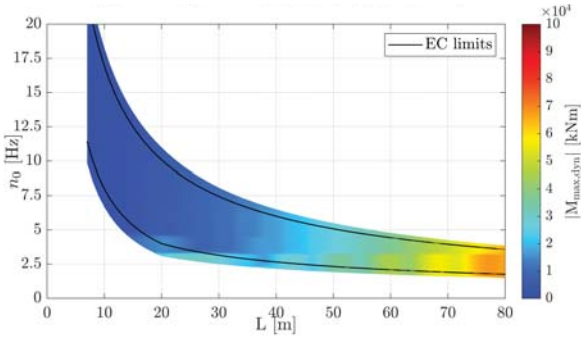

(d) $|M_{max,dyn}|$ — TM1**, incl. $(1 + 0.5\ \varphi'')$— top view

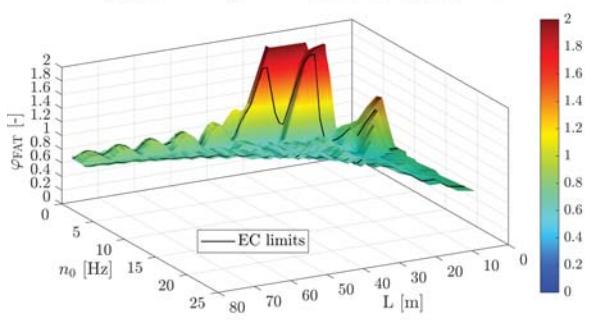

(e) $\varphi_{FAT} = |M_{max,dyn}|/M_{max,stat}$ — 3D view

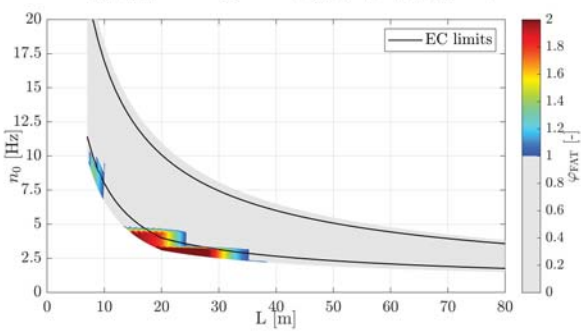

(f) $\varphi_{FAT} = |M_{max,dyn}|/M_{max,stat}$ — top view

Figure 5.137.: 'Adjusted' dynamic factor φ_{FAT} — trains of traffic mix 1 (TM1**) — v = 50 to 1.2 v_{EC} km/h — ζ_{EC} — Rayleigh like damping — no load distribution

In Figure 5.138 the above described procedure is present for the load model HSLM-A. Hence, Figures 5.138(a) and 5.138(b) show the envelope of the maximum absolute bending moment $|M_{max,dyn}|$ for the load model HSLM-A due to dynamic calculations. For each of the ten train models a speed range of v = 50-300 km/h and, again, the dynamic factor $(1 + 0.5\ \varphi'')$ according to ÖNORM EN 1991-2, Annex C [43] was considered. The two Figures 5.138(c) and 5.138(d) illustrate the resulting 'adjusted' dynamic factor φ_{FAT} after applying Equation (5.29) for the load model HSLM-A. In comparison to the results of trains TypeC1 to TypeC8 in Figure 5.137(f), the load model HSLM-A causes on more single-span structures bigger bending moments than the load model LM71.

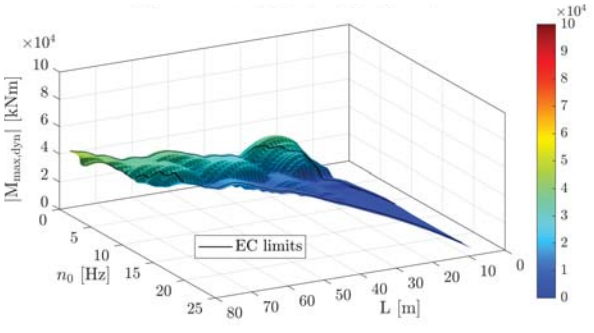

(a) $|M_{max,dyn}|$ — HSLM-A, incl. $(1 + 0.5\ \varphi'')$ — 3D view

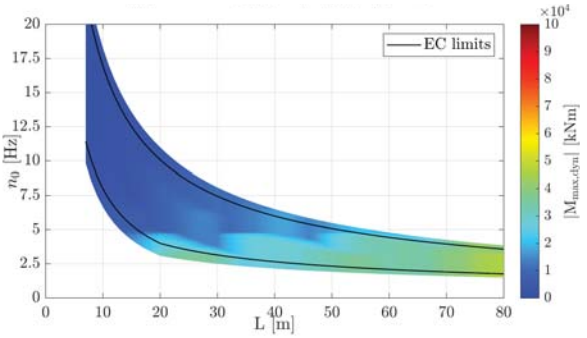

(b) $|M_{max,dyn}|$ — HSLM-A, incl. $(1 + 0.5\ \varphi'')$ — top view

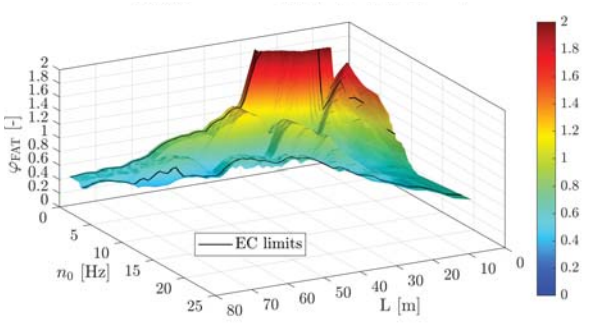

(c) $\varphi_{FAT} = |M_{max,dyn}|/M_{max,stat}$ — 3D view

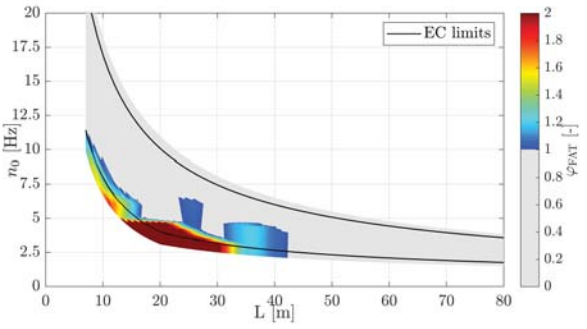

(d) $\varphi_{FAT} = |M_{max,dyn}|/M_{max,stat}$ — top view

Figure 5.138.: 'Adjusted' dynamic factor φ_{FAT} — trains of load model HSLM-A — v = 50-300 km/h — ζ_{EC} — Rayleigh like damping — no load distribution

In the next step, the final 'adjusted' dynamic factor φ_{FAT} for traffic mix 1 is determined. Therefore, the maximum values of the 'adjusted' dynamic factor φ_{FAT} of trains TypeC1 to TypeC8 — see Figure 5.137(f) — and the load model HSLM-A — see Figure 5.138(d) — are combined, which results to Figure 5.139.

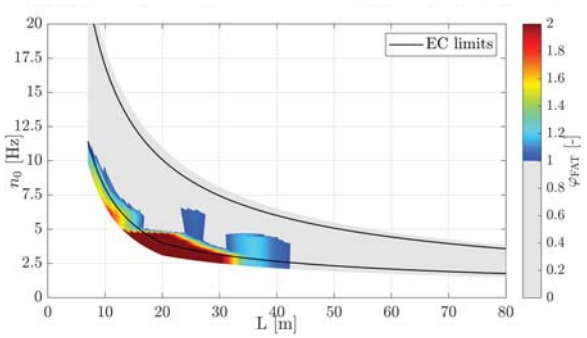

Figure 5.139.: 'Adjusted' dynamic factor φ_{FAT} — trains of traffic mix 1 with v = 50-1.2 v_{EC} km/h and load model HSLM-A with v = 50-300 km/h — ζ_{EC} — Rayleigh like damping — no load distribution

Figure 5.140, which is equivalent to Figures 5.29 and 5.31, illustrates the static equivalent constant amplitude stress ranges $\Delta\sigma_{E,2,stat}$ due to trains TypeC1 to TypeC8 (TM1), for single-span steel bridges (SSB) and single-span composite bridges (SCB).

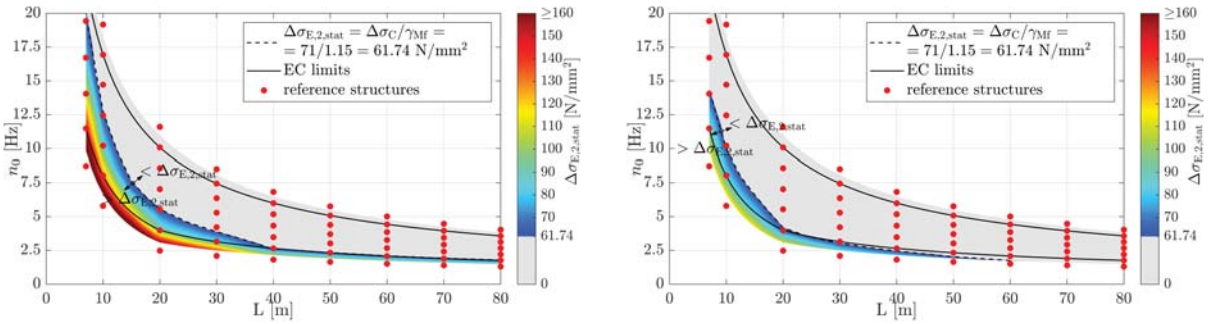

(a) SSB — static fatigue check

(b) SCB — static fatigue check

Figure 5.140.: Static fatigue check — $\Delta\sigma_{E,2,stat}$ due to static calculation of traffic mix 1 (TM1) incl. $(1+\varphi)_D$ according to Annex D of [43] performed for reference single-span steel bridges (SSB) and single-span composite bridges (SCB) → surface interpolated — no load distribution

Finally, the static equivalent constant amplitude stress ranges $\Delta\sigma_{E,2,stat}$ are multiplied by the 'adjusted' dynamic factor φ_{FAT} as stated in Equation (5.30). Consequently, Figure 5.141(a) shows the result for single-span steel bridges (SSB) and Figure 5.141(b) for single-span composite bridges (SCB). In Figures 5.141(c) to 5.141(h) the results of the dynamic fatigue check for traffic mixes TM1*, TM1** and TM1*** — see Chapter 5.4.1 — are illustrated again. Comparing the dynamic to the static fatigue check shows that, considering the 'adjusted' dynamic factor φ_{FAT} does not enable the static approach to cover the effects of the dynamic calculation. Furthermore, it seems to be more applicable to use the TS criteria, in order to avoid a FAT problem, as already concluded in Chapter 5.4.

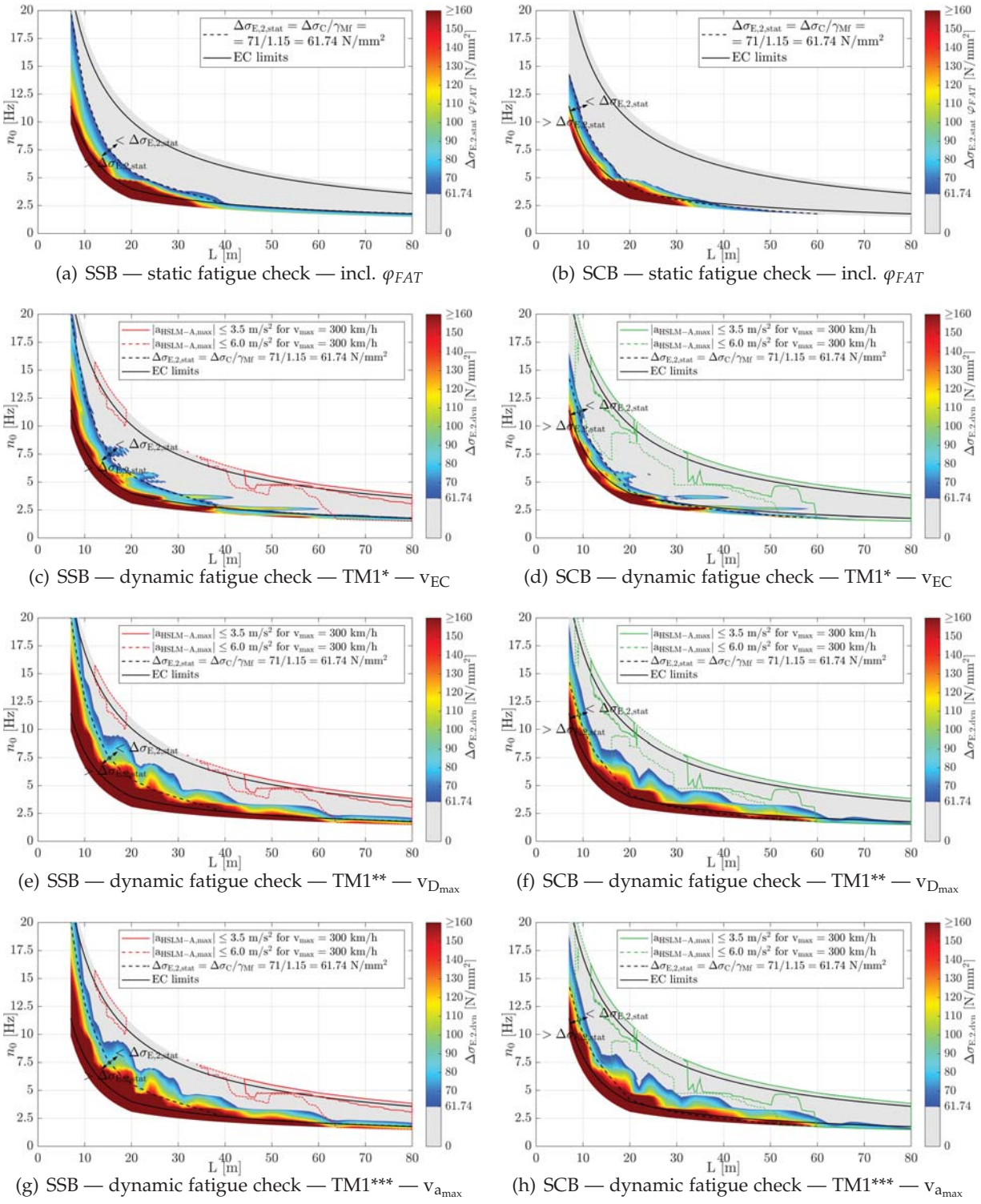

(a) SSB — static fatigue check — incl. φ_{FAT}

(b) SCB — static fatigue check — incl. φ_{FAT}

(c) SSB — dynamic fatigue check — TM1* — v_{EC}

(d) SCB — dynamic fatigue check — TM1* — v_{EC}

(e) SSB — dynamic fatigue check — TM1** — $v_{D_{max}}$

(f) SCB — dynamic fatigue check — TM1** — $v_{D_{max}}$

(g) SSB — dynamic fatigue check — TM1*** — $v_{a_{max}}$

(h) SCB — dynamic fatigue check — TM1*** — $v_{a_{max}}$

Figure 5.141.: Static fatigue check incl. 'adjusted' dynamic factor φ_{FAT} vs. dynamic fatigue check for single-span steel bridges (SSB) and single-span composite bridges (SCB) — traffic mix 1 (variants of TM1) — ζ_{EC} — Rayleigh like damping — no load distribution

5.5.2. Traffic mix 3

Subsequently, the results for traffic mix 3 are presented. Therefore, the procedure described for traffic mix 1 in Chapter 5.5.1 is applied on the 73 average passenger trains (PT) of traffic mix 3. Hence, the dynamic absolute maximum bending moments $|M_{max,dyn}|$ for each of the 73 average PT on each structure were determined. Regarding the speed range, again v = 50-1.2v_{train} for each of the 73 average trains was considered. Therefore, e.g. train TypeC19 Taurus-front was measured 6689 times in the years 2014 & 2015 — see Tabel 4.4. Hence, 6689 speed values were available, of which the maximum was picked and used as v_{train}. After determining the envelope of the dynamic absolute maximum bending moments $|M_{max,dyn}|$ regarding all 73 average PT, again, the 'adjusted' dynamic factor φ_{FAT} was calculated — see Equation (5.29) — using the static maximum bending moments $M_{max,stat}$ of the LM71 — see Figure 5.137(b). This leads to the results in Figure 5.142(a). Considering the load model HSLM-A and its 'adjusted' dynamic factor φ_{FAT} according to Figure 5.138(d), leads finally to the 'adjusted' dynamic factor φ_{FAT} for traffic mix 3, as illustrated in Figure 5.142(b). In summary, the effects due to HSLM-A overrule the ones of the 73 average PT — compare Figures 5.142(a) and 5.142(b).

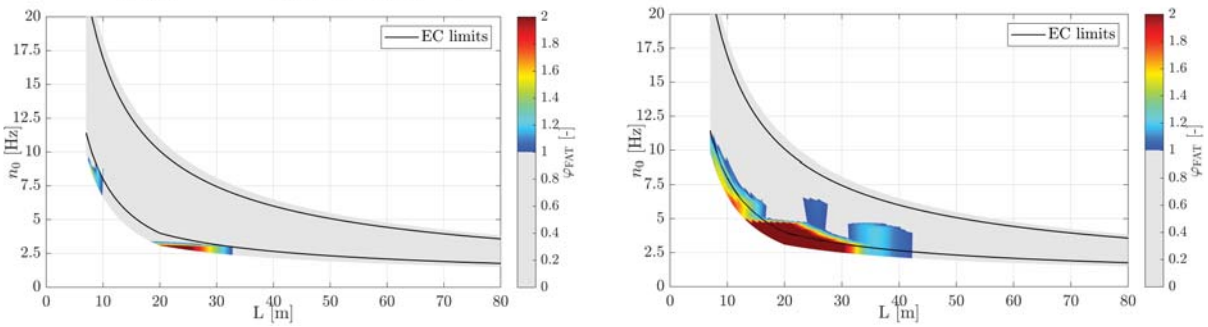

(a) Trains of traffic mix 3

(b) Trains of traffic mix 3 & load model HSLM-A

Figure 5.142.: 'Adjusted' dynamic factor φ_{FAT} — traffic mix 3 with v = 50-1.2 v_{train} km/h and load model HSLM-A with v = 50-300 km/h — ζ_{EC} — Rayleigh like damping — no load distribution

Applying the 'adjusted' dynamic factor φ_{FAT} of traffic mix 3 — see Figure 5.142(b) — according to Equation (5.30), leads for SSB to the results in Figure 5.143(a) and for SCB to the results in Figure 5.143(b). Comparing the static equivalent constant amplitude stess ranges $\Delta\sigma_{E,2,stat}$, including the 'adjusted' dynamic factor φ_{FAT}, and the dynamic equivalent constant amplitude stress ranges $\Delta\sigma_{E,2,dyn}$ to each other — see Figure 5.143 — shows again, that the static approach is not able to account for the dynamic effects.

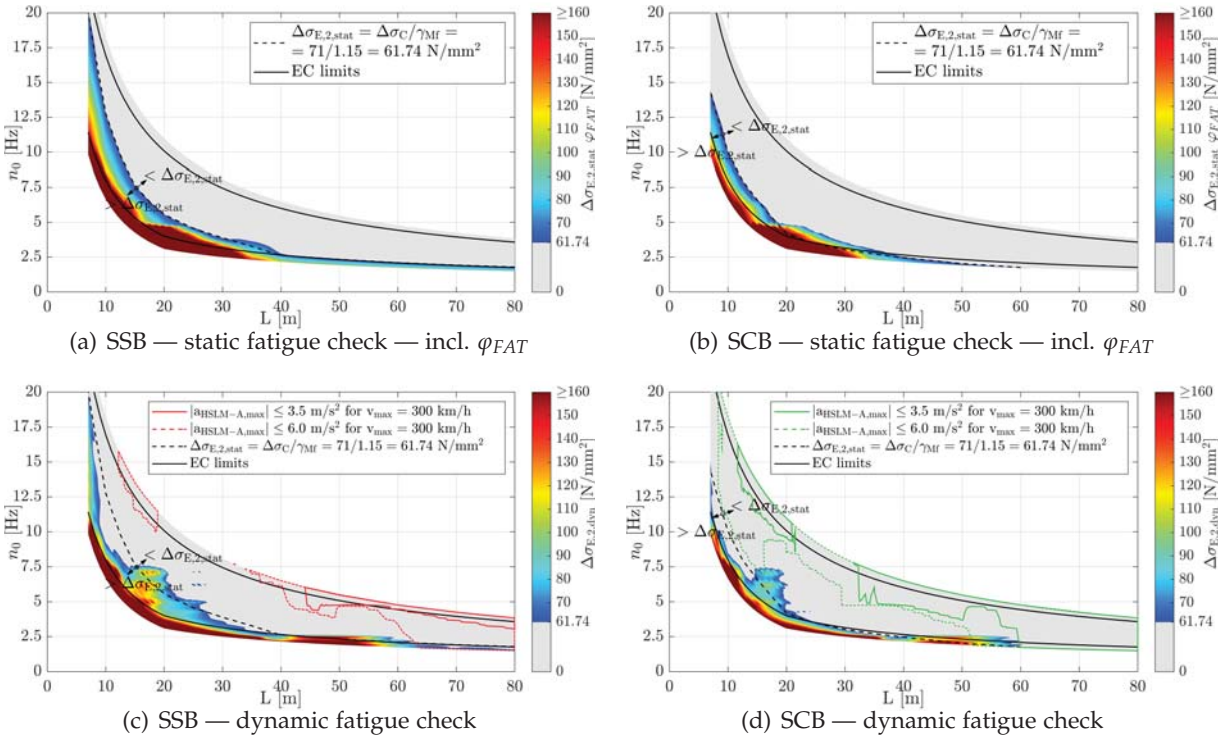

(a) SSB — static fatigue check — incl. φ_{FAT}

(b) SCB — static fatigue check — incl. φ_{FAT}

(c) SSB — dynamic fatigue check

(d) SCB — dynamic fatigue check

Figure 5.143.: Static fatigue check incl. 'adjusted' dynamic factor φ_{FAT} vs. dynamic fatigue check for single-span steel bridges (SSB) and single-span composite bridges (SCB) — traffic mix 3 (TM3) — ζ_{EC} — Rayleigh like damping — no load distribution

5.5.3. Traffic mix 4

Subsequently, the 'adjusted' dynamic factors φ_{FAT} for the trains of traffic mix 4 — see Figure 5.144(a) — and the overall result for traffic mix 4, considering the HSLM-A trains as well — see Figure 5.144(b) — are presented. Again, the impact of the load model HSLM-A exceeds the trains of the traffic mix, in this case six high-speed passenger trains.

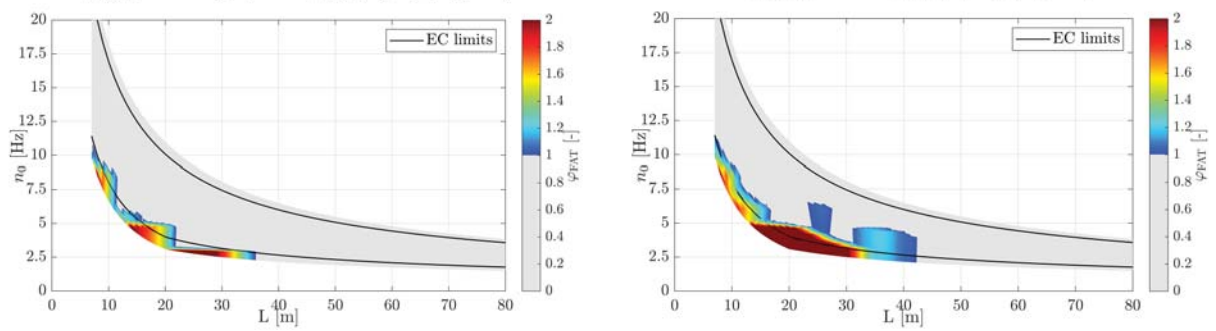

(a) Trains of traffic mix 4

(b) Trains of traffic mix 4 & load model HSLM-A

Figure 5.144.: 'Adjusted' dynamic factor φ_{FAT} — traffic mix 4 with v = 50-1.2 v_{train} km/h and load model HSLM-A with v = 50-300 km/h — ζ_{EC} — Rayleigh like damping — no load distribution

Applying the 'adjusted' dynamic factors φ_{FAT} on the static equivalent constant amplitude stress ranges $\Delta\sigma_{E,2,stat}$ — see Figures 5.145(a) and 5.145(b) — does, again, not cover the dynamic effects due to the traffic mixes TM4*, TM4** and TM4*** — see Figures 5.145(c) to 5.145(h).

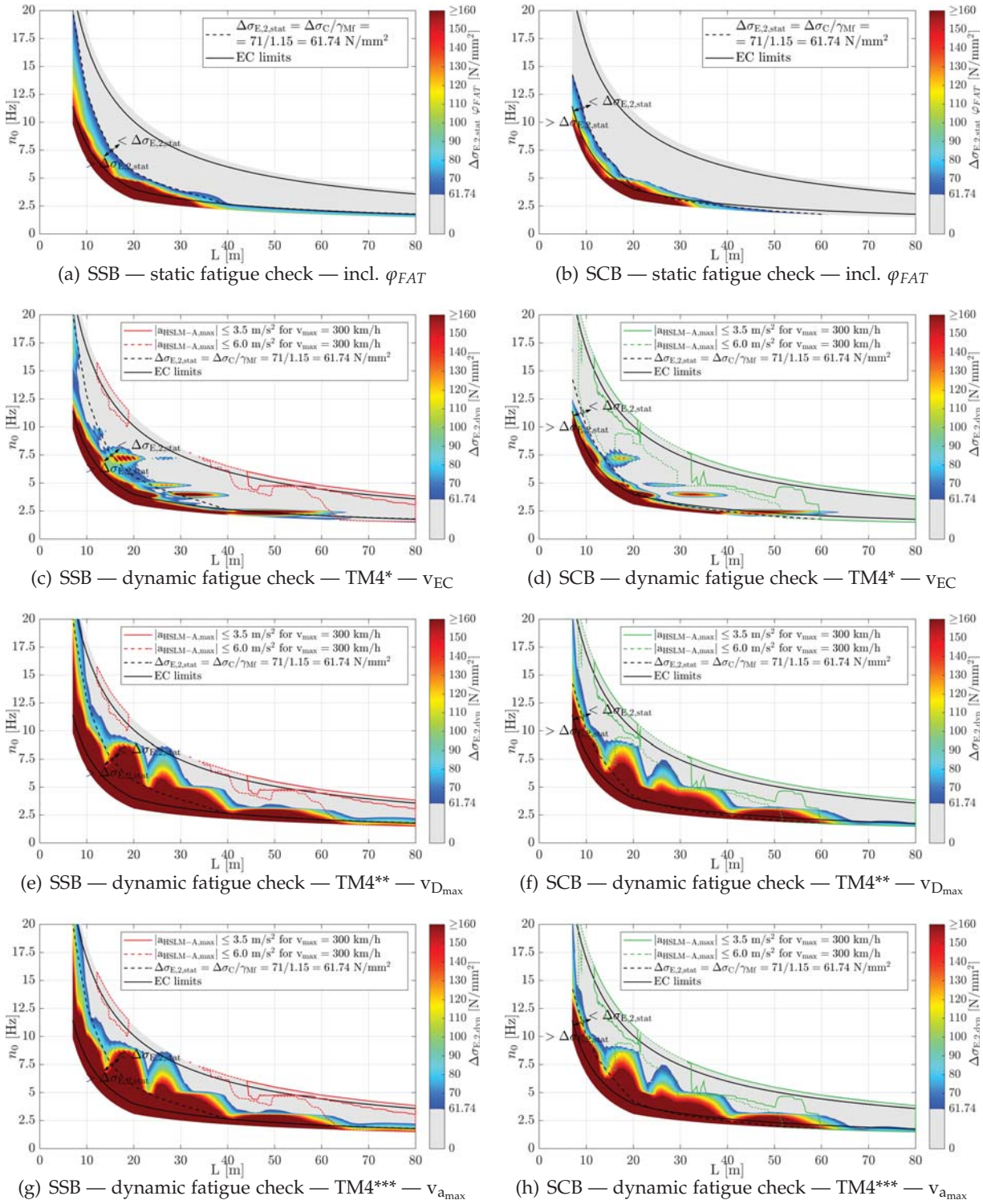

(a) SSB — static fatigue check — incl. φ_{FAT}

(b) SCB — static fatigue check — incl. φ_{FAT}

(c) SSB — dynamic fatigue check — TM4* — v_{EC}

(d) SCB — dynamic fatigue check — TM4* — v_{EC}

(e) SSB — dynamic fatigue check — TM4** — $v_{D_{max}}$

(f) SCB — dynamic fatigue check — TM4** — $v_{D_{max}}$

(g) SSB — dynamic fatigue check — TM4*** — $v_{a_{max}}$

(h) SCB — dynamic fatigue check — TM4*** — $v_{a_{max}}$

Figure 5.145.: Static fatigue check incl. 'adjusted' dynamic factor φ_{FAT} vs. dynamic fatigue check for single-span steel bridges (SSB) and single-span composite bridges (SCB) — traffic mix 4 (variants of TM4) — ζ_{EC} — Rayleigh like damping — no load distribution

5.5.4. Traffic mix 5

Subsequently, the 'adjusted' dynamic factors φ_{FAT} for the trains of traffic mix 5 — see Figure 5.146(a) — and the overall result for traffic mix 5, considering the HSLM-A trains as well — see Figure 5.146(b) — are illustrated. Again, the load model HSLM-A causes bigger dynamic absolute bending moments $|M_{max,dyn}|$ than the trains of the traffic mix, in this case the eight trains of traffic mix 5. Consequently, the 'adjusted' dynamic factors φ_{FAT} of the load model HSLM-A overrule the ones of the eight service trains — compare Figures 5.146(a) and 5.146(b).

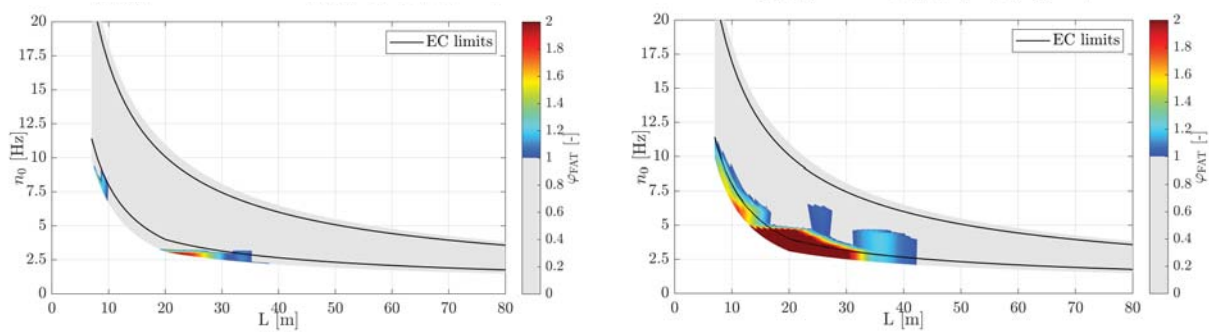

(a) Trains of traffic mix 5

(b) Trains of traffic mix 5 & load model HSLM-A

Figure 5.146.: 'Adjusted' dynamic factor φ_{FAT} — traffic mix 5 with v = 50-1.2 v_{train} km/h and load model HSLM-A with v = 50-300 km/h — ζ_{EC} — Rayleigh like damping — no load distribution

Furthermore, the static equivalent constant amplitude stress ranges $\Delta\sigma_{E,2,stat}$, enhanced by the 'adjusted' dynamic factors φ_{FAT}, are compared to the dynamic equivalent constant amplitude stress ranges $\Delta\sigma_{E,2,dyn}$ for the traffic mixes TM5*, TM5** and TM5*** in Figure 5.147. However, the static concept is, again, not able to account for the dynamic effects — compare Figures 5.147(a) and 5.147(b) to Figures 5.147(c) to 5.147(h).

5.5.5. Conclusion

The static approach, which enhances the static equivalent constant amplitude stress range $\Delta\sigma_{E,2,stat}$ by multiplying it with the 'adjusted' dynamic factor φ_{FAT}, according to Equation (5.30), is not able to account for the dynamic effects, represented by the dynamic equivalent constant amplitude stress ranges $\Delta\sigma_{E,2,dyn}$, with respect to the investigated traffic mixes TM1*, TM1**, TM1***, TM3-st, TM4*, TM4**, TM4***,TM5*, TM5** and TM5***.

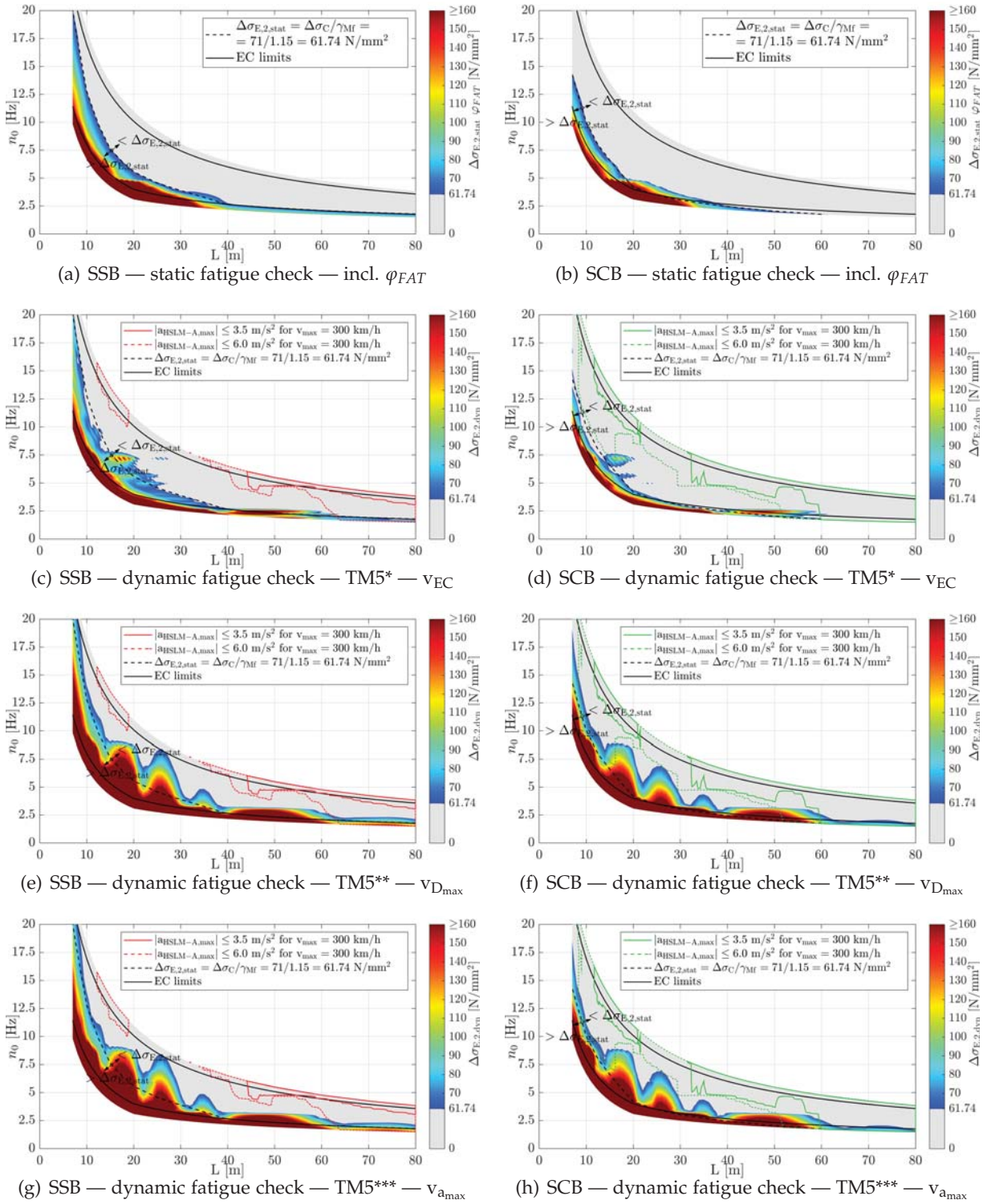

(a) SSB — static fatigue check — incl. φ_{FAT}

(b) SCB — static fatigue check — incl. φ_{FAT}

(c) SSB — dynamic fatigue check — TM5* — v_{EC}

(d) SCB — dynamic fatigue check — TM5* — v_{EC}

(e) SSB — dynamic fatigue check — TM5** — $v_{D_{max}}$

(f) SCB — dynamic fatigue check — TM5** — $v_{D_{max}}$

(g) SSB — dynamic fatigue check — TM5*** — $v_{a_{max}}$

(h) SCB — dynamic fatigue check — TM5*** — $v_{a_{max}}$

Figure 5.147.: Static fatigue check incl. 'adjusted' dynamic factor φ_{FAT} vs. dynamic fatigue check for single-span steel bridges (SSB) and single-span composite bridges (SCB) — traffic mix 5 (variants of TM5) — ζ_{EC} — Rayleigh like damping — no load distribution

6. Arch bridge

In this chapter, the main girders and arches of a representative arch bridge are investigated with respect to their fatigue behaviour. Therefore, the geometry of the structure, which was provided by the *Deutsche Bahn* (DB), is first presented. Subsequently, assumptions regarding the modelling of the arch bridge and the computational approaches are discussed. Furthermore, preliminary studies, which compare the different computational approaches, are conducted, leading subsequently to the traffic safety design check (TS). Furthermore, the fatigue limit state design checks (FLS), first using static simulations and afterwards dynamic calculations, are performed for two different train mixes. Finally, the critical cross sections, which are sensitive for the dynamic stress spectra due to high-speed trains, of the main structural members — main girder and arch — are presented. The arch bridge was assumed to be located between the cities of Linz and Vienna, in order to allow for the application of the measured traffic mix 2.

6.1. Overview

6.1.1. Geometry of the studied arch bridge

Subsequently, an overview of the studied double-track arch bridge, is presented. The longitudinal view in Figure 6.1 illustrates the total span length L of 86.02 m and the maximum arch rise of 14.95 m. Furthermore, the hangers (H), which connect the arch (A) with the main girder (MG), are placed each 7.82 m, whereas the cross girders (CG) distance of the orthotropic steel deck becomes $e_{CG} = 7.82/3 = 2.607$ m. The double-track structure's width of 10.75 m (distance of the hangers) and the bearing situation are illustrated in the top view of Figure 6.1. The total of four cross beams (CB) connect the two arches of axes ① and ② with each other, in order to improve the stability out of plane.

In Figure 6.2 the standard cross section of the arch bridge is illustrated. The main girders and the arches are designed as welded box members with a height of 2.55 m and 1.0 m, respectively, whereas both have a width of 1.25 m. The direct fastened tracks (ballastless tracks) are supported by an orthotropic steel deck with open longitudinal stiffeners (LS), which transfer the loads to the cross beams. The areas besides the direct fastened track are covered with a ballast bed of an average height of 0.4 m.

Figure 6.3 gives an overview with respect to the position of the different cross sections, which are illustrated in detail in Figure 6.4. Consequently, three different main girder cross types (MG_a, MG_b and MG_c,) were considered. On the other hand, the geometry of the arch (A_a), the hangers (H_a) and cross beams (CB_a) stay constant. Furthermore, two different longitudinal stiffener (LS_a and LS_b) and cross girder (CG_a CB_b) variants were applied. Regarding the deck plate (DP) four options were considered. Two of them carry the direct fastened track — see cross sections DPC_a and DPC_b — and the other two are situated in the area of the ballast bed and consequently only consider the deck plate itself — see cross sections DP_a and DP_b. Furthermore, Figure 6.5 gives an overview regarding the design of the direct fastened track. The direct fastened track is interrupted by gaps of 0.1 m, illustrated in the section view B-B, each 5.2133 m.

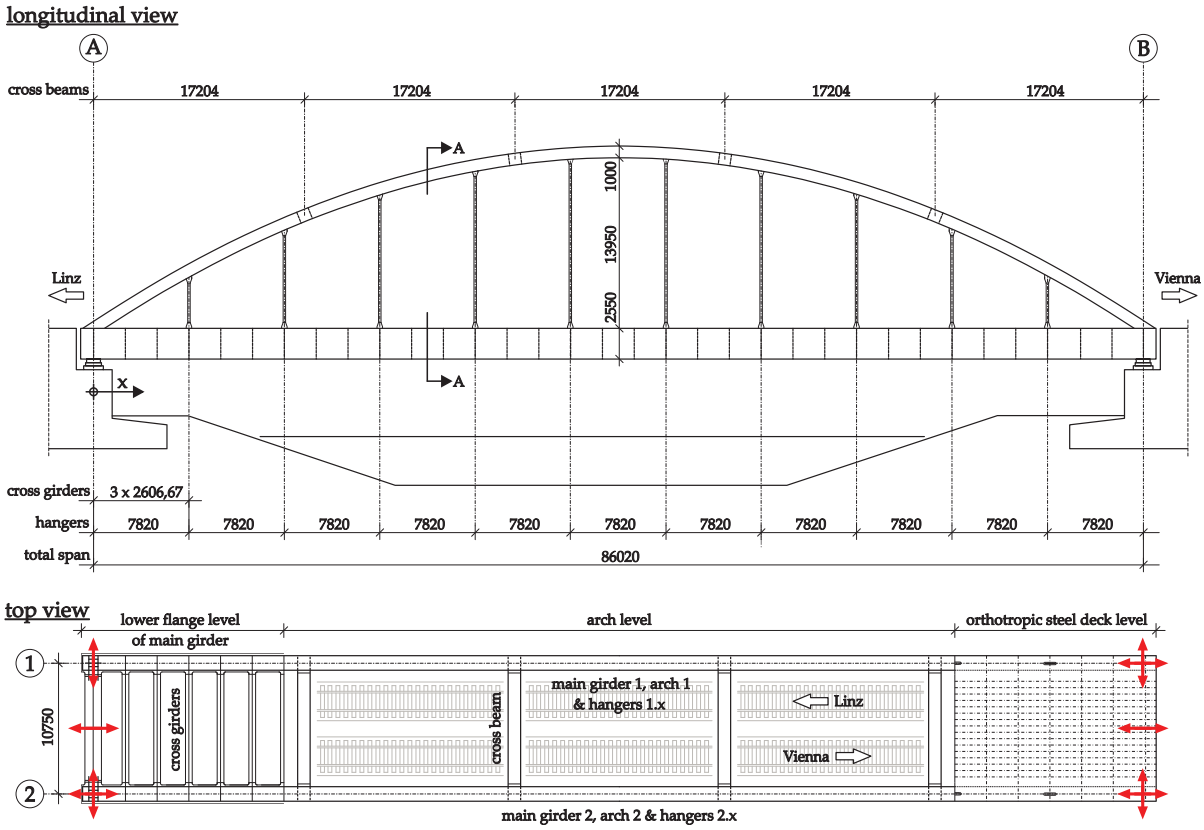

Figure 6.1.: Arch bridge — longitudinal and top view — artificial location of the arch bridge between the cities of Linz and Vienna

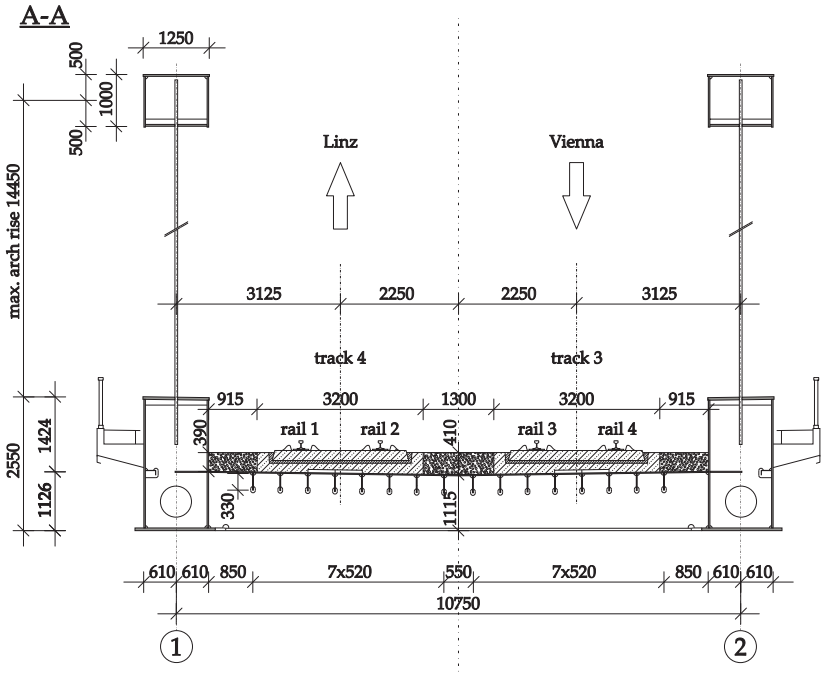

Figure 6.2.: Arch bridge — section view A-A — artificial location of the arch bridge between the cities of Linz and Vienna

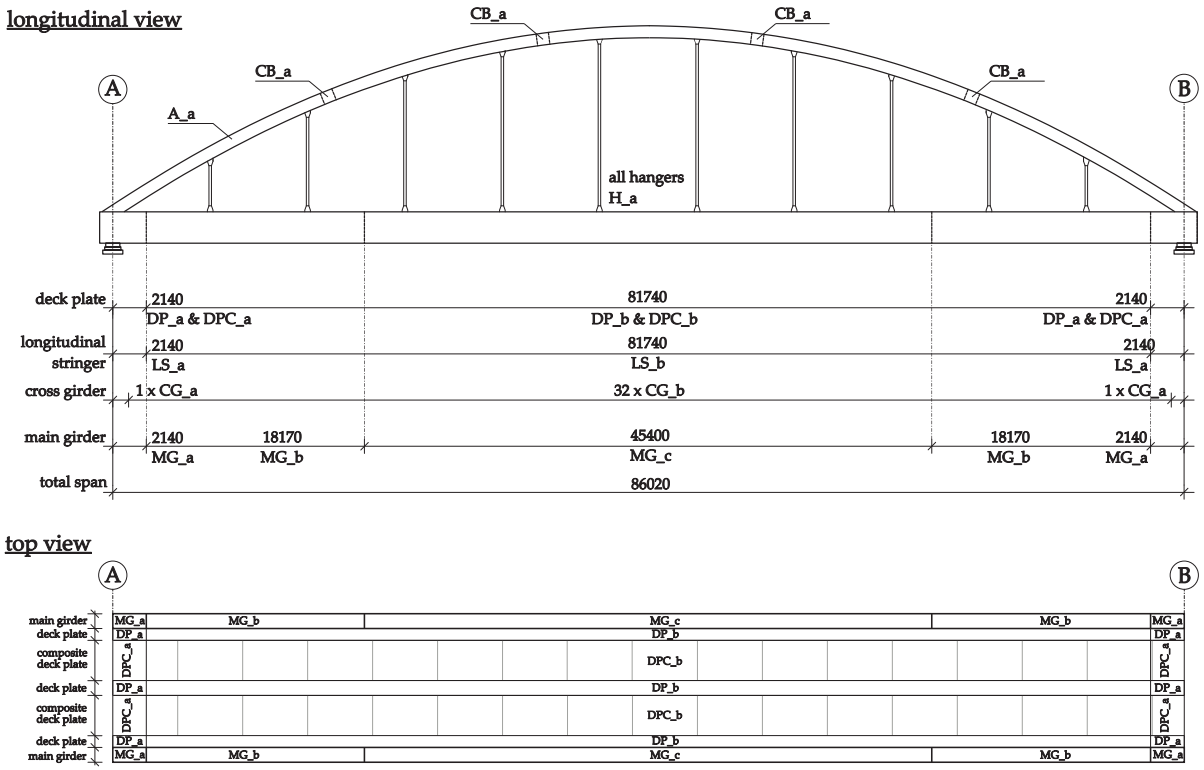

Figure 6.3.: Arch bridge — overview of cross section position and their notation

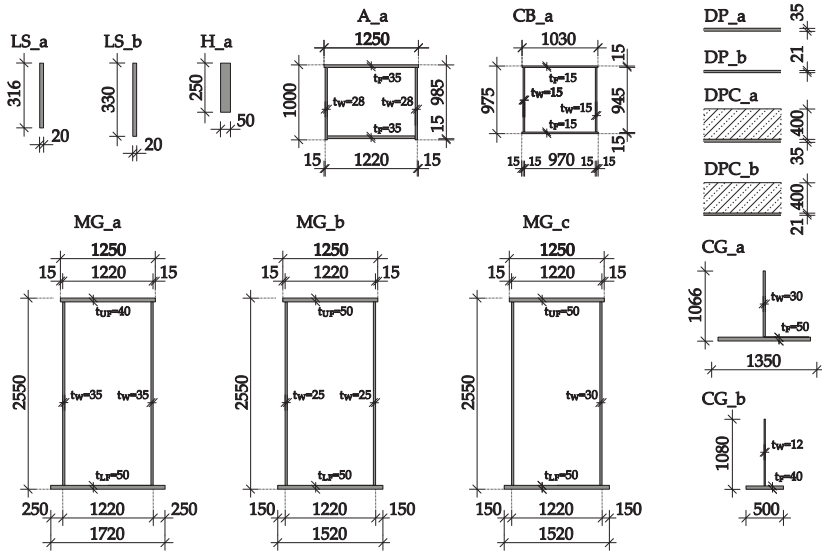

Figure 6.4.: Arch bridge — cross sections— longitudinal stiffeners (LS), deck plate (DP), hangers (H), arches (A), cross beams (CB), cross girders (CG) and main girders (MG)

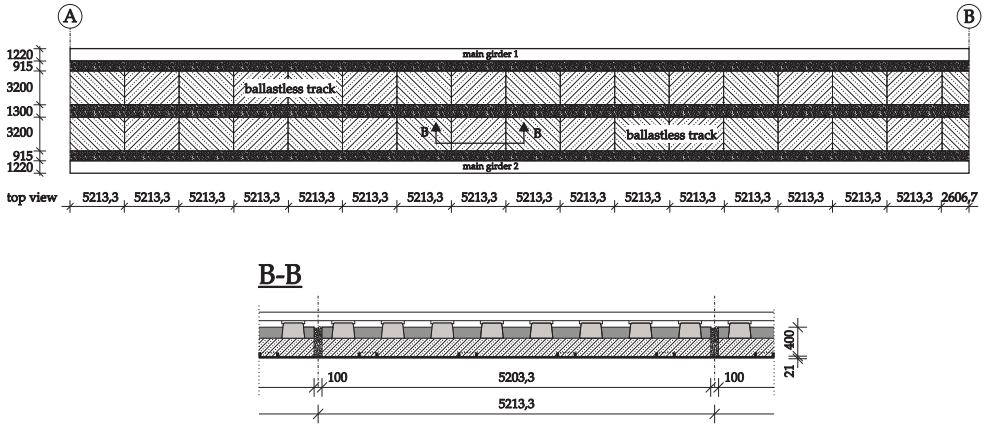

Figure 6.5.: Arch bridge — ballastless track

6.1.2. Damping variants

All subsequently performed dynamic calculations use the Rayleigh like damping, whereas the two parameters α and β are specified for the first two bending modes and damping ratios $\zeta_1 = \zeta_2 = 0.5$ — see Equation (3.127).

6.1.3. Traffic mixes

Subsequently, the variants of traffic mix 1 (EC trains TypeC1 to TypeC8) with the speed variants v_{EC} and $v_{D_{max}}$ — the traffic mixes **TM1*** and **TM1**** — are considered — see Tables 4.1 and 4.2.
Furthermore, from traffic mix 2 (measurements of real trains) the variant **TM2-dt** for the double track structure is applied — see Table 4.8. Therefore, on track 4 towards Linz 40934 real trains (RT) and on track 3 towards Vienna 53668 RT are assigned.
However, as already mentioned in the previous chapters, the traffic volume is scaled to 24.95 10^6 t/year/track and 100 years of design life for all studied traffic mixes.

6.2. Computational approach

In the following chapter, the computational concept, with respect to the before discussed arch bridge, is demonstrated.
First, the numerical model, which is created using the software Dlubal RFEM [11], is covered. Furthermore, the loading assumptions for the static and dynamic simulation of the train crossing are presented. Additionally, the determination of the natural frequencies and corresponding mode shapes is, in an exemplary manner, shown.
Second, the analytical approach, using the software package Matlab [34], which is also applied to simulate the dynamic train crossing, is briefly discussed.
However, all subsequently illustrated dynamic calculations use the *moving load model*, which is explained in Chapter 3.

6.2.1. Modelling — numerical solution — RFEM

All cross sections — see Figure 6.4 — were modelled as beam elements, except the ones concerning the cover plate (cross sections DP_a, DP_b, DPC_a and DPC_b). Latter were modelled as orthotropic surfaces in RFEM, which allows to consider different stiffnesses in both surface directions. These characteristics were necessary, as the areas with the direct fastened track (cross sections DPC_a and DPC_b) were modelled in a simplified manner as rigid composite members in global longitudinal direction (X axis) and without bond between steel and concrete (no composite effect) in global transverse direction (Y-axis), whereas the gaps, within the direct fastened track, were considered according to Figure 6.5. The other cover plates (section DP_a and DP_b) were modelled as isotropic steel plates. Furthermore, all eccentricities were considered according to the geometry in Figure 6.1 and 6.2. For the Young's modulus of steel $E_a = 210000\ N/mm^2$ and of concrete $E_a = 33000\ N/mm^2$ were used, whereas the densities $\gamma_a = 7850\ kg/m^3$ for steel, $\gamma_{bb} = 2000\ kg/m^3$ for the ballast bed and $\gamma_c = 2500\ kg/m^3$ for concrete were considered. The track's transition zone from open track to structure was in a conservative approach not modelled.
The static loads of load model LM71 and of the trains TypeC1 to TypeC8 were modelled as line loads and concentrated loads along the rail axis (e.g. for track 3, consequently along rail axis 3 and 4 — see Figure 6.2), using the RFEM add-on RF-MOVE. This add-on allowed to move the entire trains with a step size of $\Delta X = 0.25$ m across the arch bridge. Hence, each resulting load case represents a train position on the structure, which was subsequently statically analysed.
On the other hand, the dynamic crossing of a single axle was modelled using concentrated loads fixed in position, but with amplitudes variable in time — see Figure 6.6. These loads were placed each 2.607 m, according to the cross girder distance e_{CG}, along the rail axes. Hence, the dynamic calculation was first performed for the crossing of one single axle load. Subsequently, the results for an entire train were obtained by superposing the results of the single axle. Furthermore, the dynamic calculation in RFEM was performed applying the direct time integration and the modal analysis, as illustrated in Chapters 6.3.1 and 6.3.2.

6.2.2. Analytical solution — Matlab

The analytical approach, which is explained in detail in Chapter 3.5.2, is subsequently also applied on the arch bridge. This concept needs as input parameters from the numerical model, the natural frequencies ω_j, the corresponding mode shapes ϕ_j — the first four mode shapes are

shown Figure 6.7 — the modal masses m_j^* and the normal stress $\sigma_{P_j,i}$ at the investigated point P_i due to the mode shape ϕ_j, which are all determined using the above described program REFM [11]. After importing these variables for each considered mode shape j, the crossing of one train axle is simulated and the result for an entire train, again, obtained by superposition. The number of considered mode shapes is defined in the following Chapters.

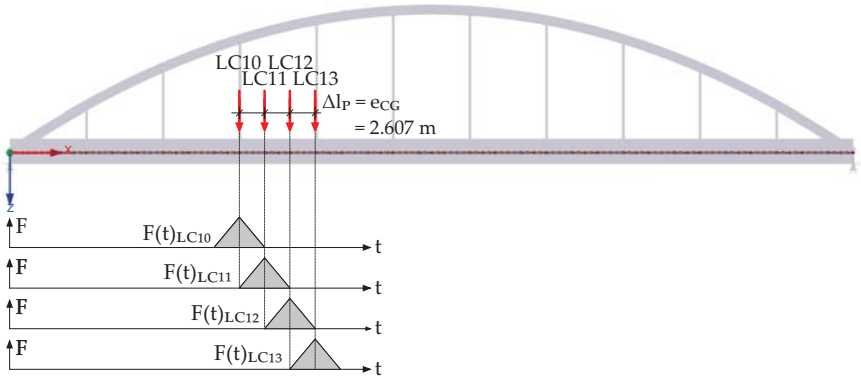

Figure 6.6.: Modelling of dynamic loading — crossing of one train axle in RFEM

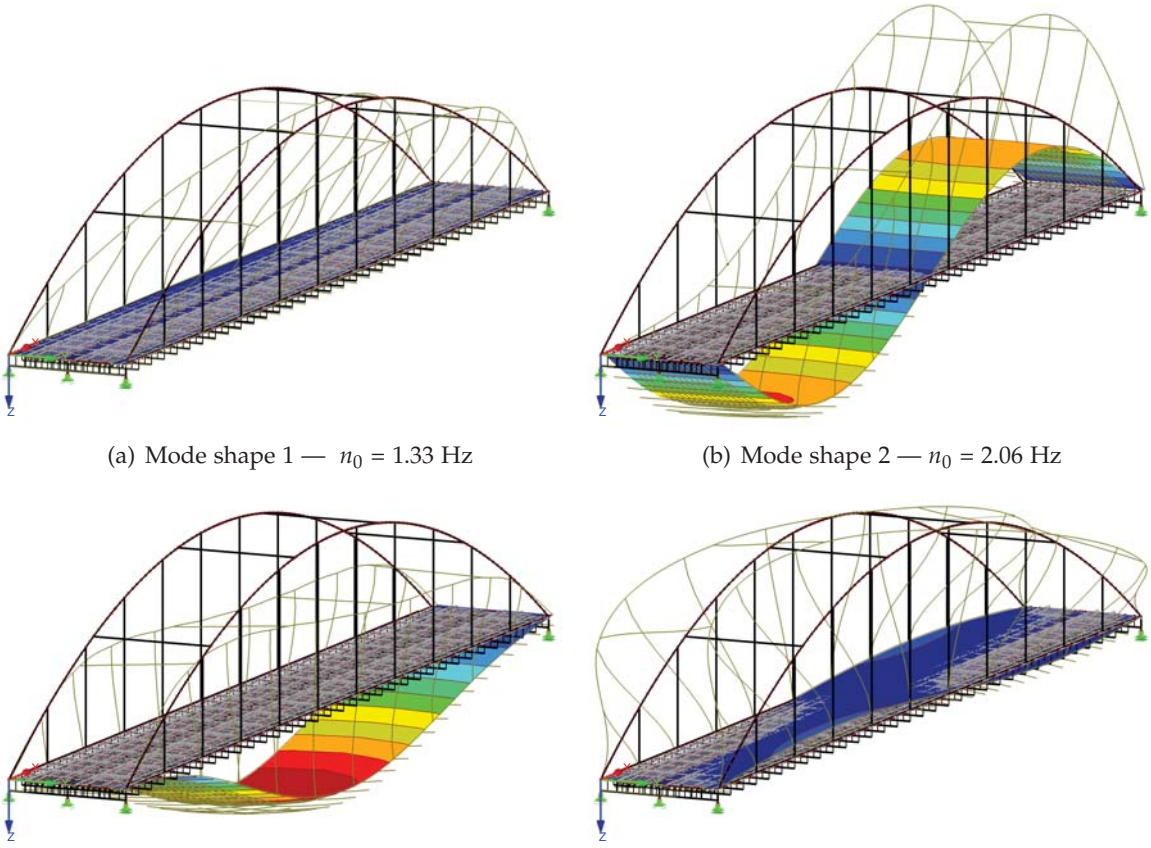

(a) Mode shape 1 — n_0 = 1.33 Hz

(b) Mode shape 2 — n_0 = 2.06 Hz

(c) Mode shape 3 — n_0 = 2.91 Hz

(d) Mode shape 4 — n_0 = 2.97 Hz

Figure 6.7.: First four mode shapes — RFEM

6.3. Preliminary studies

Subsequently, the preliminary studies with the goal to compare the simulations of the dynamic train crossing of the numerical approach (RFEM) and the analytical concept (Matlab), to each other, are presented.
Within the numerical solutions two options are available. First, the direct time integration, which solves the entire system of equations — hereinafter called *RFEM direct time integration* — and second, the modal analysis, which solves for a selected number of mode shapes the resulting single-degree of freedom systems numerically — hereinafter called *RFEM modal analysis*.
Furthermore, the analytical approach with Matlab — hereinafter called *Matlab modal analysis* — uses again the concept of the modal analysis, but solves each single-degree of freedom system analytically instead of numerically.

First, the internal forces and resulting stresses and subsequently the vertical bridge deck acceleration are studied with respect to the three computational options mentioned above.

6.3.1. Internal forces and stresses

In this chapter, the high-speed passenger train TypeC3 — see Figure 2.18 — crosses the arch bridge on track 3 towards Vienna with a constant speed of v = 193 km/h. Subsequently, the resulting internal forces M_y, N and M_z and the corresponding normal stresses σ — see Figure 6.8 — are illustrated for main girder 2 (MG2) and arch 2 (A2) at the positions x = 21.505 m (quarter-point) and x = 43.01 m (midspan) along the structure's longitudinal axis — see Figure 6.1. For the numerical simulation a time step of Δt = 0.0005 s was selected, representing a conservative approach, as due to the requirements in [10], in this case, a time step of only Δt = 0.0016 s would be required. However, for the analytical solution a time step of Δt = 0.01 s is sufficient. For the approaches using the modal analysis 60 mode shapes were used as these cover the natural frequency range up to 30 Hz as required in [37] — see also page 27. Furthermore, the analytical approach was performed with 100 sinus functions — see Figure 3.17.

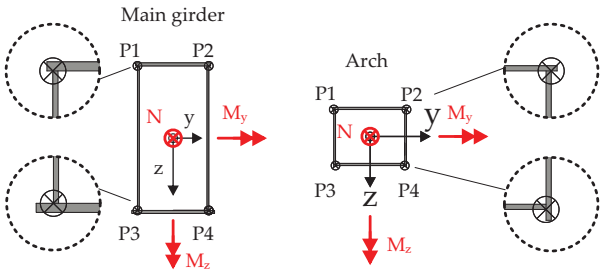

Figure 6.8.: Definition of points P1 to P4 on mono-symmetric cross sections for main girder and arch

Results at main girder 2 — x = 21.505 m (quarter-point)

Figure 6.9 shows the bending moment M_y varying over time for the MG2 at the quarter-point (x = 21.505m with cross section MG_c — see Figure 6.4) due to the crossing of train TypeC3. The reference solution (RFEM direct time integration) is approximated very well by the numerical modal analysis (RFEM modal analysis) and the analytical modal analysis (Matlab modal analysis) with 60 mode shapes only.

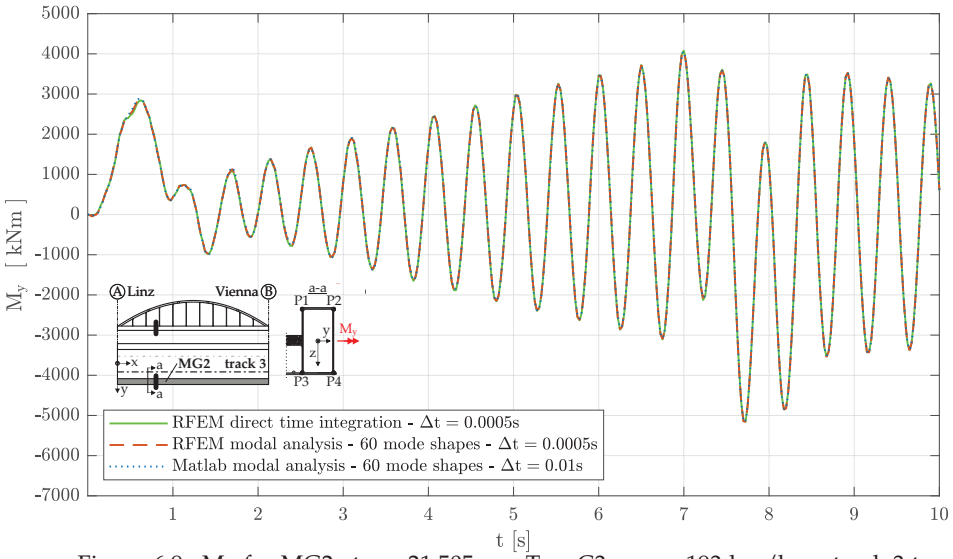

Figure 6.9.: M_y for MG2 at x = 21.505m— TypeC3 — v = 193 km/h on track 3 to Vienna— ζ_{EC} (Rayleigh) — comparison of RFEM and Matlab results

In general, the solution of the direct integration for the normal force N is approximated sufficiently by the two modal analysis options. However, the peak values are overestimated by both modal analysis calculations — see Figure 6.10.

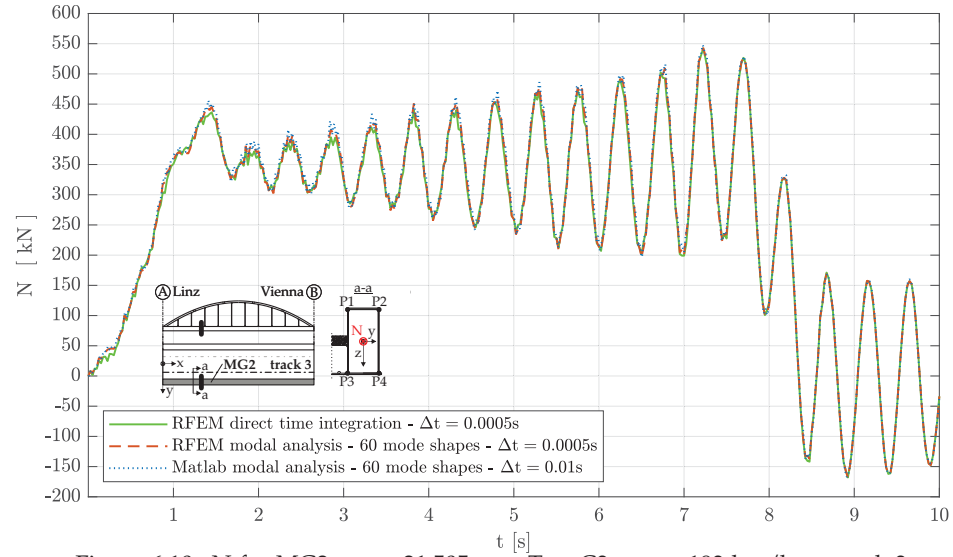

Figure 6.10.: N for MG2 at x = 21.505m — TypeC3 — v = 193 km/h on track 3 to Vienna— ζ_{EC} (Rayleigh) — comparison of RFEM and Matlab results

Furthermore, the bending moment M_z is approximated well by two modal analysis simulations, although some peak values — see in Figure 6.11 e.g. at t = 0.6 s — are not sufficiently represented.

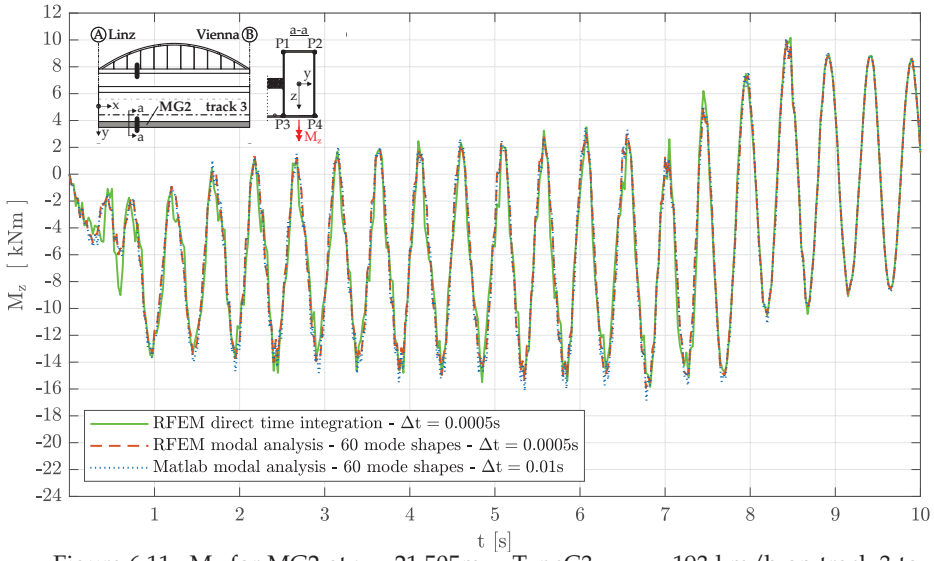

Figure 6.11.: M_z for MG2 at x = 21.505m— TypeC3 — v = 193 km/h on track 3 to Vienna— ζ_{EC} (Rayleigh) — comparison of RFEM and Matlab results

However, the before mentioned deviations of the modal analysis simulations with respect to the direct integration have little impact on the resulting normal stresses σ of MG2 at the points P1 to P4 — see Figure 6.12.

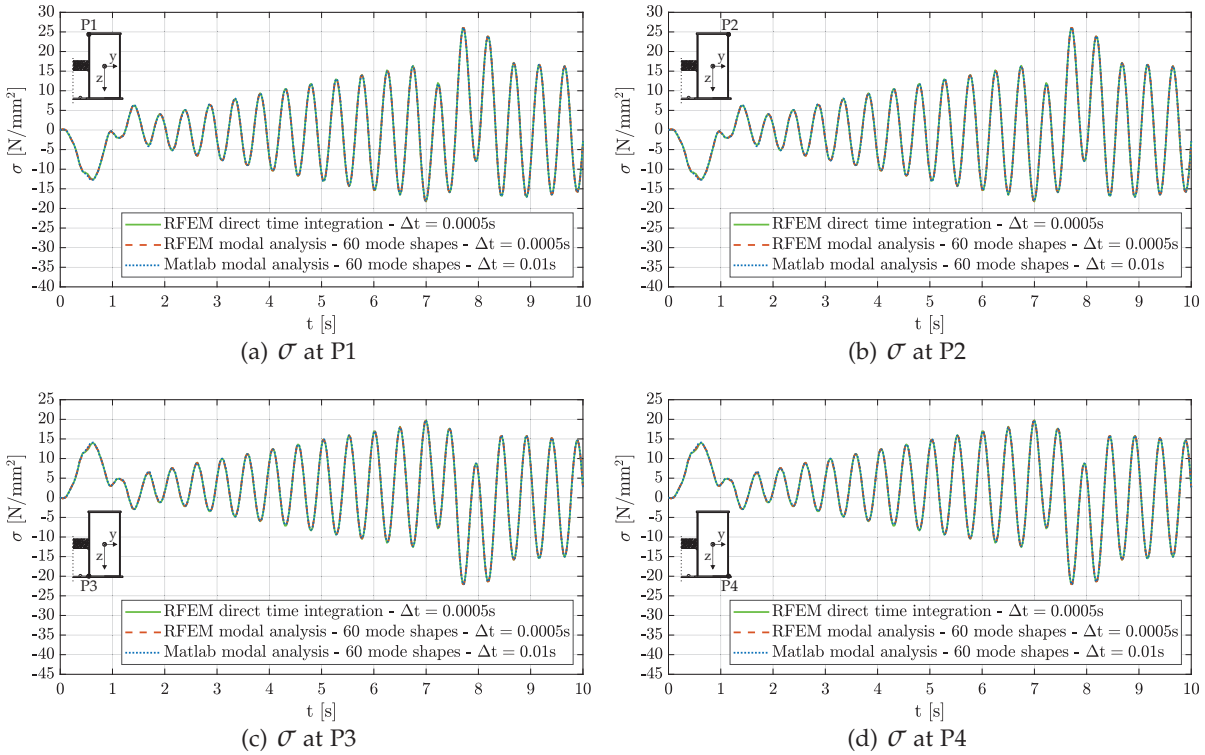

(a) σ at P1

(b) σ at P2

(c) σ at P3

(d) σ at P4

Figure 6.12.: σ for MG2 at x = 21.505m — TypeC3 — v = 193 km/h on track 3 to Vienna— ζ_{EC} (Rayleigh) — comparison of RFEM and Matlab results

Results at main girder 2 — x = 43.01 m (midspan)

Figure 6.13 presents the results of M_y for MG 2 at midspan (x = 43.01 m with cross section MG_c — see Figure 6.4). In general, the modal analysis simulations approximate the direct time integration very well again. However, some peak values (e.g. at 1 s) are overestimated.

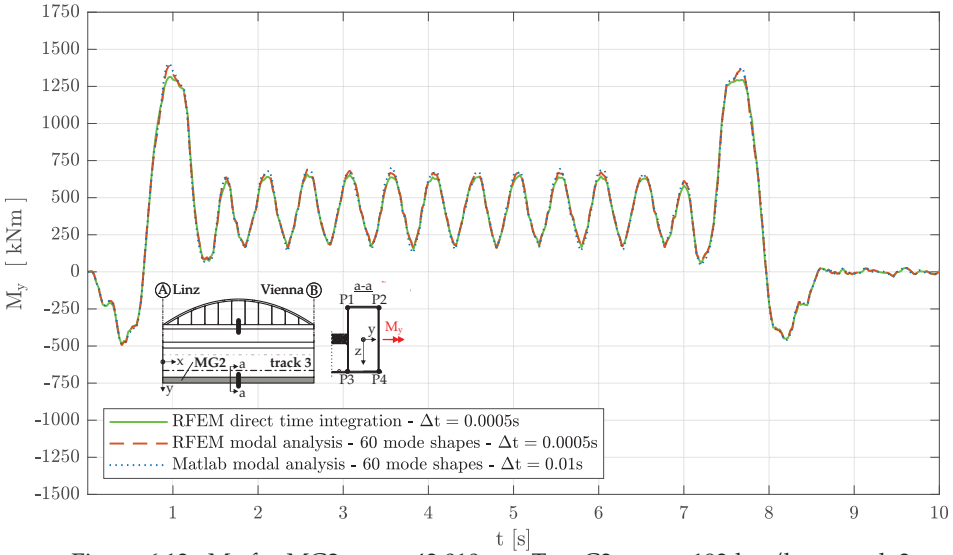

Figure 6.13.: M_y for MG2 at x = 43.010m— TypeC3 — v = 193 km/h on track 3 to Vienna— ζ_{EC} (Rayleigh) — comparison of RFEM and Matlab results

The solutions of the three computational approaches, with respect to the normal force N in Figure 6.14, result into very similar results. Furthermore, the bending moment M_z in Figure 6.15

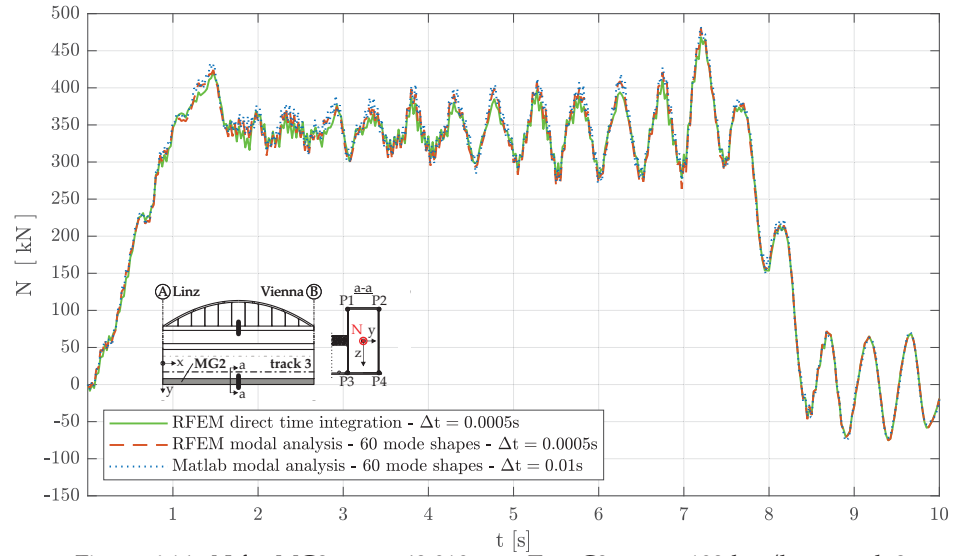

Figure 6.14.: N for MG2 at x = 43.010m — TypeC3 — v = 193 km/h on track 3 to Vienna— ζ_{EC} (Rayleigh) — comparison of RFEM and Matlab results

is approximated in similar quality like the one at the before discussed position x = 21.505 m — see Figure 6.11.

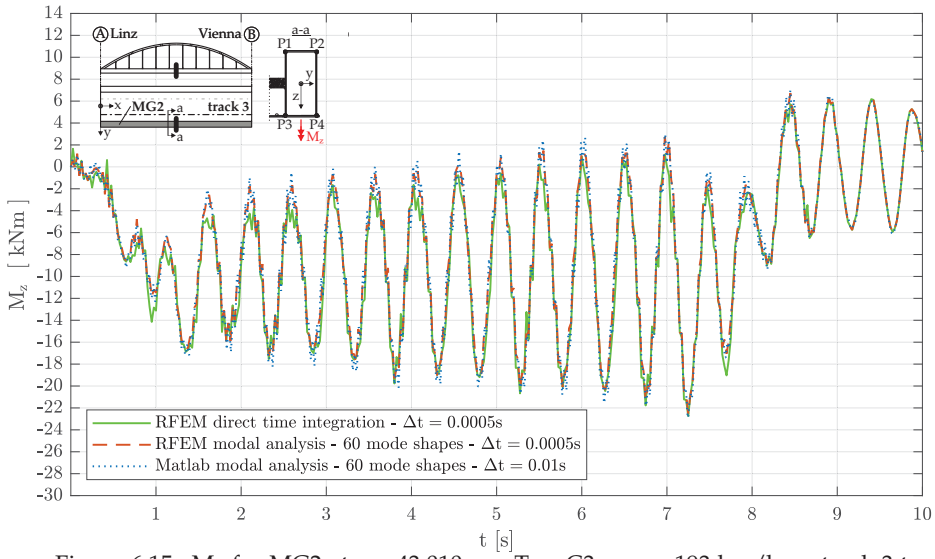

Figure 6.15.: M_z for MG2 at x = 43.010m— TypeC3 — v = 193 km/h on track 3 to Vienna— ζ_{EC} (Rayleigh) — comparison of RFEM and Matlab results

Again, the impacts of the before discussed deviations on the normal stresses σ are very limited for the points P1 to P4 on MG2 — see Figure 6.16. However, as the normal stresses σ are dominated by the effects due to the bending M_y, the peak values at t = 1 s are consequently overestimated.

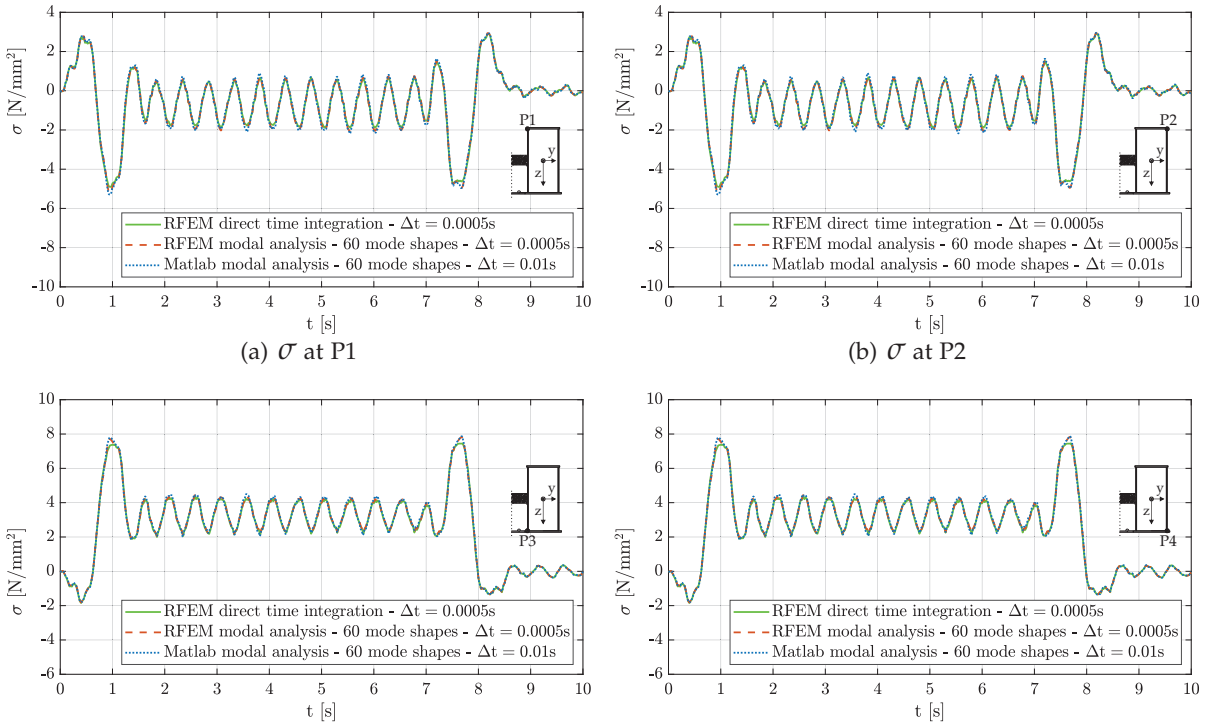

(a) σ at P1

(b) σ at P2

(c) σ at P3

(d) σ at P4

Figure 6.16.: σ for MG2 at x = 43.010m — TypeC3 — v = 193 km/h on track 3 to Vienna— ζ_{EC} (Rayleigh) — comparison of RFEM and Matlab results

Results at arch 2 — x = 21.505 m (quarter-point)

The bending moments M_y varying with time for arch 2 at position x = 21.505 m with cross section A_a — see Figure 6.4 — are illustrated in Figure 6.17. Again, all three simulation approaches lead to very similar results.

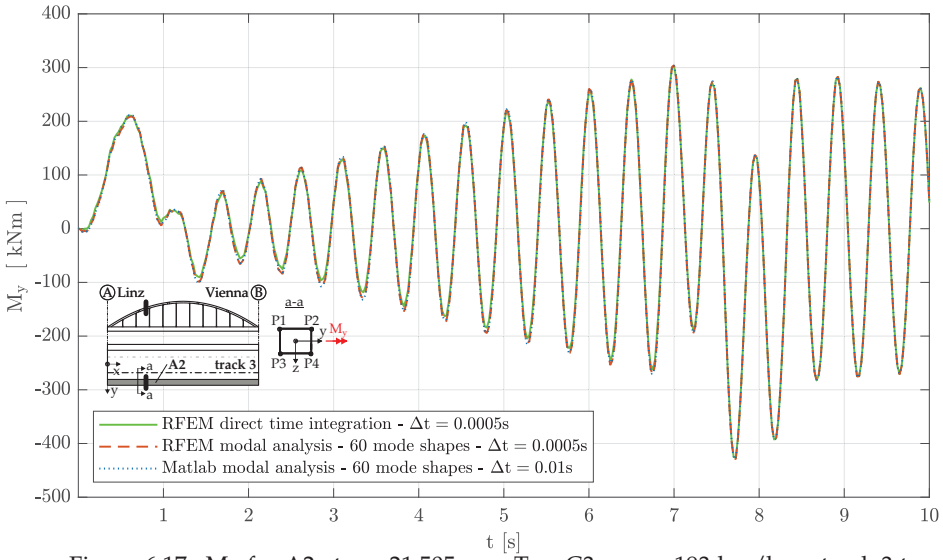

Figure 6.17.: M_y for A2 at x = 21.505m — TypeC3 — v = 193 km/h on track 3 to Vienna— ζ_{EC} (Rayleigh) — comparison of RFEM and Matlab results

The modal analysis variants are able to describe the solution for the normal force N of the direct time integration very well again, although the little osculations in the time range t = 2-6.5 s of Figure 6.18 differ slightly.

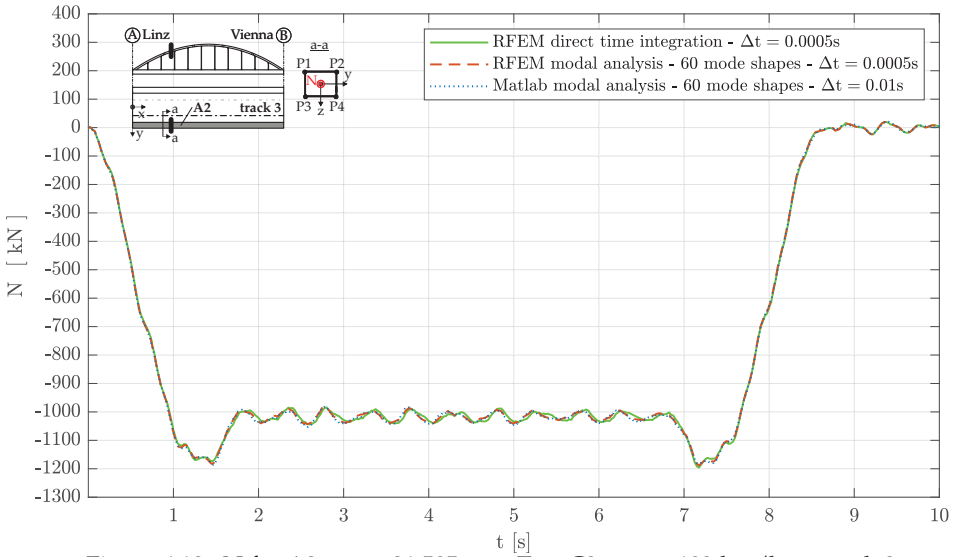

Figure 6.18.: N for A2 at x = 21.505m — TypeC3 — v = 193 km/h on track 3 to Vienna— ζ_{EC} (Rayleigh) — comparison of RFEM and Matlab results

The three computational approaches lead, regarding the bending moment M_z in Figure 6.19, to solutions, which deviate more, than the before discussed ones, from each other. Especially, the

two modal analysis approaches cause different results as well.

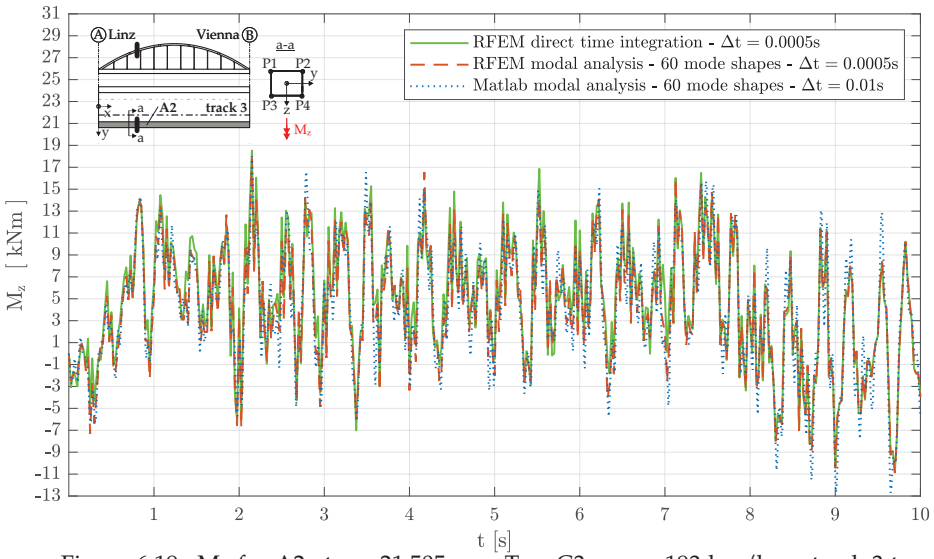

Figure 6.19.: M_z for A2 at x = 21.505m — TypeC3 — v = 193 km/h on track 3 to Vienna— ζ_{EC} (Rayleigh) — comparison of RFEM and Matlab results

However, the impact on the normal stresses σ are again very limited, as these are dominated by the normal force N and the bending moment M_y — see Figure 6.20.

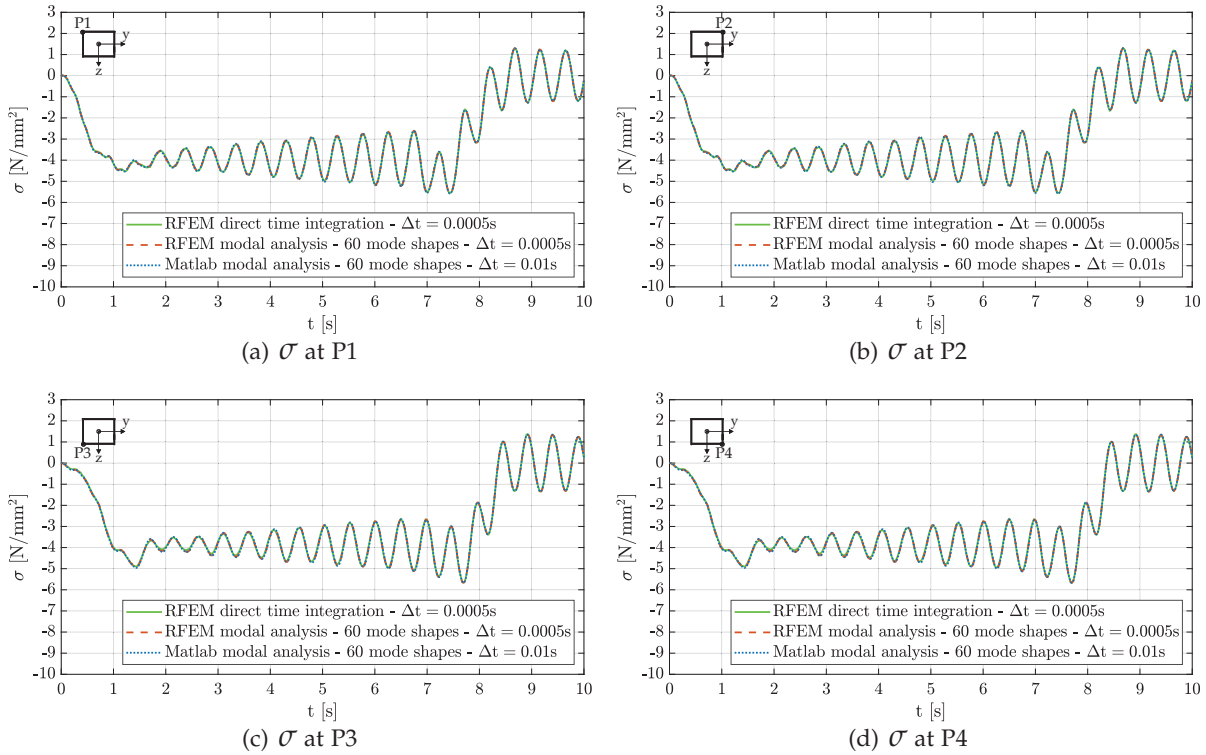

(a) σ at P1

(b) σ at P2

(c) σ at P3

(d) σ at P4

Figure 6.20.: σ for A2 at x = 21.505m — TypeC3 — v = 193 km/h on track 3 to Vienna— ζ_{EC} (Rayleigh) — comparison of RFEM and Matlab results

Results at arch 2 — x = 43.01 m (midspan)

In Figure 6.21 the bending moment M_y for arch 2 at midspan with cross section A_a — see Figure 6.4 — is shown. The 60 mode shapes, which were considered in the modal analysis approaches, are clearly not sufficient to estimate the reference solution of the direct time integration in the time range 1.5-7 s.

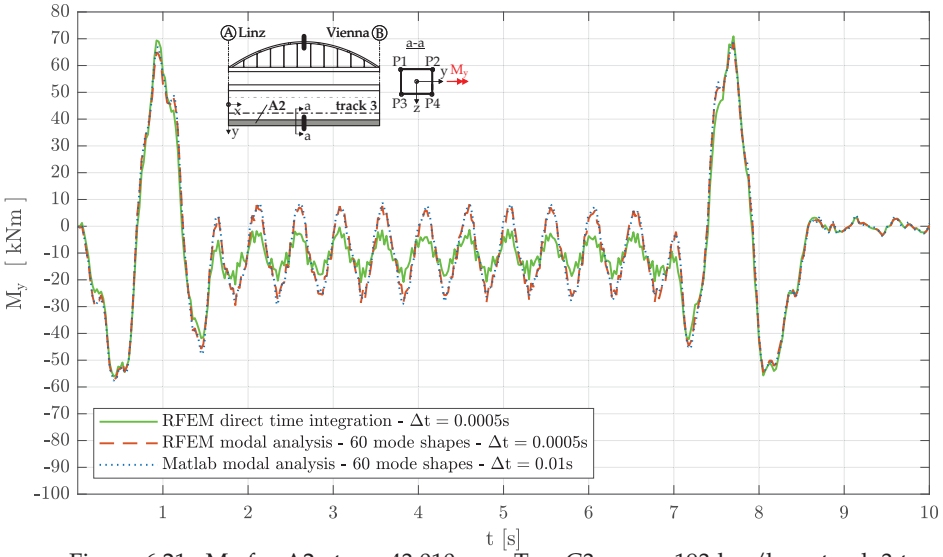

Figure 6.21.: M_y for A2 at x = 43.010m — TypeC3 — v = 193 km/h on track 3 to Vienna— ζ_{EC} (Rayleigh) — comparison of RFEM and Matlab results

On the other hand, the normal force N is approximated very well by both modal analysis approaches, as demonstrated in Figure 6.22.

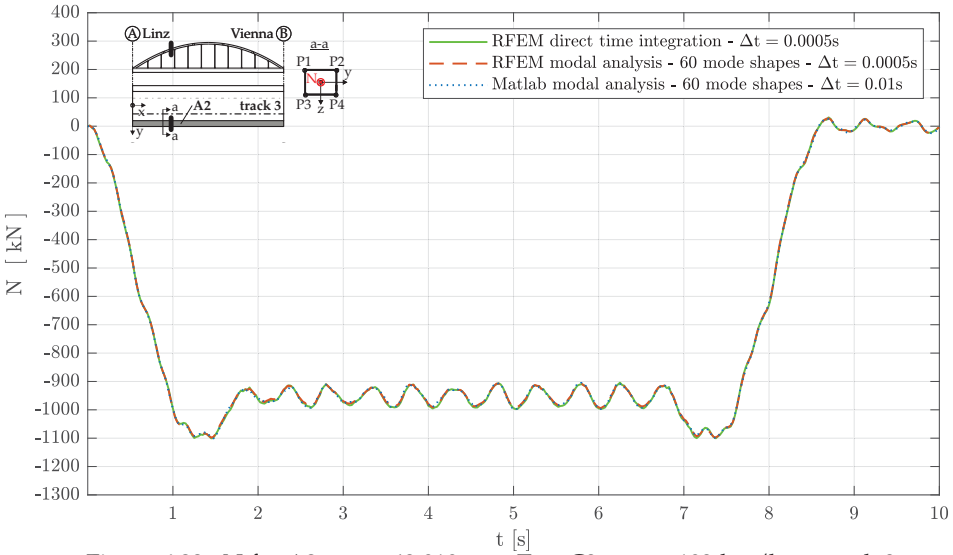

Figure 6.22.: N for A2 at x = 43.010m — TypeC3 — v = 193 km/h on track 3 to Vienna— ζ_{EC} (Rayleigh) — comparison of RFEM and Matlab results

Like at the position x = 21.505 m for arch 2, all three computational approaches lead with

respect to the bending moment M_z to different solutions — see Figure 6.23. However, the normal

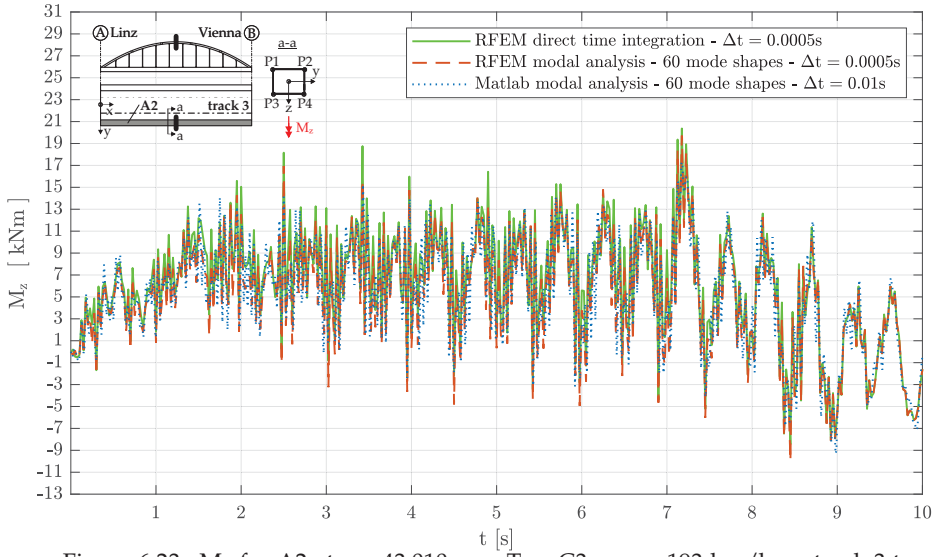

Figure 6.23.: M_z for A2 at x = 43.010m — TypeC3 — v = 193 km/h on track 3 to Vienna— ζ_{EC} (Rayleigh) — comparison of RFEM and Matlab results

stresses σ at midspan for arch 2 are clearly dominated by the normal force N and consequently the above discussed deviations do have a neglectable impact — see Figure 6.24.

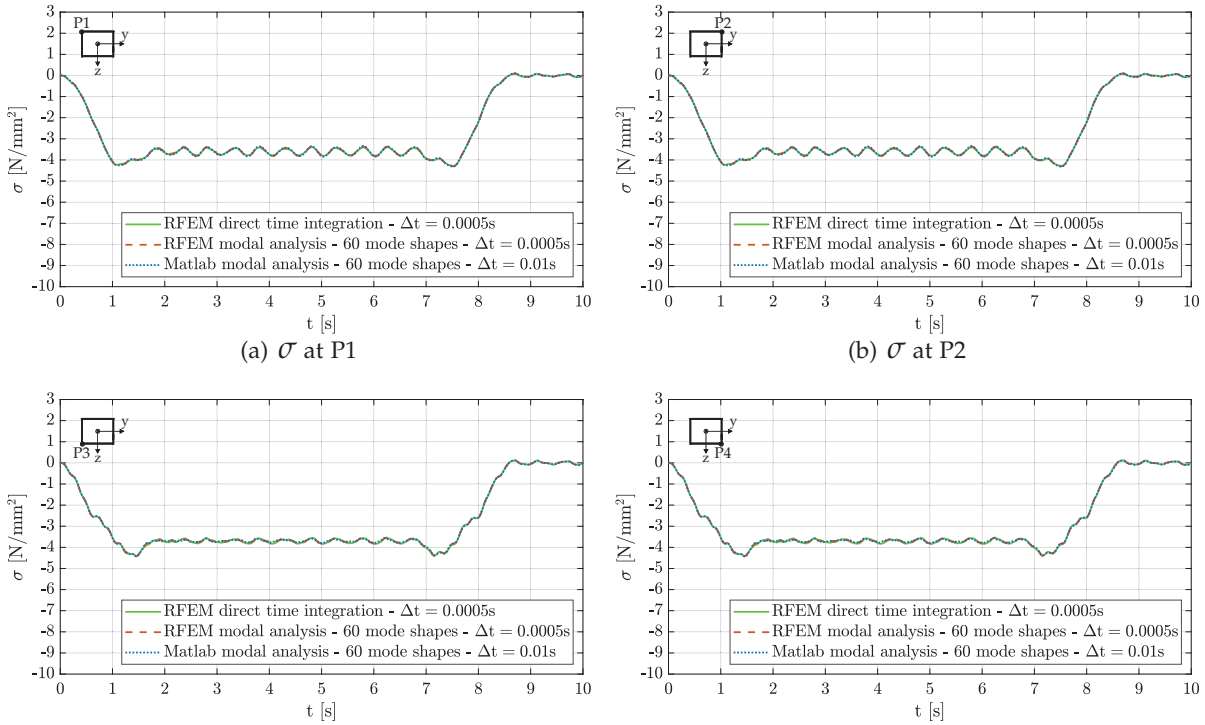

(a) σ at P1

(b) σ at P2

(c) σ at P3

(d) σ at P4

Figure 6.24.: σ for A2 at x = 43.010m — TypeC3 — v = 193 km/h on track 3 to Vienna— ζ_{EC} (Rayleigh) — comparison of RFEM and Matlab results

6.3.2. Accelerations

In this chapter, the three different computational concepts, with respect to the vertical bridge deck acceleration a, are compared to each other. Therefore, a single axle of 200 kN crosses the structure on track 3 in direction to Vienna with a constant speed of v = 187.68 km/h. All subsequently shown Figures are related to the vertical bridge deck acceleration in the center of track 3 at the position x = 21.329 m.
Figure 6.25 shows the results of the direct time integration method performed with RFEM. The loads for the dynamic calculation were placed according to the cross girder distance, hence, $\Delta l_P = e_{CG} = 2.607$ m — see Figure 6.6. Furthermore, different time steps Δt were considered, whereas the solution already converged for Δt = 0.0005 s. However, significant peak values, with no physical explanation, emerged. The maximum value of these peaks is reached when the axle load reaches x = 21.329 m, which is at about 0.41 s. Furthermore, the peaks appear each 0.05 s, which is equal to the time the single axle needs to travel between the cross girders $\Delta t_{\Delta l_P}$. In [48] similar problems regarding the numerical solution were reported and suspected, that the loading was modelled too rough, hence, Δl_P was chosen too big.

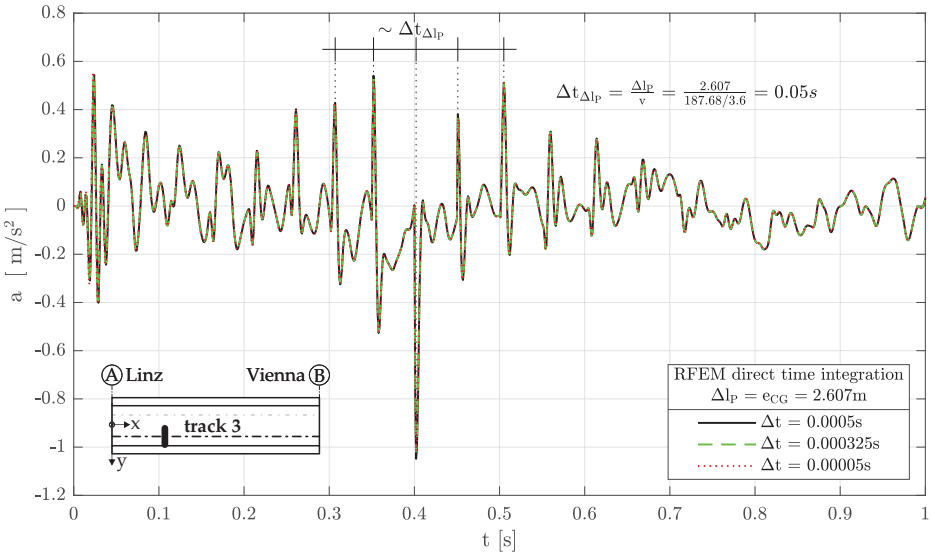

Figure 6.25.: Acceleration a at x = 21.329m on track 3 — single axle 200kN — v = 187.68 km/h on track 3 to Vienna — ζ_{EC} (Rayleigh) — RFEM direct time integration — distance of single forces $\Delta l_P = e_{CG} = 2.607$ m — variation of time steps Δt

Consequently, the number of single forces, which simulate the crossing of the single axle, was doubled, hence, the distance between the forces was set to $\Delta l_P = 1.303$ m. The results are illustrated in Figure 6.26. The amplitudes of the peaks were reduced, but the number of peaks was doubled.

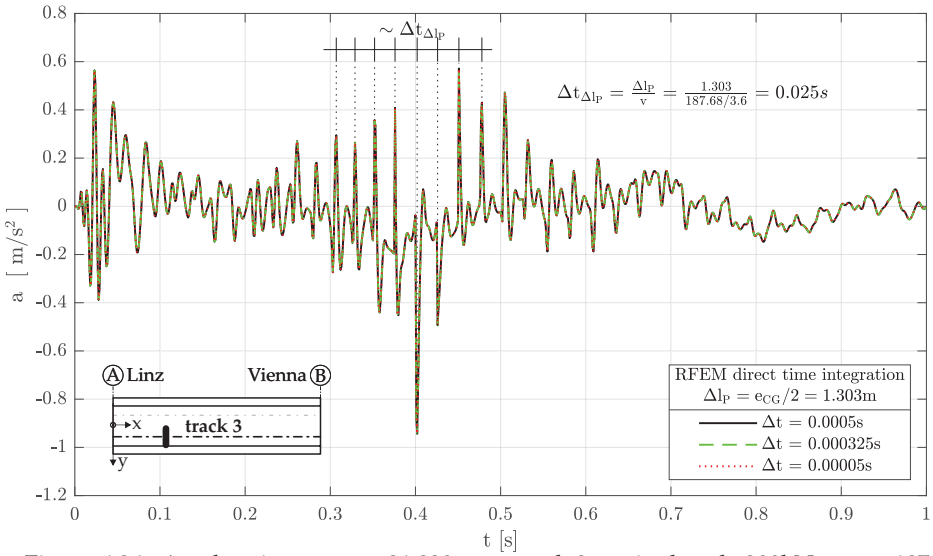

Figure 6.26.: Acceleration a at x = 21.329m on track 3 — single axle 200kN — v = 187.68 km/h on track 3 to Vienna — ζ_{EC} (Rayleigh) — RFEM direct time integration — distance of single forces $\Delta l_P = e_{CG}/2 = 1.303$ m — variation of time steps Δt

However, performing the modal analysis using RFEM leads for different numbers of considered mode shapes to the results illustrated in Figure 6.27 and converges, including the peaks, to the results of the variant using direct time integration in Figure 6.26. On the other hand,

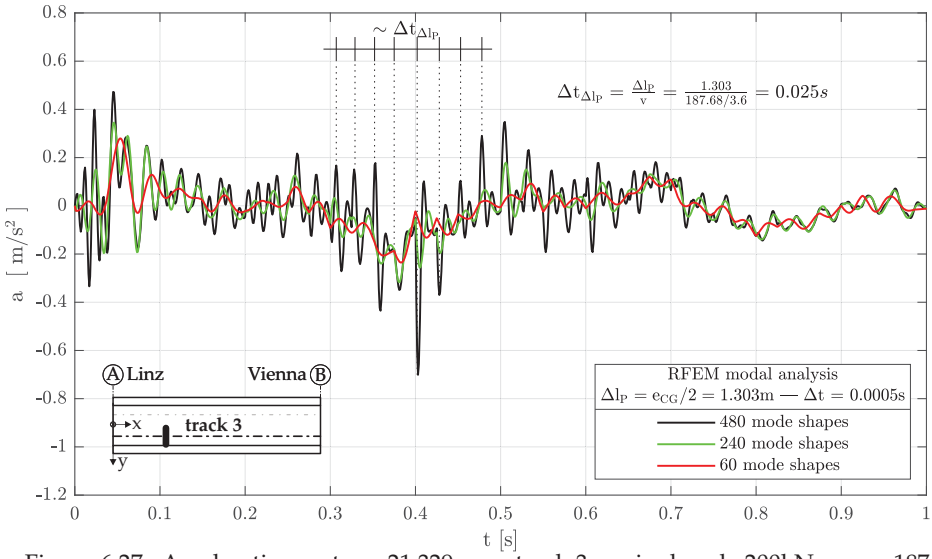

Figure 6.27.: Acceleration a at x = 21.329m on track 3 — single axle 200kN — v = 187.68 km/h on track 3 to Vienna — ζ_{EC} (Rayleigh) — RFEM modal analysis — distance of single forces $\Delta l_P = e_{CG}/2 = 1.303m$ — variation of numbers of considered mode shapes

performing the simulation with the analytical approach, using Matlab, leads for different numbers of considered mode shapes to the results in Figure 6.28. First, 60 mode shapes, like for the calculation of the internal forces in Chapter 6.3.1, were considered — see Figure 6.28(a). Each of these 60 mode shapes was approximated with 10, 100 and 150 sine functions, whereas the solution converged with 100 sine functions. This procedure was repeated for 240, 480 and 960 mode shapes — see Figure 6.28.

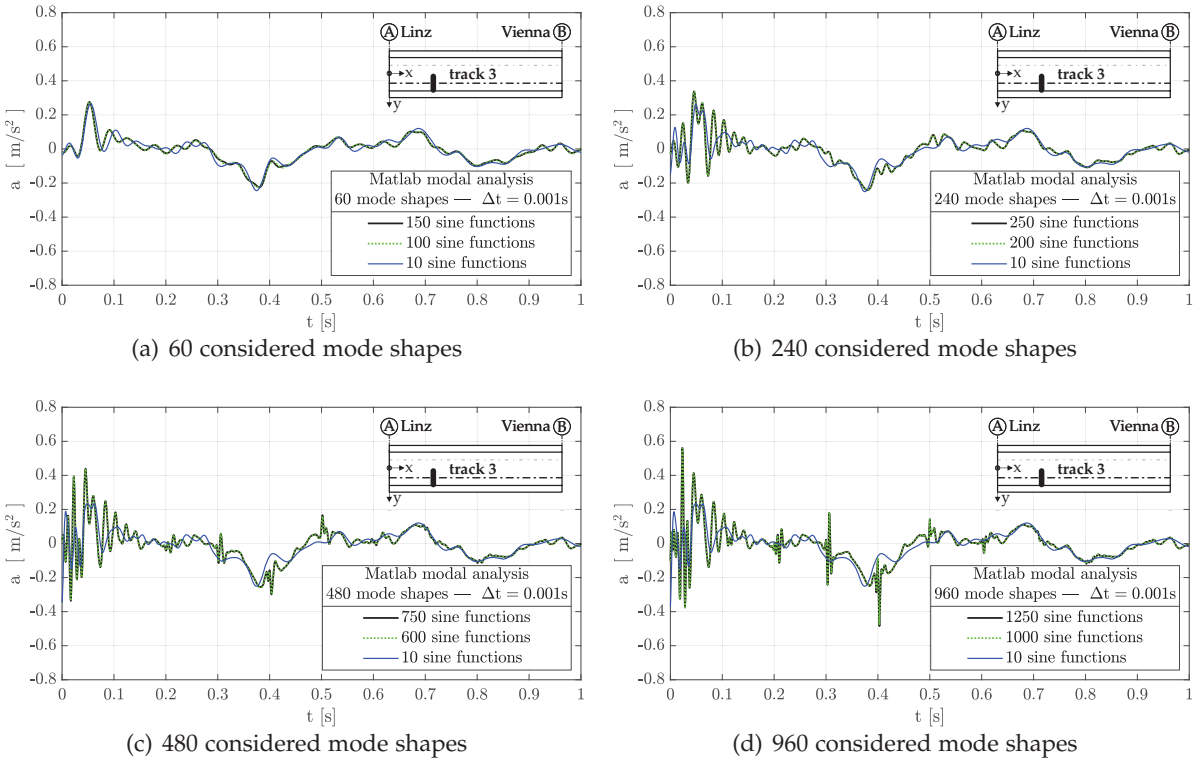

(a) 60 considered mode shapes

(b) 240 considered mode shapes

(c) 480 considered mode shapes

(d) 960 considered mode shapes

Figure 6.28.: Acceleration a at x = 21.329m on track 3 — single axle 200kN — v = 187.68 km/h on track 3 to Vienna — ζ_{EC} (Rayleigh) — Modal analysis with Matlab — variation of numbers of considered mode shapes — numbers of sine functions needed for converged solution

The variant of 960 mode shapes converged with 1000 sine functions, which was subsequently — see Figure 6.29 — compared to the solution of the direct time integration using RFEM of Figure 6.26. The two methods produce the same results for the first 0.1 s only — see Figure 6.29. Although, the results produced by the method using the analytical approach seemed much more trustworthy than the numerical ones obtained with RFEM, as the latter strongly depend on the load approximation governed by the number of considered point forces, hence, the distance Δl_P, an additional study was performed.
Therefore, a fourth computational approach according to Chapter 3.5.2 on page 72 was considered. Hence, the single degree of freedom systems, which result due to the modal analysis, were solved so far analytically with Matlab and numerically with RFEM. This fourth procedure solves the single degree of freedom systems now numerically in Matlab as well. Figure 6.30 demonstrates the results due to the numerical and analytical approach in Matlab, which confirms the latter concept definitely.
Therefore, the analytical approach using Matlab was subsequently applied for the traffic safety design check.

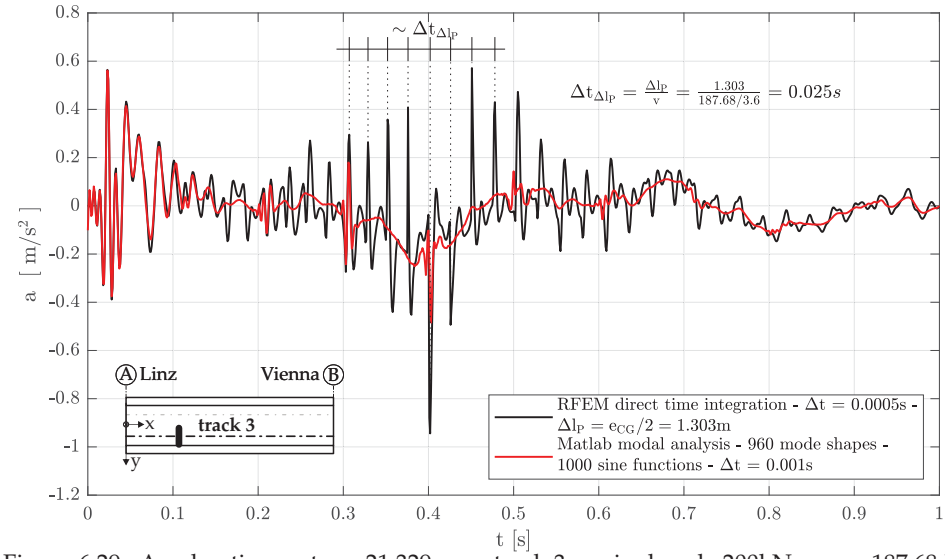

Figure 6.29.: Acceleration a at x = 21.329m on track 3 — single axle 200kN — v = 187.68 km/h on track 3 to Vienna — ζ_{EC} (Rayleigh) — RFEM direct integration vs. Matlab modal analysis

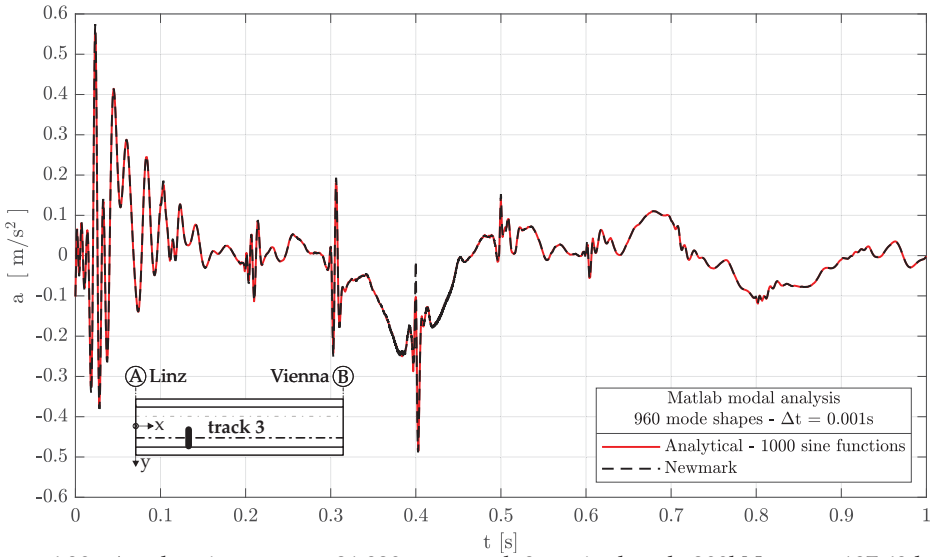

Figure 6.30.: Acceleration a at x = 21.329m on track 3 — single axle 200kN — v = 187.68 km/h on track 3 to Vienna — ζ_{EC} (Rayleigh) — Matlab modal analysis — Analytical solution vs. Newmark

6.4. Traffic safety design check — acceleration criterion

The traffic safety design check was performed for the ten HSLM-A trains — see Figure 2.20 — passing on track 3 towards Vienna with speeds v ranging from 50 to 300 km/h. The absolute maximum vertical bridge deck acceleration for all ten HSLM-A trains $|a_{HSLM-A,max}|$ was calculated at 403 points along the axis of track 3 and is illustrated in Figure 6.31. Additionally, the traffic safety criterion for new structures with direct fastened track $|a_{max}| = 5.0$ m/s^2 is plotted. The structure fulfills the criterion except at the bearings. This may result as the transition zone from open track to structure was, as a conservative approach, not modelled. However, Figure 6.32 shows for the position x = 21.329 m on track 3, which is close to the quarter point, the results for the speed range v = 50-300 km/h. Besides the envelope of all ten HSLM-A trains, the individual results for the trains HSLM-A2, HSLM-A7, HSLM-A8 and HSLM-A9 are plotted

as well. Furthermore, in Table 6.1 the critical speeds of these four trains, the train car lengths L_D and the corresponding excitation frequencies n_{L_D} are shown. The latter are all very similar to the structure's first bending frequency — see Figure 6.7(b) — and consequently cause resonance.

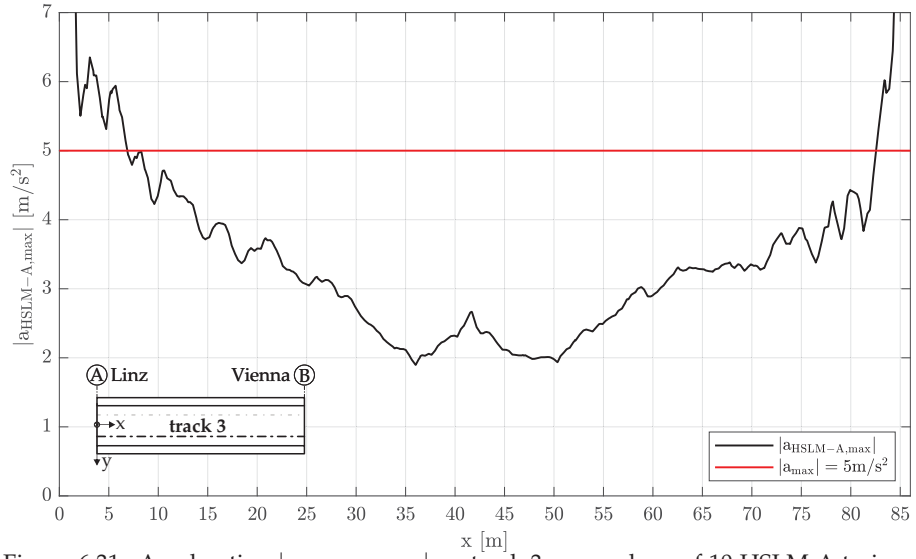

Figure 6.31.: Acceleration $|a_{HSLM-A,max}|$ on track 3 — envelope of 10 HSLM-A trains and speed range 50-300 km/h on track 3 — ζ_{EC} (Rayleigh) — Matlab modal analysis

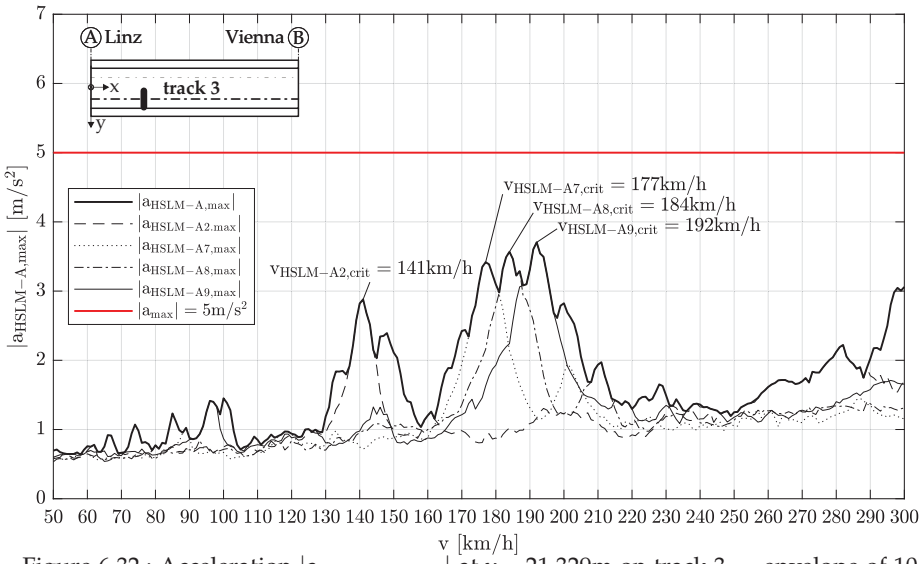

Figure 6.32.: Acceleration $|a_{HSLM-A,max}|$ at x = 21.329m on track 3 — envelope of 10 HSLM-A trains on track 3 — ζ_{EC} (Rayleigh) — Matlab modal analysis

HSLM-i	$v_{HSLM-i,crit}$ [km/h]	L_D [m]	$n_{L_D} = \frac{v_{HSLM-i,crit}}{3.6\ L_D}$ [Hz]
A9	192	26	2.05
A8	184	25	2.04
A7	177	24	2.05
A2	141	19	2.06

Table 6.1.: Critical speeds and excitation frequency of specific HSLM-A trains

6.5. Fatigue design check — conventional static approach

In this chapter, the static equivalent constant amplitude stress range $\Delta\sigma_{E,2}$ is calculated, using two options like in the case of the single-span bridges in Chapter 5.
First, the method using the load model LM71 and the damage equivalent factor λ is applied at two cross sections on the main girder and at two cross sections on the arch.
Subsequently, the more accurate crossing of the trains TypeC1 to TypeC8 (traffic mix TM1) is simulated statically for 100 years in service and the resulting stress range spectra evaluated, using *Miner's rule*, at the S-N curve, which is again iterated until $D_{stat} = 1.0$ results. The resulting level of the S-N curve provides consequently the static equivalent constant amplitude stress range $\Delta\sigma_{E,2}$, leading to a utilisation factor of 1.0 for the fatigue design verification.

6.5.1. $\Delta\sigma_{E,2}$ based on load model LM71 and stress range

According to Equation (2.27) the static equivalent constant amplitude stress range $\Delta\sigma_{E,2}$ becomes

$$\Delta\sigma_{E,2} = \lambda\ \Phi_2\ \Delta\sigma_{LM71} \tag{6.1}$$

whereas $\Delta\sigma_{LM71}$ is calculated with the maximum and minimum normal stress due to load model LM71

$$\Delta\sigma_{LM71} = |\Delta\sigma_{LM71,max} - \Delta\sigma_{LM71,min}| \tag{6.2}$$

The damage equivalent factor is

$$\lambda = \lambda_1\ \lambda_2\ \lambda_3\ \lambda_4 \leq\ \lambda_{max} \tag{6.3}$$

Rewriting Equation (2.16) for the 'dynamic' factor Φ_2 and carefully maintained track, leads to

$$\Phi_2 = \frac{1.44}{\sqrt{L_\Phi} - 0.2} + 0.82 \tag{6.4}$$

As subsequently the main girder and the arch are studied, the determinant length L_Φ is set to half the span length, according to ÖNORM EN 1991-2, Table 6.2 [43].
On the other hand, the critical length of the influence line, which is needed for the factor λ_1, is regulated in ÖNORM EN 1993-2, 9.5.2 (2) [46], but no guideline is provided for arch bridges. Furthermore, in [21] is stated to use 0.4 times the span length for the critical length for both, arch and main girder with respect to the bending moment. However, the following assumptions regarding the critical length were made and subsequently used for arch and main girder. In general, the damage equivalent factor λ_1 was derived from single-span bridges at the midspan cross section. The bending influence line has the same shape as the stress influence line for these structures. In case the stress influence line depends on more than one internal force influence line, the stress influence line shall be used in order to determine the critical length. Therefore, in this doctoral thesis, the length associated to the absolute maximum stress due to a single load crossing the bridge on one track, as this one produces the maximum damage D_{stat}, is used — see Figure 6.33(c) for point P4. This means, that the critical length L_{λ_1} is the distance between

the zero points of the influence line of the total stresses ($\sigma_N + \sigma_{M_y} + \sigma_{M_z}$) in each point (P1 to P4) of the analysed cross section.

Subsequently, the above described concept is applied on main girder 2 at x = 20.85 m and at x = 43.01 m. Furthermore, the cross sections at x = 0 m, x = 23.46 m and x = 43.01 m for arch 2 are investigated. The procedure is for all five cross sections the same and is described, in an exemplary manner, for main girder 2 at x = 20.85 m. Figure 6.33 shows the influence lines for the main girder 2 at the location x = 20.85 m due to the crossing of a single axle load of 1 kN on track 4 and track 3, respectively. Figure 6.33(a) shows the influence lines for the internal forces M_y, M_z and N due to loads on track 4, whereas Figure 6.33(b) shows the ones for loads on track 3. Next, Figure 6.33(c) considers again the loads on track 4 and illustrates the resulting influence lines for the total normal stresses at the points P1 to P4 of the cross section MG2. In Figure 6.33(d) the stress influence lines due to loads on track 3 are plotted.
In Table 6.2 the determination of the static equivalent constant amplitude stress range $\Delta\sigma_{E,2}$ is summarized for each point P1 to P4 on the cross section. Subsequently, a few comments are made, in an exemplary manner, regarding the main steps for point P1. Hence, for point P1 the load model LM71 was first positioned twice on track 4 in the most unfavourable way on the influence line P1 of Figure 6.33(c). Once in order to determine the maximum normal stress $\Delta\sigma_{\mathrm{p,max}} = 19.8\ \mathrm{N/mm^2}$ and the second time to determine the minimum normal stress $\Delta\sigma_{\mathrm{p,min}} = -22.7\ \mathrm{N/mm^2}$, which together lead to $|\Delta\sigma_{\mathrm{p}}| = 42.5\ \mathrm{N/mm^2}$ for loads on track 4. The same procedure was performed for track 3 leading to $|\Delta\sigma_{\mathrm{p}}| = 60.6\ \mathrm{N/mm^2}$. Furthermore, the critical lengths L_{λ_1} were extracted for P1 from Figure 6.33(c) and 6.33(d). Additionally, it was assumed that there is no traffic simultaneously on track 3 and track 4, hence, n for the calculation of λ_4 is set to zero — see Equation (2.30). Finally, after evaluating Equation (6.1) for point P1, the static equivalent constant amplitude stress range $\Delta\sigma_{\mathrm{E,2,n=0}}$ results to $41.9\ \mathrm{N/mm^2}$.
On the following pages, the results for main girder 2 and arch 2 are presented.

Results at main girder 2 — x = 20.85 m (quarter-point)

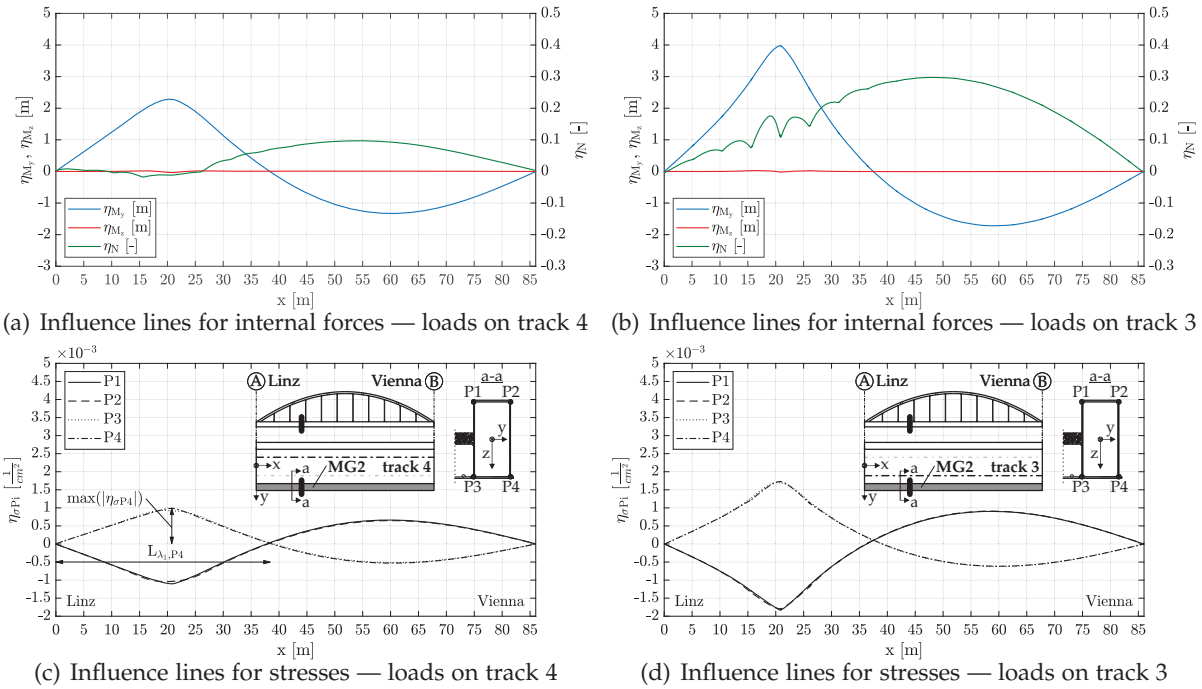

(a) Influence lines for internal forces — loads on track 4 (b) Influence lines for internal forces — loads on track 3

(c) Influence lines for stresses — loads on track 4 (d) Influence lines for stresses — loads on track 3

Figure 6.33.: Influence lines for axle load of 1 kN on one track — cross section MG2 at x = 20.85m

Point	P1		P2		P3		P4	
Track	4	3	4	3	4	3	4	3
$\Delta\sigma_{p,max}$ [N/mm^2]	19.8	27.8	19.2	28.1	20.7	33.3	20.6	33.0
$\Delta\sigma_{p,min}$ [N/mm^2]	-22.7	-32.8	-22.7	-33.1	-15.0	-18.3	-15.6	-18.1
$\lvert\Delta\sigma_p\rvert$ [N/mm^2]	**42.5**	**60.6**	**42.0**	**61.2**	**35.7**	**51.6**	**36.2**	**51.1**
$\Delta\sigma_1/\Delta\sigma_{1+2} = \lvert\Delta\sigma_p\rvert_{track3}/\lvert\Delta\sigma_p\rvert_{track3+track4}$ [-]	0.588		0.593		0.591		0.585	
L_{λ_1} [m]	37.76	36.29	38.02	36.17	39.08	39.02	38.74	39.17
λ_1 [-]	0.640	0.640	0.640	0.640	0.640	0.640	0.640	0.640
λ_2 [-]	1							
λ_3 [-]	1							
λ_4 [-]	0.719		0.719		0.719		0.719	
$\lambda_{4,n=0}$ [-]	0.607		0.610		0.609		0.605	
λ_{max} [-]	1.4							
λ [-]	0.460	0.460	0.460	0.460	0.460	0.460	0.460	0.460
$\lambda_{n=0}$ [-]	**0.388**	**0.388**	**0.390**	**0.390**	**0.390**	**0.390**	**0.390**	**0.387**
L_Φ [-]	43.01							
Φ_2 [-]	**1.046**							
$\Delta\sigma_{E,2}$ [N/mm^2]	49.6		49.7		42.0		42.0	
$\Delta\sigma_{E,2,n=0}$ [N/mm^2]	**41.9**		**42.1**		**35.6**		**35.3**	

Table 6.2.: Equivalent constant amplitude stress range $\Delta\sigma_{E,2}$ due to LM71 — cross section MG2 at x = 20.85m

Results at main girder 2 — x = 43.01 m (midspan)

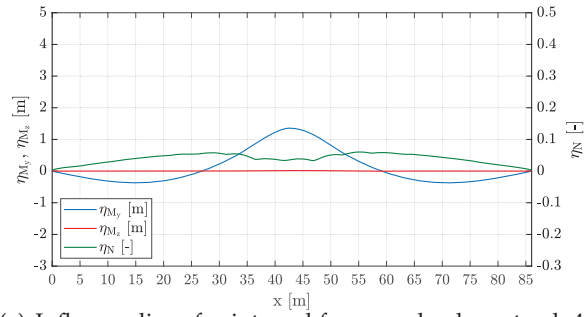

(a) Influence lines for internal forces — loads on track 4

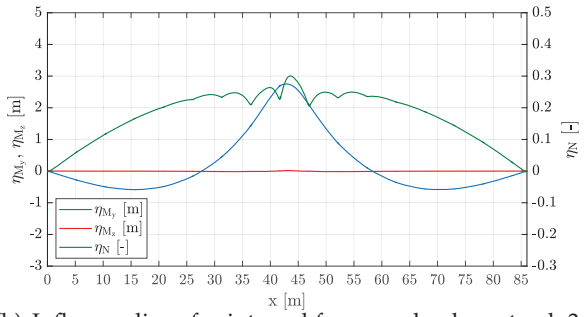

(b) Influence lines for internal forces — loads on track 3

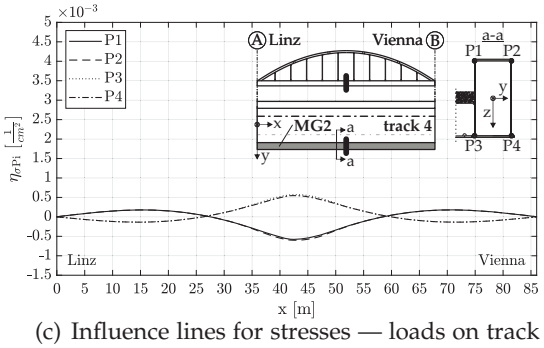

(c) Influence lines for stresses — loads on track 4

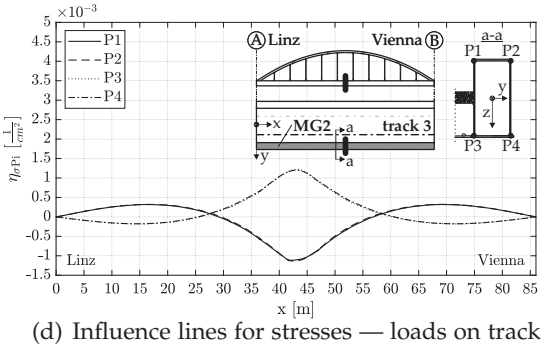

(d) Influence lines for stresses — loads on track 3

Figure 6.34.: Influence lines for axle load of 1 kN on one track — cross section MG2 at x = 43.01m

Point	P1		P2		P3		P4	
Track	4	3	4	3	4	3	4	3
$\Delta\sigma_{p,max}$ [N/mm^2]	6.0	11.1	5.9	11.4	10.7	20.5	10.2	20.9
$\Delta\sigma_{p,min}$ [N/mm^2]	-10.2	-17.5	-10.7	-17.2	-4.2	-5.7	-4.3	-5.5
$\mathbf{\lvert\Delta\sigma_p\rvert}$ **[N/mm^2]**	**16.2**	**28.6**	**16.6**	**28.6**	**14.9**	**26.2**	**14.5**	**26.4**
$\Delta\sigma_1/\Delta\sigma_{1+2} = \lvert\Delta\sigma_p\rvert_{track3}/\lvert\Delta\sigma_p\rvert_{track3+track4}$ [-]	0.638		0.632		0.637		0.646	
L_{λ_1} [m]	30.89	27.68	30.89	26.91	33.88	34.39	33.76	35.15
λ_1 [-]	0.648	0.655	0.648	0.656	0.642	0.641	0.642	0.640
λ_2 [-]	1							
λ_3 [-]	1							
λ_4 [-]	0.739		0.736		0.739		0.743	
$\lambda_{4,n=0}$ [-]	0.646		0.641		0.645		0.652	
λ_{max} [-]	1.4							
λ [-]	0.479	0.484	0.477	0.483	0.474	0.474	0.477	0.475
$\mathbf{\lambda_{n=0}}$ **[-]**	**0.419**	**0.423**	**0.415**	**0.420**	**0.414**	**0.413**	**0.419**	**0.417**
$\boldsymbol{L_\Phi}$ [-]	43.01							
$\mathbf{\Phi_2}$ [-]	**1.046**							
$\Delta\sigma_{E,2}$ [N/mm^2]	22.6		22.8		20.4		20.4	
$\mathbf{\Delta\sigma_{E,2,n=0}}$ **[N/mm^2]**	**19.8**		**19.8**		**17.8**		**17.9**	

Table 6.3.: Equivalent constant amplitude stress range $\Delta\sigma_{E,2}$ due to LM71 — cross section MG2 at x = 43.01m

Results at arch 2 — x = 0 m (bearing)

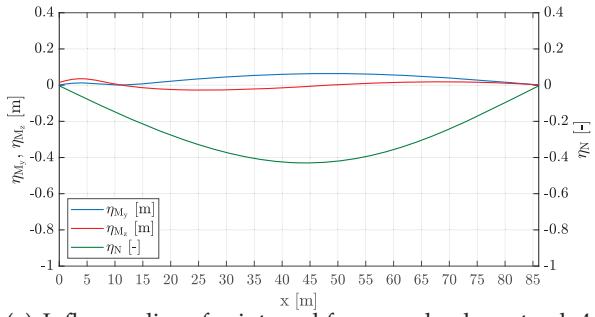

(a) Influence lines for internal forces — loads on track 4

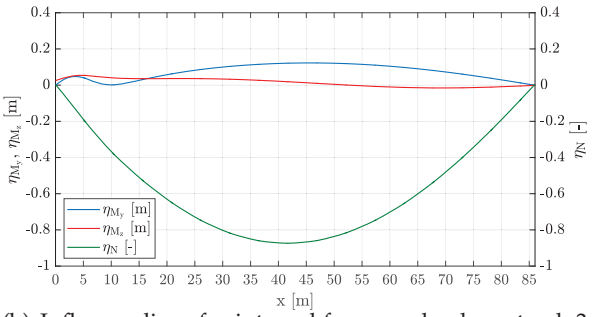

(b) Influence lines for internal forces — loads on track 3

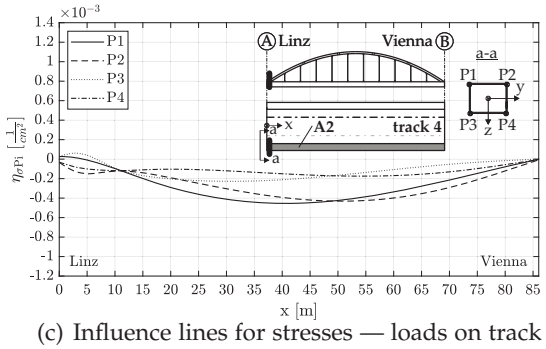

(c) Influence lines for stresses — loads on track 4

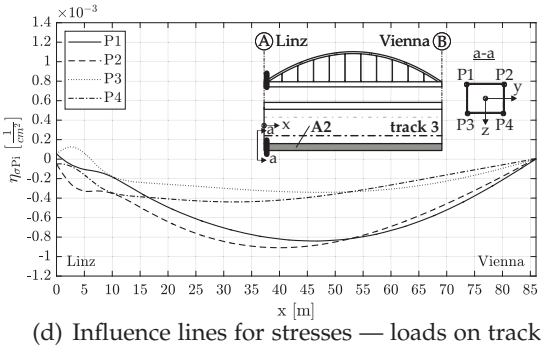

(d) Influence lines for stresses — loads on track 3

Figure 6.35.: Influence lines for axle load of 1 kN on one track — cross section A2 at x = 0m

Point	P1		P2		P3		P4	
Track	4	3	4	3	4	3	4	3
$\Delta\sigma_{p,max}$ [N/mm^2]	0.2	0.1	0.0	0.0	0.5	0.9	0.0	0.0
$\Delta\sigma_{p,min}$ [N/mm^2]	-20.6	-40.2	-20.5	-44.7	-9.6	-17.6	-9.2	-21.9
$\lvert\Delta\sigma_p\rvert$ [N/mm^2]	**20.7**	**40.4**	**20.5**	**44.7**	**10.1**	**18.5**	**9.2**	**21.9**
$\Delta\sigma_1/\Delta\sigma_{1+2} = \lvert\Delta\sigma_p\rvert_{track3}/\lvert\Delta\sigma_p\rvert_{track3+track4}$ [-]	0.660		0.685		0.648		0.703	
L_{λ_1} [m]	81.68	84.91	86.02	86.02	79.42	79.92	86.02	86.02
λ_1 [-]	0.610	0.610	0.610	0.610	0.611	0.610	0.610	0.610
λ_2 [-]	1							
λ_3 [-]	1							
λ_4 [-]	0.750		0.763		0.744		0.772	
$\lambda_{4,n=0}$ [-]	0.665		0.688		0.654		0.705	
λ_{max} [-]	1.4							
λ [-]	0.458	0.458	0.465	0.465	0.454	0.454	0.471	0.471
$\lambda_{n=0}$ [-]	**0.406**	**0.406**	**0.420**	**0.420**	**0.399**	**0.399**	**0.430**	**0.430**
L_Φ [-]	43.01							
Φ_2 [-]	**1.046**							
$\Delta\sigma_{E,2}$ [N/mm^2]	29.3		31.8		13.6		15.3	
$\Delta\sigma_{E,2,n=0}$ [N/mm^2]	**25.9**		**28.7**		**11.9**		**14.0**	

Table 6.4.: Equivalent constant amplitude stress range $\Delta\sigma_{E,2}$ due to LM71 — cross section A2 at x = 0m

Results at arch 2 — x = 23.46 m (quarter-point)

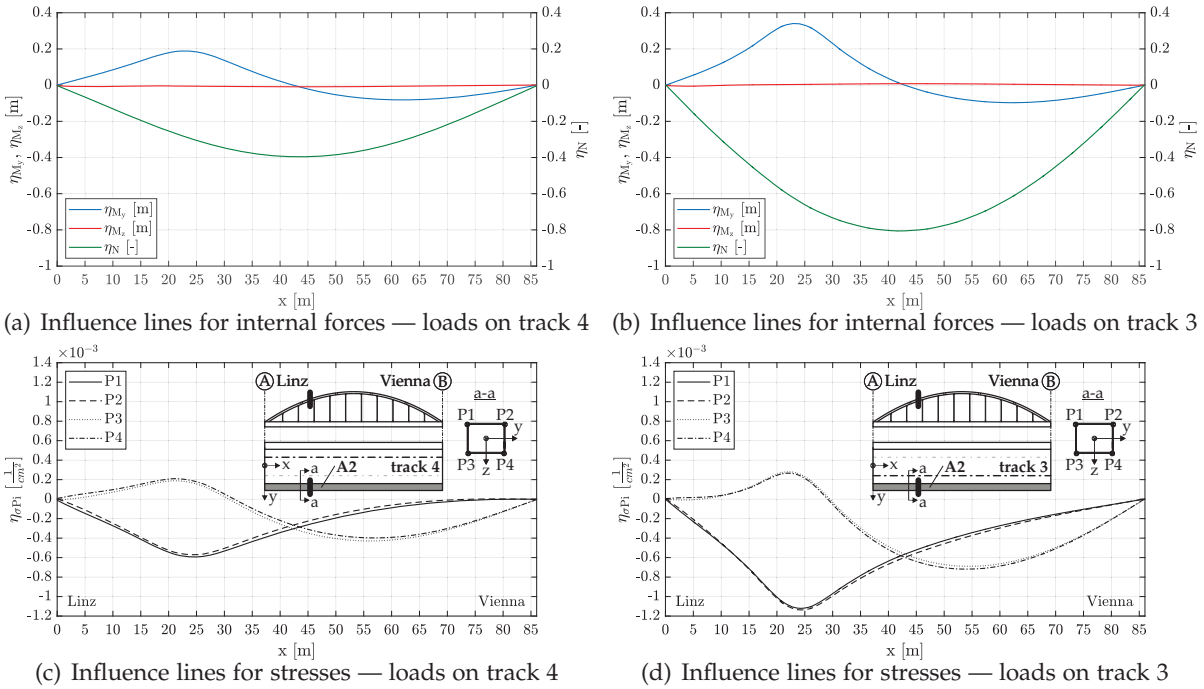

(a) Influence lines for internal forces — loads on track 4

(b) Influence lines for internal forces — loads on track 3

(c) Influence lines for stresses — loads on track 4

(d) Influence lines for stresses — loads on track 3

Figure 6.36.: Influence lines for axle load of 1 kN on one track — cross section A2 at x = 23.46m

Point	P1		P2		P3		P4	
Track	4	3	4	3	4	3	4	3
$\Delta\sigma_{p,max}$ [N/mm^2]	0.0	0.0	0.0	0.0	3.2	3.9	4.0	3.8
$\Delta\sigma_{p,min}$ [N/mm^2]	-19.2	-37.5	-17.4	-38.5	-14.4	-24.0	-13.2	-25.0
$\mathbf{\lvert\Delta\sigma_p\rvert}$ **[N/mm^2]**	**19.2**	**37.5**	**17.4**	**38.5**	**17.6**	**27.9**	**17.2**	**28.8**
$\Delta\sigma_1/\Delta\sigma_{1+2} = \lvert\Delta\sigma_p\rvert_{track3}/\lvert\Delta\sigma_p\rvert_{track3+track4}$ [-]	0.662		0.689		0.613		0.627	
L_{λ_1} [m]	86.02	86.02	75.20	86.02	55.27	56.58	54.30	56.81
λ_1 [-]	0.610	0.610	0.615	0.610	0.630	0.630	0.630	0.630
λ_2 [-]	1							
λ_3 [-]	1							
λ_4 [-]	0.751		0.765		0.726		0.733	
$\lambda_{4,n=0}$ [-]	0.666		0.692		0.625		0.636	
λ_{max} [-]	1.4							
λ [-]	0.458	0.458	0.470	0.466	0.458	0.458	0.462	0.462
$\mathbf{\lambda_{n=0}}$ **[-]**	**0.407**	**0.407**	**0.425**	**0.422**	**0.393**	**0.393**	**0.401**	**0.401**
$\boldsymbol{L_\Phi}$ [-]	43.01							
$\mathbf{\Phi_2}$ [-]	**1.046**							
$\Delta\sigma_{E,2}$ [N/mm^2]	27.2		27.4		21.8		22.2	
$\mathbf{\Delta\sigma_{E,2,n=0}}$ **[N/mm^2]**	**24.1**		**24.8**		**18.7**		**19.3**	

Table 6.5.: Equivalent constant amplitude stress range $\Delta\sigma_{E,2}$ due to LM71 — cross section A2 at x = 23.46m

Results at arch 2 — x = 43.01 m (midspan)

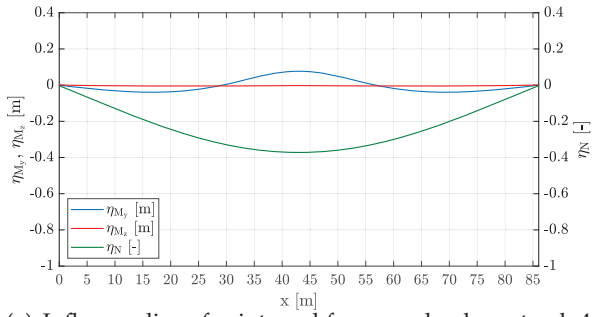

(a) Influence lines for internal forces — loads on track 4

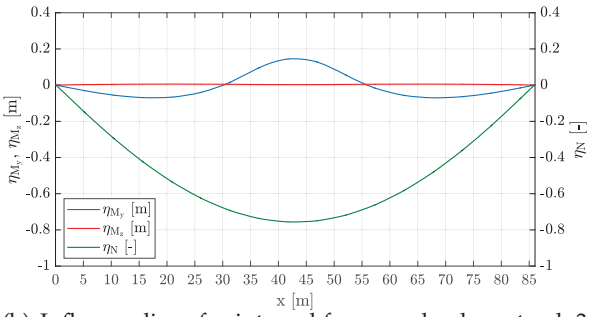

(b) Influence lines for internal forces — loads on track 3

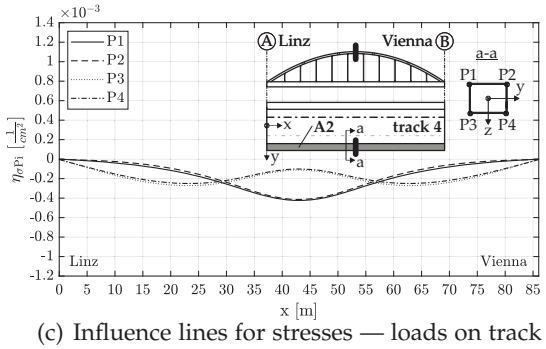

(c) Influence lines for stresses — loads on track 4

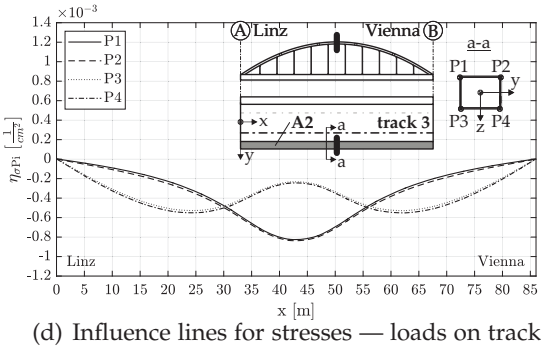

(d) Influence lines for stresses — loads on track 3

Figure 6.37.: Influence lines for axle load of 1 kN on one track — cross section A2 at x = 43.01m

Point	P1		P2		P3		P4	
Track	4	3	4	3	4	3	4	3
$\Delta\sigma_{p,max}$ [N/mm^2]	0.0	0.0	0.0	0.0	0.0	0.0	0.0	0.0
$\Delta\sigma_{p,min}$ [N/mm^2]	-13.9	-26.9	-12.8	-28.2	-13.9	-27.0	-12.8	-28.3
$\lvert\Delta\sigma_p\rvert$ [N/mm^2]	**13.9**	**26.9**	**12.8**	**28.2**	**13.9**	**27.0**	**12.8**	**28.3**
$\Delta\sigma_1/\Delta\sigma_{1+2} = \lvert\Delta\sigma_p\rvert_{track3}/\lvert\Delta\sigma_p\rvert_{track3+track4}$ [-]	0.660		0.688		0.661		0.689	
L_Φ [m]	86.02	86.02	86.02	86.02	86.02	86.02	86.02	86.02
λ_1 [-]	0.610	0.610	0.610	0.610	0.610	0.610	0.610	0.610
λ_2 [-]	1							
λ_3 [-]	1							
λ_4 [-]	0.750		0.764		0.750		0.765	
$\lambda_{4,n=0}$ [-]	0.665		0.690		0.665		0.692	
λ_{max} [-]	1.4							
λ [-]	0.458	0.458	0.466	0.466	0.458	0.458	0.466	0.466
$\lambda_{n=0}$ [-]	**0.406**	**0.406**	**0.421**	**0.421**	**0.406**	**0.406**	**0.422**	**0.422**
L_Φ [-]	43.01							
Φ_2 [-]	**1.046**							
$\Delta\sigma_{E,2}$ [N/mm^2]	19.5		20.0		19.6		20.0	
$\Delta\sigma_{E,2,n=0}$ [N/mm^2]	**17.3**		**18.1**		**17.4**		**18.1**	

Table 6.6.: Equivalent constant amplitude stress range $\Delta\sigma_{E,2}$ due to LM71 — cross section A2 at x = 43.01m

6.5.2. $\Delta\sigma_{E,2}$ based on service trains TypeC1 to TypeC8 and damage accumulation

The second variant to determine the static equivalent constant amplitude stress range $\Delta\sigma_{E,2}$ uses the trains TypeC1 to TypeC8 (traffic mix TM1) — see Figure 2.18 and Table 2.3. The individual crossing of these eight trains on track 3 and track 4 respectively was simulated statically considering the dynamic factor $(1+\varphi)_D$ according to Equation (2.12) and ÖNORM EN 1991-2, Annex D [43]. The resulting stress moment ranges were counted — by applying the reservoir method according to Figure 5.11 — at 165 equidistant cross sections for the main girders ($\Delta x = e_{CG}/4 = 0.652$ m), whereas cross sections left and right of the cross girders were considered, and at 107 cross sections for the arches ($\Delta x = e_{CG}/3 = 0.869$ m plus 2 at quarter-points, 1 at midspan and 4 at cross beam connections). Each cross section is described by four critical points as illustrated in Figure 6.8. The resulting stress range spectra for each train were then, according to Table 2.3, combined to the design life stress spectra of each point P_i (i=1...4) in each cross section along the main girders and arches. Subsequently, the stress range spectra were evaluated, using *Miner's rule*, at the S-N curve. The level of the S-N curve was again iterated until the damage $D_{stat} = 1.0$ resulted (for train crossings on both tracks individually, with 24.95 10^6 t/year/track and for 100 years of service life), which led consequently to the static equivalent constant amplitude stress range $\Delta\sigma_{E,2}$. This iteration was performed for each point P_i (i=1...4) in all cross sections separately. The results of the process described above, are presented in Figure 6.38 as $\Delta\sigma_{E,2,TypeC1-C8,stat}$ and compared to the ones obtained by the variant using the load model LM71 and damage equivalent factors λ of Chapter 6.5.1, labeled as $\Delta\sigma_{E,2,LM71}$. Hence, Figure 6.38(a) illustrates the results for main girder 2 (MG2) and Figure 6.38(b) the ones for arch 2 (A2). In general, the static equivalent constant amplitude stress ranges $\Delta\sigma_{E,2,LM71}$ due to the load model LM71 are able to estimate the results of the trains TypeC1 to TypeC8 $\Delta\sigma_{E,2,TypeC1-C8,stat}$ for the MG2 very well, but underestimate them partly for A2.

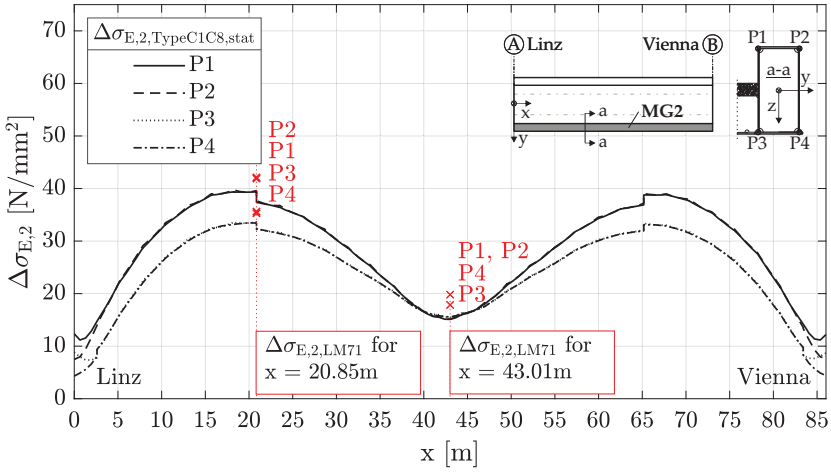

(a) Main girder 2 (MG2)

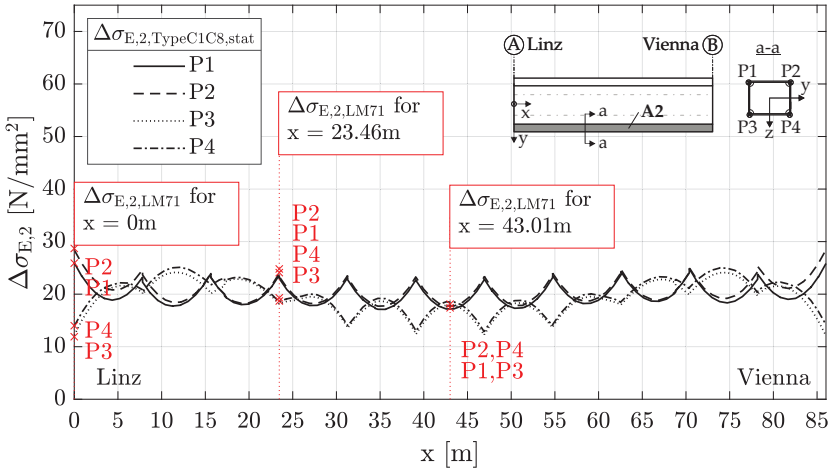

(b) Arch 2 (A2)

Figure 6.38.: Comparison of equivalent constant amplitude stress ranges $\Delta\sigma_{E,2}$ due to LM71 and TypeC1-C8 (traffic mix TM1)

6.5.3. Minimum fatigue strength for 100 years of design life

In this chapter, the level of the S-N curve, for the subsequently performed evaluation of the stress range spectra due to the dynamic simlation of the traffic mixes, is defined. Hence, the minimum fatigue strength, that is necessary for the design life of 100 years, is subsequently set. Therefore, two variants were chosen.

The first variant (Var. I) is defined as the maximum static equivalent constant amplitude stress range $\Delta\sigma_{E,2,TypeC1-C8,stat}$ along the member, due to the trains TypeC1 to TypeC8 (traffic mix TM1) of the previous Chapter 6.5.2. The results are illustrated as a red line in Figure 6.39(a) for the main girder 2 (MG2) and in Figure 6.39(b) for the arch 2 (A2). Hence, the maximum equivalent stress range $\Delta\sigma_{E,2,TypeC1-C8,stat}$ for all points P_i along e.g. MG2 is 39.73 N/mm^2. Consequently, this value is used as $\Delta\sigma_{C,I}$ to define the S-N curve at 2 million cycles for all points P_i of MG2 for the damage accumulation calculations in the following chapters. Therefore, the fatigue verification for the static stress range spectra, based on traffic mix TM1, is fulfilled along the whole main girder.

The second variant (Var. II) considers the relevant detail (diaphragm of box girder) for this type of construction, which is simplified assumed to be the detail category 71 divided by the partial safety factor $\gamma_{MF} = 1.15$, which leads to $\Delta\sigma_{C,II} = 61.74$ N/mm^2, like in the case of the single-span bridges of Chapter 5.[1] Hence, this value is used as $\Delta\sigma_{C,II}$ to define the S-N curve at 2 million cycles for all points P_i of all analysed cross sections in the members for the damage accumulation calculations in the following chapters. In conclusion, the S-N curves of all points

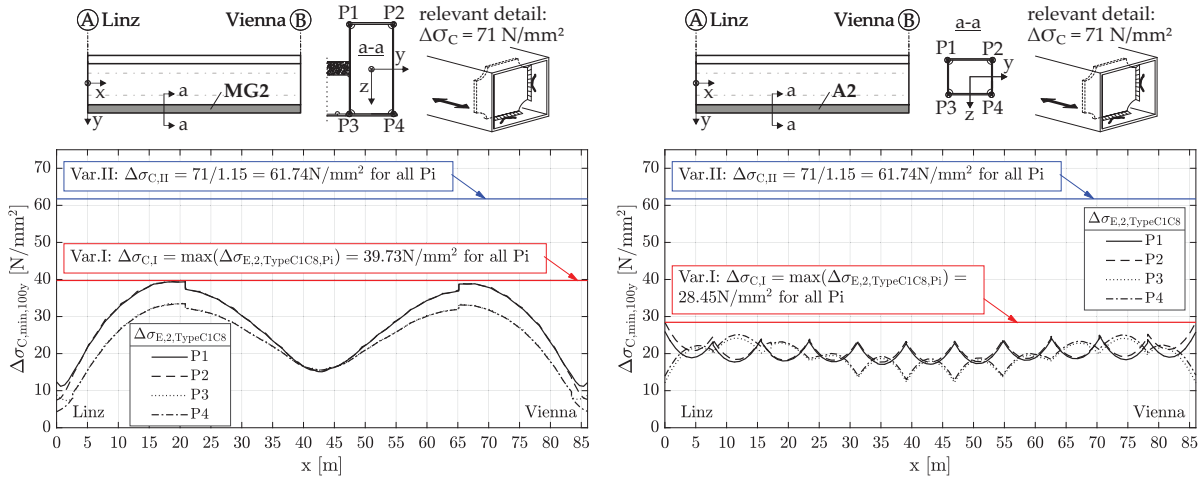

(a) Main girder 2 (MG2) (b) Arch 2 (A2)

Figure 6.39.: Minimum detail category variants $\Delta\sigma_{C,i}$ along members MG2 and A2 — equally valid for MG1 and A1 — to fulfil the fatigue verification

P_i for the damage accumulation calculations in the following chapters are set to subsequent values $\Delta\sigma_C$ at 2 million cycles:

- Var.I
  - Main girders (MG1 and MG2): $\Delta\sigma_{C,I} = 39.73$ N/mm^2
  - Arches (A1 and A2): $\Delta\sigma_{C,I} = 28.45$ N/mm^2
- Var.II
  - All members (MG1, MG2, A1 and A2): $\Delta\sigma_{C,II} = 61.74$ N/mm^2

[1] Here the detail category 80 ($l \leq 50$ mm) considering the partial safety factor $\gamma_{MF} = 1.35$ (detail not inspectable) is applicable as well, which would lead to a similar value $\Delta\sigma_{C,II}$ of 59.26 N/mm^2

6.6. Fatigue design check — static versus dynamic — TM1

In this chapter, the trains TypeC1 to TypeC8, according to Figure 2.18, are considered. These eight trains cross tracks 3 and 4 individually, according to traffic mix 1 — see Table 4.1 — and cause on each track a traffic volume of 24.95 10^6 t/year for the entire design life of 100 years.
First, the crossing of the trains is simulated statically, considering the dynamic factor $(1+\varphi)_D$ according to Equation (2.12), as already in Chapter 6.5.2 performed. The difference here is, that the resulting static stress range spectra for the entire design life are evaluated at the fixed S-N curves defined in the Chapter 6.5.3 (Var.I and Var.II), to get an objective comparison with the dynamic simulation, using the same fatigue strength $\Delta\sigma_C$.
Furthermore, the crossing of the eight trains was simulated dynamically with the analytical approach using Matlab, according to Chapter 6.3.1. Therefore, the train speeds according to TM1* and TM1** were applied — see Table 4.2. Consequently, the resulting stress range spectra, due to the traffic mixes TM1* and TM1**, were evaluated at the S-N curves defined by Var.I and Var.II according to the previous Chapter 6.5.3.

6.6.1. Static fatigue design — traffic mix TM1

Subsequently, the static stress range spectra, due to the trains TypeC1 to TypeC8 for the entire design life, are evaluated at the S-N curves defined in Chapter 6.5.3 and the resulting damage values D_{stat} are plotted for each member along the structure's longitudinal axis.

Var.I: maximum value of minimum fatigue strength — $\Delta\sigma_{C,I}$

The S-N curves for all points P_i of the main girders (MG1 and MG2) were set to $\Delta\sigma_{C,I} = 39.73$ N/mm^2 and the ones of the arches (A1 and A2) were set to $\Delta\sigma_{C,I} = 28.45$ N/mm^2. Figure 6.40 illustrates the resulting damage D_{stat} for MG1, MG2, A1 and A2. Notice, per definition $D_{stat} = 1.0$ for point P2 of cross section MG2 at x = 17.7 m and for point P2 of cross section A2 at x = 0 m — compare Figures 6.40(c) with 6.39(a) and 6.40(d) with 6.39(b).

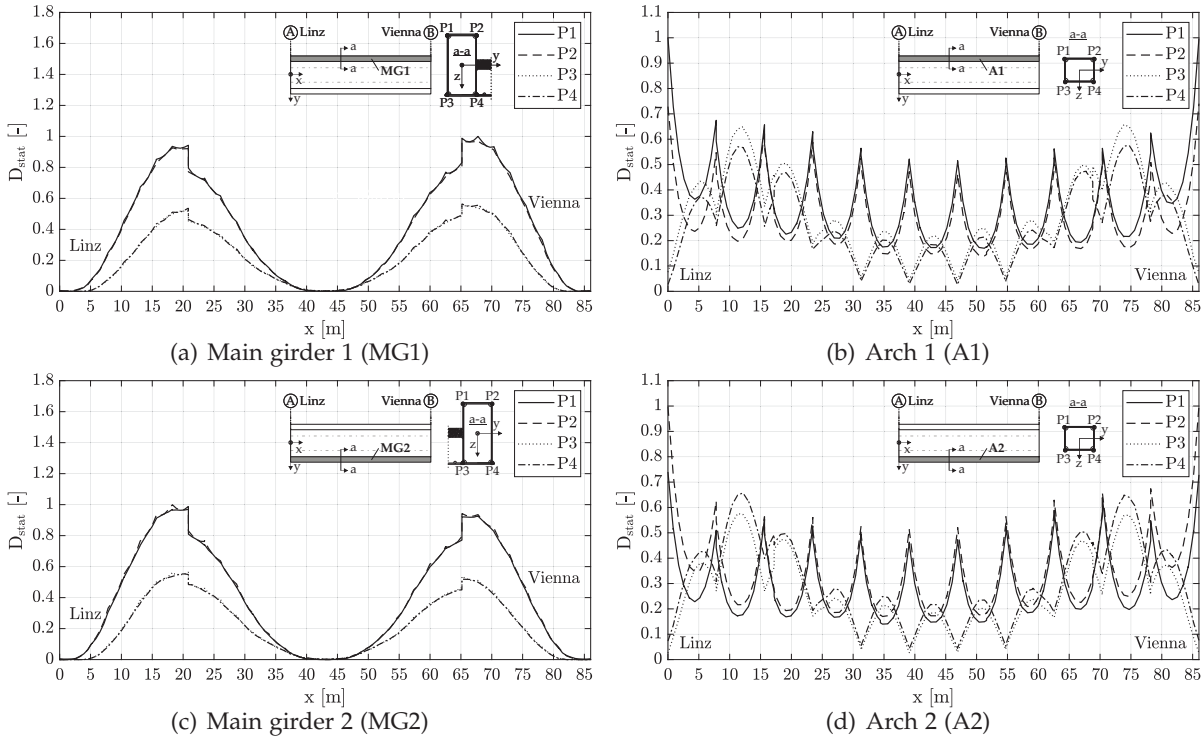

(a) Main girder 1 (MG1)
(b) Arch 1 (A1)
(c) Main girder 2 (MG2)
(d) Arch 2 (A2)

Figure 6.40.: Damage D_{stat} along members — train mix TM1 — static — $\Delta\sigma_{C,I}$

Var.II: fatigue strength according to relevant detail — $\Delta\sigma_{C,II} = 61.74 \mathrm{N/mm^2}$

Subsequently, the S-N curves were set to $\Delta\sigma_{C,II} = 61.74$ N/mm^2 at 2 million load cycles for all points P_i of all members (MG1, MG2, A1 and A2). Figure 6.41 shows the resulting damage values D_{stat} for each member separately. In comparison to the results of Var.I in Figure 6.40 the damage D_{stat} was severely reduced by increasing the levels of the S-N curves.

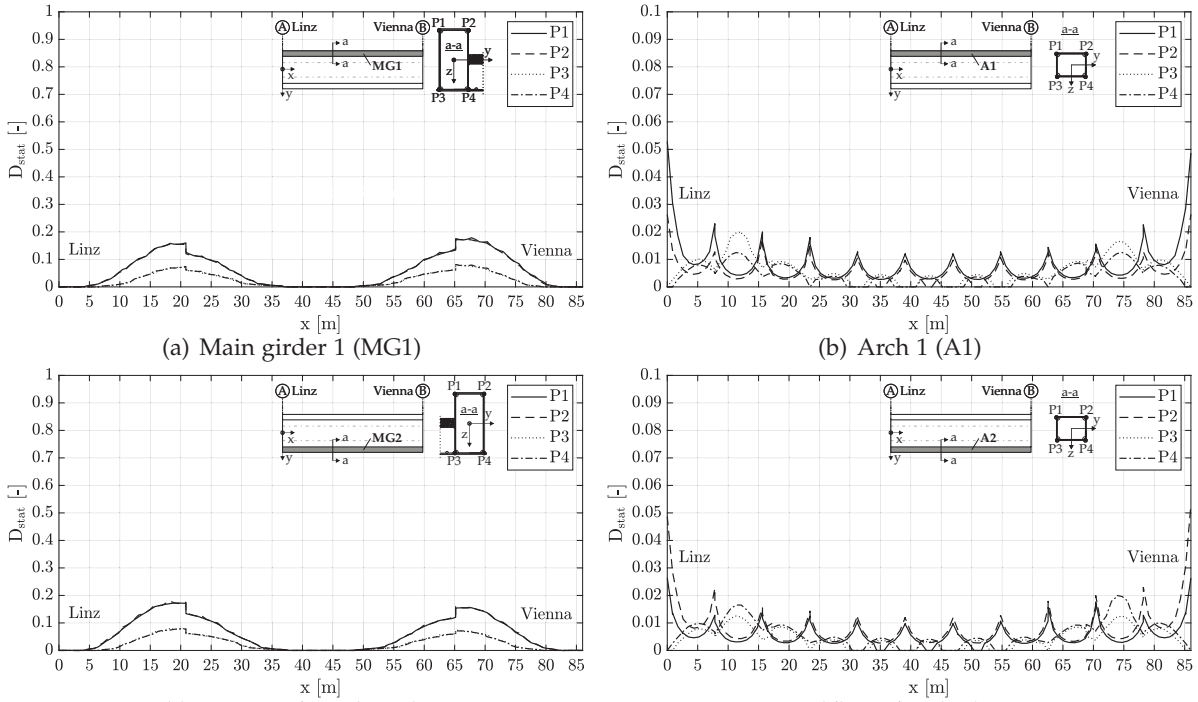

(a) Main girder 1 (MG1) (b) Arch 1 (A1)

(c) Main girder 2 (MG2) (d) Arch 2 (A2)

Figure 6.41.: Damage D_{stat} along members — train mix TM1 — static — $\Delta\sigma_{C,II}$

6.6.2. Dynamic fatigue design — traffic mix TM1* — train speed v_{EC}

In this chapter, the dynamic calculations were performed using the speeds v_{EC} according to Table 4.2. The resulting dynamic stress range spectra, for the entire design life of 100 years, were again evaluated at the S-N curve variants Var.I and Var.II.

Var.I: maximum value of minimum fatigue strength — $\Delta\sigma_{C,I}$

Figure 6.42 illustrates the damage D_{dyn}, which results due to the dynamic stress ranges being evaluated at the S-N curves of Var.I. Additionally, Figure 6.43 shows the damage ratios D_{dyn}/D_{stat}, which are obtained by dividing the damages D_{dyn} of Figure 6.42 by the damages D_{stat} of Figures 6.40, whereas zero values are plotted and undefined values are not illustrated.

Var.II: fatigue strength according to relevant detail — $\Delta\sigma_{C,II} = 61.74$ N/mm^2

Evaluating the same dynamic stress ranges as before at the S-N curves of variant Var.II leads to the damage D_{dyn} results in Figure 6.44 and the corresponding ratios D_{dyn}/D_{stat} in Figure 6.45. Hence, a severe reduction of the damage D_{dyn} due to the increased S-N curves resulted. However, the ratios D_{dyn}/D_{stat} for the main girders are about 1.2, whereas for the arches the static results are mostly not reached by the dynamic calculation.

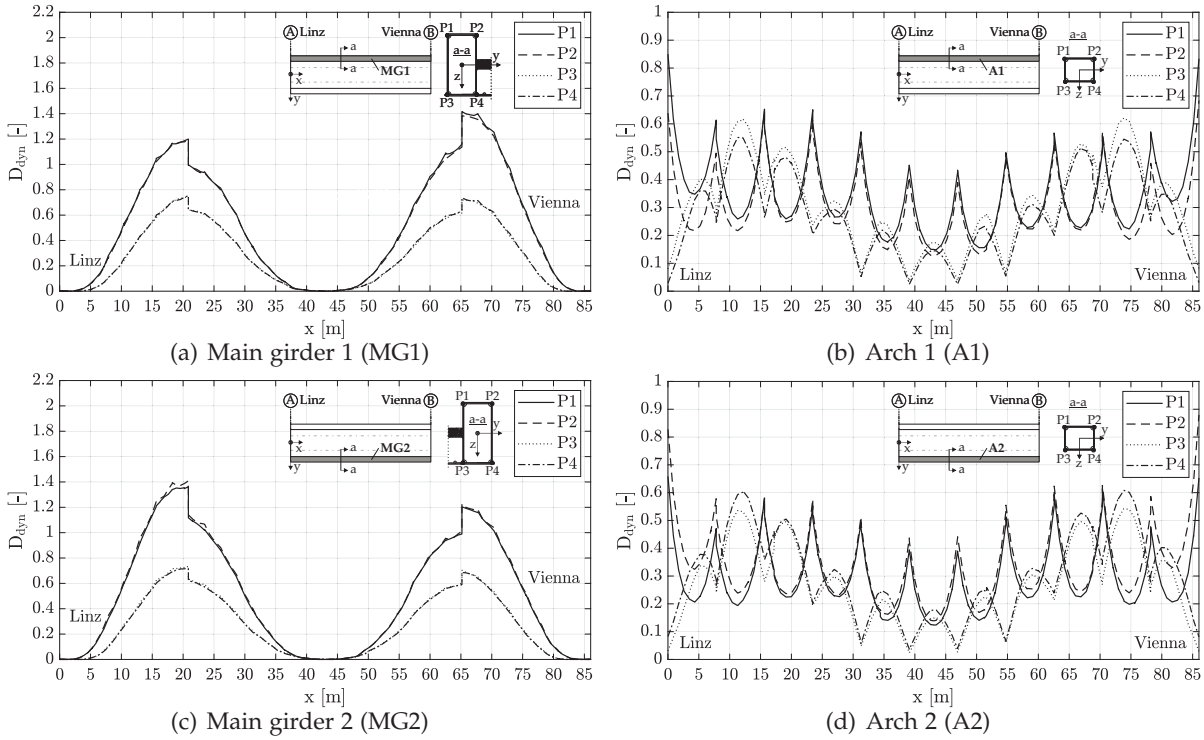

(a) Main girder 1 (MG1) (b) Arch 1 (A1)

(c) Main girder 2 (MG2) (d) Arch 2 (A2)

Figure 6.42.: Damage D_{dyn} along members — train mix TM1* — dynamic — v_{EC} — ζ_{EC} (Rayleigh) — $\Delta\sigma_{C,I}$

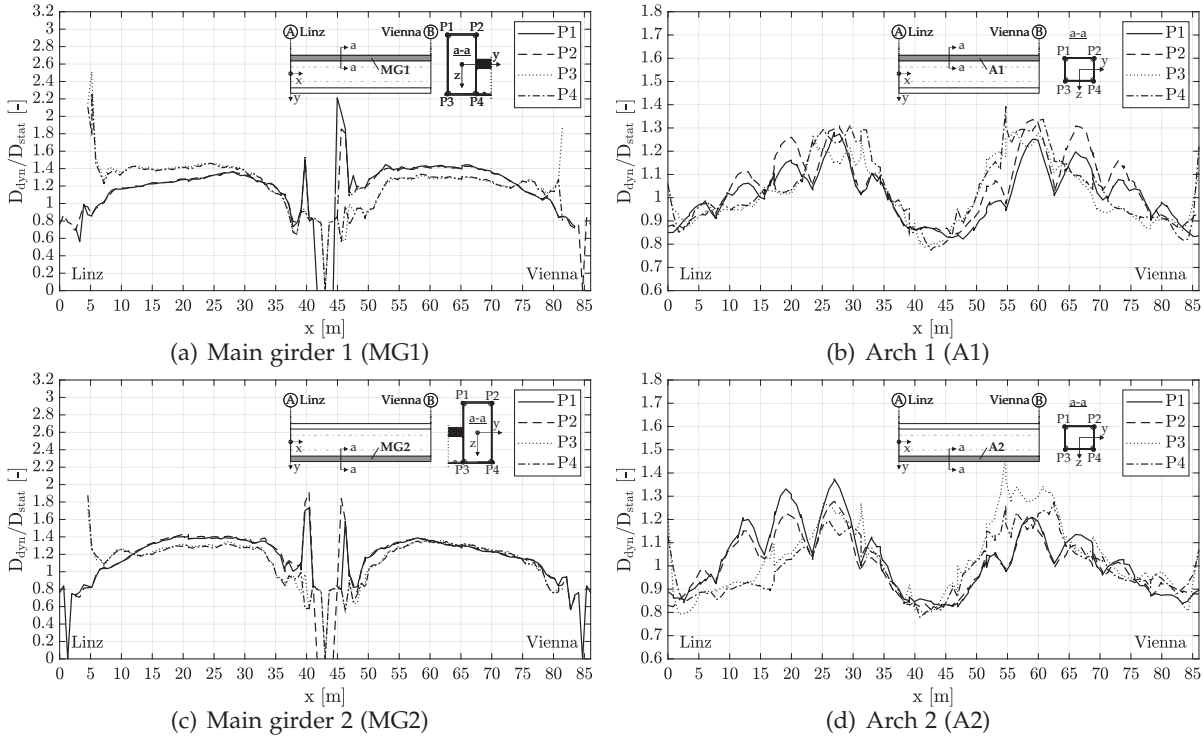

(a) Main girder 1 (MG1) (b) Arch 1 (A1)

(c) Main girder 2 (MG2) (d) Arch 2 (A2)

Figure 6.43.: Ratio D_{dyn}/D_{stat} along members — train mix TM1* — dynamic — v_{EC} — ζ_{EC} (Rayleigh) — $\Delta\sigma_{C,I}$

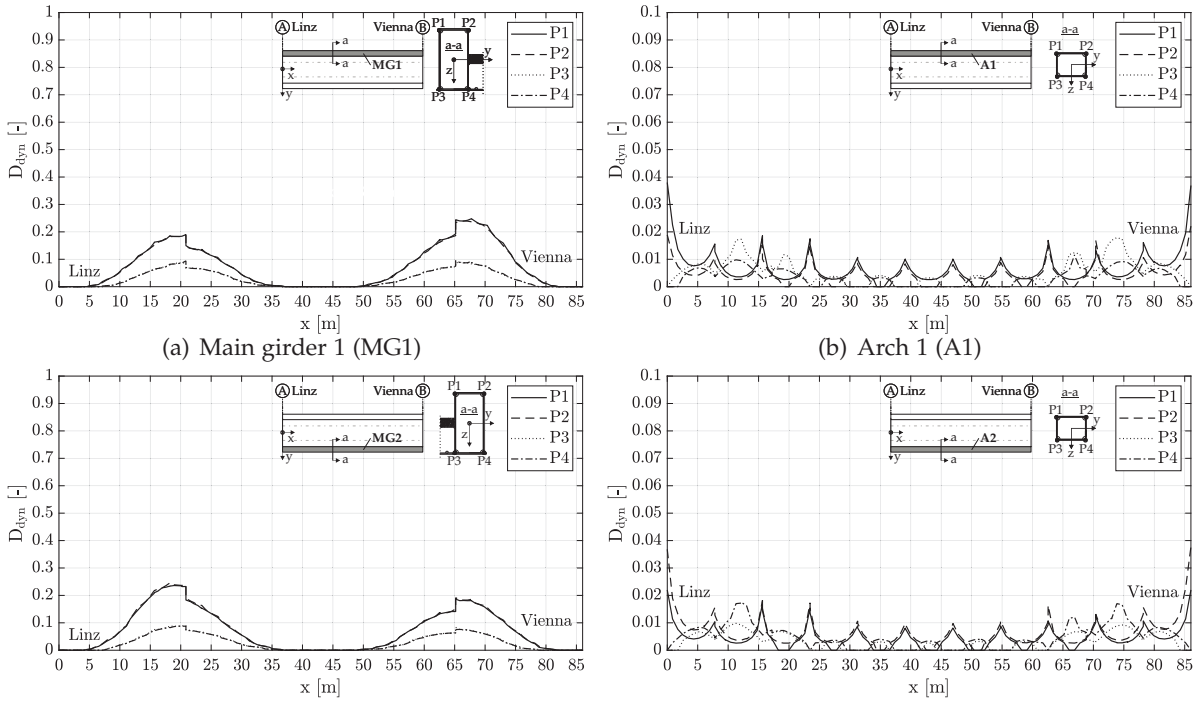

(a) Main girder 1 (MG1) (b) Arch 1 (A1)

(c) Main girder 2 (MG2) (d) Arch 2 (A2)

Figure 6.44.: Damage D_{dyn} along members — train mix TM1* — dynamic — v_{EC} — ζ_{EC} (Rayleigh) — $\Delta\sigma_{C,II}$

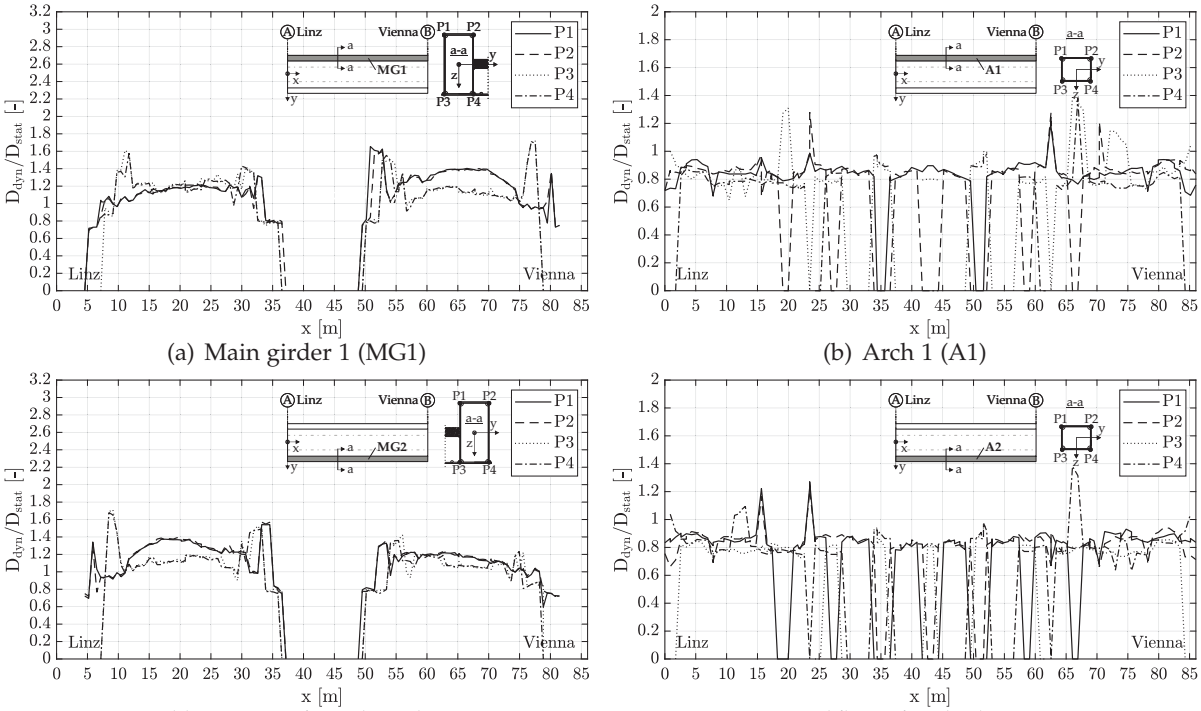

(a) Main girder 1 (MG1) (b) Arch 1 (A1)

(c) Main girder 2 (MG2) (d) Arch 2 (A2)

Figure 6.45.: Ratio D_{dyn}/D_{stat} along members — train mix TM1* — dynamic — v_{EC} — ζ_{EC} (Rayleigh) — $\Delta\sigma_{C,II}$

6.6.3. Dynamic fatigue design — traffic mix TM1** — train speed $v_{D_{max}}$

In this chapter, again, the eight trains TypeC1 to TypeC8 were simulated dynamically, but now crossing the structure on track 3 an track 4 with the speed $v_{D_{max}}$ according to traffic mix TM1**. Hence, for each point P_i on each cross section of each single member, the maximum damage D_{dyn} for each train type (considering the trains speed range v = 50-1.2v_{EC}) was determined and combined to the total traffic volume of 24.95 10^6 t/year/track and 100 years. Consequently, the subsequent illustrated results represent the biggest possible damage D_{dyn}, which the trains TypeC1 to TypeC8 can produce due to the crossing of this particular arch bridge model.

In Figure 6.46 the dynamic stress range spectra due to TM1** were evaluated at the S-N curves according to variant Var.I. For both main girders, the maximum damage D_{dyn} is about 5.0 — see Figures 6.46(a) and 6.46(c) — whereas the maximum damage D_{dyn} with respect to the arches is only slightly above 1.0 — see Figures 6.46(b) and 6.46(d). Figure 6.47 shows again the ratios D_{dyn}/D_{stat} for TM1** and the S-N curve level of variant Var.I.

Figure 6.48 shows again the results for the S-N curve variant Var.II. The increase of the S-N curve levels to $\Delta\sigma_{C,II} = 61.74$ N/mm^2 led to damage values $D_{dyn} < 1.0$ for all points P_i along all members. Consequently, even if all eight trains TypeC1 to TypeC8 cross the structure for 100 years and a traffic volume of 24.95 10^6 t/year/track, with the speed $v_{D_{max}}$, leading to the maximum possible damage D_{dyn} in each point P_i of all considered members, the FAT design criterion is still fulfilled in case of the detail category 71 is the decisive one. Additionally, Figure 6.49 shows the ratios D_{dyn}/D_{stat} for TM1** and the S-N curve level of variant II.

Var.I: maximum value of minimum fatigue strength — $\Delta\sigma_{C,I}$

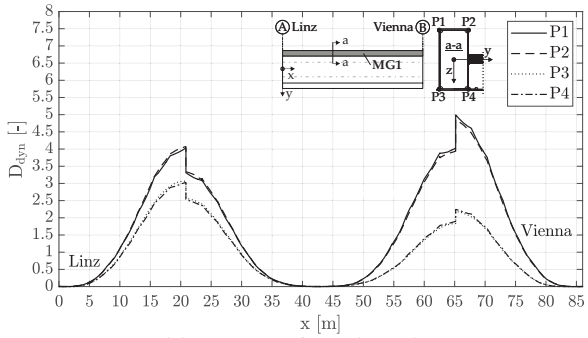

(a) Main girder 1 (MG1)

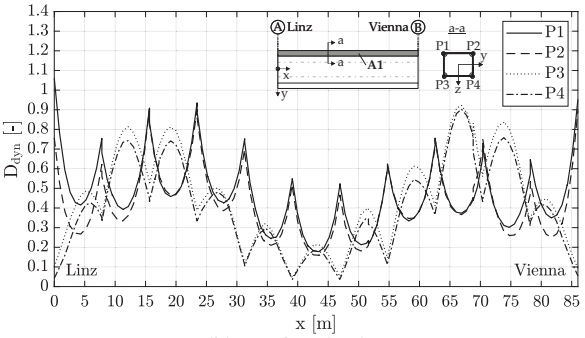

(b) Arch 1 (A1)

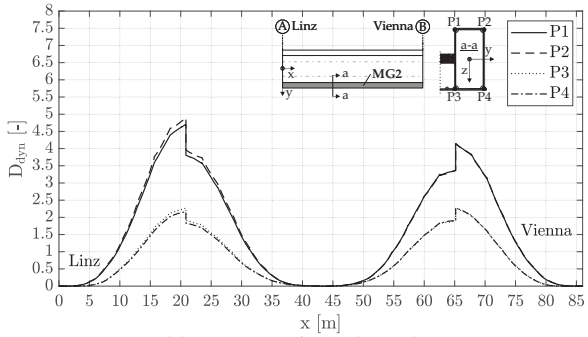

(c) Main girder 2 (MG2)

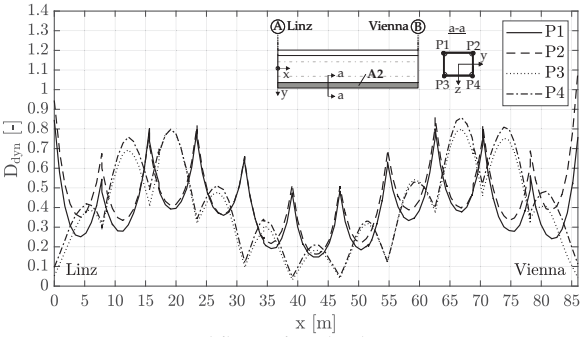

(d) Arch 2 (A2)

Figure 6.46.: Damage D_{dyn} along members — train mix TM1** — dynamic — $v_{D_{max}}$ — ζ_{EC} (Rayleigh) — $\Delta\sigma_{C,I}$

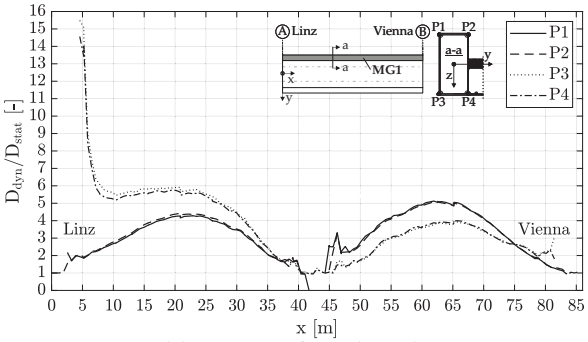

(a) Main girder 1 (MG1)

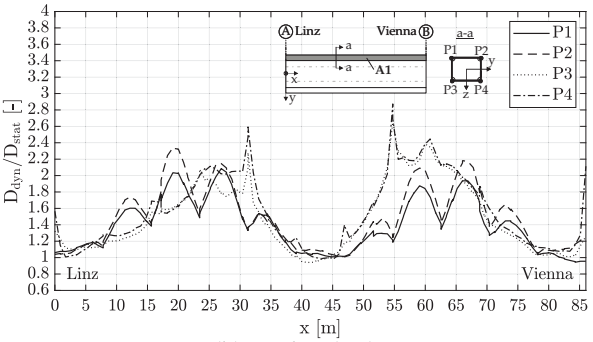

(b) Arch 1 (A1)

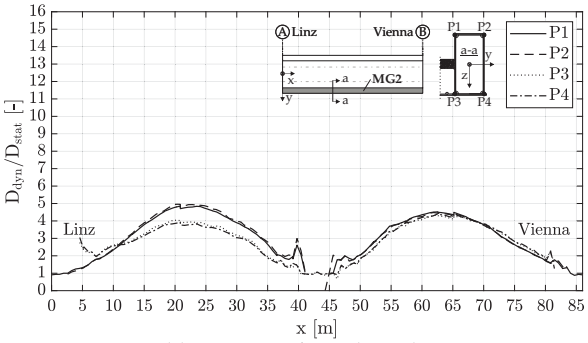

(c) Main girder 2 (MG2)

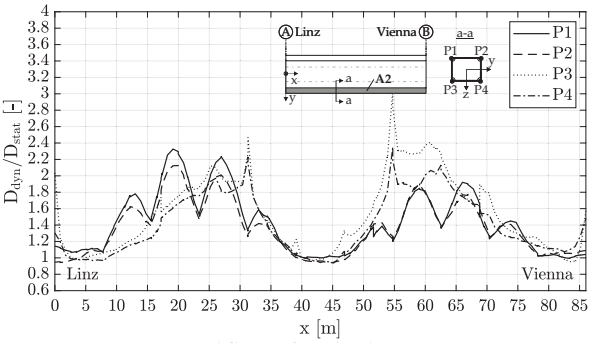

(d) Arch 2 (A2)

Figure 6.47.: Ratio D_{dyn}/D_{stat} along members — train mix TM1** — dynamic — $v_{D_{max}}$ — ζ_{EC} (Rayleigh) — $\Delta\sigma_{C,I}$

Var.II: fatigue strength according to relevant detail — $\Delta\sigma_{C,II} = 61.74 N/mm^2$

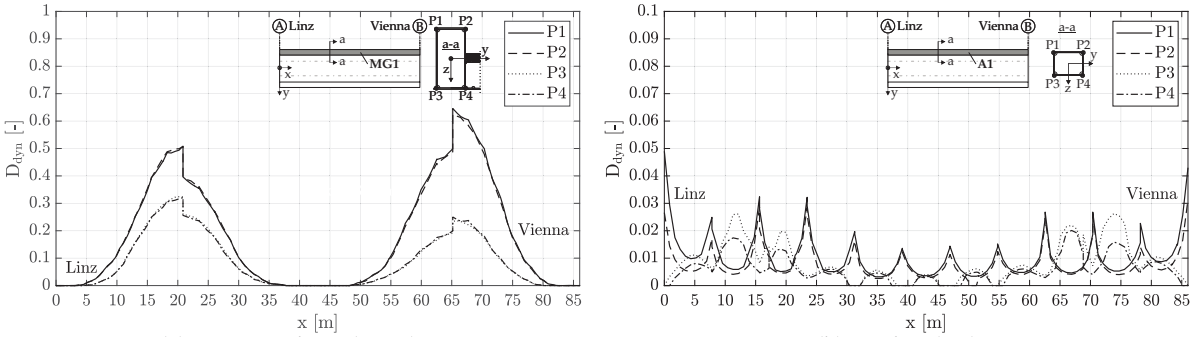

(a) Main girder 1 (MG1) (b) Arch 1 (A1)

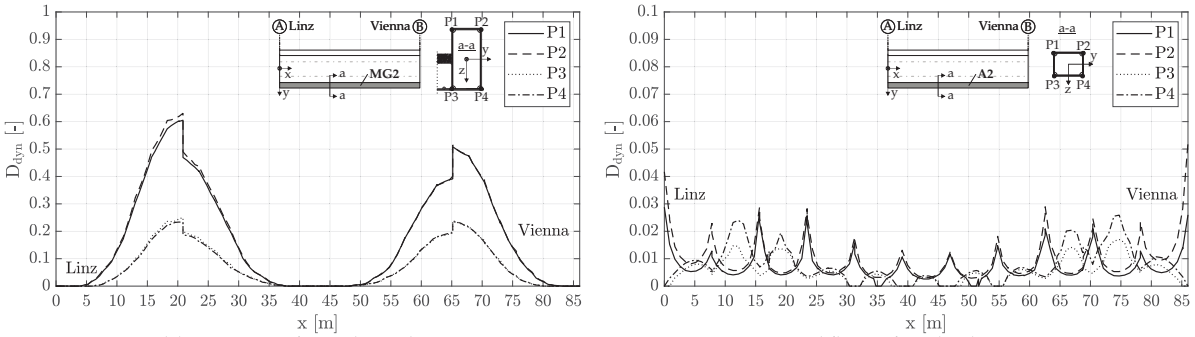

(c) Main girder 2 (MG2) (d) Arch 2 (A2)

Figure 6.48.: Damage D_{dyn} along members —— train mix TM1** — dynamic — $v_{D_{max}}$ — ζ_{EC} (Rayleigh) — $\Delta\sigma_{C,II}$

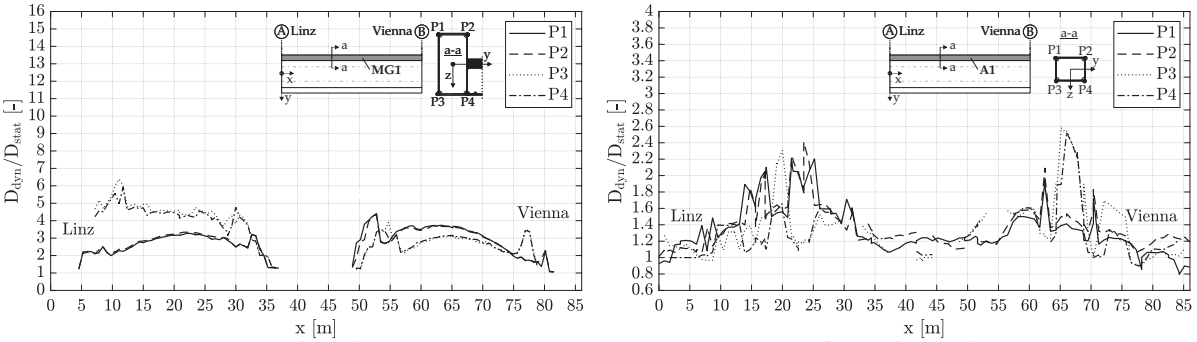

(a) Main girder 1 (MG1) (b) Arch 1 (A1)

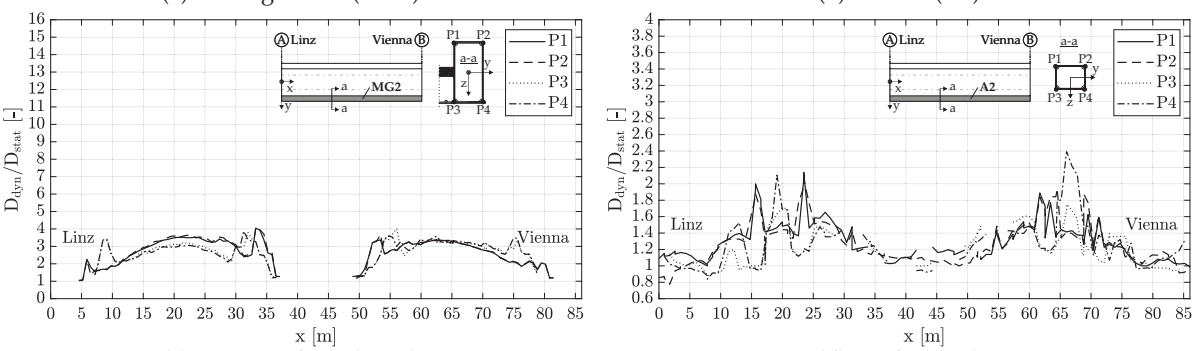

(c) Main girder 2 (MG2) (d) Arch 2 (A2)

Figure 6.49.: Ratio D_{dyn}/D_{stat} along members —— train mix TM1** — dynamic — $v_{D_{max}}$ — ζ_{EC} (Rayleigh) — $\Delta\sigma_{C,II}$

6.7. Dynamic fatigue design check — traffic mix TM2

Subsequently, the 94602 measured real trains with the corresponding train speeds were considered on both tracks according to traffic mix TM2-dt — see Figure 4.8. The resulting dynamic stress ranges, were again evaluated at the two S-N curve varaints Var.I and Var.II.
The results for the S-N curve variant Var.I are shown in Figure 6.50, whereas the ratios D_{dyn}/D_{stat}, which are obtained by using the damages of Figures 6.50 and 6.40, are illustrated in Figure 6.51.

Hence, if the S-N curve level, which leads for the static case (TypeC1 to TypeC8 of traffic mix TM1), at the decisive point P_i, to a damage of $D_{stat} = 1.0$, were considered, then due to the traffic mix TM2-dt a damage D_{dyn} of about 0.9 at the decisive point P1 at the main girder MG1 would result — see Figure 6.50(a). The maximum damage D_{dyn} in the cross section of the arch, due to TM2-dt and the S-N curve variant Var.I is significantly smaller, about 0.2 — see Figure 6.50(b).

However, if the S-N curve variant Var.II is considered, which represents the very likely decisive detail category 71, then the maximum damage D_{dyn} of all members is below 0.05 — see Figure 6.52. Furthermore, the ratios D_{dyn}/D_{stat} in Figure 6.53 are all far below 1.0 as well.

6.8. Conclusion

The considered individual cross-sections of the main members (main girders, arches) of the studied arch bridge are not prone to a FLS problem for the considered detail category 71. Neither traffic mix TM2-st, which represents a real traffic mix due to measurements, nor traffic mix TM1**, which represents the service trains of *EC mix*, crossing the arch bridge for 100 years with the most unfavourable train speeds, is causing a damgage $D_{dyn} > 1.0$ in any main girder or arch.

Var.I: maximum value of minimum fatigue strength — $\Delta\sigma_{C,I}$

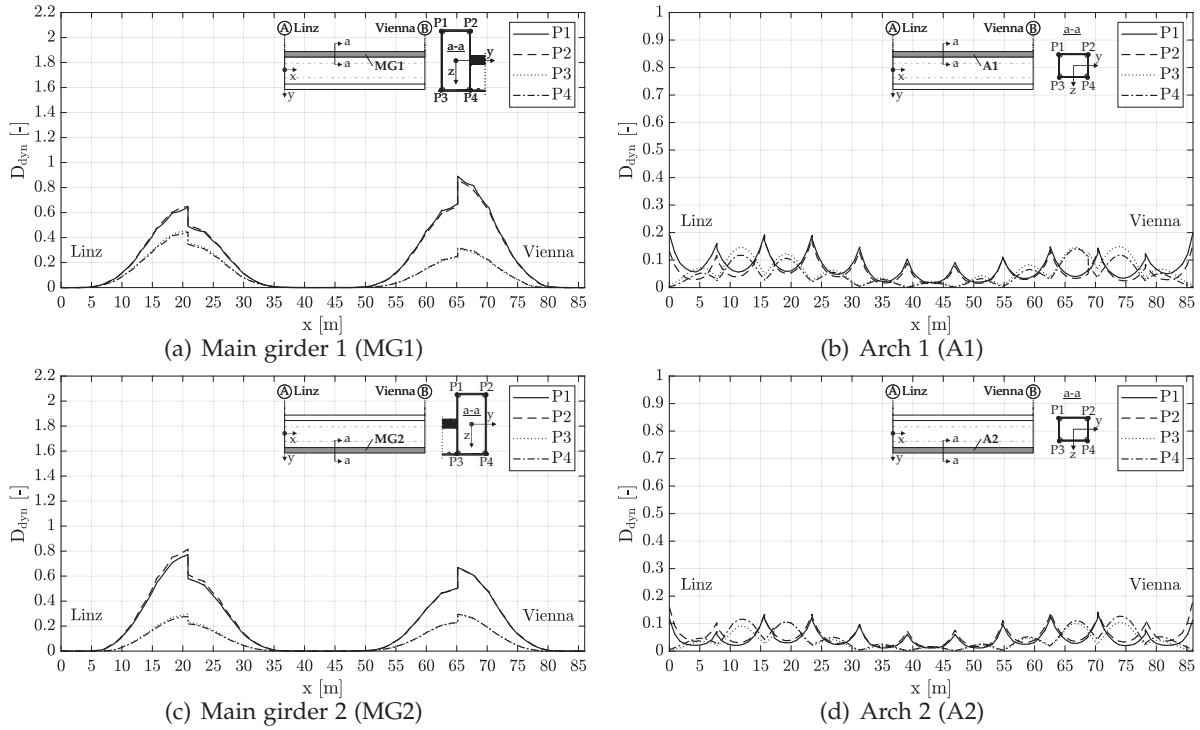

(a) Main girder 1 (MG1) (b) Arch 1 (A1)

(c) Main girder 2 (MG2) (d) Arch 2 (A2)

Figure 6.50.: Damage D_{dyn} along members — train mix TM2 — dynamic — v_{train} — ζ_{EC} (Rayleigh) — $\Delta\sigma_{C,I}$

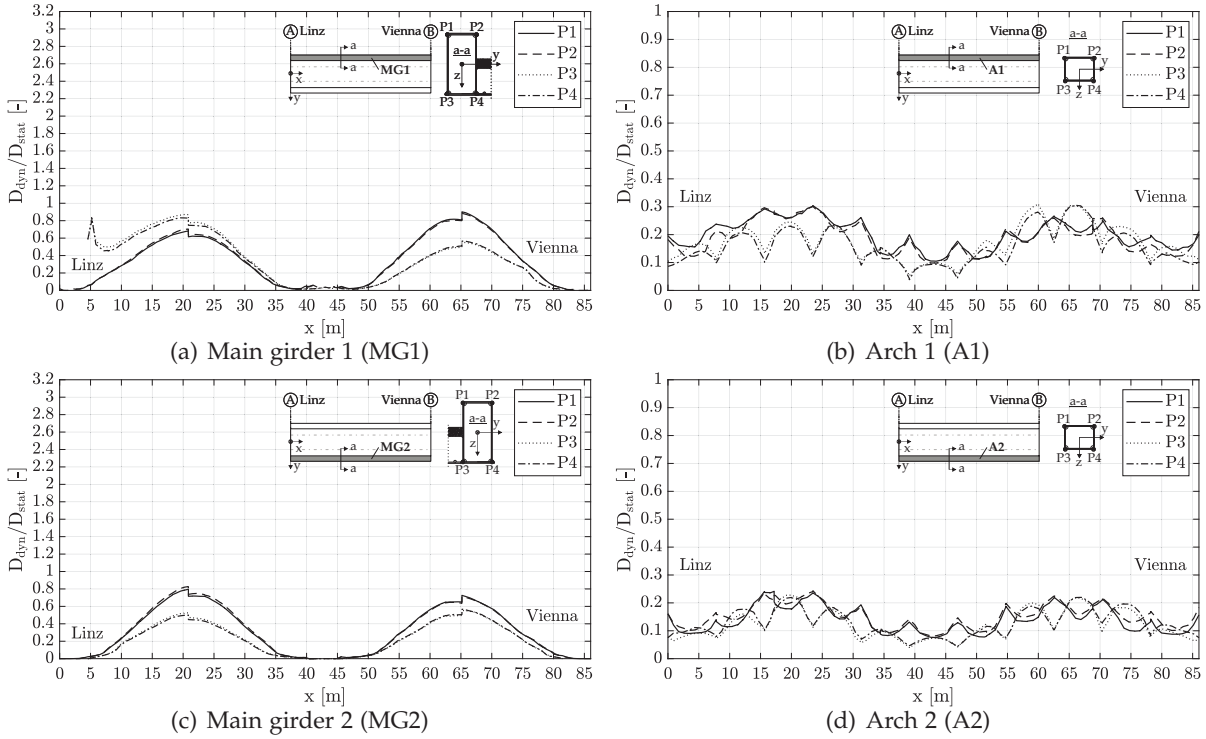

(a) Main girder 1 (MG1) (b) Arch 1 (A1)

(c) Main girder 2 (MG2) (d) Arch 2 (A2)

Figure 6.51.: Ratio D_{dyn}/D_{stat} along members — train mix TM2 — dynamic — v_{train} — ζ_{EC} (Rayleigh) — $\Delta\sigma_{C,I}$

Var.II: fatigue strength according to relevant detail — $\Delta\sigma_{C,II} = 61.74\mathrm{N/mm^2}$

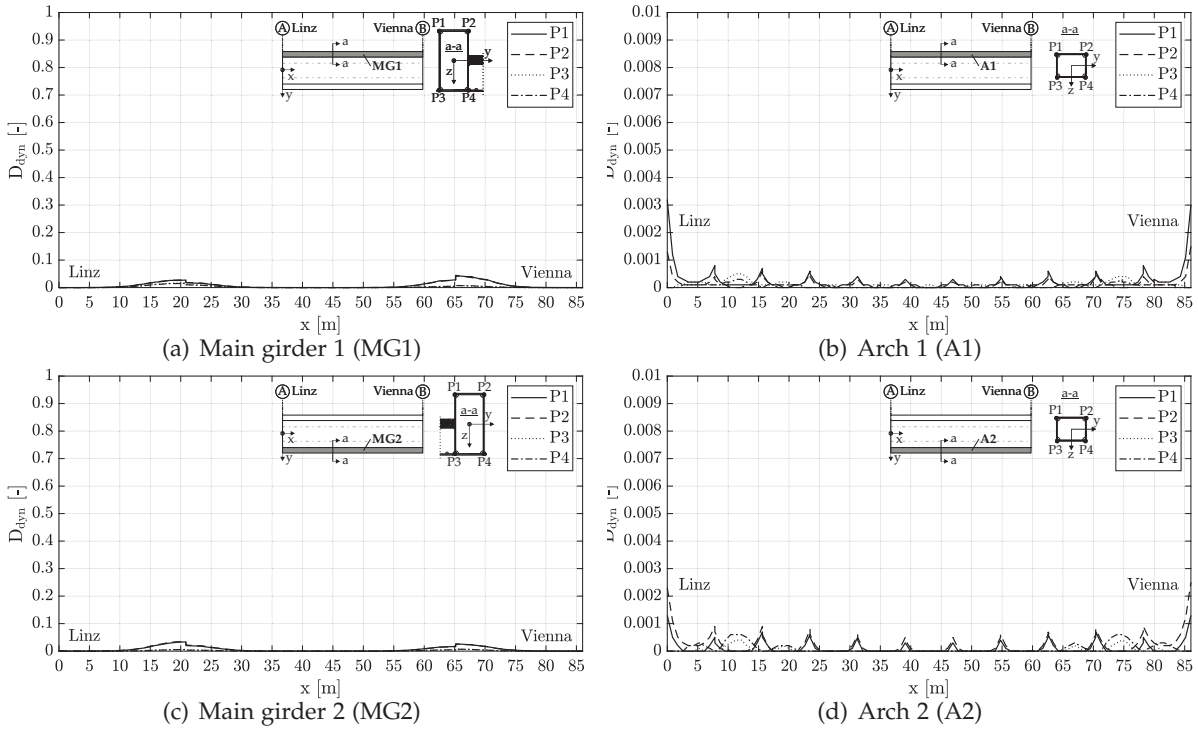

(a) Main girder 1 (MG1) (b) Arch 1 (A1)

(c) Main girder 2 (MG2) (d) Arch 2 (A2)

Figure 6.52.: Damage D_{dyn} along members — train mix TM2 — dynamic — v_{train} — ζ_{EC} (Rayleigh) — $\Delta\sigma_{C,II}$

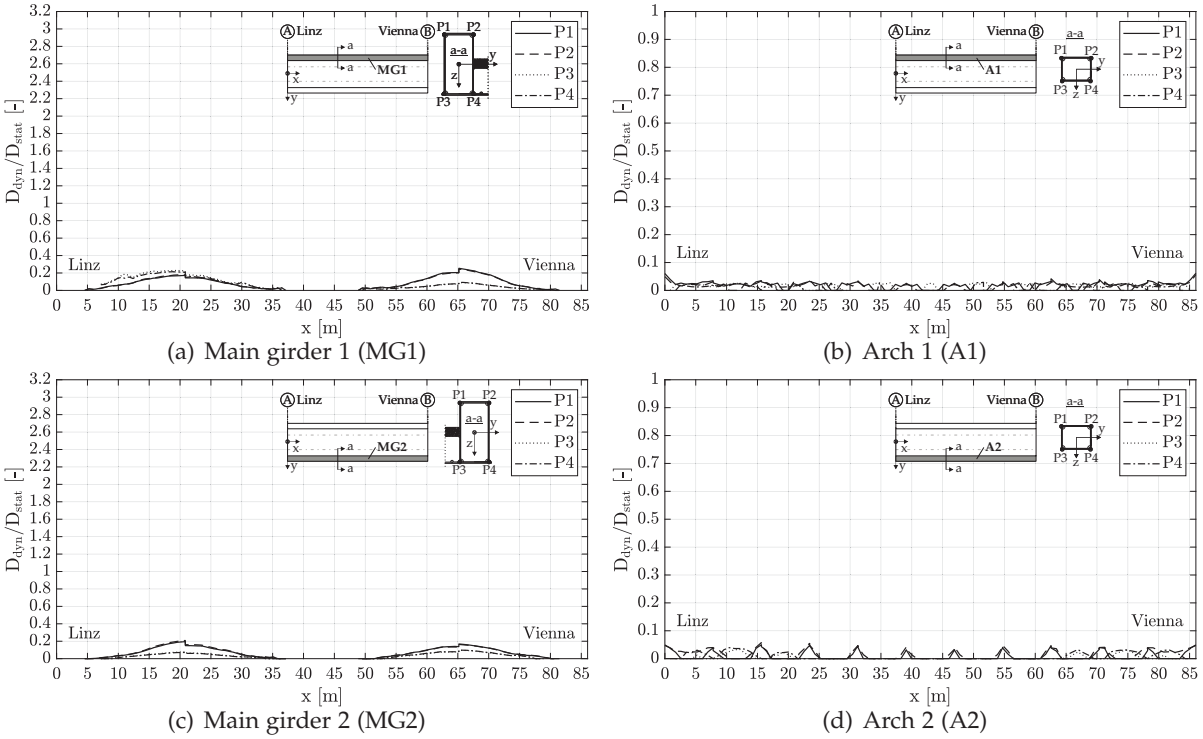

(a) Main girder 1 (MG1) (b) Arch 1 (A1)

(c) Main girder 2 (MG2) (d) Arch 2 (A2)

Figure 6.53.: Ratio D_{dyn}/D_{stat} along members — train mix TM2 — dynamic — v_{train} — ζ_{EC} (Rayleigh) — $\Delta\sigma_{C,II}$

7. Summary and concluding remarks

In this thesis, the impact of high-speed railway traffic on the fatigue behaviour of steel and composite railway bridges is investigated. It discusses whether the common static approach (load model LM71 with damage equivalent factor λ) accounts also for the resonance effects, which might occur due to the dynamic crossing of high-speed passenger trains.

Therefore, in the first part of the thesis, a parameter study of pre-designed single-span steel and composite bridges is performed. A new calculation approach, based on the existing non-dimensional representation of dynamic train crossing simulations, is developed with respect to the fatigue design check, which allows to consider a wide range of input parameters:

- Five traffic mixes:
  - TM1 — 8 trains and train mix according to ÖNORM EN 1991-2 (*EC-mix*), which is the basis for the fatigue design of new steel and composite bridges
  - TM2 — 94602 measured passenger, freight and special trains according to monitoring point *Enns*, which is located on the high-speed line *Westbahn* between the two cities of *Linz* and *Vienna*.
  - TM3 — 77217 measured passenger trains according to monitoring point *Enns*, which is located on the high-speed line *Westbahn* between the two cities of *Linz* and *Vienna*.
  - TM4 — 6 high-speed trains, which represent a possible high-speed train mix in Austria
  - TM5 — 4 high-speed trains and 4 freight trains representing a possible mixed train mix in Austria
- Three train speed variants
  - v_{EC} or v_{Train} — train speeds according to ÖNORM EN 1991-2 [43] or measured data
  - $v_{D_{max}}$ — train speed within speed range of each train, which produces the maximum dynamic damage D_{dyn}
  - $v_{a_{max}}$ — train speed within speed range of each train, which produces the maximum vertical bridge deck acceleration $|a_{max}|$
- Two damping variants
  - ζ_{EC} — according to ÖNORM EN 1991-2 [43]
  - ζ_{V1} — according to ÖNORM EN 1991-2 [43] but at least 1.0 %
- Two load distribution variants
  - without load distribution, hence each axle load is represented by one single load
  - with load distribution, hence each axle load is represented by three single loads according to ÖNORM EN 1991-2 [43]
- New/ Existing single-span steel and composite bridges are distinguished due to their traffic safety (TS) vertical bridge deck acceleration criterion
  - $|a_{HSLM-A,max}| \leq 3.5\ m/s^2$ for new bridge structures

- $|a_{HSLM-A,max}| \leq 6.0$ m/s^2 for existing bridge structures

For all studied bridges these criteria are checked.

Furthermore, the influence of two different train models (*moving load model* and *2D multi-body model*) on the damage D_{dyn} is investigated.
The results of the dynamic parameter study led to the following conclusions — see Chapter 5.4.6:

- The common static approach for the fatigue design verification of steel and composite railway bridges (load model LM71 with damage equivalent factor λ) is not sufficient to account for resonance effects due to the dynamic simulation.
- New/ existing single-span steel bridges and new single-span composite bridges in general do not have a fatigue problem (considering a minimum fatigue strength of FAT-71 with $\Delta\sigma_C = 71/1.15 = 61.74$ N/mm^2), if they fulfil the TS criteria.
- Existing single-span composite bridges in general do not have a fatigue problem (considering FAT-71 with $\Delta\sigma_C = 71/1.15 = 61.74$ N/mm^2), if they fulfil the TS criteria, besides few exceptions stated in Chapter 5.4.6.
- The speed variants $v_{D_{max}}$ and $v_{a_{max}}$ lead to very similar results, hence, one can use the speed $v_{a_{max}}$, which leads to the maximum vertical bridge deck acceleration $|a_{max}|$, in order to calculate the maximum dynamic damage D_{dyn}.
- Increasing the damping ratio from ζ_{EC} to ζ_{V1} improves the situation for one particular single-span steel or composite structure, as the damping effects are simply enhanced. On the other hand, the influence on the entire population of the bridge structures (L and n_0 ranges) is not severe, as the number of bridges that fulfil the TS criteria increases in about the same range as the number of bridges that do not fulfil the fatigue limit state (FLS) criteria decreases.
- The influence of the load distribution is of neglectable magnitude and only present for spans up to L = 15 m.
- Furthermore, the load model *moving load model* proves to be sufficient and usually conservative in comparison to the computationally much more expensive *2D multi-body model* — see Chapter 5.2.1.

Moreover, the accuracy of the static approach in Austria is checked, which additionally enhances the static fatigue load by the percentage the internal forces of the dynamic calculation exceed the ones of the static calculation.
As discussed in Chapter 5.5.5, this simplified static approach is not able to account for the dynamic effects, represented by the above presented dynamic parameter study.

Finally, the main girders and arches of a representative arch bridge were investigated with respect to their fatigue behaviour due to high-speed railway traffic. Therefore, the traffic mixes TM1 and TM2 were considered. Due to the complexity of the structure, four different computational approaches were compared to each other. The calculations of the internal forces led for all approaches to similar results, whereas for the vertical bridge deck acceleration severe differences resulted due to the different load approximation methods — see Chapter 6.3.2. However, as discussed in Chapter 6.8, the dynamic effects exceeded the ones due to the static calculation, but with respect to the common minimum detail category FAT-71 ($\Delta\sigma_C = 71/1.15 = 61.74$ N/mm^2) the arch bridge is not prone to fatigue problems.

Bibliography

[1] Adam, C.; Salcher, P. "Dynamic effects of high-speed trains on simple bridge structures." In: *Structural Engineering and Mechanics* 51 (4 2014), pp. 581–599.

[2] Albuquerque, C.; de Castro, P.M.S.T.; Calçada, Rui. "Efficient crack analysis of dynamically loaded structures using a modal superposition of stress intensity factors." In: *Engineering Fracture Mechanics* 93 (2012), pp. 75–91.

[3] Albuquerque, Carlos; Silva ,António L.L.; de Jesus, Abìlio M.P.; Calçada, Rui. "An efficient methodology for fatigue damage assessment of bridge details using modal superposition of stress intensity factors." In: *International Journal of Fatigue* 81 (2015), pp. 61–77.

[4] Baur, Karl Gerhard. *Drehgestelle - Bogies*. Freiburg im Breisgau: EK-Verlag, 2006.

[5] Brandstetter, Georg. "Analyse einfacher Tragwerksmodelle zur dynamischen Berechnung von Eisenbahnbrücken mit Schwerpunkt Schotteroberbau." Doctoral thesis. Technical University of Vienna, 2018.

[6] Calgaro, J-A; Tschumi, M; Gulvanessian, H. *Designers' Guide to Eurocode 1: Actions on Bridges. EN 1991-2, EN 1991-1-1, -1-3 TO -1-7 AND EN 1990 ANNEX A2*. London: Thomas Telford Ltd, 2010.

[7] Calgaro, J-A; Tschumi, M; Gulvanessian, H. *Designers' Guide to Eurocode: Basis of structural design. EN 1990*. 2nd ed. London: Thomas Telford Ltd, 2012.

[8] Clough, Ray W.; Penzien, Joseph. *Dynamics of structures*. 2nd ed. Computers and Structures, 2003.

[9] Craig, R.R.Jr.; Kurdila, A.J. *Fundamentals of Structural Dynamics*. 2nd ed. Hoboken: John Wiley & Sons, 2006.

[10] Dlubal. *RF-DYNAM Pro. Program Description*. Tiefenbach, Germany: Dlubal Software GmbH, 2019.

[11] Dlubal. *RFEM 5.19.01*. Tiefenbach, Germany: Dlubal Software GmbH, 2019.

[12] European Rail Research Institute (ERRI). *Confirmation of values against experi mental data*. 1999.

[13] European Rail Research Institute (ERRI). *Rail bridges for speeds > 200km/h Final report. Part A: Synthesis of the results of D 214 research. Part B: Proposed UIC Leaflet*. 1999.

[14] European Rail Research Institute (ERRI). *Recommendations for calculating damping in rail bridge decks*. 1999.

[15] Fink, Josef; Mähr, Tobias. *Simplified method to calculate the dynamic response of railway-bridges on the basis of response spectra*. Budapest: 6th International Conference on Bridges across the Danube 2007.

[16] Fink, Josef; Mähr, Tobias. "Vereinfachte Methode zur Berechnung der dynamischen Antwort von Eisenbahnbrücken bei Zugüberfahrt." In: *Stahlbau* 76 (10 2007), pp. 710–721.

[17] Frýba, Ladislav. *Dynamics of railway bridges*. 2nd ed. London: Thomas Telford, 1996.

[18] Frýba, Ladislav. "Dynamische Beanspruchungen von Eisenbahnbrücken und ihre Einflüsse auf die Ermüdung." In: *Stahlbau* 67 (8 1998), pp. 627–633.

[19] Frýba, Ladislav. *Vibration of solids and structures under moving loads*. 3rd ed. London: Thomas Telford, 1999.

[20] Gasch, Robert; Knothe, Klaus; Liebich, Robert. *Strukturdynamik. Diskrete Systeme und Kontinua*. 2nd ed. Berlin: Springer Vieweg, 2012.

[21] Geißler, Karsten. *Handbuch Brückenbau. Entwurf, Konstruktion, Berechnung, Bewertung und Ertüchtigung*. Berlin: Wilhelm Ernst & Sohn, 2014.

[22] Haibach, E. *Betriebsfestigkeit. Verfahren und Daten zur Bauteilberechnung*. Berlin: Springer-Verlag, 2006.

[23] Hauser, Andreas; Adam Christoph. *Abschätzung der Schwingungsantwort von Brückentragwerken für Hochgeschwindigkeitszüge*. Vienna: D-A-CH Tagung 27.9. - 28.9.2007 Österreichischen Gesellschaft für Erdbebeningenieurwesen und Baudynamik.

[24] Hendy, C.R.; Murphy, C.J. *Designers' guide to EN 1993-2 Eurocode 3: Design of steel structures. Part 2: Steel bridges*. London: Thomas Telford Ltd, 2007.

[25] Horas, Cláudio S.; Alencar, Guilherme; De Jesus, Abílio M.P.; Calçada, Rui. "Application of the modal superposition technique combined with analytical elastoplastic approaches to assess the fatigue crack initiation on structural components." In: *Engineering Fracture Mechanics* 185 (2017), pp. 271–283.

[26] Horas, Cláudio S.; Alencar, Guilherme; De Jesus, Abílio M.P.; Calçada, Rui. "Development of an efficient approach for fatigue crack initiation and propagation analysis of bridge critical details using the modal superposition technique." In: *Engineering Failure Analysis* 89 (2018), pp. 118–137.

[27] Inman, D.J. *Engineering Vibration*. 4th ed. New Jersey: Pearson Education, Inc., 2014.

[28] International Union of Railways (UIC). *UIC Code 702. Static Loading Diagrams to be Taken into Consideration for the Design of Rail-carrying Structures on Lines Used by International Services*. 3rd ed. Paris, 2003.

[29] International Union of Railways (UIC). *UIC Code 776-1. Loads to be Considered in Railway Bridge Design*. 5th ed. Paris, 2006.

[30] Knothe, K.; Stichel, S. *Schienenfahrzeugdynamik*. Berlin: Springer-Verlag, 2003.

[31] Li, Huile; Frangopol, Dan M.; Soliman, Mohamed, Xia, He. "Fatigue reliability assessment of railway bridges based on probabilistic dynamic analysis of a coupled train-bridge system." In: *Journal of Structural Engineering* 142 (3 2016), p. 04015158.

[32] Mähr, Tobias Christoph. "Theoretische und experimentelle Untersuchungen zum dynamischen Verhalten von Eisenbahnbrücken mit Schotteroberbau unter Verkehrslast." Doctoral thesis. Technical University of Vienna, 2008.

[33] Mähr, Tobias; Fink, Josef. "Adoption of the response spectra method for calculating the dynamic response of railway bridges." In: *Steel Construction* 3 (4 2010), pp. 212–217.

[34] MATLAB. *MATLAB R2017a*. Natick, Massachusetts, United States: MathWorks, 2017.

[35] ÖBB Infrastruktur. *B 45. Technische Richtlinie für Eisenbahnbrücken und sonstige Konstruktive Ingenieurbauwerke*. 2011.

[36] ÖBB Infrastruktur. *Planungsgrundsätze für Eisenbahnbrücken*. 2008.

[37] ÖBB Infrastruktur. *Richtlinie für die dynamische Berechnung von Eisenbahnbrücken*. 2011.

[38] ÖNORM B 1991-2. *Eurocode 1 - Actions on structures. Part 2: Traffic loads on bridges - National specifications concerning ÖNORM EN 1991-2 and national supplements*. Austrian Standards Institute, 2011.

[39] ÖNORM B 1991-2. *Eurocode 1 - Actions on structures. Part 2: Traffic loads on bridges - National specifications concerning ÖNORM EN 1991-2 and national supplements*. Austrian Standards Institute, 2018.

[40] ÖNORM EN 10025-2. *Hot rolled products of structural steels. Part 2: Technical delivery conditions for non-alloy structural steels*. Austrian Standards Institute, 2018.

[41] ÖNORM EN 1990. *Eurocode - Basis of structural design*. Austrian Standards Institute, 2013.

[42] ÖNORM EN 1990/A1. *Eurocode - Basis of structural design. Amendment 1: Application for bridges*. Austrian Standards Institute, 2013.

[43] ÖNORM EN 1991-2. *Eurocode 1 - Actions on structures. Part 2: Traffic loads on bridges*. Austrian Standards Institute, 2012.

[44] ÖNORM EN 1993-1-5. *Eurocode 3 - Design of steel structures. Part 1-5: Plated structural elements*. Austrian Standards Institute, 2020.

[45] ÖNORM EN 1993-1-9. *Eurocode 3 - Design of steel structures. Part 1-9: Fatigue*. Austrian Standards Institute, 2013.

[46] ÖNORM EN 1993-2. *Eurocode 3 - Design of steel structures. Part 2: Steel bridges*. Austrian Standards Institute, 2010.

[47] Papula, L. *Mathematik für Ingenieure und Naturwissenschaftler Band 2*. 14th ed. Wiesbaden: Springer Vieweg, 2015.

[48] Pircher, Heinz. "Lösung baudynamischer Probleme mittels analytischer Zeitintegration und modaler Analyse." Doctoral thesis. Graz University of Technology, Faculty of Civil Engineering, 2006.

[49] Pommersberger, G.; Siebke, H. "Das Belastungsbild UIC 71, die neue Bemessungsgrundlage für den Eisenbahnbrückenbau." German. In: *Eisenbahntechnische Rundschau* 25 (1/2 1976).

[50] Rail Cargo Austria AG. *Güterwagen und innovative Transport- und Umschlagslösungen der Rail Cargo Group*. 2015. URL: `http://www.railcargowagon.at/de/Unsere_Fahrzeuge/wagen_folder.pdf` (visited on 09/01/2017).

[51] Rauert, Tim. "Zum Einfluss baulicher Randbedingungen auf das dynamische Verhalten von WIB-Eisenbahnbrücken." Doctoral thesis. RWTH Aachen University, Faculty of Civil Engineering, 2011.

[52] Ribeiro, D.; Calçada, Rui; Delgado, R. *Fatigue on metallic railway bridges: methodology of analysis and application to Alcácer do Sal Bridge*. Porto: IABMAS 2006.

[53] Salcher, P.; Adam, C. “Ein Bemessungsbehelf zur schnellen dynamischen Bewertung von einfachen Eisenbahnbrücken.” In: *Bauingenieur* 93 (6 2018), pp. 233–241.

[54] Salcher, P.; Adam, C. “Quick assessment of high-speed railway bridges based on a non-dimensional parameter representation.” In: *Advances in Structural Engineering* 20 (11 2017), pp. 1623–1631.

[55] Salcher, Patrick. “Reliability assessment of railway bridges designed for high-speed traffic: Modelling strategies and stochastic simulation.” Doctoral thesis. University of Innsbruck, 2015.

[56] Savin, Eric. “Dynamic amplification factor and response spectrum for evaluation of vibrations of beams under successive moving loads.” In: *Journal of Sound and Vibration* 248 (2 2001), pp. 267–288.

[57] Schörghofer, Andreas; Unterweger, Harald; Seidl, Florian; Kettler, Markus. “Dynamische Berechnung von Eisenbahnbrücken. Lastmodell HSLM-A ausreichend für zugehörige Hochgeschwindigkeitszüge?” In: *EI-Eisenbahningenieur* (3 2020), pp. 62–66.

[58] Sousa Figueiredo, Helder Miguel. “Dinâmica de pontes mistas aço-betão em linhas de alta velocidade.” Masterthesis. Universidade do Porto, Faculdade de Engenharia, 2007.

[59] Spengler, M. “Dynamik von Eisenbahnbrücken unter Hochgeschwindigkeitsverkehr.” Doctoral thesis. Technical University of Darmstadt, 2010.

[60] Unterweger, Harald. *Stahl- und Verbundbrücken*. Graz University of Technology, 2011.

[61] Unterweger, Harald; Schörghofer, Andreas. “Neue Züge in Hochgeschwindigkeitsnetz – Eignung der Zugsignatur als Ersatz für dynamische Berechnungen an Brücken.” Graz University of Technology, Faculty of Civil Engineering, not published, 2019.

[62] Unterweger, Harald; Taras, Andreas; Schörghofer, Andreas. “Tragsicherheit von Bestandsbrücken für neue Hochgeschwindigkeitszüge — Teil 1. Analyse der maßgebenden Zugparameter und deren Grenzwerte.” In: *EI-Eisenbahningenieur* (4 2016), pp. 40–44.

[63] Unterweger, Harald; Taras, Andreas; Schörghofer, Andreas. “Tragsicherheit von Bestandsbrücken für neue Hochgeschwindigkeitszüge — Teil 2. Selektion kritischer Einzeltragwerke und objektiver Zugvergleich.” In: *EI-Eisenbahningenieur* (5 2016), pp. 62–66.

[64] Weber, Benedikt. *Vorlesung Tragwerksdynamik*. 3rd ed. Zumikon: Instiut für Baustatik und Konstruktion an der ETH Zürich, 2002.

[65] Weber, Wilmar. “Schwingbeiwerte und sogenannte ”dynamische Beiwerte” (”Schwingfaktoren”) von Eisenbahnbrücken.” German. In: *Stahlbau* 67 (8 1998), pp. 659–666.

[66] Matthias Zacher Manfred; Baeßler. “Dynamic behaviour of ballast on railway bridges.” In: *Dynamics fo High-Speed Railway Bridges: Selected and revised papers from the course on 'Dynamics of High-Speed Railway Brdiges', Porto, Portugal, 20-23 September 2005* ().

[67] Zhai, Wanming; Han, Zhaoling; Chen, Zhaowei; Ling, Liang; Zhu Shengyang. “Train–track–bridge dynamic interaction: a state-of-the-art review.” In: *Vehicle System Dynamics* 57 (7 2019), pp. 984–1027.

[68] Zhou, H.; Liu, K.; Shi, G.; Wang, Y.Q.; Shi, Y.J.; De Roeck, G. “Fatigue assessment of a composite railway bridge for high speed trains. Part I: Modeling and fatigue critical details.” In: *Journal of Constructional Steel Research* 82 (2013), pp. 234–245.

[69] Zhou, H.; Liu, K.; Shi, G.; Wang, Y.Q.; Shi, Y.J.; De Roeck, G. "Fatigue assessment of a composite railway bridge for high speed trains. Part II: Conditions for which a dynamic analysis is needed." In: *Journal of Constructional Steel Research* 82 (2013), pp. 246–254.

[70] Zhou, H.; Shi, G.; Wang, Y.Q.; Chen, H.; De Roeck, G. "Fatigue evaluation of a composite railway bridge based on fracture mechanics through global–local dynamic analysis." In: *Journal of Constructional Steel Research* 122 (2016), pp. 1–13.

[71] Ziegler, Franz. *Technische Mechanik der festen und flüssigen Körper*. 3rd ed. Wien New York: Springer-Verlag, 1985.

Appendix

Appendix A.

Train data

A.1. Trains according to design codes

Axle Nr.	Mass [t]	Distance [mm]	Axle Nr.	Mass [t]	Distance [mm]	Axle Nr.	Mass [t]	Distance [mm]
1	22.5	0	19	11	3600	37	11	11500
2	22.5	2200	20	11	2600	38	11	2600
3	22.5	2200	21	11	11500	39	11	3600
4	22.5	6900	22	11	2600	40	11	2600
5	22.5	2200	23	11	3600	41	11	11500
6	22.5	2200	24	11	2600	42	11	2600
7	11	3200	25	11	11500	43	11	3600
8	11	2600	26	11	2600	44	11	2600
9	11	11500	27	11	3600	45	11	11500
10	11	2600	28	11	2600	46	11	2600
11	11	3600	29	11	11500	47	11	3600
12	11	2600	30	11	2600	48	11	2600
13	11	11500	31	11	3600	49	11	11500
14	11	2600	32	11	2600	50	11	2600
15	11	3600	33	11	11500	51	11	3600
16	11	2600	34	11	2600	52	11	2600
17	11	11500	35	11	3600	53	11	11500
18	11	2600	36	11	2600	54	11	2600

Table A.1.: TypeC1 — according to ÖNORM EN 1991-2 [43] Annex D

Axle Nr.	Mass [t]	Distance [mm]
1	22.5	0
2	22.5	3300
3	22.5	6700
4	22.5	3300
5	11	3900
6	11	2500
7	11	16500
8	11	2500
9	11	5000
10	11	2500
11	11	16500
12	11	2500
13	11	5000
14	11	2500
15	11	16500
16	11	2500
17	11	5000
18	11	2500
19	11	16500
20	11	2500
21	11	5000
22	11	2500
23	11	16500
24	11	2500
25	11	5000
26	11	2500
27	11	16500
28	11	2500
29	11	5000
30	11	2500
31	11	16500
32	11	2500
33	11	5000
34	11	2500
35	11	16500
36	11	2500
37	11	5000
38	11	2500
39	11	16500
40	11	2500
41	11	5000
42	11	2500
43	11	16500
44	11	2500

Table A.2.: TypeC2 — according to ÖNORM EN 1991-2 [43] Annex D

Axle Nr.	Mass [t]	Distance [mm]
1	20	0
2	20	3000
3	20	8460
4	20	3000
5	15	4450
6	15	2500
7	15	16500
8	15	2500
9	15	4900
10	15	2500
11	15	16500
12	15	2500
13	15	4900
14	15	2500
15	15	16500
16	15	2500
17	15	4900
18	15	2500
19	15	16500
20	15	2500
21	15	4900
22	15	2500
23	15	16500
24	15	2500
25	15	4900
26	15	2500
27	15	16500
28	15	2500
29	15	4900
30	15	2500
31	15	16500
32	15	2500
33	15	4900
34	15	2500
35	15	16500
36	15	2500
37	15	4900
38	15	2500
39	15	16500
40	15	2500
41	15	4900
42	15	2500
43	15	16500
44	15	2500
45	15	4900
46	15	2500
47	15	16500
48	15	2500
49	15	4900
50	15	2500
51	15	16500
52	15	2500
53	15	4900
54	15	2500
55	15	16500
56	15	2500
57	20	4450
58	20	3000
59	20	8460
60	20	3000

Table A.3.: TypeC3 — according to ÖNORM EN 1991-2 [43] Annex D

Axle Nr.	Mass [t]	Distance [mm]	Axle Nr.	Mass [t]	Distance [mm]	Axle Nr.	Mass [t]	Distance [mm]
1	22.5	0	33	22.5	1800	65	22.5	1800
2	22.5	2100	34	22.5	5700	66	22.5	1800
3	22.5	2100	35	22.5	1800	67	22.5	4000
4	22.5	4400	36	22.5	1800	68	22.5	1800
5	22.5	2100	37	22.5	4000	69	22.5	1800
6	22.5	2100	38	22.5	1800	70	22.5	5700
7	22.5	4000	39	22.5	1800	71	22.5	1800
8	22.5	1800	40	22.5	5700	72	22.5	1800
9	22.5	1800	41	22.5	1800	73	22.5	4000
10	22.5	5700	42	22.5	1800	74	22.5	1800
11	22.5	1800	43	22.5	4000	75	22.5	1800
12	22.5	1800	44	22.5	1800	76	22.5	5700
13	22.5	4000	45	22.5	1800	77	22.5	1800
14	22.5	1800	46	22.5	5700	78	22.5	1800
15	22.5	1800	47	22.5	1800	79	22.5	4000
16	22.5	5700	48	22.5	1800	80	22.5	1800
17	22.5	1800	49	22.5	4000	81	22.5	1800
18	22.5	1800	50	22.5	1800	82	22.5	5700
19	22.5	4000	51	22.5	1800	83	22.5	1800
20	22.5	1800	52	22.5	5700	84	22.5	1800
21	22.5	1800	53	22.5	1800	85	22.5	4000
22	22.5	5700	54	22.5	1800	86	22.5	1800
23	22.5	1800	55	22.5	4000	87	22.5	1800
24	22.5	1800	56	22.5	1800	88	22.5	5700
25	22.5	4000	57	22.5	1800	89	22.5	1800
26	22.5	1800	58	22.5	5700	90	22.5	1800
27	22.5	1800	59	22.5	1800	91	22.5	4000
28	22.5	5700	60	22.5	1800	92	22.5	1800
29	22.5	1800	61	22.5	4000	93	22.5	1800
30	22.5	1800	62	22.5	1800	94	22.5	5700
31	22.5	4000	63	22.5	1800	95	22.5	1800
32	22.5	1800	64	22.5	5700	96	22.5	1800

Table A.4.: TypeC5 — according to ÖNORM EN 1991-2 [43] Annex D

Axle Nr.	Mass [t]	Distance [mm]
1	17	0
2	17	3000
3	17	11000
4	17	3000
5	17	3300
6	17	3000
7	17	15700
8	17	3000
9	17	15700
10	17	3000

Axle Nr.	Mass [t]	Distance [mm]
11	17	15700
12	17	3000
13	17	15700
14	17	3000
15	17	15700
16	17	3000
17	17	15700
18	17	3000
19	17	15700
20	17	3000

Axle Nr.	Mass [t]	Distance [mm]
21	17	15700
22	17	3000
23	17	15700
24	17	3000
25	17	15700
26	17	3000
27	17	3300
28	17	3000
29	17	11000
30	17	3000

Table A.5.: TypeC4 — according to ÖNORM EN 1991-2 [43] Annex D

Axle Nr.	Mass [t]	Distance [mm]
1	22.5	0
2	22.5	2100
3	22.5	2100
4	22.5	4400
5	22.5	2100
6	22.5	2100
7	7	3900
8	7	6500
9	7	3800
10	7	6500
11	22.5	3700
12	22.5	1800
13	22.5	12800
14	22.5	1800
15	7	3700
16	7	6500
17	22.5	3500
18	22.5	1800
19	22.5	8000
20	22.5	1800
21	22.5	3200
22	22.5	1800
23	22.5	8000
24	22.5	1800
25	7	3500
26	7	6500

Axle Nr.	Mass [t]	Distance [mm]
27	22.5	3700
28	22.5	1800
29	22.5	12800
30	22.5	1800
31	22.5	3600
32	22.5	1800
33	22.5	12800
34	22.5	1800
35	22.5	3600
36	22.5	1800
37	22.5	12800
38	22.5	1800
39	7	3700
40	7	6500
41	7	3800
42	7	6500
43	22.5	3500
44	22.5	1800
45	22.5	8000
46	22.5	1800
47	22.5	3200
48	22.5	1800
49	22.5	8000
50	22.5	1800
51	7	3500

Axle Nr.	Mass [t]	Distance [mm]
52	7	6500
53	22.5	3700
54	22.5	1800
55	22.5	12800
56	22.5	1800
57	22.5	3400
58	22.5	1800
59	22.5	8000
60	22.5	1800
61	7	3500
62	7	6500
63	7	3800
64	7	6500
65	22.5	3500
66	22.5	1800
67	22.5	8000
68	22.5	1800
69	22.5	3200
70	22.5	1800
71	22.5	8000
72	22.5	1800
73	22.5	3400
74	22.5	1800
75	22.5	12800
76	22.5	1800

Table A.6.: TypeC6 — according to ÖNORM EN 1991-2 [43] Annex D

Axle Nr.	Mass [t]	Distance [mm]
1	22.5	0
2	22.5	2200
3	22.5	2200
4	22.5	6900
5	22.5	2200
6	22.5	2200
7	22.5	3000
8	22.5	1800
9	22.5	11000
10	22.5	1800
11	22.5	3200
12	22.5	1800
13	22.5	11000
14	22.5	1800
15	22.5	3200
16	22.5	1800
17	22.5	11000
18	22.5	1800
19	22.5	3200
20	22.5	1800
21	22.5	11000
22	22.5	1800
23	22.5	3200
24	22.5	1800
25	22.5	11000
26	22.5	1800
27	22.5	3200
28	22.5	1800
29	22.5	11000
30	22.5	1800
31	22.5	3200
32	22.5	1800
33	22.5	11000
34	22.5	1800
35	22.5	3200
36	22.5	1800
37	22.5	11000
38	22.5	1800
39	22.5	3200
40	22.5	1800
41	22.5	11000
42	22.5	1800
43	22.5	3200
44	22.5	1800
45	22.5	11000
46	22.5	1800

Table A.7.: TypeC7 — according to ÖNORM EN 1991-2 [43] Annex D

Axle Nr.	Mass [t]	Distance [mm]
1	22.5	0
2	22.5	2200
3	22.5	2200
4	22.5	6900
5	22.5	2200
6	22.5	2200
7	22.5	3500
8	22.5	5500
9	22.5	4200
10	22.5	5500
11	22.5	4200
12	22.5	5500
13	22.5	4200
14	22.5	5500
15	22.5	4200
16	22.5	5500
17	22.5	4200
18	22.5	5500
19	22.5	4200
20	22.5	5500
21	22.5	4200
22	22.5	5500
23	22.5	4200
24	22.5	5500
25	22.5	4200
26	22.5	5500
27	22.5	4200
28	22.5	5500
29	22.5	4200
30	22.5	5500
31	22.5	4200
32	22.5	5500
33	22.5	4200
34	22.5	5500
35	22.5	4200
36	22.5	5500
37	22.5	4200
38	22.5	5500
39	22.5	4200
40	22.5	5500
41	22.5	4200
42	22.5	5500
43	22.5	4200
44	22.5	5500
45	22.5	4200
46	22.5	5500

Table A.8.: TypeC8 — according to ÖNORM EN 1991-2 [43] Annex D

A.2. Trains according to literature

Axle Nr.	Mass [t]	Distance [mm]	Axle Nr.	Mass [t]	Distance [mm]	Axle Nr.	Mass [t]	Distance [mm]
1	17.2	0	9	18.2	14750	17	18.7	14750
2	17.2	2700	10	18.2	2750	18	18.7	2750
3	18.7	13975	11	18.3	14750	19	18.5	14750
4	18.7	2750	12	18.3	2750	20	18.6	2750
5	18.6	14750	13	18.7	14750	21	18.2	14750
6	18.7	2750	14	18.7	2750	22	18.2	2750
7	17.5	14750	15	18.6	14750	23	17.5	13975
8	17.5	2750	16	18.6	2750	24	17.6	2700

Table A.9.: EC250-Brutto18 — according to [61]

Axle Nr.	Mass [t]	Distance [mm]	Axle Nr.	Mass [t]	Distance [mm]	Axle Nr.	Mass [t]	Distance [mm]
1	17.5	0	17	19.9	6800	33	17.0	6800
2	17.2	2300	18	18.2	2750	34	17.0	2300
3	18.7	17200	19	20.1	16900	35	17.1	17200
4	18.7	2300	20	18.3	2750	36	17.1	2300
5	18.6	6800	21	19.9	6650	37	20.1	6800
6	18.7	2600	22	18.7	2750	38	20.1	2600
7	17.5	16900	23	20.1	16900	39	20.0	16900
8	17.5	2600	24	18.6	2750	40	20.0	2600
9	19.9	6650	25	17.7	6800	41	17.7	6800
10	18.2	2600	26	18.7	2750	42	17.7	2300
11	18.3	16900	27	17.9	17200	43	18.0	17200
12	18.3	2600	28	18.6	2750	44	18.0	2300
13	18.7	6800	29	20.6	6800	45	17.6	6950
14	18.7	2300	30	18.2	2750	46	17.6	2300
15	18.6	17200	31	20.6	16900	47	17.6	17200
16	18.6	2300	32	17.6	2700	48	17.6	2300

Table A.10.: ICE4-K3-12cars — according to [61]

Car type	Axle Nr.	Load [N]	Distance [mm]	Car type	Axle Nr.	Load [N]	Distance [mm]
Taurus	1	217782	0	Taurus	33	217782	6040
	2	217782	3000		34	217782	3000
	3	217782	6900		35	217782	6900
	4	217782	3000		36	217782	3000
Bmpz-2	5	142073	5640	Bmpz-2	37	142073	5640
	6	142073	2500		38	142073	2500
	7	142073	16500		39	142073	16500
	8	142073	2500		40	142073	2500
Ampz	9	136678	5000	Ampz	41	136678	5000
	10	136678	2500		42	136678	2500
	11	136678	16500		43	136678	16500
	12	136678	2500		44	136678	2500
Ampz	13	136678	5000	Ampz	45	136678	5000
	14	136678	2500		46	136678	2500
	15	136678	16500		47	136678	16500
	16	136678	2500		48	136678	2500
Ampz	17	136678	5000	Ampz	49	136678	5000
	18	136678	2500		50	136678	2500
	19	136678	16500		51	136678	16500
	20	136678	2500		52	136678	2500
Arbmpz	21	138149	5000	Arbmpz	53	138149	5000
	22	138149	2500		54	138149	2500
	23	138149	16500		55	138149	16500
	24	138149	2500		56	138149	2500
Bmpz-1	25	143545	5000	Bmpz-1	57	143545	5000
	26	143545	2500		58	143545	2500
	27	143545	16500		59	143545	16500
	28	143545	2500		60	143545	2500
Afmpz	29	144526	5000	Afmpz	61	144526	5000
	30	144526	2500		62	144526	2500
	31	144526	16500		63	144526	16500
	32	144526	2500		64	144526	2500

Table A.11.: TypeC19 — adapted according to [32]

			Taurus	Ampz	Afmpz	ARbmpz	Bmpz-1	Bmpz-2
Masses and moments of inertia	m_P	mass of the car body [kg]	52400	43530	46330	44130	46330	45730
	I_P	mass moment of inertia of the car body [kgm^2]	890008.4	2700100	2900100	2800100	2900100	2900100
	m_{B1}, m_{B2}	masses of the bogies 1 and 2 [kg]	13200	2300	3600	2300	2300	2300
	I_{B1}, I_{B2}	mass moments of inertia of the bogies 1 and 2 [kgm^2]	7300	1600	1760	1600	1600	1600
	m_{W1}, m_{W2}, m_{W3}, m_{W4}	masses of the wheel-sets 1 to 4 [kg]	2500	1900	1900	1900	1900	1900
Spring and damping constants	k_{11}, k_{12}, k_{13}, k_{14}	primary suspension stiffness [kN/m]	4000	1600	1600	1600	1600	1600
	c_{11}, c_{12}, c_{13}, c_{14}	primary suspension damping [kNs/m]	80	30	30	30	30	30
	k_{21}, k_{22}	secondary suspension stiffness [kN/m]	2800	320	320	320	320	320
	c_{21}, c_{22}	secondary suspension damping [kNs/m]	200	30	30	30	30	30
Geometry	x_{PB}	distance of the car body's center of gravity to the connection of the secondary suspension system [m]	4.95	9.50	9.50	9.50	9.50	9.50
	x_{BW}	distance of the bogie's center of gravity to the connection of the primary suspension system [m]	1.50	1.25	1.25	1.25	1.25	1.25

Table A.12.: TypeC19 — input values for 2D multi-body model — adapted according to [32]

A.3. Trains according to the monitoring station Enns

Axle Nr.	Mass [t]		Distance [mm]	
	μ	σ	μ	σ
1	16.9	0.36	0	0.0
2	16.8	0.43	2501	1.6
3	15.9	0.38	15352	23.9
4	16.3	0.43	2501	1.6
5	12.4	0.45	3698	3.0
6	12.4	0.46	2501	1.5
7	11.9	0.56	16358	26.6
8	11.9	0.55	2500	1.5
9	12.1	0.70	3479	2.9
10	12.1	0.72	2500	1.5
11	12.1	0.45	16358	26.2
12	12.2	0.46	2500	1.5
13	12.0	0.62	3479	2.5
14	12.0	0.64	2500	1.6
15	12.2	0.47	16357	26.1
16	12.2	0.49	2500	1.6
17	12.1	0.43	3477	3.0
18	12.0	0.43	2500	1.6
19	12.5	0.45	16358	25.2
20	12.6	0.43	2501	1.5
21	16.1	0.41	3699	3.2
22	16.3	0.53	2501	1.6
23	16.4	0.46	15353	24.1
24	17.0	0.61	2501	1.7

Table A.13.: DOSTO

Axle	Mass [t]		Distance [mm]	
	μ	σ	μ	σ
1	14.6	0.33	0	0.0
2	14.2	0.36	2699	1.7
3	14.6	0.37	16307	36.8
4	14.5	0.38	2699	1.7
5	13.9	0.34	4205	4.8
6	14.3	0.31	2699	2.0
7	13.7	0.41	16302	31.4
8	13.4	0.40	2698	1.9
9	14.2	0.35	4212	6.4
10	14.6	0.32	2700	2.0
11	14.4	0.57	16305	31.7
12	14.2	0.59	2699	1.9
13	12.3	0.42	4210	4.5
14	12.3	0.43	2699	1.7
15	12.2	0.42	16309	30.7
16	12.3	0.43	2699	1.7
17	14.1	0.74	4204	5.1
18	14.5	0.71	2699	1.9
19	14.4	0.40	16305	30.7
20	14.3	0.37	2699	1.8
21	13.3	0.46	4212	6.2
22	13.8	0.44	2699	2.0
23	14.2	0.34	16304	31.4
24	14.0	0.32	2699	1.9
25	14.6	0.39	4212	4.5
26	14.7	0.40	2699	1.7
27	14.0	0.35	16308	32.7
28	14.5	0.37	2699	1.7

Table A.14.: TypeC14 (ICE-T1 411)

Axle Nr.	Mass [t]		Distance [mm]		Axle Nr.	Mass [t]		Distance [mm]	
	μ	σ	μ	σ		μ	σ	μ	σ
1	16,6	0,27	0	0,0	25	16,6	0,29	6118	3,7
2	16,4	0,34	2500	1,6	26	16,4	0,34	2500	1,6
3	15,7	0,24	15353	22,3	27	15,7	0,27	15354	21,8
4	15,9	0,31	2500	1,6	28	16,0	0,31	2500	1,6
5	11,9	0,31	3698	3,1	29	11,9	0,39	3698	3,2
6	11,9	0,29	2500	1,7	30	11,9	0,39	2500	1,6
7	11,4	0,37	16359	24,9	31	11,5	0,52	16358	26,0
8	11,4	0,36	2500	1,6	32	11,4	0,52	2500	1,7
9	11,6	0,56	3478	3,0	33	11,7	0,64	3479	3,1
10	11,6	0,58	2500	1,6	34	11,7	0,66	2500	1,6
11	11,4	0,48	16359	24,9	35	11,5	0,36	16359	24,1
12	11,4	0,48	2500	1,7	36	11,5	0,36	2500	1,6
13	11,6	0,55	3478	2,5	37	11,7	0,65	3479	2,5
14	11,6	0,56	2500	1,6	38	11,6	0,67	2500	1,6
15	11,5	0,50	16359	25,0	39	11,6	0,37	16360	28,0
16	11,5	0,51	2500	1,7	40	11,6	0,36	2500	1,8
17	11,4	0,56	3478	3,0	41	11,5	0,38	3478	3,0
18	11,3	0,55	2500	1,8	42	11,5	0,38	2500	1,7
19	12,0	0,54	16360	23,9	43	12,2	0,49	16360	25,5
20	12,0	0,53	2500	1,6	44	12,2	0,46	2500	1,7
21	15,7	0,31	3699	3,1	45	15,7	0,21	3699	3,2
22	15,9	0,39	2500	1,6	46	15,8	0,27	2500	1,7
23	16,2	0,33	15353	22,3	47	16,0	0,24	15353	23,5
24	16,7	0,45	2500	1,8	48	16,5	0,37	2500	1,7

Table A.15.: 2xDOSTO

Axle Nr.	Mass [t]		Distance [mm]		Axle Nr.	Mass [t]		Distance [mm]	
	μ	σ	μ	σ		μ	σ	μ	σ
1	21.4	0.41	0	0.0	33	21.3	0.43	6008	12.6
2	21.1	0.60	3000	2.8	34	21.1	0.64	2999	1.8
3	21.1	0.36	6900	8.1	35	21.0	0.38	6900	4.5
4	21.3	0.87	2999	2.0	36	21.3	0.84	2999	1.7
5	12.7	0.55	5633	21.4	37	13.0	0.47	5635	20.7
6	12.6	0.52	2500	2.7	38	12.9	0.44	2500	2.2
7	12.2	0.49	16494	53.8	39	12.4	0.44	16493	47.0
8	12.2	0.47	2500	2.0	40	12.4	0.42	2500	1.9
9	12.8	0.49	4990	11.6	41	13.0	0.46	4990	12.7
10	12.7	0.46	2500	2.0	42	13.0	0.43	2500	1.9
11	12.5	0.50	16494	47.9	43	12.8	0.46	16495	46.0
12	12.6	0.47	2500	2.0	44	12.8	0.43	2500	1.9
13	12.8	0.45	4990	9.0	45	13.0	0.45	4991	10.1
14	12.7	0.43	2500	1.9	46	12.9	0.41	2500	1.9
15	12.6	0.45	16494	44.1	47	12.7	0.45	16495	43.1
16	12.6	0.43	2500	1.9	48	12.7	0.42	2500	1.9
17	13.0	0.47	4991	7.1	49	13.1	0.46	4991	8.1
18	13.0	0.45	2500	2.1	50	13.0	0.42	2500	2.0
19	12.8	0.43	16493	44.1	51	12.8	0.43	16494	47.0
20	12.9	0.41	2500	1.9	52	12.8	0.40	2500	1.9
21	13.5	0.28	4990	5.9	53	13.5	0.28	4990	6.8
22	13.4	0.23	2500	2.0	54	13.4	0.23	2500	2.0
23	12.0	0.26	16494	42.3	55	12.1	0.26	16495	47.2
24	12.1	0.22	2499	2.0	56	12.1	0.23	2499	1.9
25	12.4	0.33	4990	5.1	57	12.6	0.33	4990	5.4
26	12.3	0.30	2499	2.0	58	12.5	0.31	2500	2.0
27	12.2	0.38	16495	46.6	59	12.3	0.38	16495	54.3
28	12.3	0.35	2500	1.9	60	12.3	0.34	2499	2.1
29	13.1	0.28	4991	4.7	61	13.2	0.30	4990	5.2
30	13.1	0.23	2500	1.9	62	13.2	0.25	2500	2.0
31	14.0	0.22	16492	46.3	63	14.0	0.20	16497	54.1
32	13.9	0.20	2500	2.1	64	14.0	0.22	2500	2.4

Table A.16.: TypeC19-Taurus-front and TypeC19-Taurus-back (Railjet)

Axle Nr.	Mass [t]		Distance [mm]	
	μ	σ	μ	σ
1	21.3	0.48	0	0.0
2	21.1	0.59	3000	1.5
3	21.1	0.36	6899	3.6
4	21.2	0.86	2999	1.4
5	12.9	0.97	5630	21.4
6	12.8	0.96	2500	4.0
7	12.4	0.94	16493	45.5
8	12.4	0.95	2500	3.8
9	12.9	0.96	4978	35.5
10	12.8	0.95	2500	2.4
11	12.7	0.94	16492	45.9
12	12.7	0.95	2500	2.5
13	13.0	0.49	4978	35.3
14	12.9	0.48	2500	2.1
15	12.8	0.47	16492	44.1
16	12.8	0.46	2500	2.2
17	13.0	0.54	4979	36.0
18	13.0	0.52	2500	3.2
19	12.8	0.49	16492	42.9
20	12.9	0.48	2500	3.0
21	13.4	0.41	4979	36.1
22	13.4	0.36	2500	2.1
23	12.1	0.35	16492	42.1
24	12.2	0.34	2500	2.0
25	12.4	0.80	4979	36.0
26	12.4	0.79	2500	2.3
27	12.2	0.83	16494	47.2
28	12.3	0.83	2500	2.2
29	13.0	1.08	4980	35.6
30	13.0	1.05	2500	2.4
31	13.7	1.25	16491	48.9
32	13.8	1.26	2500	2.5

Table A.17.: TypeC19*-Taurus-front and TypeC19*-Taurus-back (Railjet)

Axle	Mass [t]		Distance [mm]	
	μ	σ	μ	σ
1	21.0	0.44	0	0.0
2	21.4	0.45	3000	1.2
3	20.8	0.38	6899	3.3
4	21.7	0.49	3000	1.2
5	12.5	1.67	5628	14.3
6	12.6	1.68	2501	6.7
7	12.5	1.70	16494	57.9
8	12.5	1.75	2501	6.7
9	12.2	1.67	4878	16.5
10	12.2	1.69	2501	4.3
11	12.1	1.69	16496	43.1
12	12.2	1.73	2500	4.3
13	12.8	0.66	4879	14.7
14	12.8	0.68	2501	4.2
15	12.7	0.63	16492	35.2
16	12.8	0.66	2501	4.3
17	12.7	0.70	4877	14.2
18	12.8	0.70	2500	3.7
19	12.7	0.70	16494	37.9
20	12.7	0.72	2500	3.7
21	12.6	0.86	4874	14.6
22	12.7	0.85	2501	3.7
23	12.6	0.93	16490	33.8
24	12.7	0.94	2501	3.6
25	12.8	0.86	4873	14.5
26	12.8	0.87	2501	5.2
27	12.8	0.97	16487	35.6
28	12.8	0.99	2501	5.2
29	11.5	1.66	4873	13.8
30	11.5	1.65	2501	5.2
31	11.2	1.79	16497	45.7
32	11.2	1.79	2501	5.2
33	11.1	2.30	4875	14.7
34	11.2	2.29	2501	6.6
35	10.9	2.53	16503	52.3
36	10.9	2.55	2501	6.6

Table A.18.: TypeC19** (Railjet)

Axle Nr.	Mass [t]		Distance [mm]	
	μ	σ	μ	σ
1	13.3	0.70	0	0.0
2	13.2	0.53	2300	1.4
3	11.0	0.22	12258	14.0
4	11.1	0.16	2800	1.3
5	10.6	0.44	11954	8.0
6	10.7	0.36	2799	2.0
7	12.3	0.82	12270	8.6
8	12.3	0.77	2300	1.0

Table A.19.: Talent 4023

Axle	Mass [t]		Distance [mm]	
	μ	σ	μ	σ
1	12.9	0.75	0	0.0
2	12.6	0.85	2300	1.2
3	10.9	0.41	12263	11.3
4	10.9	0.43	2799	1.3
5	10.1	0.30	11952	9.8
6	10.1	0.32	2798	1.6
7	11.0	0.54	11952	9.5
8	11.0	0.55	2799	1.6
9	13.0	0.91	12273	9.2
10	12.9	0.84	2300	1.1

Table A.20.: Talent 4024

Axle Nr.	Mass [t]		Distance [mm]	
	μ	σ	μ	σ
1	13.7	0.28	0	0.0
2	13.5	0.27	2300	0.8
3	12.7	0.27	13945	15.1
4	12.6	0.33	2300	1.0
5	9.6	0.68	5184	3.1
6	9.6	0.69	2299	1.1

Axle Nr.	Mass [t]		Distance [mm]	
	μ	σ	μ	σ
7	9.6	0.70	16329	23.8
8	9.6	0.72	2299	1.1
9	12.8	0.57	5186	5.8
10	12.7	0.59	2300	0.8
11	13.8	0.54	13941	13.5
12	13.8	0.56	2300	0.9

Table A.21.: Train 4020

Axle Nr.	Mass [t]		Distance [mm]	
	μ	σ	μ	σ
1	13.6	0.28	0	0.0
2	13.4	0.23	2300	0.8
3	12.7	0.26	13946	12.9
4	12.6	0.28	2299	0.9
5	9.4	0.10	5187	3.3
6	9.5	0.11	2299	1.1
7	9.4	0.16	16333	20.9
8	9.4	0.15	2299	1.1
9	12.7	0.25	5189	2.5
10	12.6	0.22	2300	1.0
11	13.5	0.28	13944	15.8
12	13.5	0.28	2300	0.9

Axle Nr.	Mass [t]		Distance [mm]	
	μ	σ	μ	σ
13	13.7	0.32	6809	3.3
14	13.4	0.21	2300	1.0
15	12.7	0.18	13946	13.4
16	12.6	0.21	2300	1.0
17	9.4	0.14	5185	2.8
18	9.4	0.14	2299	1.1
19	9.4	0.12	16337	18.5
20	9.4	0.12	2299	1.1
21	12.7	0.25	5188	3.3
22	12.6	0.23	2300	1.0
23	13.6	0.21	13944	15.7
24	13.7	0.22	2300	0.8

Table A.22.: 2xTrain 4020

Axle Nr.	Mass [t]		Distance [mm]		Axle Nr.	Mass [t]		Distance [mm]	
	μ	σ	μ	σ		μ	σ	μ	σ
1	13.4	0.23	0	0.0	19	9.3	0.11	16316	25.9
2	13.3	0.21	2300	1.1	20	9.3	0.08	2299	1.2
3	12.5	0.05	13940	19.4	21	12.6	0.13	5190	2.1
4	12.5	0.11	2300	0.9	22	12.6	0.18	2300	0.7
5	9.3	0.13	5183	2.4	23	13.2	0.19	13933	5.8
6	9.3	0.11	2299	0.9	24	13.3	0.16	2299	1.0
7	9.4	0.06	16309	19.2	25	13.4	0.20	6807	2.4
8	9.4	0.07	2299	1.4	26	13.3	0.18	2300	0.9
9	12.4	0.07	5191	2.5	27	12.4	0.07	13948	22.3
10	12.4	0.10	2300	0.7	28	12.4	0.09	2301	1.3
11	13.4	0.18	13932	16.9	29	9.3	0.13	5189	2.8
12	13.5	0.20	2300	1.1	30	9.3	0.10	2300	1.1
13	13.5	0.21	6808	1.7	31	9.3	0.06	16320	19.8
14	13.4	0.23	2301	0.9	32	9.4	0.07	2300	0.9
15	12.5	0.21	13941	6.9	33	12.5	0.10	5187	2.5
16	12.5	0.20	2300	1.0	34	12.5	0.12	2301	0.9
17	9.4	0.03	5187	1.5	35	13.6	0.28	13943	22.0
18	9.4	0.06	2300	1.2	36	13.7	0.27	2300	1.0

Table A.23.: 3xTrain 4020

Axle Nr.	Mass [t]		Distance [mm]		Axle Nr.	Mass [t]		Distance [mm]	
	μ	σ	μ	σ		μ	σ	μ	σ
1	13.8	0.22	0	0.0	25	13.7	0.23	6806	2.2
2	13.6	0.20	2300	1.0	26	13.5	0.21	2300	1.2
3	12.6	0.19	13946	11.4	27	12.6	0.15	13944	14.8
4	12.6	0.20	2300	0.8	28	12.5	0.16	2300	0.9
5	9.5	0.13	5184	4.0	29	9.5	0.14	5185	4.9
6	9.5	0.12	2299	1.3	30	9.5	0.14	2299	1.2
7	9.4	0.15	16330	25.4	31	9.5	0.16	16329	22.8
8	9.4	0.12	2299	1.2	32	9.5	0.14	2299	1.1
9	12.8	0.25	5186	4.4	33	12.7	0.26	5186	3.0
10	12.7	0.23	2300	0.9	34	12.7	0.24	2300	1.2
11	13.4	0.19	13944	14.3	35	13.5	0.25	13945	13.0
12	13.5	0.21	2300	0.9	36	13.6	0.24	2300	1.0
13	13.6	0.23	6807	2.9	37	13.6	0.26	6806	3.0
14	13.4	0.22	2300	1.0	38	13.4	0.25	2300	1.1
15	12.7	0.22	13948	13.6	39	12.7	0.17	13948	13.4
16	12.6	0.21	2300	1.0	40	12.7	0.17	2300	0.9
17	9.4	0.15	5184	3.8	41	9.5	0.17	5183	5.4
18	9.4	0.14	2299	1.3	42	9.5	0.18	2299	1.2
19	9.5	0.16	16330	19.9	43	9.5	0.13	16331	27.6
20	9.5	0.14	2299	1.2	44	9.5	0.11	2299	1.2
21	12.6	0.20	5189	4.3	45	12.8	0.30	5185	3.6
22	12.6	0.17	2300	1.0	46	12.7	0.27	2300	1.1
23	13.5	0.25	13948	13.1	47	13.7	0.15	13945	16.3
24	13.6	0.22	2300	0.9	48	13.8	0.13	2300	1.2

Table A.24.: 4xTrain 4020

Axle Nr.	Mass [t]		Distance [mm]		Axle Nr.	Mass [t]		Distance [mm]	
	μ	σ	μ	σ		μ	σ	μ	σ
1	13.3	0.94	0	0.0	11	13.7	1.21	5442	43.2
2	12.6	0.95	2300	0.9	12	13.1	1.15	2300	0.8
3	11.4	0.94	12279	141.4	13	11.6	1.02	12280	141.1
4	11.4	0.96	2798	1.4	14	11.6	1.04	2798	1.4
5	10.6	0.93	11971	159.2	15	10.6	0.91	11971	159.4
6	10.6	0.94	2799	0.9	16	10.6	0.90	2798	1.1
7	11.7	1.07	11970	159.0	17	11.5	0.96	11969	159.0
8	11.7	1.07	2799	1.1	18	11.5	0.97	2798	1.3
9	13.5	1.11	12287	140.8	19	13.1	0.96	12287	142.2
10	13.7	1.16	2300	0.9	20	13.3	0.96	2300	0.9

Table A.25.: 2xTalent 4024

Axle Nr.	Mass [t]		Distance [mm]		Axle Nr.	Mass [t]		Distance [mm]	
	μ	σ	μ	σ		μ	σ	μ	σ
1	0.0	0.00	0	0.0	16	10.0	0.00	2799	0.0
2	13.7	0.00	2302	0.0	17	10.1	0.00	11974	0.0
3	13.5	0.00	12242	0.0	18	10.6	0.00	2798	0.0
4	11.1	0.00	2799	0.0	19	10.7	0.00	12265	0.0
5	11.2	0.00	11941	0.0	20	12.0	0.00	2299	0.0
6	10.0	0.00	2799	0.0	21	12.3	0.00	5439	0.0
7	10.0	0.00	11938	0.0	22	14.5	0.00	2299	0.0
8	10.4	0.00	2799	0.0	23	13.7	0.00	12252	0.0
9	10.4	0.00	12238	0.0	24	11.4	0.00	2800	0.0
10	11.9	0.00	2299	0.0	25	11.4	0.00	11946	0.0
11	11.8	0.00	5439	0.0	26	10.0	0.00	2799	0.0
12	14.5	0.00	2299	0.0	27	10.0	0.00	11948	0.0
13	13.6	0.00	12264	0.0	28	10.5	0.00	2799	0.0
14	11.4	0.00	2799	0.0	29	10.5	0.00	12279	0.0
15	11.4	0.00	11922	0.0	30	12.1	0.00	2301	0.0

Table A.26.: 3xTalent 4024

Axle Nr.	Mass [t]		Distance [mm]		Axle Nr.	Mass [t]		Distance [mm]	
	μ	σ	μ	σ		μ	σ	μ	σ
1	20,9	0,30	0	0,0	13	12,7	0,37	5215	18,5
2	21,4	0,22	2999	1,1	14	12,6	0,39	2499	1,4
3	20,8	0,23	6900	2,6	15	12,8	0,38	15808	21,2
4	21,6	0,30	2999	1,1	16	12,7	0,39	2499	1,4
5	12,5	0,37	5982	10,3	17	12,4	0,43	5227	13,7
6	12,5	0,37	2499	1,4	18	12,4	0,42	2508	17,8
7	12,5	0,36	15808	21,4	19	12,3	0,39	16493	28,6
8	12,5	0,37	2499	1,4	20	12,3	0,42	2508	17,8
9	12,2	0,42	5218	17,5	21	12,1	0,26	4875	14,5
10	12,2	0,42	2542	24,8	22	12,2	0,27	2500	1,4
11	12,4	0,38	16464	31,8	23	12,1	0,32	16516	25,2
12	12,3	0,40	2542	25,1	24	12,0	0,32	2499	1,5

Table A.27.: PT-24-1

Axle	Mass [t]		Distance [mm]	
	μ	σ	μ	σ
1	20.9	0.37	0	0.0
2	21.1	0.37	2999	1.3
3	20.7	0.32	6900	3.4
4	21.4	0.42	3000	1.3
5	12.2	0.42	5627	18.0
6	12.2	0.45	2501	6.9
7	12.2	0.45	16505	32.5
8	12.1	0.45	2501	6.8
9	12.3	0.42	4872	16.8
10	12.3	0.44	2524	27.2
11	12.4	0.45	16474	34.3
12	12.3	0.47	2524	27.4
13	12.7	0.39	5223	19.0
14	12.7	0.41	2499	1.5
15	12.7	0.41	15799	31.2
16	12.7	0.42	2500	1.5
17	12.3	0.43	5219	18.5
18	12.4	0.43	2524	27.6
19	12.2	0.46	16474	41.2
20	12.2	0.48	2523	27.4
21	12.3	0.42	4867	17.0
22	12.3	0.44	2502	9.7
23	12.2	0.43	16502	35.4
24	12.2	0.44	2502	9.6

Table A.28.: PT-24-2

Axle	Mass [t]		Distance [mm]	
	μ	σ	μ	σ
1	21.0	0.32	0	0.0
2	21.4	0.24	3000	1.0
3	20.8	0.23	6900	2.8
4	21.6	0.29	2999	1.1
5	12.5	0.38	5983	11.1
6	12.6	0.41	2499	2.0
7	12.6	0.40	15808	32.2
8	12.6	0.42	2500	1.5
9	12.2	0.45	5214	13.9
10	12.3	0.46	2543	23.9
11	12.4	0.38	16463	29.7
12	12.3	0.40	2544	24.2
13	12.8	0.40	4856	17.2
14	12.8	0.41	2499	1.5
15	12.9	0.41	16514	26.6
16	12.8	0.43	2500	1.5
17	12.4	0.46	4870	13.0
18	12.4	0.47	2514	23.8
19	12.4	0.41	16489	29.4
20	12.3	0.42	2515	23.7
21	12.1	0.29	4870	16.9
22	12.1	0.31	2499	1.8
23	12.1	0.28	16519	27.3
24	12.0	0.32	2499	1.7

Table A.29.: PT-24-3

Axle Nr.	Mass [t]		Distance [mm]	
	μ	σ	μ	σ
1	21.3	0.36	0	0.0
2	21.6	0.30	3002	9.7
3	21.1	0.26	6904	22.3
4	21.7	0.36	3002	10.0
5	13.3	0.20	5604	21.3
6	13.6	0.23	2500	9.0
7	13.5	0.19	16524	86.1
8	13.5	0.25	2501	9.3
9	11.7	0.20	5179	18.6
10	11.8	0.20	2501	8.4
11	11.6	0.31	17023	45.1
12	11.7	0.27	2503	8.2

Axle Nr.	Mass [t]		Distance [mm]	
	μ	σ	μ	σ
13	13.4	0.44	5125	21.6
14	13.5	0.42	2599	8.7
15	13.5	0.41	16413	43.1
16	13.6	0.38	2599	8.8
17	13.8	0.39	4772	20.8
18	13.9	0.41	2599	8.9
19	13.7	0.47	16415	46.8
20	13.8	0.49	2599	8.7
21	12.6	0.39	4812	21.6
22	12.7	0.39	2500	8.2
23	12.4	0.36	16524	46.5
24	12.6	0.36	2500	8.2

Table A.30.: PT-24-4

Axle	Mass [t]		Distance [mm]	
	μ	σ	μ	σ
1	21.4	0.36	0	0.0
2	21.7	0.32	3000	4.6
3	21.2	0.34	6901	10.2
4	21.8	0.34	3000	4.7
5	13.4	0.20	5600	13.8
6	13.6	0.23	2498	4.4
7	13.5	0.15	16519	38.9
8	13.5	0.17	2499	4.4
9	13.6	0.23	4853	13.8
10	13.8	0.24	2498	4.4
11	13.5	0.27	16526	39.7
12	13.5	0.27	2499	4.2
13	13.6	0.41	4805	25.0
14	13.6	0.42	2595	7.5
15	13.1	0.37	16418	41.9
16	13.2	0.36	2595	7.5
17	13.6	0.29	4782	18.7
18	13.7	0.33	2597	4.2
19	13.4	0.42	16418	20.8
20	13.5	0.46	2597	4.2
21	12.4	0.23	4810	15.1
22	12.4	0.21	2499	4.1
23	12.2	0.21	16528	24.4
24	12.3	0.19	2498	4.1

Table A.31.: PT-24-5

Axle	Mass [t]		Distance [mm]	
	μ	σ	μ	σ
1	20.9	0.41	0	0.0
2	21.0	0.36	3000	1.3
3	20.7	0.37	6899	3.8
4	21.2	0.42	3000	1.5
5	12.0	0.28	5625	9.4
6	12.0	0.34	2500	1.9
7	12.0	0.29	16498	34.7
8	12.0	0.33	2500	1.9
9	12.4	0.41	4879	14.2
10	12.4	0.44	2508	17.4
11	12.3	0.40	16476	35.8
12	12.4	0.44	2508	17.5
13	12.7	0.39	5232	14.1
14	12.7	0.42	2500	1.8
15	12.6	0.39	15791	35.3
16	12.7	0.42	2500	1.8
17	12.3	0.43	5213	18.1
18	12.3	0.45	2541	26.1
19	12.1	0.42	16447	41.0
20	12.2	0.46	2540	25.8
21	12.4	0.40	5216	17.2
22	12.5	0.42	2500	1.7
23	12.5	0.41	15791	35.4
24	12.5	0.43	2500	1.7

Table A.32.: PT-24-6

Axle Nr.	Mass [t]		Distance [mm]	
	μ	σ	μ	σ
1	21.0	0.36	0	0.0
2	21.0	0.36	3000	1.3
3	20.7	0.37	6898	3.6
4	21.2	0.46	3000	1.5
5	12.0	0.26	5625	9.4
6	12.1	0.33	2500	1.9
7	11.9	0.30	16499	35.1
8	11.9	0.33	2500	2.1
9	12.4	0.40	4873	16.1
10	12.4	0.42	2514	23.2
11	12.3	0.40	16471	35.9
12	12.3	0.45	2514	23.7

Axle Nr.	Mass [t]		Distance [mm]	
	μ	σ	μ	σ
13	12.8	0.44	4873	14.6
14	12.9	0.46	2500	1.9
15	12.7	0.41	16495	53.8
16	12.7	0.43	2500	1.8
17	12.3	0.37	4854	17.2
18	12.4	0.40	2545	24.0
19	12.1	0.43	16444	38.3
20	12.1	0.46	2544	23.5
21	12.5	0.44	5210	14.7
22	12.6	0.47	2500	1.8
23	12.5	0.45	15786	32.7
24	12.6	0.49	2500	2.1

Table A.33.: PT-24-7

Axle	Mass [t]		Distance [mm]	
	μ	σ	μ	σ
1	21.7	0.34	0	0.0
2	21.9	0.25	3009	16.9
3	21.6	0.24	6921	39.2
4	22.2	0.34	3009	16.9
5	12.7	0.47	5628	34.6
6	12.6	0.44	2506	14.1
7	12.8	0.45	16540	98.9
8	12.8	0.44	2507	14.1
9	13.7	0.45	4825	32.5
10	13.7	0.46	2605	14.3
11	13.8	0.37	16429	84.3
12	13.7	0.37	2605	14.8
13	13.4	0.37	4787	29.1
14	13.5	0.38	2606	14.5
15	13.3	0.44	16428	85.0
16	13.3	0.45	2606	14.6
17	11.6	0.27	5139	32.3
18	11.6	0.31	2509	13.9
19	11.7	0.24	17031	99.3
20	11.6	0.24	2508	14.0
21	13.5	0.25	5188	30.0
22	13.6	0.20	2507	14.7
23	13.5	0.30	16533	145.2
24	13.4	0.24	2506	14.8

Table A.34.: PT-24-8

Axle	Mass [t]		Distance [mm]	
	μ	σ	μ	σ
1	21.8	0.32	0	0.0
2	21.9	0.30	3013	18.6
3	21.6	0.31	6931	43.3
4	22.1	0.30	3013	18.9
5	12.4	0.28	5631	35.6
6	12.4	0.27	2510	15.5
7	12.5	0.28	16559	104.6
8	12.5	0.28	2510	15.5
9	13.4	0.42	4831	30.3
10	13.5	0.38	2609	16.0
11	13.5	0.37	16451	96.2
12	13.5	0.36	2609	16.4
13	13.0	0.37	4803	32.9
14	13.1	0.36	2608	15.9
15	13.5	0.47	16447	89.6
16	13.4	0.43	2608	16.6
17	13.4	0.26	4824	39.3
18	13.5	0.27	2510	15.9
19	13.6	0.22	16564	105.1
20	13.6	0.22	2510	15.7
21	13.4	0.18	4871	32.0
22	13.5	0.17	2510	16.1
23	13.4	0.20	16559	118.0
24	13.4	0.17	2510	15.6

Table A.35.: PT-24-9

Axle Nr.	Mass [t]		Distance [mm]	
	μ	σ	μ	σ
1	20.9	0.33	0	0.0
2	21.4	0.27	3000	1.2
3	20.8	0.27	6900	3.4
4	21.6	0.33	2999	1.1
5	12.6	0.43	5984	24.3
6	12.6	0.45	2499	1.6
7	12.7	0.45	15799	35.5
8	12.6	0.46	2500	1.5
9	12.7	0.44	5588	11.0
10	12.7	0.45	2500	1.6
11	12.8	0.42	15800	33.5
12	12.7	0.44	2500	1.5
13	12.9	0.43	5587	10.7
14	12.8	0.44	2500	1.7
15	13.0	0.40	15800	34.8
16	12.9	0.42	2500	1.5
17	12.7	0.46	5232	10.9
18	12.7	0.46	2502	1.8
19	12.7	0.44	16494	36.3
20	12.6	0.46	2501	1.9
21	12.2	0.29	4878	11.7
22	12.2	0.29	2500	1.5
23	12.0	0.27	16510	42.9
24	12.0	0.31	2500	1.6

Table A.36.: PT-24-10

Axle	Mass [t]		Distance [mm]	
	μ	σ	μ	σ
1	20.9	0.46	0	0.0
2	20.9	0.44	3000	1.3
3	20.7	0.41	6898	3.9
4	21.1	0.48	3000	1.4
5	11.9	0.23	5626	20.5
6	11.9	0.32	2500	2.0
7	12.0	0.32	16494	41.9
8	12.0	0.39	2500	1.9
9	12.5	0.44	4880	11.1
10	12.5	0.49	2502	2.1
11	12.4	0.45	16484	30.7
12	12.5	0.49	2502	2.2
13	12.6	0.37	5235	11.0
14	12.7	0.40	2500	1.9
15	12.5	0.34	15784	29.9
16	12.6	0.39	2500	1.8
17	12.4	0.32	5584	11.1
18	12.4	0.37	2500	1.9
19	12.4	0.31	15787	33.4
20	12.4	0.36	2500	1.7
21	12.3	0.31	5585	11.1
22	12.3	0.35	2500	1.9
23	12.3	0.31	15787	33.2
24	12.4	0.36	2500	1.7

Table A.37.: PT-24-11

Axle	Mass [t]		Distance [mm]	
	μ	σ	μ	σ
1	20,9	0,41	0	0,0
2	20,9	0,38	3000	1,3
3	20,6	0,35	6898	3,6
4	21,2	0,42	3000	1,4
5	11,9	0,22	5625	15,7
6	11,9	0,29	2500	2,0
7	12,0	0,29	16501	44,8
8	12,0	0,35	2500	2,0
9	12,3	0,40	4881	11,4
10	12,4	0,44	2502	2,0
11	12,3	0,42	16481	34,0
12	12,4	0,45	2502	2,1
13	12,6	0,34	5232	12,6
14	12,6	0,35	2500	1,8
15	12,5	0,29	15788	29,8
16	12,5	0,34	2500	1,9
17	12,4	0,27	5585	9,7
18	12,4	0,31	2500	2,0
19	12,4	0,29	15789	32,3
20	12,5	0,32	2500	1,7
21	12,3	0,43	5230	13,3
22	12,3	0,47	2501	2,1
23	12,2	0,46	16479	32,9
24	12,2	0,47	2502	2,7

Table A.38.: PT-24-12

Axle Nr.	Mass [t]		Distance [mm]	
	μ	σ	μ	σ
1	21.4	0.29	0	0.0
2	21.7	0.29	3000	1.4
3	21.2	0.26	6899	3.4
4	21.8	0.32	3000	1.2
5	13.8	0.57	5619	15.5
6	14.0	0.58	2500	1.3
7	15.0	0.73	16483	23.7
8	15.1	0.80	2500	1.5
9	12.9	0.42	4871	14.3
10	12.9	0.42	2500	1.9
11	12.5	0.40	16493	28.6
12	12.6	0.39	2500	1.8

Axle Nr.	Mass [t]		Distance [mm]	
	μ	σ	μ	σ
13	12.9	0.47	4870	12.2
14	12.9	0.50	2500	1.5
15	13.1	0.37	16491	26.9
16	13.3	0.37	2499	1.7
17	11.7	0.35	4869	9.8
18	11.8	0.34	2501	1.7
19	11.7	0.29	16478	24.0
20	11.8	0.32	2501	1.6
21	12.2	0.56	4864	9.9
22	12.3	0.56	2501	1.8
23	12.6	0.38	16469	24.7
24	12.6	0.38	2501	1.8

Table A.39.: PT-24-13

Axle	Mass [t]		Distance [mm]	
	μ	σ	μ	σ
1	20.9	0.32	0	0.0
2	21.4	0.26	3000	1.1
3	20.8	0.26	6900	3.1
4	21.7	0.37	2999	1.1
5	12.4	0.37	5985	20.9
6	12.4	0.37	2499	1.5
7	12.4	0.37	15803	31.5
8	12.3	0.39	2499	1.6
9	12.5	0.33	5590	11.4
10	12.5	0.34	2499	1.5
11	12.5	0.36	15803	31.6
12	12.5	0.38	2499	1.4
13	12.4	0.46	5232	14.9
14	12.4	0.45	2507	16.7
15	12.5	0.41	16490	37.1
16	12.5	0.41	2507	16.9
17	12.7	0.38	5230	16.0
18	12.7	0.38	2499	1.6
19	12.7	0.41	15804	32.2
20	12.6	0.42	2499	1.6
21	12.5	0.44	5233	12.1
22	12.5	0.44	2503	8.9
23	12.4	0.46	16495	35.4
24	12.4	0.47	2503	8.9
25	12.2	0.29	4877	10.7
26	12.2	0.30	2500	1.6
27	12.0	0.28	16512	37.2
28	12.0	0.30	2499	1.5

Table A.40.: PT-28-1

Axle	Mass [t]		Distance [mm]	
	μ	σ	μ	σ
1	20.9	0.32	0	0.0
2	21.4	0.26	3000	1.1
3	20.8	0.26	6900	2.7
4	21.7	0.35	2999	1.1
5	12.4	0.48	5629	17.1
6	12.5	0.50	2504	12.1
7	12.4	0.52	16502	32.0
8	12.4	0.53	2503	12.1
9	12.6	0.46	5234	13.5
10	12.6	0.47	2499	1.5
11	12.7	0.47	15806	24.0
12	12.7	0.48	2500	1.5
13	12.5	0.51	5229	15.3
14	12.5	0.51	2515	24.1
15	12.6	0.46	16489	31.5
16	12.5	0.47	2515	24.1
17	12.8	0.48	5228	18.5
18	12.8	0.49	2499	1.5
19	12.8	0.50	15807	22.9
20	12.8	0.52	2499	1.4
21	12.6	0.52	5230	13.5
22	12.5	0.52	2506	13.9
23	12.5	0.50	16494	31.7
24	12.5	0.53	2505	14.2
25	12.2	0.30	4877	12.5
26	12.2	0.31	2500	1.5
27	12.0	0.32	16517	31.9
28	12.0	0.33	2499	1.5

Table A.41.: PT-28-2

Axle	Mass [t]		Distance [mm]	
	μ	σ	μ	σ
1	20.9	0.44	0	0.0
2	21.1	0.44	3000	1.3
3	20.7	0.36	6899	3.6
4	21.4	0.52	3000	1.3
5	12.1	0.49	5627	13.9
6	12.1	0.52	2501	2.2
7	12.1	0.48	16493	33.7
8	12.1	0.51	2501	2.3
9	12.4	0.57	4879	13.3
10	12.5	0.61	2501	3.8
11	12.5	0.50	16485	37.0
12	12.5	0.54	2502	3.8
13	12.6	0.45	4879	14.0
14	12.7	0.50	2500	1.8
15	12.7	0.44	16494	41.8
16	12.6	0.49	2500	1.9
17	12.6	0.43	4876	15.5
18	12.6	0.48	2501	6.4
19	12.6	0.44	16496	46.8
20	12.6	0.47	2501	6.0
21	12.4	0.54	4874	14.4
22	12.4	0.58	2501	2.3
23	12.3	0.58	16484	41.0
24	12.3	0.61	2501	2.2
25	12.2	0.59	4873	12.8
26	12.3	0.63	2502	6.8
27	12.1	0.66	16489	41.1
28	12.2	0.68	2502	6.6

Table A.42.: PT-28-3

Axle	Mass [t]		Distance [mm]	
	μ	σ	μ	σ
1	20.9	0.37	0	0.0
2	20.9	0.33	3000	1.3
3	20.6	0.32	6899	3.6
4	21.1	0.39	3000	1.3
5	12.1	0.29	5626	8.2
6	12.1	0.33	2500	1.6
7	12.0	0.33	16492	40.0
8	12.0	0.36	2500	1.8
9	12.3	0.38	4880	12.2
10	12.3	0.40	2503	7.0
11	12.3	0.40	16481	34.5
12	12.3	0.46	2503	6.7
13	12.8	0.38	4880	14.4
14	12.8	0.44	2500	1.6
15	12.6	0.35	16493	34.0
16	12.6	0.39	2500	1.4
17	12.3	0.42	4865	18.2
18	12.3	0.45	2522	26.9
19	12.2	0.43	16465	35.3
20	12.2	0.46	2521	26.1
21	12.5	0.38	5220	14.7
22	12.5	0.41	2500	2.1
23	12.5	0.42	15791	33.8
24	12.6	0.43	2500	1.7
25	12.3	0.45	5583	13.3
26	12.3	0.45	2499	1.5
27	12.4	0.44	15791	31.1
28	12.5	0.44	2500	1.6

Table A.43.: PT-28-4

Axle	Mass [t]		Distance [mm]	
	μ	σ	μ	σ
1	20.9	0.48	0	0.0
2	21.0	0.44	3000	1.3
3	20.7	0.41	6899	3.6
4	21.3	0.49	3000	1.4
5	12.0	0.29	5627	14.6
6	12.1	0.37	2500	1.7
7	12.0	0.34	16497	40.2
8	12.0	0.38	2500	1.7
9	12.5	0.50	4880	14.0
10	12.6	0.55	2506	15.2
11	12.4	0.49	16480	33.7
12	12.5	0.51	2506	15.1
13	12.8	0.41	5231	17.4
14	12.8	0.45	2500	2.1
15	12.6	0.41	15787	42.5
16	12.7	0.43	2500	1.7
17	12.4	0.47	5227	19.0
18	12.4	0.47	2512	22.8
19	12.3	0.47	16473	40.6
20	12.3	0.52	2513	22.6
21	12.4	0.47	4872	15.2
22	12.4	0.49	2502	8.4
23	12.4	0.45	16487	33.7
24	12.4	0.47	2503	8.6
25	12.2	0.50	4873	14.3
26	12.3	0.52	2507	16.4
27	12.2	0.49	16475	45.3
28	12.2	0.53	2507	16.3

Table A.44.: PT-28-5

Axle	Mass [t]		Distance [mm]	
	μ	σ	μ	σ
1	20.9	0.45	0	0.0
2	21.0	0.39	3000	1.2
3	20.7	0.39	6899	3.9
4	21.2	0.47	3000	1.5
5	12.0	0.30	5627	17.2
6	12.1	0.37	2500	1.8
7	12.1	0.35	16496	36.1
8	12.1	0.40	2500	2.1
9	12.4	0.49	4880	13.4
10	12.5	0.53	2506	14.8
11	12.4	0.50	16480	34.5
12	12.4	0.53	2506	14.7
13	12.7	0.45	5234	13.7
14	12.7	0.47	2500	1.8
15	12.6	0.43	15787	32.8
16	12.7	0.46	2500	1.8
17	12.3	0.52	5223	19.5
18	12.4	0.54	2521	26.6
19	12.3	0.50	16466	41.0
20	12.3	0.53	2521	26.4
21	12.5	0.46	5225	16.1
22	12.6	0.47	2500	1.8
23	12.5	0.45	15789	32.7
24	12.6	0.48	2500	1.8
25	12.2	0.52	5227	13.4
26	12.3	0.53	2505	13.7
27	12.2	0.54	16483	37.8
28	12.3	0.57	2505	13.7

Table A.45.: PT-28-6

Axle	Mass [t]		Distance [mm]	
	μ	σ	μ	σ
1	20.9	0.43	0	0.0
2	21.0	0.40	3000	1.3
3	20.6	0.37	6898	3.9
4	21.2	0.45	3000	1.5
5	12.0	0.27	5627	17.4
6	12.0	0.33	2500	1.9
7	12.0	0.33	16497	39.8
8	12.1	0.39	2500	1.9
9	12.5	0.49	4882	12.2
10	12.5	0.53	2503	8.7
11	12.4	0.45	16484	34.8
12	12.5	0.48	2503	8.7
13	12.7	0.40	5237	12.6
14	12.7	0.43	2500	1.8
15	12.6	0.41	15787	33.7
16	12.7	0.45	2500	1.8
17	12.3	0.48	5229	15.8
18	12.4	0.50	2507	16.1
19	12.2	0.46	16480	37.8
20	12.3	0.50	2507	15.8
21	12.4	0.41	5231	14.4
22	12.5	0.42	2500	1.9
23	12.4	0.40	15789	34.9
24	12.5	0.43	2500	1.7
25	12.3	0.42	5584	10.7
26	12.3	0.44	2500	1.9
27	12.3	0.40	15787	34.2
28	12.4	0.43	2500	1.7

Table A.46.: PT-28-7

Axle	Mass [t]		Distance [mm]	
	μ	σ	μ	σ
1	20.9	0.36	0	0.0
2	21.3	0.30	3000	1.2
3	20.8	0.26	6899	3.3
4	21.7	0.44	2999	1.2
5	12.7	0.58	5633	25.0
6	12.7	0.58	2502	2.2
7	12.7	0.58	16495	36.5
8	12.6	0.58	2501	2.0
9	12.8	0.54	5231	13.8
10	12.8	0.55	2500	1.4
11	12.9	0.55	15800	36.7
12	12.8	0.56	2500	1.6
13	12.9	0.53	5588	11.7
14	12.9	0.54	2499	1.7
15	12.9	0.55	15802	38.8
16	12.9	0.55	2500	1.7
17	13.0	0.56	5586	11.7
18	13.0	0.57	2500	1.7
19	13.1	0.57	15801	35.4
20	13.1	0.55	2500	1.5
21	12.9	0.62	5231	11.7
22	12.9	0.64	2502	1.9
23	12.8	0.64	16496	36.6
24	12.8	0.64	2501	1.9
25	12.3	0.32	4877	11.1
26	12.3	0.34	2500	1.7
27	12.1	0.32	16510	45.5
28	12.1	0.34	2499	1.8

Table A.47.: PT-28-8

Axle	Mass [t]		Distance [mm]	
	μ	σ	μ	σ
1	20.9	0.41	0	0.0
2	21.1	0.44	3000	1.3
3	20.7	0.36	6899	3.6
4	21.4	0.55	3000	1.3
5	12.2	0.45	5627	16.0
6	12.2	0.48	2500	2.2
7	12.2	0.48	16497	47.7
8	12.2	0.50	2500	1.9
9	12.5	0.55	4878	15.0
10	12.5	0.57	2502	2.3
11	12.5	0.55	16484	37.1
12	12.5	0.57	2502	2.2
13	12.8	0.49	5235	13.3
14	12.8	0.50	2500	1.8
15	12.7	0.50	15794	36.3
16	12.7	0.50	2500	1.8
17	12.7	0.50	5587	11.6
18	12.7	0.50	2500	1.8
19	12.8	0.51	15794	31.4
20	12.8	0.50	2499	1.7
21	12.5	0.59	5231	13.1
22	12.5	0.59	2502	2.1
23	12.4	0.56	16485	34.2
24	12.4	0.56	2502	2.2
25	12.2	0.39	4870	13.9
26	12.2	0.41	2501	2.1
27	12.1	0.43	16495	38.8
28	12.1	0.45	2501	2.3

Table A.48.: PT-28-9

Axle	Mass [t]		Distance [mm]	
	μ	σ	μ	σ
1	20.9	0.31	0	0.0
2	21.3	0.25	2999	1.2
3	20.7	0.28	6900	3.3
4	21.6	0.36	2999	1.2
5	12.3	0.25	5981	10.7
6	12.3	0.24	2499	1.5
7	12.3	0.29	15813	18.1
8	12.3	0.30	2499	1.4
9	12.4	0.36	5239	9.9
10	12.4	0.40	2502	2.1
11	12.2	0.42	16501	23.4
12	12.2	0.44	2501	1.7
13	12.5	0.34	4882	9.4
14	12.4	0.36	2502	2.1
15	12.5	0.37	16506	27.7
16	12.4	0.40	2501	1.9
17	12.6	0.32	5232	11.7
18	12.6	0.31	2499	1.6
19	12.6	0.35	15803	30.0
20	12.6	0.35	2499	1.6
21	12.3	0.36	5230	10.7
22	12.3	0.37	2501	1.8
23	12.5	0.31	16497	31.1
24	12.5	0.31	2501	2.1
25	12.3	0.30	4879	9.4
26	12.3	0.29	2499	1.7
27	12.0	0.28	16521	28.7
28	12.0	0.32	2499	1.4

Table A.49.: PT-28-10

Axle	Mass [t]		Distance [mm]	
	μ	σ	μ	σ
1	20.8	0.32	0	0.0
2	21.2	0.19	2999	0.9
3	20.6	0.28	6900	2.7
4	21.6	0.29	2999	1.2
5	12.2	0.27	5991	10.9
6	12.2	0.28	2499	1.3
7	12.3	0.27	15817	17.4
8	12.2	0.30	2499	1.5
9	12.3	0.33	5234	12.4
10	12.2	0.34	2501	1.6
11	12.1	0.38	16504	20.1
12	12.0	0.39	2502	1.6
13	12.4	0.30	5221	16.3
14	12.4	0.32	2499	1.6
15	12.6	0.34	15815	17.8
16	12.5	0.37	2499	1.6
17	12.5	0.40	5582	11.7
18	12.5	0.39	2499	1.5
19	12.6	0.41	15817	16.9
20	12.5	0.40	2499	1.3
21	12.4	0.45	5236	11.0
22	12.5	0.45	2500	2.0
23	12.3	0.46	16511	17.0
24	12.3	0.46	2500	1.6
25	12.0	0.27	4876	15.6
26	12.0	0.25	2499	1.6
27	12.0	0.35	16530	24.0
28	12.0	0.36	2499	1.5

Table A.50.: PT-28-11

Axle	Mass [t]		Distance [mm]	
	μ	σ	μ	σ
1	20.9	0.45	0	0.0
2	21.0	0.41	3000	1.3
3	20.6	0.39	6898	3.7
4	21.2	0.44	3000	1.4
5	12.0	0.27	5628	19.3
6	12.0	0.35	2500	2.0
7	12.1	0.36	16497	45.2
8	12.1	0.42	2500	1.7
9	12.6	0.55	4881	12.0
10	12.6	0.58	2502	2.1
11	12.6	0.57	16484	32.9
12	12.6	0.60	2502	2.0
13	12.8	0.47	5236	11.2
14	12.8	0.48	2500	1.8
15	12.7	0.47	15786	32.0
16	12.7	0.51	2500	1.9
17	12.6	0.45	5585	11.4
18	12.6	0.47	2500	2.0
19	12.6	0.43	15788	34.8
20	12.6	0.46	2500	1.8
21	12.6	0.47	5585	11.8
22	12.6	0.50	2500	1.9
23	12.5	0.45	15786	32.5
24	12.6	0.47	2500	1.7
25	12.2	0.55	5223	12.9
26	12.3	0.57	2502	2.4
27	12.2	0.54	16485	35.0
28	12.3	0.58	2502	2.3

Table A.51.: PT-28-12

Axle	Mass [t]		Distance [mm]	
	μ	σ	μ	σ
1	20.8	0.50	0	0.0
2	20.9	0.48	3000	1.5
3	20.6	0.43	6899	3.8
4	21.1	0.47	3000	1.5
5	12.1	0.29	5625	10.0
6	12.1	0.36	2500	1.7
7	12.0	0.29	16499	34.4
8	12.0	0.34	2500	1.8
9	12.5	0.61	4880	17.7
10	12.5	0.62	2501	2.2
11	12.5	0.52	16479	34.3
12	12.5	0.54	2502	2.2
13	12.5	0.37	5240	12.1
14	12.6	0.40	2500	1.9
15	12.4	0.36	15787	31.8
16	12.5	0.38	2500	1.8
17	12.4	0.38	5583	11.7
18	12.5	0.40	2500	1.8
19	12.4	0.37	15789	35.6
20	12.5	0.39	2500	1.4
21	11.9	0.40	5216	16.5
22	12.0	0.43	2503	1.8
23	12.2	0.41	16491	36.1
24	12.2	0.45	2502	2.0
25	12.2	0.38	5232	11.1
26	12.2	0.40	2500	1.6
27	12.2	0.39	15797	31.9
28	12.3	0.40	2500	1.7

Table A.52.: PT-28-13

Axle	Mass [t]		Distance [mm]	
	μ	σ	μ	σ
1	20.8	0.46	0	0.0
2	21.0	0.43	3000	1.3
3	20.6	0.38	6899	3.9
4	21.2	0.44	2999	1.5
5	12.0	0.22	5629	28.1
6	12.0	0.28	2500	1.6
7	12.1	0.37	16499	32.8
8	12.1	0.41	2500	1.9
9	12.6	0.45	4882	10.5
10	12.6	0.49	2502	2.7
11	12.2	0.47	16482	31.7
12	12.3	0.48	2502	2.2
13	12.6	0.40	5235	11.0
14	12.7	0.40	2500	2.2
15	12.6	0.37	15788	38.2
16	12.7	0.41	2500	2.1
17	12.3	0.50	5230	12.6
18	12.4	0.53	2501	2.1
19	12.4	0.41	16482	35.3
20	12.4	0.42	2502	2.5
21	12.1	0.40	4879	11.2
22	12.1	0.42	2502	1.9
23	12.3	0.47	16484	32.2
24	12.4	0.48	2502	2.4
25	12.3	0.41	5237	9.7
26	12.4	0.42	2500	1.7
27	12.4	0.38	15789	30.0
28	12.4	0.39	2500	1.6

Table A.53.: PT-28-14

Axle	Mass [t]		Distance [mm]	
	μ	σ	μ	σ
1	20.8	0.39	0	0.0
2	21.2	0.41	3000	1.2
3	20.6	0.34	6899	3.6
4	21.5	0.52	2999	1.3
5	12.1	0.37	5630	15.3
6	12.1	0.38	2502	8.7
7	12.1	0.39	16495	37.0
8	12.0	0.39	2502	8.7
9	12.2	0.43	4884	16.5
10	12.2	0.45	2504	12.4
11	12.2	0.42	16491	37.7
12	12.2	0.44	2504	12.4
13	12.4	0.38	5234	14.0
14	12.4	0.38	2500	1.6
15	12.4	0.42	15798	35.6
16	12.4	0.41	2500	1.6
17	12.2	0.45	5228	17.0
18	12.2	0.45	2517	24.7
19	12.2	0.48	16479	41.5
20	12.2	0.48	2516	24.6
21	12.4	0.44	5229	17.5
22	12.4	0.44	2500	1.6
23	12.4	0.44	15798	33.8
24	12.4	0.44	2500	1.5
25	12.2	0.50	5228	14.3
26	12.2	0.50	2504	12.5
27	12.1	0.48	16488	35.3
28	12.1	0.48	2504	12.5
29	12.0	0.43	4875	16.2
30	12.0	0.43	2504	12.2
31	11.9	0.41	16498	38.2
32	11.9	0.42	2503	12.4

Table A.54.: PT-32-1

Axle	Mass [t]		Distance [mm]	
	μ	σ	μ	σ
1	20.8	0.38	0	0.0
2	21.4	0.28	2999	1.1
3	20.8	0.27	6900	2.9
4	21.8	0.38	2999	1.1
5	12.4	0.29	5985	14.8
6	12.4	0.30	2499	1.5
7	12.4	0.30	15807	29.4
8	12.4	0.31	2499	1.5
9	12.6	0.31	5591	12.6
10	12.6	0.32	2499	1.5
11	12.7	0.29	15802	26.4
12	12.6	0.31	2499	1.5
13	12.5	0.45	5229	17.7
14	12.5	0.46	2519	26.0
15	12.6	0.40	16476	41.1
16	12.5	0.42	2519	26.2
17	12.9	0.37	5226	17.1
18	13.0	0.38	2499	1.4
19	13.0	0.35	15805	27.5
20	13.0	0.36	2499	1.6
21	12.7	0.42	5231	14.5
22	12.7	0.45	2507	17.4
23	12.7	0.44	16491	35.4
24	12.6	0.45	2507	17.4
25	12.2	0.35	4876	13.2
26	12.2	0.38	2500	1.5
27	12.2	0.27	16513	30.3
28	12.1	0.31	2499	1.4
29	12.6	0.39	4876	10.2
30	12.6	0.40	2500	1.7
31	12.5	0.35	16507	31.7
32	12.5	0.37	2499	1.8

Table A.55.: PT-32-2

Axle	Mass [t]		Distance [mm]	
	μ	σ	μ	σ
1	20.8	0.39	0	0.0
2	21.0	0.38	3000	1.3
3	20.6	0.35	6899	3.7
4	21.2	0.41	3000	1.4
5	12.3	0.42	5627	15.7
6	12.3	0.44	2502	9.5
7	12.4	0.48	16491	44.3
8	12.4	0.52	2502	9.7
9	12.0	0.34	4881	12.0
10	12.0	0.40	2500	1.9
11	12.0	0.34	16491	39.7
12	12.0	0.38	2500	1.8
13	12.5	0.56	4880	13.3
14	12.5	0.60	2506	15.1
15	12.5	0.51	16477	35.1
16	12.5	0.53	2506	15.0
17	12.8	0.49	5234	13.5
18	12.9	0.50	2500	1.9
19	12.7	0.48	15785	33.2
20	12.8	0.51	2500	1.8
21	12.3	0.48	5220	17.9
22	12.3	0.50	2524	27.3
23	12.2	0.50	16461	44.0
24	12.3	0.53	2524	27.1
25	12.4	0.41	5223	17.0
26	12.5	0.42	2500	1.8
27	12.3	0.38	15789	31.0
28	12.4	0.41	2500	1.7
29	12.2	0.34	5583	11.6
30	12.2	0.37	2500	1.8
31	12.2	0.31	15790	35.7
32	12.3	0.35	2500	1.7

Table A.56.: PT-32-3

Axle	Mass [t]		Distance [mm]	
	μ	σ	μ	σ
1	20.7	0.40	0	0.0
2	21.0	0.30	3000	1.4
3	20.6	0.36	6899	3.7
4	21.2	0.35	3000	1.4
5	12.7	0.50	5629	16.0
6	12.7	0.51	2506	14.0
7	12.8	0.57	16483	35.3
8	12.8	0.58	2506	14.0
9	12.9	0.55	4879	18.3
10	12.8	0.56	2507	15.4
11	12.8	0.50	16476	33.8
12	12.8	0.54	2507	15.2
13	12.2	0.30	4868	13.5
14	12.2	0.35	2500	1.8
15	12.3	0.37	16499	38.0
16	12.2	0.40	2500	1.8
17	12.9	0.44	4881	16.0
18	12.9	0.47	2506	14.7
19	12.9	0.45	16475	31.9
20	12.9	0.48	2506	14.6
21	13.3	0.36	5233	14.4
22	13.3	0.38	2500	2.0
23	13.2	0.37	15787	34.9
24	13.2	0.40	2500	1.9
25	12.7	0.46	5223	18.0
26	12.7	0.47	2523	27.3
27	12.5	0.47	16465	46.5
28	12.5	0.50	2523	27.0
29	12.9	0.40	5222	17.6
30	12.9	0.41	2500	1.7
31	12.9	0.42	15791	30.4
32	13.0	0.44	2500	1.8

Table A.57.: PT-32-4

Axle	Mass [t]		Distance [mm]	
	μ	σ	μ	σ
1	20.8	0.42	0	0.0
2	21.0	0.34	3000	1.5
3	20.6	0.39	6899	3.9
4	21.2	0.40	2999	1.5
5	12.0	0.28	5629	16.6
6	12.1	0.36	2500	1.7
7	12.0	0.34	16498	38.4
8	12.0	0.40	2500	2.1
9	12.5	0.59	4882	12.5
10	12.5	0.65	2505	13.7
11	12.4	0.53	16480	33.4
12	12.5	0.57	2505	13.9
13	12.7	0.48	5237	14.0
14	12.8	0.53	2500	1.7
15	12.7	0.47	15786	30.5
16	12.8	0.50	2500	1.8
17	12.4	0.47	5230	17.0
18	12.4	0.50	2509	18.6
19	12.2	0.46	16481	33.4
20	12.2	0.51	2509	18.5
21	12.5	0.39	5232	16.1
22	12.6	0.41	2500	1.8
23	12.5	0.38	15790	36.1
24	12.5	0.41	2500	1.6
25	12.4	0.36	5585	10.4
26	12.5	0.39	2500	2.0
27	12.3	0.36	15788	33.9
28	12.4	0.38	2500	1.6
29	12.1	0.43	5224	15.2
30	12.1	0.45	2506	14.4
31	11.9	0.42	16482	35.8
32	12.0	0.47	2506	14.4

Table A.58.: PT-32-5

Axle	Mass [t]		Distance [mm]	
	μ	σ	μ	σ
1	20.7	0.43	0	0.0
2	21.1	0.38	3000	1.3
3	20.6	0.35	6899	4.5
4	21.4	0.46	3000	1.4
5	12.3	0.53	5631	17.0
6	12.3	0.54	2503	10.0
7	12.2	0.60	16493	40.0
8	12.2	0.62	2503	10.0
9	12.4	0.64	4881	16.1
10	12.4	0.64	2508	17.4
11	12.3	0.54	16482	36.3
12	12.3	0.56	2508	17.7
13	12.4	0.41	4877	15.1
14	12.4	0.45	2500	1.9
15	12.3	0.40	16498	41.6
16	12.3	0.43	2501	2.0
17	12.4	0.57	4873	18.2
18	12.5	0.59	2520	26.5
19	12.4	0.63	16472	42.9
20	12.4	0.64	2520	26.5
21	12.6	0.60	5229	16.7
22	12.6	0.61	2500	1.9
23	12.6	0.57	15796	35.6
24	12.6	0.59	2500	2.1
25	12.3	0.62	5222	17.8
26	12.3	0.63	2513	22.7
27	12.2	0.54	16483	41.8
28	12.2	0.55	2513	22.6
29	12.2	0.64	4870	17.0
30	12.2	0.64	2505	13.7
31	12.1	0.61	16492	38.8
32	12.1	0.62	2505	13.7

Table A.59.: PT-32-6

Axle	Mass [t]		Distance [mm]	
	μ	σ	μ	σ
1	20.9	0.41	0	0.0
2	21.0	0.37	3000	1.3
3	20.6	0.36	6899	3.3
4	21.2	0.44	3000	1.3
5	12.3	0.45	5626	19.2
6	12.3	0.47	2504	14.1
7	12.3	0.52	16487	42.6
8	12.3	0.55	2504	13.9
9	12.0	0.27	4880	13.7
10	12.0	0.34	2500	1.6
11	12.0	0.31	16495	30.2
12	12.0	0.32	2500	1.8
13	12.5	0.49	4879	12.1
14	12.5	0.52	2505	12.0
15	12.3	0.44	16481	41.0
16	12.4	0.46	2505	12.1
17	12.7	0.49	5234	12.5
18	12.8	0.50	2500	1.7
19	12.6	0.48	15789	32.4
20	12.7	0.50	2500	1.8
21	12.2	0.45	5214	18.9
22	12.2	0.45	2538	26.8
23	12.1	0.43	16449	43.4
24	12.2	0.46	2538	26.9
25	12.4	0.42	5218	16.0
26	12.4	0.43	2500	1.8
27	12.3	0.39	15791	29.9
28	12.4	0.39	2500	1.8
29	12.1	0.42	5225	11.8
30	12.2	0.45	2505	14.1
31	12.1	0.41	16485	32.7
32	12.1	0.43	2505	14.0

Table A.60.: PT-32-7

Axle	Mass [t]		Distance [mm]	
	μ	σ	μ	σ
1	20.9	0.38	0	0.0
2	21.4	0.29	2999	1.1
3	20.8	0.26	6900	3.1
4	21.8	0.40	2999	1.1
5	12.3	0.40	5638	33.0
6	12.3	0.41	2501	2.2
7	12.4	0.38	16497	37.0
8	12.3	0.39	2501	1.9
9	12.4	0.31	5235	13.3
10	12.4	0.32	2499	1.6
11	12.4	0.29	15801	36.1
12	12.4	0.30	2499	1.6
13	12.5	0.27	5590	12.0
14	12.5	0.28	2499	1.6
15	12.6	0.27	15802	34.5
16	12.5	0.30	2499	1.6
17	12.4	0.43	5233	12.1
18	12.4	0.44	2501	2.0
19	12.5	0.42	16496	35.3
20	12.5	0.43	2501	1.9
21	12.6	0.31	5232	13.8
22	12.6	0.32	2499	1.4
23	12.6	0.29	15801	34.2
24	12.6	0.31	2500	1.5
25	12.5	0.42	5235	11.7
26	12.5	0.43	2501	1.9
27	12.5	0.45	16494	42.1
28	12.5	0.46	2501	1.9
29	12.2	0.32	4878	10.3
30	12.2	0.33	2500	1.7
31	12.0	0.26	16512	37.9
32	12.0	0.28	2500	1.7

Table A.61.: PT-32-8

Axle	Mass [t]		Distance [mm]	
	μ	σ	μ	σ
1	20.8	0.40	0	0.0
2	21.2	0.45	3000	1.2
3	20.7	0.33	6899	3.6
4	21.5	0.54	3000	1.3
5	12.1	0.40	5630	17.1
6	12.1	0.42	2501	2.1
7	12.1	0.43	16496	43.9
8	12.1	0.44	2501	1.8
9	12.5	0.50	4884	10.8
10	12.5	0.52	2502	2.1
11	12.5	0.48	16490	33.5
12	12.5	0.51	2501	2.0
13	12.6	0.43	5238	11.8
14	12.6	0.44	2500	1.7
15	12.6	0.43	15796	31.6
16	12.6	0.44	2500	1.9
17	12.5	0.45	5589	11.9
18	12.5	0.45	2500	1.9
19	12.5	0.41	15793	35.9
20	12.5	0.42	2500	1.8
21	12.5	0.44	5588	11.7
22	12.5	0.45	2500	1.9
23	12.6	0.42	15791	35.7
24	12.6	0.42	2500	1.7
25	12.3	0.54	5230	12.4
26	12.3	0.55	2501	2.0
27	12.2	0.51	16489	36.2
28	12.2	0.51	2502	2.0
29	12.1	0.42	4876	10.9
30	12.1	0.45	2501	2.4
31	12.0	0.42	16496	39.8
32	12.0	0.45	2501	2.5

Table A.62.: PT-32-9

Axle	Mass [t]		Distance [mm]	
	μ	σ	μ	σ
1	20.7	0.33	0	0.0
2	21.5	0.28	3000	1.1
3	20.8	0.25	6900	2.7
4	22.0	0.37	2999	1.0
5	12.3	0.40	5635	15.7
6	12.3	0.40	2508	17.8
7	12.3	0.39	16493	26.1
8	12.2	0.41	2508	17.9
9	12.5	0.32	5236	16.5
10	12.5	0.33	2499	1.3
11	12.5	0.32	15807	23.0
12	12.5	0.34	2499	1.4
13	12.7	0.32	5593	13.7
14	12.6	0.31	2499	1.4
15	12.8	0.29	15806	18.6
16	12.8	0.29	2499	1.5
17	12.4	0.42	5222	17.5
18	12.4	0.42	2534	27.5
19	12.6	0.44	16469	36.4
20	12.5	0.45	2534	27.9
21	12.9	0.34	5221	18.9
22	12.8	0.35	2499	1.5
23	12.9	0.35	15807	17.9
24	12.9	0.36	2500	1.5
25	12.6	0.39	5229	15.2
26	12.6	0.40	2510	20.4
27	12.4	0.41	16492	31.3
28	12.4	0.45	2510	20.3
29	12.2	0.31	4874	14.4
30	12.2	0.34	2499	1.4
31	12.2	0.29	16517	29.4
32	12.1	0.31	2499	1.5
33	12.5	0.40	4874	13.2
34	12.6	0.40	2503	13.1
35	12.5	0.39	16508	31.5
36	12.4	0.40	2503	13.1

Table A.63.: PT-36-1

Axle	Mass [t]		Distance [mm]	
	μ	σ	μ	σ
1	20.7	0.39	0	0.0
2	21.2	0.47	2999	1.2
3	20.7	0.33	6900	3.5
4	21.5	0.58	2999	1.3
5	12.2	0.35	5631	17.5
6	12.2	0.35	2506	15.5
7	12.2	0.34	16497	31.6
8	12.1	0.36	2506	15.4
9	12.4	0.46	4881	15.0
10	12.4	0.48	2503	10.7
11	12.4	0.43	16503	48.1
12	12.4	0.42	2503	10.5
13	12.5	0.42	5236	13.1
14	12.5	0.42	2499	1.6
15	12.6	0.44	15797	28.6
16	12.6	0.44	2499	1.6
17	12.3	0.48	5226	20.4
18	12.3	0.49	2527	27.7
19	12.3	0.44	16469	34.4
20	12.3	0.44	2527	27.7
21	12.6	0.46	5222	19.4
22	12.6	0.46	2499	1.6
23	12.6	0.47	15802	26.9
24	12.6	0.46	2500	1.5
25	12.2	0.48	5230	14.9
26	12.3	0.49	2506	14.8
27	12.2	0.45	16491	29.2
28	12.2	0.45	2506	14.6
29	12.1	0.33	4873	15.8
30	12.1	0.34	2501	5.0
31	12.0	0.36	16505	29.1
32	11.9	0.37	2501	4.7
33	12.2	0.44	4876	13.3
34	12.2	0.45	2503	11.2
35	12.1	0.46	16501	42.8
36	12.1	0.46	2503	11.1

Table A.64.: PT-36-2

Axle	Mass [t]		Distance [mm]	
	μ	σ	μ	σ
1	20.8	0.42	0	0.0
2	21.0	0.44	3000	1.3
3	20.6	0.35	6899	4.0
4	21.2	0.53	3000	1.5
5	12.2	0.40	5629	22.0
6	12.2	0.44	2502	2.3
7	12.2	0.44	16492	35.8
8	12.2	0.47	2501	2.1
9	11.9	0.29	4883	12.3
10	11.9	0.32	2501	2.3
11	12.0	0.32	16499	29.7
12	12.0	0.36	2501	2.1
13	12.3	0.47	4880	15.7
14	12.3	0.48	2506	14.7
15	12.0	0.59	16485	34.0
16	12.0	0.61	2506	14.5
17	12.5	0.53	5233	15.1
18	12.5	0.54	2500	1.6
19	12.4	0.50	15792	33.3
20	12.5	0.52	2500	1.8
21	12.1	0.43	5223	16.4
22	12.2	0.44	2520	26.0
23	11.9	0.52	16470	44.4
24	12.0	0.53	2519	26.3
25	12.3	0.46	5225	15.8
26	12.3	0.47	2500	2.0
27	12.2	0.42	15794	29.5
28	12.3	0.44	2500	1.8
29	12.0	0.52	5226	14.8
30	12.0	0.52	2506	15.1
31	12.0	0.45	16483	36.0
32	12.0	0.47	2506	15.6
33	11.8	0.38	4868	16.0
34	11.8	0.38	2508	16.7
35	11.9	0.35	16487	35.2
36	11.9	0.40	2508	16.6

Table A.65.: PT-36-3

Axle	Mass [t]		Distance [mm]	
	μ	σ	μ	σ
1	20.7	0.41	0	0.0
2	20.9	0.35	3000	1.3
3	20.6	0.35	6899	3.4
4	21.3	0.42	3000	1.4
5	12.5	0.30	5626	12.6
6	12.4	0.35	2500	1.8
7	12.5	0.37	16501	39.5
8	12.5	0.42	2500	2.2
9	12.0	0.28	4882	12.3
10	12.0	0.34	2500	1.7
11	12.0	0.30	16498	37.2
12	11.9	0.34	2500	1.6
13	12.5	0.53	4880	15.3
14	12.5	0.56	2508	17.8
15	12.5	0.52	16480	36.2
16	12.5	0.53	2508	17.7
17	12.9	0.50	5233	15.9
18	12.9	0.50	2500	1.7
19	12.7	0.50	15791	32.6
20	12.8	0.52	2500	1.7
21	12.3	0.51	5217	20.6
22	12.3	0.52	2527	27.8
23	12.2	0.50	16462	46.9
24	12.2	0.52	2526	27.7
25	12.5	0.41	5223	16.6
26	12.5	0.42	2500	1.7
27	12.4	0.39	15788	32.0
28	12.4	0.41	2500	1.7
29	12.3	0.36	5584	12.2
30	12.3	0.37	2500	1.8
31	12.2	0.33	15793	29.5
32	12.3	0.34	2500	1.8
33	11.9	0.46	5225	16.7
34	11.9	0.45	2509	18.5
35	11.9	0.47	16487	62.8
36	11.9	0.50	2509	18.5

Table A.66.: PT-36-4

Axle	Mass [t]		Distance [mm]	
	μ	σ	μ	σ
1	21.5	0.23	0	0.0
2	21.8	0.23	2999	0.9
3	21.3	0.24	6900	3.2
4	22.0	0.36	2999	1.1
5	12.5	0.37	5620	14.0
6	12.6	0.35	2510	20.5
7	12.6	0.37	16455	26.1
8	12.6	0.37	2510	20.4
9	11.8	0.21	4874	16.7
10	11.9	0.20	2501	1.3
11	11.9	0.20	16472	20.9
12	11.9	0.19	2501	1.3
13	12.8	0.48	4869	10.7
14	12.8	0.46	2499	1.3
15	13.0	0.44	16491	24.2
16	13.0	0.42	2499	1.3
17	13.2	0.48	4875	10.6
18	13.2	0.45	2499	1.5
19	13.2	0.43	16485	30.4
20	13.3	0.41	2499	2.0
21	15.9	0.47	4672	11.6
22	15.8	0.47	2499	1.2
23	16.2	0.52	17385	23.8
24	16.4	0.50	2499	2.3
25	15.8	0.39	4465	9.0
26	15.6	0.39	2499	1.2
27	16.2	0.43	17383	25.0
28	16.3	0.43	2499	1.2
29	9.7	0.94	4665	12.3
30	9.8	0.94	2501	2.0
31	9.0	0.88	16491	38.3
32	9.0	0.87	2501	1.7
33	8.5	1.59	4875	13.1
34	8.6	1.61	2500	2.1
35	7.8	1.16	16495	41.9
36	7.8	1.17	2500	1.7

Table A.67.: PT-36-5

Axle	Mass [t]		Distance [mm]	
	μ	σ	μ	σ
1	20.8	0.65	0	0.0
2	21.3	0.44	3010	18.3
3	20.8	0.34	6922	41.5
4	21.8	0.67	3009	18.3
5	13.3	0.22	5638	36.7
6	13.4	0.24	2508	15.6
7	13.4	0.28	16554	93.4
8	13.3	0.27	2508	15.8
9	13.4	0.39	4876	30.5
10	13.4	0.39	2508	15.4
11	13.3	0.44	16562	94.7
12	13.3	0.43	2508	15.6
13	13.5	0.43	4849	39.7
14	13.6	0.46	2548	50.4
15	13.6	0.36	16510	104.6
16	13.6	0.37	2548	50.6
17	13.8	0.52	4804	40.7
18	13.9	0.54	2606	18.1
19	13.8	0.58	16451	82.6
20	13.8	0.57	2606	18.3
21	13.7	0.67	4786	34.8
22	13.8	0.71	2590	40.3
23	13.8	0.84	16467	100.7
24	13.7	0.83	2591	40.7
25	13.5	0.43	4809	40.3
26	13.5	0.44	2555	51.2
27	13.5	0.51	16506	104.6
28	13.4	0.45	2555	51.4
29	13.3	0.31	4844	41.0
30	13.3	0.33	2508	15.6
31	13.4	0.31	16554	89.8
32	13.4	0.30	2508	15.7
33	13.3	0.26	4869	32.6
34	13.4	0.25	2508	15.4
35	13.4	0.30	16553	90.7
36	13.2	0.29	2508	15.5

Table A.68.: PT-36-6

Axle	Mass [t]		Distance [mm]	
	μ	σ	μ	σ
1	20.7	0.44	0	0.0
2	20.9	0.37	3000	1.2
3	20.5	0.36	6898	3.9
4	21.1	0.39	3000	1.5
5	12.1	0.29	5631	20.2
6	12.1	0.32	2500	1.8
7	12.3	0.35	16498	44.2
8	12.2	0.40	2500	2.3
9	12.2	0.45	4885	10.0
10	12.2	0.49	2502	2.2
11	12.1	0.39	16489	33.0
12	12.2	0.42	2502	2.1
13	12.2	0.29	5241	11.3
14	12.2	0.31	2500	1.9
15	12.2	0.28	15790	35.3
16	12.2	0.31	2500	1.8
17	12.1	0.40	5234	11.3
18	12.1	0.42	2502	2.4
19	12.0	0.43	16486	35.8
20	12.1	0.47	2502	2.2
21	12.0	0.22	5238	10.9
22	12.1	0.25	2500	1.7
23	12.0	0.23	15792	31.8
24	12.1	0.26	2500	1.7
25	12.0	0.23	5588	11.4
26	12.0	0.24	2500	1.8
27	11.9	0.22	15790	32.7
28	12.0	0.25	2500	1.6
29	11.8	0.41	5226	12.0
30	11.9	0.42	2502	2.2
31	11.9	0.37	16490	35.8
32	11.9	0.41	2502	2.3
33	11.8	0.37	4878	12.0
34	11.9	0.40	2502	2.1
35	11.9	0.39	16489	33.2
36	11.9	0.41	2502	2.4

Table A.69.: PT-36-7

Axle	Mass [t]		Distance [mm]	
	μ	σ	μ	σ
1	20.9	0.61	0	0.0
2	21.5	0.60	2997	32.1
3	20.9	0.62	6939	616.1
4	21.8	0.73	2997	32.1
5	12.7	1.31	5627	44.5
6	12.7	1.32	2505	14.8
7	12.6	1.30	16489	42.4
8	12.6	1.36	2505	14.9
9	12.5	1.32	4877	18.9
10	12.6	1.34	2501	6.6
11	12.5	1.23	16498	39.2
12	12.5	1.28	2501	6.6
13	12.7	0.72	4880	17.4
14	12.7	0.74	2501	5.6
15	12.6	0.73	16498	36.4
16	12.6	0.76	2500	5.4
17	12.7	0.68	4879	15.9
18	12.7	0.69	2500	3.1
19	12.7	0.68	16498	32.4
20	12.7	0.69	2500	3.3
21	12.7	1.09	4876	15.8
22	12.7	1.08	2501	4.0
23	12.7	1.14	16493	32.8
24	12.7	1.15	2501	4.1
25	12.9	0.98	4874	16.2
26	13.0	0.99	2500	3.3
27	13.0	1.16	16495	40.3
28	13.0	1.19	2500	3.3
29	11.6	1.30	4871	14.7
30	11.6	1.29	2501	5.0
31	11.3	1.51	16500	41.4
32	11.3	1.50	2501	5.0
33	11.1	1.45	4875	13.8
34	11.2	1.45	2501	5.6
35	10.8	1.78	16508	41.6
36	10.7	1.76	2500	5.6
37	10.7	2.34	4877	49.4
38	10.7	2.34	2502	32.5
39	10.3	2.53	16470	619.3
40	10.3	2.54	2502	32.5

Table A.70.: PT-40-1

Axle	Mass [t]		Distance [mm]	
	μ	σ	μ	σ
1	21.0	0.29	0	0.0
2	21.6	0.24	3000	0.9
3	20.8	0.24	6900	2.6
4	21.8	0.29	2999	1.0
5	16.0	0.45	5427	12.6
6	16.1	0.47	2499	1.0
7	15.5	0.44	17407	23.1
8	15.7	0.42	2499	1.1
9	16.2	0.35	4474	13.7
10	16.3	0.36	2499	1.3
11	15.4	0.37	17401	26.8
12	15.7	0.37	2499	1.3
13	13.3	0.48	4676	13.0
14	13.3	0.49	2499	1.6
15	13.1	0.47	16511	26.5
16	13.3	0.47	2499	1.4
17	13.0	0.43	4882	12.0
18	13.1	0.43	2499	1.3
19	12.8	0.50	16516	19.1
20	12.9	0.47	2499	1.4
21	11.8	0.21	4872	10.6
22	11.9	0.20	2500	1.3
23	11.8	0.26	16495	21.9
24	11.9	0.27	2500	1.5
25	12.5	0.37	4871	13.7
26	12.6	0.36	2505	14.7
27	12.5	0.40	16488	21.4
28	12.7	0.42	2505	14.9
29	10.4	1.13	4867	15.2
30	10.5	1.14	2501	9.8
31	10.3	1.22	16517	38.3
32	10.3	1.24	2501	10.1
33	9.8	1.00	4871	18.2
34	9.8	1.03	2499	1.6
35	9.2	1.03	16530	32.7
36	9.2	1.05	2500	1.6
37	8.8	1.37	4872	11.1
38	8.8	1.40	2499	1.4
39	8.1	1.09	16525	33.9
40	8.0	1.12	2499	1.5

Table A.71.: PT-40-2

Axle	Mass [t]		Distance [mm]	
	μ	σ	μ	σ
1	20.5	0.33	0	0.0
2	21.6	0.29	2999	1.4
3	20.6	0.25	6900	3.1
4	22.1	0.43	2999	1.3
5	12.2	0.23	5997	18.3
6	12.2	0.22	2500	1.6
7	12.3	0.20	15799	33.4
8	12.3	0.22	2500	1.6
9	12.3	0.22	5602	11.7
10	12.3	0.21	2500	1.8
11	12.4	0.23	15803	34.8
12	12.3	0.24	2500	1.5
13	12.4	0.26	5600	12.8
14	12.4	0.25	2500	1.6
15	12.6	0.27	15800	33.7
16	12.6	0.27	2500	1.5
17	12.4	0.38	5242	12.7
18	12.4	0.38	2502	1.7
19	12.4	0.32	16496	40.1
20	12.3	0.32	2501	1.7
21	12.1	0.30	4888	12.4
22	12.1	0.30	2500	1.7
23	12.1	0.24	16506	36.1
24	12.0	0.23	2500	1.7
25	12.4	0.38	4875	10.7
26	12.4	0.35	2501	2.3
27	12.3	0.37	16494	36.8
28	12.2	0.37	2501	2.3
29	12.3	0.40	4884	11.8
30	12.2	0.38	2501	2.0
31	12.4	0.38	16489	38.8
32	12.3	0.36	2501	2.0
33	12.3	0.35	4882	12.1
34	12.3	0.34	2502	2.4
35	12.2	0.41	16499	41.4
36	12.1	0.40	2501	2.1
37	12.2	0.36	4878	10.6
38	12.1	0.35	2501	2.2
39	12.1	0.35	16492	46.4
40	12.0	0.35	2501	2.1

Table A.72.: PT-40-3

Axle Nr.	Mass [t]		Distance [mm]		Axle Nr.	Mass [t]		Distance [mm]	
	μ	σ	μ	σ		μ	σ	μ	σ
1	20.7	0.40	0	0.0	25	12.8	0.39	4868	24.2
2	21.4	0.27	3000	3.9	26	12.7	0.40	2512	22.2
3	20.8	0.24	6901	8.3	27	12.7	0.34	16488	33.3
4	22.0	0.44	3000	3.8	28	12.7	0.36	2512	22.4
5	13.4	0.20	5630	17.6	29	12.0	0.22	4866	18.6
6	13.5	0.18	2500	3.4	30	12.0	0.22	2501	3.4
7	13.6	0.28	16517	36.9	31	11.9	0.23	16501	27.4
8	13.5	0.25	2500	3.5	32	11.9	0.23	2501	3.5
9	13.9	0.26	4857	17.3	33	13.1	0.42	4880	12.5
10	13.9	0.28	2499	3.6	34	13.0	0.44	2500	3.3
11	13.8	0.34	16520	27.3	35	12.9	0.60	16518	27.3
12	13.7	0.32	2499	3.6	36	12.8	0.58	2500	3.5
13	13.7	0.46	4819	16.7	37	13.5	0.49	4878	12.2
14	13.7	0.44	2598	3.7	38	13.3	0.48	2500	3.3
15	13.4	0.54	16407	27.1	39	13.3	0.48	16515	28.1
16	13.4	0.52	2598	3.8	40	13.3	0.46	2500	3.3
17	13.1	0.42	4807	17.9	41	16.2	0.40	4677	13.6
18	13.1	0.43	2499	3.4	42	16.1	0.41	2500	3.3
19	13.0	0.42	16520	29.9	43	15.7	0.39	17418	30.5
20	13.0	0.43	2499	3.4	44	15.8	0.37	2500	3.2
21	12.6	0.40	4857	16.3	45	16.3	0.38	4469	13.3
22	12.5	0.39	2514	23.1	46	16.2	0.38	2500	3.3
23	12.6	0.37	16488	33.7	47	15.7	0.42	17417	30.2
24	12.5	0.39	2514	23.1	48	15.7	0.38	2500	3.3

Table A.73.: PT-48-1

Axle Nr.	Mass [t]		Distance [mm]		Axle Nr.	Mass [t]		Distance [mm]	
	μ	σ	μ	σ		μ	σ	μ	σ
1	21.1	0.33	0	0.0	25	12.8	0.86	4866	18.5
2	21.6	0.31	3000	1.1	26	12.9	0.81	2506	17.2
3	21.0	0.29	6899	3.0	27	12.7	0.83	16485	38.1
4	21.9	0.36	3000	1.1	28	12.8	0.80	2506	17.3
5	13.5	1.05	5626	13.4	29	12.4	1.07	4874	13.8
6	13.6	1.06	2504	13.2	30	12.4	1.00	2501	1.8
7	13.7	1.28	16487	47.2	31	12.3	1.06	16493	31.3
8	13.8	1.39	2504	13.0	32	12.4	1.03	2501	1.6
9	12.9	0.75	4876	15.6	33	12.2	1.14	4874	12.3
10	12.9	0.78	2501	4.9	34	12.3	1.13	2501	6.8
11	12.8	0.68	16502	48.9	35	12.1	1.26	16498	31.2
12	13.0	0.71	2500	5.0	36	12.2	1.31	2501	6.9
13	12.8	0.61	4883	12.3	37	12.4	1.24	4874	16.3
14	12.9	0.63	2501	6.8	38	12.5	1.26	2504	13.5
15	12.8	0.66	16498	34.8	39	12.3	1.50	16493	33.2
16	13.0	0.67	2501	6.8	40	12.4	1.56	2504	13.4
17	13.1	1.17	4875	16.5	41	12.7	2.20	4868	19.1
18	13.2	1.14	2509	20.1	42	12.8	2.27	2500	3.7
19	13.1	0.97	16482	47.3	43	12.7	2.40	16494	38.1
20	13.2	1.03	2509	20.0	44	12.8	2.47	2500	3.7
21	12.4	1.72	4861	20.7	45	9.0	1.68	4866	14.8
22	12.6	1.70	2500	1.8	46	9.1	1.68	2501	3.7
23	12.4	1.71	16497	34.1	47	8.4	1.55	16517	49.2
24	12.5	1.75	2500	1.7	48	8.4	1.55	2500	3.9

Table A.74.: PT-48-2

Axle Nr.	Mass [t]		Distance [mm]		Axle Nr.	Mass [t]		Distance [mm]	
	μ	σ	μ	σ		μ	σ	μ	σ
1	20.2	0.40	0	0.0	25	12.6	0.27	5240	13.6
2	21.8	0.31	2999	1.1	26	12.6	0.27	2499	1.4
3	20.6	0.23	6901	3.1	27	12.5	0.27	15810	16.1
4	22.3	0.45	2999	1.2	28	12.5	0.26	2499	1.3
5	12.2	0.19	6002	14.3	29	12.1	0.32	5231	13.2
6	12.3	0.19	2499	1.2	30	12.1	0.30	2510	19.9
7	12.3	0.17	15806	17.0	31	12.1	0.28	16491	25.5
8	12.3	0.18	2499	1.5	32	12.0	0.32	2510	20.4
9	12.0	0.27	5239	21.9	33	12.3	0.18	5230	12.9
10	12.0	0.25	2550	19.9	34	12.3	0.18	2499	1.1
11	12.2	0.30	16453	26.2	35	12.4	0.18	15811	16.9
12	12.1	0.33	2550	19.6	36	12.3	0.20	2500	1.5
13	12.4	0.23	5234	19.1	37	12.0	0.28	5228	15.4
14	12.4	0.22	2499	1.1	38	12.0	0.26	2510	19.7
15	12.6	0.20	15809	19.1	39	12.2	0.30	16489	25.4
16	12.6	0.21	2499	1.3	40	12.2	0.33	2510	19.8
17	12.3	0.33	5243	16.4	41	12.2	0.18	4877	13.0
18	12.3	0.33	2510	20.1	42	12.2	0.19	2502	1.4
19	12.3	0.32	16492	24.4	43	12.1	0.20	16501	16.5
20	12.2	0.34	2510	20.1	44	12.0	0.18	2503	1.5
21	12.0	0.32	4894	19.5	45	12.0	0.29	4871	9.2
22	12.0	0.31	2499	1.4	46	12.0	0.27	2505	12.4
23	12.2	0.28	16517	18.6	47	12.0	0.27	16497	23.9
24	12.1	0.26	2500	1.2	48	12.0	0.30	2505	12.3

Table A.75.: PT-48-3

Axle Nr.	Mass [t]		Distance [mm]		Axle Nr.	Mass [t]		Distance [mm]	
	μ	σ	μ	σ		μ	σ	μ	σ
1	20.6	0.46	0	0.0	25	12.3	0.34	4873	21.3
2	21.1	0.37	3002	9.2	26	12.4	0.38	2514	23.5
3	20.5	0.34	6904	20.8	27	12.3	0.38	16490	58.8
4	21.4	0.35	3002	9.5	28	12.4	0.43	2514	23.5
5	15.4	0.35	5437	22.1	29	12.2	0.35	4871	25.8
6	15.3	0.38	2502	7.9	30	12.3	0.38	2515	23.1
7	15.9	0.40	17415	62.8	31	12.1	0.36	16488	65.3
8	16.1	0.48	2502	7.8	32	12.2	0.41	2515	23.1
9	15.3	0.31	4484	20.3	33	12.6	0.38	4858	22.1
10	15.3	0.37	2502	7.7	34	12.7	0.39	2501	7.8
11	15.9	0.41	17414	61.6	35	12.6	0.37	16515	66.6
12	16.1	0.47	2502	7.7	36	12.7	0.38	2502	7.9
13	13.1	0.51	4688	20.9	37	13.0	0.46	4812	25.9
14	13.1	0.55	2502	7.8	38	13.1	0.46	2600	8.0
15	13.2	0.51	16517	60.2	39	13.3	0.38	16407	44.6
16	13.3	0.53	2502	7.9	40	13.3	0.40	2600	8.4
17	12.6	0.62	4889	20.6	41	13.6	0.32	4821	21.8
18	12.7	0.64	2502	7.8	42	13.7	0.37	2502	7.9
19	12.9	0.48	16515	58.5	43	13.6	0.29	16518	68.1
20	12.9	0.50	2502	7.7	44	13.7	0.30	2501	8.2
21	11.6	0.15	4887	19.1	45	13.3	0.26	4853	20.5
22	11.6	0.21	2503	8.1	46	13.4	0.31	2502	7.9
23	11.6	0.16	16505	55.2	47	13.3	0.22	16521	97.8
24	11.7	0.21	2504	7.7	48	13.3	0.24	2502	8.1

Table A.76.: PT-48-4

Axle Nr.	Mass [t]		Distance [mm]		Axle Nr.	Mass [t]		Distance [mm]	
	μ	σ	μ	σ		μ	σ	μ	σ
1	20.3	0.41	0	0.0	25	12.5	0.25	5239	10.9
2	21.7	0.31	2999	1.2	26	12.5	0.26	2499	1.8
3	20.5	0.32	6900	2.9	27	12.6	0.25	15800	39.3
4	22.3	0.42	2999	1.2	28	12.5	0.27	2499	1.6
5	12.1	0.22	6002	20.7	29	12.4	0.24	5595	12.0
6	12.2	0.23	2499	1.5	30	12.4	0.24	2499	1.6
7	12.2	0.23	15802	33.7	31	12.4	0.24	15801	31.1
8	12.1	0.25	2499	1.6	32	12.4	0.24	2499	1.4
9	12.4	0.30	5608	14.7	33	12.3	0.44	5239	9.7
10	12.3	0.31	2499	1.5	34	12.2	0.44	2501	2.2
11	12.4	0.30	15805	26.8	35	12.3	0.34	16491	34.8
12	12.3	0.34	2500	1.6	36	12.3	0.36	2501	2.1
13	12.4	0.30	5606	15.0	37	12.5	0.19	5233	10.2
14	12.4	0.30	2499	1.4	38	12.4	0.20	2499	1.4
15	12.6	0.28	15801	29.7	39	12.4	0.21	15799	33.7
16	12.6	0.29	2499	1.5	40	12.3	0.22	2500	1.4
17	12.5	0.38	5251	13.5	41	12.3	0.40	5235	9.9
18	12.5	0.37	2501	1.9	42	12.3	0.39	2501	1.8
19	12.4	0.38	16495	34.5	43	12.2	0.34	16498	30.0
20	12.4	0.38	2501	2.0	44	12.1	0.34	2502	1.8
21	12.0	0.26	4896	14.6	45	12.6	0.31	4878	8.2
22	12.0	0.28	2499	1.5	46	12.6	0.30	2499	2.4
23	12.0	0.21	16509	35.6	47	12.5	0.30	16512	34.8
24	12.0	0.20	2499	1.5	48	12.4	0.34	2499	1.4

Table A.77.: PT-48-5

Axle Nr.	Mass [t]		Distance [mm]		Axle Nr.	Mass [t]		Distance [mm]	
	μ	σ	μ	σ		μ	σ	μ	σ
1	20.8	0.25	0	0.0	27	13.6	0.69	16915	26.0
2	21.5	0.16	3000	1.1	28	13.7	0.74	2499	1.5
3	20.8	0.19	6900	2.5	29	12.3	0.30	4932	9.7
4	21.9	0.23	2999	1.0	30	12.4	0.33	2499	1.2
5	12.5	0.21	5995	9.5	31	12.3	0.26	16516	21.8
6	12.6	0.22	2499	1.1	32	12.4	0.24	2499	1.2
7	12.6	0.22	15808	17.2	33	12.9	0.31	4881	11.6
8	12.7	0.24	2499	1.2	34	13.0	0.31	2499	1.4
9	12.4	0.31	5225	18.1	35	12.8	0.33	16515	24.1
10	12.5	0.31	2547	20.4	36	12.9	0.33	2499	1.8
11	12.5	0.32	16460	25.9	37	9.3	1.28	4867	10.5
12	12.6	0.33	2548	20.4	38	9.4	1.29	2499	2.4
13	12.9	0.32	5220	13.3	39	8.6	1.17	16541	41.3
14	13.0	0.32	2499	1.4	40	8.6	1.22	2500	2.2
15	13.0	0.31	15809	17.9	41	7.9	1.36	4876	12.8
16	13.1	0.37	2499	1.9	42	7.9	1.39	2500	2.3
17	13.2	0.26	5594	9.4	43	7.4	0.88	16536	37.7
18	13.3	0.27	2499	1.1	44	7.3	0.92	2500	2.4
19	13.2	0.27	15807	16.0	45	9.0	1.06	4870	11.0
20	13.4	0.30	2499	1.2	46	9.1	1.09	2500	2.1
21	12.9	0.43	5230	13.6	47	8.5	1.04	16533	34.1
22	13.0	0.47	2512	22.7	48	8.5	1.07	2500	2.4
23	12.8	0.29	16489	25.2	49	7.9	1.51	4875	13.2
24	12.9	0.28	2512	22.3	50	8.0	1.55	2499	1.6
25	14.6	0.83	4930	15.1	51	7.5	0.98	16535	37.6
26	14.8	0.86	2499	1.6	52	7.5	1.03	2500	1.4

Table A.78.: PT-52-1

Axle Nr.	Mass [t]		Distance [mm]		Axle Nr.	Mass [t]		Distance [mm]	
	μ	σ	μ	σ		μ	σ	μ	σ
1	20.9	0.26	0	0.0	27	12.5	0.22	15779	30.2
2	21.4	0.27	3000	1.2	28	12.6	0.26	2499	1.4
3	20.7	0.23	6898	3.1	29	12.2	0.37	5216	13.7
4	21.6	0.29	3000	1.2	30	12.4	0.36	2546	22.5
5	12.6	0.29	5633	11.1	31	12.1	0.30	16435	37.2
6	12.8	0.33	2500	1.8	32	12.2	0.32	2545	22.1
7	12.6	0.30	16484	33.3	33	12.4	0.20	5221	17.4
8	12.8	0.32	2499	2.0	34	12.5	0.21	2499	1.5
9	12.2	0.23	4891	12.3	35	12.2	0.20	15780	26.9
10	12.3	0.28	2499	1.5	36	12.4	0.21	2499	1.2
11	12.1	0.31	16487	29.0	37	8.8	1.42	5233	11.0
12	12.2	0.31	2500	1.6	38	8.8	1.43	2501	1.9
13	13.6	0.78	4938	8.8	39	8.3	1.19	16519	43.1
14	13.8	0.79	2499	1.5	40	8.4	1.19	2501	2.0
15	14.4	0.89	16879	33.6	41	7.9	1.41	4883	14.2
16	14.6	0.91	2499	1.9	42	8.0	1.42	2501	2.1
17	12.5	0.26	4934	15.4	43	7.2	1.01	16519	41.2
18	12.7	0.26	2509	19.8	44	7.3	1.03	2501	2.0
19	12.5	0.39	16471	30.7	45	8.2	1.17	4874	12.4
20	12.7	0.38	2509	19.9	46	8.3	1.18	2501	2.3
21	13.0	0.23	5234	13.3	47	7.6	0.84	16513	77.9
22	13.1	0.24	2499	1.5	48	7.7	0.84	2501	2.4
23	12.8	0.28	15775	27.7	49	7.1	1.05	4875	14.7
24	12.9	0.30	2499	1.3	50	7.2	1.06	2500	1.8
25	12.5	0.27	5591	9.8	51	6.8	0.64	16518	56.0
26	12.7	0.27	2499	2.1	52	6.9	0.64	2501	1.8

Table A.79.: PT-52-2

Axle Nr.	Mass [t]		Distance [mm]		Axle Nr.	Mass [t]		Distance [mm]	
	μ	σ	μ	σ		μ	σ	μ	σ
1	21.0	0.47	0	0.0	27	12.2	0.62	16477	35.9
2	21.5	0.38	3000	1.2	28	12.3	0.59	2507	17.8
3	20.8	0.37	6899	3.6	29	12.2	0.78	4870	14.6
4	21.7	0.39	3000	1.2	30	12.3	0.75	2502	8.8
5	13.8	1.00	5625	12.8	31	12.2	0.89	16482	27.7
6	14.0	1.04	2501	6.5	32	12.3	0.87	2502	8.7
7	14.1	1.02	16487	29.8	33	12.7	0.76	4874	12.0
8	14.4	1.16	2501	6.3	34	12.8	0.79	2500	1.9
9	12.9	0.88	4872	15.0	35	12.7	0.99	16492	30.1
10	13.0	0.90	2500	1.8	36	12.8	1.04	2500	1.9
11	12.9	0.89	16494	32.4	37	12.8	1.26	4877	15.6
12	13.1	0.95	2500	1.7	38	12.9	1.28	2504	13.2
13	12.9	0.66	4883	13.5	39	12.8	1.35	16491	38.5
14	13.0	0.68	2502	10.6	40	12.9	1.41	2503	13.4
15	12.9	0.67	16490	27.8	41	13.5	1.69	4873	18.3
16	13.1	0.69	2502	10.8	42	13.6	1.73	2502	10.9
17	12.6	0.65	4875	21.2	43	13.6	1.97	16493	35.9
18	12.7	0.65	2510	20.5	44	13.7	2.04	2502	10.8
19	12.6	0.64	16472	47.5	45	11.1	2.05	4865	16.9
20	12.8	0.66	2510	20.4	46	11.2	2.08	2503	10.4
21	11.6	0.95	4859	19.7	47	10.3	2.39	16500	52.6
22	11.7	0.90	2501	6.5	48	10.3	2.42	2502	10.6
23	11.5	1.10	16490	27.9	49	9.4	2.12	4870	13.6
24	11.6	1.10	2501	6.4	50	9.5	2.12	2501	6.6
25	12.3	0.66	4862	19.3	51	8.8	2.07	16509	38.8
26	12.5	0.61	2507	17.7	52	8.9	2.10	2501	6.7

Table A.80.: PT-52-3

Axle Nr.	Mass [t]		Distance [mm]		Axle Nr.	Mass [t]		Distance [mm]	
	μ	σ	μ	σ		μ	σ	μ	σ
1	20.9	0.29	0	0.0	29	11.9	0.61	4873	15.8
2	21.4	0.36	3000	1.2	30	12.0	0.59	2501	1.7
3	20.8	0.25	6898	3.9	31	11.9	0.64	16487	27.2
4	21.7	0.35	3000	1.5	32	12.1	0.65	2501	1.6
5	14.2	0.81	5622	14.7	33	12.7	0.69	4876	12.2
6	14.4	0.82	2500	1.4	34	12.9	0.71	2501	6.3
7	14.4	0.85	16484	26.1	35	12.7	0.64	16495	41.8
8	14.7	0.98	2500	2.4	36	12.9	0.66	2501	6.4
9	13.0	0.84	4872	14.5	37	12.9	0.77	4880	12.4
10	13.2	0.91	2500	1.6	38	13.0	0.78	2500	1.8
11	13.2	0.99	16501	30.9	39	13.0	0.71	16488	28.7
12	13.4	1.05	2500	1.7	40	13.2	0.77	2500	1.5
13	12.8	0.60	4881	14.2	41	14.1	1.20	4877	13.5
14	12.9	0.58	2503	12.4	42	14.2	1.21	2500	1.8
15	12.9	0.62	16487	32.7	43	14.3	1.19	16493	30.9
16	13.2	0.63	2503	12.1	44	14.5	1.30	2500	1.7
17	12.4	0.83	4877	19.0	45	13.5	1.20	4866	16.0
18	12.5	0.79	2510	20.9	46	13.7	1.24	2500	1.9
19	12.4	0.81	16479	33.2	47	13.9	1.31	16493	54.7
20	12.6	0.82	2510	21.0	48	14.1	1.44	2500	1.7
21	11.4	0.85	4861	21.2	49	10.9	1.51	4861	14.9
22	11.6	0.83	2504	13.5	50	11.0	1.50	2501	2.5
23	11.3	0.98	16486	36.8	51	9.8	1.57	16510	54.5
24	11.4	1.03	2503	13.4	52	9.8	1.59	2501	1.8
25	12.0	0.60	4863	19.6	53	9.5	1.58	4872	11.4
26	12.2	0.59	2508	18.7	54	9.6	1.60	2501	1.8
27	12.1	0.72	16476	36.7	55	8.4	1.21	16502	37.5
28	12.3	0.79	2508	18.8	56	8.4	1.23	2501	1.8

Table A.81.: PT-56-1

Axle Nr.	Mass [t]		Distance [mm]		Axle Nr.	Mass [t]		Distance [mm]	
	μ	σ	μ	σ		μ	σ	μ	σ
1	21.0	0.42	0	0.0	29	12.9	0.51	4865	12.6
2	21.5	0.22	3000	1.1	30	13.0	0.53	2501	1.7
3	20.9	0.24	6898	2.0	31	12.8	0.51	16491	20.7
4	21.7	0.40	3000	1.2	32	12.9	0.52	2501	2.1
5	15.6	0.50	5422	12.8	33	13.0	0.52	4873	13.7
6	15.5	0.52	2500	1.4	34	13.1	0.56	2501	1.9
7	16.1	0.49	17406	23.3	35	12.9	0.66	16497	18.6
8	16.2	0.49	2500	1.3	36	13.0	0.68	2501	1.8
9	15.8	0.57	4470	13.2	37	14.3	0.73	4871	14.5
10	15.8	0.59	2500	1.6	38	14.5	0.65	2500	1.3
11	15.8	0.47	17412	31.0	39	14.7	0.74	16510	23.1
12	16.0	0.52	2500	1.7	40	15.0	0.85	2500	1.5
13	12.8	0.51	4669	11.4	41	13.6	0.80	4877	18.2
14	12.8	0.60	2499	1.3	42	13.7	0.76	2500	1.5
15	13.2	0.38	16509	25.4	43	14.2	0.74	16507	27.4
16	13.2	0.40	2500	1.5	44	14.3	0.81	2500	1.7
17	13.2	0.48	4872	11.3	45	13.4	0.80	4868	12.9
18	13.2	0.53	2500	1.2	46	13.5	0.88	2500	1.6
19	13.4	0.37	16512	21.6	47	13.4	0.52	16511	25.2
20	13.5	0.36	2500	1.0	48	13.5	0.55	2499	1.5
21	11.9	0.17	4872	12.5	49	13.7	0.53	4870	10.0
22	11.9	0.19	2501	1.2	50	13.8	0.58	2499	1.4
23	11.8	0.19	16496	20.0	51	13.6	0.50	16512	28.9
24	11.8	0.18	2501	1.3	52	13.6	0.51	2499	1.6
25	12.6	0.46	4870	9.5	53	13.2	0.67	4869	8.8
26	12.7	0.43	2502	1.8	54	13.2	0.73	2500	1.5
27	12.7	0.35	16490	20.6	55	13.3	0.58	16511	24.1
28	12.8	0.36	2501	1.7	56	13.5	0.60	2500	1.6

Table A.82.: PT-56-2

Axle Nr.	Mass [t]		Distance [mm]		Axle Nr.	Mass [t]		Distance [mm]	
	μ	σ	μ	σ		μ	σ	μ	σ
1	21.0	0.55	0	0.0	29	13.2	0.60	4662	12.0
2	21.5	0.40	3000	1.1	30	13.3	0.63	2500	2.0
3	20.9	0.43	6897	3.4	31	13.0	0.71	16486	39.3
4	21.8	0.46	3000	1.2	32	13.2	0.68	2500	1.9
5	12.5	0.38	5632	28.0	33	13.6	0.58	4875	9.7
6	12.7	0.35	2502	1.7	34	13.8	0.61	2500	2.4
7	12.4	0.38	16472	31.2	35	13.6	0.54	16487	45.8
8	12.6	0.42	2502	1.7	36	13.7	0.49	2500	2.2
9	11.7	0.17	4875	10.4	37	13.2	0.59	4873	10.6
10	11.9	0.17	2502	1.4	38	13.3	0.63	2500	1.9
11	11.8	0.15	16485	24.0	39	13.1	0.74	16491	46.1
12	11.9	0.15	2501	1.5	40	13.3	0.71	2500	1.9
13	13.3	0.42	4877	13.3	41	14.2	0.82	4874	12.2
14	13.4	0.44	2500	1.6	42	14.4	0.79	2500	2.8
15	12.9	0.49	16495	41.5	43	13.5	0.77	16487	67.9
16	13.1	0.48	2500	1.5	44	13.6	0.80	2500	1.7
17	13.1	0.42	4874	13.9	45	14.7	0.81	4876	16.8
18	13.2	0.46	2500	1.8	46	14.9	0.75	2500	1.8
19	12.8	0.71	16494	53.2	47	14.2	0.70	16493	29.2
20	12.9	0.66	2500	1.7	48	14.3	0.82	2500	1.9
21	15.9	0.54	4671	11.5	49	12.7	0.66	4867	16.5
22	16.0	0.52	2500	2.4	50	12.9	0.66	2501	2.1
23	15.7	0.66	17395	41.4	51	12.7	0.56	16475	31.5
24	16.1	0.66	2500	2.1	52	12.8	0.54	2501	2.2
25	16.2	0.54	4469	14.9	53	12.6	0.56	4869	12.4
26	16.3	0.54	2499	1.6	54	12.7	0.55	2501	2.3
27	15.5	0.54	17390	32.2	55	12.6	0.57	16478	31.6
28	15.9	0.51	2500	1.3	56	12.8	0.55	2501	2.2

Table A.83.: PT-56-3

Appendix B.

Single-span steel bridges

B.1. Design of the individual single-span steel bridges

B.1.1. Studied section type

Open cross sections — see Figure B.1

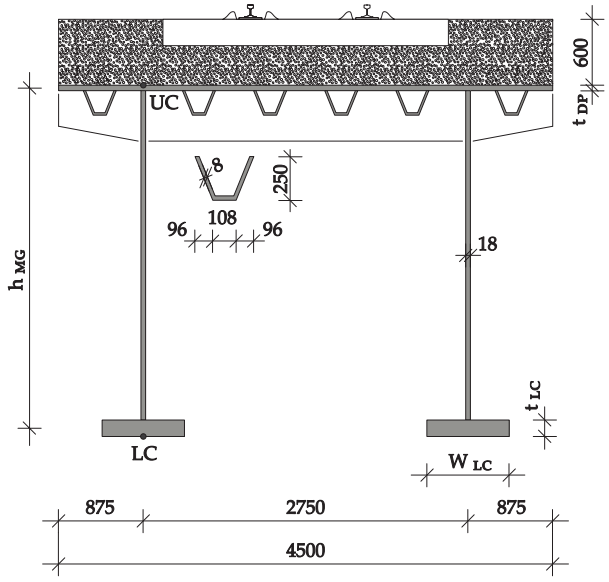

Figure B.1.: Single-span steel bridges — geometry overview — material S355

B.1.2. General approach

a.) ULS design for each bridge (S355) of length L due to LM71, SW/2 and permanent loads in order to determine the "base" section geometry ($h_{MG} \approx L/12 \Rightarrow$ w_{LC}, t_{LC} and t_{DP}). Simplified approach $\sigma_{global} \leq 0.6 * f_{yd}$.

b.) Varying the geometry of the "base" section geometry in order to reach different n_0 — see Figures B.2 and B.3

According to [41], [42] and [35]:

$$E_d = \gamma_{G,j,sup} * G_{k,j,sup} + \gamma_{Q,1} * Q_{k,1} \tag{B.1}$$

with:
$$\begin{aligned}
\gamma_{G,j,sup} &= 1.35 \\
\gamma_{Q,LM71} &= 1.45 \\
\gamma_{Q,SW/2} &= 1.20 \\
Q_{LM71} &= M_{y,LM71,k} * \alpha * \Phi_2 \\
Q_{SW/2} &= M_{y,SW/2,k} * \Phi_2 \\
\alpha &= 1.21 \\
\Phi_2 &= \frac{1.44}{\sqrt{L_\Phi} - 0.2} + 0.82 \\
L_\Phi &= L \\
\gamma_a &= 7850 \text{ kg/m}^3 \\
\gamma_{bb} &= 2000 \text{ kg/m}^3
\end{aligned}$$

B.1.3. Studied individual bridges

$$\mu = \gamma_a * A_a + \gamma_{bb} * A_{bb} \tag{B.2}$$

with:
$$\begin{aligned}
\gamma_a &= 7850 \text{ kg/m}^3 \\
\gamma_{bb} &= 2000 \text{ kg/m}^3 \\
A_{bb} &= 4.5 * 0.6 = 2.7 \text{ m}^2
\end{aligned}$$

$$n_0 = \frac{\pi}{2 * L} * \sqrt{\frac{EI_y}{\mu}} \tag{B.3}$$

Nr.	Name	L [m]	h_{MG} [mm]	t_{DP} [mm]	w_{LC} [mm]	t_{LC} [mm]	EI_y [Nm^2]	μ [kg/m]	n_0 [Hz]	ζ_{EC} [%]	FB [%]
1	SSB7-0	7	435	20	200	20	4.834E+08	6523.1	8.73	2.302	-25
2	SSB7-1	7	555	20	240	20	8.427E+08	6569.5	11.48	2.302	0
3	SSB7-2	7	640	20	300	20	1.270E+09	6612.4	14.05	2.302	25
4	SSB7-3	7	695	20	340	25	1.813E+09	6666.5	16.72	2.302	50
5	SSB7-4	7	775	20	385	25	2.462E+09	6706.7	19.42	2.302	75
6	SSB7-5	7	820	20	420	30	3.226E+09	6765.5	22.14	2.302	100
7	SSB7-6	7	900	20	440	30	4.062E+09	6797.5	24.78	2.302	125
8	SSB10-0	10	540	20	290	20	8.943E+08	6581.0	5.79	2.079	-25
9	SSB10-1	10	675	20	340	25	1.746E+09	6660.8	8.04	2.079	0
10	SSB10-2	10	770	20	410	30	2.851E+09	6746.6	10.21	2.079	25
11	SSB10-3	10	890	20	480	30	4.276E+09	6813.5	12.44	2.079	50
12	SSB10-4	10	935	20	560	40	6.103E+09	6950.4	14.72	2.079	75
13	SSB10-5	10	1050	20	600	40	8.142E+09	7008.0	16.93	2.079	100
14	SSB10-6	10	1155	20	660	40	1.053E+10	7075.4	19.17	2.079	125
15	SSB20-0	20	735	20	425	30	2.690E+09	6743.8	2.48	0.796	-25
16	SSB20-1	20	1000	20	550	40	7.157E+09	6962.5	3.98	0.796	0
17	SSB20-2	20	1340	20	600	40	1.415E+10	7090.0	5.55	0.796	25
18	SSB20-3	20	1675	20	600	40	2.303E+10	7184.7	7.03	0.796	50
19	SSB20-4	20	1870	20	700	50	3.534E+10	7411.0	8.58	0.796	75
20	SSB20-5	20	2055	20	800	60	5.044E+10	7666.0	10.07	0.796	100
21	SSB20-6	20	2175	20	1000	80	7.158E+10	8199.5	11.60	0.796	125
22	SSB30-0	30	1300	20	460	30	9.951E+09	6920.0	2.09	0.500	-25
23	SSB30-1	30	1685	20	600	40	2.344E+10	7187.5	3.15	0.500	0
24	SSB30-2	30	2055	20	700	50	4.357E+10	7463.3	4.22	0.500	25
25	SSB30-3	30	2435	25	800	50	7.195E+10	7825.1	5.29	0.500	50
26	SSB30-4	30	2755	25	900	60	1.083E+11	8134.0	6.37	0.500	75
27	SSB30-5	30	3100	25	950	70	1.533E+11	8426.3	7.45	0.500	100
28	SSB30-6	30	3435	25	1000	80	2.072E+11	8731.5	8.50	0.500	125
29	SSB40-0	40	1720	20	600	40	2.457E+10	7197.4	1.81	0.500	-25
30	SSB40-1	40	2150	20	800	60	5.599E+10	7692.9	2.65	0.500	0
31	SSB40-2	40	2675	25	900	60	1.019E+11	8111.3	3.48	0.500	25
32	SSB40-3	40	3175	25	1000	70	1.655E+11	8502.4	4.33	0.500	50
33	SSB40-4	40	3650	25	1000	90	2.485E+11	8947.8	5.17	0.500	75
34	SSB40-5	40	4120	25	1000	110	3.496E+11	9391.8	5.99	0.500	100

Continued on next page

Table B.1 – continued from previous page

Nr.	Name	L [m]	h_{MG} [mm]	t_{DP} [mm]	w_{LC} [mm]	t_{LC} [mm]	EI_y [Nm^2]	μ [kg/m]	n_0 [Hz]	ζ_{EC} [%]	FB [%]
35	SSB40-6	40	4650	25	1000	120	4.694E+11	9697.2	6.83	0.500	125
36	SSB50-0	50	2350	25	600	40	5.220E+10	7551.3	1.65	0.500	-25
37	SSB50-1	50	2800	30	800	60	1.129E+11	8228.4	2.33	0.500	0
38	SSB50-2	50	3435	30	900	70	1.992E+11	8641.9	3.02	0.500	25
39	SSB50-3	50	4115	30	900	80	3.1192E+11	8974.0	3.70	0.500	50
40	SSB50-4	50	4715	30	1000	90	4.607E+11	9424.7	4.39	0.500	75
41	SSB50-5	50	5310	30	1000	110	6.469E+11	9904.1	5.08	0.500	100
42	SSB50-6	50	5850	35	1000	120	8.749E+11	10388.2	5.77	0.500	125
43	SSB60-0	60	3000	30	600	40	9.502E+10	7910.9	1.51	0.500	-25
44	SSB60-1	60	3575	30	800	60	1.916E+11	8447.4	2.08	0.500	0
45	SSB60-2	60	4325	30	950	70	3.356E+11	8948.4	2.67	0.500	25
46	SSB60-3	60	5050	30	1000	90	5.344E+11	9519.4	3.27	0.500	50
47	SSB60-4	60	5750	30	1000	120	7.961E+11	10184.0	3.86	0.500	76
48	SSB60-5	60	6450	30	1000	150	1.114E+12	10848.6	4.42	0.500	100
49	SSB60-6	60	7125	35	1000	160	1.503E+12	11370.8	5.02	0.500	125
50	SSB70-0	70	3700	30	600	40	1.532E+11	8108.8	1.39	0.500	-25
51	SSB70-1	70	4360	35	800	60	3.108E+11	8845.2	1.90	0.500	0
52	SSB70-2	70	4990	35	1000	90	5.507E+11	9678.4	2.42	0.500	25
53	SSB70-3	70	5820	35	1000	120	8.658E+11	10379.7	2.93	0.500	50
54	SSB70-4	70	6685	35	1000	150	1.277E+12	11090.9	3.44	0.500	75
55	SSB70-5	70	7565	35	1000	180	1.790E+12	11806.3	3.95	0.500	100
56	SSB70-6	70	8350	40	1000	200	2.432E+12	12515.3	4.47	0.500	125
57	SSB80-0	80	4450	30	600	40	2.345E+11	8320.7	1.30	0.500	-25
58	SSB80-1	80	5250	35	800	60	4.690E+11	9096.7	1.76	0.500	0
59	SSB80-2	80	6175	35	1000	70	7.864E+11	9702.1	2.21	0.500	25
60	SSB80-3	80	7000	35	1000	110	1.247E+12	10557.6	2.67	0.500	50
61	SSB80-4	80	7850	35	1000	170	1.901E+12	11731.3	3.12	0.500	75
62	SSB80-5	80	8875	35	1000	200	2.642E+12	12487.7	3.57	0.500	100
63	SSB80-6	80	9800	40	1000	220	3.576E+12	13236.2	4.03	0.500	125

Note: abbr. of structure name, e.g. **SSB20-3**: **S**ingle-span**S**teel**B**ridge Length=**20**m **-** Nr.**3**

Table B.1.: Single-span steel bridges — geometry

B.1.4. Utilization factors for ULS of the individual bridges

Nr.	Name	η_{ULS} [%]			
		with LM71		with SW/2	
		UC	LC	UC	LC
1	SSB7-0	37	132	26	94
2	SSB7-1	27	96	19	68
3	SSB7-2	22	72	15	51
4	SSB7-3	18	53	13	38
5	SSB7-4	15	43	11	31
6	SSB7-5	14	33	10	24
7	SSB7-6	12	29	9	21
8	SSB10-0	45	160	34	120
9	SSB10-1	32	99	24	75
10	SSB10-2	25	66	19	50
11	SSB10-3	21	50	16	38
12	SSB10-4	18	34	14	26
13	SSB10-5	16	28	12	21
14	SSB10-6	14	23	11	18
15	SSB20-0	78	212	69	188
16	SSB20-1	50	99	44	88
17	SSB20-2	35	65	32	58
18	SSB20-3	28	50	25	44
19	SSB20-4	23	34	21	31
20	SSB20-5	21	24	18	22
21	SSB20-6	19	16	17	14
22	SSB30-0	78	198	73	186
23	SSB30-1	54	99	51	93
24	SSB30-2	42	62	40	58
25	SSB30-3	30	45	28	43
26	SSB30-4	26	32	24	30
27	SSB30-5	22	25	21	23
28	SSB30-6	20	19	19	18
29	SSB40-0	88	161	80	146
30	SSB40-1	65	78	59	70
31	SSB40-2	44	55	40	50
32	SSB40-3	36	39	33	35
33	SSB40-4	30	29	28	26
34	SSB40-5	26	23	24	21
35	SSB40-6	23	19	21	18

Nr.	Name	η_{ULS} [%]			
		with LM71		with SW/2	
		UC	LC	UC	LC
36	SSB50-0	81	161	73	144
37	SSB50-1	56	84	51	76
38	SSB50-2	44	57	40	51
39	SSB50-3	36	42	33	38
40	SSB50-4	31	32	28	29
41	SSB50-5	27	26	24	24
42	SSB50-6	22	22	20	20
43	SSB60-0	78	163	70	148
44	SSB60-1	61	89	55	80
45	SSB60-2	48	59	44	53
46	SSB60-3	40	42	36	38
47	SSB60-4	34	32	31	29
48	SSB60-5	30	24	27	22
49	SSB60-6	25	22	23	20
50	SSB70-0	83	165	76	151
51	SSB70-1	60	93	54	85
52	SSB70-2	50	56	45	51
53	SSB70-3	41	42	38	38
54	SSB70-4	35	31	33	29
55	SSB70-5	31	25	29	23
56	SSB70-6	26	21	24	20
57	SSB80-0	88	167	80	151
58	SSB80-1	63	96	57	87
59	SSB80-2	51	65	47	59
60	SSB80-3	44	47	40	43
61	SSB80-4	38	32	35	30
62	SSB80-5	33	26	31	24
63	SSB80-6	28	23	26	21

UC...upper chord
LC...lower chord

$f_{yd} = f(t_{LC})$
according to [40]

Table B.2.: Single-span steel bridges — utilization for ULS

B.1.5. Suitability of individual bridges for high-speed railway lines

Nr.	Name	$\lvert a_{HSLM-A,max} \rvert$ [m/s^2]	
		v_{max} = 240 km/h	v_{max} = 300 km/h
1	SSB7-0	47.36	78.04
2	SSB7-1	17.71	38.02
3	SSB7-2	18.36	20.21
4	SSB7-3	19.06	19.06
5	SSB7-4	19.44	19.75
6	SSB7-5	9.21	20.38
7	SSB7-6	7.81	18.49
8	SSB10-0	59.84	77.74
9	SSB10-1	18.64	50.40
10	SSB10-2	9.98	18.56
11	SSB10-3	10.27	10.27
12	SSB10-4	8.35	10.58
13	SSB10-5	8.61	11.09
14	SSB10-6	8.97	8.97
15	SSB20-0	107.63	107.63
16	SSB20-1	18.83	86.55
17	SSB20-2	19.24	19.24
18	SSB20-3	12.50	19.54
19	SSB20-4	7.22	12.64
20	SSB20-5	6.16	7.14
21	SSB20-6	3.83	6.91
22	SSB30-0	47.77	47.77
23	SSB30-1	16.15	41.12
24	SSB30-2	11.31	15.61
25	SSB30-3	8.97	11.05
26	SSB30-4	8.55	8.55
27	SSB30-5	4.14	8.50
28	SSB30-6	4.08	4.99
29	SSB40-0	18.83	18.83
30	SSB40-1	17.72	17.72
31	SSB40-2	15.24	16.96
32	SSB40-3	6.68	14.52
33	SSB40-4	5.00	6.36
34	SSB40-5	4.12	6.05
35	SSB40-6	2.14	4.01
36	SSB50-0	13.56	13.56
37	SSB50-1	12.45	12.45
38	SSB50-2	6.84	11.90
39	SSB50-3	6.58	6.58
40	SSB50-4	3.17	6.27
41	SSB50-5	3.03	3.03
42	SSB50-6	2.29	2.88
43	SSB60-0	7.28	7.87
44	SSB60-1	6.79	6.79
45	SSB60-2	6.47	6.47
46	SSB60-3	6.09	6.09
47	SSB60-4	1.86	5.67
48	SSB60-5	1.76	4.07
49	SSB60-6	1.67	1.67
50	SSB70-0	5.77	5.77
51	SSB70-1	5.24	5.24
52	SSB70-2	4.85	4.85
53	SSB70-3	3.94	4.52
54	SSB70-4	3.12	4.23
55	SSB70-5	1.34	2.94
56	SSB70-6	1.27	2.77
57	SSB80-0	4.78	4.78
58	SSB80-1	4.43	4.43
59	SSB80-2	4.13	4.13
60	SSB80-3	3.00	3.82
61	SSB80-4	2.70	3.26
62	SSB80-5	1.42	2.54
63	SSB80-6	0.98	2.39

Table B.3.: Single-span steel bridges — $\lvert a_{HSLM-A,max} \rvert$ due to HSLM-A

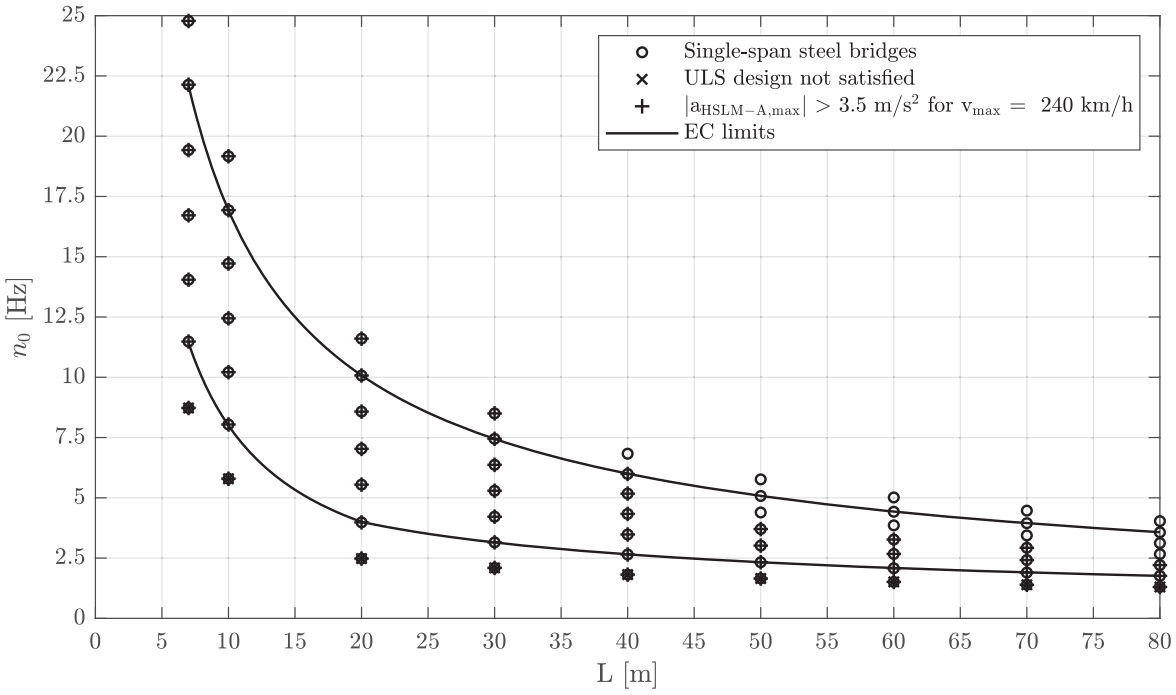

Figure B.2.: Single-span steel bridges — suitability for high-speed railway lines — v_{max} = 240 km/h

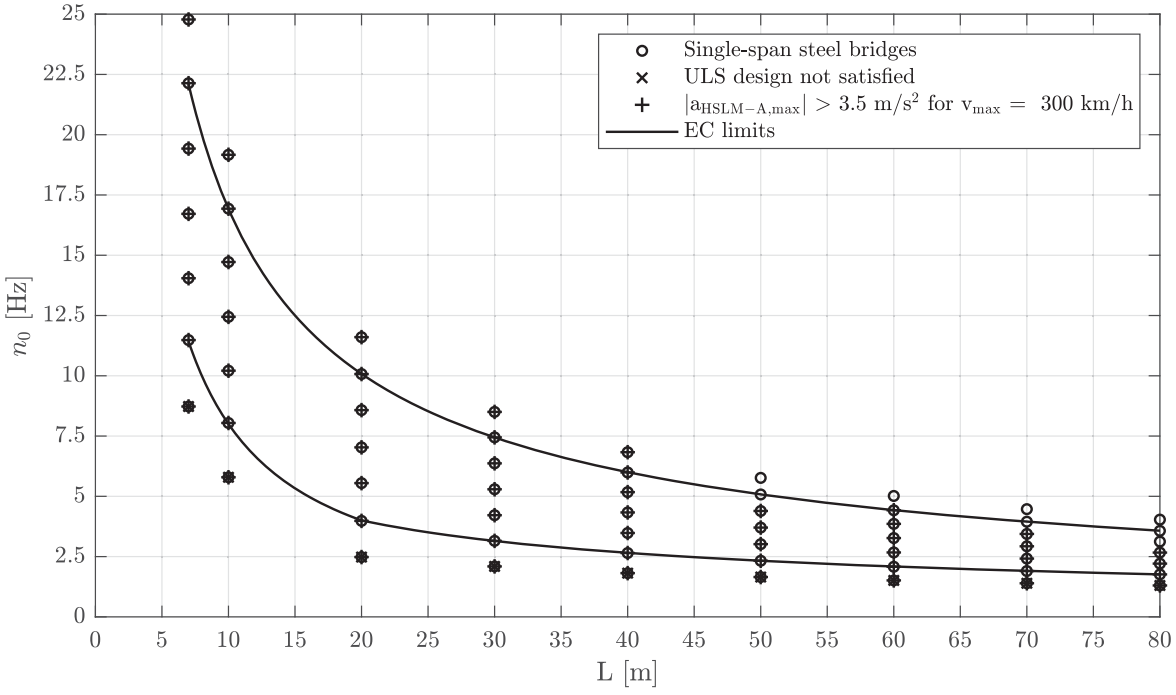

Figure B.3.: Single-span steel bridges — suitability for high-speed railway lines — v_{max} = 300 km/h

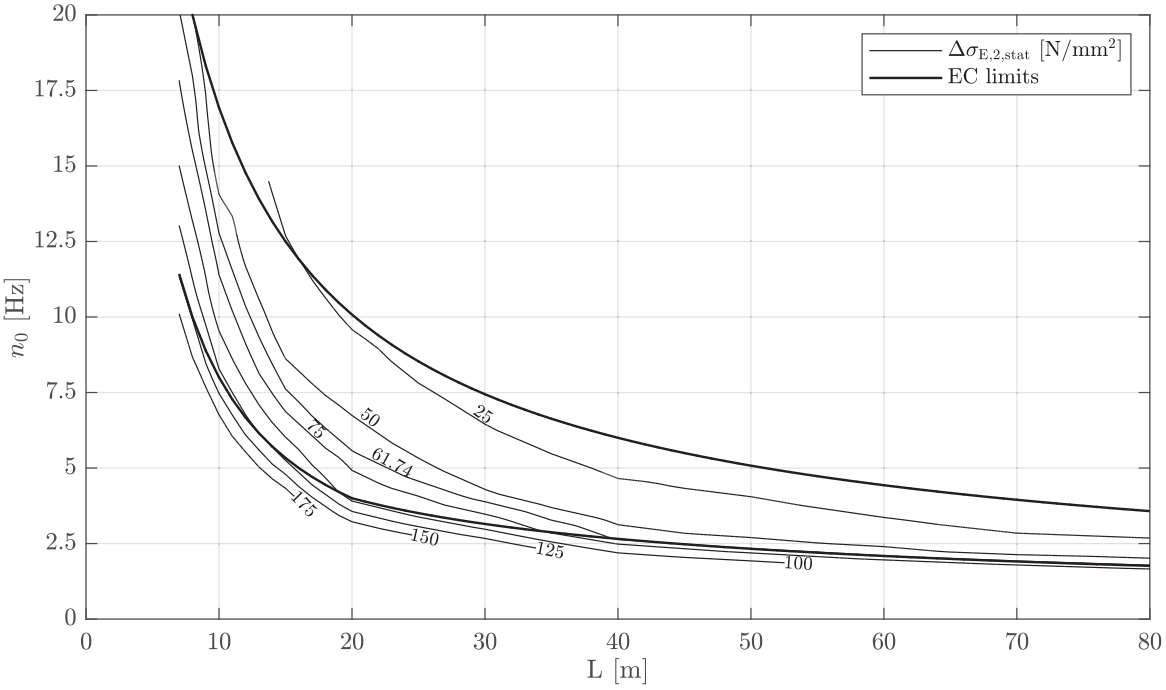

Figure B.4.: Single-span steel bridges — $\Delta\sigma_{E,2,stat}$ due to TM1 — no load distribution

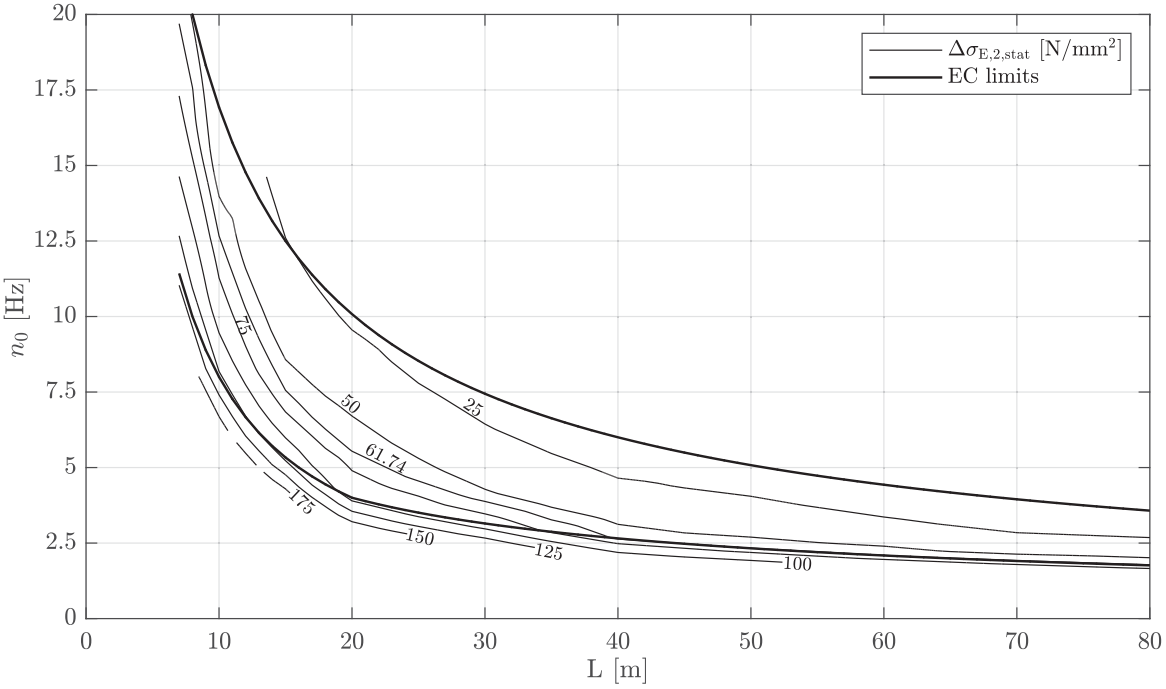

Figure B.5.: Single-span steel bridges — $\Delta\sigma_{E,2,stat}$ due to TM1 — load distribution

B.2. Results for $|a_{HSLM-A,max}|$ of single-span steel bridges due to HSLM-A

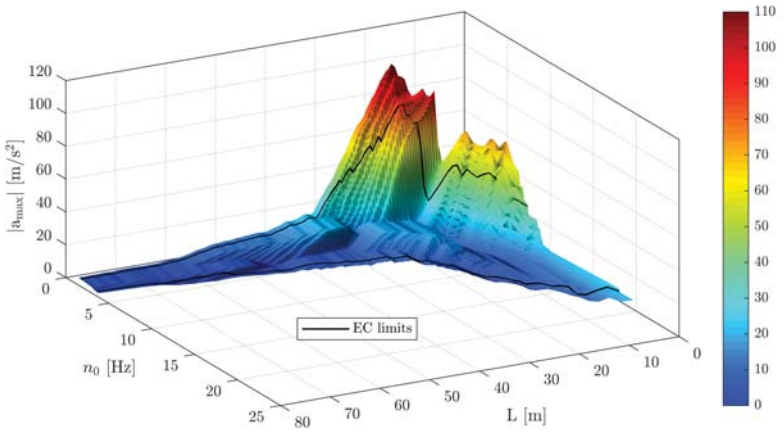

(a) 3D-view

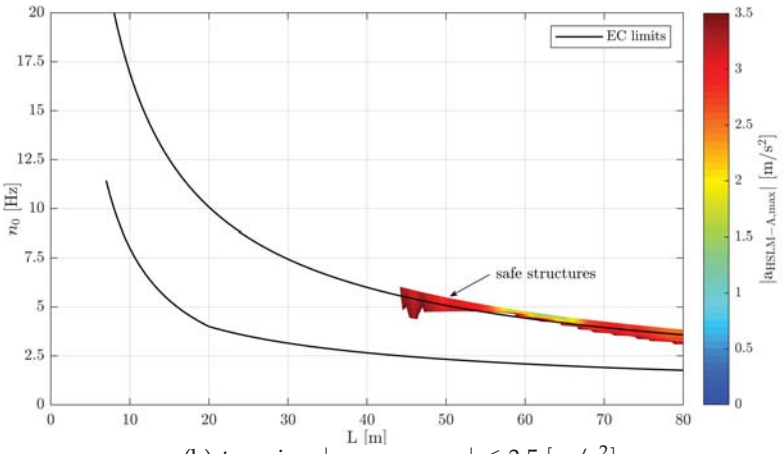

(b) top view $|a_{HSLM-A,max}| \leq 3.5$ [m/s^2]

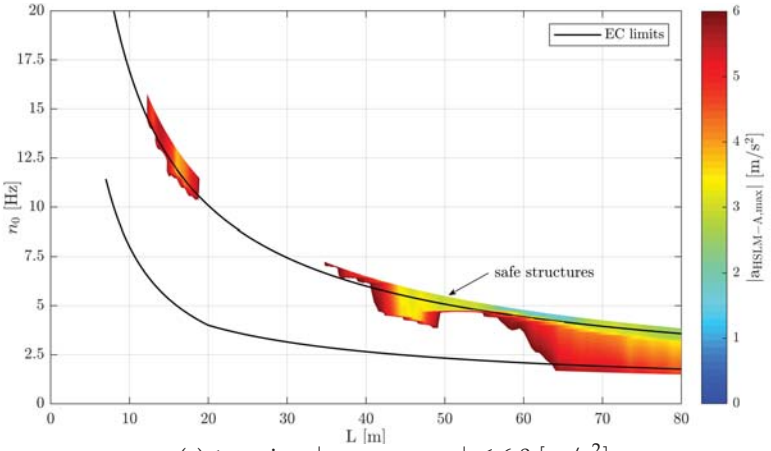

(c) top view $|a_{HSLM-A,max}| \leq 6.0$ [m/s^2]

Figure B.6.: Single-span steel bridges — vertical bridge deck acceleration $|a_{HSLM-A,max}|$ due to HSLM-A trains — v_{max} = 300 km/h — ζ_{EC} — modal damping — no load distribution

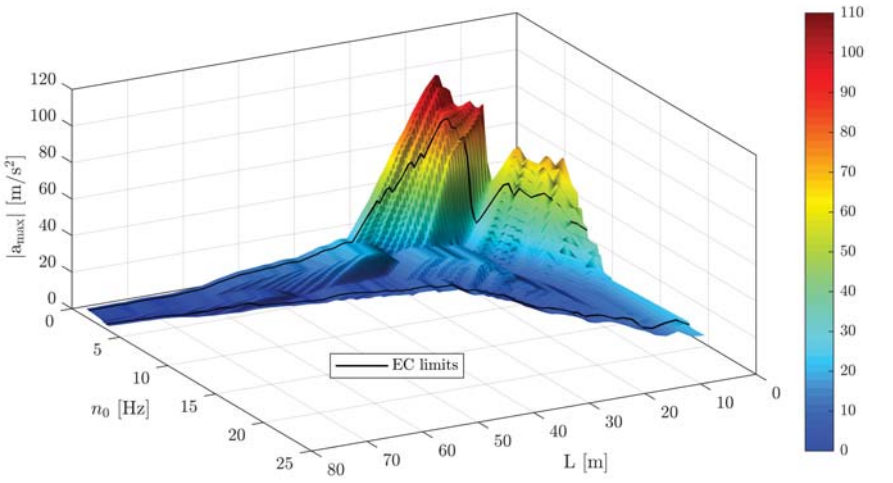

(a) 3D-view

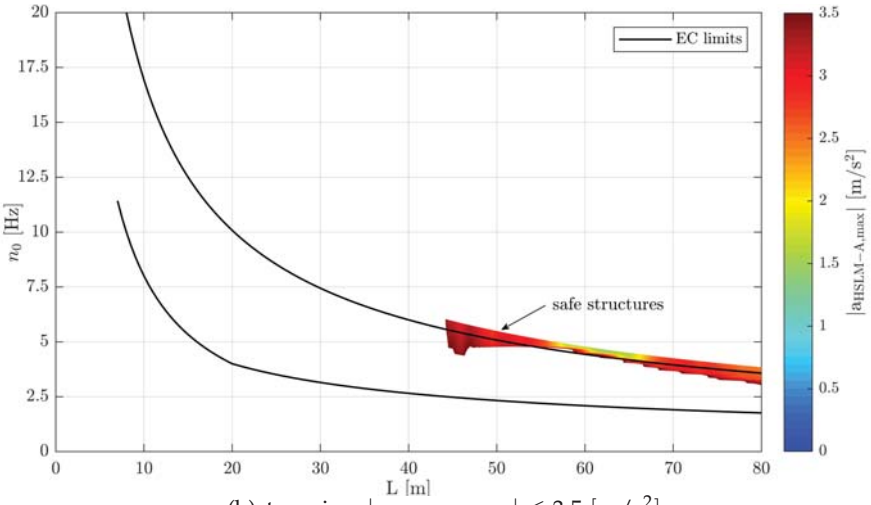

(b) top view $|a_{HSLM-A,max}| \leq 3.5$ [m/s^2]

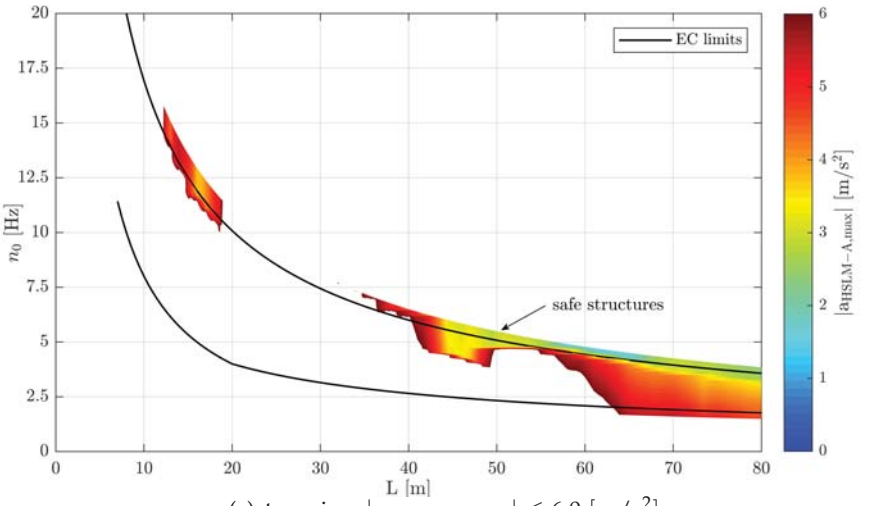

(c) top view $|a_{HSLM-A,max}| \leq 6.0$ [m/s^2]

Figure B.7.: Single-span steel bridges — vertical bridge deck acceleration $|a_{HSLM-A,max}|$ due to HSLM-A trains — v_{max} = 300 km/h — ζ_{EC} — Rayleigh like damping — no load distribution

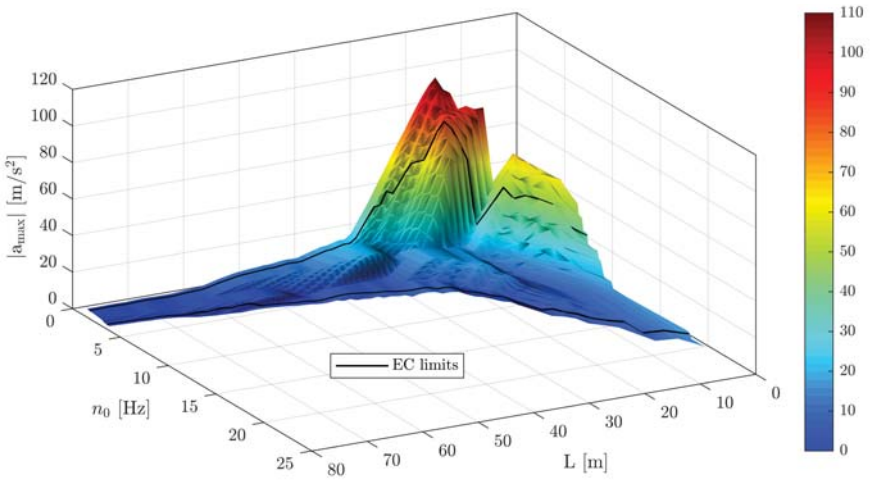

(a) 3D-view

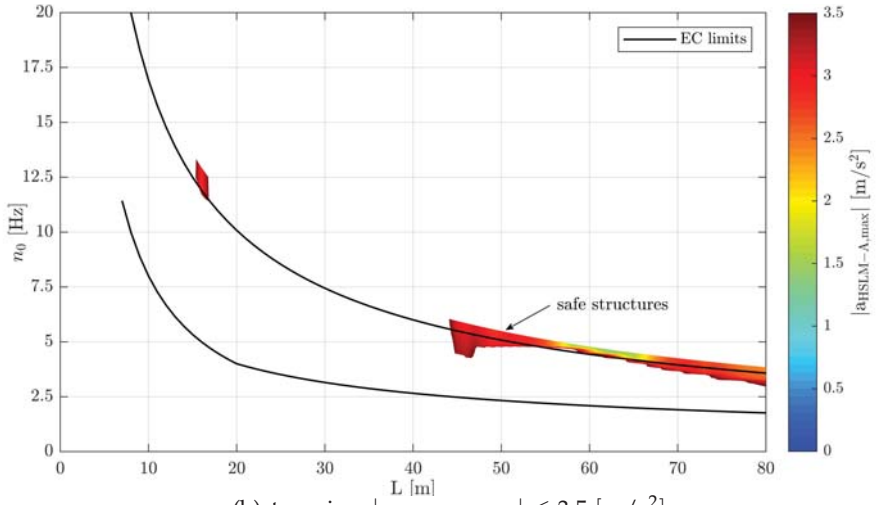

(b) top view $|a_{HSLM-A,max}| \leq 3.5$ [m/s^2]

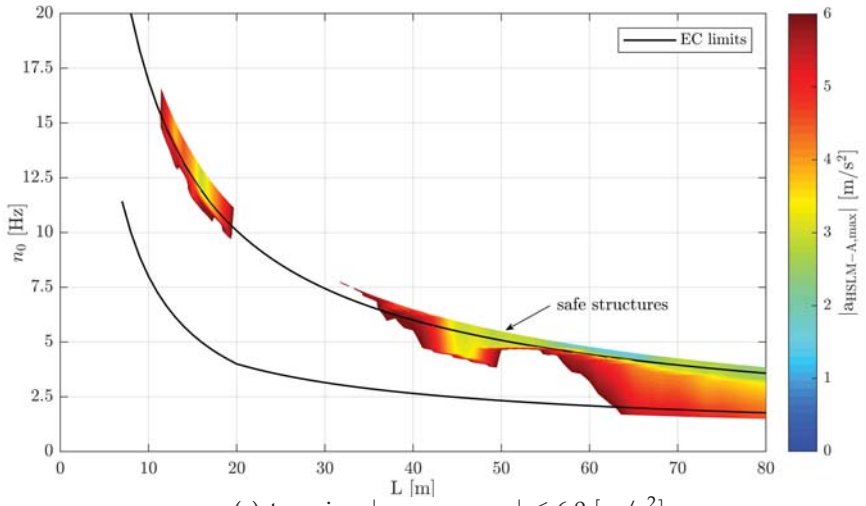

(c) top view $|a_{HSLM-A,max}| \leq 6.0$ [m/s^2]

Figure B.8.: Single-span steel bridges — vertical bridge deck acceleration $|a_{HSLM-A,max}|$ due to HSLM-A trains — v_{max} = 300 km/h — ζ_{EC} — Rayleigh like damping — with load distribution

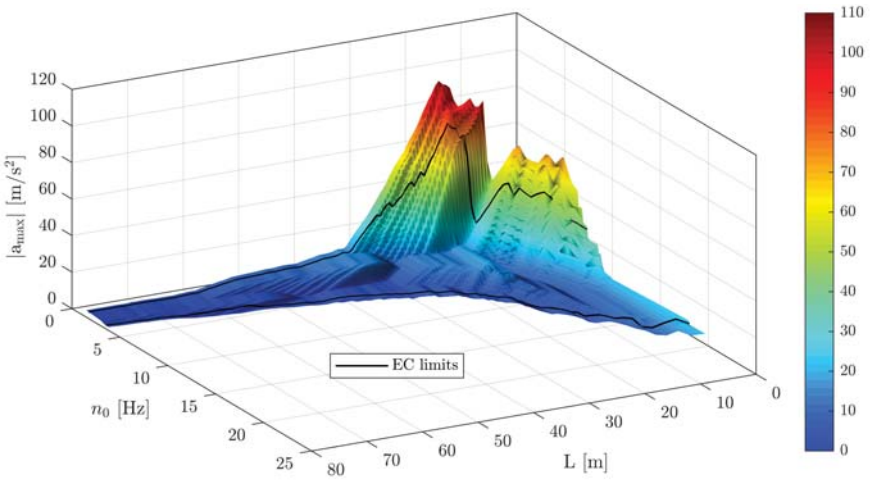

(a) 3D-view

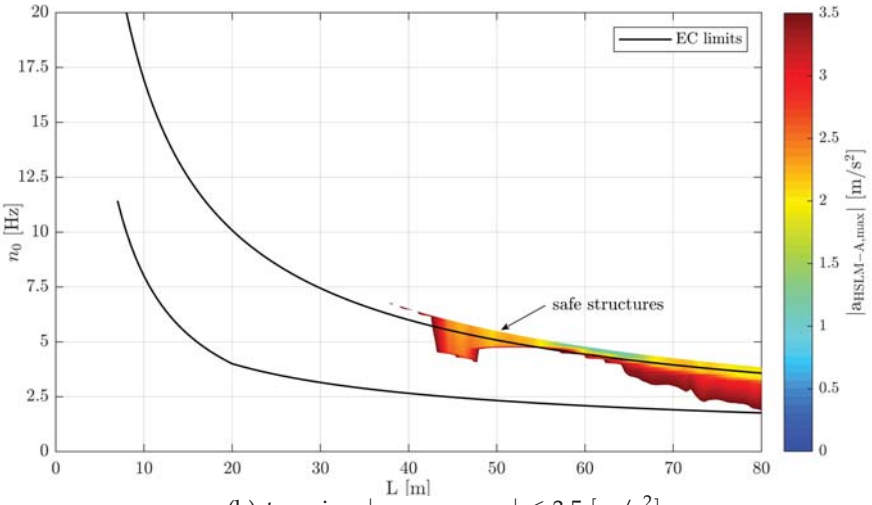

(b) top view $|a_{HSLM-A,max}| \leq 3.5$ [m/s^2]

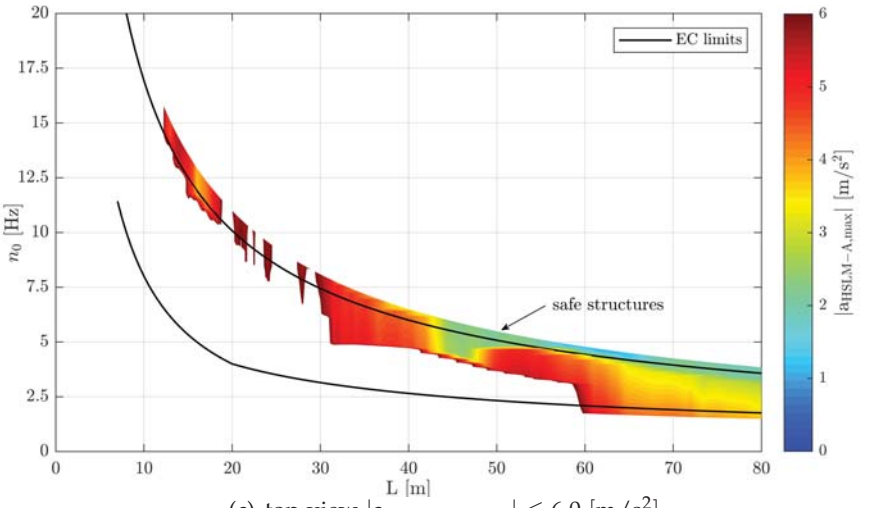

(c) top view $|a_{HSLM-A,max}| \leq 6.0$ [m/s^2]

Figure B.9.: Single-span steel bridges — vertical bridge deck acceleration $|a_{HSLM-A,max}|$ due to HSLM-A trains — v_{max} = 300 km/h — ζ_{V1} — modal damping — no load distribution

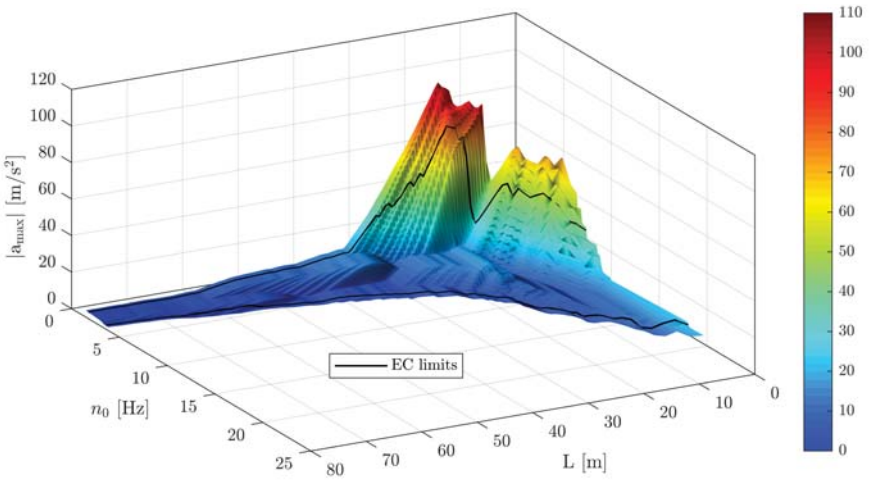

(a) 3D-view

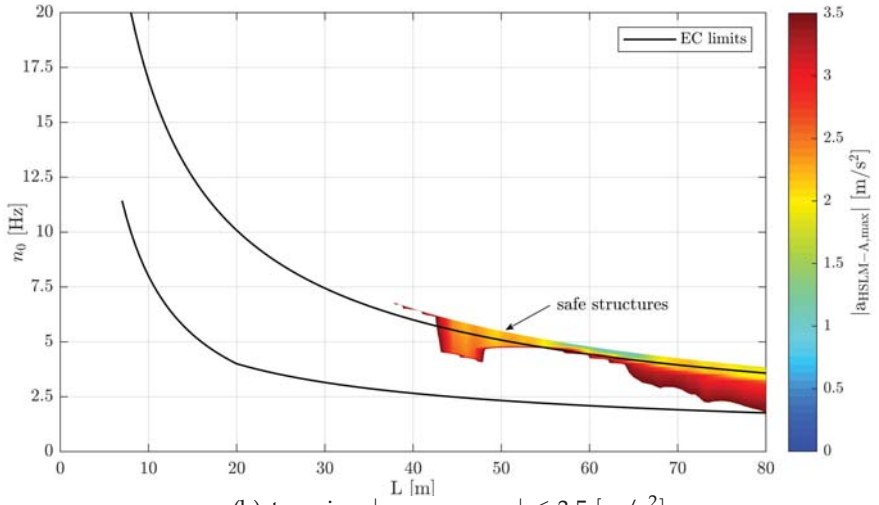

(b) top view $|a_{HSLM-A,max}| \leq 3.5$ [m/s^2]

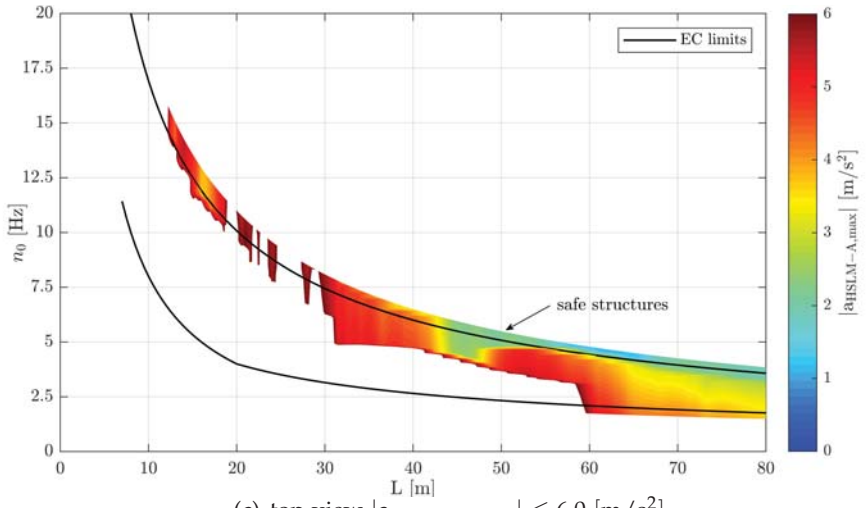

(c) top view $|a_{HSLM-A,max}| \leq 6.0$ [m/s^2]

Figure B.10.: Single-span steel bridges — vertical bridge deck acceleration $|a_{HSLM-A,max}|$ due to HSLM-A trains — v_{max} = 300 km/h — ζ_{V1} — Rayleigh like damping — no load distribution

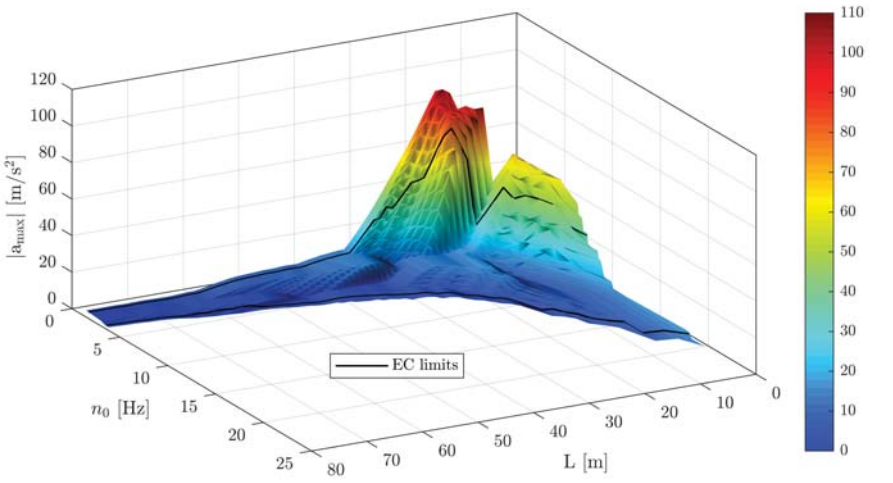

(a) 3D-view

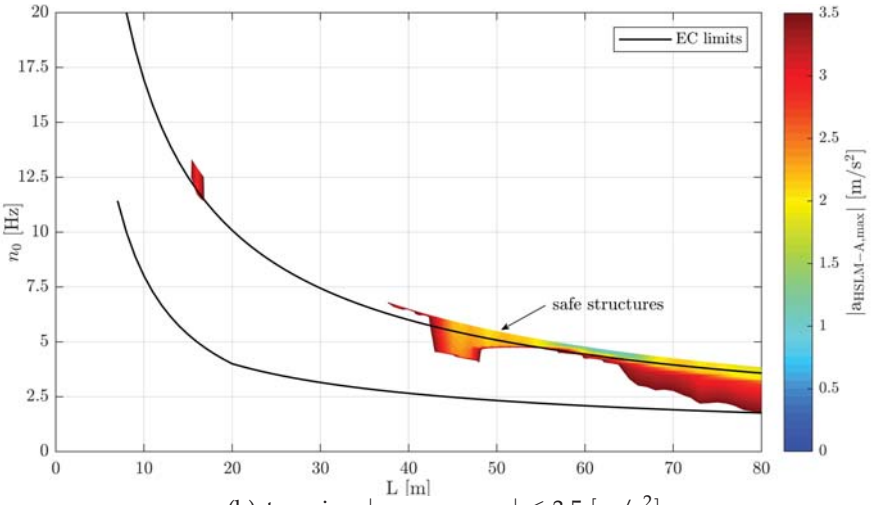

(b) top view $|a_{HSLM-A,max}| \leq 3.5$ [m/s^2]

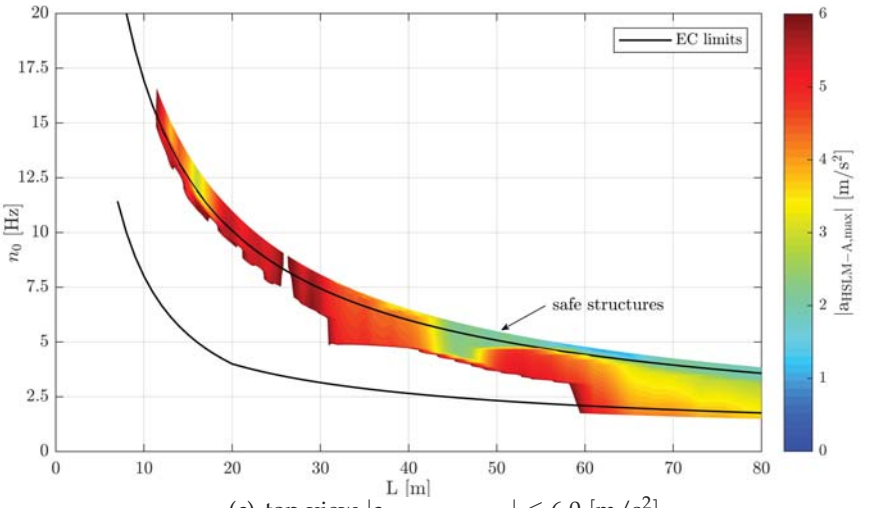

(c) top view $|a_{HSLM-A,max}| \leq 6.0$ [m/s^2]

Figure B.11.: Single-span steel bridges — vertical bridge deck acceleration $|a_{HSLM-A,max}|$ due to HSLM-A trains — v_{max} = 300 km/h — ζ_{V1} — Rayleigh like damping — with load distribution

B.3. Results for fatigue of single-span steel bridges due to TM1

B.3.1. Train speed v_{EC}

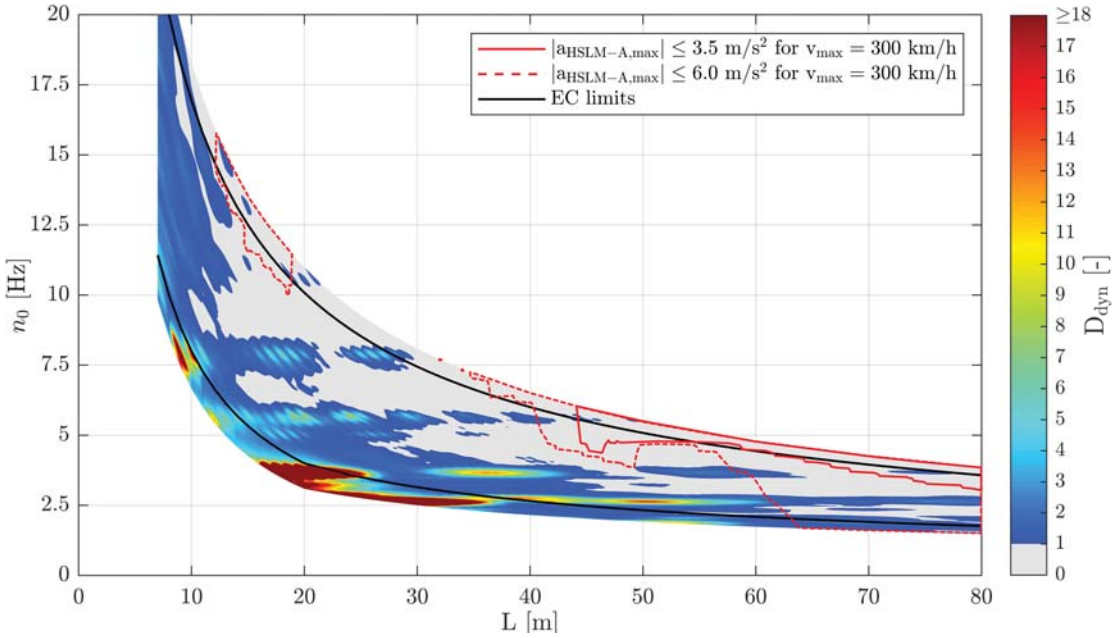

Figure B.12.: Single-span steel bridges — traffic mix TM1* — v_{EC} — ζ_{EC} — Rayleigh like damping — no load distribution — top view D_{dyn} & $|a_{HSLM-A,max}|$

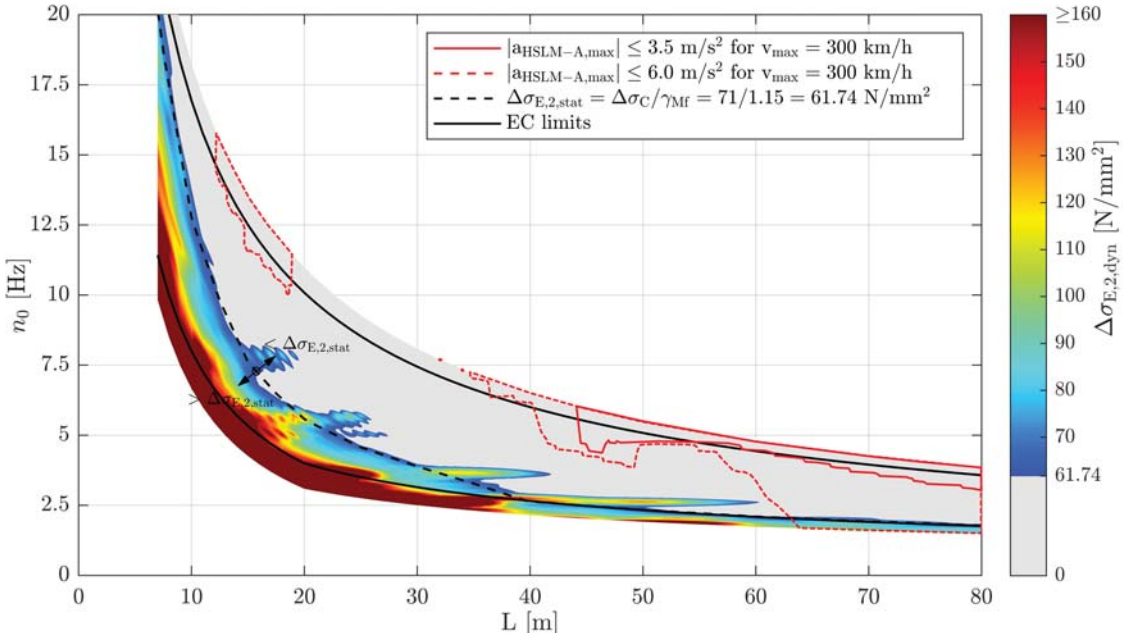

Figure B.13.: Single-span steel bridges — traffic mix TM1* — v_{EC} — ζ_{EC} — Rayleigh like damping — no load distribution — top view $\Delta\sigma_{E,2,dyn}$ & $|a_{HSLM-A,max}|$ & $\Delta\sigma_{E,2,stat}$

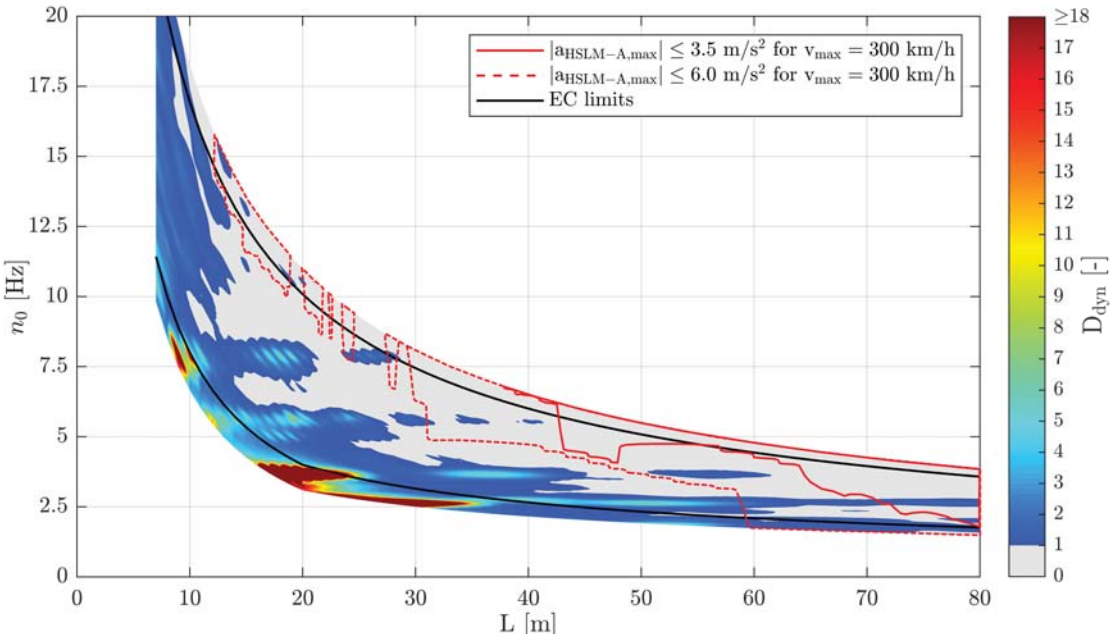

Figure B.14.: Single-span steel bridges — traffic mix TM1* — v_{EC} — ζ_{V1} — Rayleigh like damping — no load distribution — top view D_{dyn} & $|a_{HSLM-A,max}|$

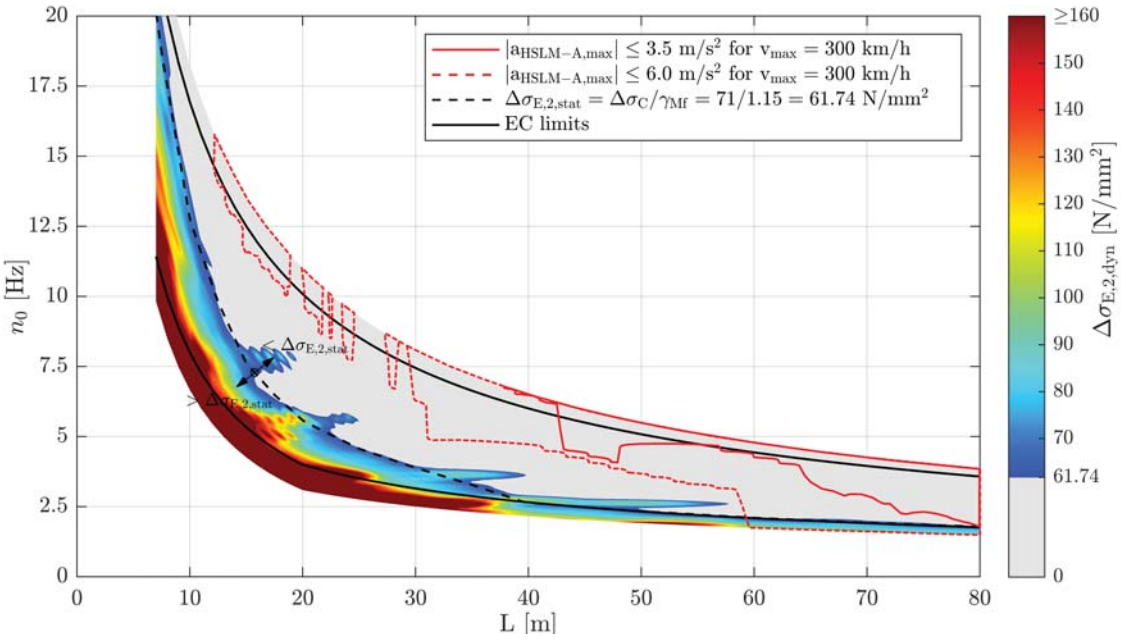

Figure B.15.: Single-span steel bridges — traffic mix TM1* — v_{EC} — ζ_{V1} — Rayleigh like damping — no load distribution — top view $\Delta\sigma_{E,2,dyn}$ & $|a_{HSLM-A,max}|$ & $\Delta\sigma_{E,2,stat}$

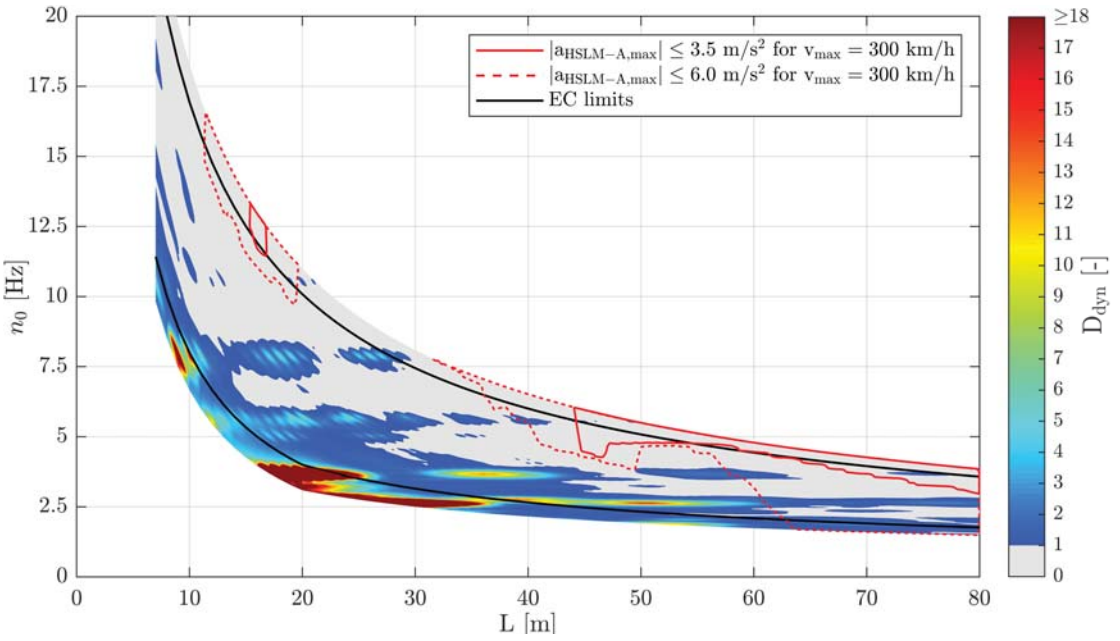

Figure B.16.: Single-span steel bridges — traffic mix TM1* — v_{EC} — ζ_{EC} — Rayleigh like damping — load distribution — top view D_{dyn} & $|a_{HSLM-A,max}|$

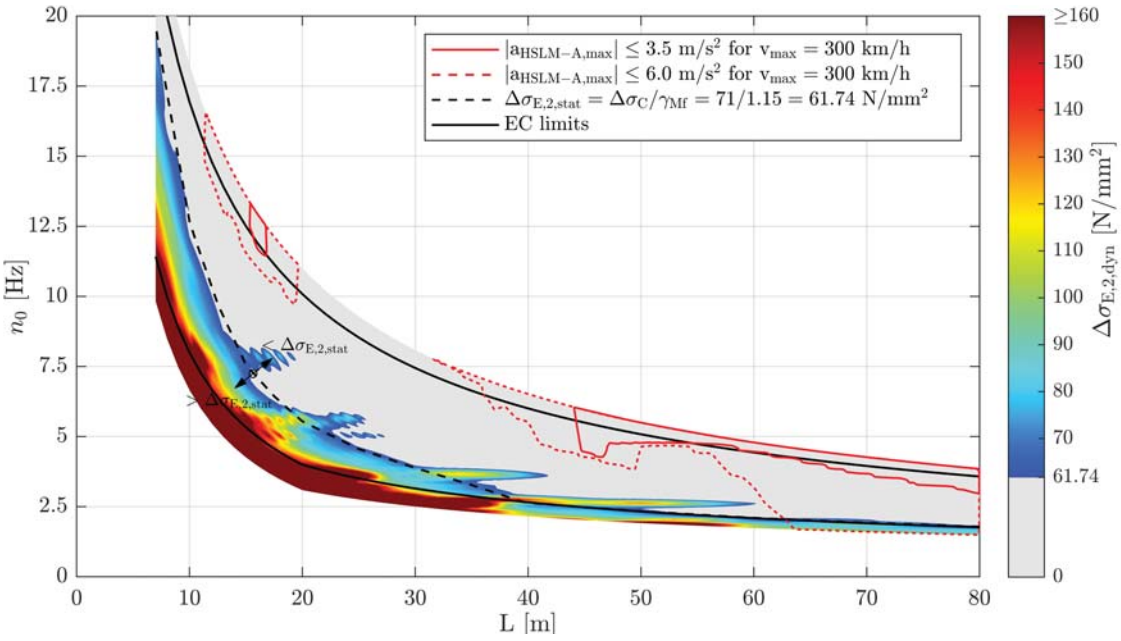

Figure B.17.: Single-span steel bridges — traffic mix TM1* — v_{EC} — ζ_{EC} — Rayleigh like damping — load distribution — top view $\Delta\sigma_{E,2,dyn}$ & $|a_{HSLM-A,max}|$ & $\Delta\sigma_{E,2,stat}$

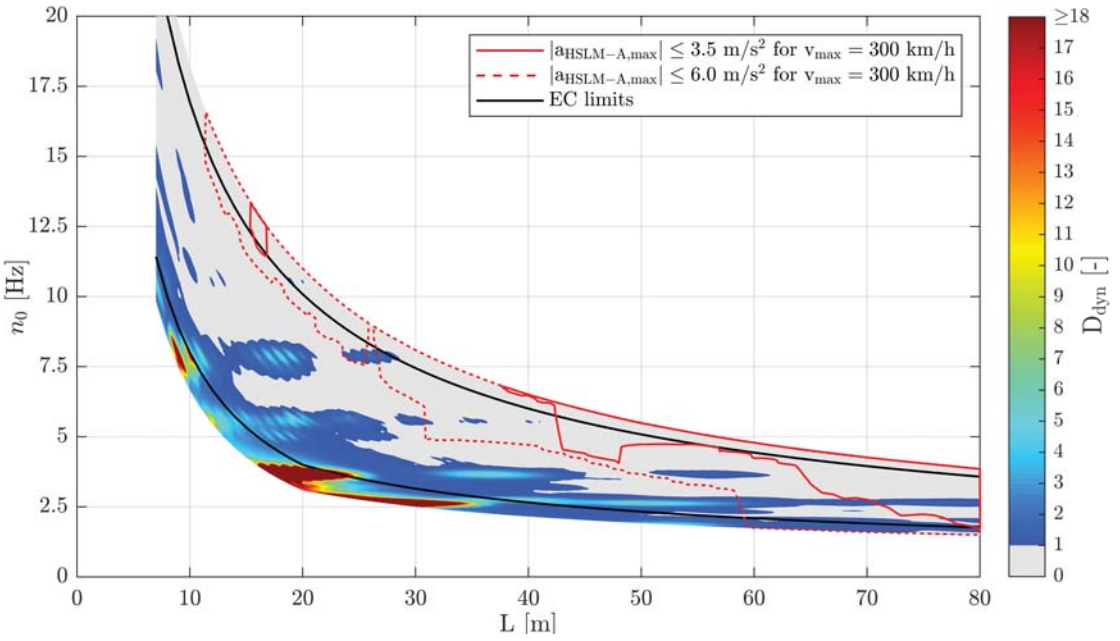

Figure B.18.: Single-span steel bridges — traffic mix TM1* — v_{EC} — ζ_{V1} — Rayleigh like damping — load distribution — top view D_{dyn} & $|a_{HSLM-A,max}|$

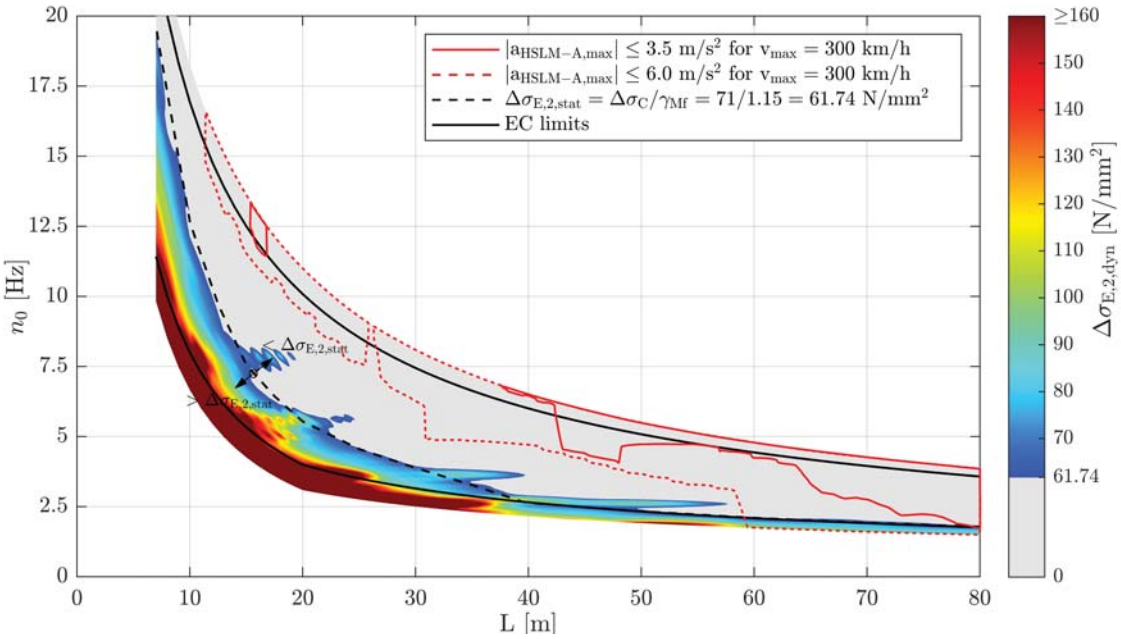

Figure B.19.: Single-span steel bridges — traffic mix TM1* — v_{EC} — ζ_{V1} — Rayleigh like damping — load distribution — top view $\Delta\sigma_{E,2,dyn}$ & $|a_{HSLM-A,max}|$ & $\Delta\sigma_{E,2,stat}$

B.3.2. Train speed $v_{D_{max}}$

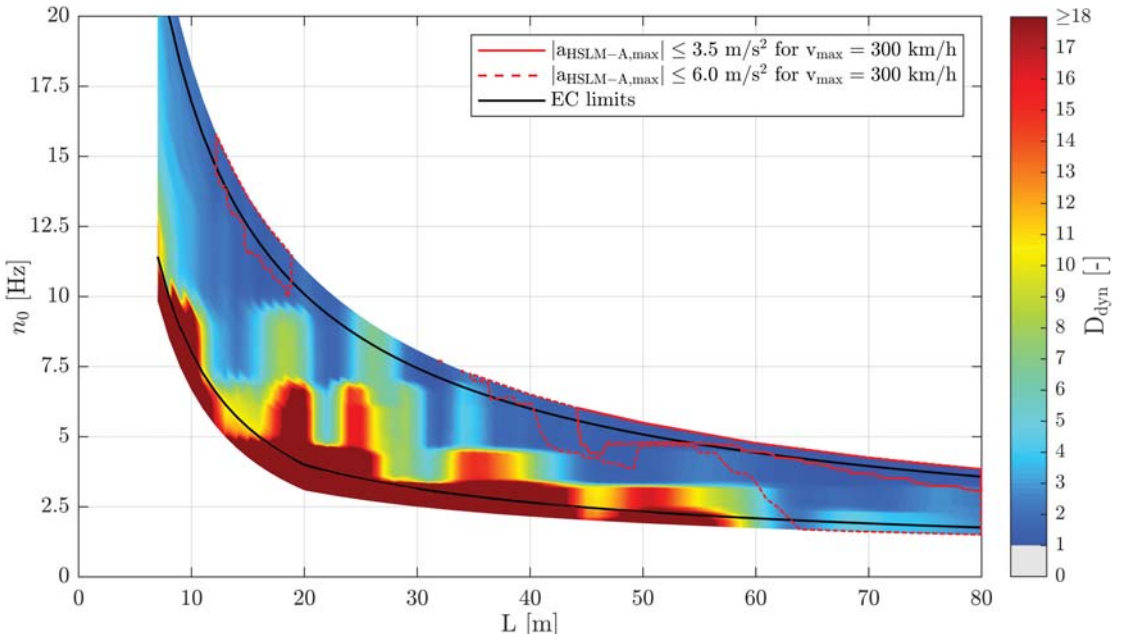

Figure B.20.: Single-span steel bridges — traffic mix TM1** — $v_{D_{max}}$ — ζ_{EC} — Rayleigh like damping — no load distribution — top view D_{dyn} & $|a_{HSLM-A,max}|$

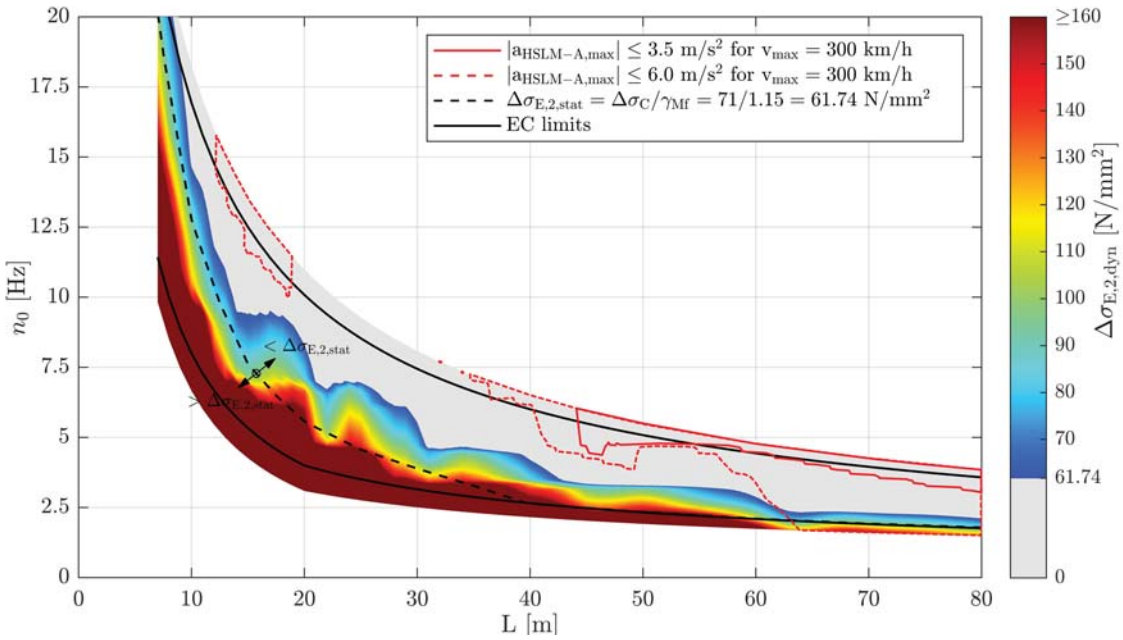

Figure B.21.: Single-span steel bridges — traffic mix TM1** — $v_{D_{max}}$ — ζ_{EC} — Rayleigh like damping — no load distribution — top view $\Delta\sigma_{E,2,dyn}$ & $|a_{HSLM-A,max}|$ & $\Delta\sigma_{E,2,stat}$

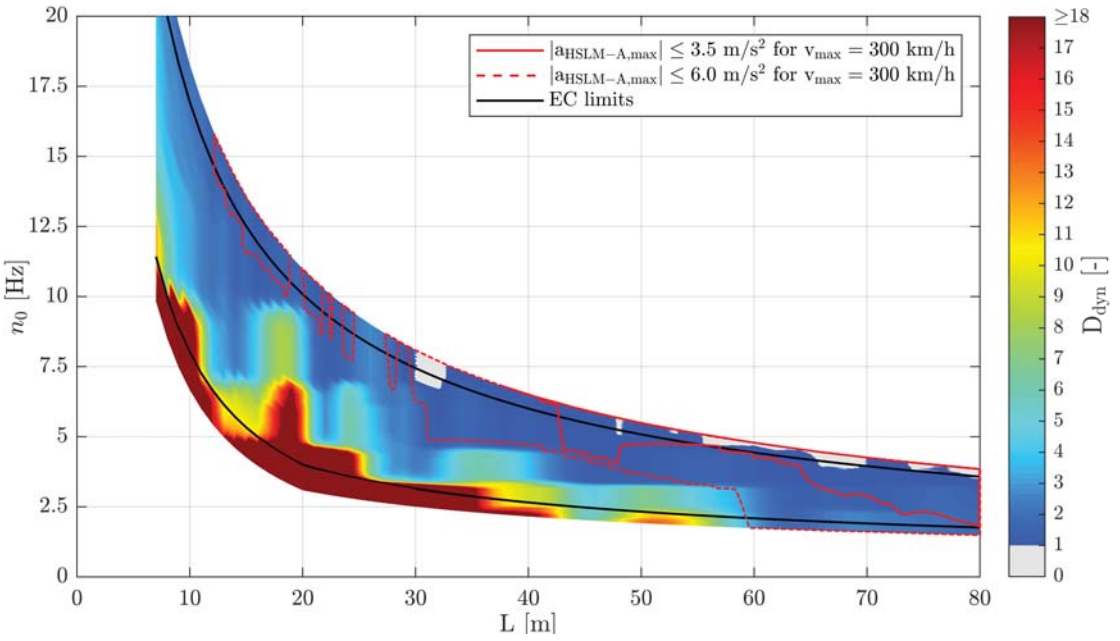

Figure B.22.: Single-span steel bridges — traffic mix TM1** — $v_{D_{max}}$ — ζ_{V1} — Rayleigh like damping — no load distribution — top view D_{dyn} & $|a_{HSLM-A,max}|$

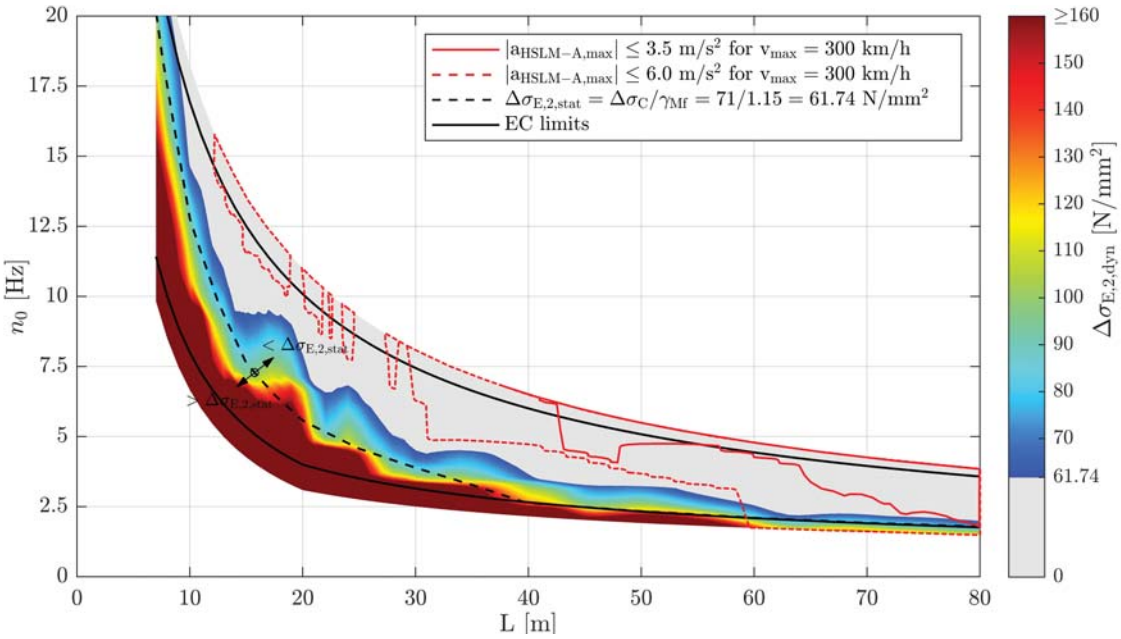

Figure B.23.: Single-span steel bridges — traffic mix TM1** — $v_{D_{max}}$ — ζ_{V1} — Rayleigh like damping — no load distribution — top view $\Delta\sigma_{E,2,dyn}$ & $|a_{HSLM-A,max}|$ & $\Delta\sigma_{E,2,stat}$

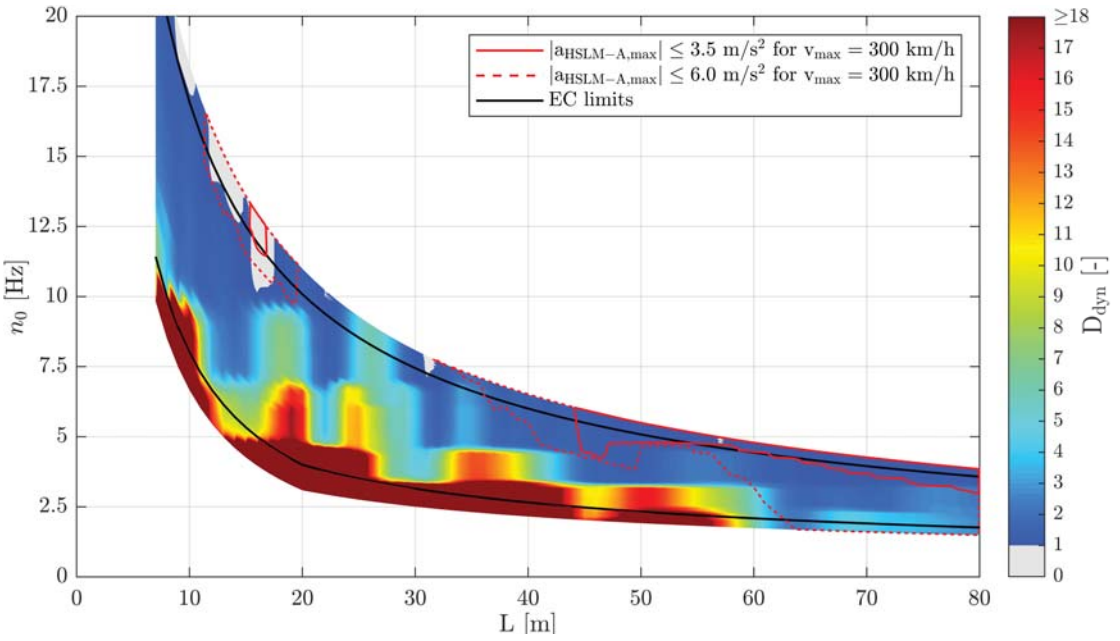

Figure B.24.: Single-span steel bridges — traffic mix TM1** — $v_{D_{max}}$ — ζ_{EC} — Rayleigh like damping — load distribution — top view D_{dyn} & $|a_{HSLM-A,max}|$

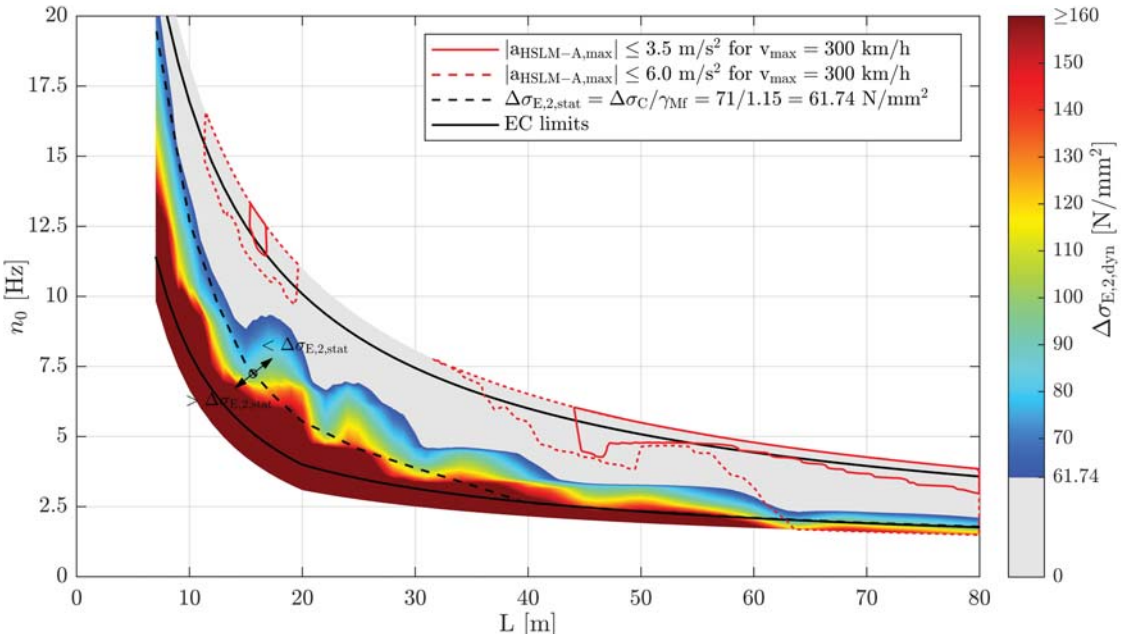

Figure B.25.: Single-span steel bridges — traffic mix TM1** — $v_{D_{max}}$ — ζ_{EC} — Rayleigh like damping — load distribution — top view $\Delta\sigma_{E,2,dyn}$ & $|a_{HSLM-A,max}|$ & $\Delta\sigma_{E,2,stat}$

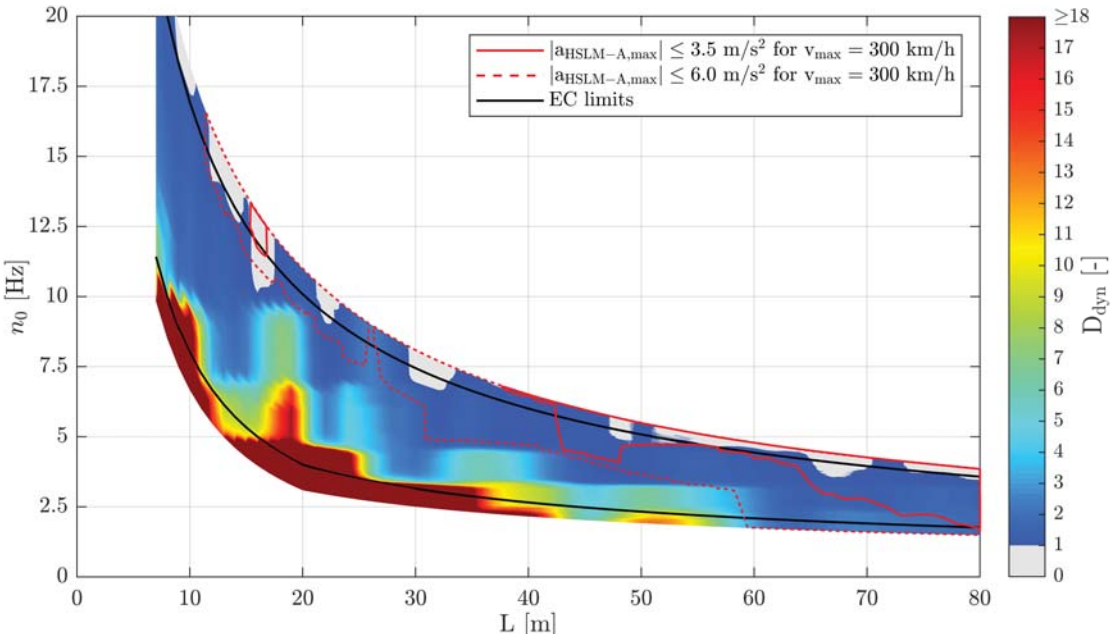

Figure B.26.: Single-span steel bridges — traffic mix TM1** — $v_{D_{max}}$ — ζ_{V1} — Rayleigh like damping — load distribution — top view D_{dyn} & $|a_{HSLM-A,max}|$

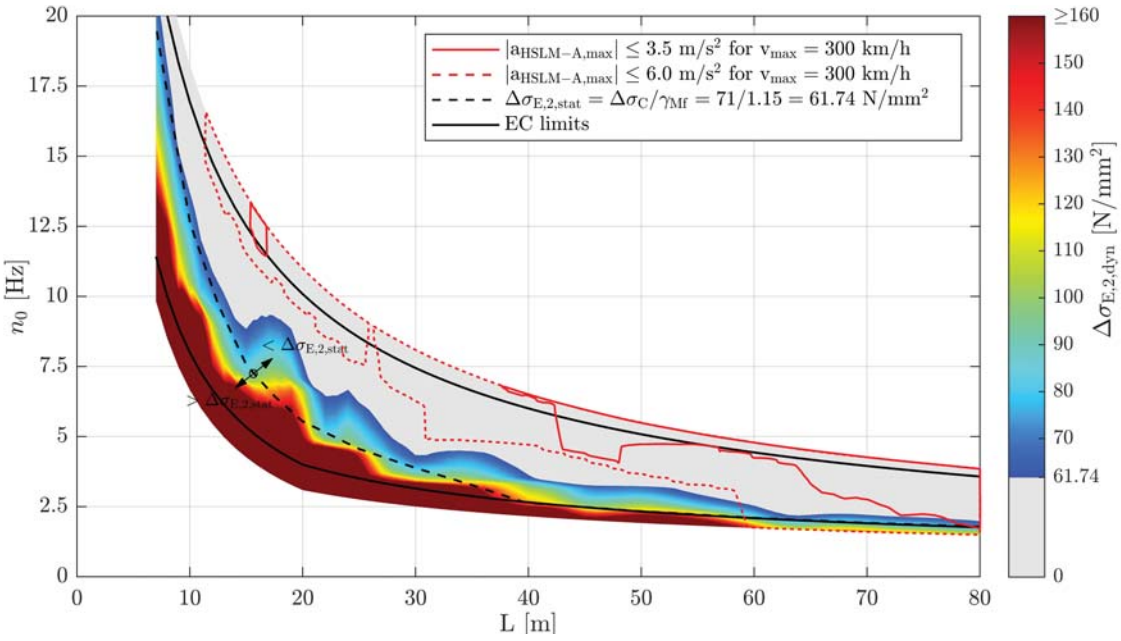

Figure B.27.: Single-span steel bridges — traffic mix TM1** — $v_{D_{max}}$ — ζ_{V1} — Rayleigh like damping — load distribution — top view $\Delta\sigma_{E,2,dyn}$ & $|a_{HSLM-A,max}|$ & $\Delta\sigma_{E,2,stat}$

B.3.3. Train speed $v_{a_{max}}$

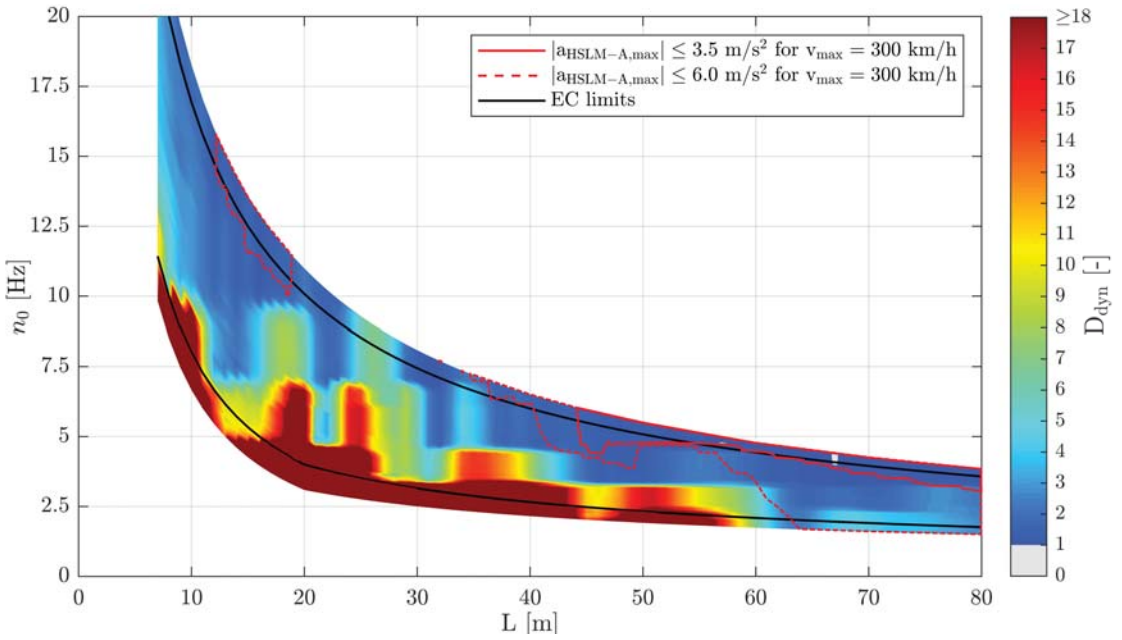

Figure B.28.: Single-span steel bridges — traffic mix TM1*** — $v_{a_{max}}$ — ζ_{EC} — Rayleigh like damping — no load distribution — top view D_{dyn} & $|a_{HSLM-A,max}|$

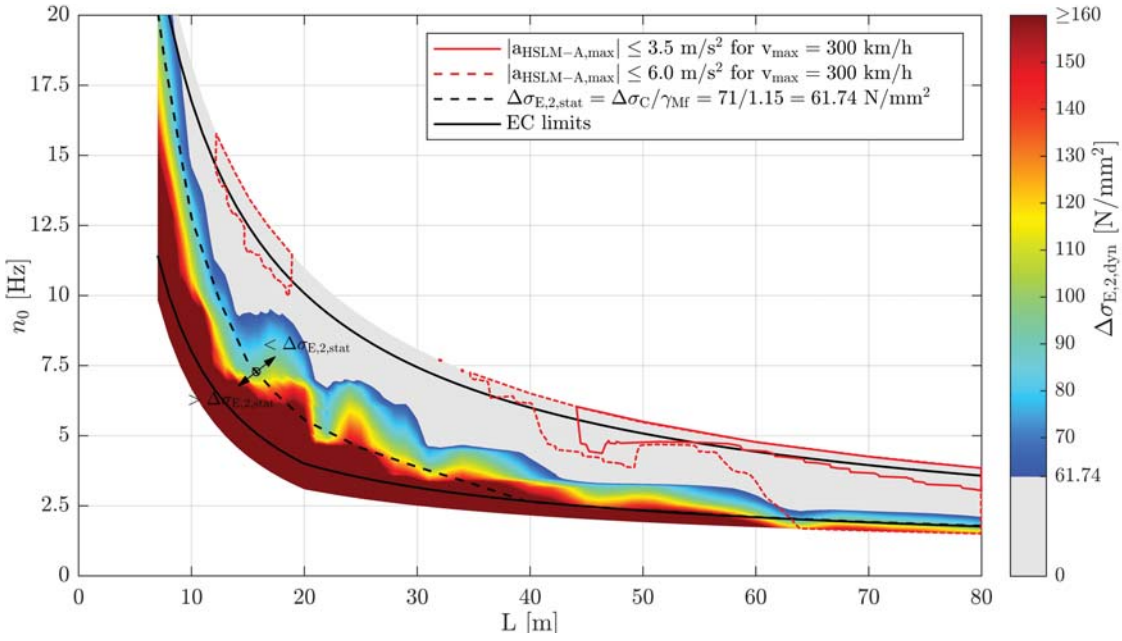

Figure B.29.: Single-span steel bridges — traffic mix TM1*** — $v_{a_{max}}$ — ζ_{EC} — Rayleigh like damping — no load distribution — top view $\Delta\sigma_{E,2,dyn}$ & $|a_{HSLM-A,max}|$ & $\Delta\sigma_{E,2,stat}$

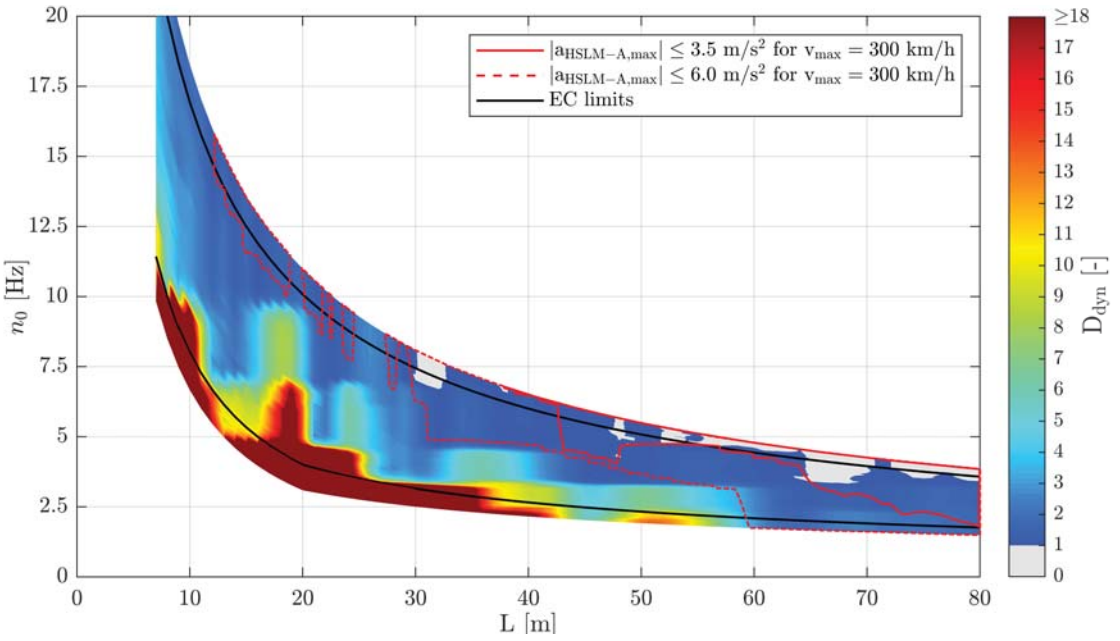

Figure B.30.: Single-span steel bridges — traffic mix TM1*** — $v_{a_{max}}$ — ζ_{V1} — Rayleigh like damping — no load distribution — top view D_{dyn} & $|a_{HSLM-A,max}|$

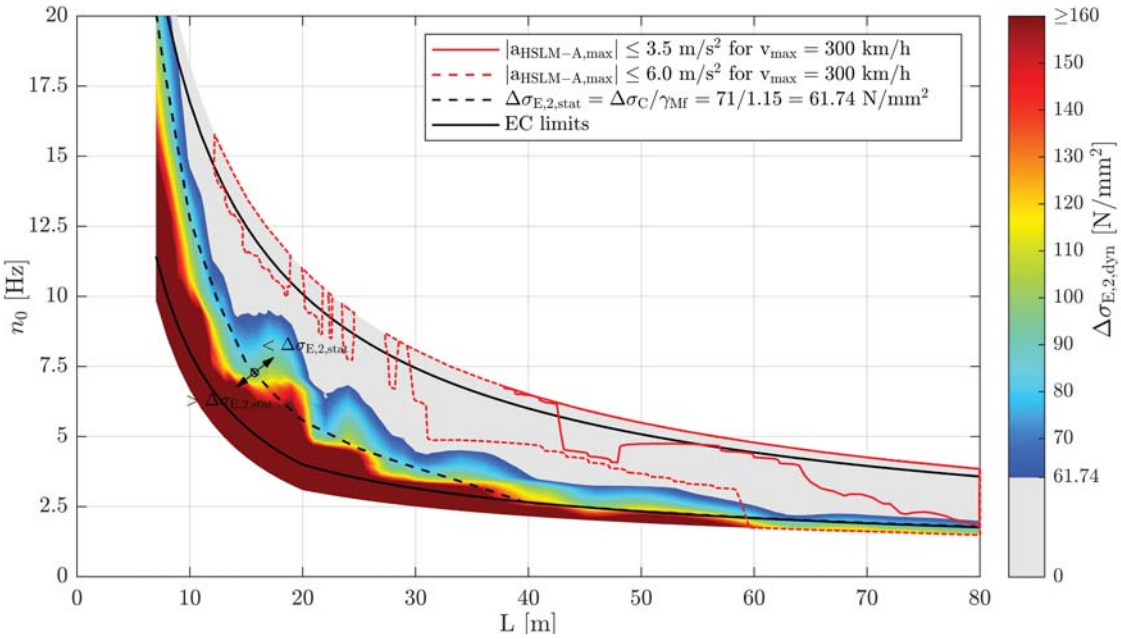

Figure B.31.: Single-span steel bridges — traffic mix TM1*** — $v_{a_{max}}$ — ζ_{V1} — Rayleigh like damping — no load distribution — top view $\Delta\sigma_{E,2,dyn}$ & $|a_{HSLM-A,max}|$ & $\Delta\sigma_{E,2,stat}$

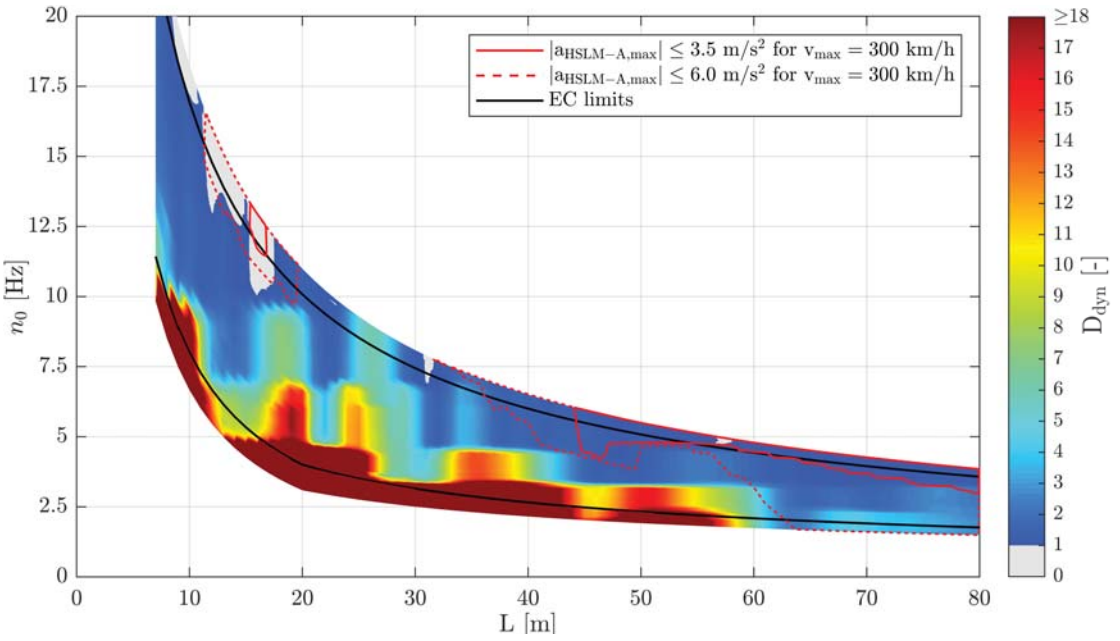

Figure B.32.: Single-span steel bridges — traffic mix TM1*** — $v_{a_{max}}$ — ζ_{EC} — Rayleigh like damping — load distribution — top view D_{dyn} & $|a_{HSLM-A,max}|$

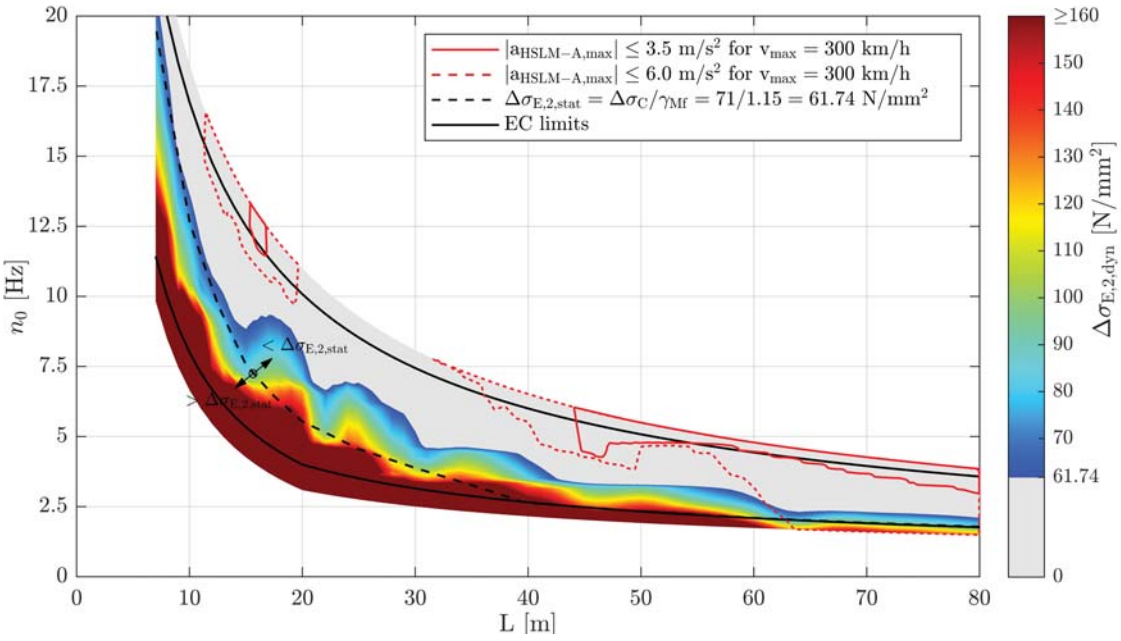

Figure B.33.: Single-span steel bridges — traffic mix TM1*** — $v_{a_{max}}$ — ζ_{EC} — Rayleigh like damping — load distribution — top view $\Delta\sigma_{E,2,dyn}$ & $|a_{HSLM-A,max}|$ & $\Delta\sigma_{E,2,stat}$

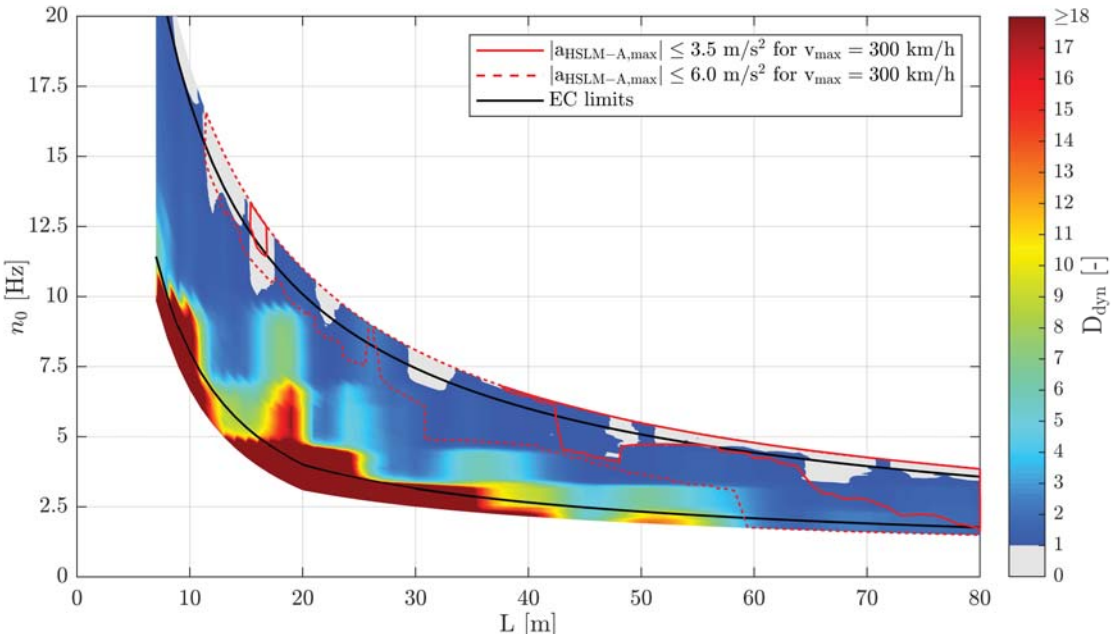

Figure B.34.: Single-span steel bridges — traffic mix TM1*** — $v_{a_{max}}$ — ζ_{V1} — Rayleigh like damping — load distribution — top view D_{dyn} & $|a_{HSLM-A,max}|$

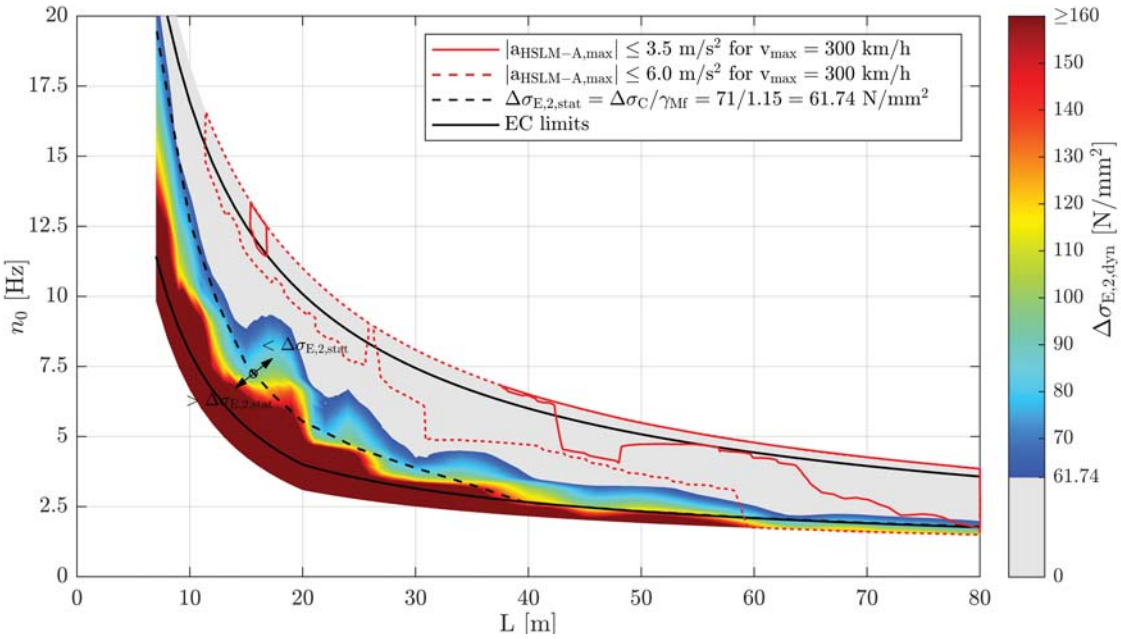

Figure B.35.: Single-span steel bridges — traffic mix TM1*** — $v_{a_{max}}$ — ζ_{V1} — Rayleigh like damping — load distribution — top view $\Delta\sigma_{E,2,dyn}$ & $|a_{HSLM-A,max}|$ & $\Delta\sigma_{E,2,stat}$

B.4. Results of single-span steel bridges due to TM2

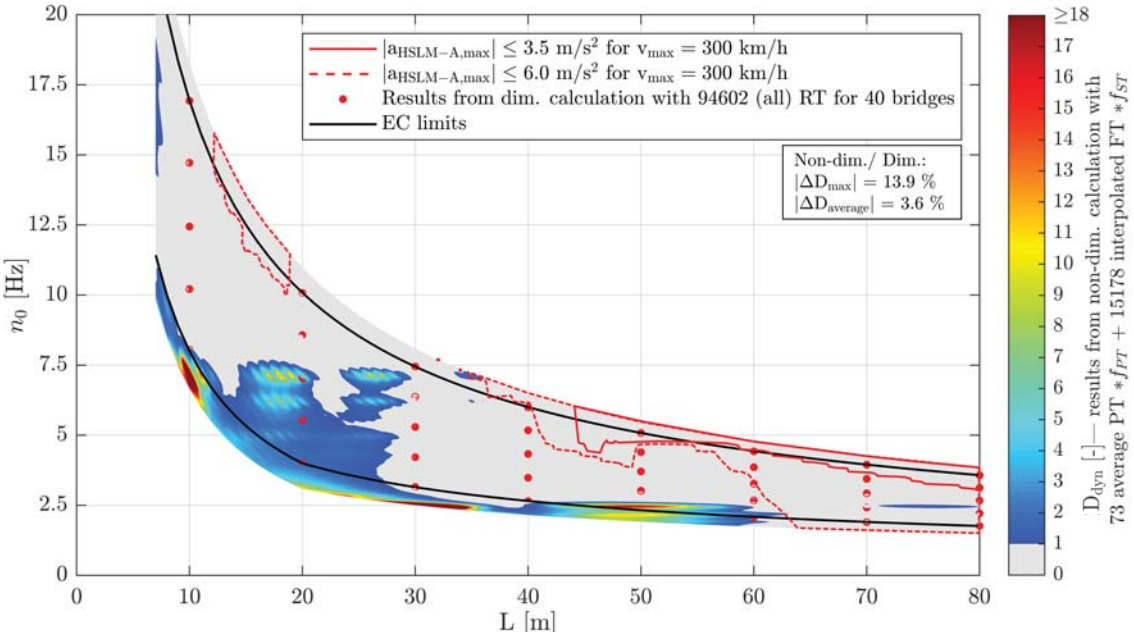

Figure B.36.: Single-span steel bridges — traffic mix TM2-st — ζ_{EC} — Rayleigh like damping — no load distribution — top view D_{dyn} & $|a_{HSLM-A,max}|$

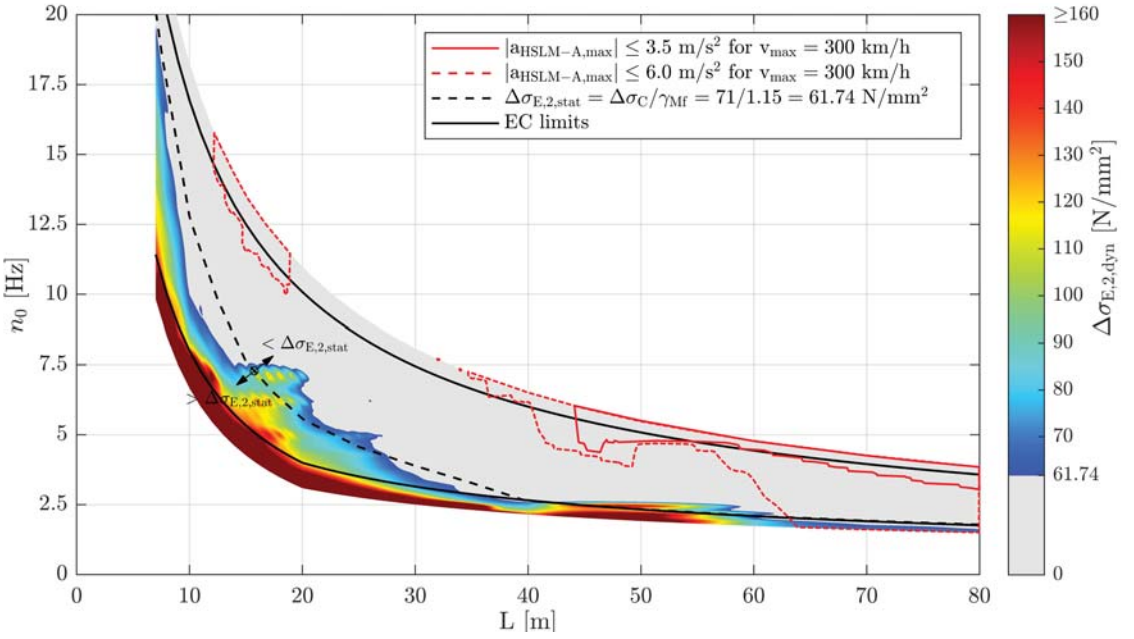

Figure B.37.: Single-span steel bridges — traffic mix TM2-st — ζ_{EC} — Rayleigh like damping — no load distribution — top view $\Delta\sigma_{E,2,dyn}$ & $|a_{HSLM-A,max}|$ & $\Delta\sigma_{E,2,stat}$

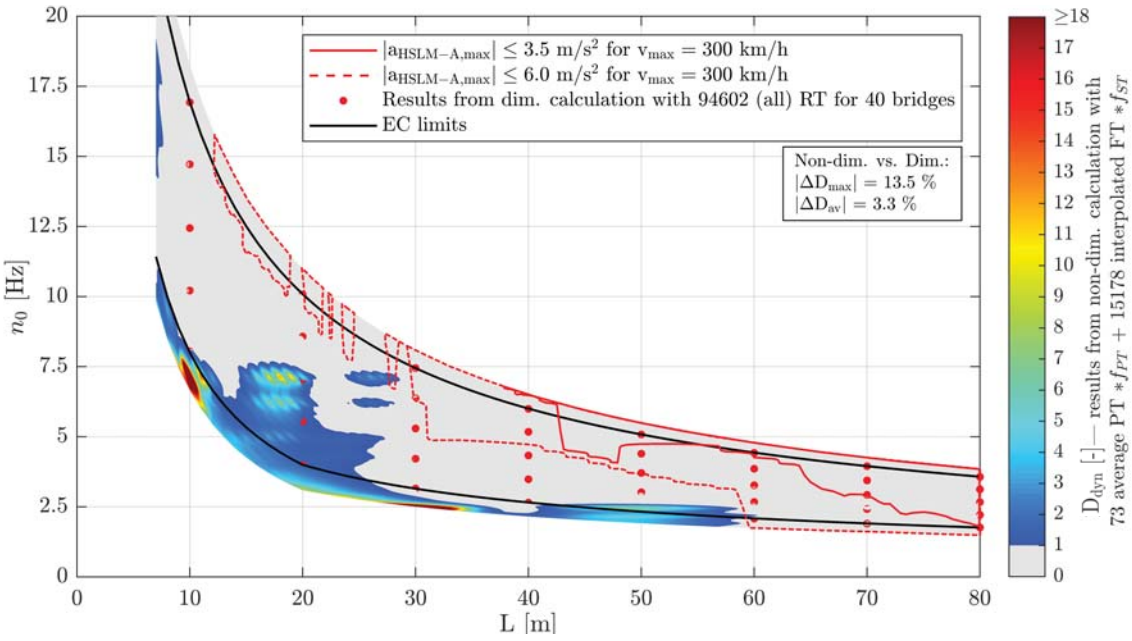

Figure B.38.: Single-span steel bridges — traffic mix TM2-st — ζ_{V1} — Rayleigh like damping — no load distribution — top view D_{dyn} & $|a_{HSLM-A,max}|$

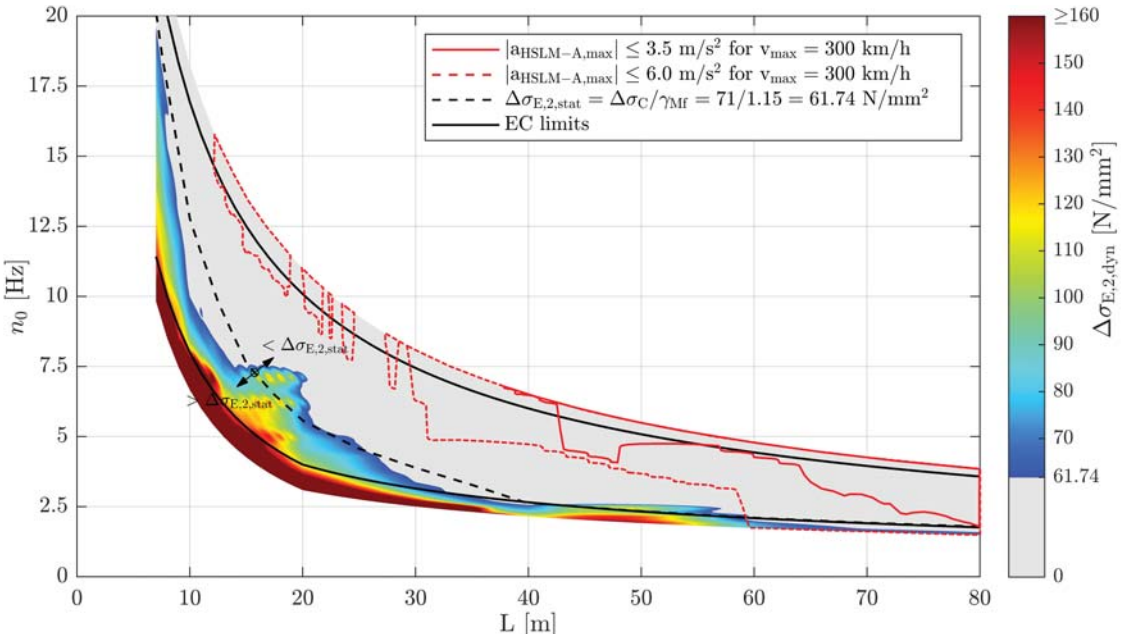

Figure B.39.: Single-span steel bridges — traffic mix TM2-st — ζ_{V1} — Rayleigh like damping — no load distribution — top view $\Delta\sigma_{E,2,dyn}$ & $|a_{HSLM-A,max}|$ & $\Delta\sigma_{E,2,stat}$

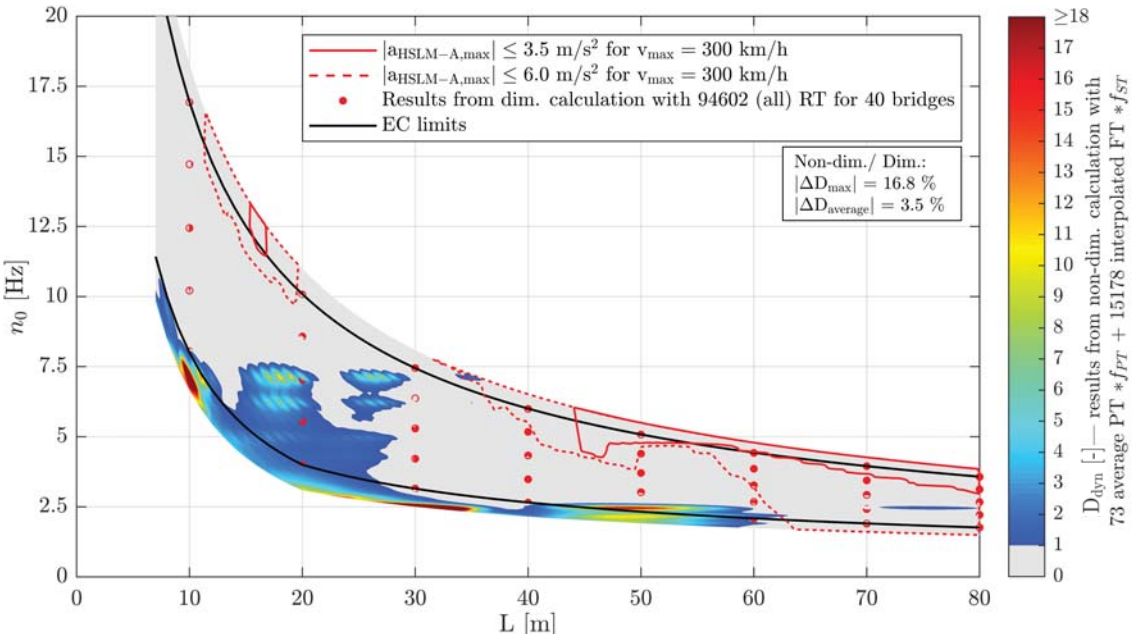

Figure B.40.: Single-span steel bridges — traffic mix TM2-st — ζ_{EC} — Rayleigh like damping — load distribution — top view D_{dyn} & $|a_{HSLM-A,max}|$

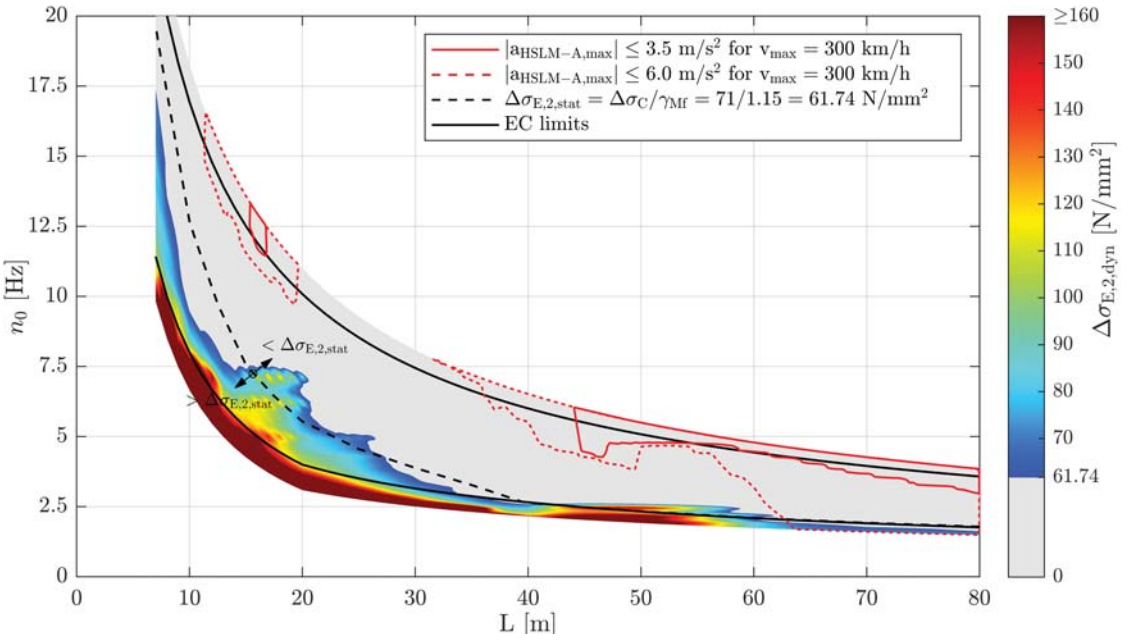

Figure B.41.: Single-span steel bridges — traffic mix TM2-st — ζ_{EC} — Rayleigh like damping — load distribution — top view $\Delta\sigma_{E,2,dyn}$ & $|a_{HSLM-A,max}|$ & $\Delta\sigma_{E,2,stat}$

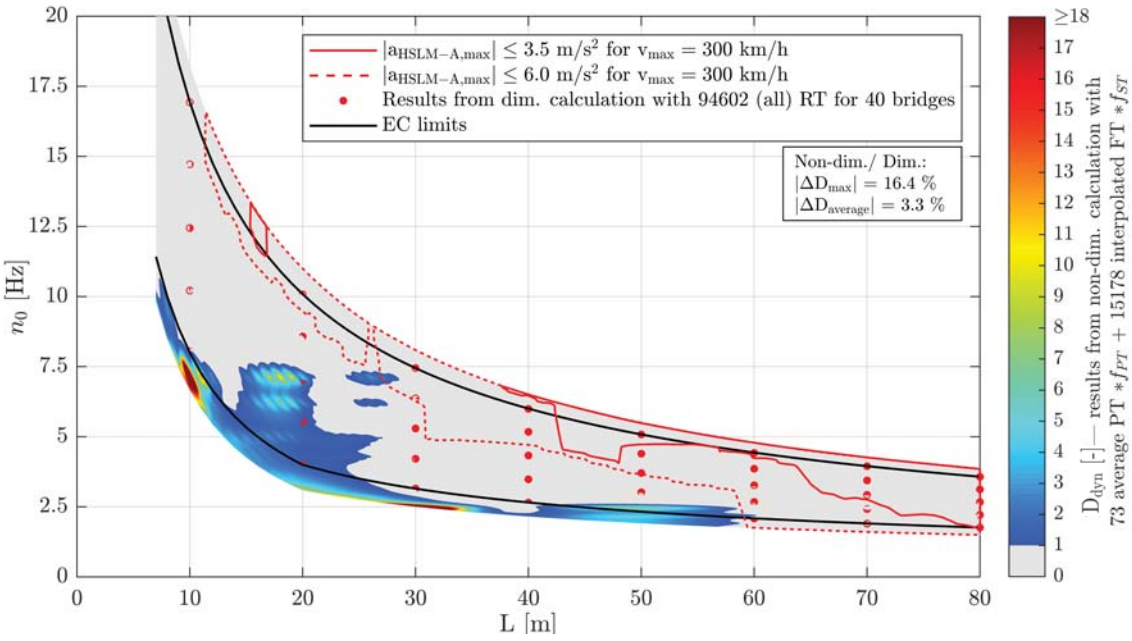

Figure B.42.: Single-span steel bridges — traffic mix TM2-st — ζ_{V1} — Rayleigh like damping — load distribution — top view D_{dyn} & $|a_{HSLM-A,max}|$

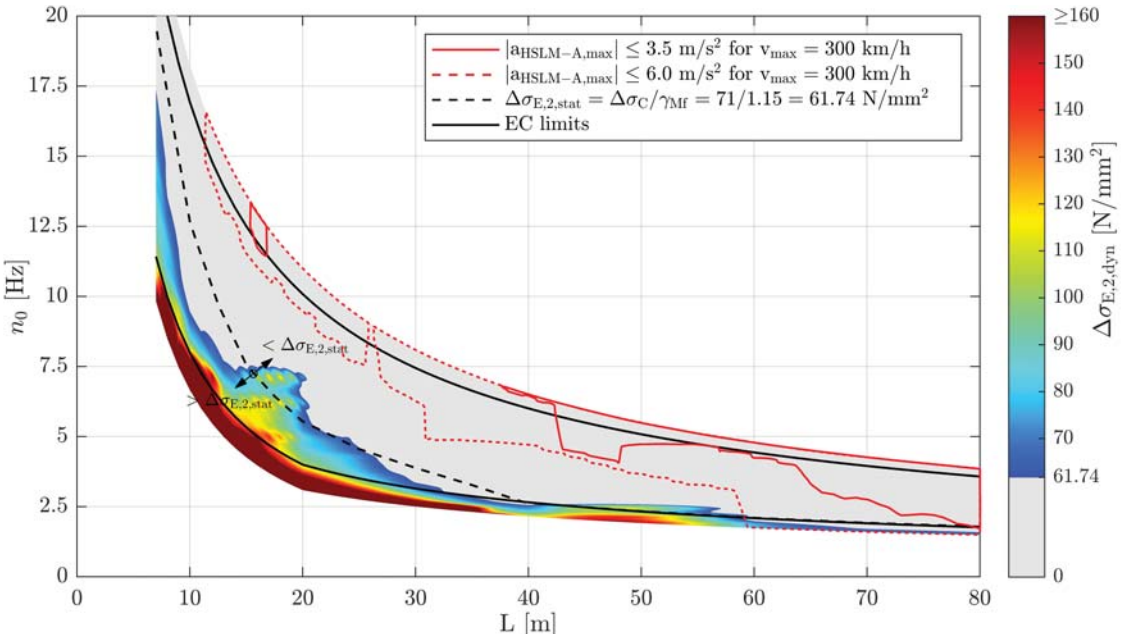

Figure B.43.: Single-span steel bridges — traffic mix TM2-st — ζ_{V1} — Rayleigh like damping — load distribution — top view $\Delta\sigma_{E,2,dyn}$ & $|a_{HSLM-A,max}|$ & $\Delta\sigma_{E,2,stat}$

B.5. Results of single-span steel bridges due to TM3

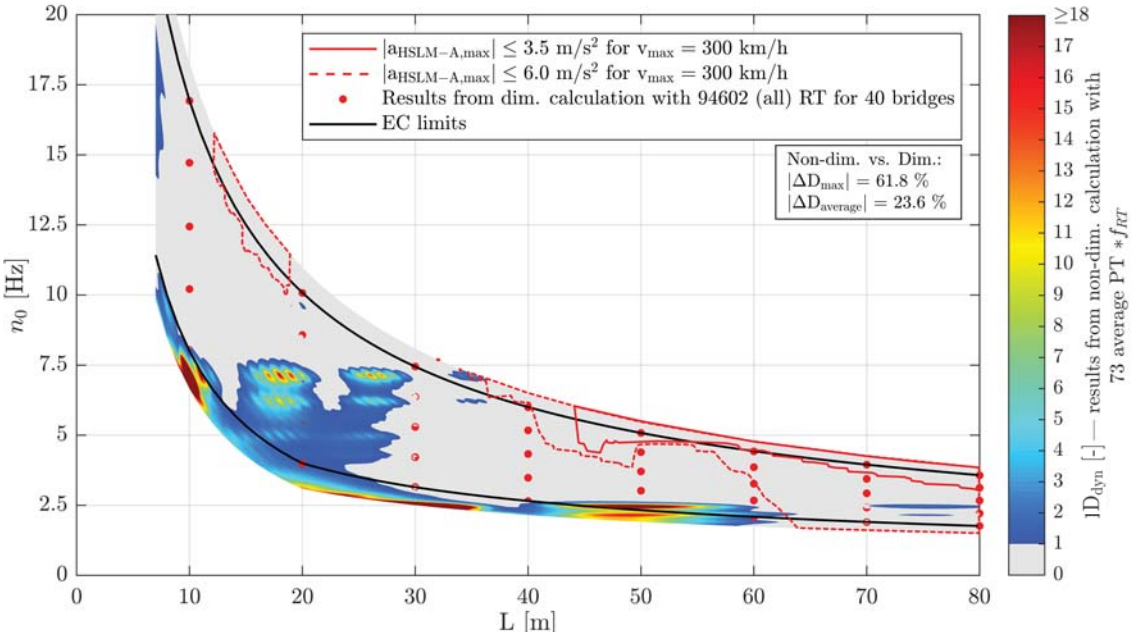

Figure B.44.: Single-span steel bridges — traffic mix TM3-st — ζ_{EC} — Rayleigh like damping — no load distribution — top view D_{dyn} & $|a_{HSLM-A,max}|$

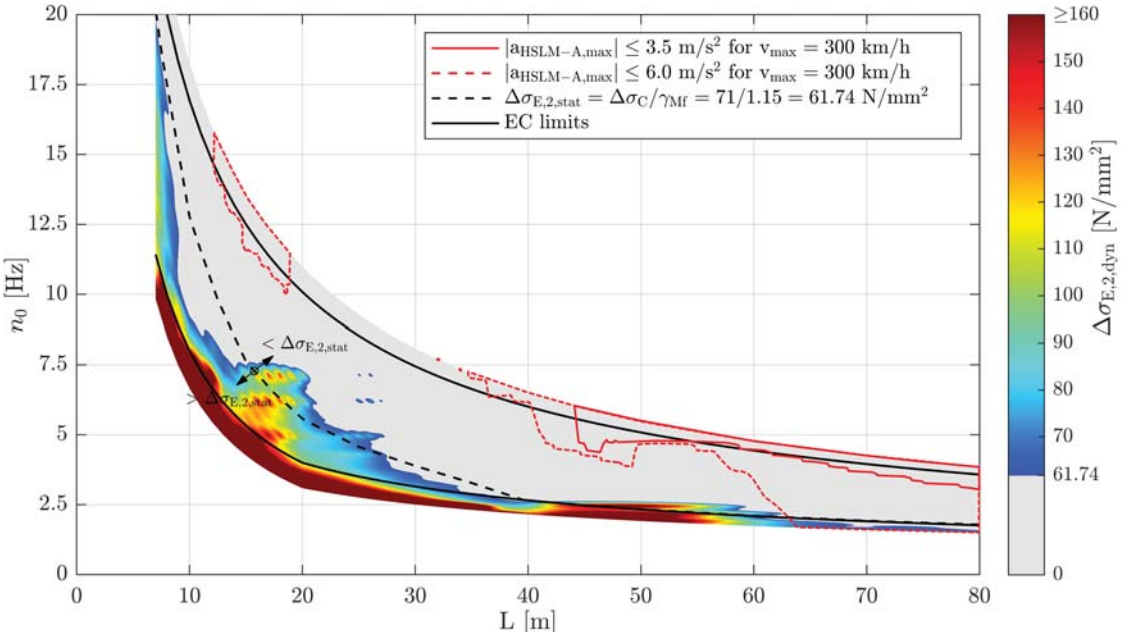

Figure B.45.: Single-span steel bridges — traffic mix TM3-st — ζ_{EC} — Rayleigh like damping — no load distribution — top view $\Delta\sigma_{E,2,dyn}$ & $|a_{HSLM-A,max}|$ & $\Delta\sigma_{E,2,stat}$

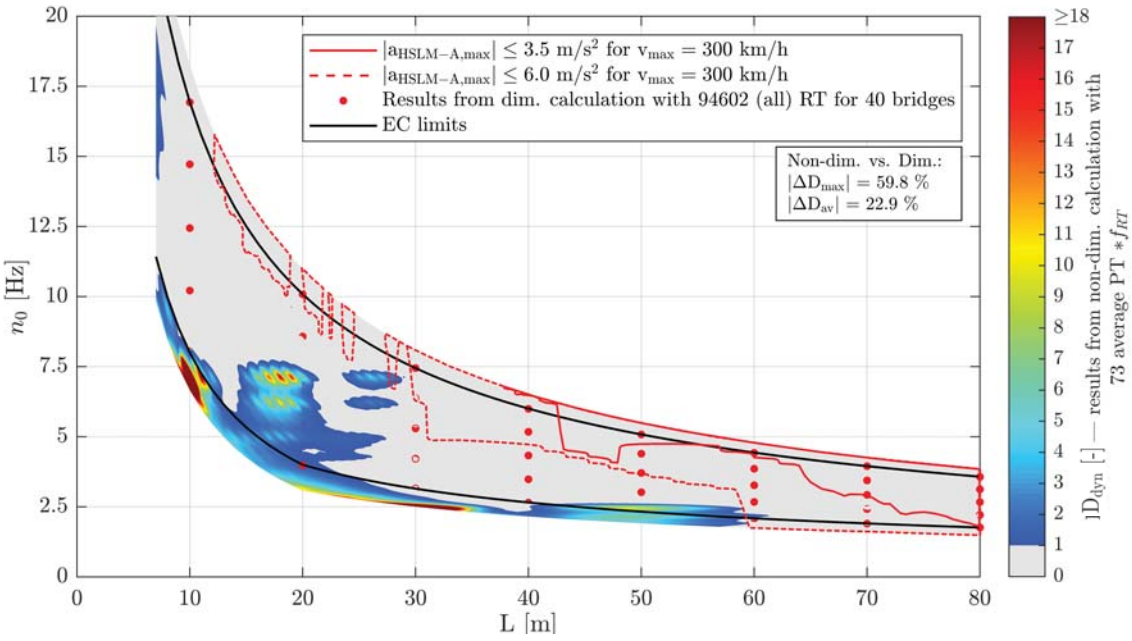

Figure B.46.: Single-span steel bridges — traffic mix TM3-st — ζ_{V1} — Rayleigh like damping — no load distribution — top view D_{dyn} & $|a_{HSLM-A,max}|$

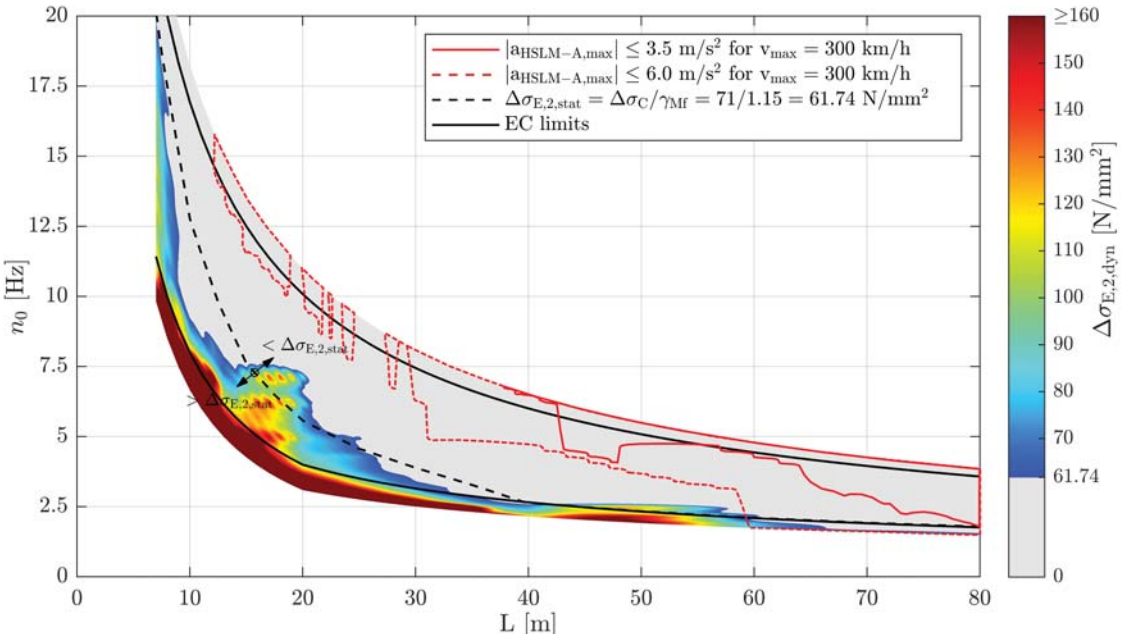

Figure B.47.: Single-span steel bridges — traffic mix TM3-st — ζ_{V1} — Rayleigh like damping — no load distribution — top view $\Delta\sigma_{E,2,dyn}$ & $|a_{HSLM-A,max}|$ & $\Delta\sigma_{E,2,stat}$

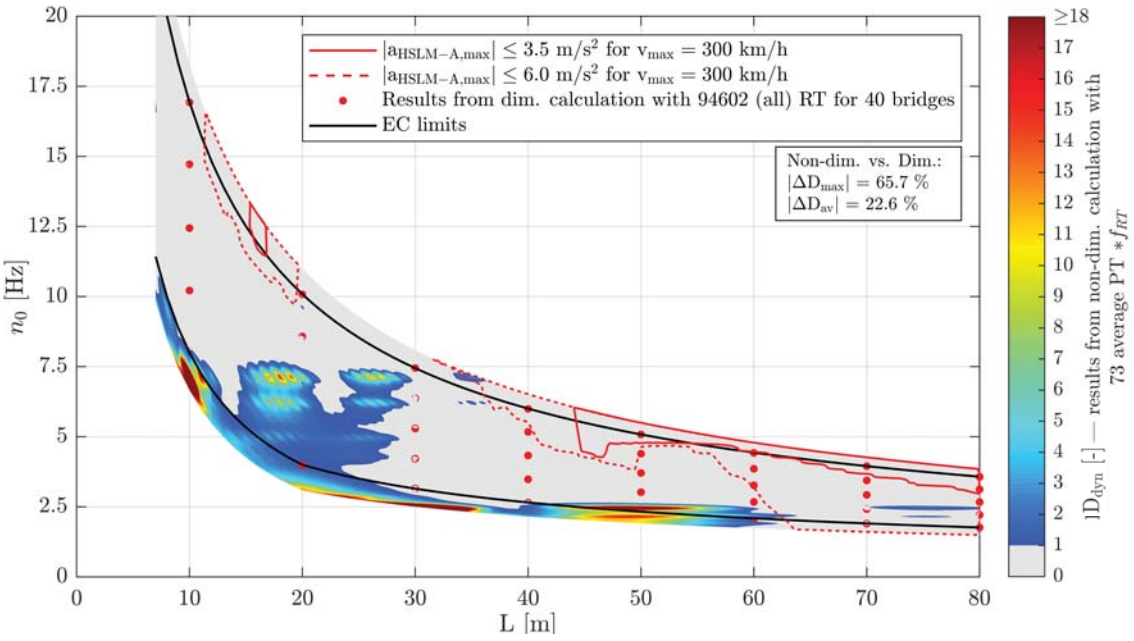

Figure B.48.: Single-span steel bridges — traffic mix TM3-st — ζ_{EC} — Rayleigh like damping — load distribution — top view D_{dyn} & $|a_{HSLM-A,max}|$

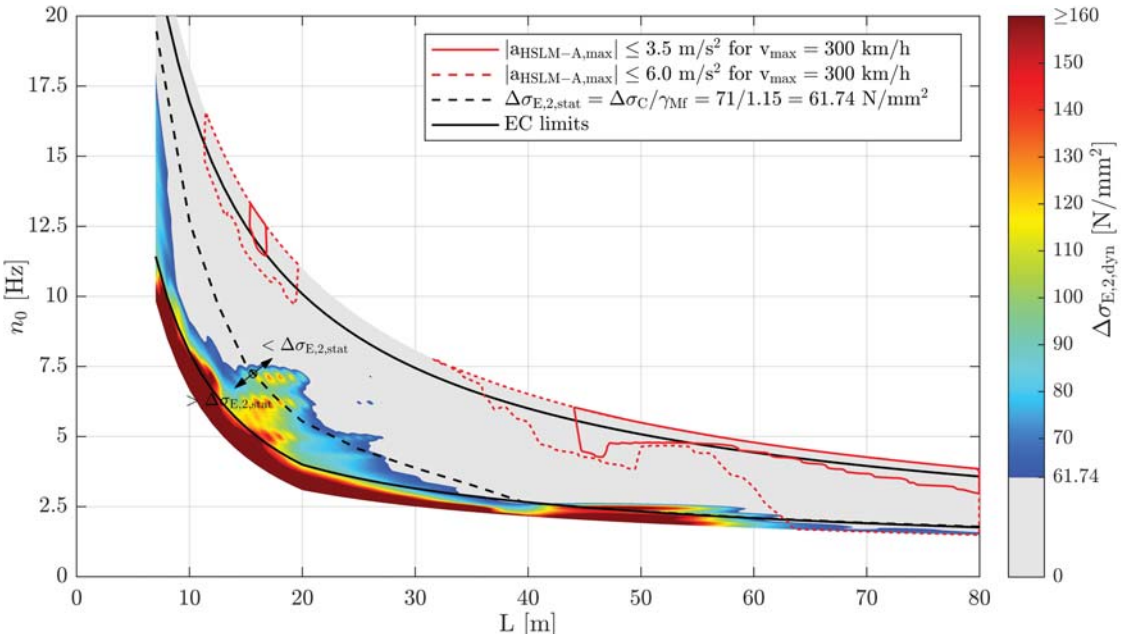

Figure B.49.: Single-span steel bridges — traffic mix TM3-st — ζ_{EC} — Rayleigh like damping — load distribution — top view $\Delta\sigma_{E,2,dyn}$ & $|a_{HSLM-A,max}|$ & $\Delta\sigma_{E,2,stat}$

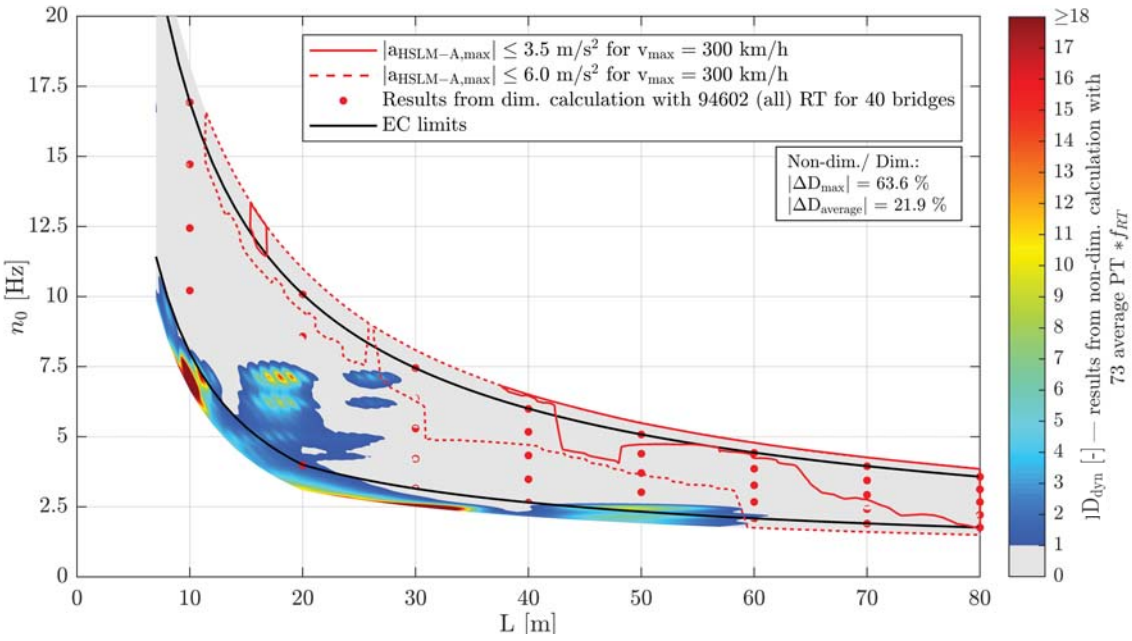

Figure B.50.: Single-span steel bridges — traffic mix TM3-st — ζ_{V1} — Rayleigh like damping — load distribution — top view D_{dyn} & $|a_{HSLM-A,max}|$

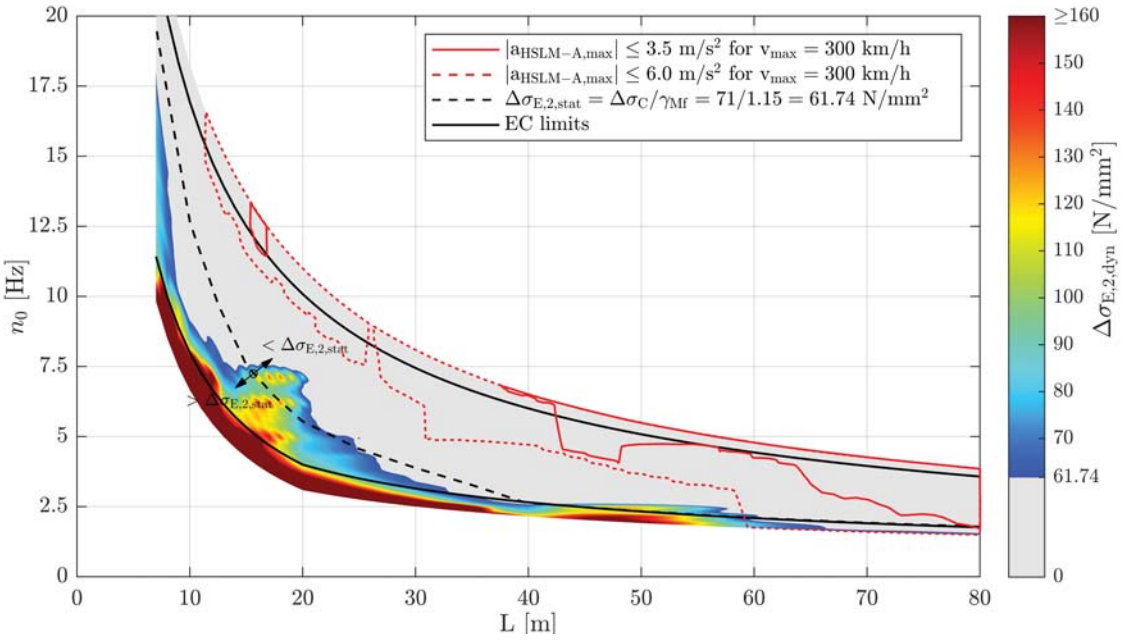

Figure B.51.: Single-span steel bridges — traffic mix TM3-st — ζ_{V1} — Rayleigh like damping — load distribution — top view $\Delta\sigma_{E,2,dyn}$ & $|a_{HSLM-A,max}|$ & $\Delta\sigma_{E,2,stat}$

B.6. Results of single-span steel bridges due to TM4

B.6.1. Train speed v_{Train}

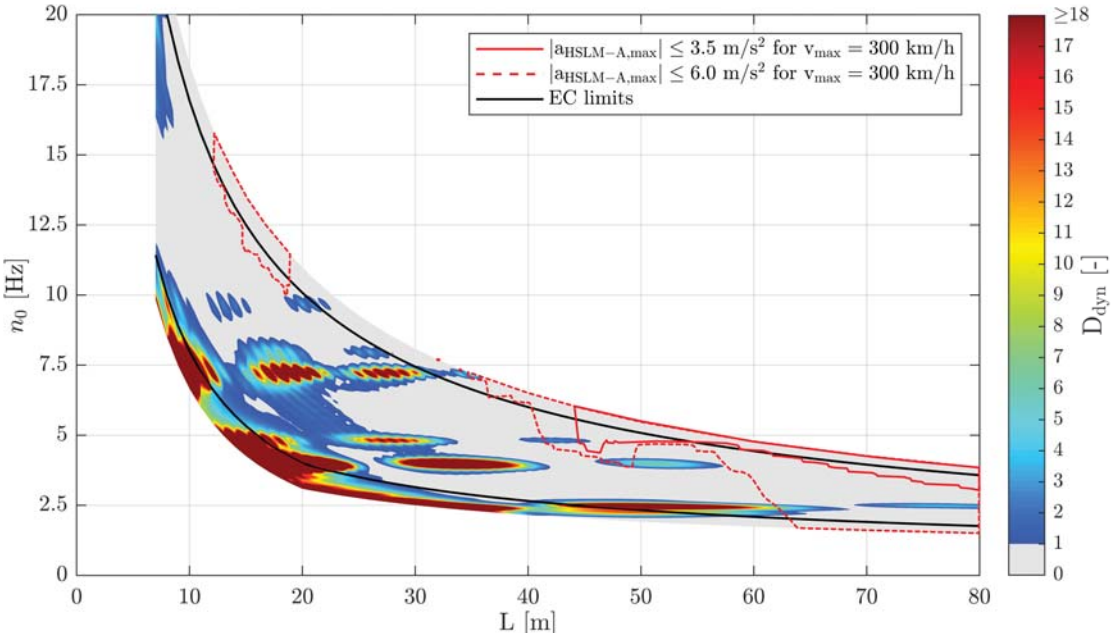

Figure B.52.: Single-span steel bridges — traffic mix TM4* — v_{Train} — ζ_{EC} — Rayleigh like damping — no load distribution — top view D_{dyn} & $|a_{HSLM-A,max}|$

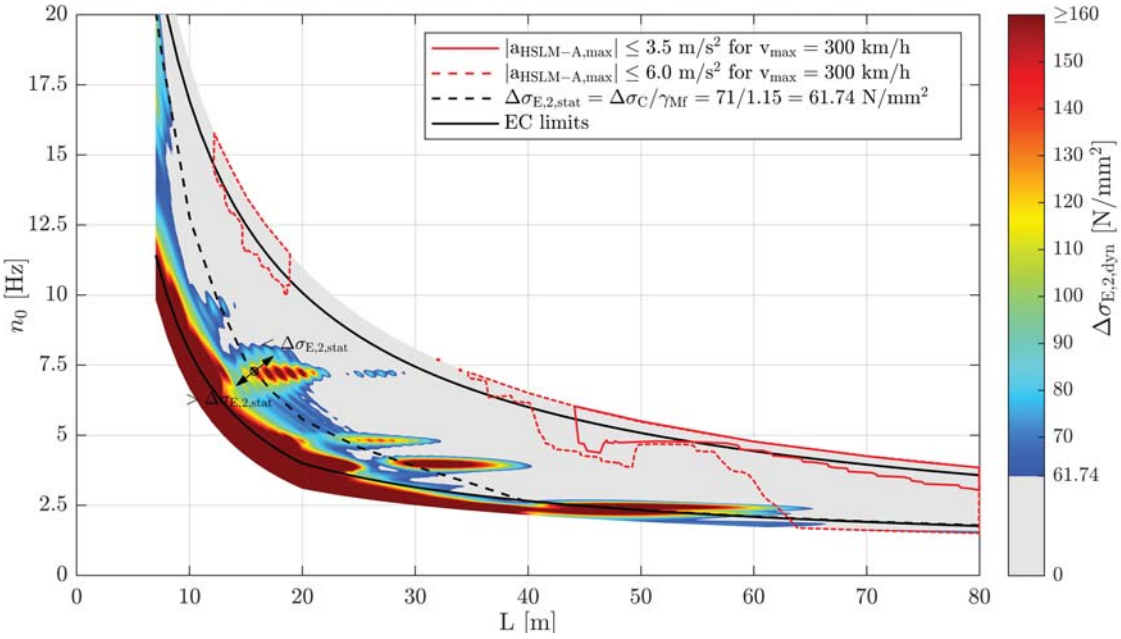

Figure B.53.: Single-span steel bridges — traffic mix TM4* — v_{Train} — ζ_{EC} — Rayleigh like damping — no load distribution — top view $\Delta\sigma_{E,2,dyn}$ & $|a_{HSLM-A,max}|$ & $\Delta\sigma_{E,2,stat}$

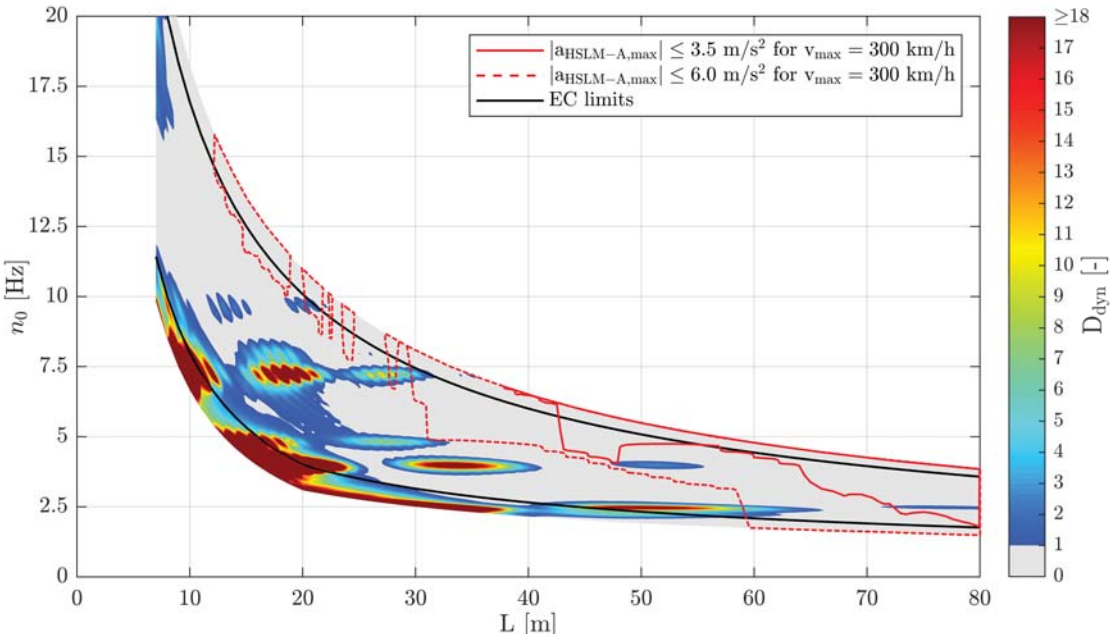

Figure B.54.: Single-span steel bridges — traffic mix TM4* — v_{Train} — ζ_{V1} — Rayleigh like damping — no load distribution — top view D_{dyn} & $|a_{HSLM-A,max}|$

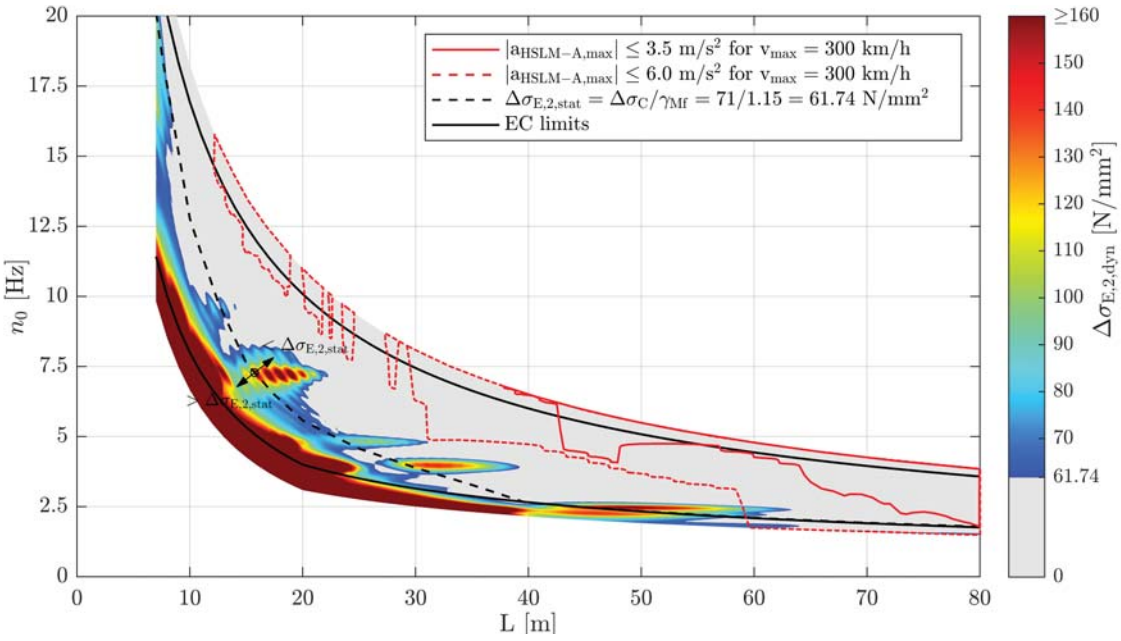

Figure B.55.: Single-span steel bridges — traffic mix TM4* — v_{Train} — ζ_{V1} — Rayleigh like damping — no load distribution — top view $\Delta\sigma_{E,2,dyn}$ & $|a_{HSLM-A,max}|$ & $\Delta\sigma_{E,2,stat}$

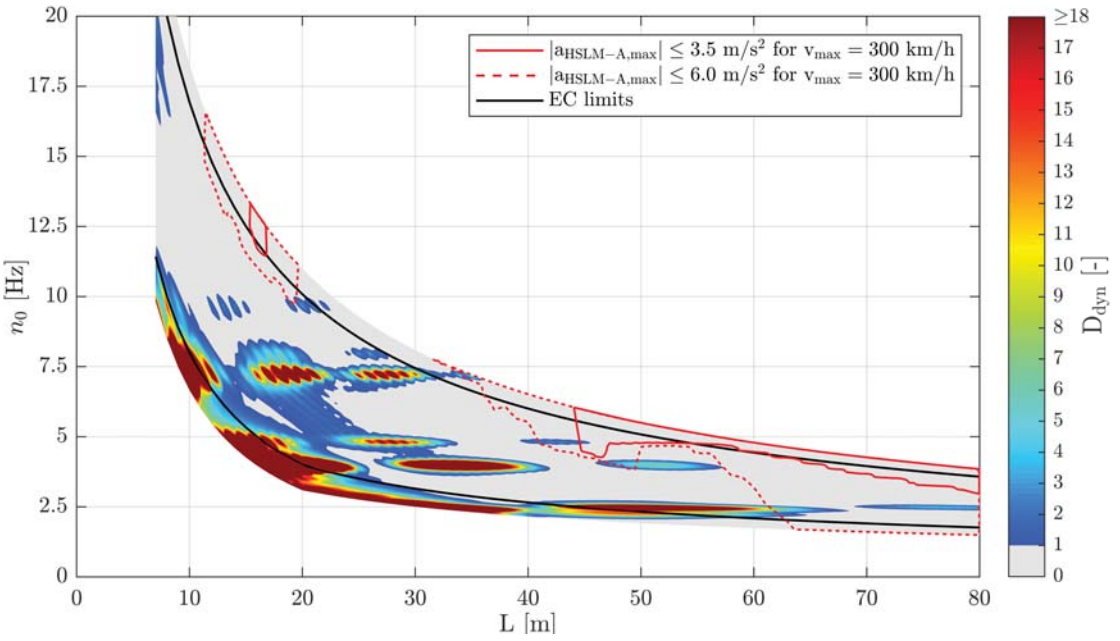

Figure B.56.: Single-span steel bridges — traffic mix TM4* — v_{Train} — ζ_{EC} — Rayleigh like damping — load distribution — top view D_{dyn} & $|a_{HSLM-A,max}|$

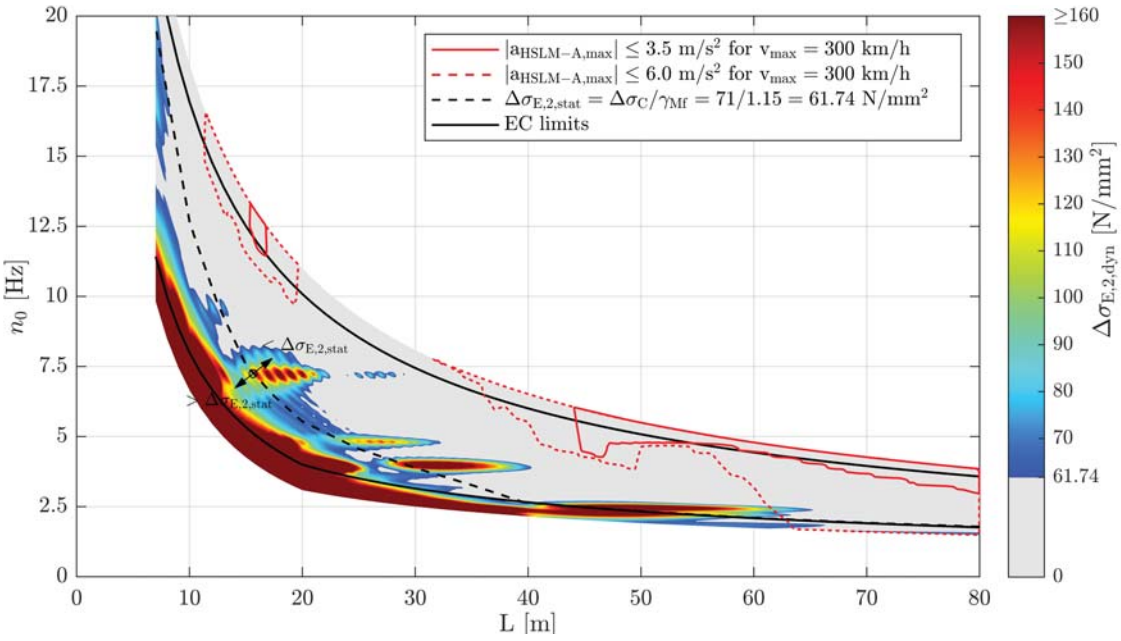

Figure B.57.: Single-span steel bridges — traffic mix TM4* — v_{Train} — ζ_{EC} — Rayleigh like damping — load distribution — top view $\Delta\sigma_{E,2,dyn}$ & $|a_{HSLM-A,max}|$ & $\Delta\sigma_{E,2,stat}$

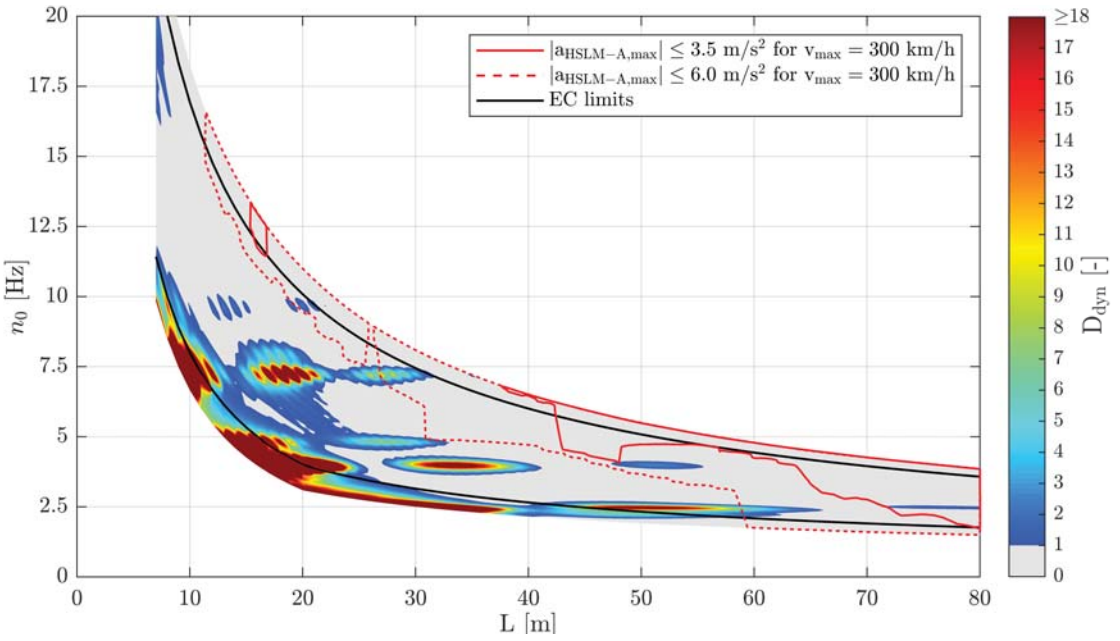

Figure B.58.: Single-span steel bridges — traffic mix TM4* — v_{Train} — ζ_{V1} — Rayleigh like damping — load distribution — top view D_{dyn} & $|a_{HSLM-A,max}|$

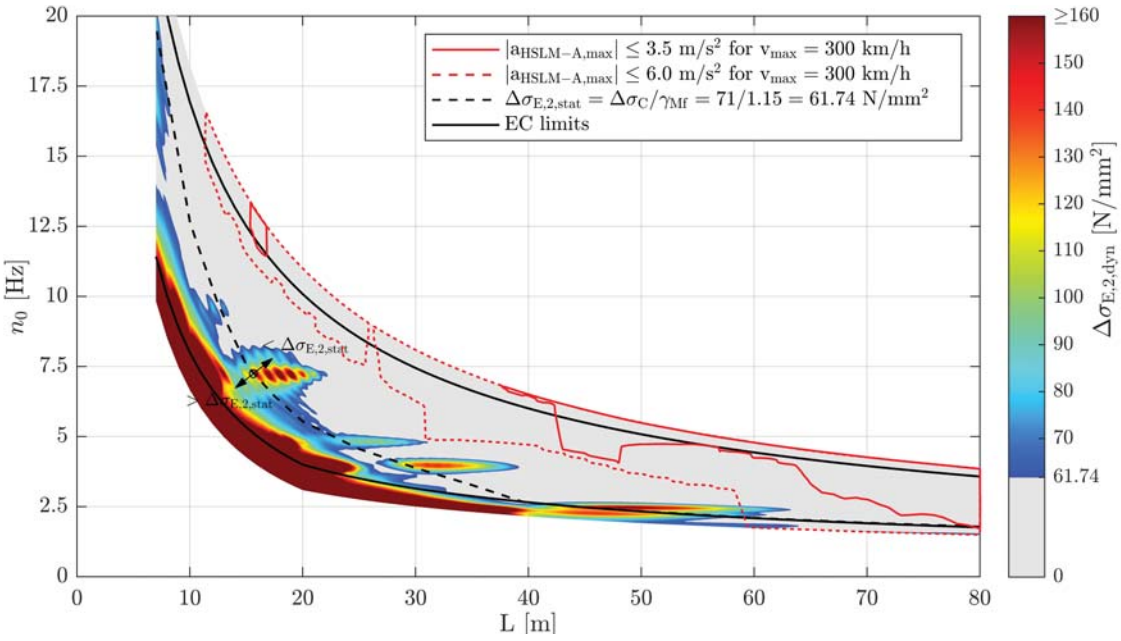

Figure B.59.: Single-span steel bridges — traffic mix TM4* — v_{Train} — ζ_{V1} — Rayleigh like damping — load distribution — top view $\Delta\sigma_{E,2,dyn}$ & $|a_{HSLM-A,max}|$ & $\Delta\sigma_{E,2,stat}$

B.6.2. Train speed $v_{D_{max}}$

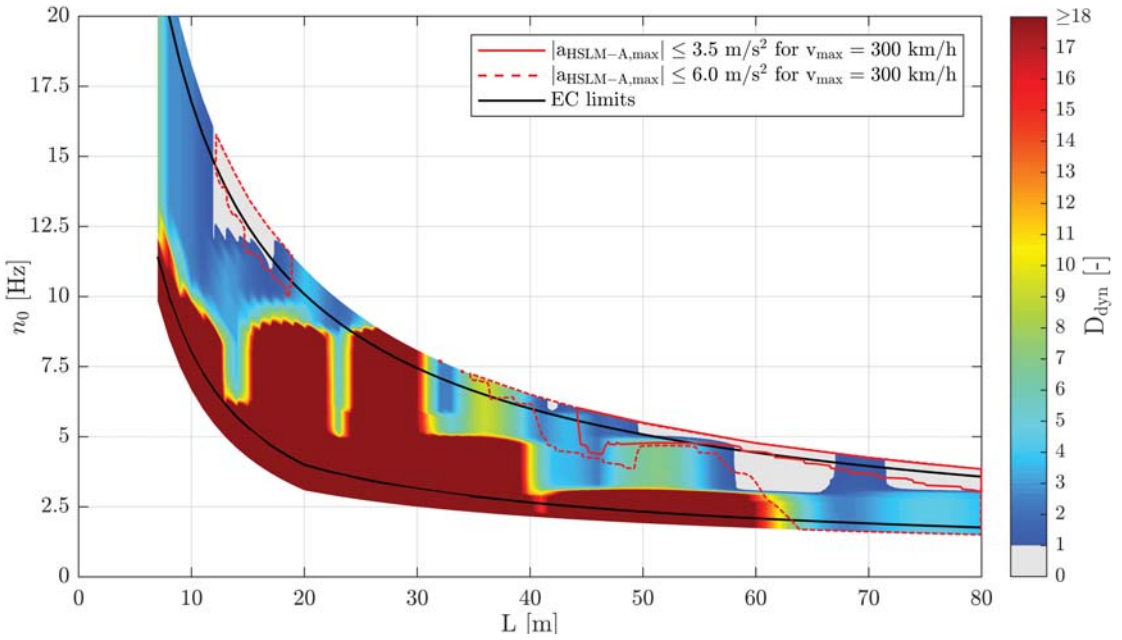

Figure B.60.: Single-span steel bridges — traffic mix TM4** — $v_{D_{max}}$ — ζ_{EC} — Rayleigh like damping — no load distribution — top view D_{dyn} & $|a_{HSLM-A,max}|$

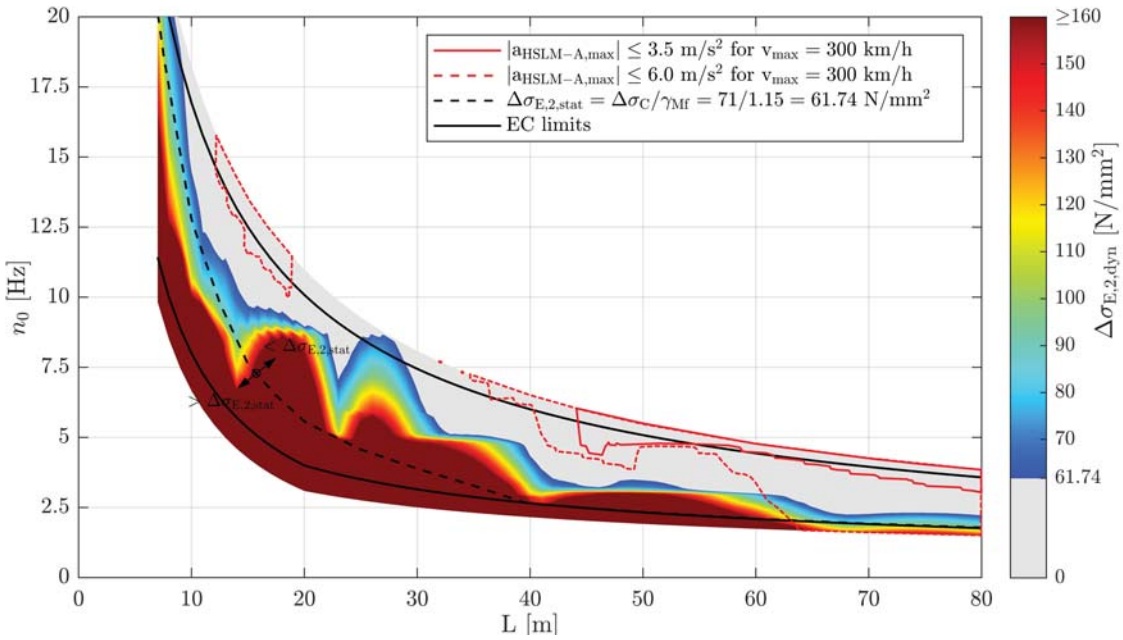

Figure B.61.: Single-span steel bridges — traffic mix TM4** — $v_{D_{max}}$ — ζ_{EC} — Rayleigh like damping — no load distribution — top view $\Delta\sigma_{E,2,dyn}$ & $|a_{HSLM-A,max}|$ & $\Delta\sigma_{E,2,stat}$

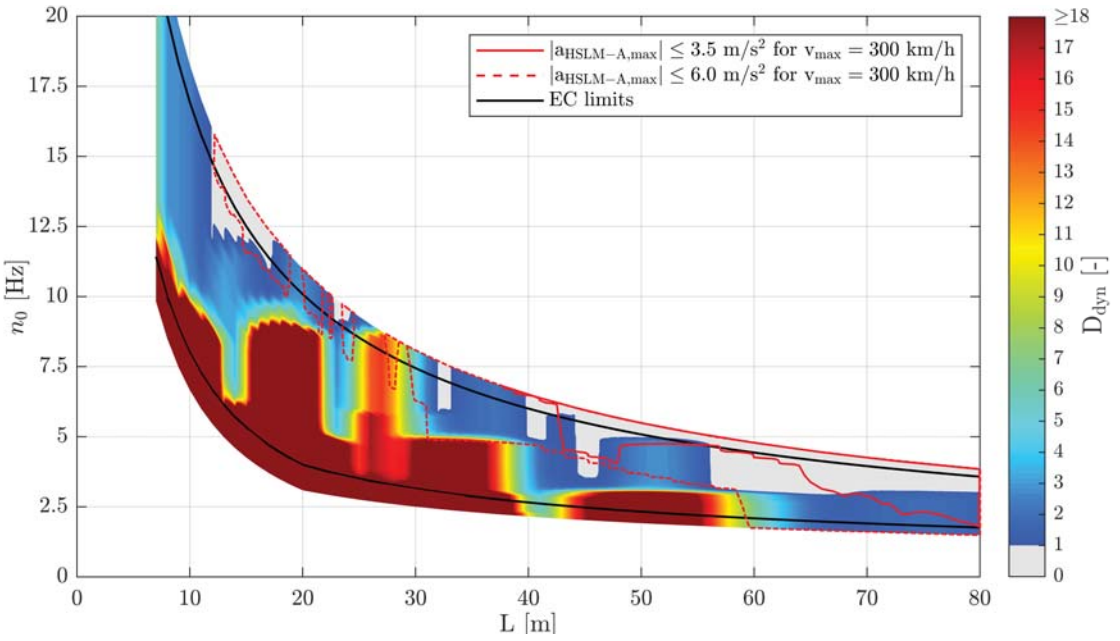

Figure B.62.: Single-span steel bridges — traffic mix TM4** — $v_{D_{max}}$ — ζ_{V1} — Rayleigh like damping — no load distribution — top view D_{dyn} & $|a_{HSLM-A,max}|$

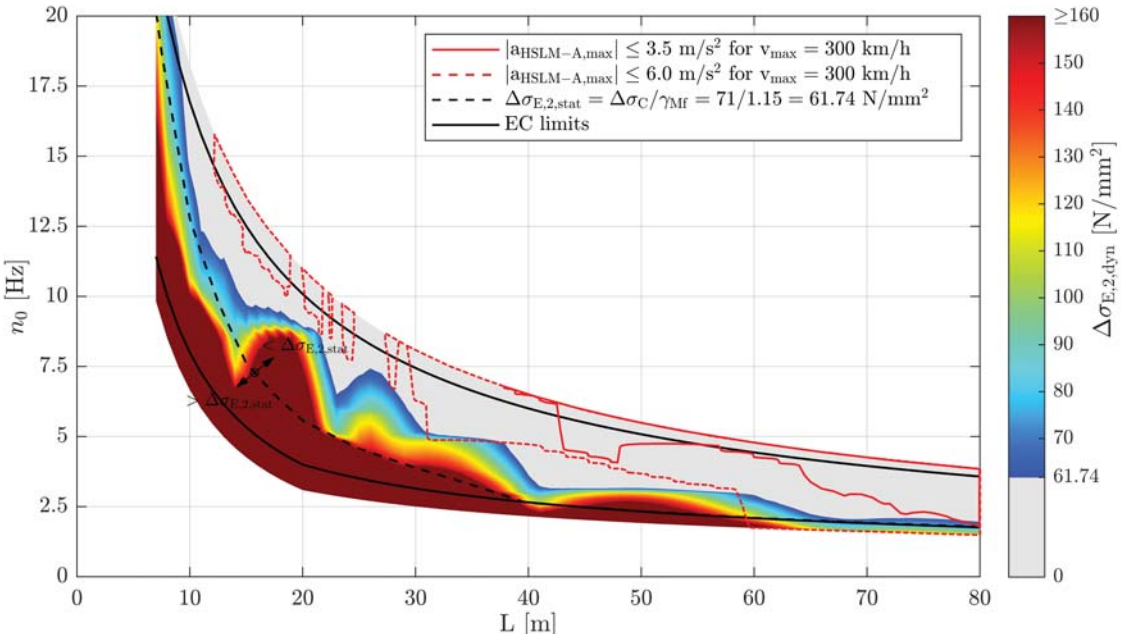

Figure B.63.: Single-span steel bridges — traffic mix TM4** — $v_{D_{max}}$ — ζ_{V1} — Rayleigh like damping — no load distribution — top view $\Delta\sigma_{E,2,dyn}$ & $|a_{HSLM-A,max}|$ & $\Delta\sigma_{E,2,stat}$

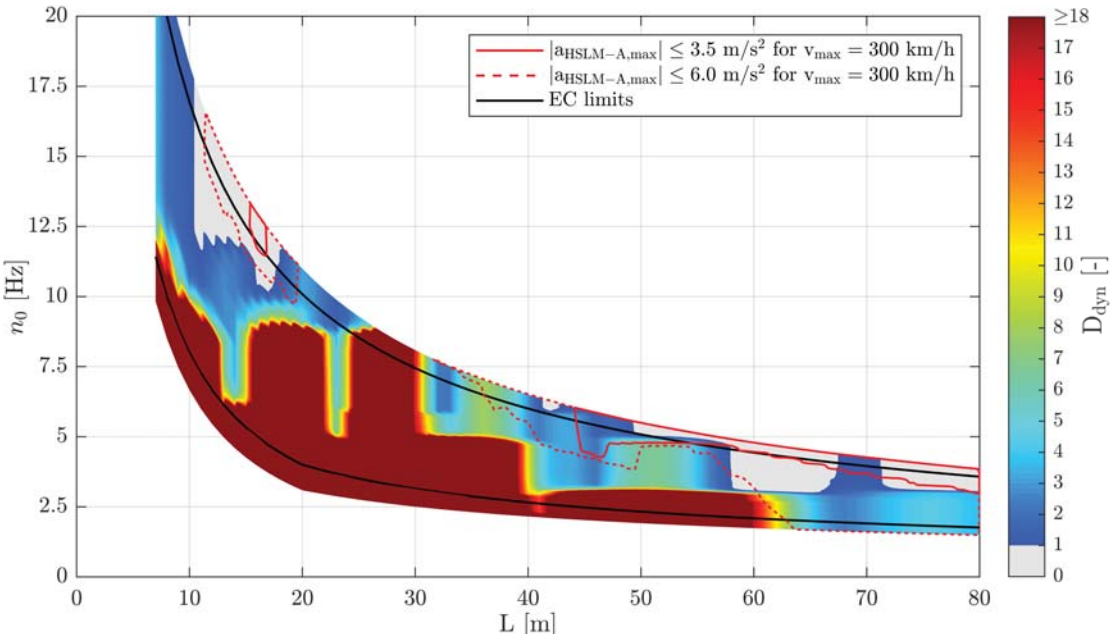

Figure B.64.: Single-span steel bridges — traffic mix TM4** — $v_{D_{max}}$ — ζ_{EC} — Rayleigh like damping — load distribution — top view D_{dyn} & $|a_{HSLM-A,max}|$

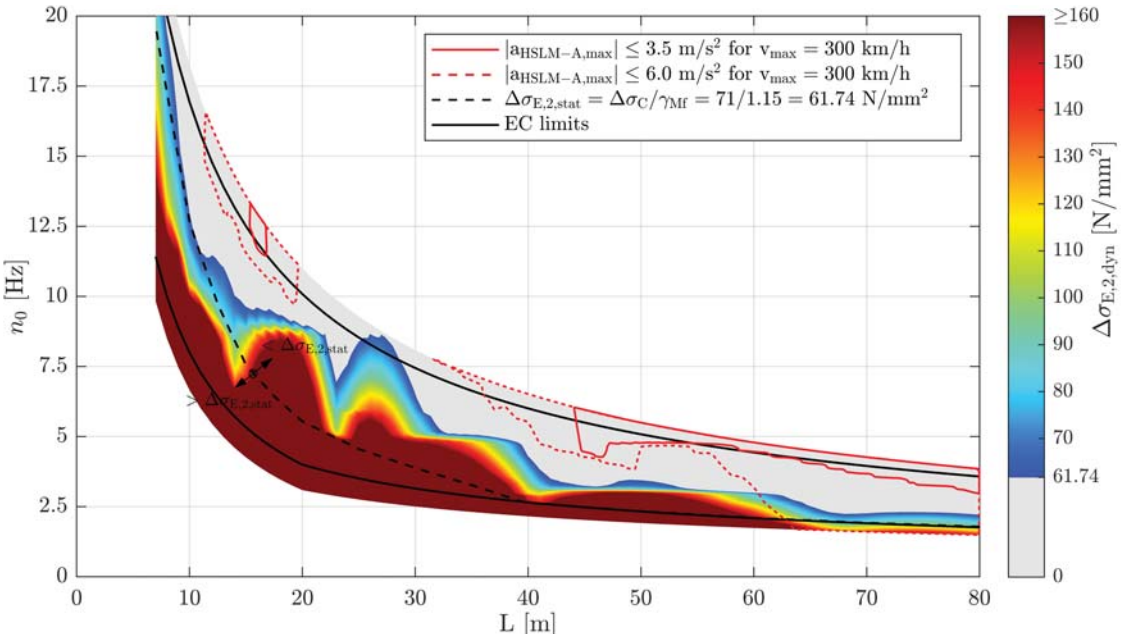

Figure B.65.: Single-span steel bridges — traffic mix TM4** — $v_{D_{max}}$ — ζ_{EC} — Rayleigh like damping — load distribution — top view $\Delta\sigma_{E,2,dyn}$ & $|a_{HSLM-A,max}|$ & $\Delta\sigma_{E,2,stat}$

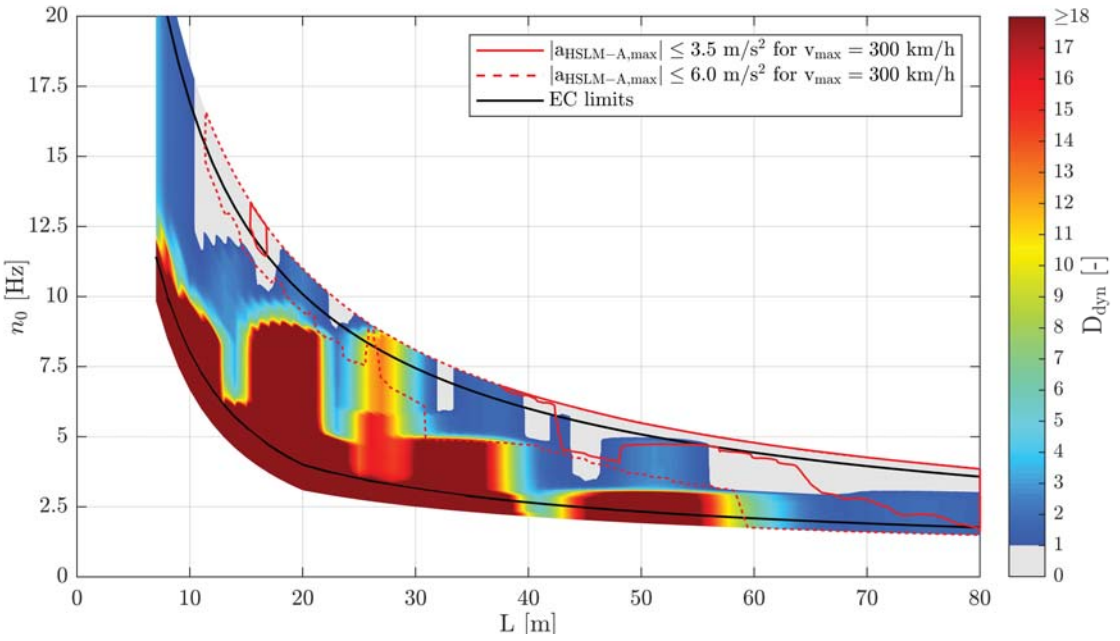

Figure B.66.: Single-span steel bridges — traffic mix TM4** — $v_{D_{max}}$ — ζ_{V1} — Rayleigh like damping — load distribution — top view D_{dyn} & $|a_{HSLM-A,max}|$

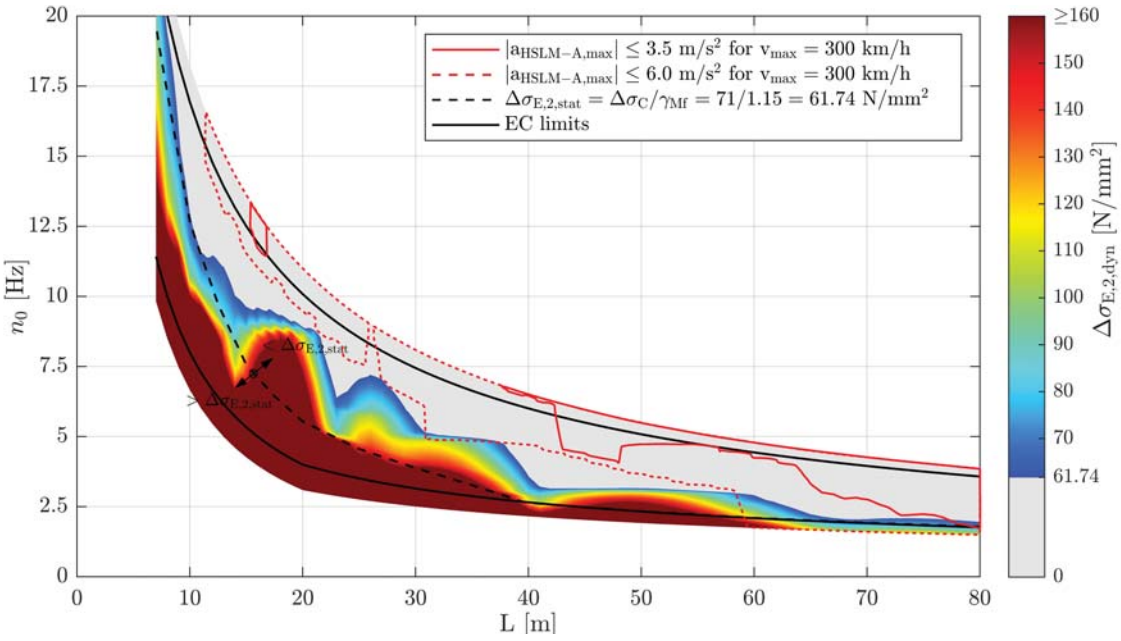

Figure B.67.: Single-span steel bridges — traffic mix TM4** — $v_{D_{max}}$ — ζ_{V1} — Rayleigh like damping — load distribution — top view $\Delta\sigma_{E,2,dyn}$ & $|a_{HSLM-A,max}|$ & $\Delta\sigma_{E,2,stat}$

B.6.3. Train speed $v_{a_{max}}$

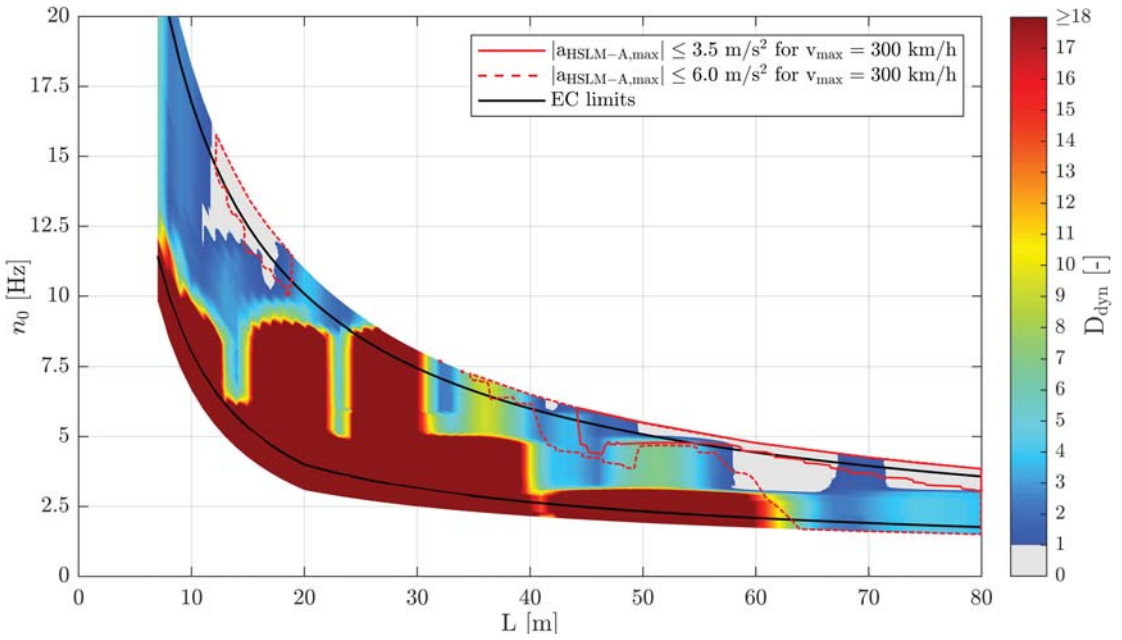

Figure B.68.: Single-span steel bridges — traffic mix TM4*** — $v_{a_{max}}$ — ζ_{EC} — Rayleigh like damping — no load distribution — top view D_{dyn} & $|a_{HSLM-A,max}|$

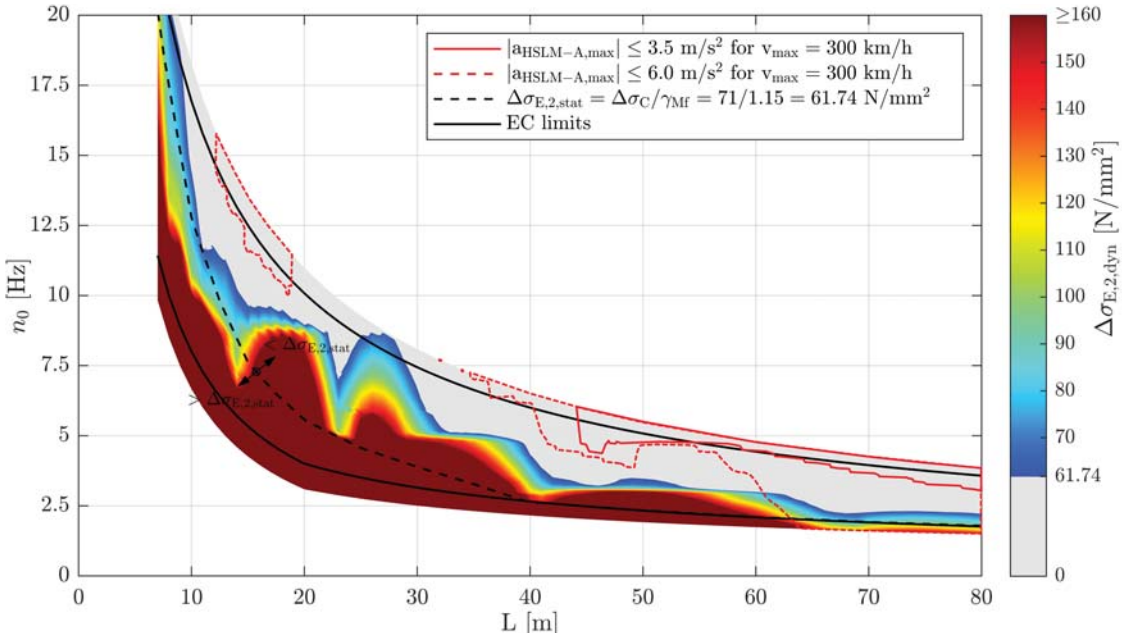

Figure B.69.: Single-span steel bridges — traffic mix TM4*** — $v_{a_{max}}$ — ζ_{EC} — Rayleigh like damping — no load distribution — top view $\Delta\sigma_{E,2,dyn}$ & $|a_{HSLM-A,max}|$ & $\Delta\sigma_{E,2,stat}$

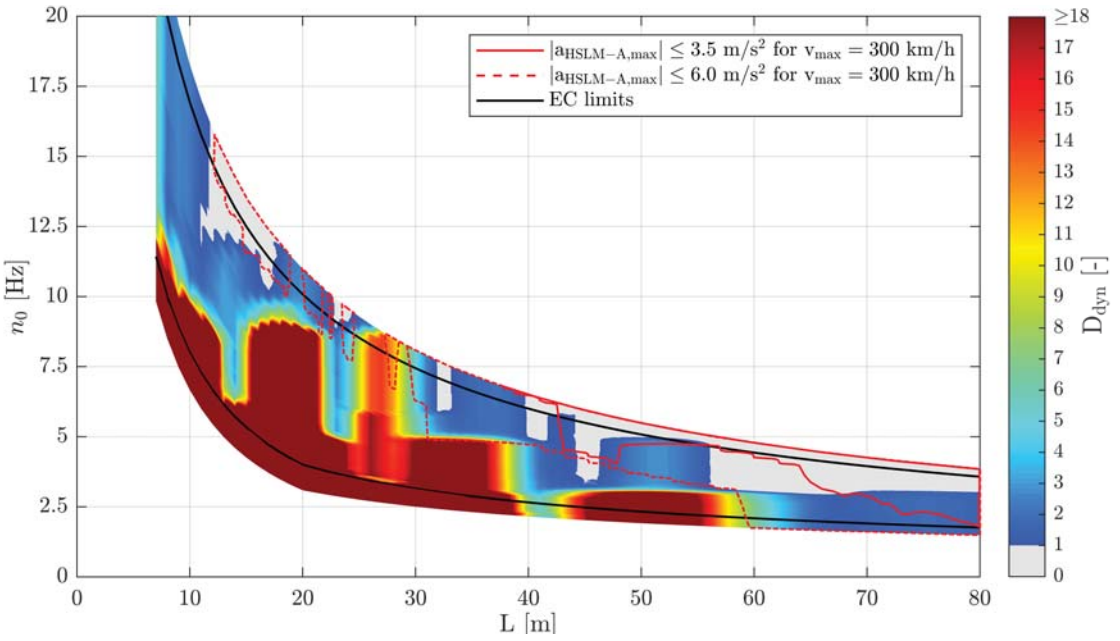

Figure B.70.: Single-span steel bridges — traffic mix TM4*** — $v_{a_{max}}$ — ζ_{V1} — Rayleigh like damping — no load distribution — top view D_{dyn} & $|a_{HSLM-A,max}|$

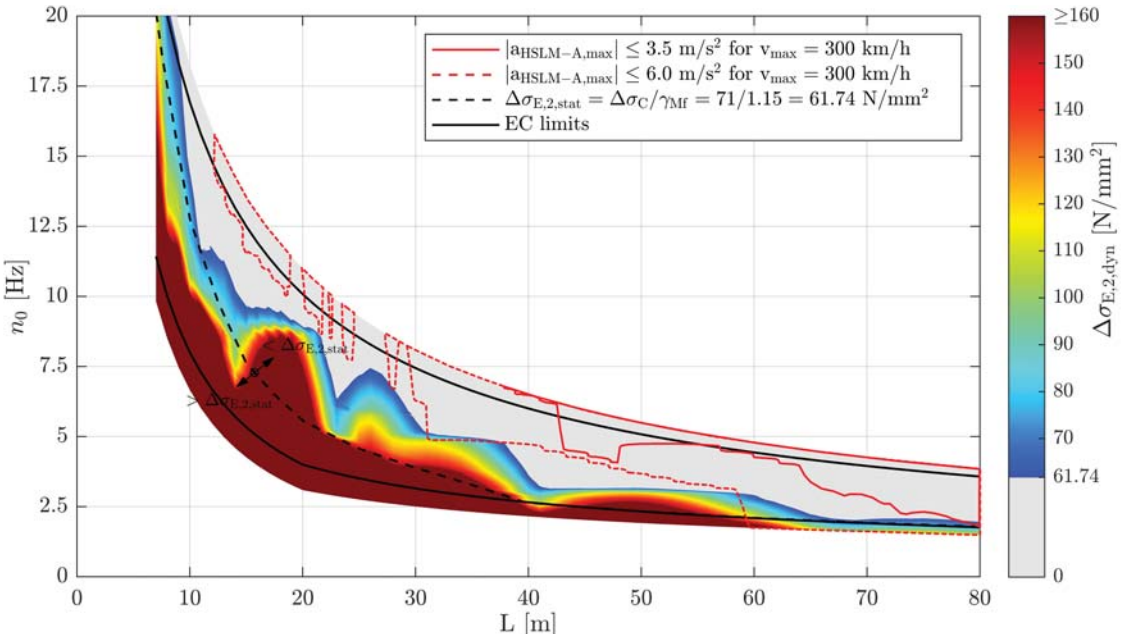

Figure B.71.: Single-span steel bridges — traffic mix TM4*** — $v_{a_{max}}$ — ζ_{V1} — Rayleigh like damping — no load distribution — top view $\Delta\sigma_{E,2,dyn}$ & $|a_{HSLM-A,max}|$ & $\Delta\sigma_{E,2,stat}$

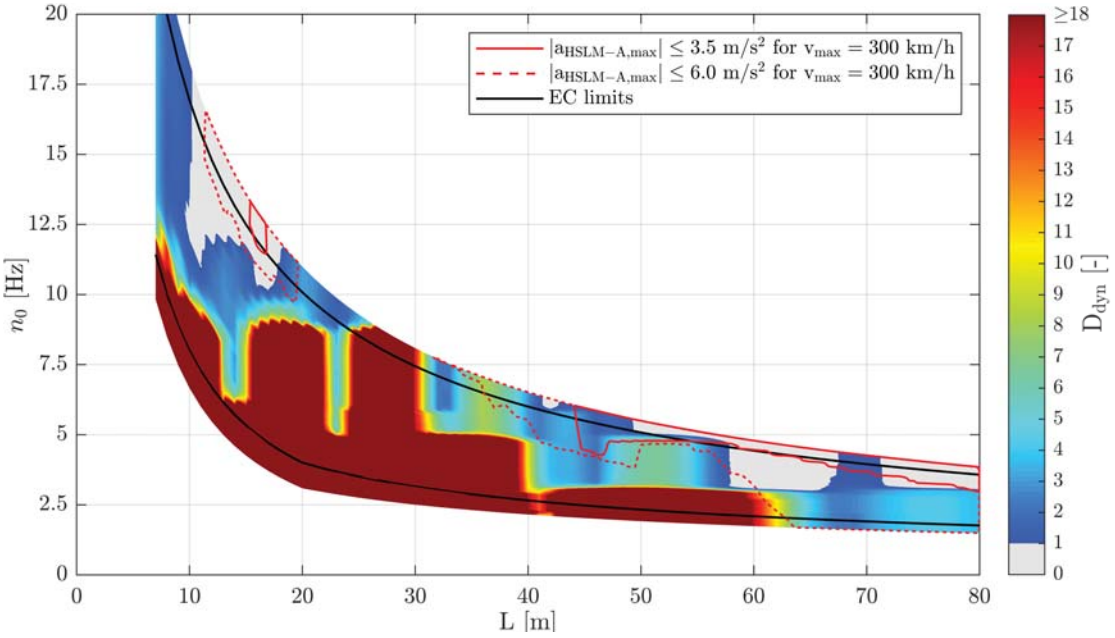

Figure B.72.: Single-span steel bridges — traffic mix TM4*** — $v_{a_{max}}$ — ζ_{EC} — Rayleigh like damping — load distribution — top view D_{dyn} & $|a_{HSLM-A,max}|$

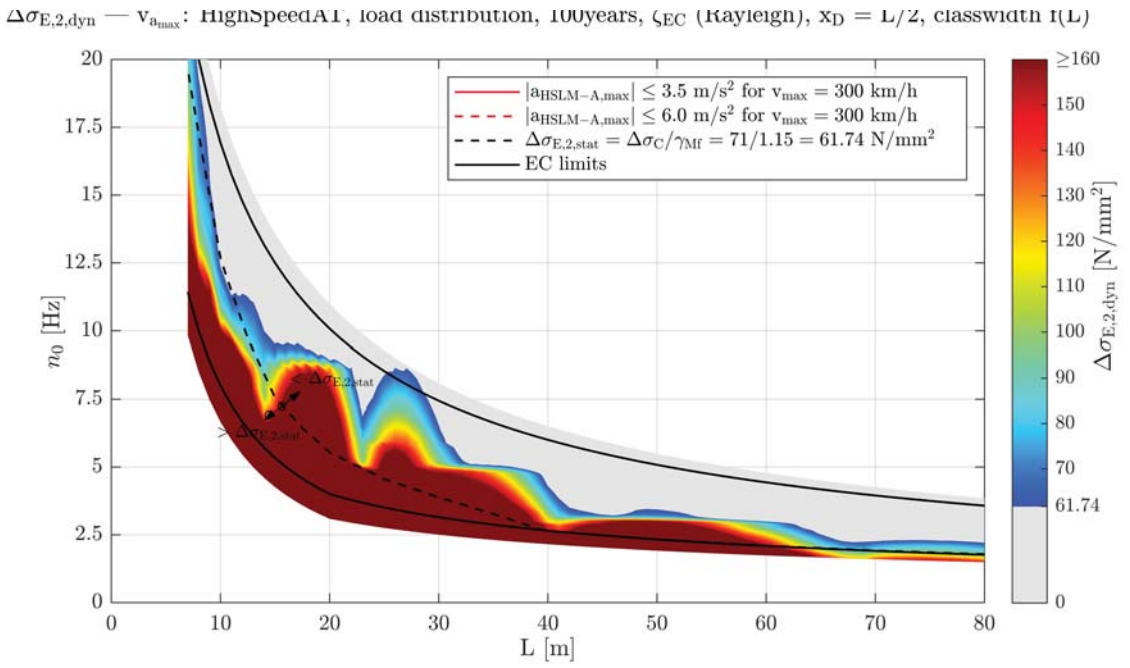

Figure B.73.: Single-span steel bridges — traffic mix TM4*** — $v_{a_{max}}$ — ζ_{EC} — Rayleigh like damping — load distribution — top view $\Delta\sigma_{E,2,dyn}$ & $|a_{HSLM-A,max}|$ & $\Delta\sigma_{E,2,stat}$

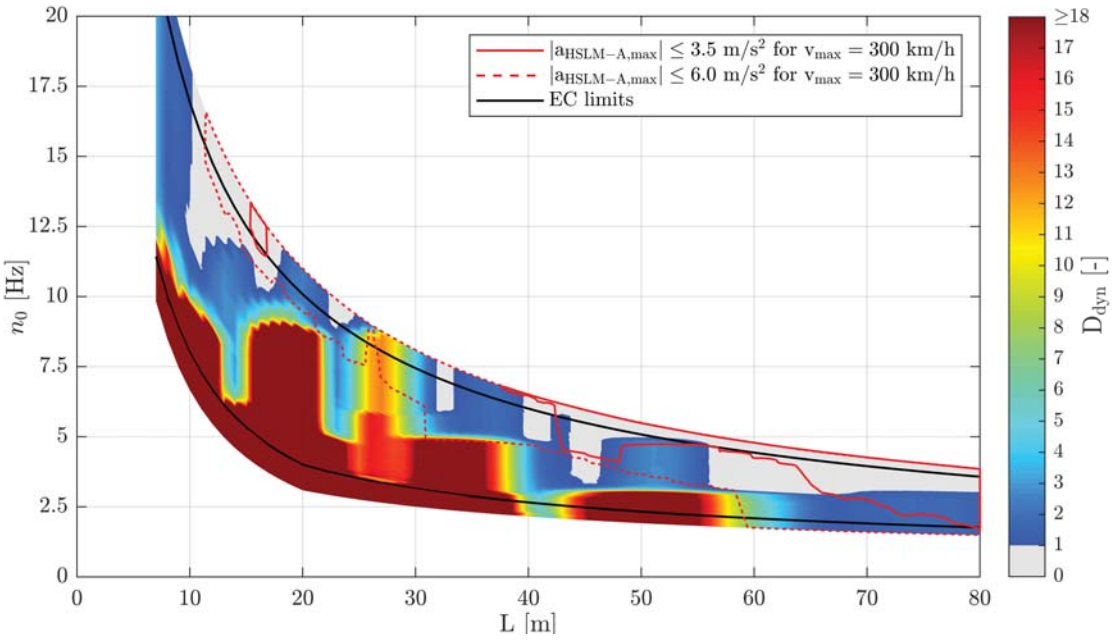

Figure B.74.: Single-span steel bridges — traffic mix TM4*** — $v_{a_{max}}$ — ζ_{V1} — Rayleigh like damping — load distribution — top view D_{dyn} & $|a_{HSLM-A,max}|$

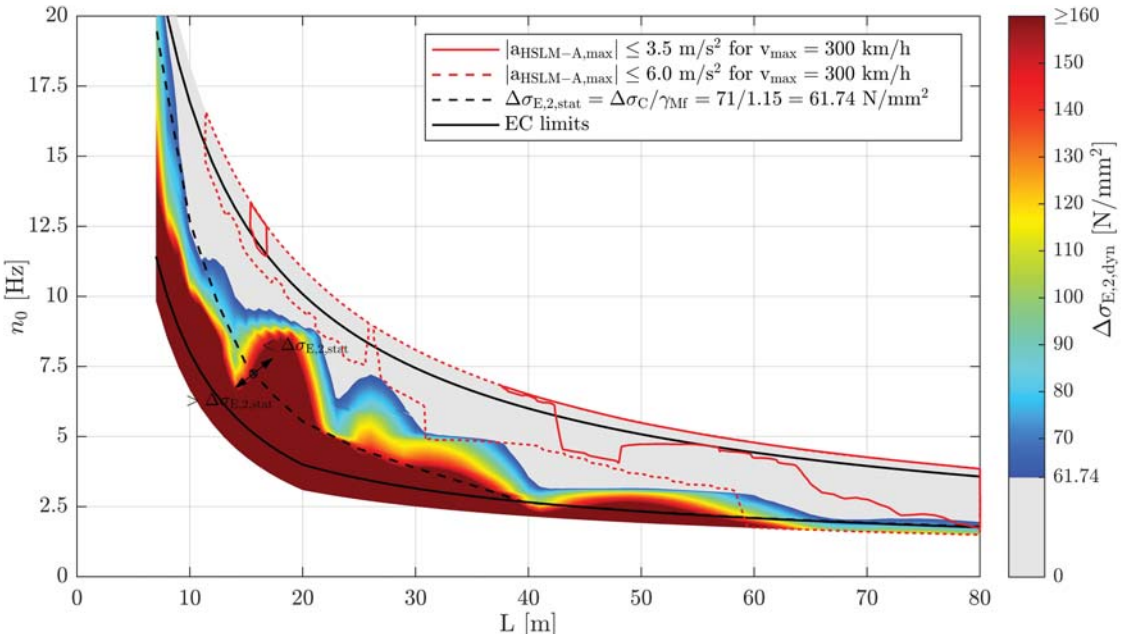

Figure B.75.: Single-span steel bridges — traffic mix TM4*** — $v_{a_{max}}$ — ζ_{V1} — Rayleigh like damping — load distribution — top view $\Delta\sigma_{E,2,dyn}$ & $|a_{HSLM-A,max}|$ & $\Delta\sigma_{E,2,stat}$

B.7. Results of single-span steel bridges due to TM5

B.7.1. Train speed v_{Train}

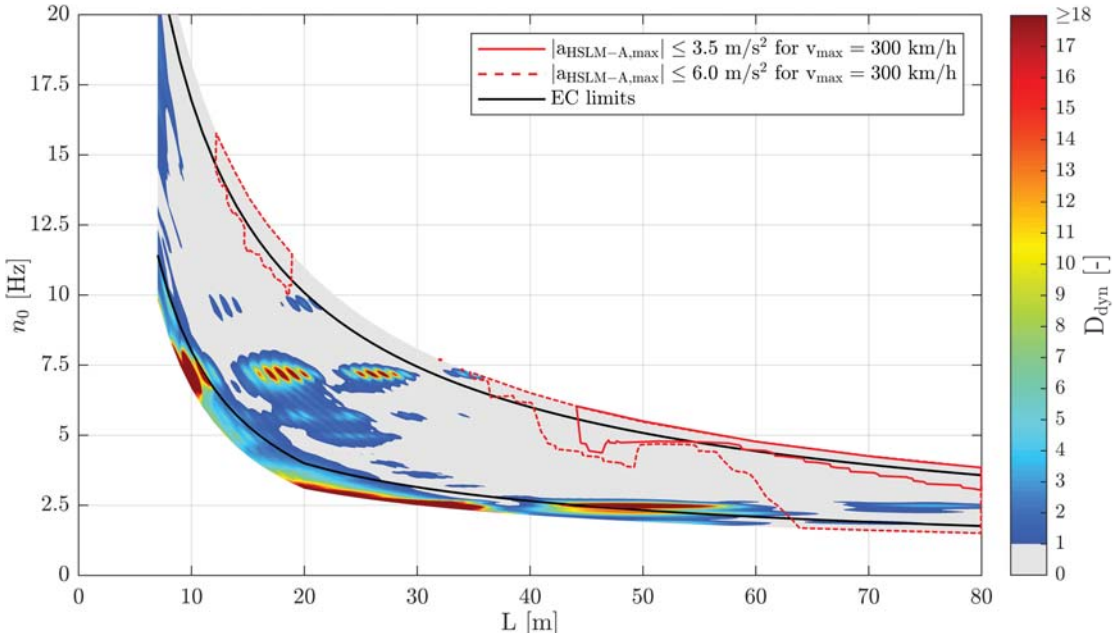

Figure B.76.: Single-span steel bridges — traffic mix TM5* — v_{Train} — ζ_{EC} — Rayleigh like damping — no load distribution — top view D_{dyn} & $|a_{HSLM-A,max}|$

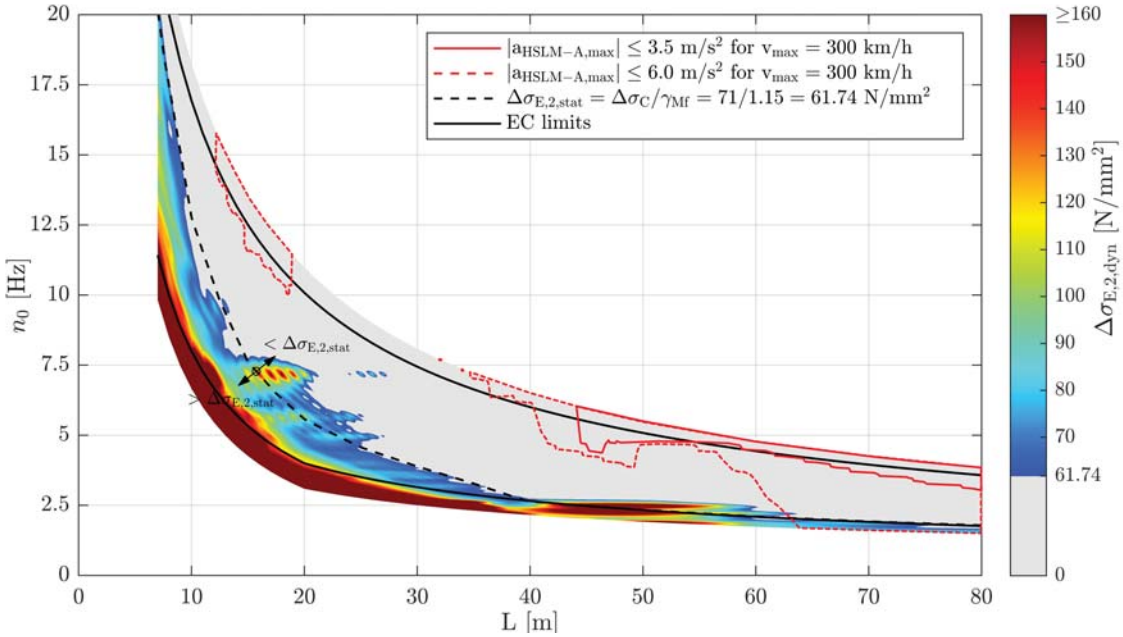

Figure B.77.: Single-span steel bridges — traffic mix TM5* — v_{Train} — ζ_{EC} — Rayleigh like damping — no load distribution — top view $\Delta\sigma_{E,2,dyn}$ & $|a_{HSLM-A,max}|$ & $\Delta\sigma_{E,2,stat}$

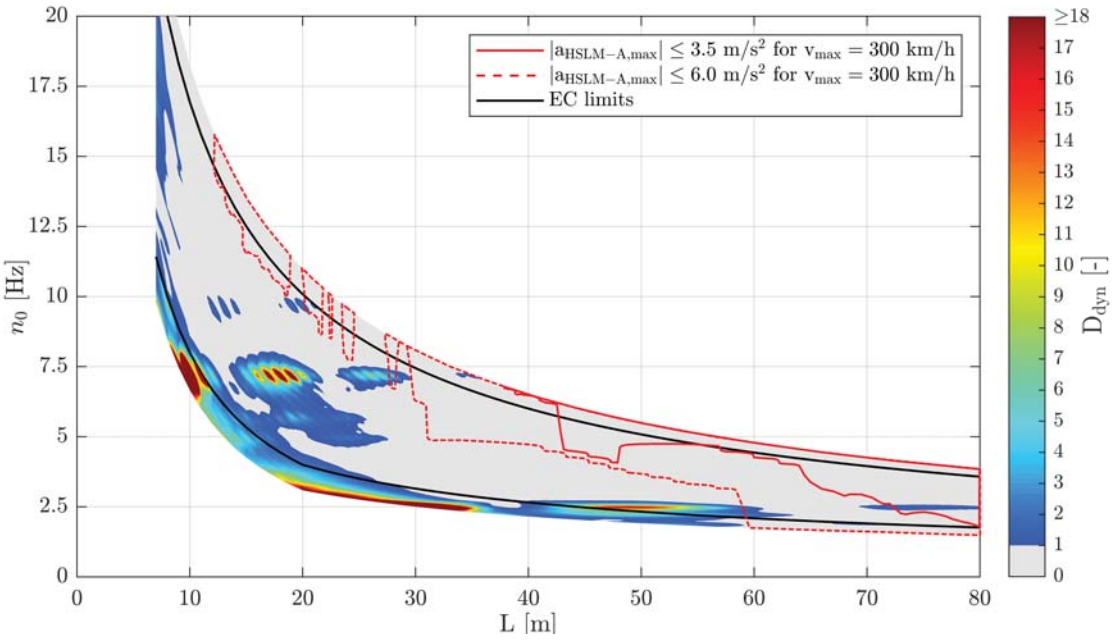

Figure B.78.: Single-span steel bridges — traffic mix TM5* — v_{Train} — ζ_{V1} — Rayleigh like damping — no load distribution — top view D_{dyn} & $|a_{HSLM-A,max}|$

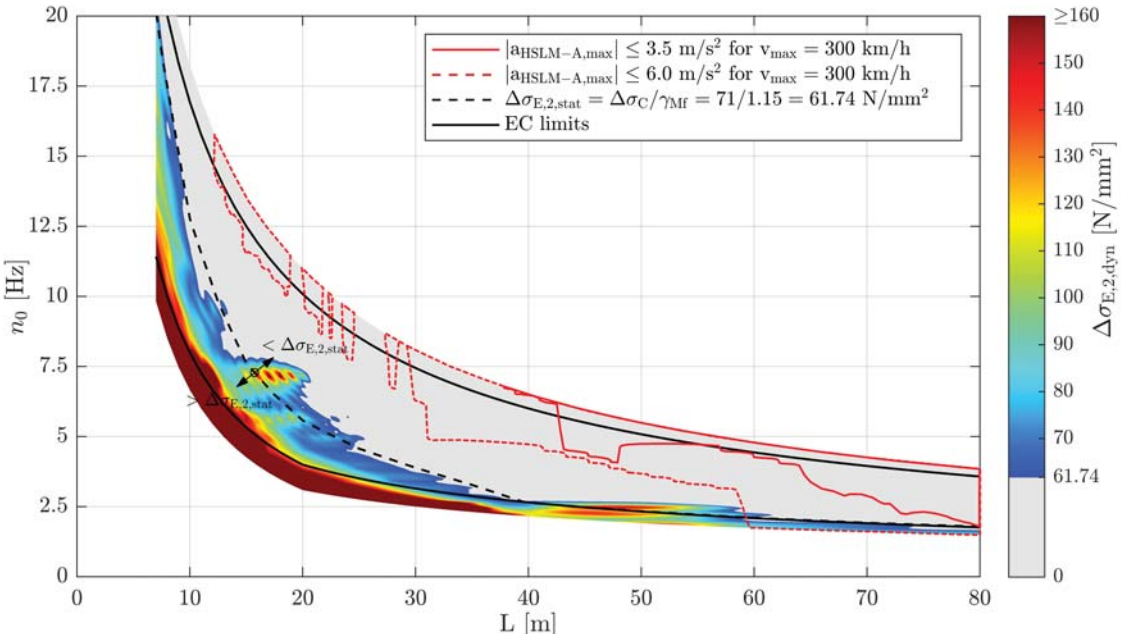

Figure B.79.: Single-span steel bridges — traffic mix TM5* — v_{Train} — ζ_{V1} — Rayleigh like damping — no load distribution — top view $\Delta\sigma_{E,2,dyn}$ & $|a_{HSLM-A,max}|$ & $\Delta\sigma_{E,2,stat}$

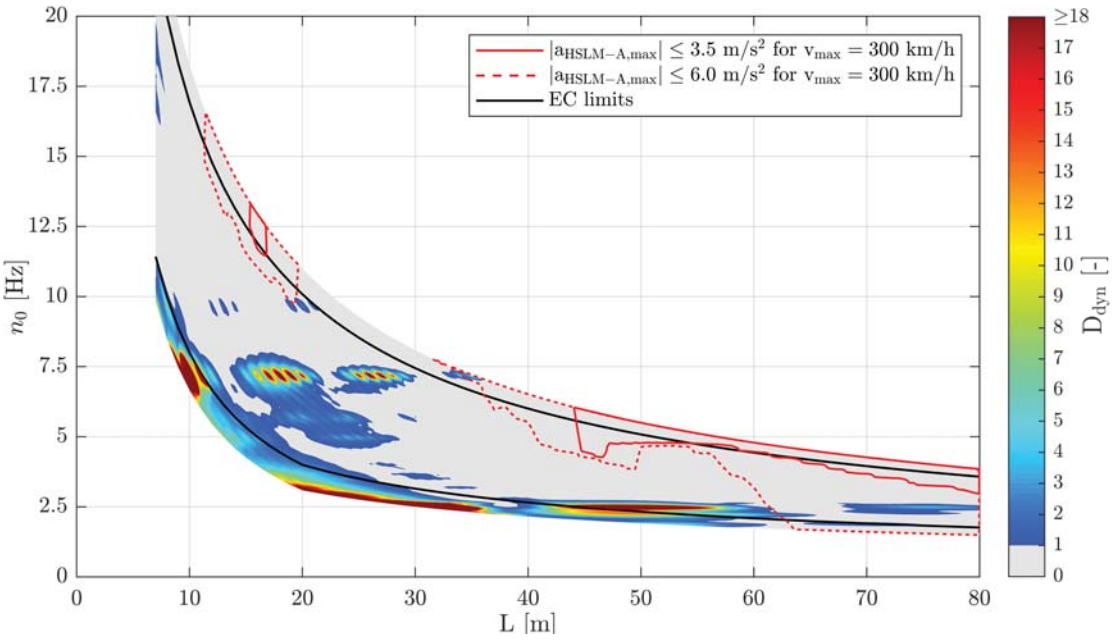

Figure B.80.: Single-span steel bridges — traffic mix TM5* — v_{Train} — ζ_{EC} — Rayleigh like damping — load distribution — top view D_{dyn} & $|a_{HSLM-A,max}|$

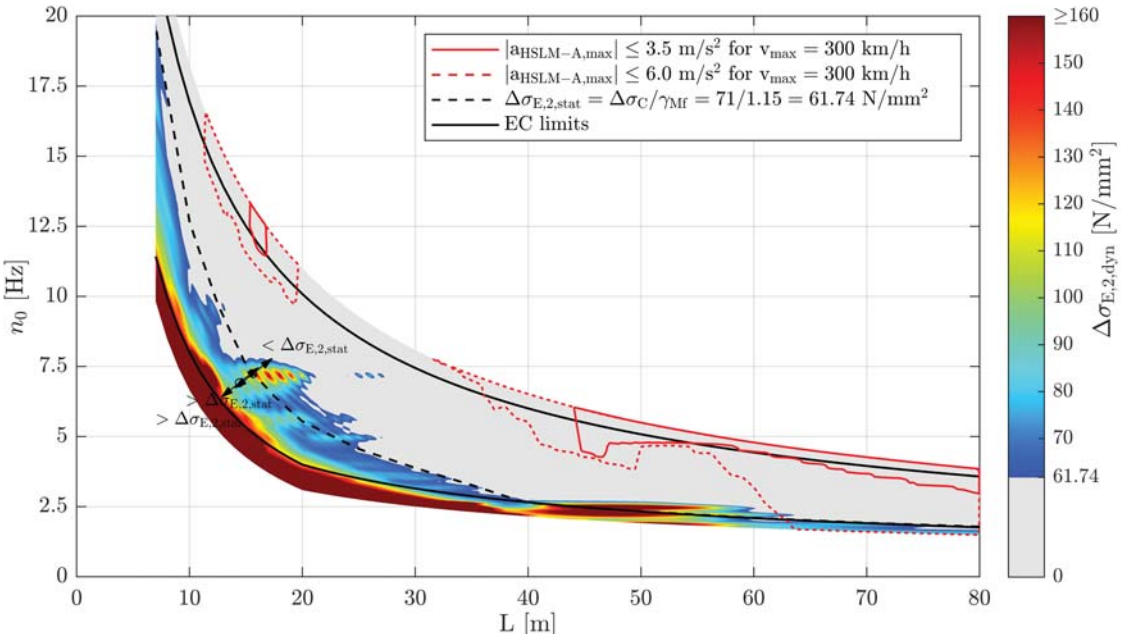

Figure B.81.: Single-span steel bridges — traffic mix TM5* — v_{Train} — ζ_{EC} — Rayleigh like damping — load distribution — top view $\Delta\sigma_{E,2,dyn}$ & $|a_{HSLM-A,max}|$ & $\Delta\sigma_{E,2,stat}$

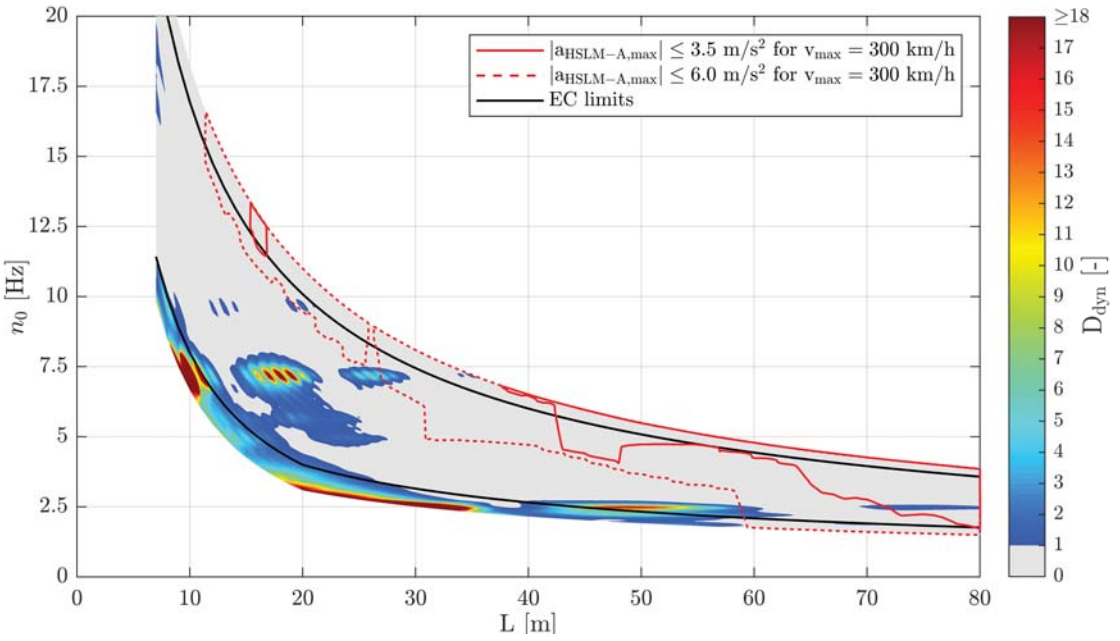

Figure B.82.: Single-span steel bridges — traffic mix TM5* — v_{Train} — ζ_{V1} — Rayleigh like damping — load distribution — top view D_{dyn} & $|a_{HSLM-A,max}|$

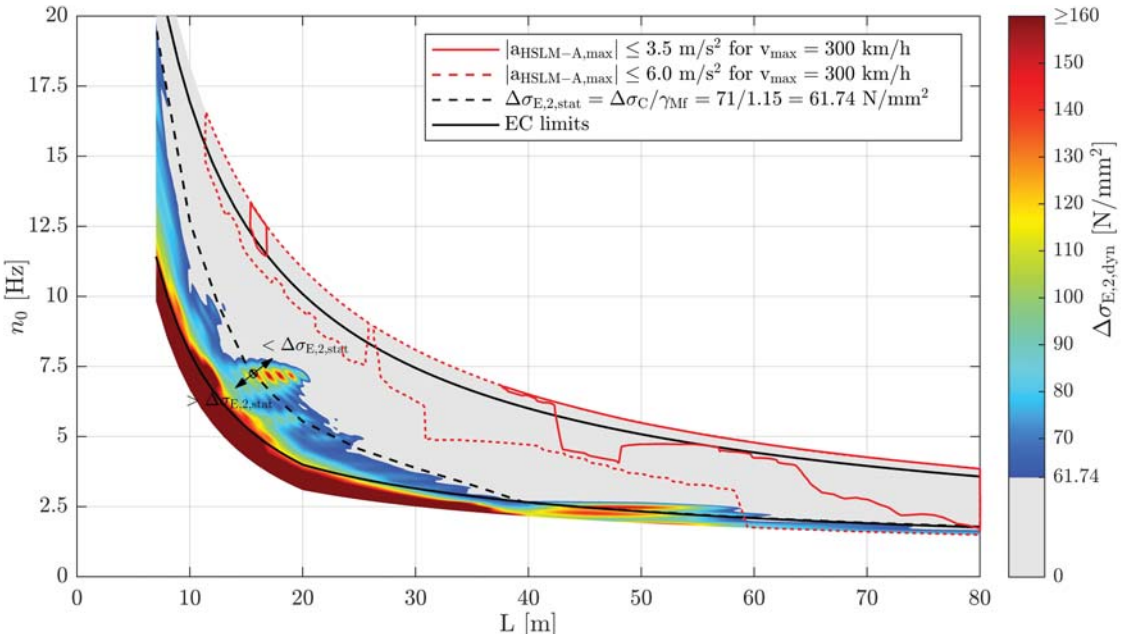

Figure B.83.: Single-span steel bridges — traffic mix TM5* — v_{Train} — ζ_{V1} — Rayleigh like damping — load distribution — top view $\Delta\sigma_{E,2,dyn}$ & $|a_{HSLM-A,max}|$ & $\Delta\sigma_{E,2,stat}$

B.7.2. Train speed $v_{D_{max}}$

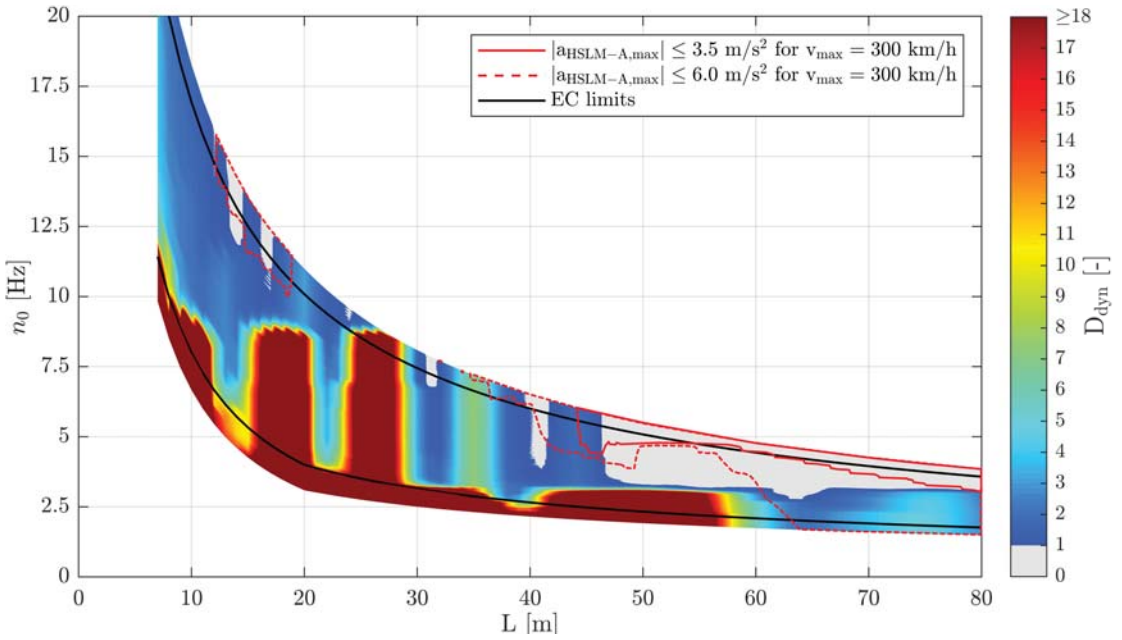

Figure B.84.: Single-span steel bridges — traffic mix TM5** — $v_{D_{max}}$ — ζ_{EC} — Rayleigh like damping — no load distribution — top view D_{dyn} & $|a_{HSLM-A,max}|$

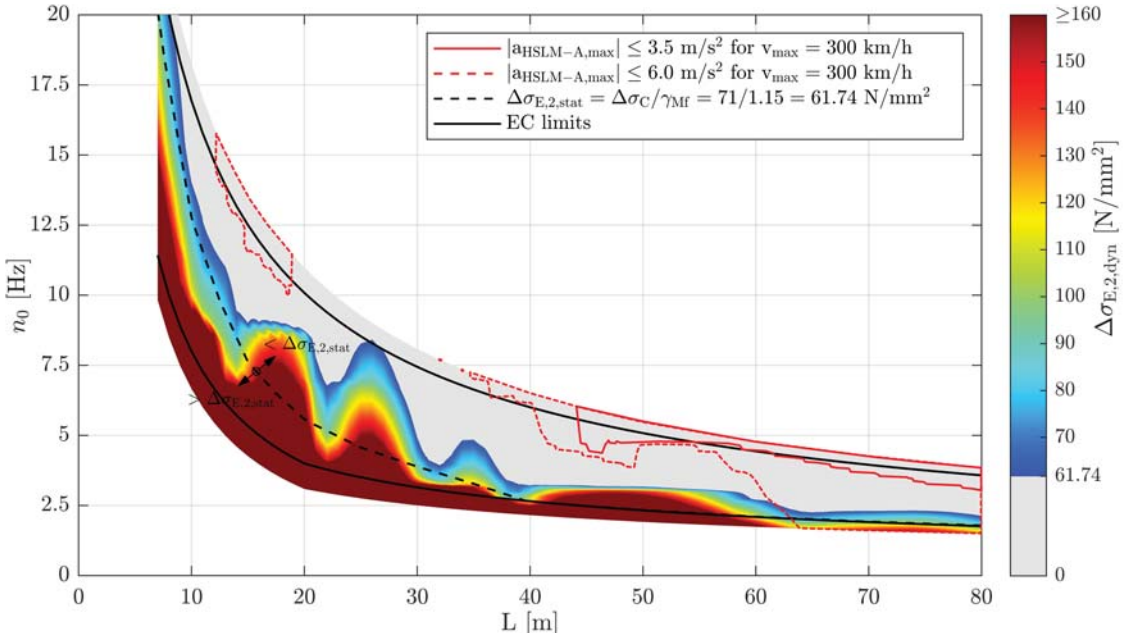

Figure B.85.: Single-span steel bridges — traffic mix TM5** — $v_{D_{max}}$ — ζ_{EC} — Rayleigh like damping — no load distribution — top view $\Delta\sigma_{E,2,dyn}$ & $|a_{HSLM-A,max}|$ & $\Delta\sigma_{E,2,stat}$

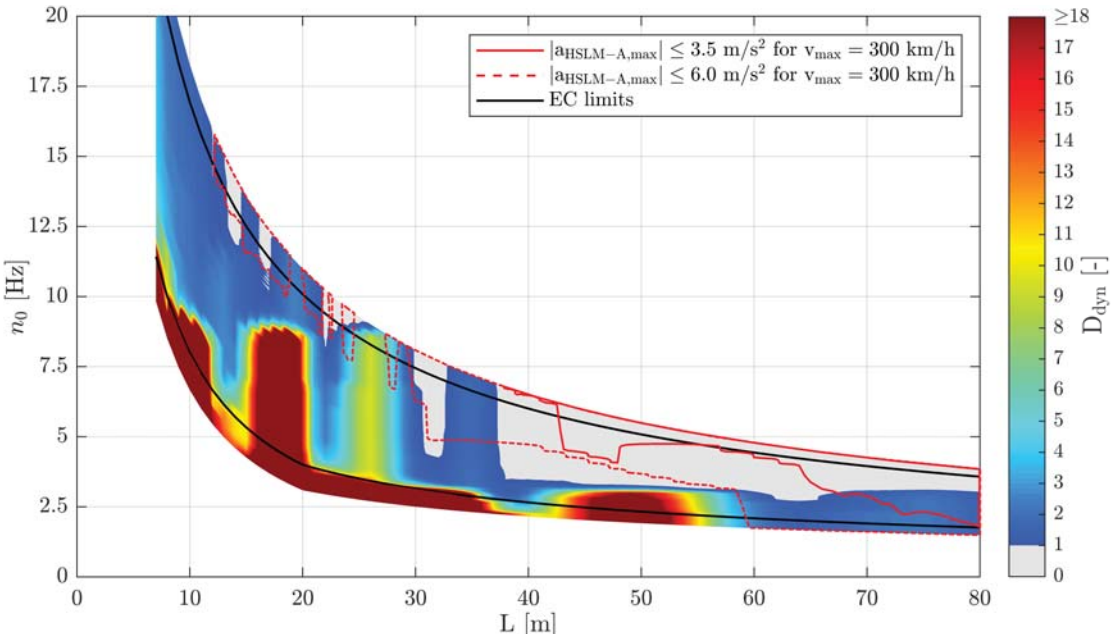

Figure B.86.: Single-span steel bridges — traffic mix TM5** — $v_{D_{max}}$ — ζ_{V1} — Rayleigh like damping — no load distribution — top view D_{dyn} & $|a_{HSLM-A,max}|$

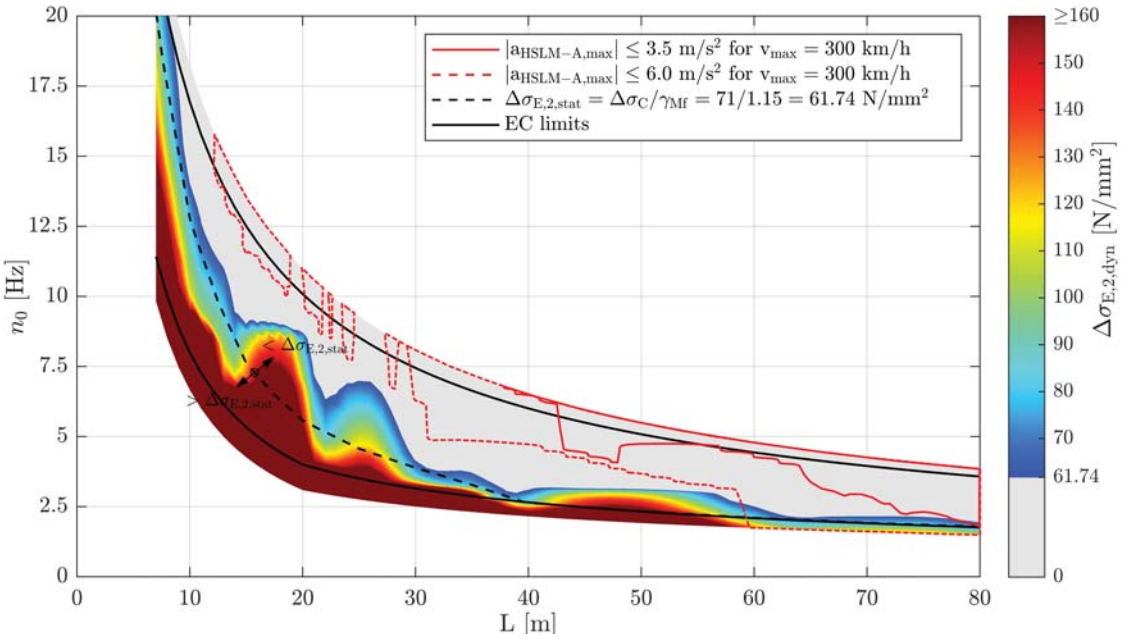

Figure B.87.: Single-span steel bridges — traffic mix TM5** — $v_{D_{max}}$ — ζ_{V1} — Rayleigh like damping — no load distribution — top view $\Delta\sigma_{E,2,dyn}$ & $|a_{HSLM-A,max}|$ & $\Delta\sigma_{E,2,stat}$

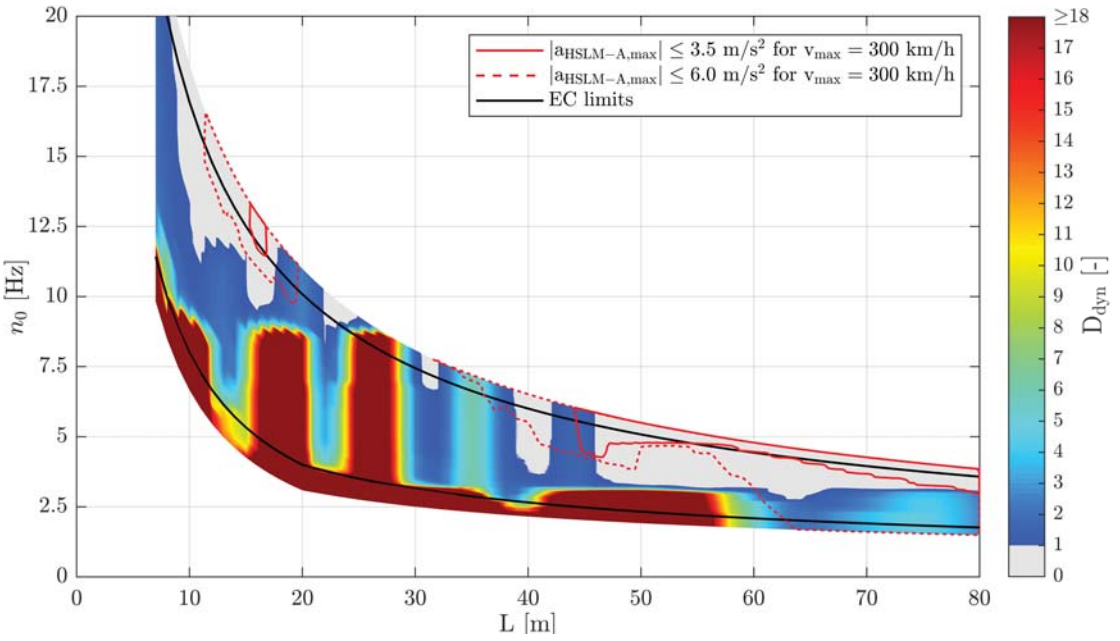

Figure B.88.: Single-span steel bridges — traffic mix TM5** — $v_{D_{max}}$ — ζ_{EC} — Rayleigh like damping — load distribution — top view D_{dyn} & $|a_{HSLM-A,max}|$

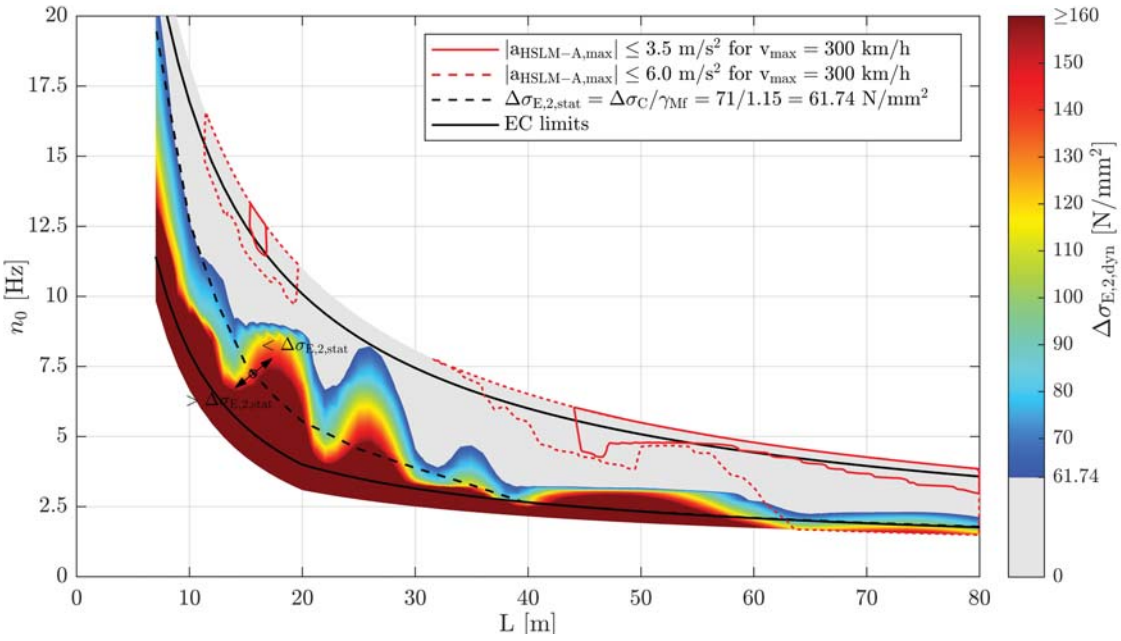

Figure B.89.: Single-span steel bridges — traffic mix TM5** — $v_{D_{max}}$ — ζ_{EC} — Rayleigh like damping — load distribution — top view $\Delta\sigma_{E,2,dyn}$ & $|a_{HSLM-A,max}|$ & $\Delta\sigma_{E,2,stat}$

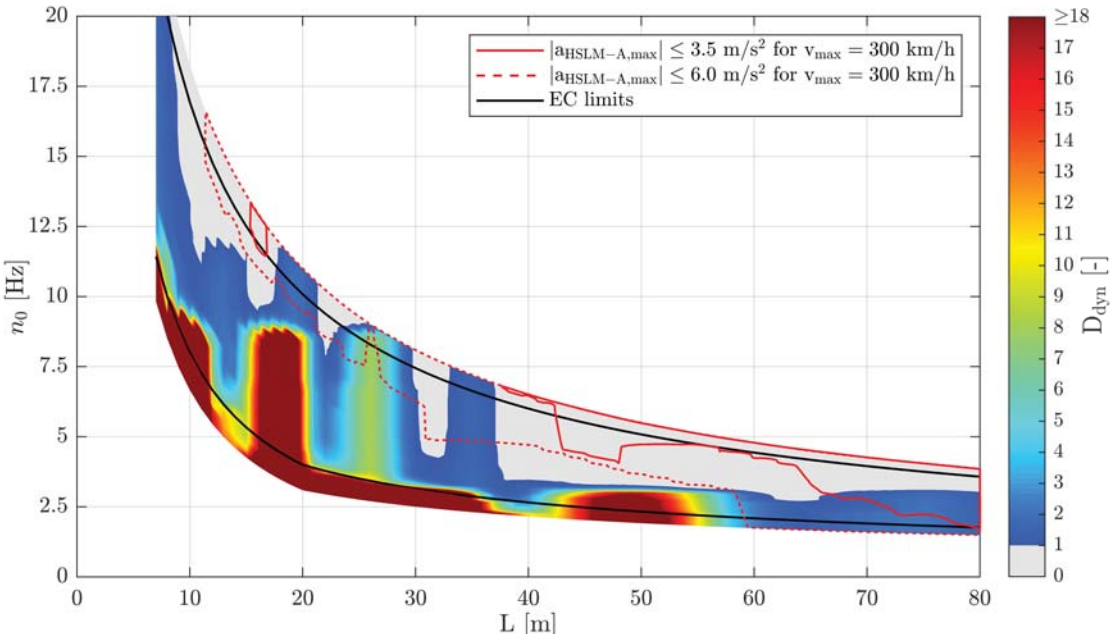

Figure B.90.: Single-span steel bridges — traffic mix TM5** — $v_{D_{max}}$ — ζ_{V1} — Rayleigh like damping — load distribution — top view D_{dyn} & $|a_{HSLM-A,max}|$

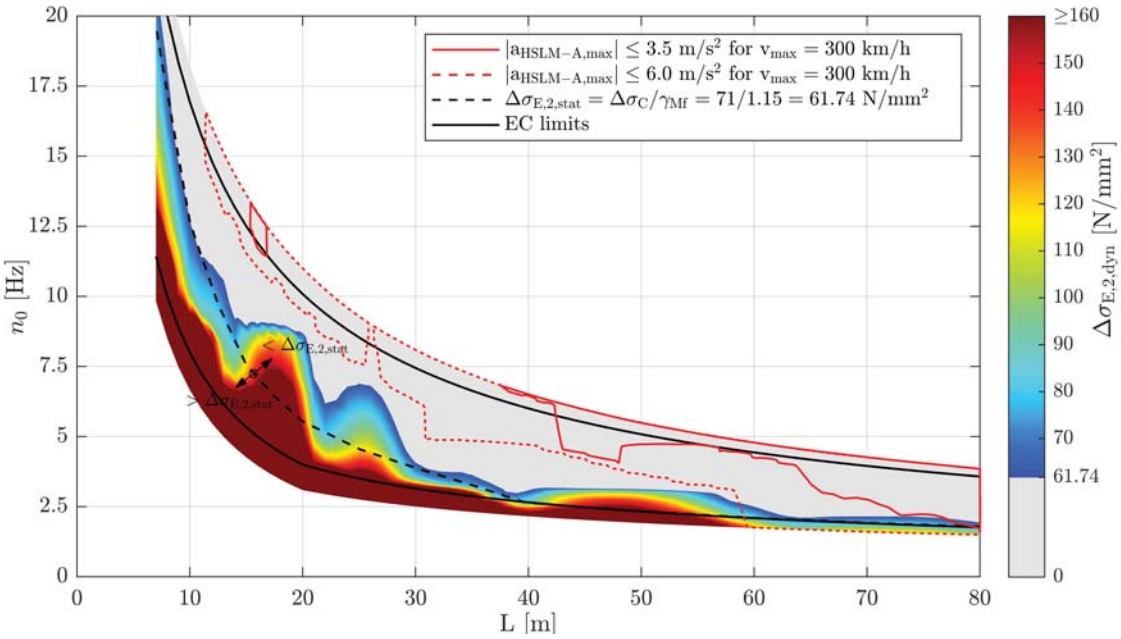

Figure B.91.: Single-span steel bridges — traffic mix TM5** — $v_{D_{max}}$ — ζ_{V1} — Rayleigh like damping — load distribution — top view $\Delta\sigma_{E,2,dyn}$ & $|a_{HSLM-A,max}|$ & $\Delta\sigma_{E,2,stat}$

B.7.3. Train speed $v_{a_{max}}$

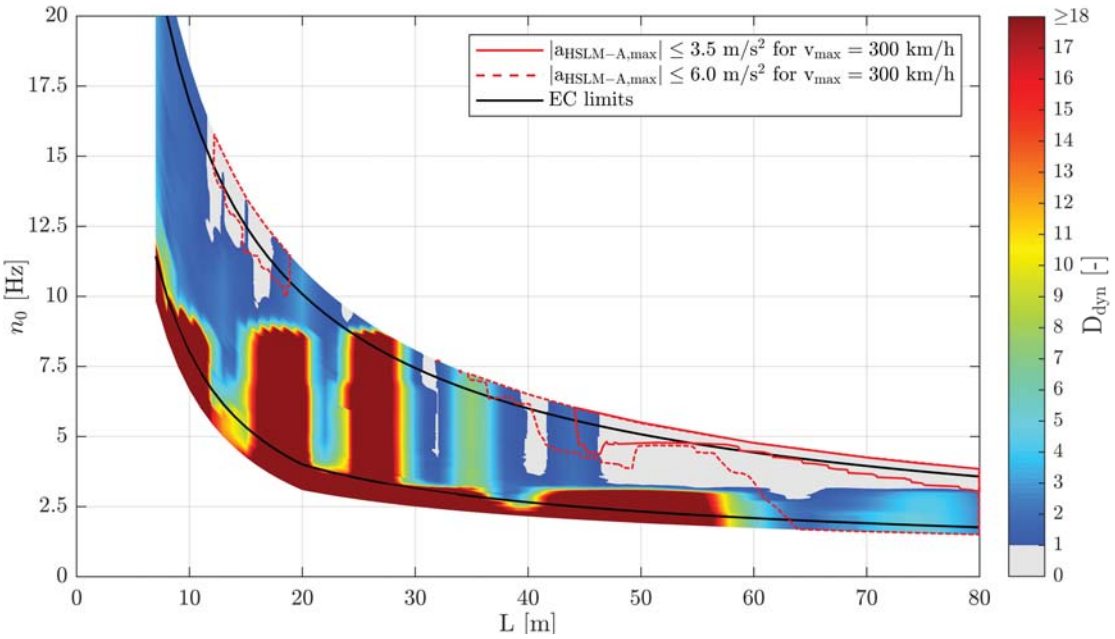

Figure B.92.: Single-span steel bridges — traffic mix TM5*** — $v_{a_{max}}$ — ζ_{EC} — Rayleigh like damping — no load distribution — top view D_{dyn} & $|a_{HSLM-A,max}|$

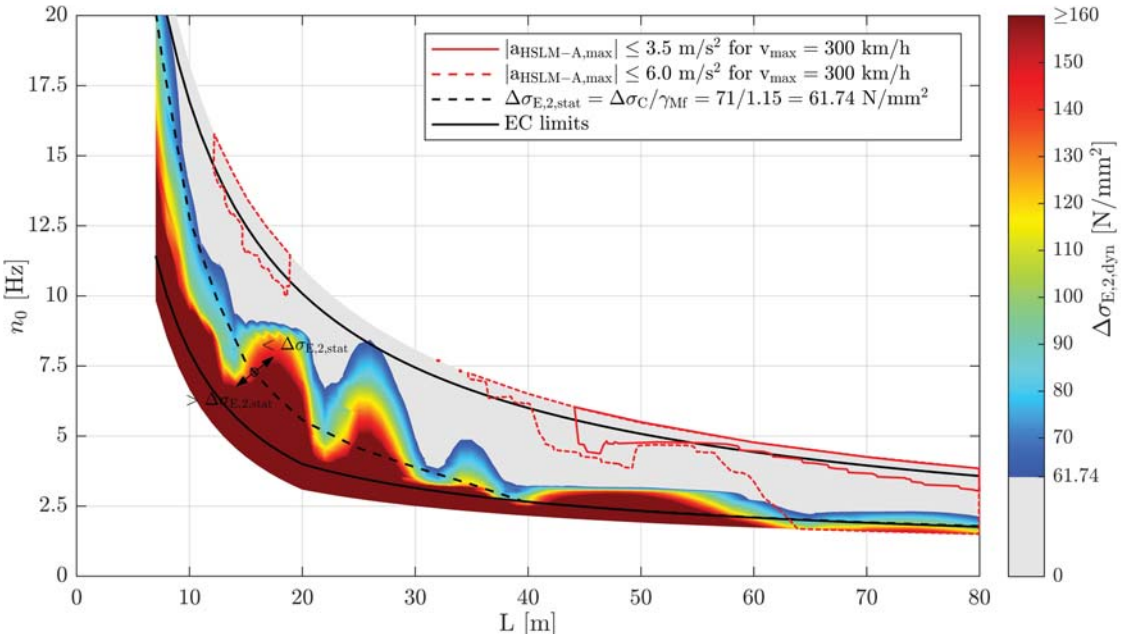

Figure B.93.: Single-span steel bridges — traffic mix TM5*** — $v_{a_{max}}$ — ζ_{EC} — Rayleigh like damping — no load distribution — top view $\Delta\sigma_{E,2,dyn}$ & $|a_{HSLM-A,max}|$ & $\Delta\sigma_{E,2,stat}$

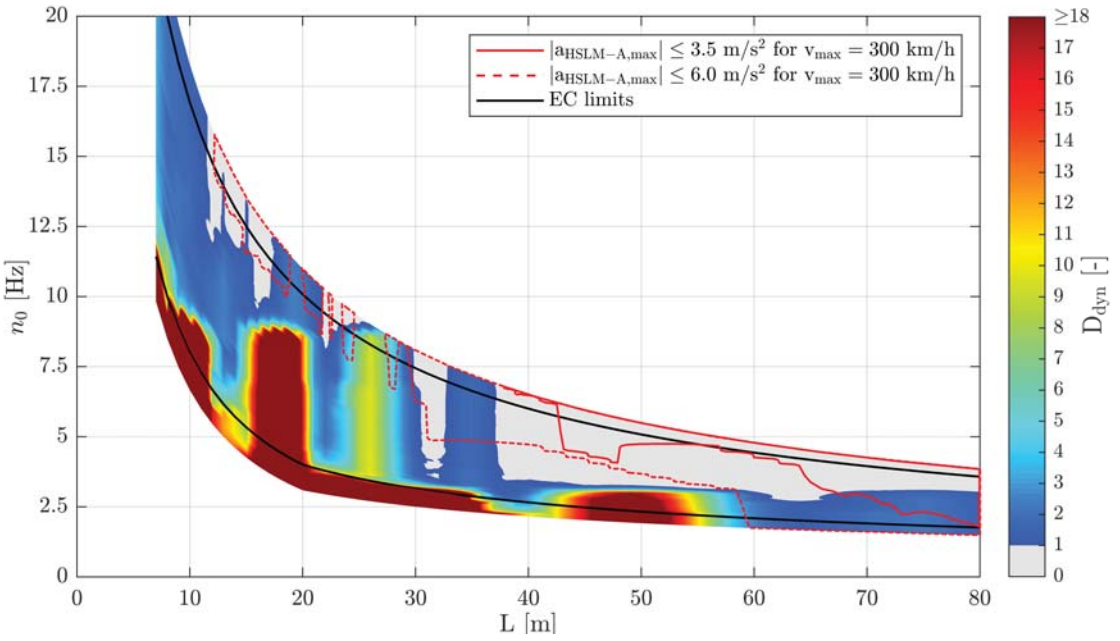

Figure B.94.: Single-span steel bridges — traffic mix TM5*** — $v_{a_{max}}$ — ζ_{V1} — Rayleigh like damping — no load distribution — top view D_{dyn} & $|a_{HSLM-A,max}|$

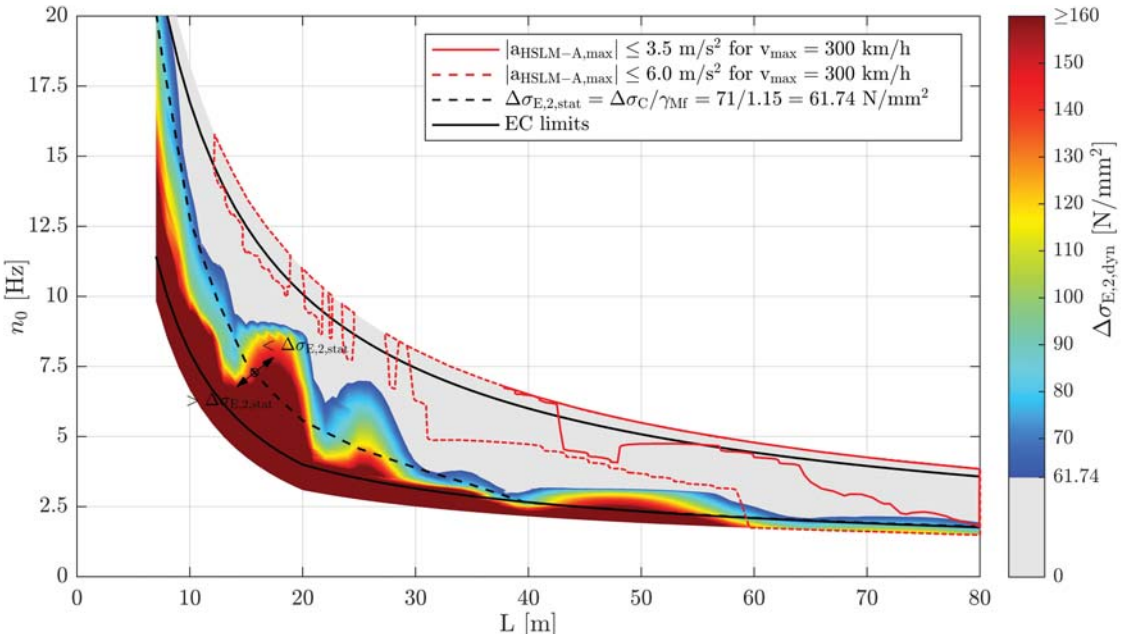

Figure B.95.: Single-span steel bridges — traffic mix TM5*** — $v_{a_{max}}$ — ζ_{V1} — Rayleigh like damping — no load distribution — top view $\Delta\sigma_{E,2,dyn}$ & $|a_{HSLM-A,max}|$ & $\Delta\sigma_{E,2,stat}$

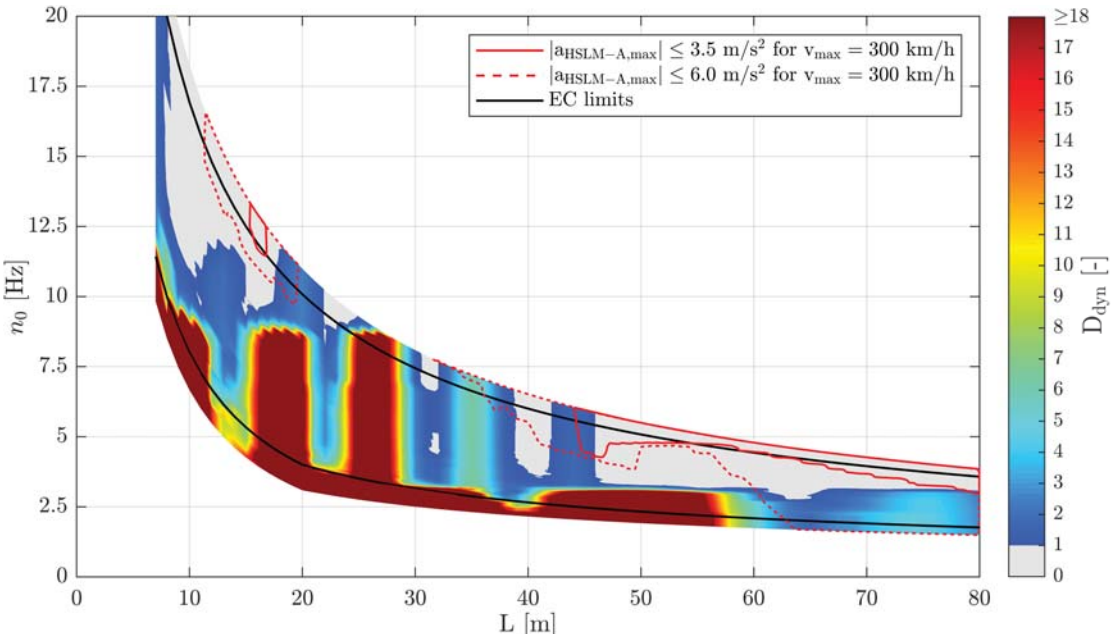

Figure B.96.: Single-span steel bridges — traffic mix TM5*** — $v_{a_{max}}$ — ζ_{EC} — Rayleigh like damping — load distribution — top view D_{dyn} & $|a_{HSLM-A,max}|$

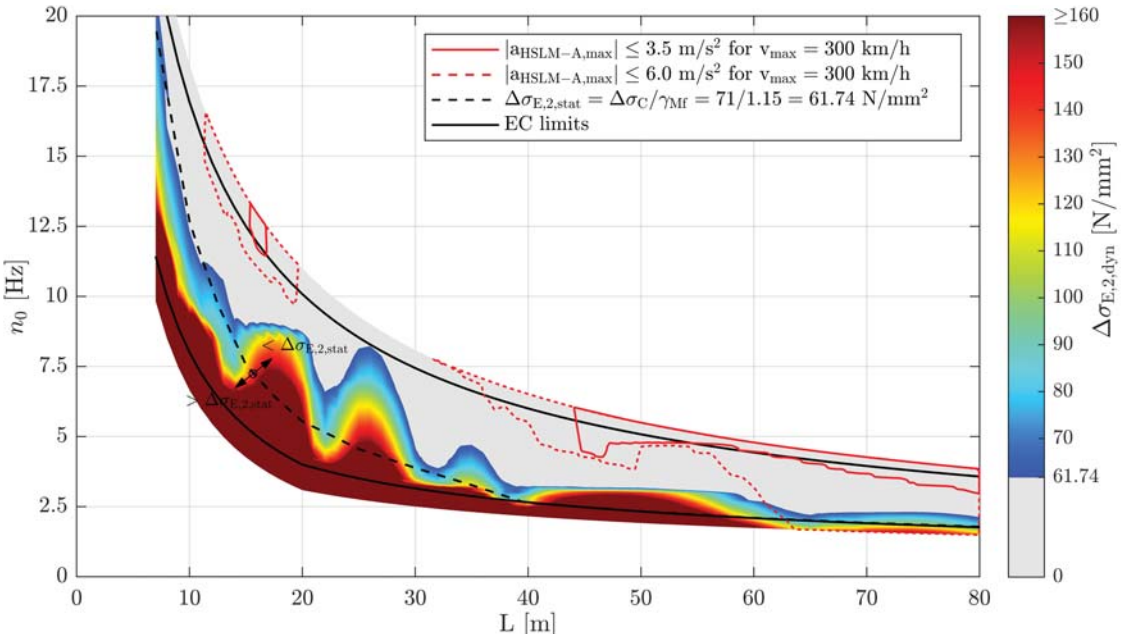

Figure B.97.: Single-span steel bridges — traffic mix TM5*** — $v_{a_{max}}$ — ζ_{EC} — Rayleigh like damping — load distribution — top view $\Delta\sigma_{E,2,dyn}$ & $|a_{HSLM-A,max}|$ & $\Delta\sigma_{E,2,stat}$

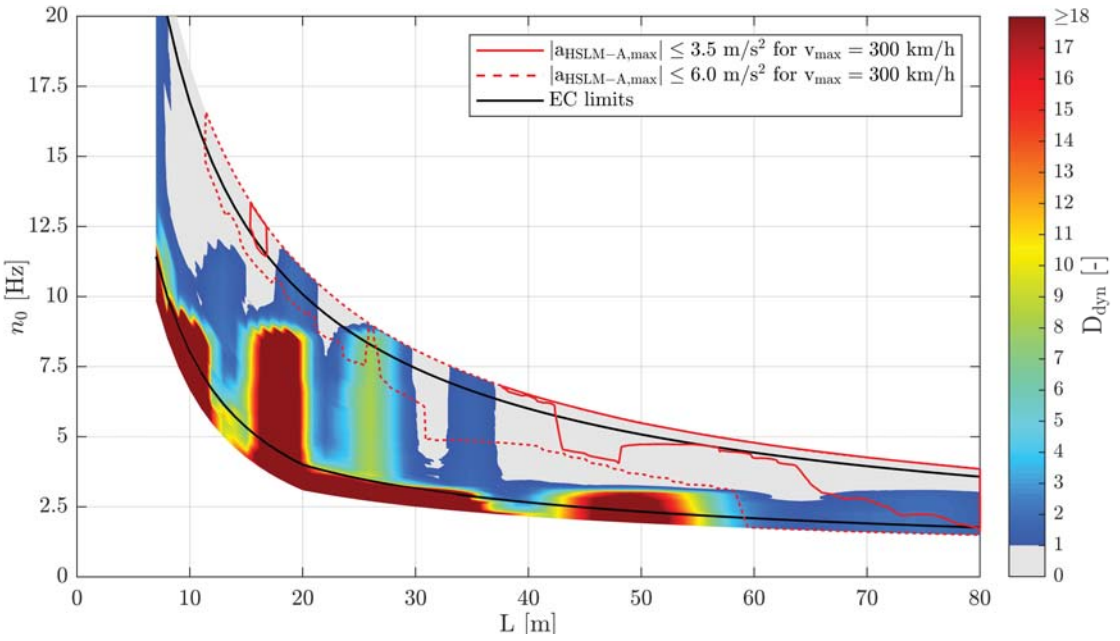

Figure B.98.: Single-span steel bridges — traffic mix TM5*** — $v_{a_{max}}$ — ζ_{V1} — Rayleigh like damping — load distribution — top view D_{dyn} & $|a_{HSLM-A,max}|$

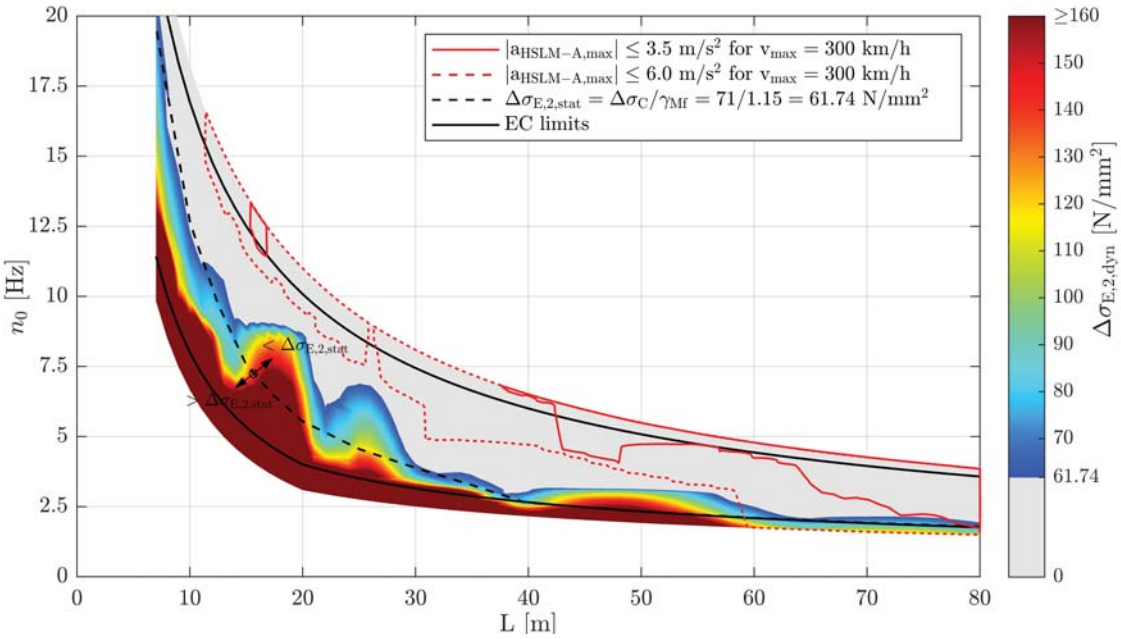

Figure B.99.: Single-span steel bridges — traffic mix TM5*** — $v_{a_{max}}$ — ζ_{ECV1} — Rayleigh like damping — load distribution — top view $\Delta\sigma_{E,2,dyn}$ & $|a_{HSLM-A,max}|$ & $\Delta\sigma_{E,2,stat}$

Appendix C.

Single-span composite bridges

C.1. Design of the individual composite bridges

C.1.1. Studied section type

Open cross sections — see Figure C.1

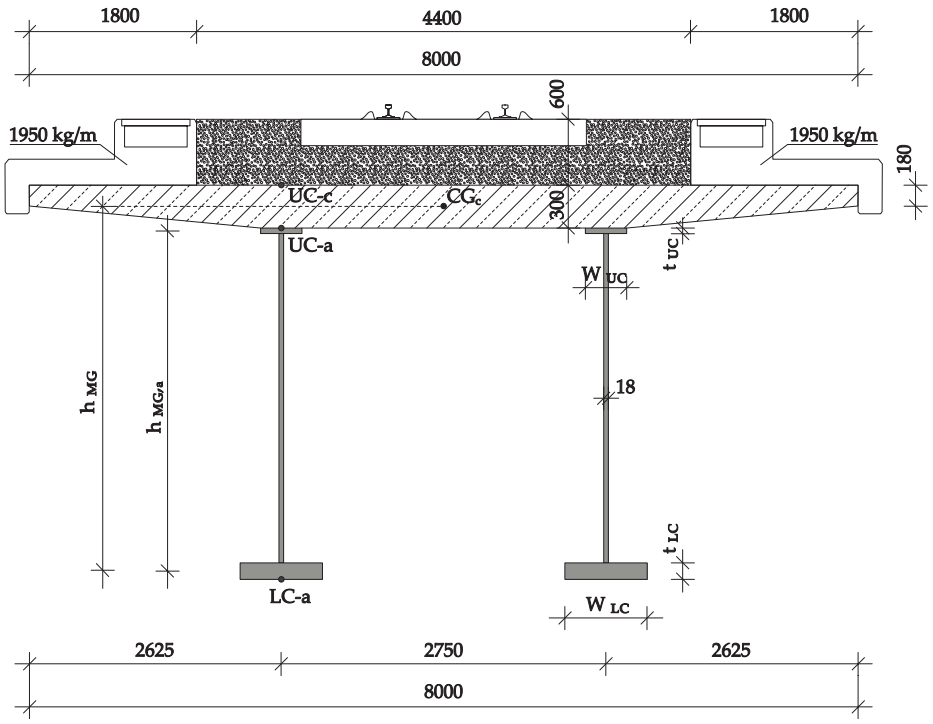

Figure C.1.: Composite bridges — geometry overview — material S355, C35/45

C.1.2. General approach

a.) ULS design for each bridge (S355, C35/45) of length L due to permanent loads and LM71, SW/2 in order to determine the "base" section geometry ($h_{MG,a} \approx L/12 \Rightarrow$ w_{UC}, t_{UC}, w_{LC} and t_{LC}). The loads were distinguished into loads acting on the steel cross section only

and on the composite cross section. In the first step the required areas of the steel-chords were estimated using Equations C.1 and C.2. In the next step the normal stresses at the points UC-c, UC-a and LC-a — see Figure C.1 — were calculated and the utilization ratios summarized in Table C.2.

b.) Varying the geometry of the "base" section geometry in order to reach different n_0 — see Figures C.2 and C.3

According to [60]:

$$A_{LC,a,requ} = \frac{\frac{M_1}{h_{MG,a}} + \frac{M_2}{h_{MG}}}{f_{yd}} - \frac{A_{web}}{6} \tag{C.1}$$

$$A_{UC,a,requ} = \frac{\frac{M_1}{h_{MG,a}} + \frac{M_2}{h_{MG}} * 0.25}{f_{yd}} - \frac{A_{web}}{6}$$

with: $M_1 = f(q_a, q_c) \ldots$ due to loads on steel cross section

$M_2 = f(q_{bb}, q_{eb}, LM71, SW/2) \ldots$ due to loads on composite cross section

According to [41], [42] and [35]:

$$E_d = \gamma_{G,j,sup} * G_{k,j,sup} + \gamma_{Q,1} * Q_{k,1} \tag{C.2}$$

with:
$$\gamma_{G,j,sup} = 1.35$$
$$\gamma_{Q,LM71} = 1.45$$
$$\gamma_{Q,SW/2} = 1.20$$
$$Q_{LM71} = M_{y,LM71,k} * \alpha * \Phi_2$$
$$Q_{SW/2} = M_{y,SW/2,k} * \Phi_2$$
$$\alpha = 1.21$$
$$\Phi_2 = \frac{1.44}{\sqrt{L_\Phi} - 0.2} + 0.82$$
$$L_\Phi = L$$
$$\gamma_a = 7850 \text{ kg/m}^3$$
$$\gamma_{bb} = 2000 \text{ kg/m}^3$$
$$q_{eb} = 19.5 \text{ kN/m}$$

C.1.3. Studied individual composite bridges

$$\mu = \gamma_a * A_a + \gamma_{bb} * A_{bb} + \gamma_c * A_c + \mu_{eb} \tag{C.3}$$

$$\begin{aligned} \text{with:} \quad \gamma_a &= 7850 \text{ kg/m}^3 \\ \gamma_{bb} &= 2000 \text{ kg/m}^3 \\ \gamma_c &= 2500 \text{ kg/m}^3 \\ \mu_{eb} &= 1950 \text{ kg/m} \\ A_{bb} &= 4.5 * 0.6 = 2.7 \text{ m}^2 \end{aligned}$$

$$n_0 = \frac{\pi}{2 * L} * \sqrt{\frac{EI_y}{\mu}} \tag{C.4}$$

Nr.	Name	L [m]	h_{MG} [mm]	w_{UC} [mm]	t_{UC} [mm]	w_{LC} [mm]	t_{LC} [mm]	EI_y [Nm^2]	μ [kg/m]	n_0 [Hz]	ζ_{EC} [%]	FB [%]
1	SCB7-0	7	375	220	20	220	20	1.094E+09	14664	8.76	2.302	-25
2	SCB7-1	7	530	220	20	250	20	1.857E+09	14717	11.39	2.302	0
3	SCB7-2	7	590	220	20	350	25	2.873E+09	14792	14.13	2.302	25
4	SCB7-3	7	655	220	20	400	30	4.049E+09	14861	16.73	2.302	50
5	SCB7-4	7	755	220	20	450	30	5.507E+09	14913	19.48	2.302	75
6	SCB7-5	7	830	220	20	450	35	7.092E+09	14969	22.06	2.302	100
7	SCB7-6	7	875	220	20	500	40	8.954E+09	15047	24.73	2.302	125
8	SCB10-0	10	505	275	20	275	20	1.978E+09	14744	5.75	2.079	-25
9	SCB10-1	10	685	275	20	335	25	3.882E+09	14839	8.03	2.079	0
10	SCB10-2	10	830	275	20	375	30	6.329E+09	14924	10.23	2.079	25
11	SCB10-3	10	950	275	20	425	35	9.454E+09	15014	12.46	2.079	50
12	SCB10-4	10	1025	275	20	515	40	1.318E+10	15125	14.66	2.079	75
13	SCB10-5	10	1150	275	20	585	40	1.762E+10	15204	16.91	2.079	100
14	SCB10-6	10	1250	275	20	615	45	2.278E+10	15299	19.17	2.079	125
15	SCB20-0	20	765	375	30	375	30	6.027E+09	15010	2.49	0.796	-25
16	SCB20-1	20	1015	375	30	600	40	1.564E+10	15279	3.97	0.796	0

Continued on next page

Table C.1 – continued from previous page

Nr.	Name	L [m]	h_{MG} [mm]	w_{UC} [mm]	t_{UC} [mm]	w_{LC} [mm]	t_{LC} [mm]	EI_y [Nm^2]	μ [kg/m]	n_0 [Hz]	ζ_{EC} [%]	FB [%]
17	SCB20-2	20	1425	375	30	625	40	3.016E+10	15411	5.49	0.796	25
18	SCB20-3	20	1675	375	30	685	50	4.998E+10	15625	7.02	0.796	50
19	SCB20-4	20	1855	375	30	810	60	7.555E+10	15900	8.56	0.796	75
20	SCB20-5	20	2055	375	30	950	65	1.066E+11	16162	10.08	0.796	100
21	SCB20-6	20	2300	375	30	995	70	1.424E+11	16355	11.59	0.796	125
22	SCB30-0	30	1300	450	35	550	35	2.171E+10	15367	2.07	0.500	-25
23	SCB30-1	30	1750	450	35	665	45	5.043E+10	15660	3.13	0.500	0
24	SCB30-2	30	2425	450	35	600	45	9.233E+10	15805	4.22	0.500	25
25	SCB30-3	30	2570	450	35	865	60	1.502E+11	16235	5.31	0.500	50
26	SCB30-4	30	2865	450	35	1000	70	2.217E+11	16601	6.38	0.500	75
27	SCB30-5	30	3300	450	35	1000	75	3.056E+11	16802	7.44	0.500	100
28	SCB30-6	30	3735	450	35	1000	80	4.064E+11	17003	8.53	0.500	125
29	SCB40-0	40	1985	550	40	550	40	5.479E+10	15715	1.83	0.500	-25
30	SCB40-1	40	2495	550	40	750	50	1.181E+11	16102	2.66	0.500	0
31	SCB40-2	40	3325	550	40	700	50	2.072E+11	16297	3.50	0.500	25
32	SCB40-3	40	3925	550	40	750	55	3.207E+11	16564	4.32	0.500	50
33	SCB40-4	40	4150	550	40	925	75	4.718E+11	17066	5.16	0.500	75
34	SCB40-5	40	4450	550	40	1000	100	6.598E+11	17628	6.01	0.500	100
35	SCB40-6	40	4925	550	40	1000	115	8.714E+11	17996	6.83	0.500	125
36	SCB50-0	50	2450	625	45	795	45	1.115E+11	16169	1.65	0.500	-25
37	SCB50-1	50	3325	625	45	730	55	2.240E+11	16484	2.38	0.500	0
38	SCB50-2	50	4215	625	45	775	55	3.828E+11	16774	3.00	0.500	25
39	SCB50-3	50	4975	625	45	830	60	5.897E+11	17101	3.70	0.500	50
40	SCB50-4	50	5515	625	45	975	70	8.567E+11	17542	4.39	0.500	75
41	SCB50-5	50	5875	625	45	1000	100	1.181E+12	18138	5.08	0.500	100
42	SCB50-6	50	6250	625	45	1000	140	1.583E+12	18866	5.76	0.500	125
43	SCB60-0	60	3100	715	50	790	50	1.933E+11	16543	1.49	0.500	-25
44	SCB60-1	60	4075	715	50	815	60	3.852E+11	16965	2.08	0.500	0
45	SCB60-2	60	5000	715	50	900	65	6.517E+11	17376	2.67	0.500	25
46	SCB60-3	60	5800	715	50	975	75	9.977E+11	17831	3.26	0.500	50

Continued on next page

Table C.1 – continued from previous page

Nr.	Name	L [m]	h_{MG} [mm]	w_{UC} [mm]	t_{UC} [mm]	w_{LC} [mm]	t_{LC} [mm]	EI_y [Nm^2]	μ [kg/m]	n_0 [Hz]	ζ_{EC} [%]	FB [%]
47	SCB60-4	60	6605	715	50	1000	85	1.414E+12	18243	3.84	0.500	75
48	SCB60-5	60	6950	715	50	1000	135	1.966E+12	19118	4.42	0.500	100
49	SCB60-6	60	7460	715	50	1000	185	2.639E+12	20041	5.01	0.500	125
50	SCB70-0	70	3715	735	60	850	60	3.274E+11	17029	1.41	0.500	-25
51	SCB70-1	70	4850	735	60	900	65	6.177E+11	17467	1.91	0.500	0
52	SCB70-2	70	5895	735	60	975	70	1.011E+12	17914	2.41	0.500	25
53	SCB70-3	70	6850	735	60	1000	85	1.548E+12	18445	2.94	0.500	50
54	SCB70-4	70	7675	735	60	1000	105	2.179E+12	18989	3.43	0.500	75
55	SCB70-5	70	8050	735	60	1000	175	3.062E+12	20184	3.95	0.500	100
56	SCB70-6	70	8750	735	60	1000	225	4.077E+12	21160	4.45	0.500	125
57	SCB80-0	80	4350	825	65	900	65	4.961E+11	17488	1.31	0.500	-25
58	SCB80-1	80	5500	825	65	1000	75	9.263E+11	18070	1.76	0.500	0
59	SCB80-2	80	6750	825	65	1000	85	1.522E+12	18579	2.22	0.500	25
60	SCB80-3	80	7500	825	65	1000	125	2.291E+12	19413	2.67	0.500	50
61	SCB80-4	80	8350	825	65	1000	165	3.272E+12	20276	3.12	0.500	75
62	SCB80-5	80	9125	825	65	1000	225	4.535E+12	21428	3.57	0.500	100
63	SCB80-6	80	9985	825	65	1000	285	6.057E+12	22605	4.02	0.500	125

Note: abbr. of structure name, e.g. **SCB20-3**: **S**ingle**C**omposite**B**ridge Length=**20**m **-** Nr.**3**

Table C.1.: Composite bridges — geometry

C.1.4. Utilization factors for ULS of the individual bridges

Nr.	Name	η_{ULS} [%]					
		with LM71			with SW/2		
		UC-c	UC-a	LC-a	UC-c	UC-a	LC-a
1	SCB7-0	83	16	122	61	21	98
2	SCB7-1	55	14	86	40	16	68
3	SCB7-2	41	15	57	30	16	45
4	SCB7-3	33	14	42	24	15	33
5	SCB7-4	26	13	34	19	13	27
6	SCB7-5	23	12	28	17	12	22
7	SCB7-6	20	12	22	15	11	17
8	SCB10-0	86	23	152	67	27	127
9	SCB10-1	52	21	92	40	22	76
10	SCB10-2	37	19	63	29	19	52
11	SCB10-3	29	17	46	22	17	38
12	SCB10-4	24	16	34	18	16	28
13	SCB10-5	20	15	27	15	14	22
14	SCB10-6	17	13	23	13	13	19
15	SCB20-0	104	46	220	93	47	203
16	SCB20-1	56	41	99	51	41	91
17	SCB20-2	37	30	67	33	30	62
18	SCB20-3	28	26	46	25	25	43
19	SCB20-4	23	23	32	21	23	30
20	SCB20-5	20	21	25	18	21	23
21	SCB20-6	17	19	20	16	18	18
22	SCB30-0	89	60	183	85	60	175
23	SCB30-1	55	47	100	52	46	96
24	SCB30-2	39	34	74	37	33	71
25	SCB30-3	32	32	44	30	31	43
26	SCB30-4	27	28	33	26	28	31
27	SCB30-5	23	24	27	22	24	26
28	SCB30-6	20	21	22	19	20	21

Continued on next page

Table C.2 – continued from previous page

Nr.	Name	η_{ULS} [%]					
		with LM71			with SW/2		
		UC-c	UC-a	LC-a	UC-c	UC-a	LC-a
29	SCB40-0	85	62	174	77	61	164
30	SCB40-1	58	50	97	53	49	91
31	SCB40-2	42	37	72	39	36	68
32	SCB40-3	34	31	54	31	30	50
33	SCB40-4	30	29	37	27	28	35
34	SCB40-5	26	27	27	24	26	26
35	SCB40-6	23	24	24	21	23	22
36	SCB50-0	88	72	154	79	70	144
37	SCB50-1	61	54	100	55	52	93
38	SCB50-2	46	42	73	42	41	68
39	SCB50-3	37	35	54	34	34	51
40	SCB50-4	32	31	41	29	30	38
41	SCB50-5	28	29	31	26	28	29
42	SCB50-6	26	27	24	23	26	23
43	SCB60-0	90	74	155	82	72	145
44	SCB60-1	64	56	98	58	55	92
45	SCB60-2	50	46	71	45	44	66
46	SCB60-3	41	39	52	37	37	49
47	SCB60-4	35	33	42	32	32	39
48	SCB60-5	31	32	31	28	31	29
49	SCB60-6	28	30	24	25	29	23
50	SCB70-0	91	77	142	84	74	134
51	SCB70-1	67	59	98	61	57	92
52	SCB70-2	53	48	71	48	46	67
53	SCB70-3	43	41	54	40	39	51
54	SCB70-4	37	36	44	34	35	42
55	SCB70-5	33	34	31	31	33	29
56	SCB70-6	30	32	25	27	31	24
57	SCB80-0	94	81	144	85	78	135
58	SCB80-1	70	64	93	64	61	88

Continued on next page

Table C.2 – continued from previous page

Nr.	Name	η_{ULS} [%]					
		with LM71			with SW/2		
		UC-c	UC-a	LC-a	UC-c	UC-a	LC-a
59	SCB80-2	55	52	70	50	50	66
60	SCB80-3	47	46	52	42	44	49
61	SCB80-4	40	41	40	37	40	38
62	SCB80-5	35	38	31	32	37	29
63	SCB80-6	31	35	25	28	34	24

UC-c...upper chord concrete
UC-a...upper chord steel
LC-a...lower chord steel
$f_{yd} = f(t_{LC})$ according to [40]

Table C.2.: Composite bridges — utilization for ULS

C.1.5. Suitability of individual composite bridges for high-speed railway lines

Nr.	Name	$\lvert a_{HSLM-A,max} \rvert$ [m/s^2]	
		v_{max} = 240 km/h	v_{max} = 300 km/h
1	SCB7-0	20.19	34.80
2	SCB7-1	7.92	18.52
3	SCB7-2	8.22	8.45
4	SCB7-3	8.57	8.57
5	SCB7-4	8.76	8.95
6	SCB7-5	4.16	9.19
7	SCB7-6	3.47	8.52
8	SCB10-0	26.81	34.60
9	SCB10-1	8.51	22.68
10	SCB10-2	4.50	8.44
11	SCB10-3	4.68	4.68
12	SCB10-4	3.82	4.81
13	SCB10-5	4.00	5.09
14	SCB10-6	4.15	4.15
15	SCB20-0	48.38	48.38
16	SCB20-1	8.31	39.39
17	SCB20-2	8.85	8.85
18	SCB20-3	5.80	9.00
19	SCB20-4	3.35	5.90
20	SCB20-5	2.81	3.43
21	SCB20-6	1.90	3.50
22	SCB30-0	21.52	21.52
23	SCB30-1	7.36	20.35
24	SCB30-2	5.37	7.40
25	SCB30-3	4.18	5.28
26	SCB30-4	4.26	4.26
27	SCB30-5	2.07	4.27
28	SCB30-6	2.08	2.30
29	SCB40-0	8.73	8.73
30	SCB40-1	8.53	8.53
31	SCB40-2	7.52	8.45
32	SCB40-3	3.42	7.44
33	SCB40-4	2.75	3.35
34	SCB40-5	2.16	3.23
35	SCB40-6	1.15	2.16
36	SCB50-0	6.31	6.31
37	SCB50-1	6.22	6.22
38	SCB50-2	3.53	6.14
39	SCB50-3	3.46	3.67
40	SCB50-4	1.70	3.37
41	SCB50-5	1.64	1.64
42	SCB50-6	1.24	1.58
43	SCB60-0	3.48	3.75
44	SCB60-1	3.37	3.37
45	SCB60-2	3.33	3.33
46	SCB60-3	3.25	3.25
47	SCB60-4	1.05	3.17
48	SCB60-5	1.00	2.29
49	SCB60-6	0.95	0.95
50	SCB70-0	2.76	2.76
51	SCB70-1	2.69	2.69
52	SCB70-2	2.62	2.62
53	SCB70-3	2.15	2.54
54	SCB70-4	1.82	2.47
55	SCB70-5	0.78	1.72
56	SCB70-6	0.75	1.64
57	SCB80-0	2.31	2.31
58	SCB80-1	2.21	2.21
59	SCB80-2	2.16	2.16
60	SCB80-3	1.63	2.08
61	SCB80-4	1.56	1.89
62	SCB80-5	0.82	1.48
63	SCB80-6	0.58	1.40

Table C.3.: Composite bridges — $|a_{max}|$ due to HSLM-A

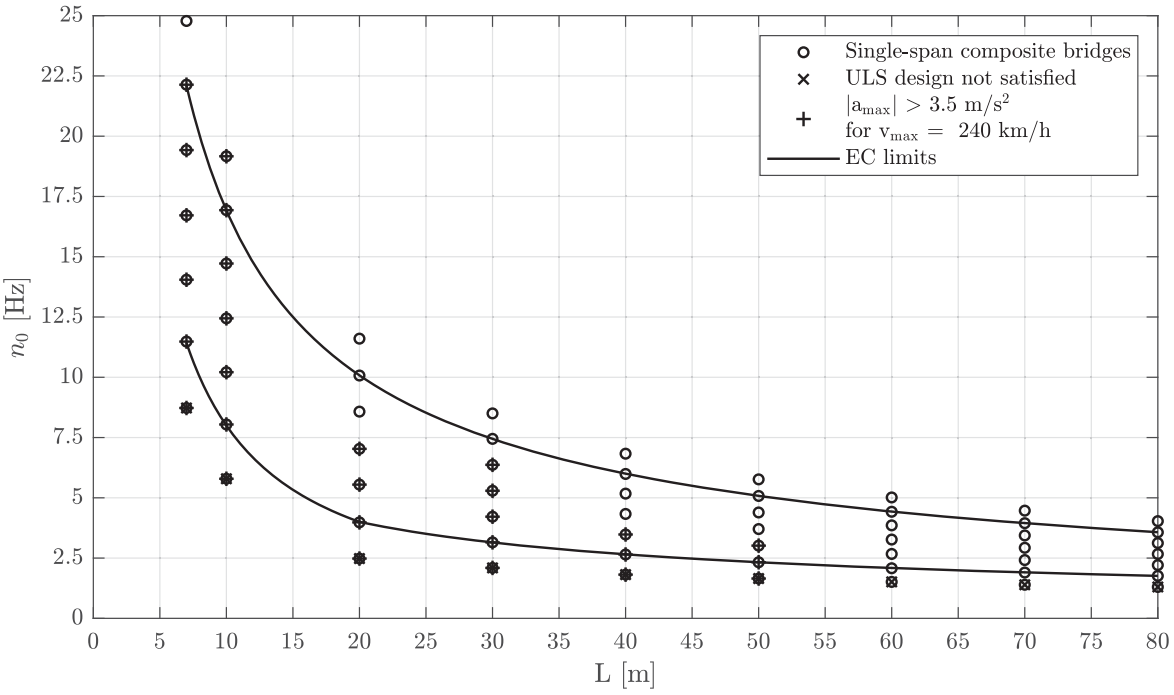

Figure C.2.: Composite bridges — suitability for high-speed railway lines — v_{max} = 240 km/h

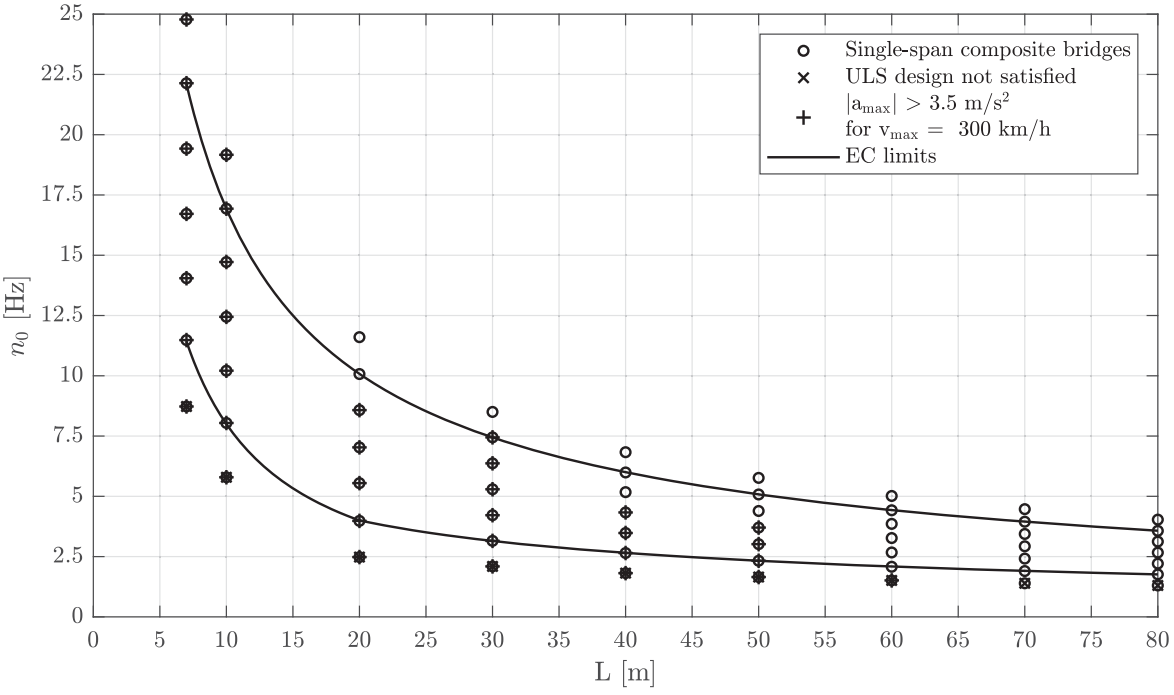

Figure C.3.: Composite bridges — suitability for high-speed railway lines — v_{max} = 300 km/h

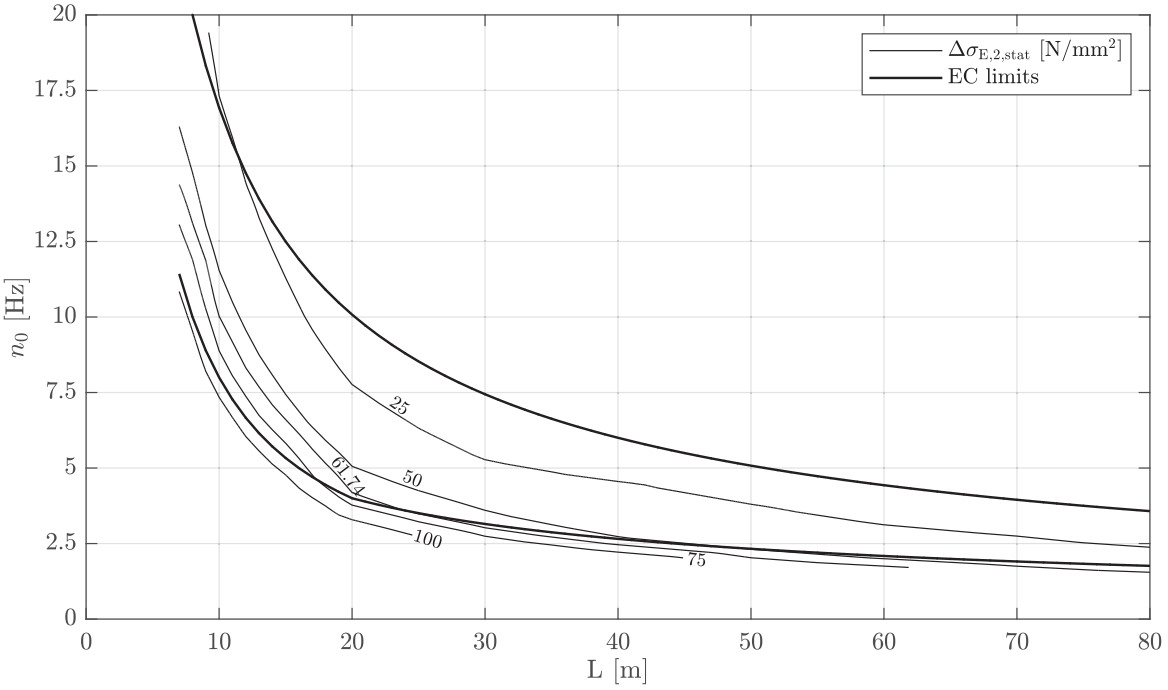

Figure C.4.: Composite bridges — $\Delta\sigma_{E,2,stat}$ due to TM1 — no load distribution

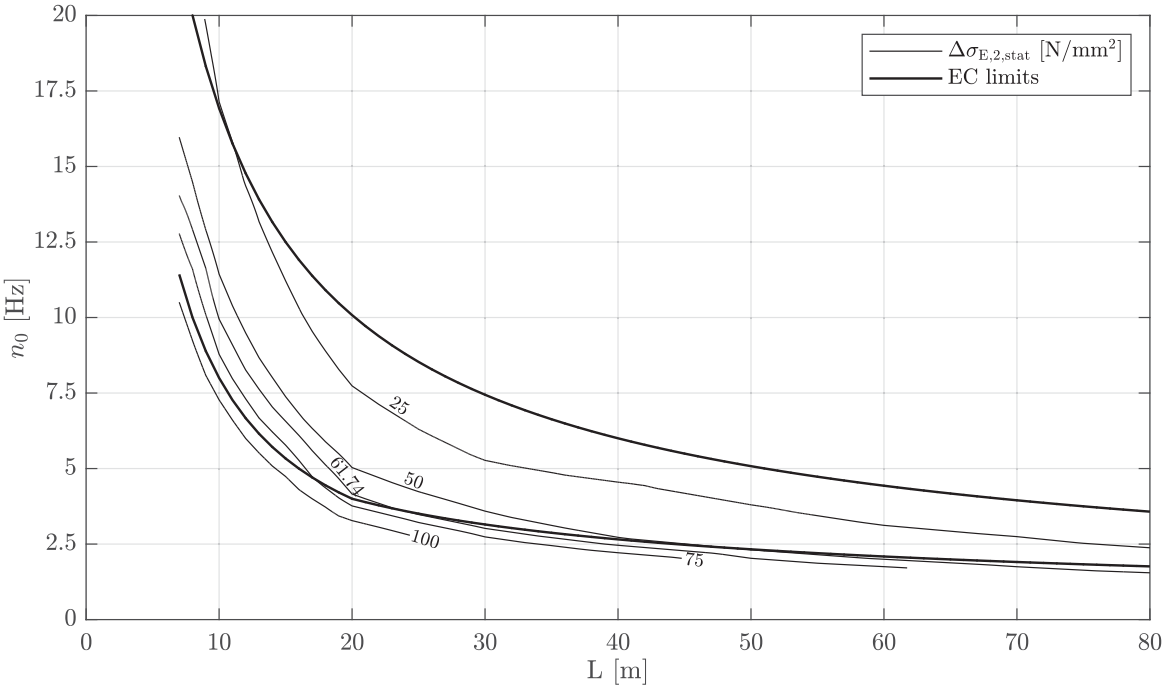

Figure C.5.: Composite bridges — $\Delta\sigma_{E,2,stat}$ due to TM1 — load distribution

C.2. Results for $|a_{HSLM-A,max}|$ of single-span composite bridges bridges due to HSLM-A

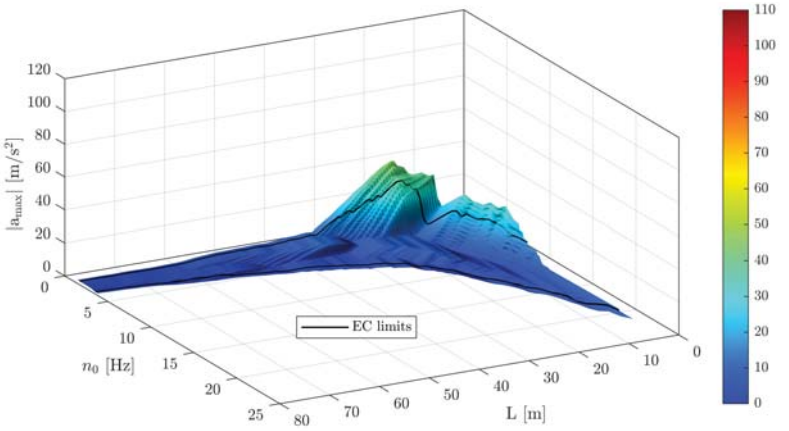

(a) 3D-view

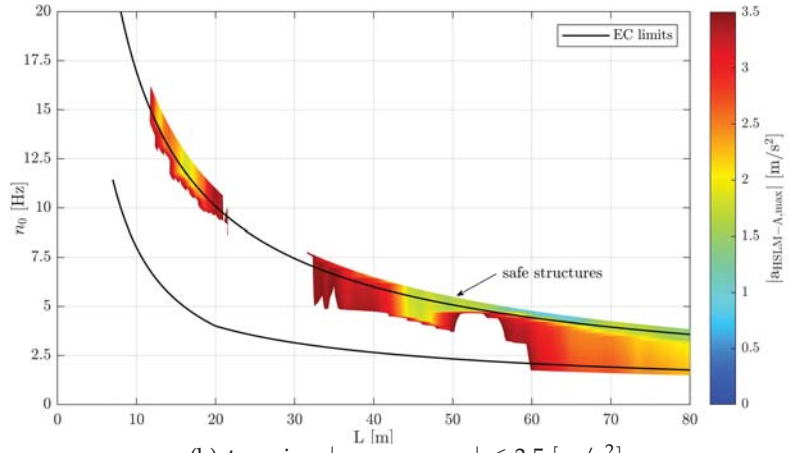

(b) top view $|a_{HSLM-A,max}| \leq 3.5$ [m/s^2]

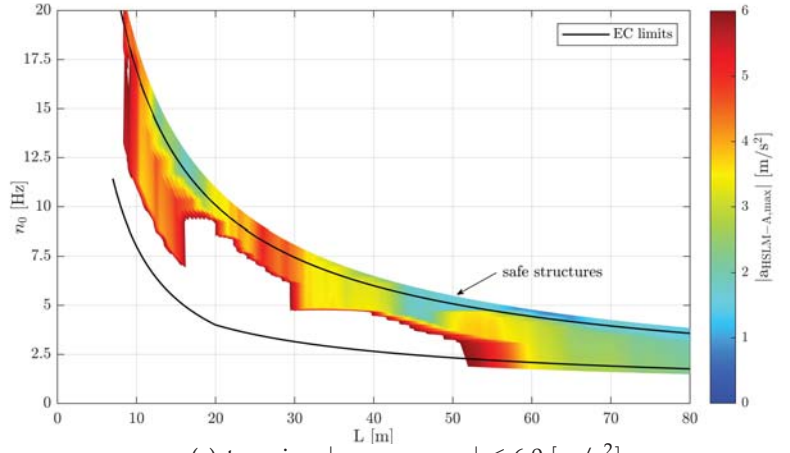

(c) top view $|a_{HSLM-A,max}| \leq 6.0$ [m/s^2]

Figure C.6.: Single-span composite bridges — vertical bridge deck acceleration $|a_{HSLM-A,max}|$ due to HSLM-A trains — v_{max} = 300 km/h — ζ_{EC} — Rayleigh like damping — no load distribution

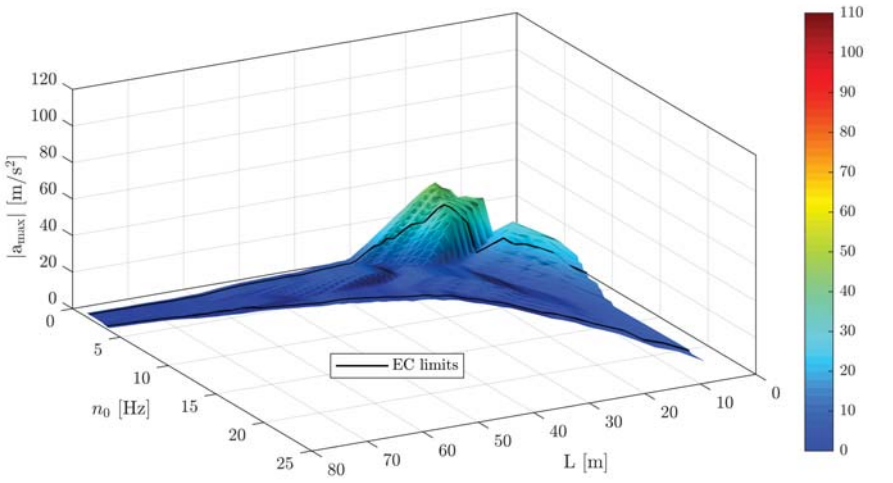

(a) 3D-view

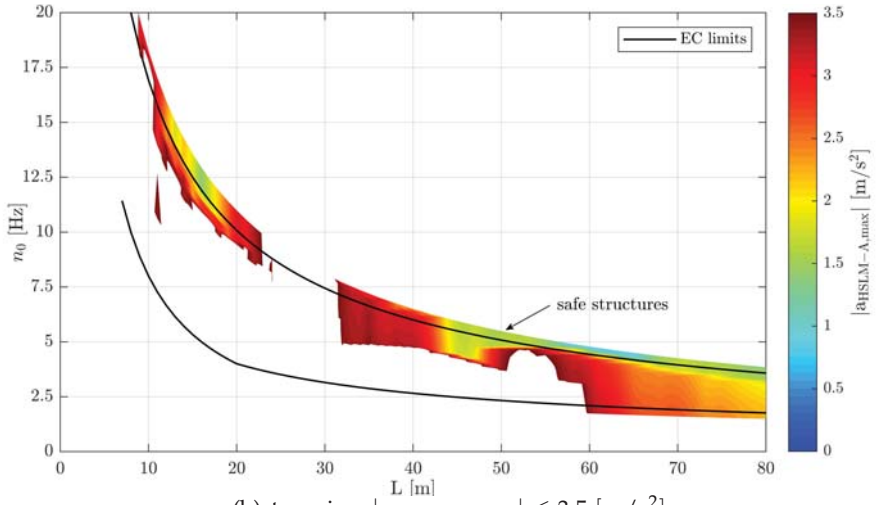

(b) top view $|a_{HSLM-A,max}| \leq 3.5$ [m/s^2]

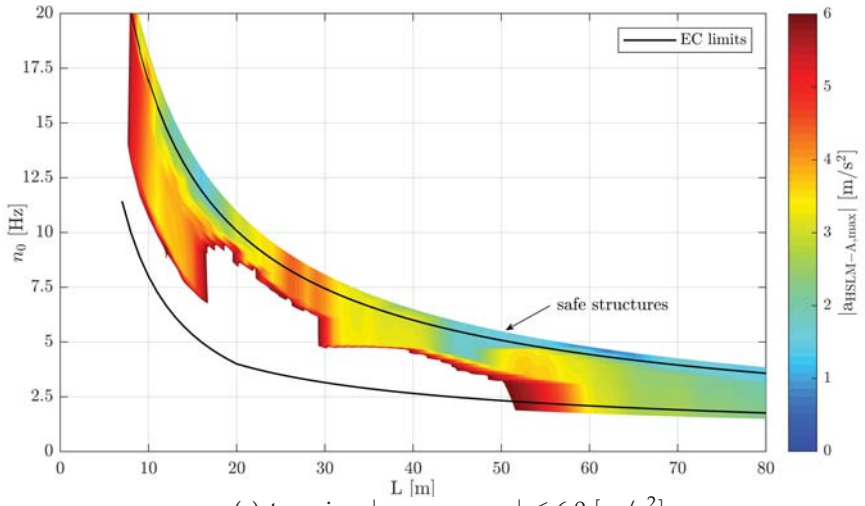

(c) top view $|a_{HSLM-A,max}| \leq 6.0$ [m/s^2]

Figure C.7.: Single-span composite bridges — vertical bridge deck acceleration $|a_{HSLM-A,max}|$ due to HSLM-A trains — v_{max} = 300 km/h — ζ_{EC} — rayleigh like damping — load distribution

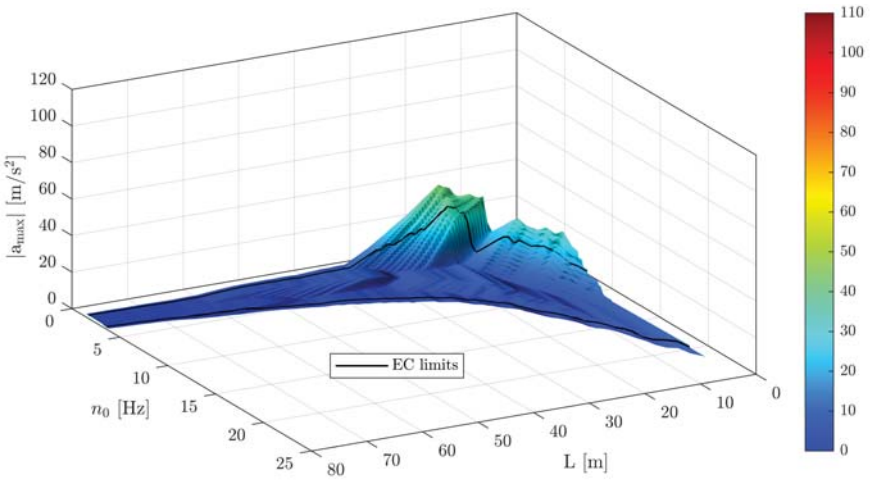

(a) 3D-view

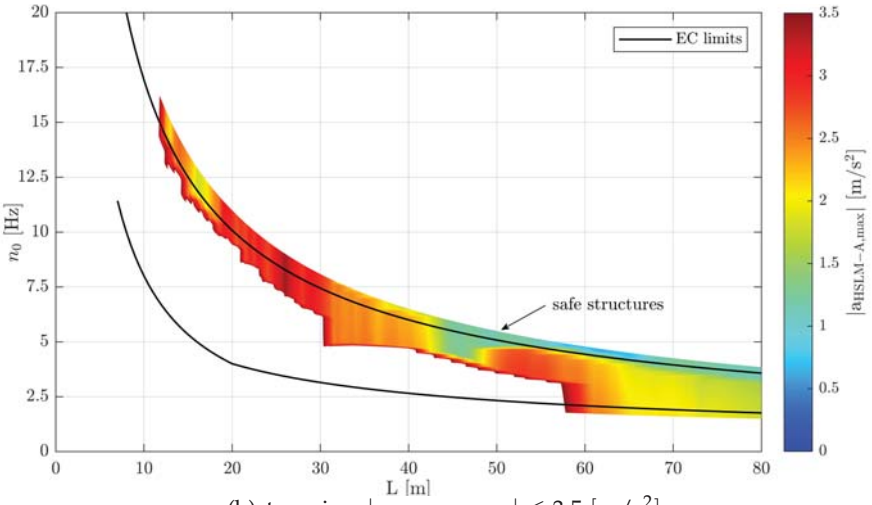

(b) top view $|a_{HSLM-A,max}| \leq 3.5$ [m/s^2]

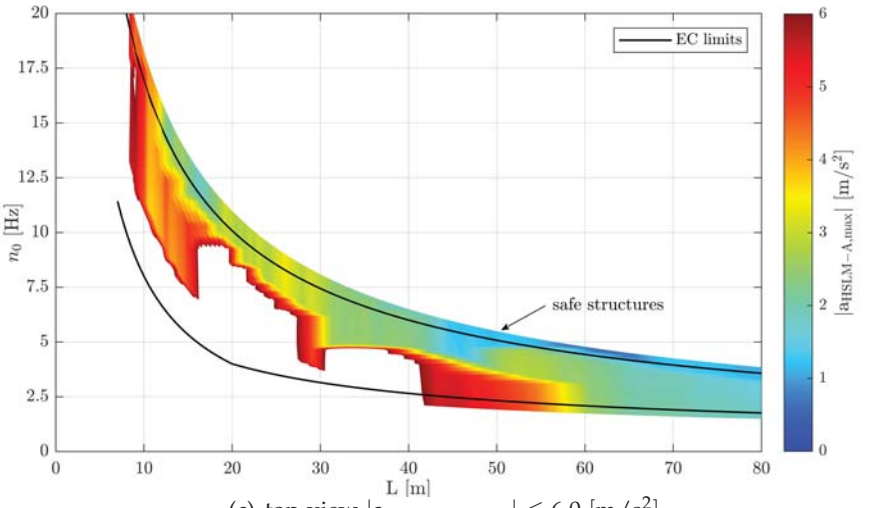

(c) top view $|a_{HSLM-A,max}| \leq 6.0$ [m/s^2]

Figure C.8.: Single-span composite bridges — vertical bridge deck acceleration $|a_{HSLM-A,max}|$ due to HSLM-A trains — v_{max} = 300 km/h — ζ_{V1} — Rayleigh like damping — no load distribution

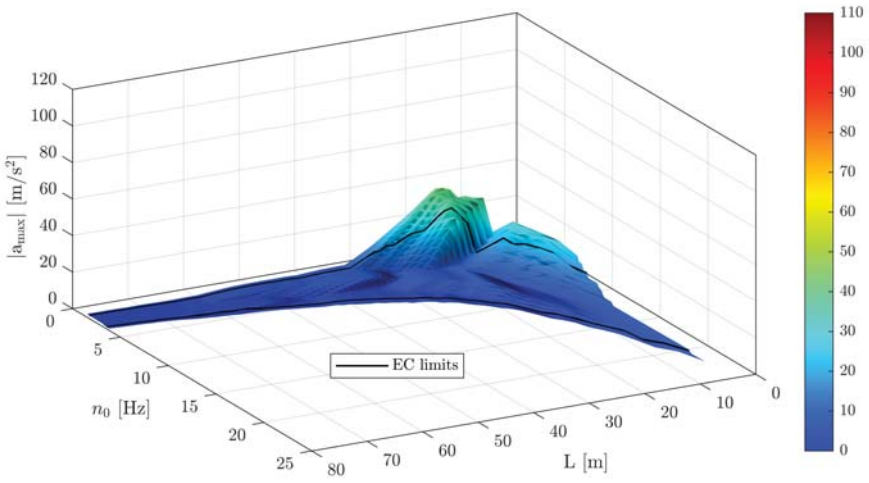

(a) 3D-view

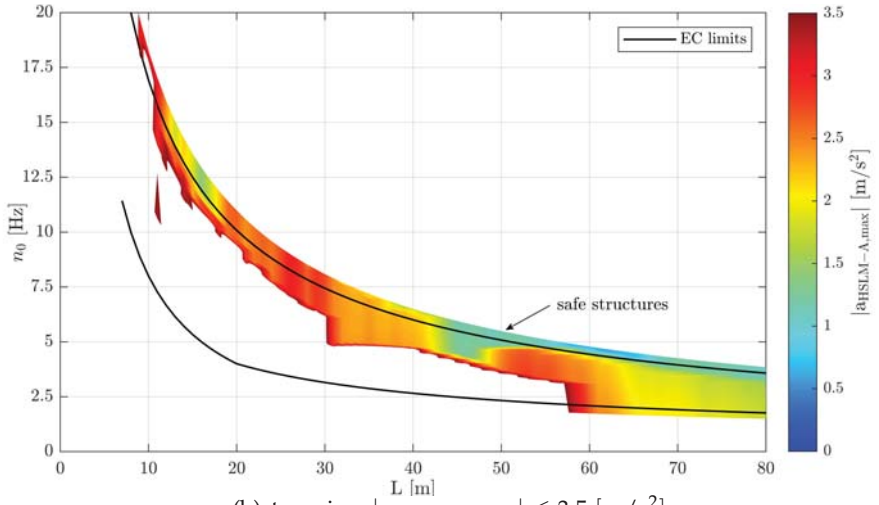

(b) top view $|a_{HSLM-A,max}| \leq 3.5$ [m/s^2]

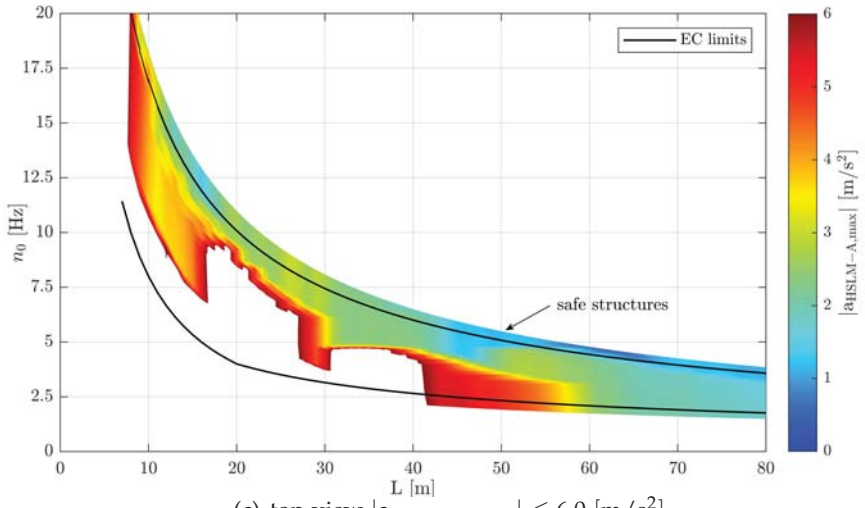

(c) top view $|a_{HSLM-A,max}| \leq 6.0$ [m/s^2]

Figure C.9.: Single-span composite bridges — vertical bridge deck acceleration $|a_{HSLM-A,max}|$ due to HSLM-A trains — v_{max} = 300 km/h — ζ_{V1} — Rayleigh like damping — with load distribution

C.3. Results for fatigue of single-span composite bridges due to TM1

C.3.1. Train speed v_{EC}

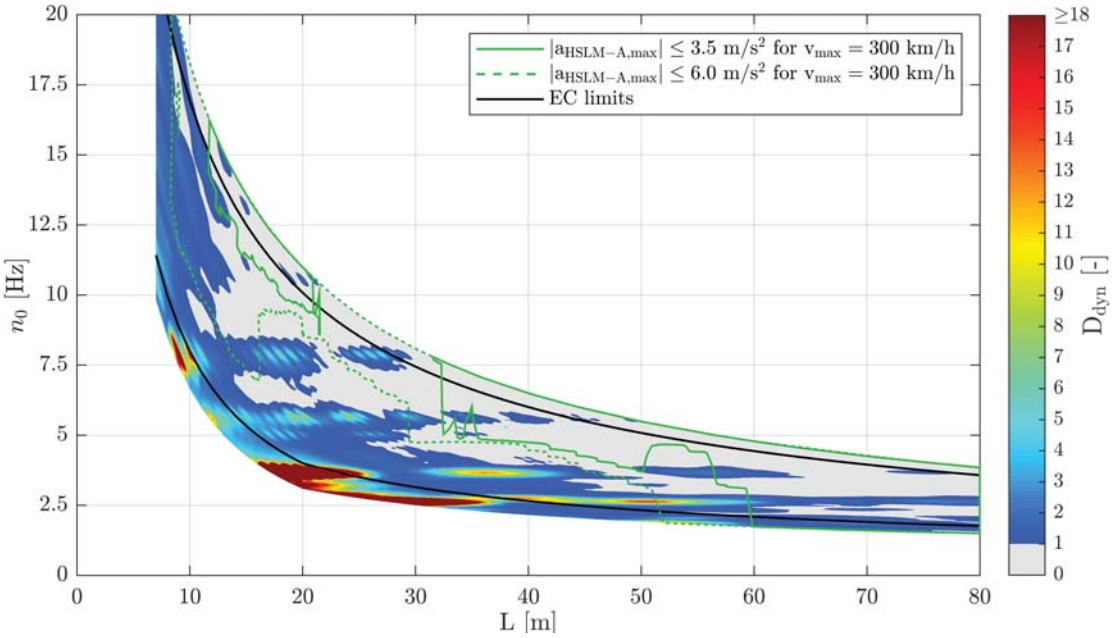

Figure C.10.: Single-span composite bridges — traffic mix TM1* — v_{EC} — ζ_{EC} — Rayleigh like damping — no load distribution — top view D_{dyn} & $|a_{HSLM-A,max}|$

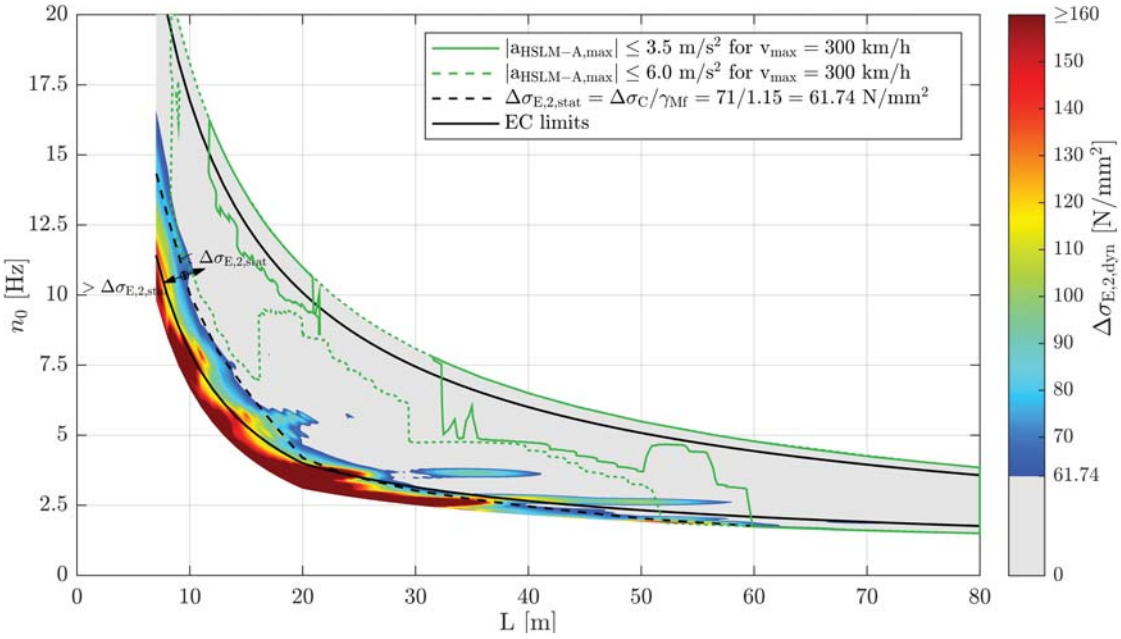

Figure C.11.: Single-span composite bridges — traffic mix TM1* — v_{EC} — ζ_{EC} — Rayleigh like damping — no load distribution — top view $\Delta\sigma_{E,2,dyn}$ & $|a_{HSLM-A,max}|$ & $\Delta\sigma_{E,2,stat}$

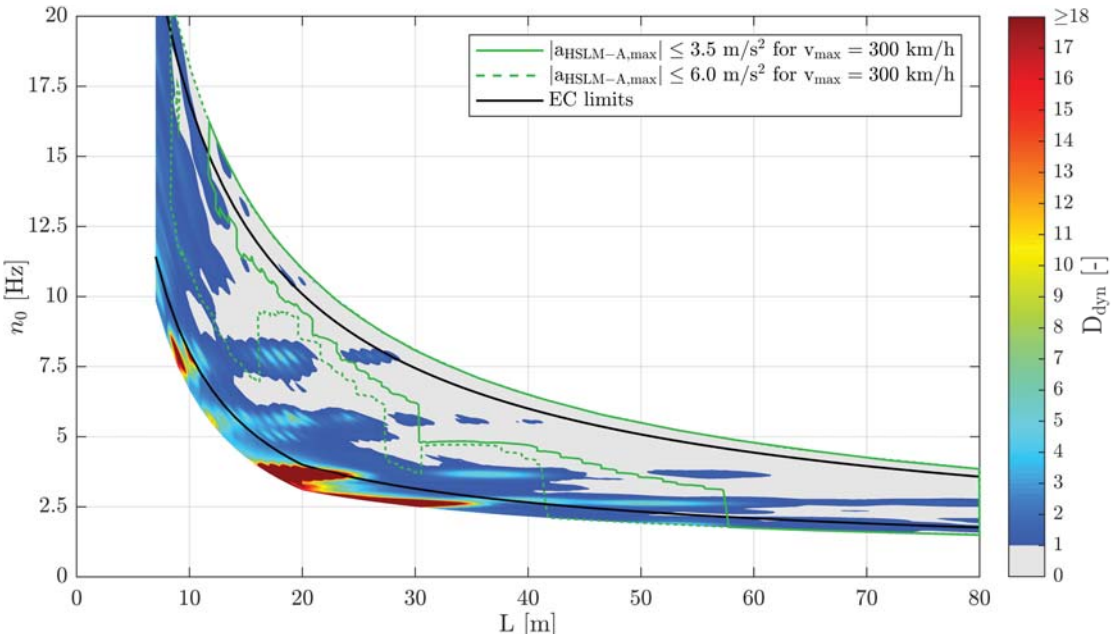

Figure C.12.: Single-span composite bridges — traffic mix TM1* — v_{EC} — ζ_{V1} — Rayleigh like damping — no load distribution — top view D_{dyn} & $|a_{HSLM-A,max}|$

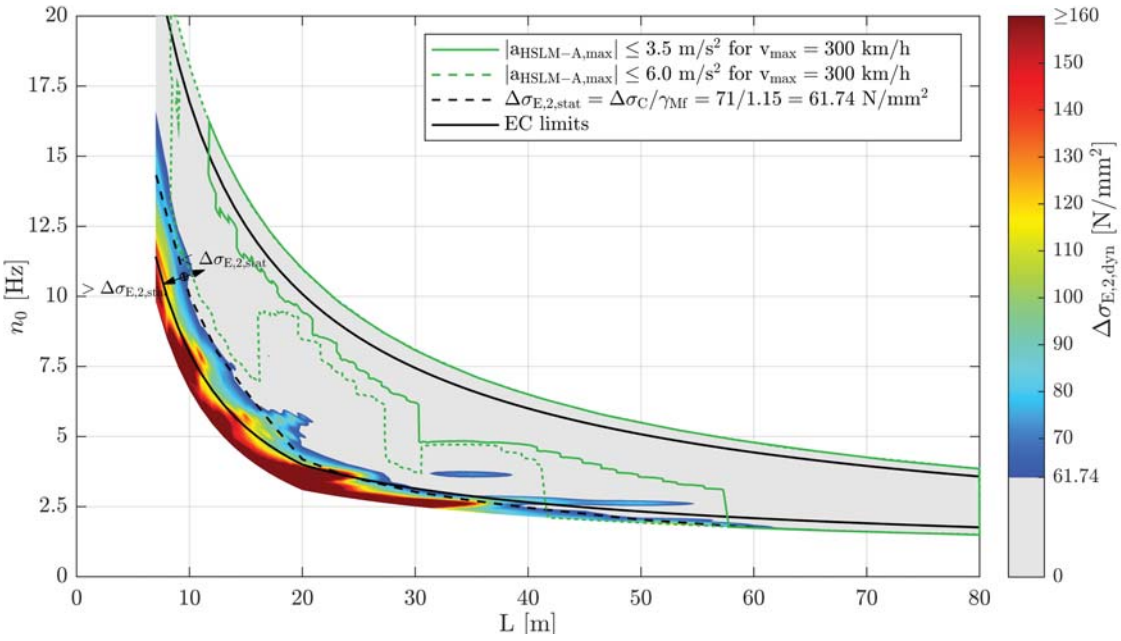

Figure C.13.: Single-span composite bridges — traffic mix TM1* — v_{EC} — ζ_{V1} — Rayleigh like damping — no load distribution — top view $\Delta\sigma_{E,2,dyn}$ & $|a_{HSLM-A,max}|$ & $\Delta\sigma_{E,2,stat}$

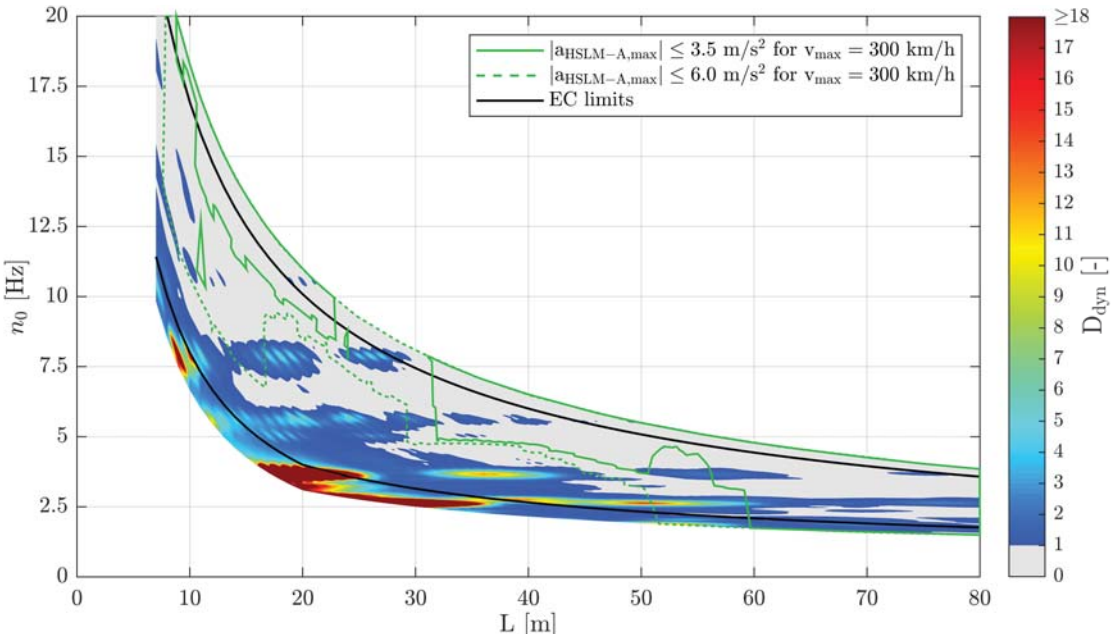

Figure C.14.: Single-span composite bridges — traffic mix TM1* — v_{EC} — ζ_{EC} — Rayleigh like damping — load distribution — top view D_{dyn} & $|a_{HSLM-A,max}|$

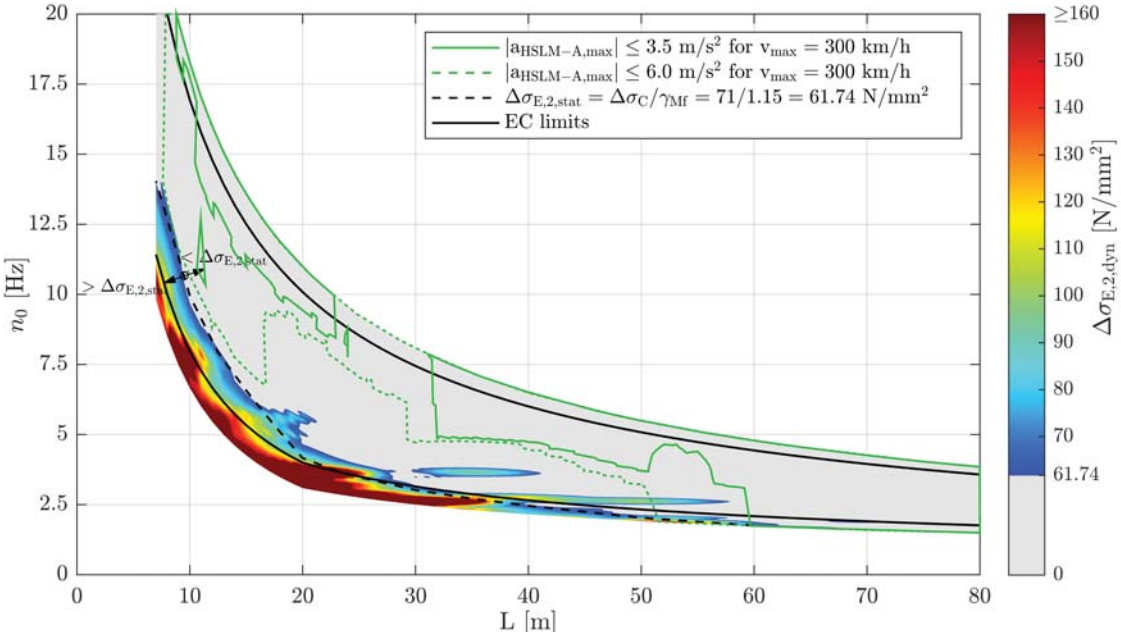

Figure C.15.: Single-span composite bridges — traffic mix TM1* — v_{EC} — ζ_{EC} — Rayleigh like damping — load distribution — top view $\Delta\sigma_{E,2,dyn}$ & $|a_{HSLM-A,max}|$ & $\Delta\sigma_{E,2,stat}$

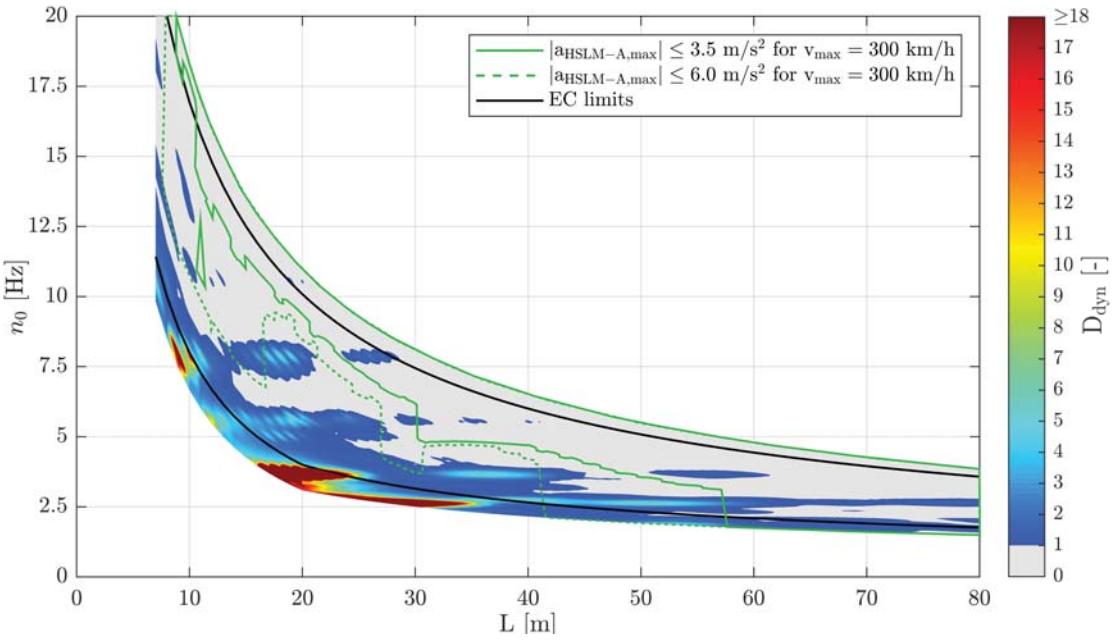

Figure C.16.: Single-span composite bridges — traffic mix TM1* — v_{EC} — ζ_{V1} — Rayleigh like damping — load distribution — top view D_{dyn} & $|a_{HSLM-A,max}|$

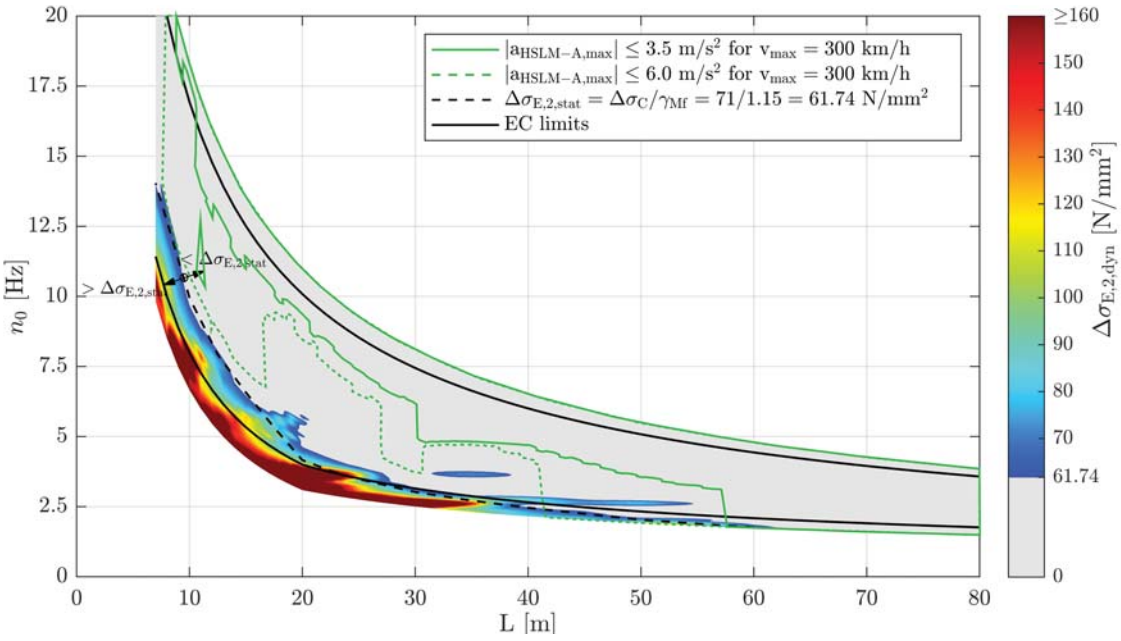

Figure C.17.: Single-span composite bridges — traffic mix TM1* — v_{EC} — ζ_{V1} — Rayleigh like damping — load distribution — top view $\Delta\sigma_{E,2,dyn}$ & $|a_{HSLM-A,max}|$ & $\Delta\sigma_{E,2,stat}$

C.3.2. Train speed $v_{D_{max}}$

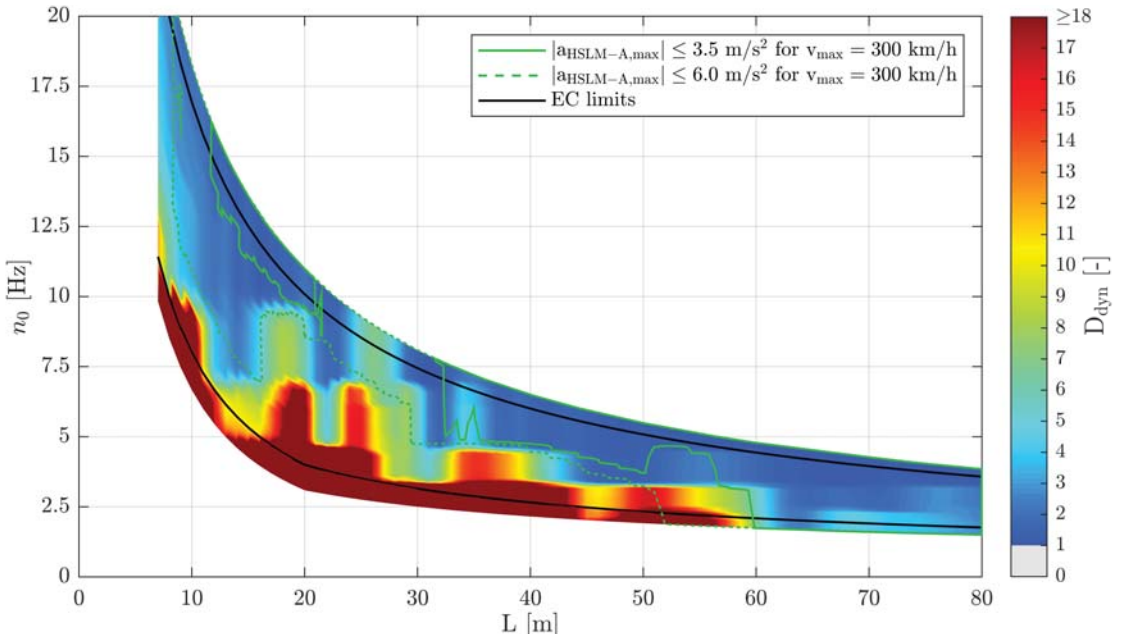

Figure C.18.: Single-span composite bridges — traffic mix TM1** — $v_{D_{max}}$ — ζ_{EC} — Rayleigh like damping — no load distribution — top view D_{dyn} & $|a_{HSLM-A,max}|$

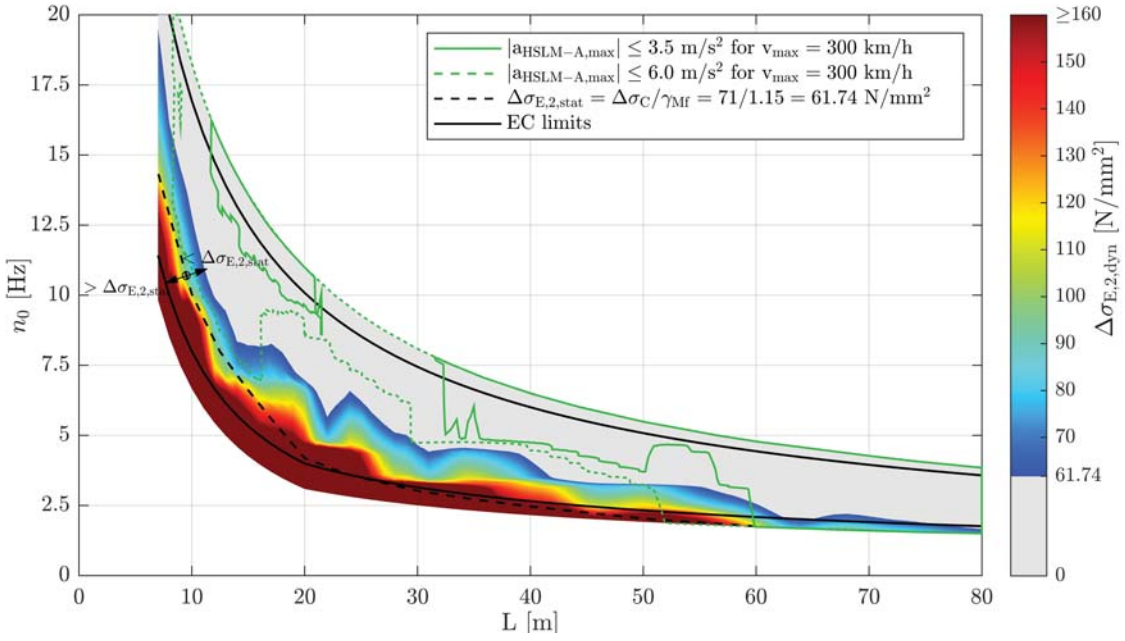

Figure C.19.: Single-span composite bridges — traffic mix TM1** — $v_{D_{max}}$ — ζ_{EC} — Rayleigh like damping — no load distribution — top view $\Delta\sigma_{E,2,dyn}$ & $|a_{HSLM-A,max}|$ & $\Delta\sigma_{E,2,stat}$

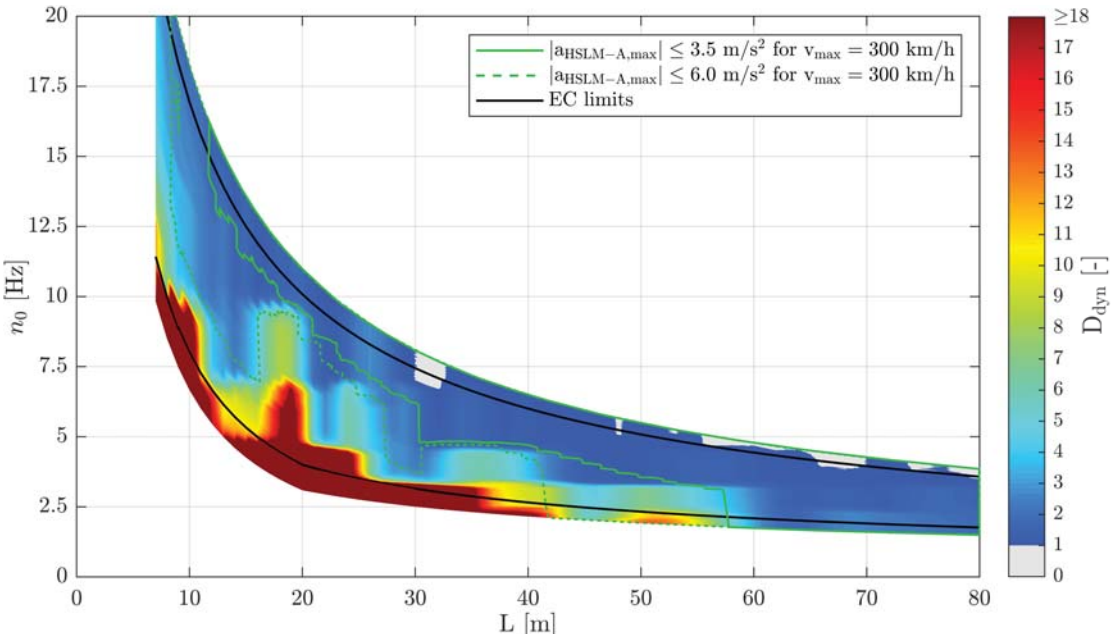

Figure C.20.: Single-span composite bridges — traffic mix TM1** — $v_{D_{max}}$ — ζ_{V1} — Rayleigh like damping — no load distribution — top view D_{dyn} & $|a_{HSLM-A,max}|$

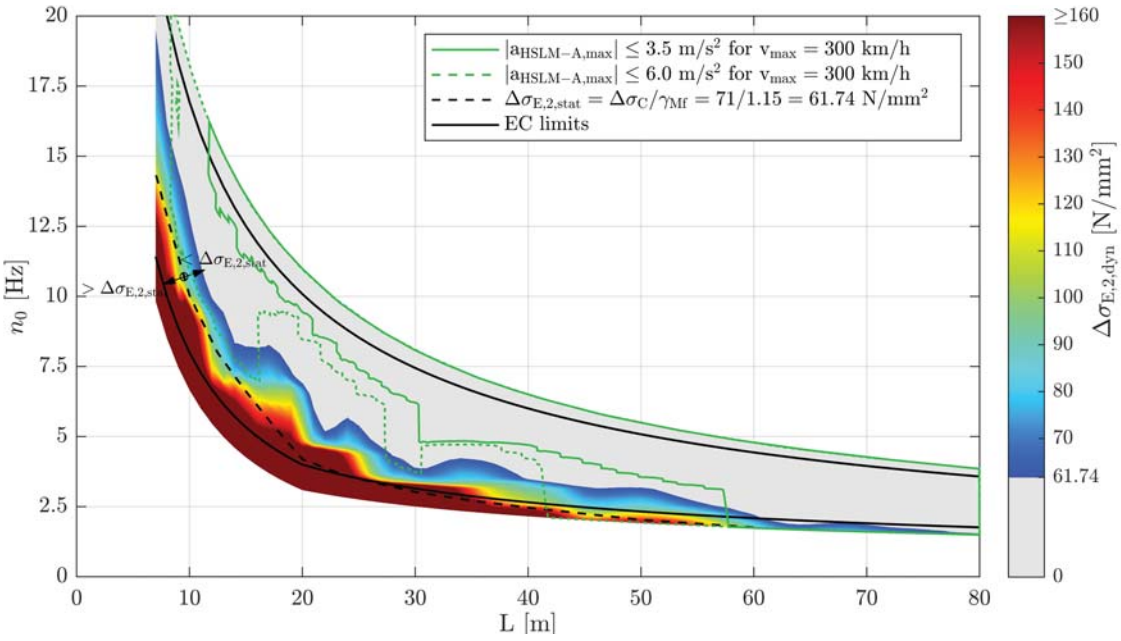

Figure C.21.: Single-span composite bridges — traffic mix TM1** — $v_{D_{max}}$ — ζ_{V1} — Rayleigh like damping — no load distribution — top view $\Delta\sigma_{E,2,dyn}$ & $|a_{HSLM-A,max}|$ & $\Delta\sigma_{E,2,stat}$

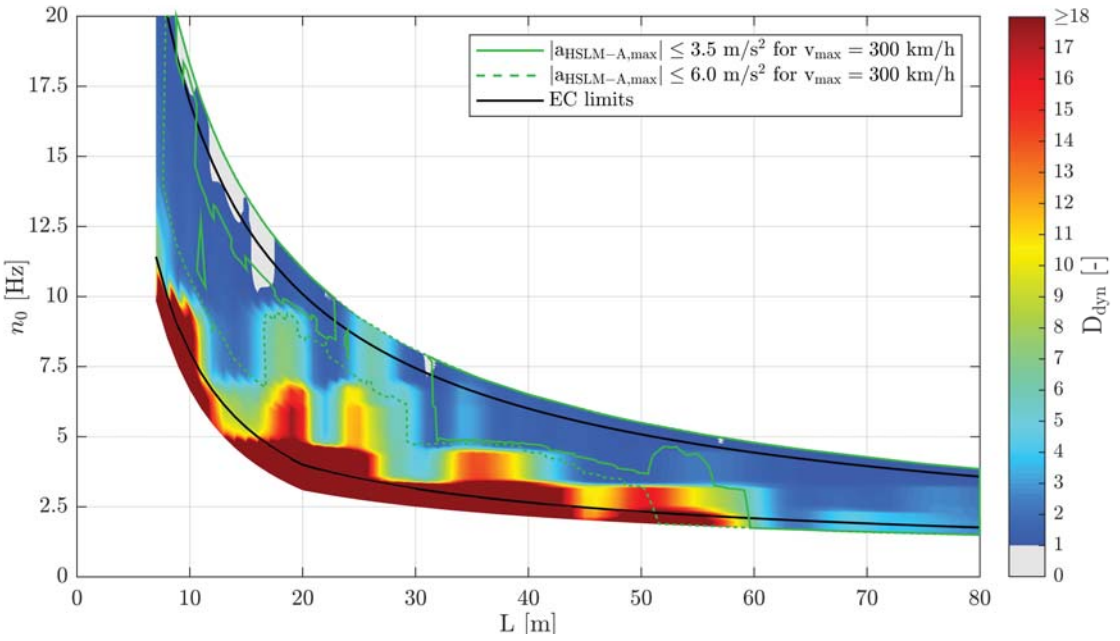

Figure C.22.: Single-span composite bridges — traffic mix TM1** — $v_{D_{max}}$ — ζ_{EC} — Rayleigh like damping — load distribution — top view D_{dyn} & $|a_{HSLM-A,max}|$

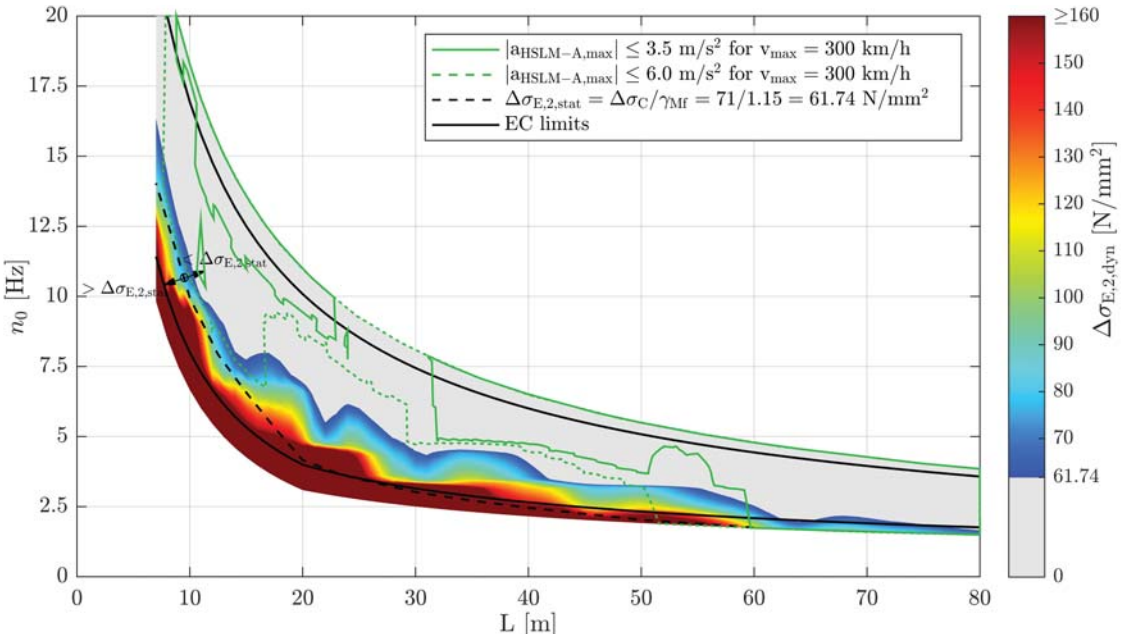

Figure C.23.: Single-span composite bridges — traffic mix TM1** — $v_{D_{max}}$ — ζ_{EC} — Rayleigh like damping — load distribution — top view $\Delta\sigma_{E,2,dyn}$ & $|a_{HSLM-A,max}|$ & $\Delta\sigma_{E,2,stat}$

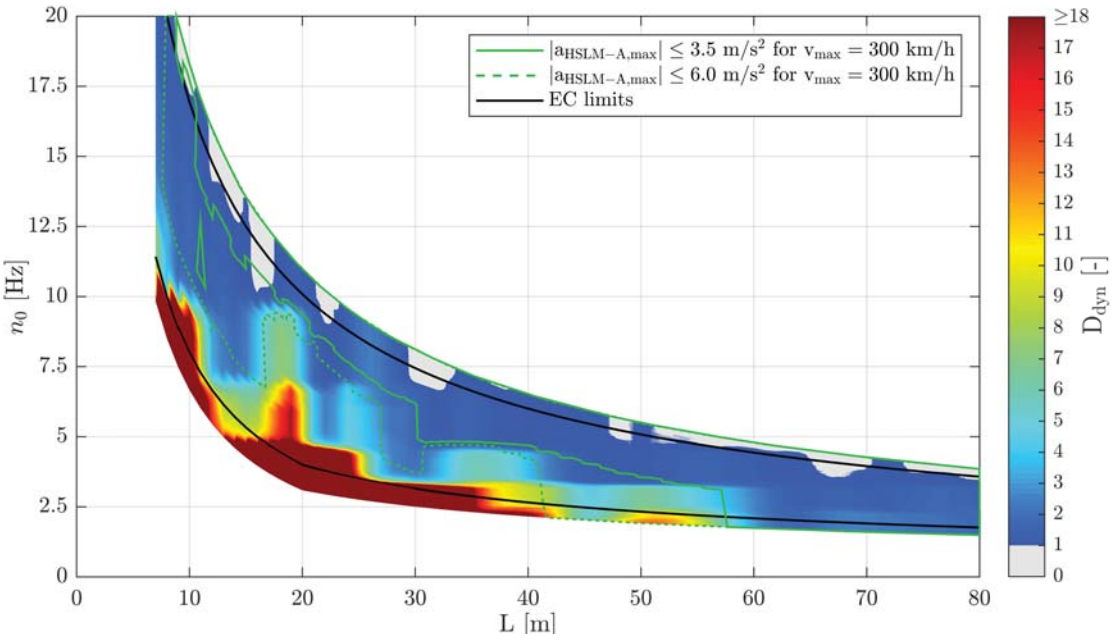

Figure C.24.: Single-span composite bridges — traffic mix TM1** — $v_{D_{max}}$ — ζ_{V1} — Rayleigh like damping — load distribution — top view D_{dyn} & $|a_{HSLM-A,max}|$

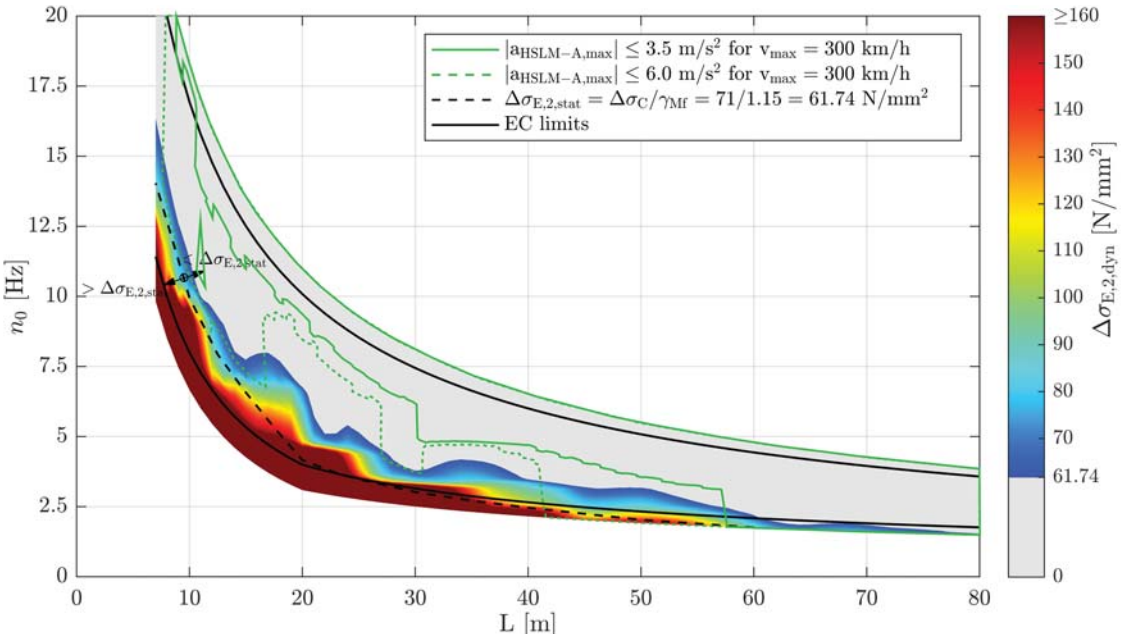

Figure C.25.: Single-span composite bridges — traffic mix TM1** — $v_{D_{max}}$ — ζ_{V1} — Rayleigh like damping — load distribution — top view $\Delta\sigma_{E,2,dyn}$ & $|a_{HSLM-A,max}|$ & $\Delta\sigma_{E,2,stat}$

C.3.3. Train speed $v_{a_{max}}$

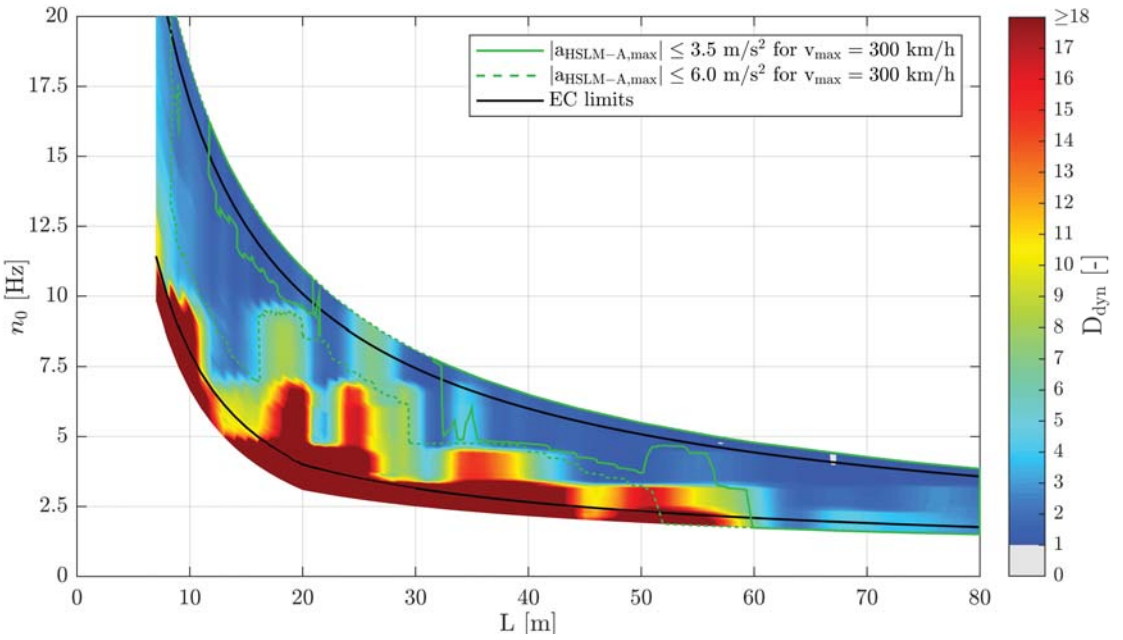

Figure C.26.: Single-span composite bridges — traffic mix TM1*** — $v_{a_{max}}$ — ζ_{EC} — Rayleigh like damping — no load distribution — top view D_{dyn} & $|a_{HSLM-A,max}|$

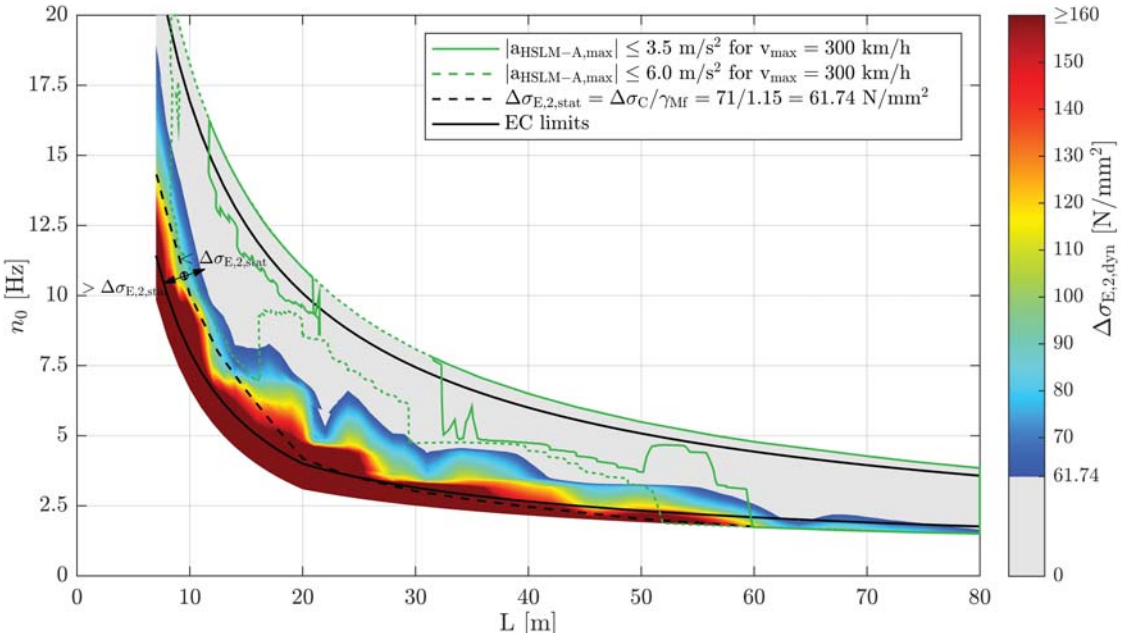

Figure C.27.: Single-span composite bridges — traffic mix TM1*** — $v_{a_{max}}$ — ζ_{EC} — Rayleigh like damping — no load distribution — top view $\Delta\sigma_{E,2,dyn}$ & $|a_{HSLM-A,max}|$ & $\Delta\sigma_{E,2,stat}$

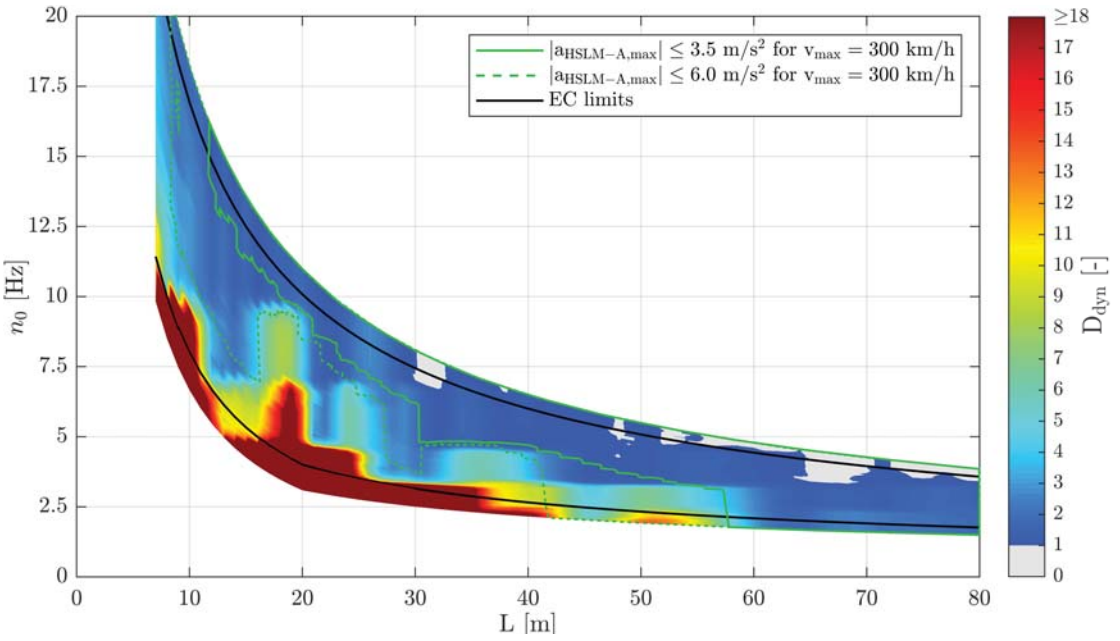

Figure C.28.: Single-span composite bridges — traffic mix TM1*** — $v_{a_{max}}$ — ζ_{V1} — Rayleigh like damping — no load distribution — top view D_{dyn} & $|a_{HSLM-A,max}|$

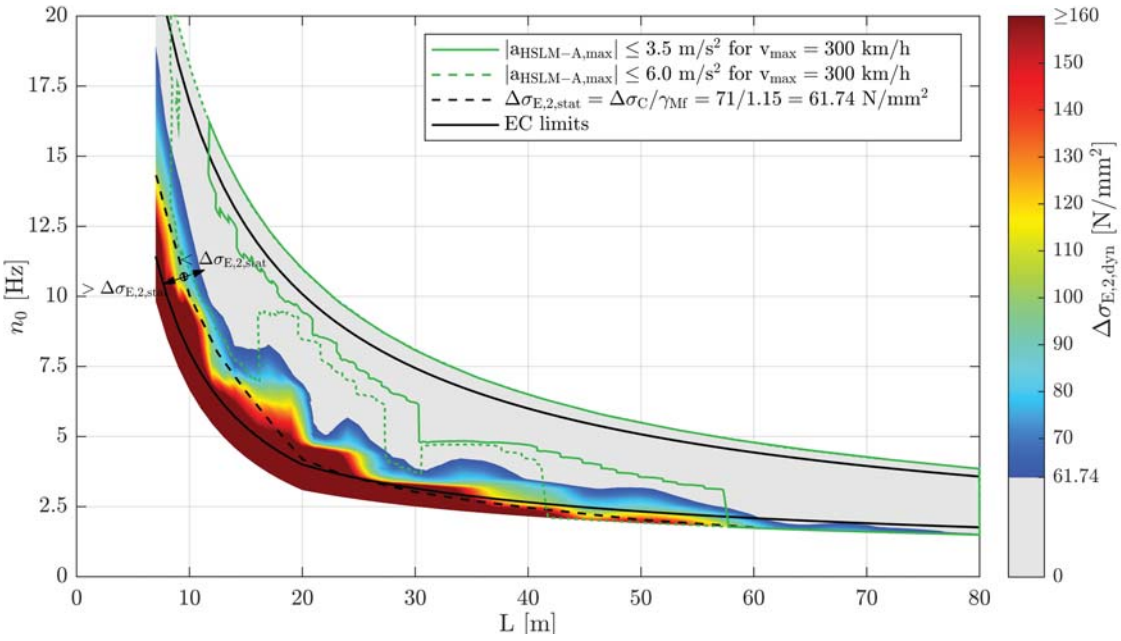

Figure C.29.: Single-span composite bridges — traffic mix TM1*** — $v_{a_{max}}$ — ζ_{V1} — Rayleigh like damping — no load distribution — top view $\Delta\sigma_{E,2,dyn}$ & $|a_{HSLM-A,max}|$ & $\Delta\sigma_{E,2,stat}$

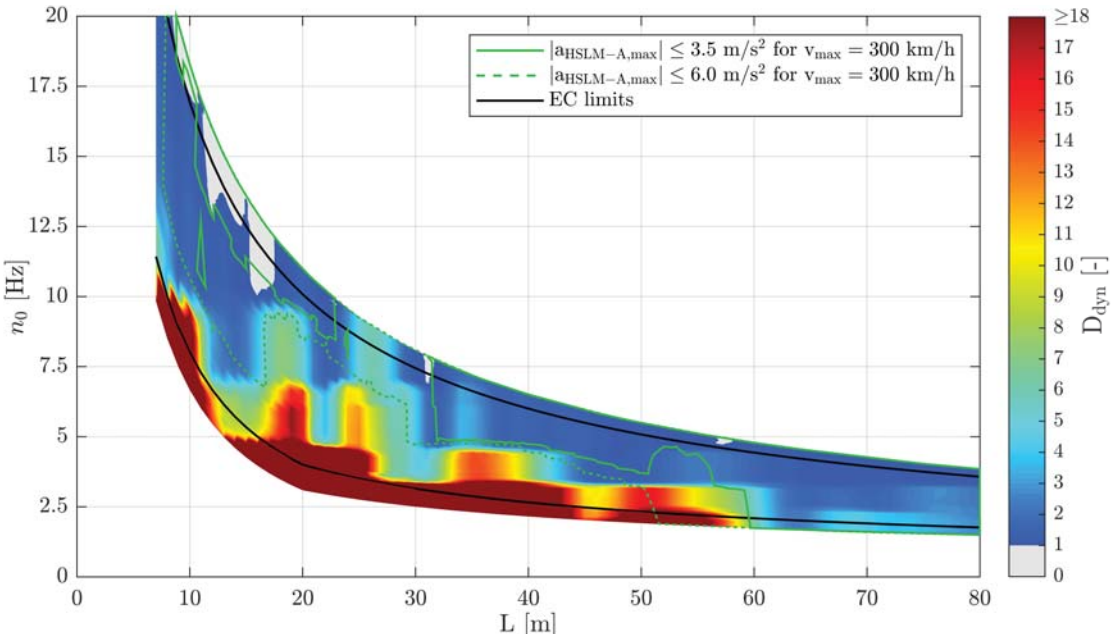

Figure C.30.: Single-span composite bridges — traffic mix TM1*** — $v_{a_{max}}$ — ζ_{EC} — Rayleigh like damping — load distribution — top view D_{dyn} & $|a_{HSLM-A,max}|$

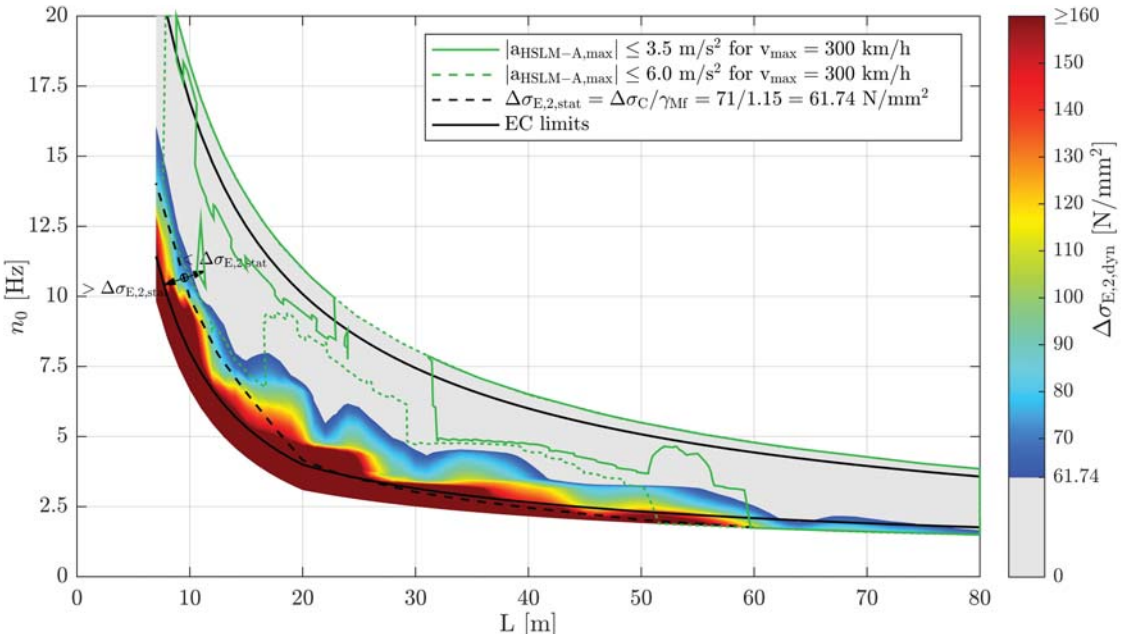

Figure C.31.: Single-span composite bridges — traffic mix TM1*** — $v_{a_{max}}$ — ζ_{EC} — Rayleigh like damping — load distribution — top view $\Delta\sigma_{E,2,dyn}$ & $|a_{HSLM-A,max}|$ & $\Delta\sigma_{E,2,stat}$

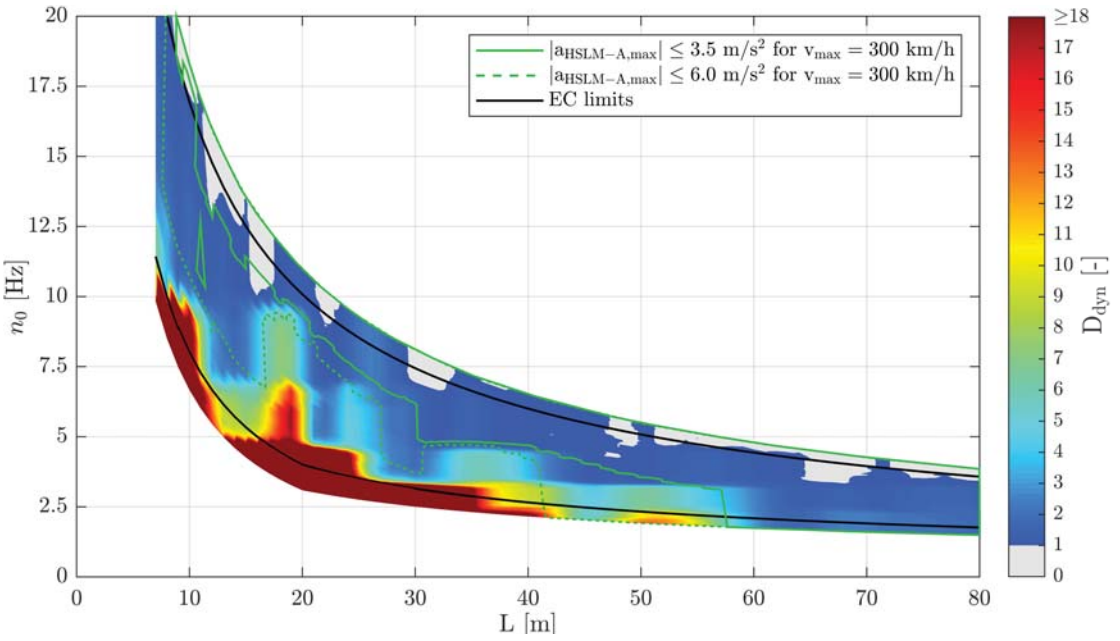

Figure C.32.: Single-span composite bridges — traffic mix TM1*** — $v_{a_{max}}$ — ζ_{V1} — Rayleigh like damping — load distribution — top view D_{dyn} & $|a_{HSLM-A,max}|$

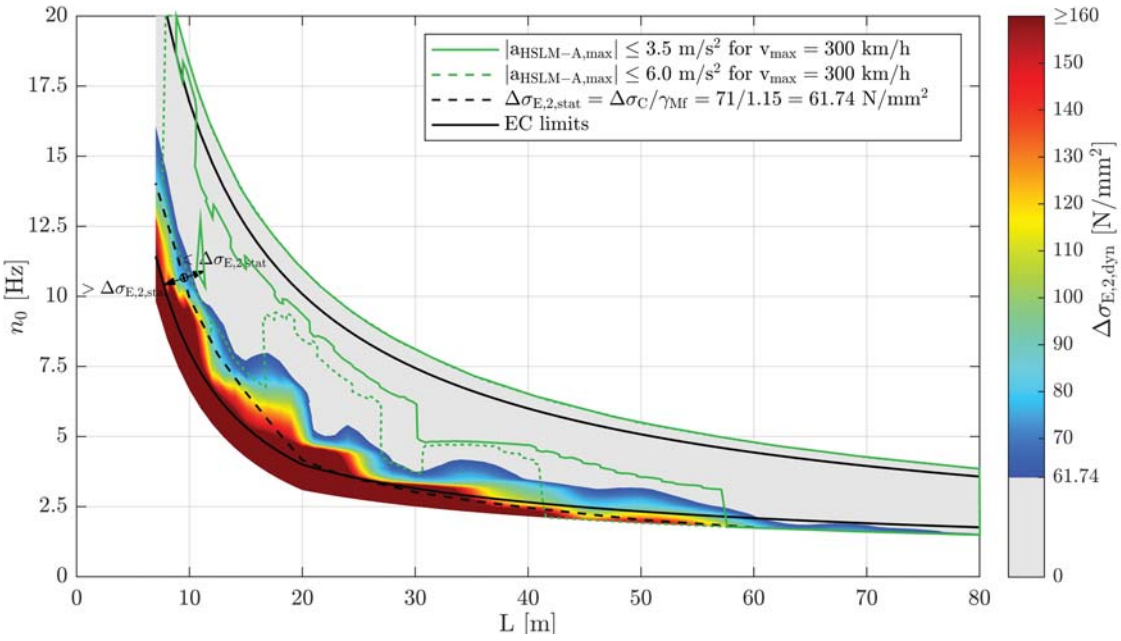

Figure C.33.: Single-span composite bridges — traffic mix TM1*** — $v_{a_{max}}$ — ζ_{V1} — Rayleigh like damping — load distribution — top view $\Delta\sigma_{E,2,dyn}$ & $|a_{HSLM-A,max}|$ & $\Delta\sigma_{E,2,stat}$

C.4. Results of single-span composite bridges due to TM2

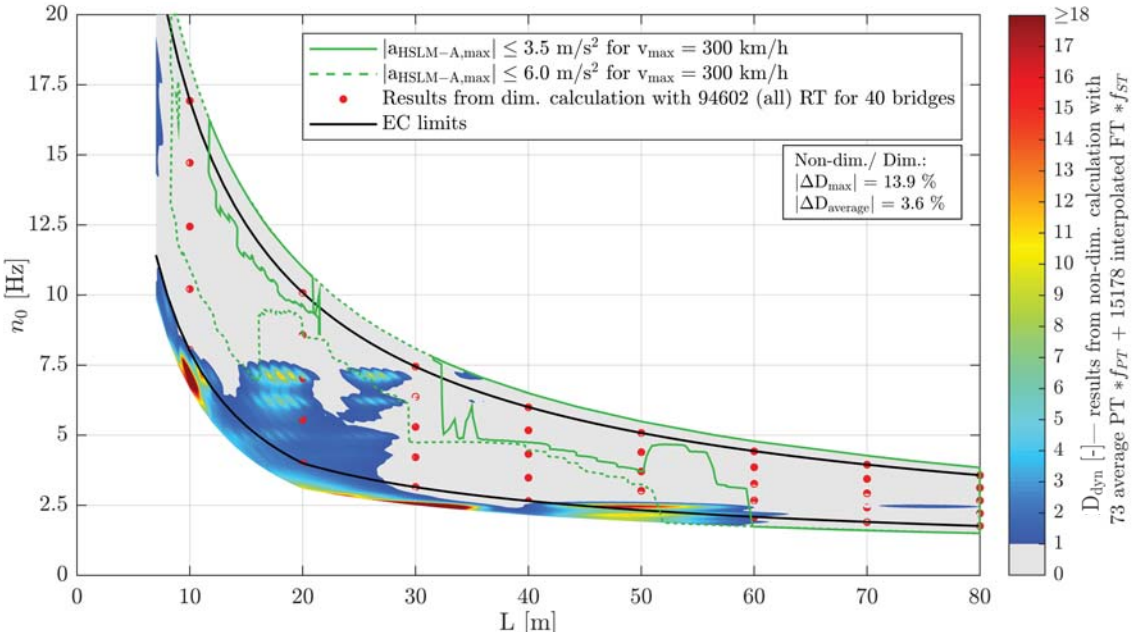

Figure C.34.: Single-span composite bridges — traffic mix TM2-st — ζ_{EC} — Rayleigh like damping — no load distribution — top view D_{dyn} & $|a_{HSLM-A,max}|$

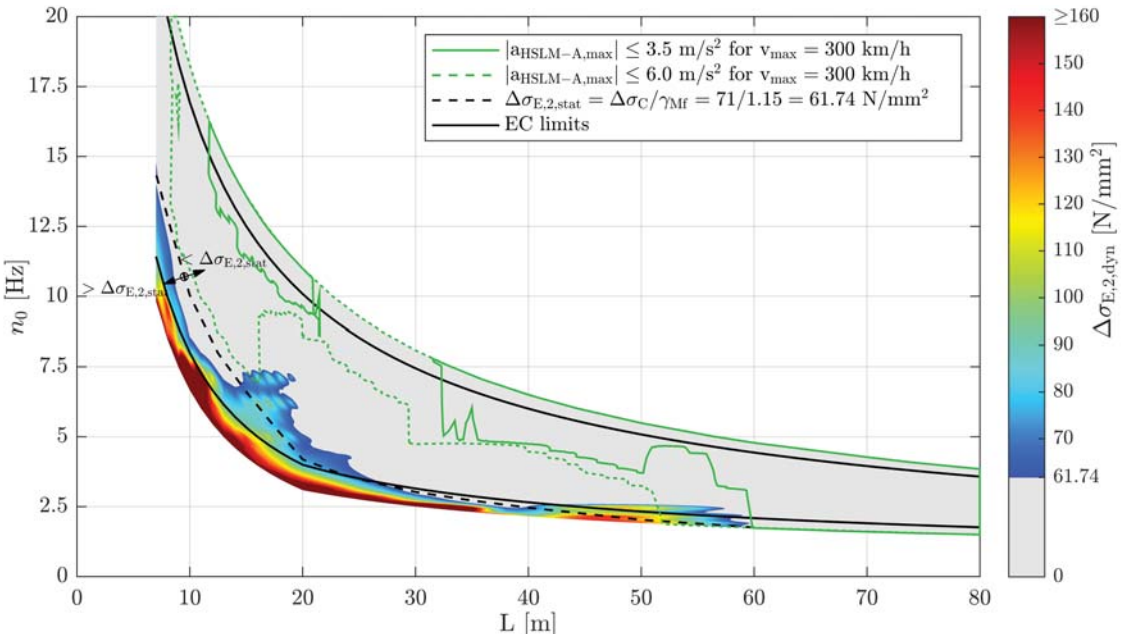

Figure C.35.: Single-span composite bridges — traffic mix TM2-st — ζ_{EC} — Rayleigh like damping — no load distribution — top view $\Delta\sigma_{E,2,dyn}$ & $|a_{HSLM-A,max}|$ & $\Delta\sigma_{E,2,stat}$

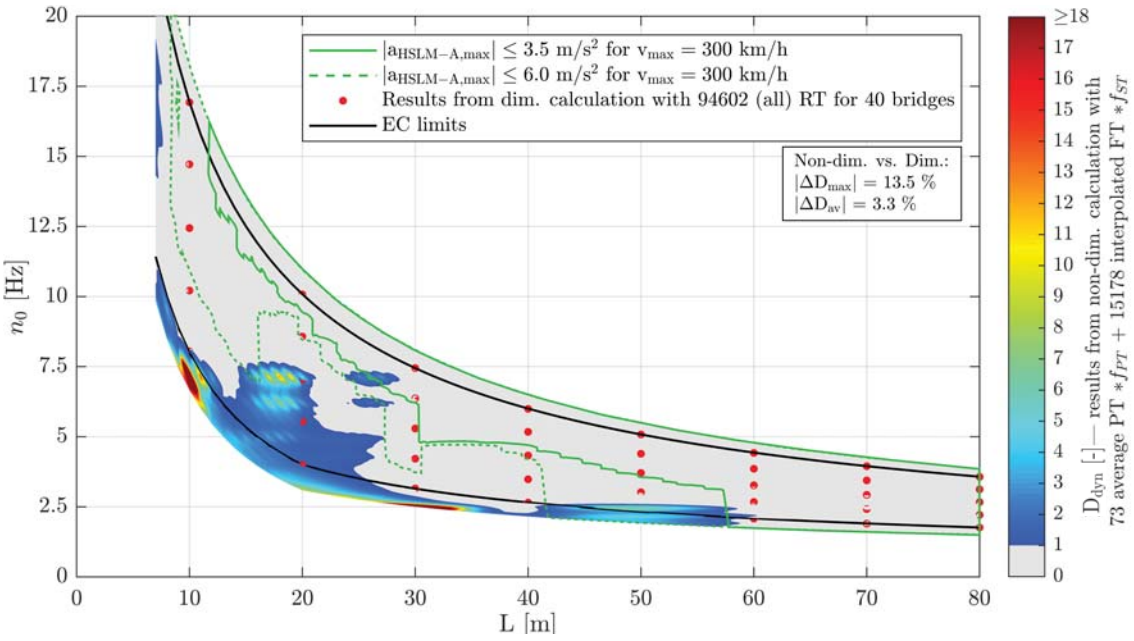

Figure C.36.: Single-span composite bridges — traffic mix TM2-st — ζ_{V1} — Rayleigh like damping — no load distribution — top view D_{dyn} & $|a_{HSLM-A,max}|$

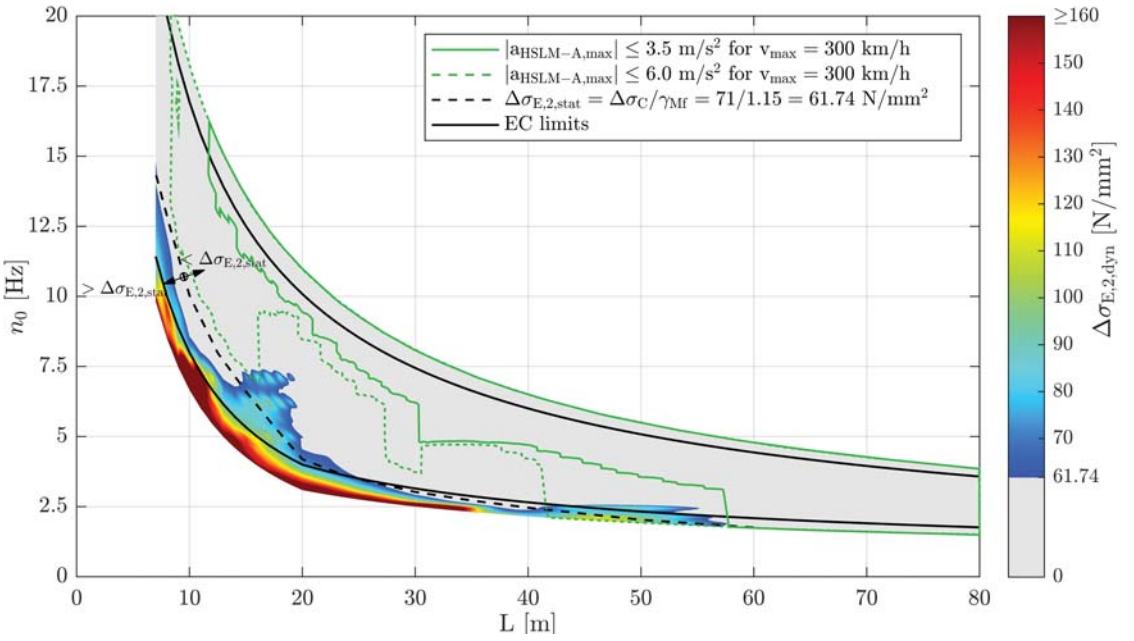

Figure C.37.: Single-span composite bridges — traffic mix TM2-st — ζ_{V1} — Rayleigh like damping — no load distribution — top view $\Delta\sigma_{E,2,dyn}$ & $|a_{HSLM-A,max}|$ & $\Delta\sigma_{E,2,stat}$

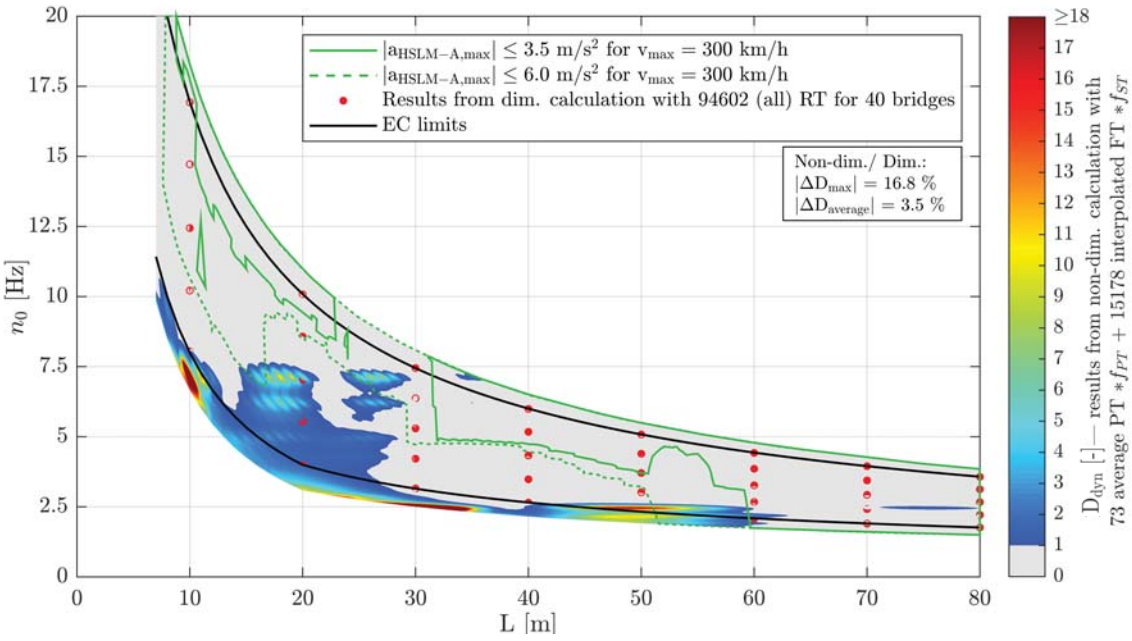

Figure C.38.: Single-span composite bridges — traffic mix TM2-st — ζ_{EC} — Rayleigh like damping — load distribution — top view D_{dyn} & $|a_{HSLM-A,max}|$

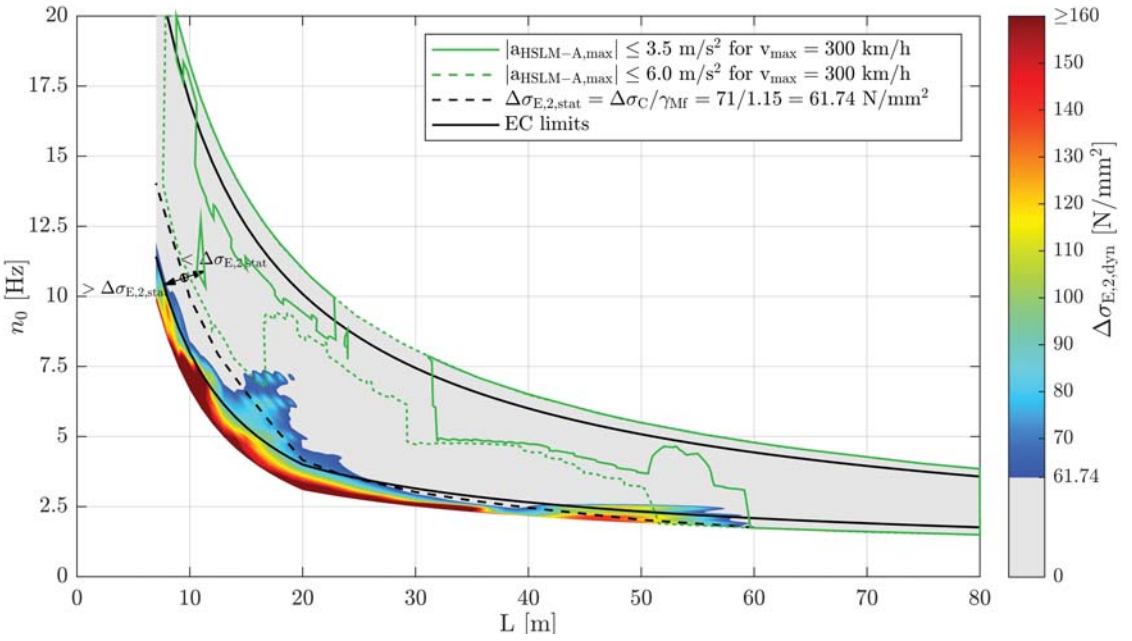

Figure C.39.: Single-span composite bridges — traffic mix TM2-st — ζ_{EC} — Rayleigh like damping — load distribution — top view $\Delta\sigma_{E,2,dyn}$ & $|a_{HSLM-A,max}|$ & $\Delta\sigma_{E,2,stat}$

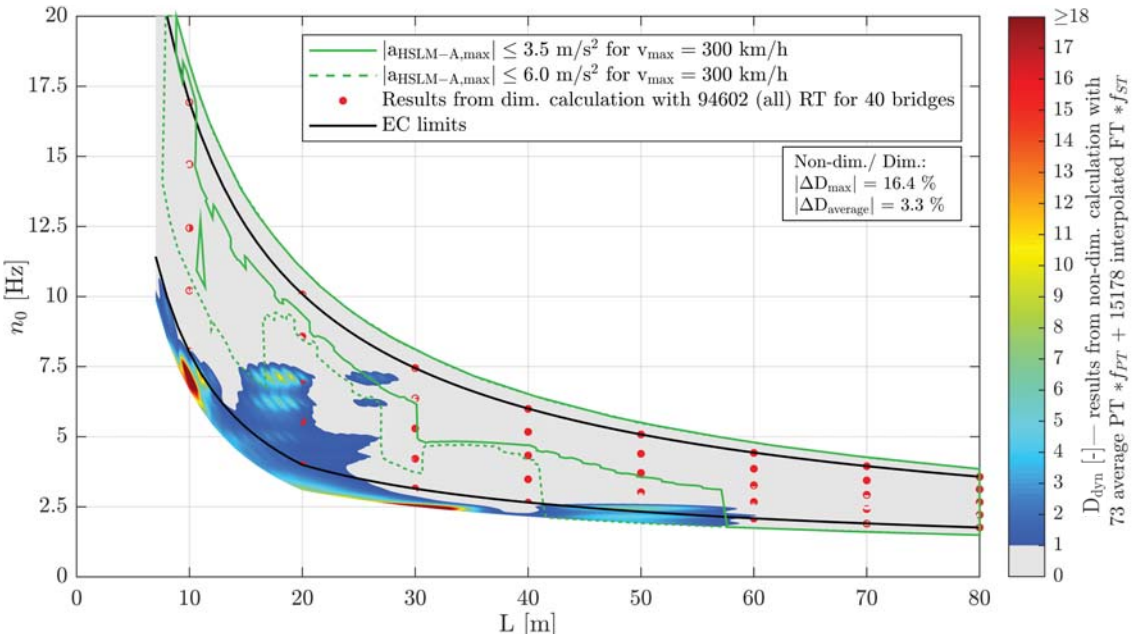

Figure C.40.: Single-span composite bridges — traffic mix TM2-st — ζ_{V1} — Rayleigh like damping — load distribution — top view D_{dyn} & $|a_{HSLM-A,max}|$

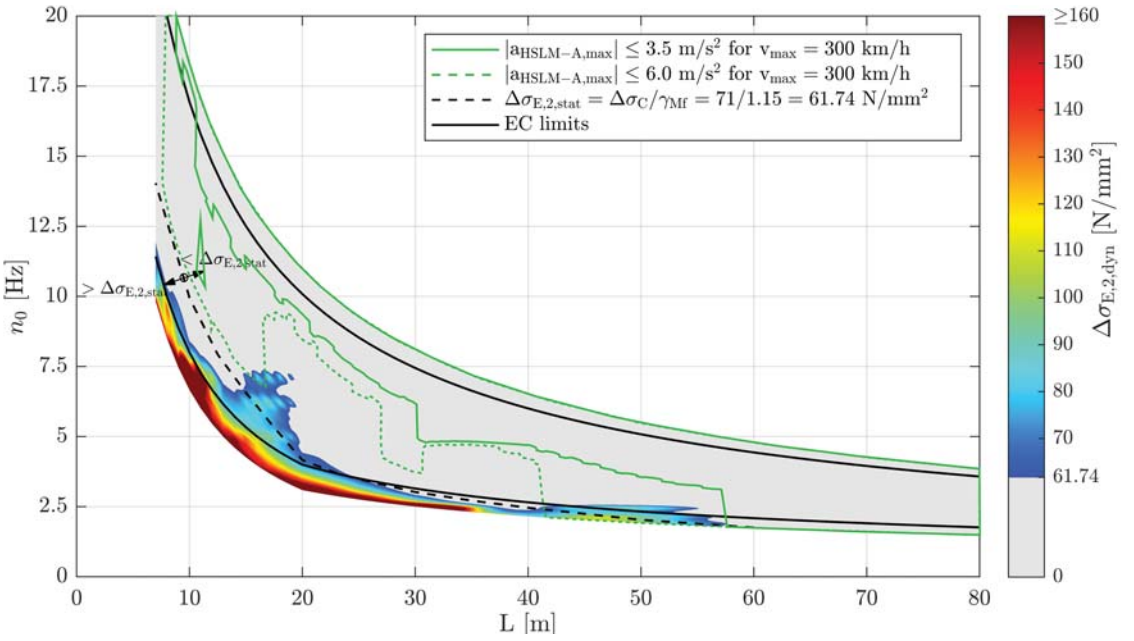

Figure C.41.: Single-span composite bridges — traffic mix TM2-st — ζ_{V1} — Rayleigh like damping — load distribution — top view $\Delta\sigma_{E,2,dyn}$ & $|a_{HSLM-A,max}|$ & $\Delta\sigma_{E,2,stat}$

C.5. Results of single-span steel bridges due to TM3

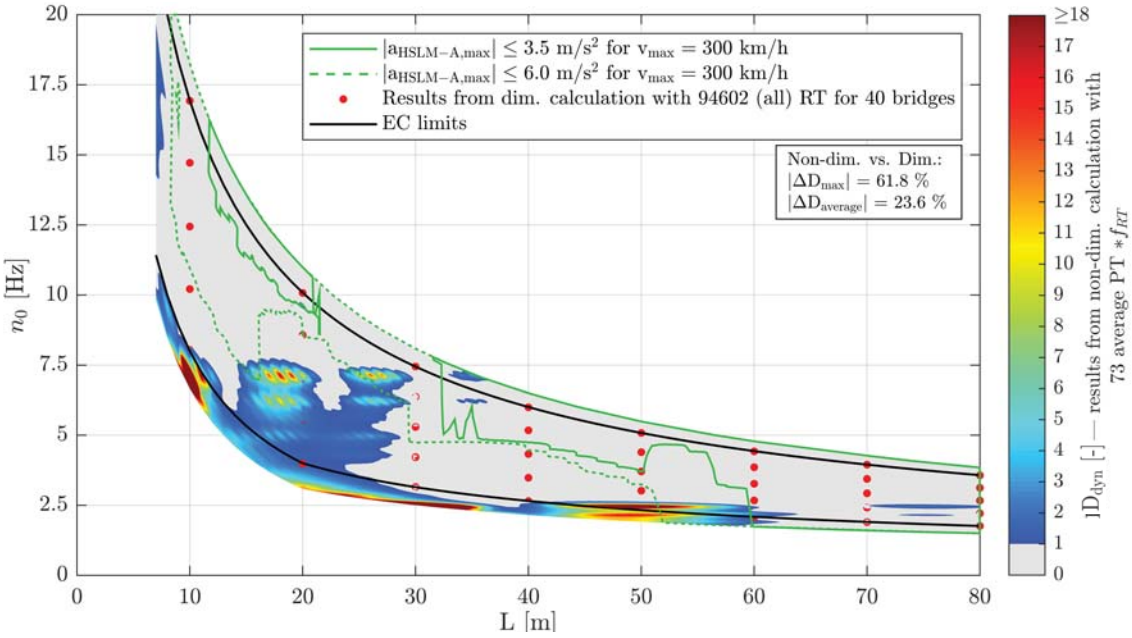

Figure C.42.: Single-span composite bridges — traffic mix TM3-st — ζ_{EC} — Rayleigh like damping — no load distribution — top view D_{dyn} & $|a_{HSLM-A,max}|$

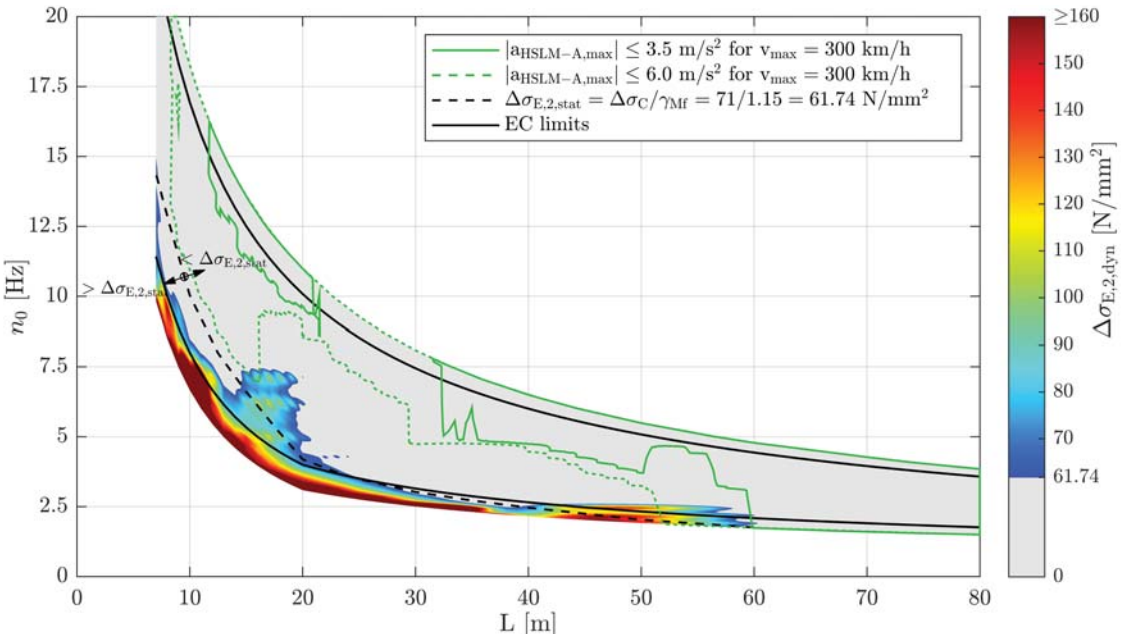

Figure C.43.: Single-span composite bridges — traffic mix TM3-st — ζ_{EC} — Rayleigh like damping — no load distribution — top view $\Delta\sigma_{E,2,dyn}$ & $|a_{HSLM-A,max}|$ & $\Delta\sigma_{E,2,stat}$

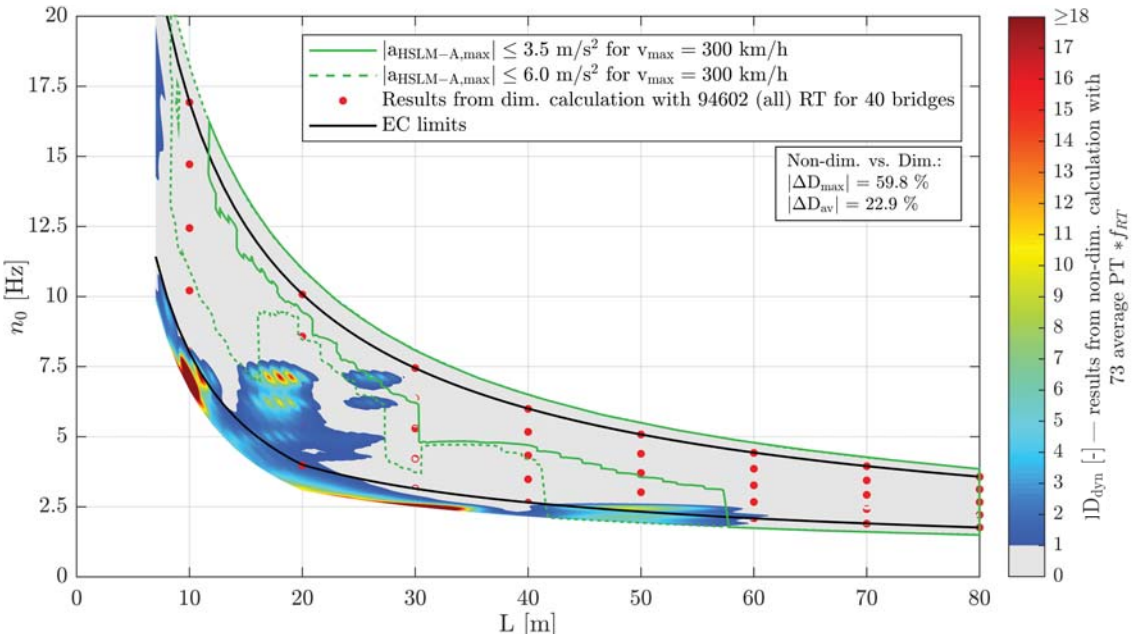

Figure C.44.: Single-span composite bridges — traffic mix TM3-st — ζ_{V1} — Rayleigh like damping — no load distribution — top view D_{dyn} & $|a_{HSLM-A,max}|$

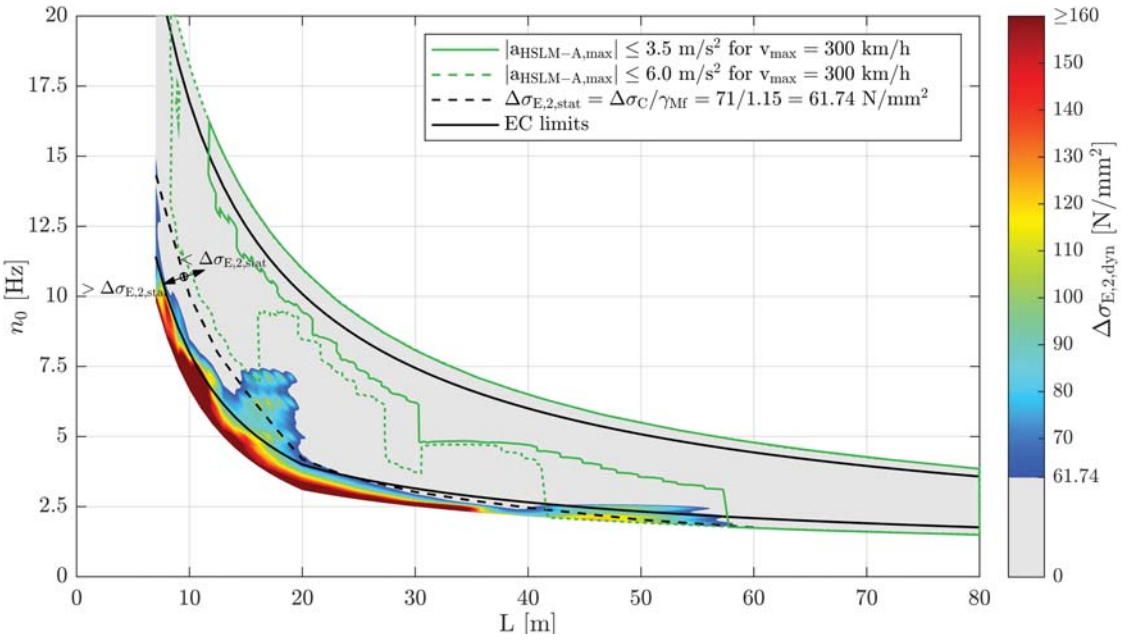

Figure C.45.: Single-span composite bridges — traffic mix TM3-st — ζ_{V1} — Rayleigh like damping — no load distribution — top view $\Delta\sigma_{E,2,dyn}$ & $|a_{HSLM-A,max}|$ & $\Delta\sigma_{E,2,stat}$

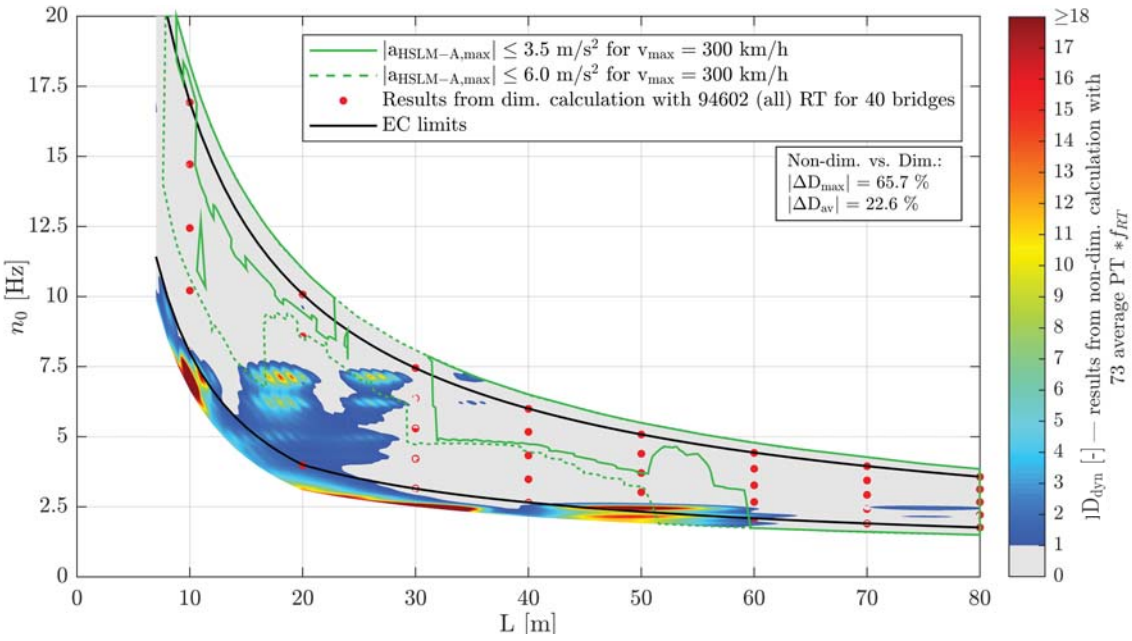

Figure C.46.: Single-span composite bridges — traffic mix TM3-st — ζ_{EC} — Rayleigh like damping — load distribution — top view D_{dyn} & $|a_{HSLM-A,max}|$

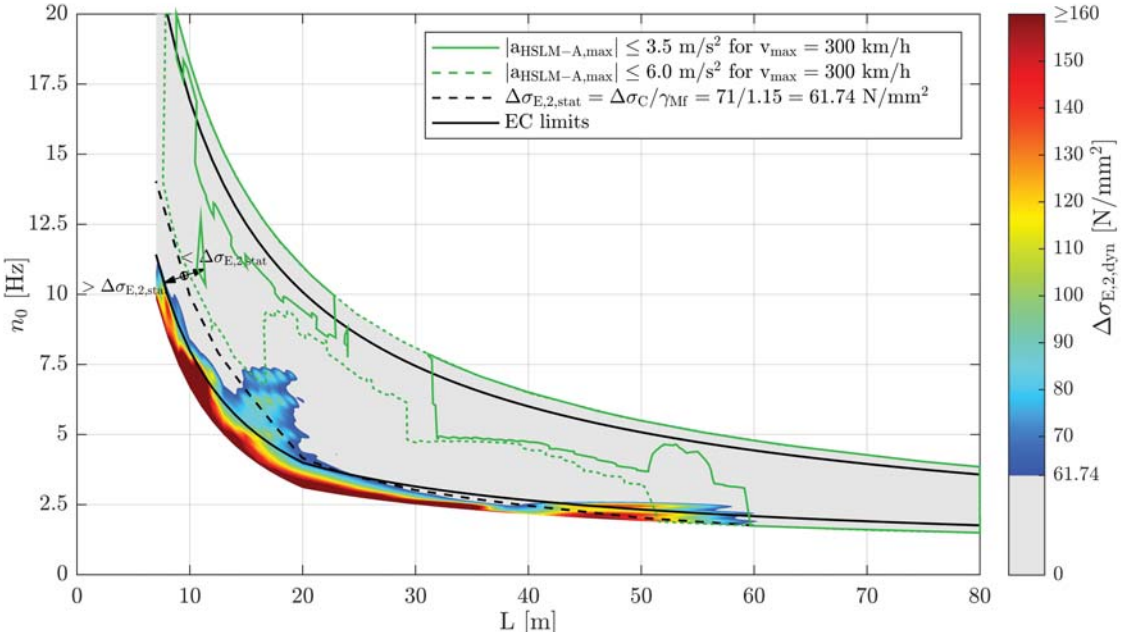

Figure C.47.: Single-span composite bridges — traffic mix TM3-st — ζ_{EC} — Rayleigh like damping — load distribution — top view $\Delta\sigma_{E,2,dyn}$ & $|a_{HSLM-A,max}|$ & $\Delta\sigma_{E,2,stat}$

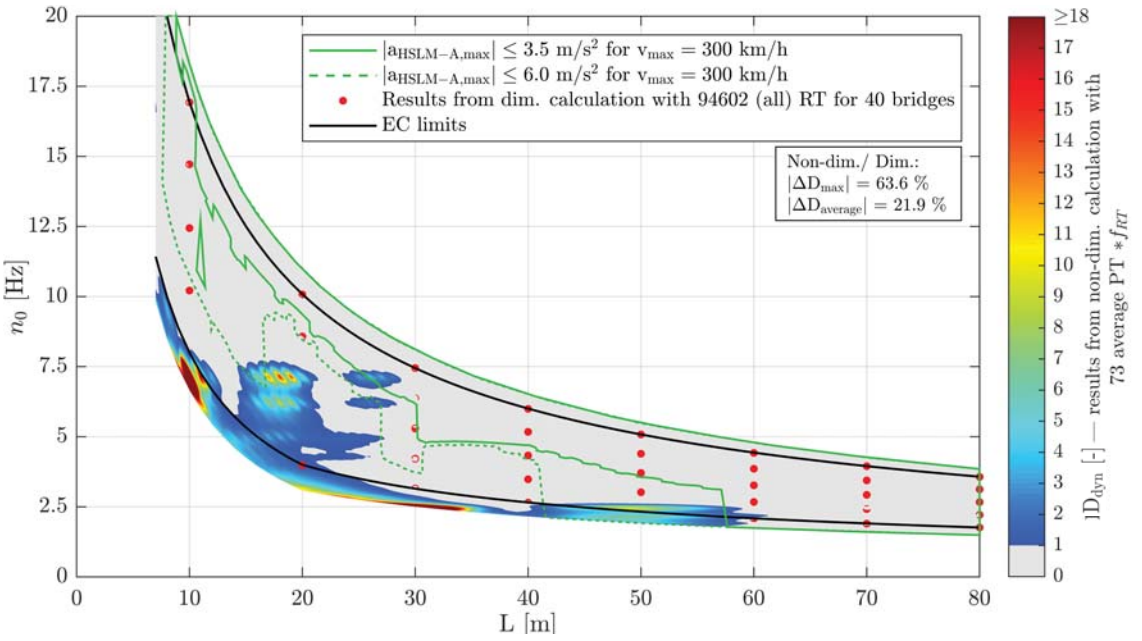

Figure C.48.: Single-span composite bridges — traffic mix TM3-st — ζ_{V1} — Rayleigh like damping — load distribution — top view D_{dyn} & $|a_{HSLM-A,max}|$

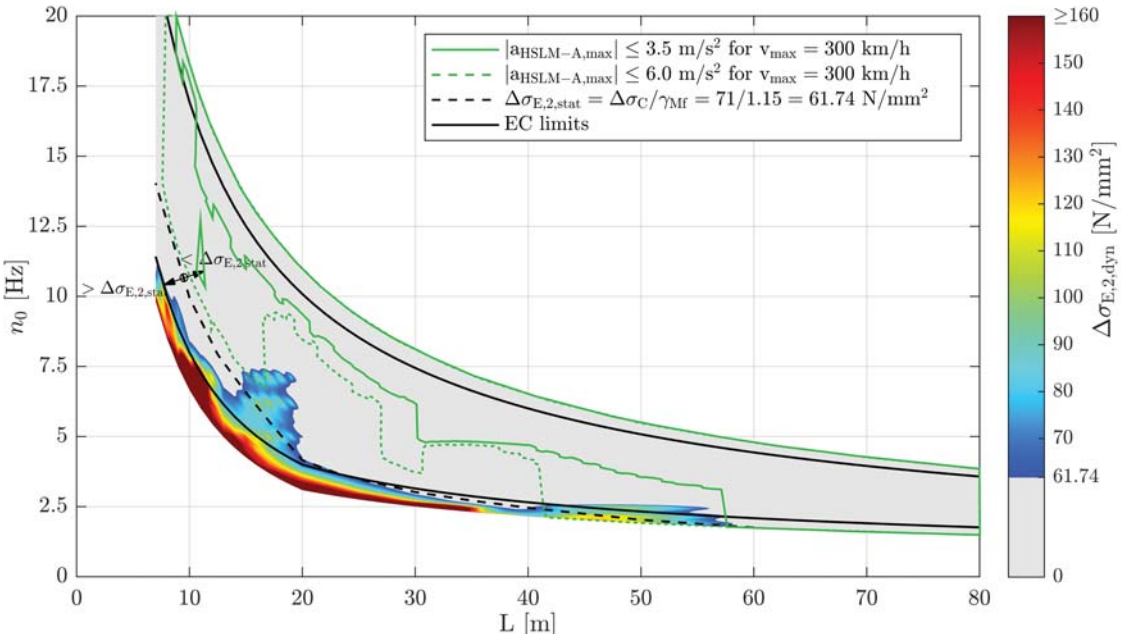

Figure C.49.: Single-span composite bridges — traffic mix TM3-st — ζ_{V1} — Rayleigh like damping — load distribution — top view $\Delta\sigma_{E,2,dyn}$ & $|a_{HSLM-A,max}|$ & $\Delta\sigma_{E,2,stat}$

C.6. Results of single-span composite bridges due to TM4

C.6.1. Train speed v_{Train}

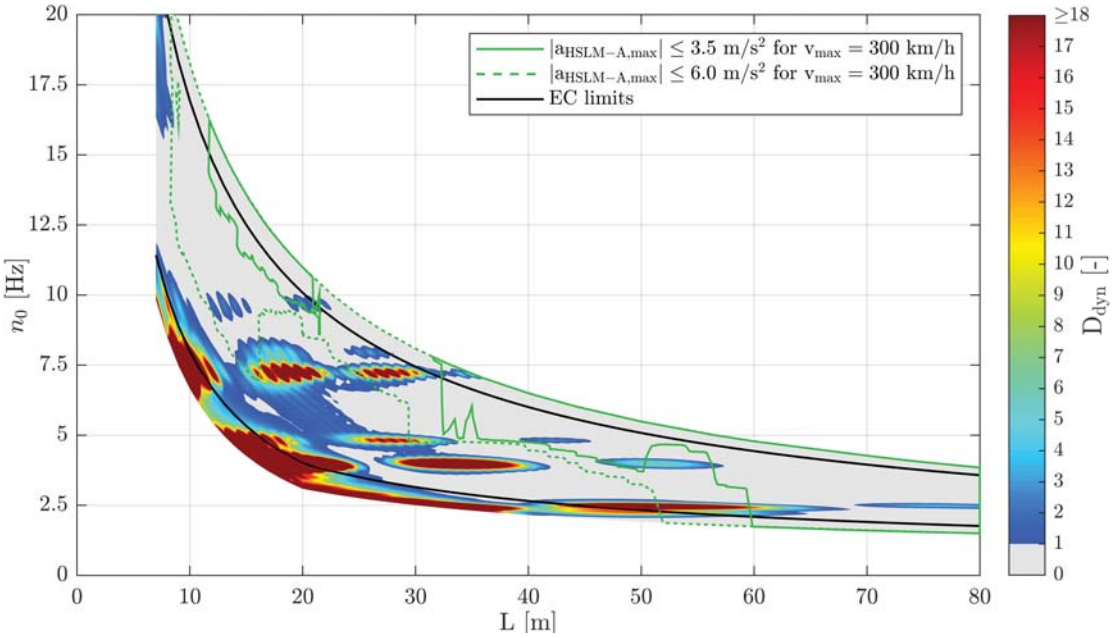

Figure C.50.: Single-span composite bridges — traffic mix TM4* — v_{Train} — ζ_{EC} — Rayleigh like damping — no load distribution — top view D_{dyn} & $|a_{HSLM-A,max}|$

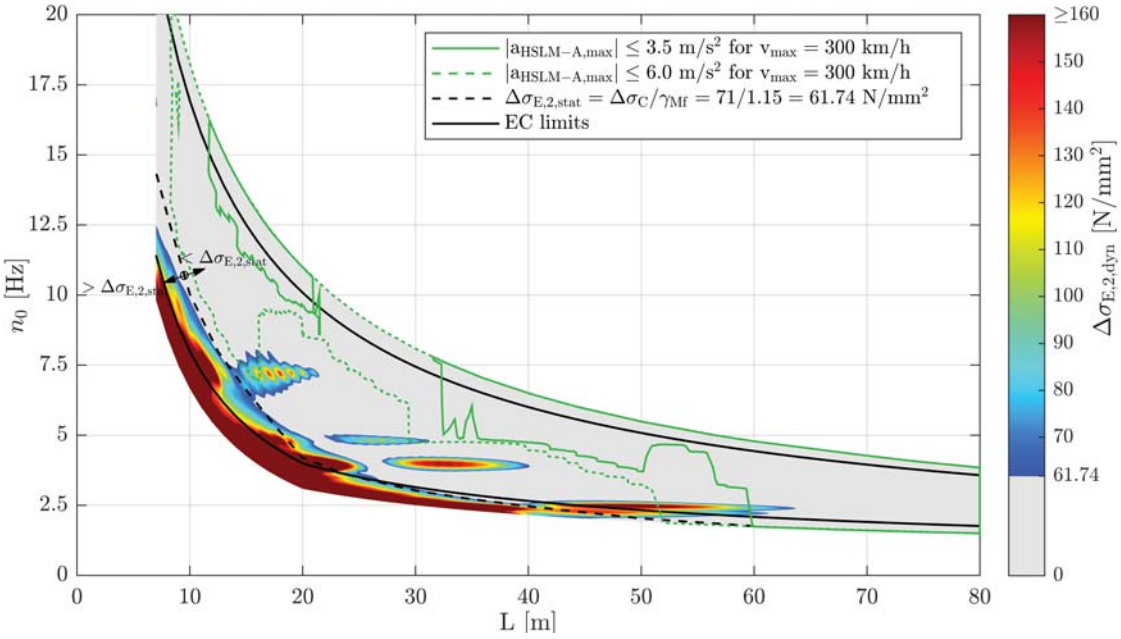

Figure C.51.: Single-span composite bridges — traffic mix TM4* — v_{Train} — ζ_{EC} — Rayleigh like damping — no load distribution — top view $\Delta\sigma_{E,2,dyn}$ & $|a_{HSLM-A,max}|$ & $\Delta\sigma_{E,2,stat}$

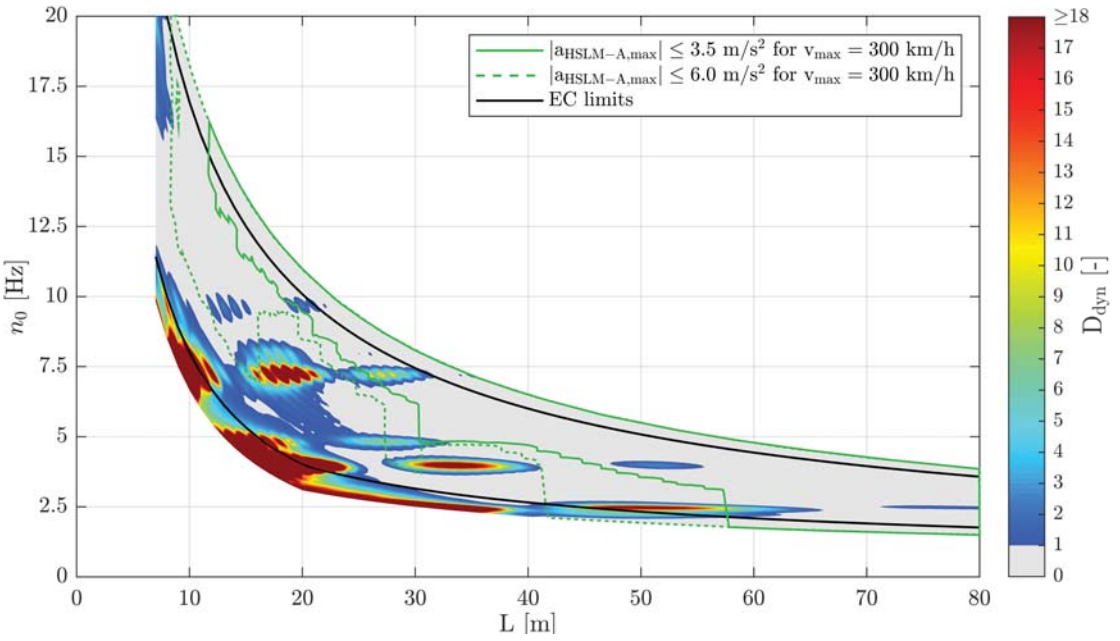

Figure C.52.: Single-span composite bridges — traffic mix TM4* — v_{Train} — ζ_{V1} — Rayleigh like damping — no load distribution — top view D_{dyn} & $|a_{HSLM-A,max}|$

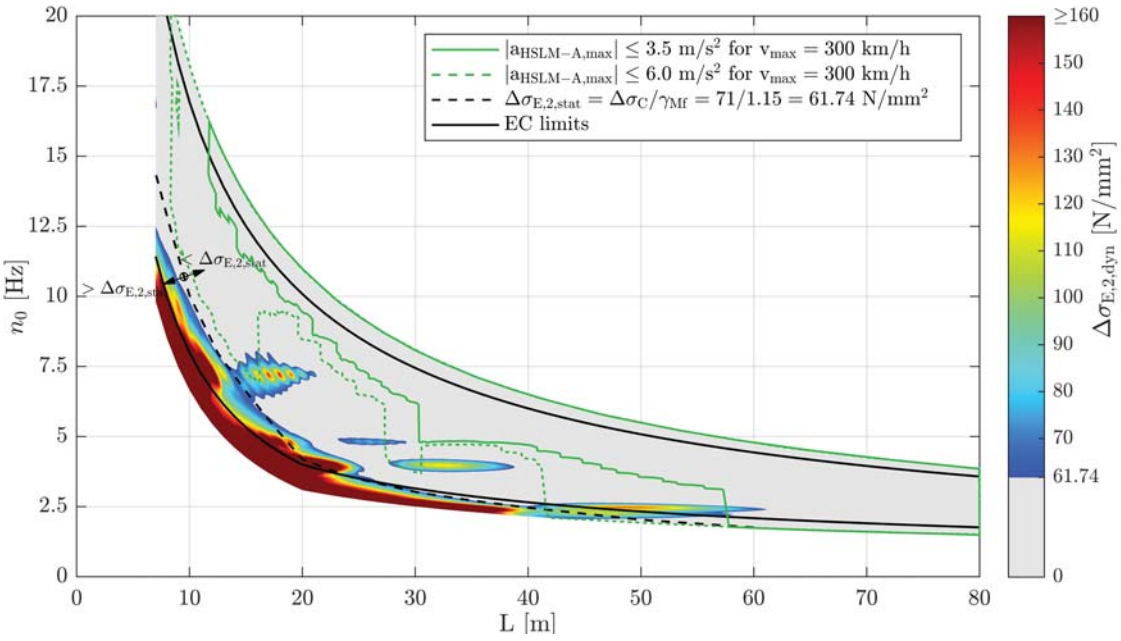

Figure C.53.: Single-span composite bridges — traffic mix TM4* — v_{Train} — ζ_{V1} — Rayleigh like damping — no load distribution — top view $\Delta\sigma_{E,2,dyn}$ & $|a_{HSLM-A,max}|$ & $\Delta\sigma_{E,2,stat}$

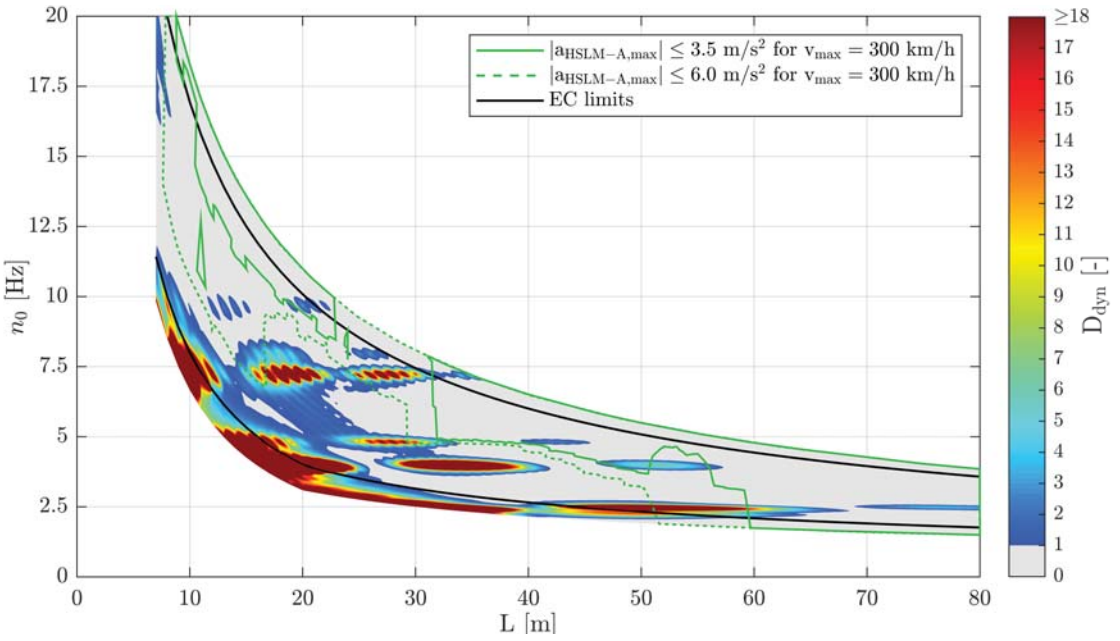

Figure C.54.: Single-span composite bridges — traffic mix TM4* — v_{Train} — ζ_{EC} — Rayleigh like damping — load distribution — top view D_{dyn} & $|a_{HSLM-A,max}|$

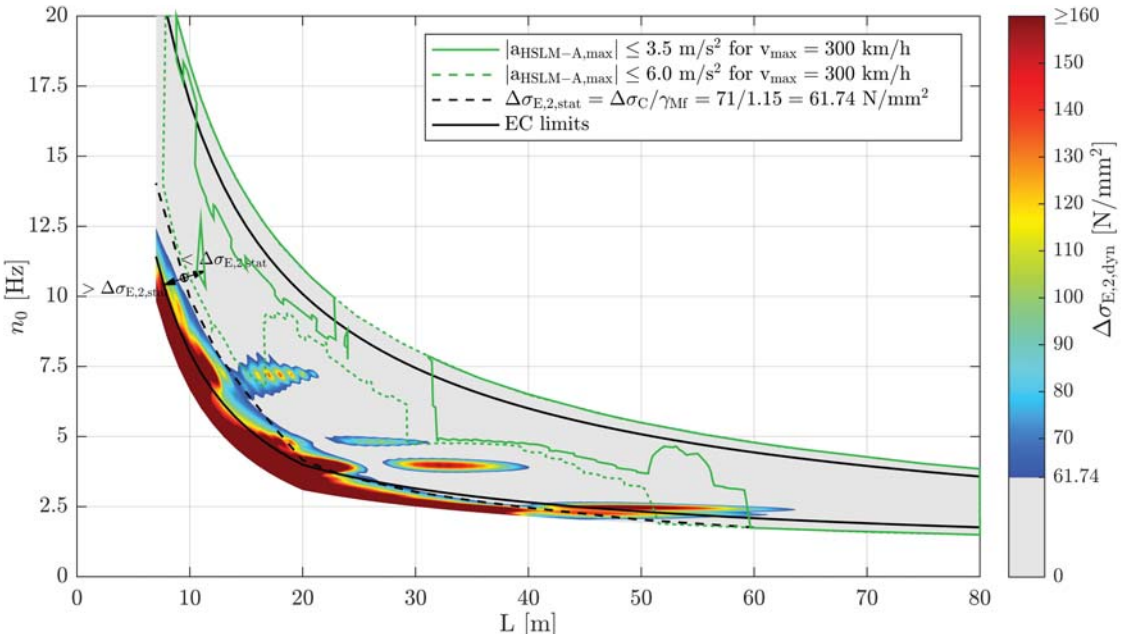

Figure C.55.: Single-span composite bridges — traffic mix TM4* — v_{Train} — ζ_{EC} — Rayleigh like damping — load distribution — top view $\Delta\sigma_{E,2,dyn}$ & $|a_{HSLM-A,max}|$ & $\Delta\sigma_{E,2,stat}$

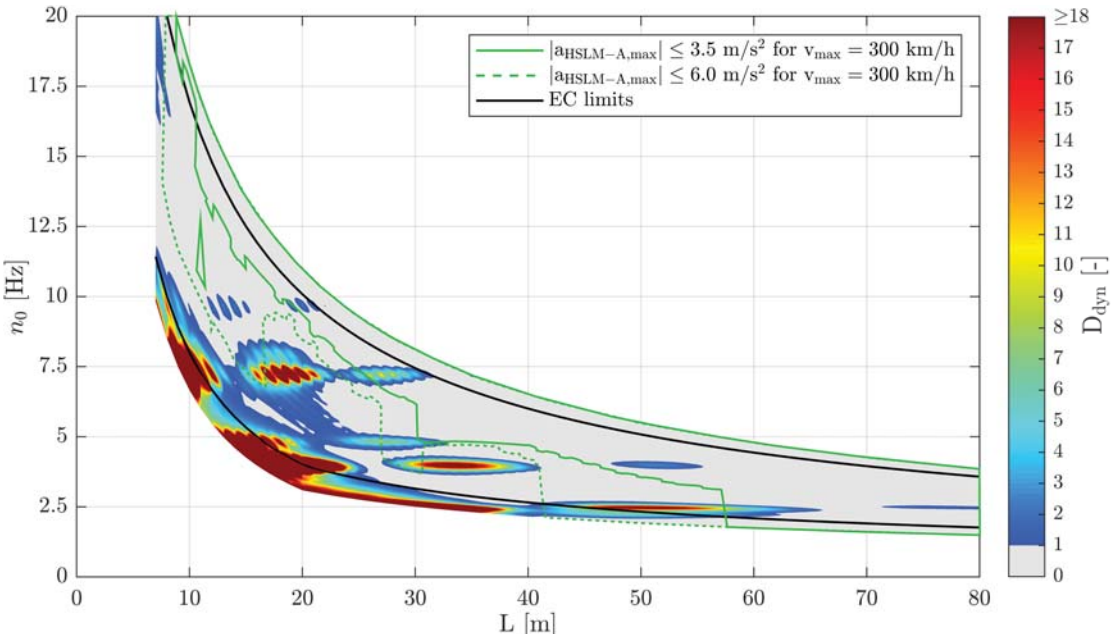

Figure C.56.: Single-span composite bridges — traffic mix TM4* — v_{Train} — ζ_{V1} — Rayleigh like damping — load distribution — top view D_{dyn} & $|a_{HSLM-A,max}|$

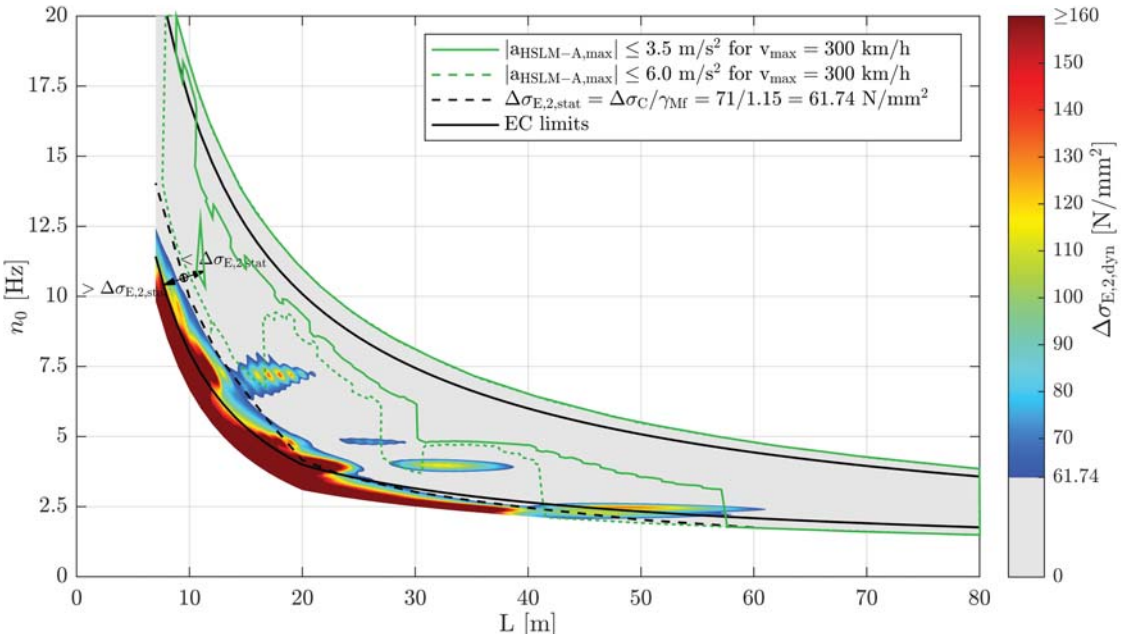

Figure C.57.: Single-span composite bridges — traffic mix TM4* — v_{Train} — ζ_{V1} — Rayleigh like damping — load distribution — top view $\Delta\sigma_{E,2,dyn}$ & $|a_{HSLM-A,max}|$ & $\Delta\sigma_{E,2,stat}$

C.6.2. Train speed $v_{D_{max}}$

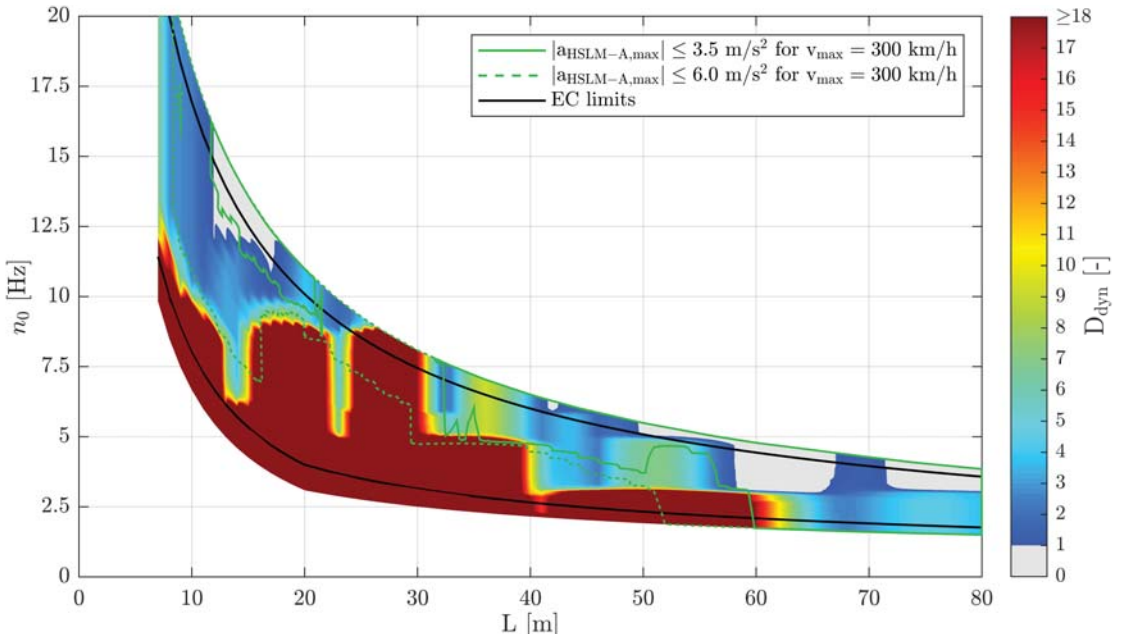

Figure C.58.: Single-span composite bridges — traffic mix TM4** — $v_{D_{max}}$ — ζ_{EC} — Rayleigh like damping — no load distribution — top view D_{dyn} & $|a_{HSLM-A,max}|$

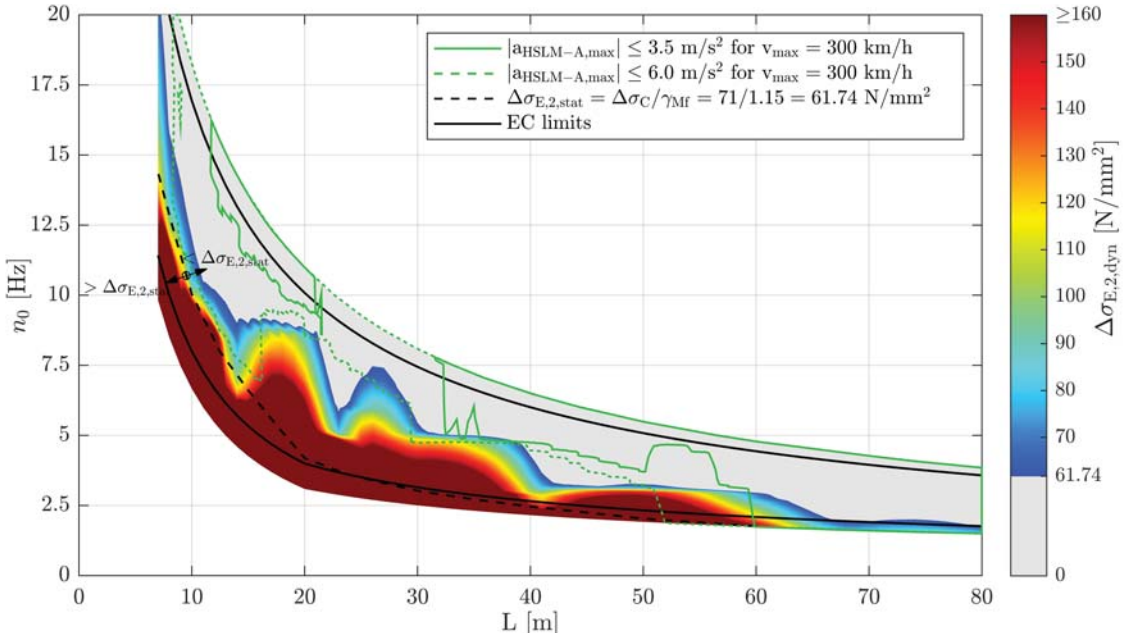

Figure C.59.: Single-span composite bridges — traffic mix TM4** — $v_{D_{max}}$ — ζ_{EC} — Rayleigh like damping — no load distribution — top view $\Delta\sigma_{E,2,dyn}$ & $|a_{HSLM-A,max}|$ & $\Delta\sigma_{E,2,stat}$

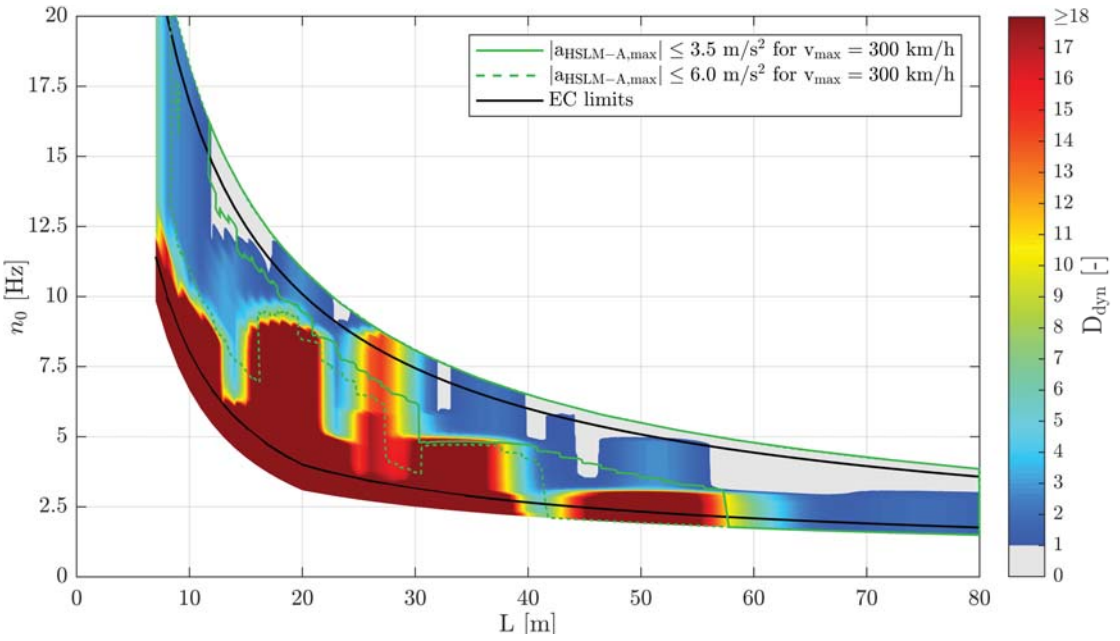

Figure C.60.: Single-span composite bridges — traffic mix TM4** — $v_{D_{max}}$ — ζ_{V1} — Rayleigh like damping — no load distribution — top view D_{dyn} & $|a_{HSLM-A,max}|$

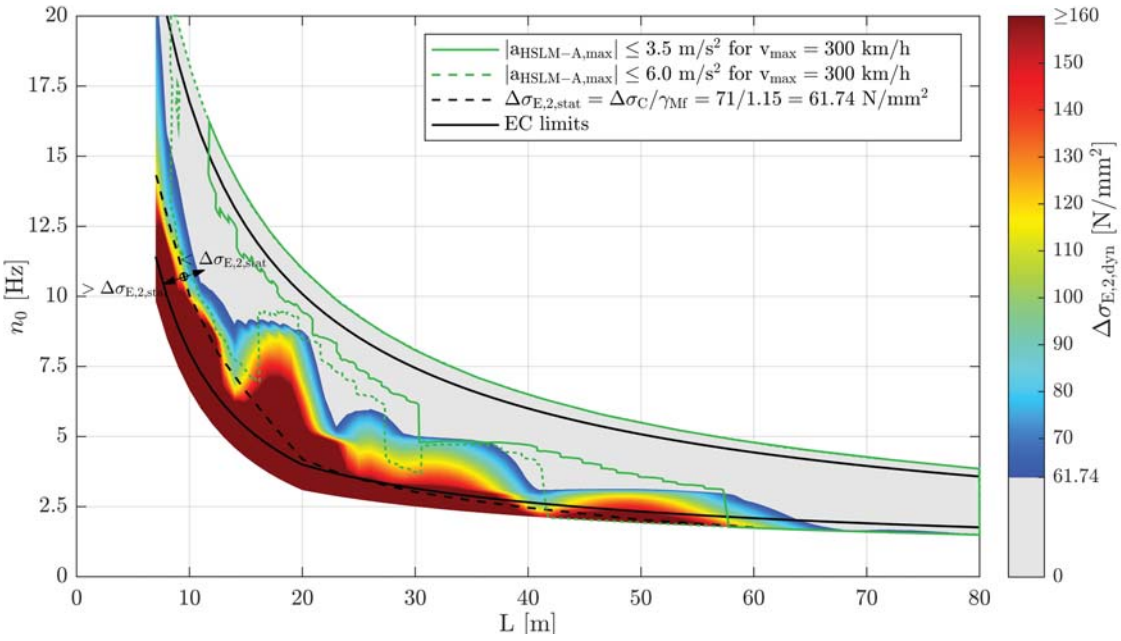

Figure C.61.: Single-span composite bridges — traffic mix TM4** — $v_{D_{max}}$ — ζ_{V1} — Rayleigh like damping — no load distribution — top view $\Delta\sigma_{E,2,dyn}$ & $|a_{HSLM-A,max}|$ & $\Delta\sigma_{E,2,stat}$

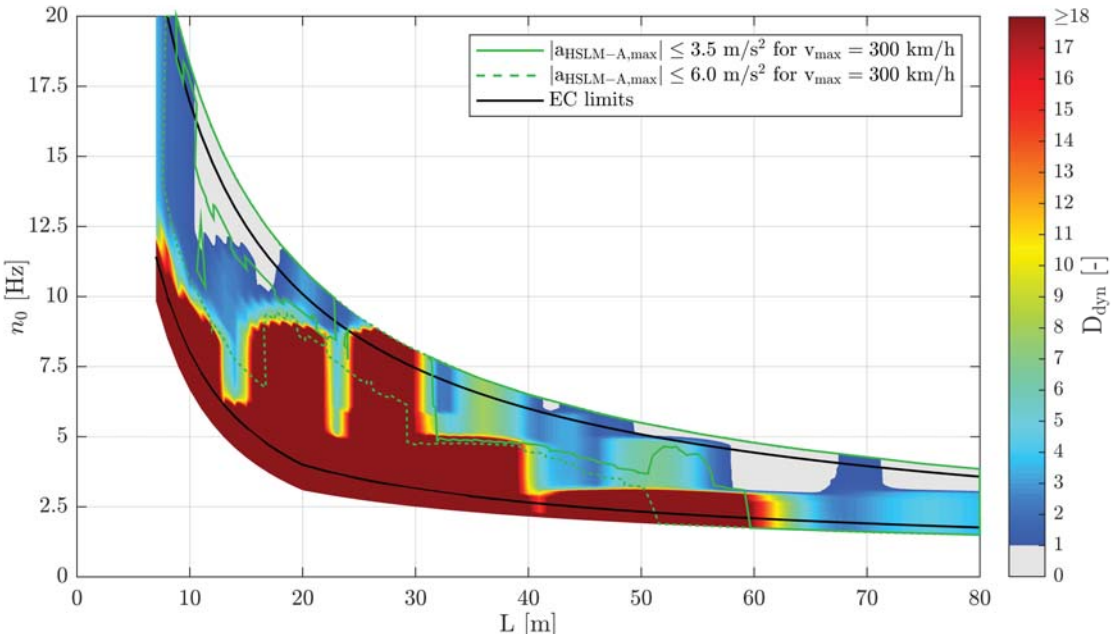

Figure C.62.: Single-span composite bridges — traffic mix TM4** — $v_{D_{max}}$ — ζ_{EC} — Rayleigh like damping — load distribution — top view D_{dyn} & $|a_{HSLM-A,max}|$

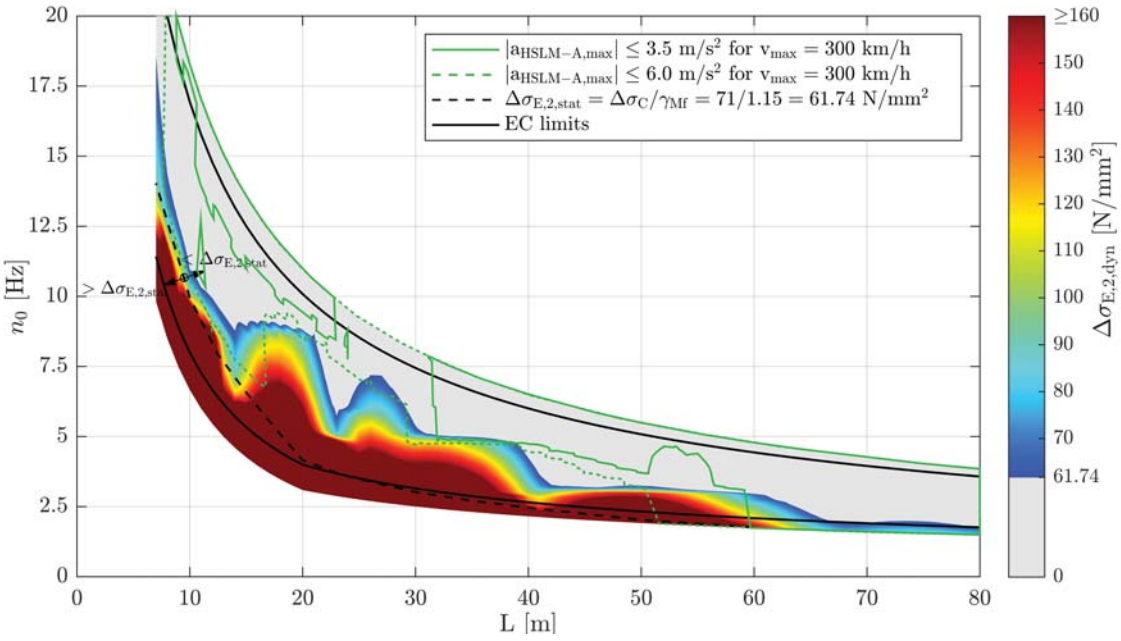

Figure C.63.: Single-span composite bridges — traffic mix TM4** — $v_{D_{max}}$ — ζ_{EC} — Rayleigh like damping — load distribution — top view $\Delta\sigma_{E,2,dyn}$ & $|a_{HSLM-A,max}|$ & $\Delta\sigma_{E,2,stat}$

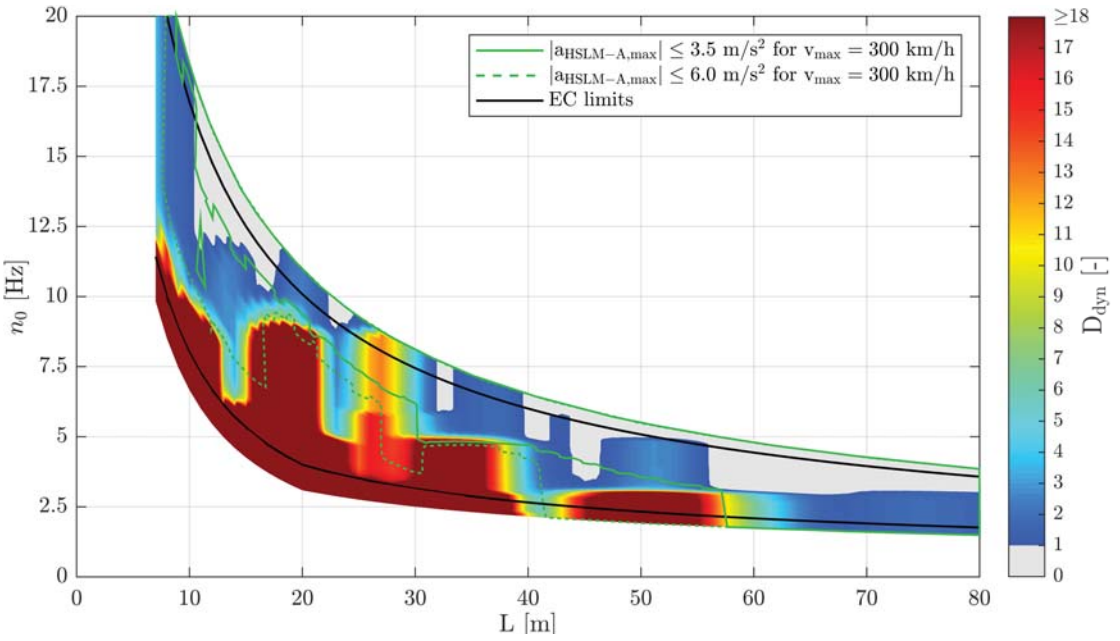

Figure C.64.: Single-span composite bridges — traffic mix TM4** — $v_{D_{max}}$ — ζ_{V1} — Rayleigh like damping — load distribution — top view D_{dyn} & $|a_{HSLM-A,max}|$

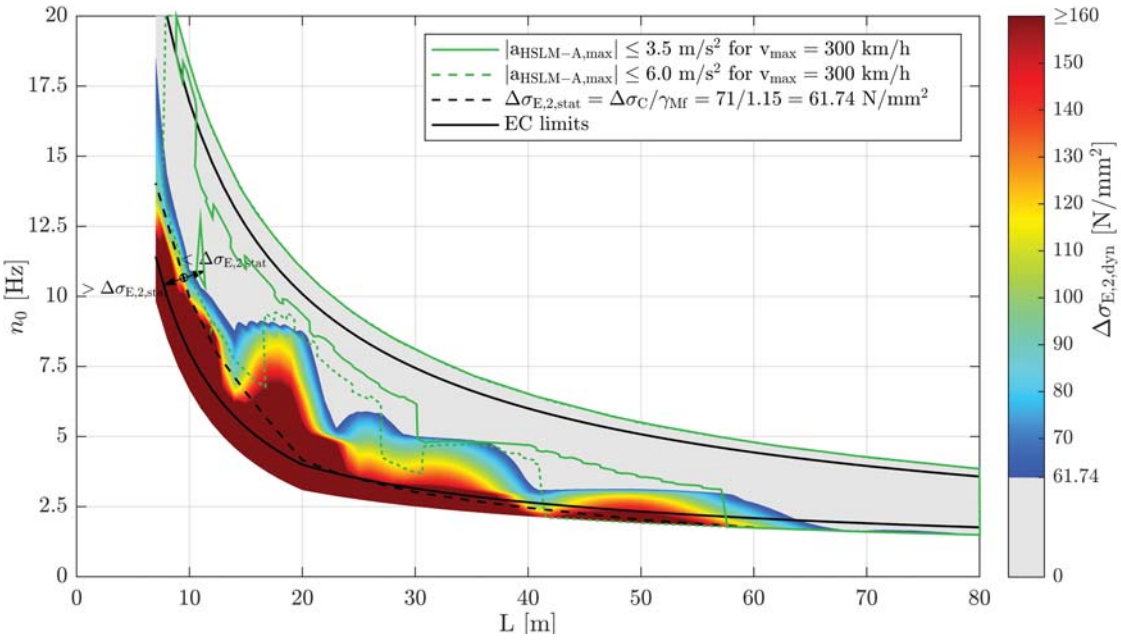

Figure C.65.: Single-span composite bridges — traffic mix TM4** — $v_{D_{max}}$ — ζ_{V1} — Rayleigh like damping — load distribution — top view $\Delta\sigma_{E,2,dyn}$ & $|a_{HSLM-A,max}|$ & $\Delta\sigma_{E,2,stat}$

C.6.3. Train speed $v_{a_{max}}$

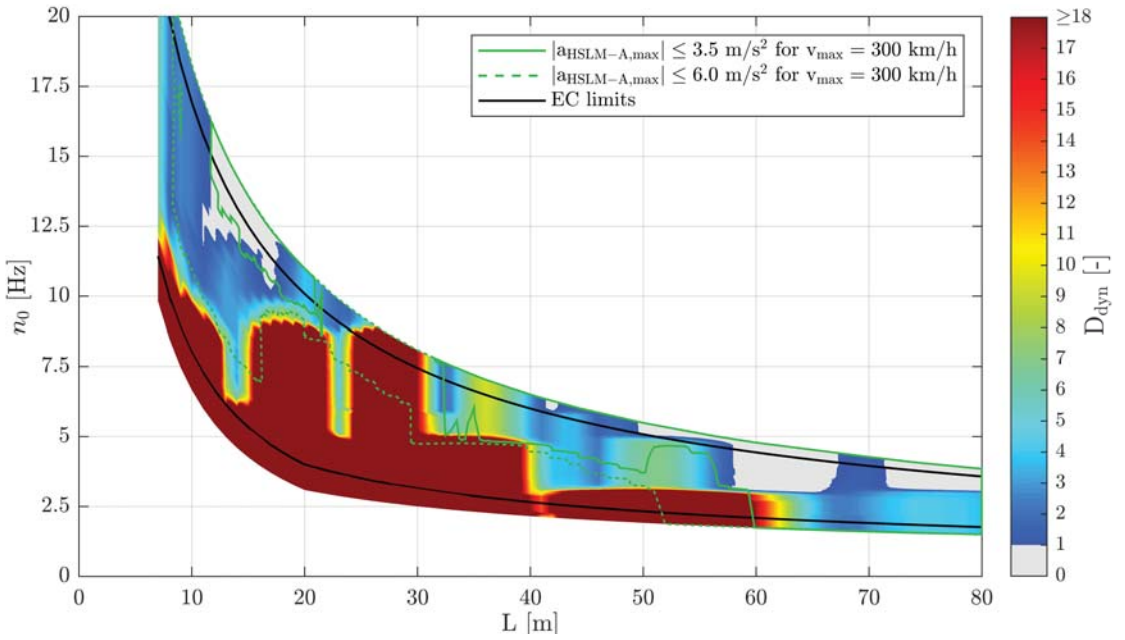

Figure C.66.: Single-span composite bridges — traffic mix TM4*** — $v_{a_{max}}$ — ζ_{EC} — Rayleigh like damping — no load distribution — top view D_{dyn} & $|a_{HSLM-A,max}|$

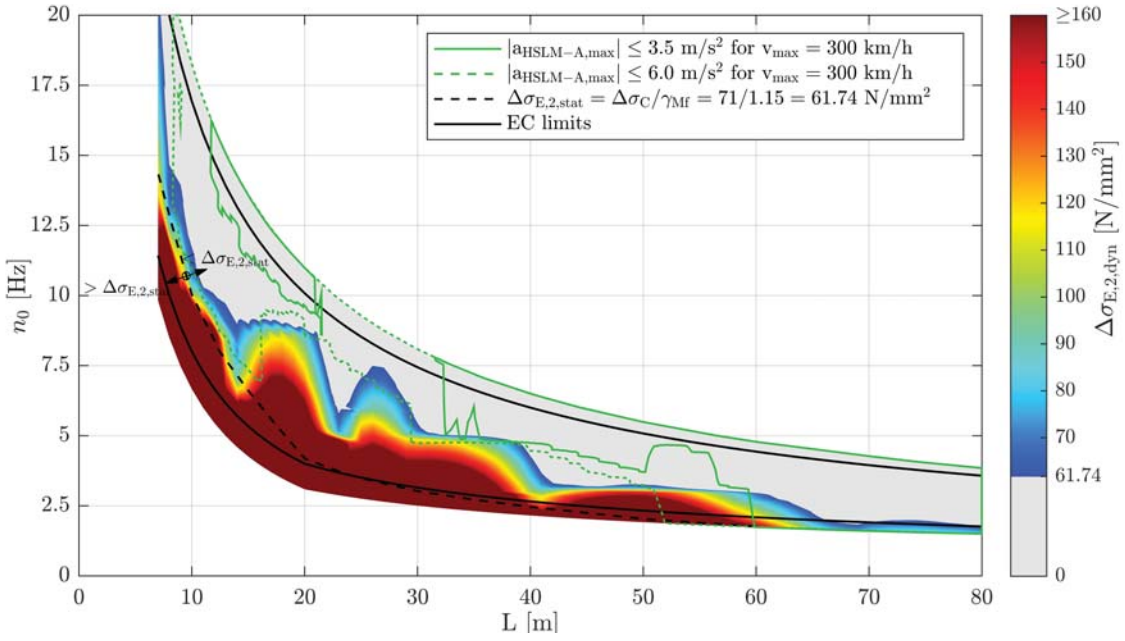

Figure C.67.: Single-span composite bridges — traffic mix TM4*** — $v_{a_{max}}$ — ζ_{EC} — Rayleigh like damping — no load distribution — top view $\Delta\sigma_{E,2,dyn}$ & $|a_{HSLM-A,max}|$ & $\Delta\sigma_{E,2,stat}$

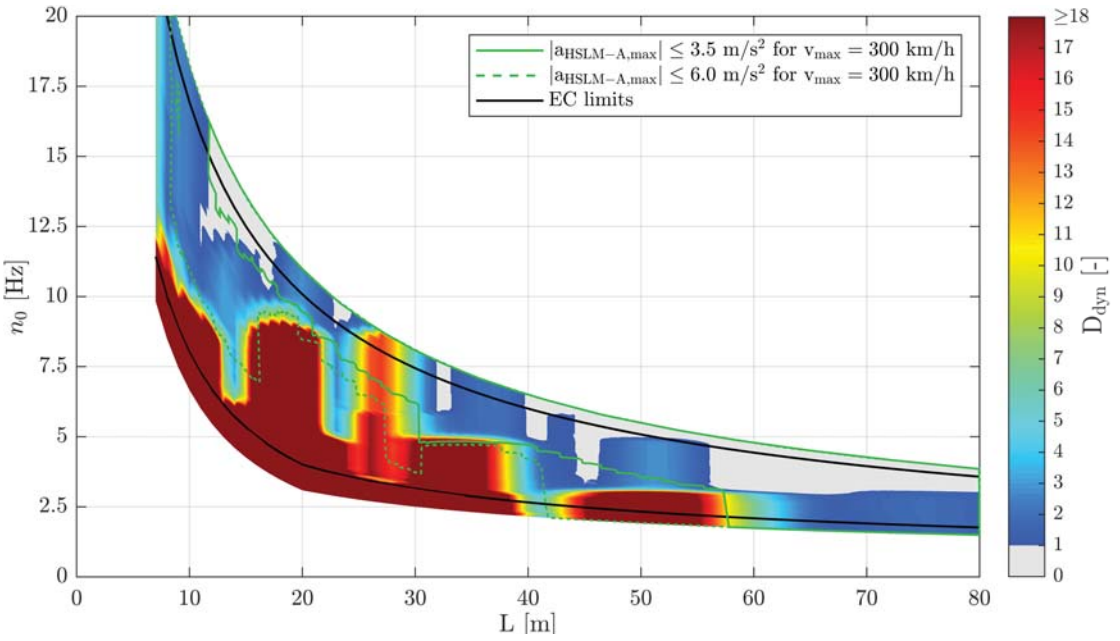

Figure C.68.: Single-span composite bridges — traffic mix TM4*** — $v_{a_{max}}$ — ζ_{V1} — Rayleigh like damping — no load distribution — top view D_{dyn} & $|a_{HSLM-A,max}|$

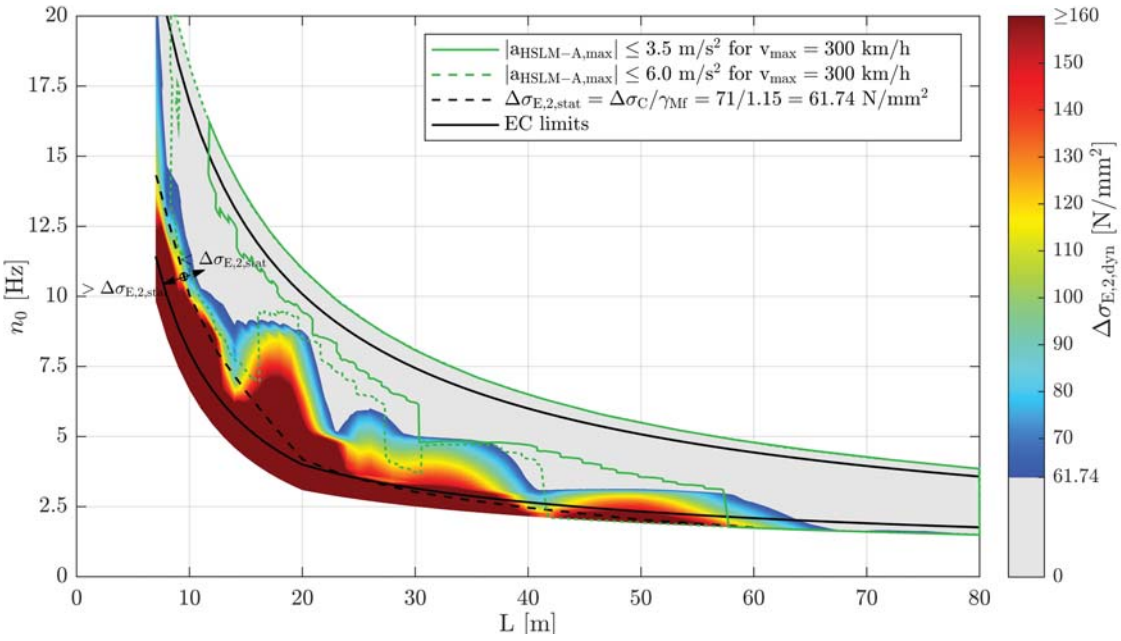

Figure C.69.: Single-span composite bridges — traffic mix TM4*** — $v_{a_{max}}$ — ζ_{V1} — Rayleigh like damping — no load distribution — top view $\Delta\sigma_{E,2,dyn}$ & $|a_{HSLM-A,max}|$ & $\Delta\sigma_{E,2,stat}$

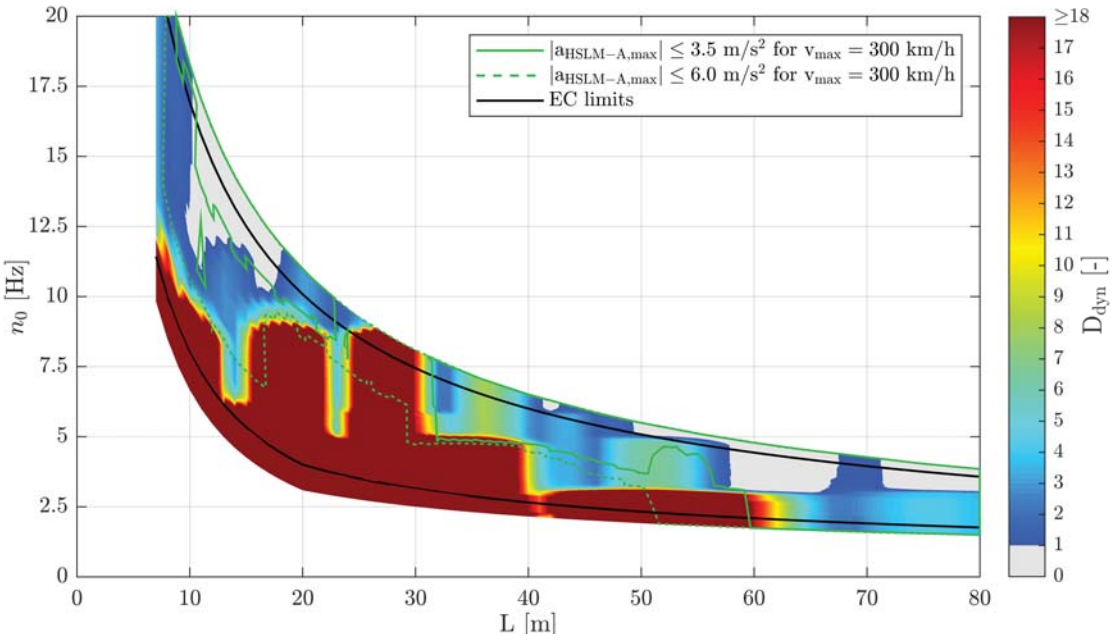

Figure C.70.: Single-span composite bridges — traffic mix TM4*** — $v_{a_{max}}$ — ζ_{EC} — Rayleigh like damping — load distribution — top view D_{dyn} & $|a_{HSLM-A,max}|$

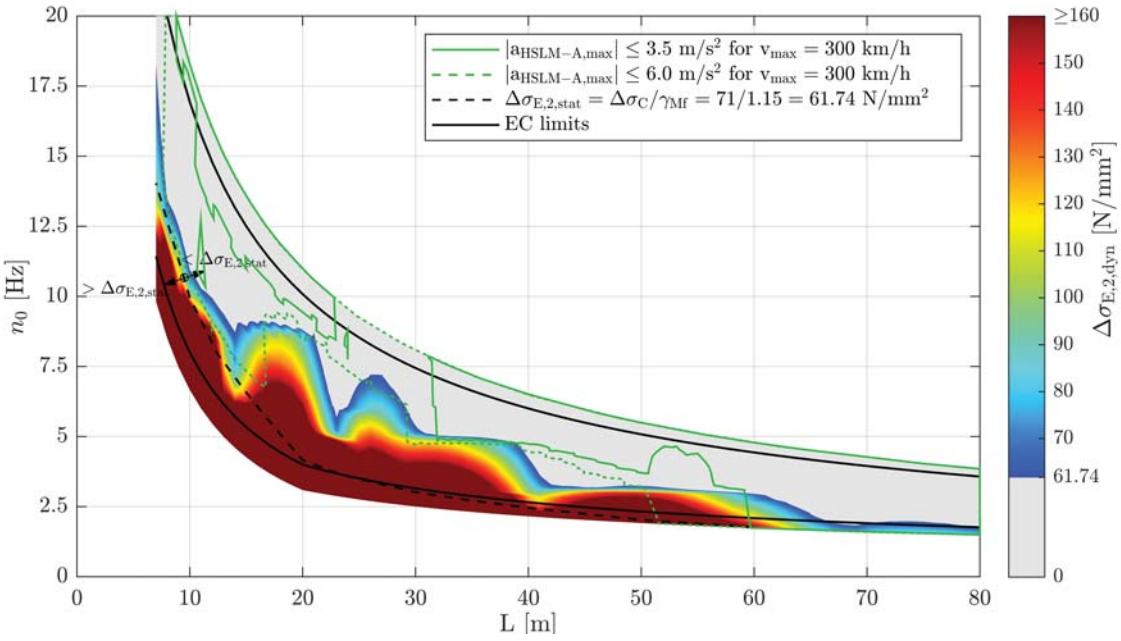

Figure C.71.: Single-span composite bridges — traffic mix TM4*** — $v_{a_{max}}$ — ζ_{EC} — Rayleigh like damping — load distribution — top view $\Delta\sigma_{E,2,dyn}$ & $|a_{HSLM-A,max}|$ & $\Delta\sigma_{E,2,stat}$

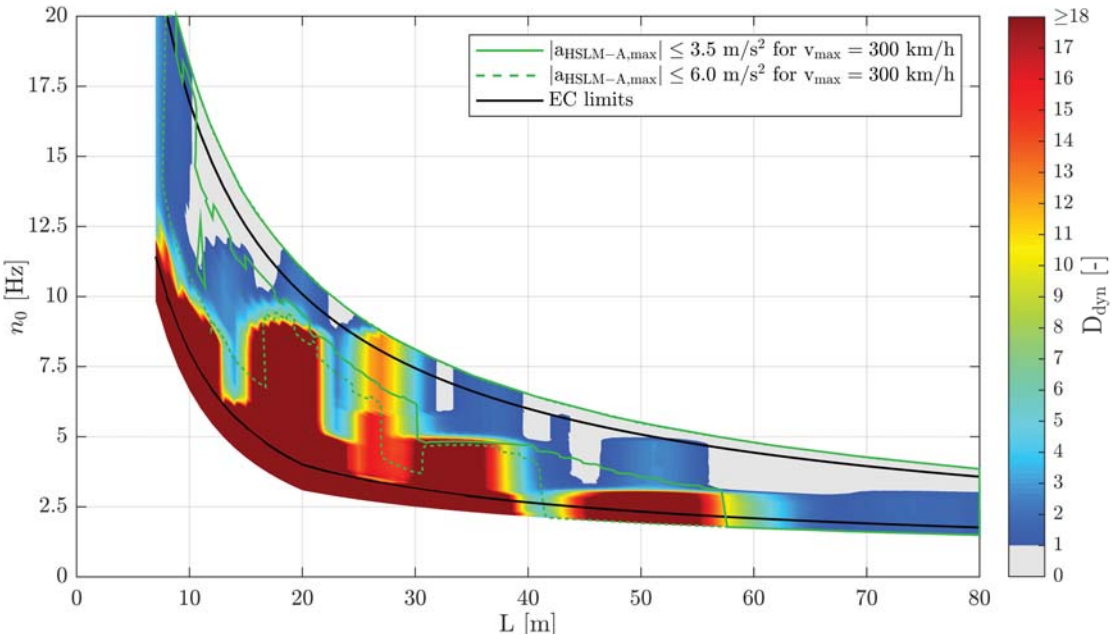

Figure C.72.: Single-span composite bridges — traffic mix TM4*** — $v_{a_{max}}$ — ζ_{V1} — Rayleigh like damping — load distribution — top view D_{dyn} & $|a_{HSLM-A,max}|$

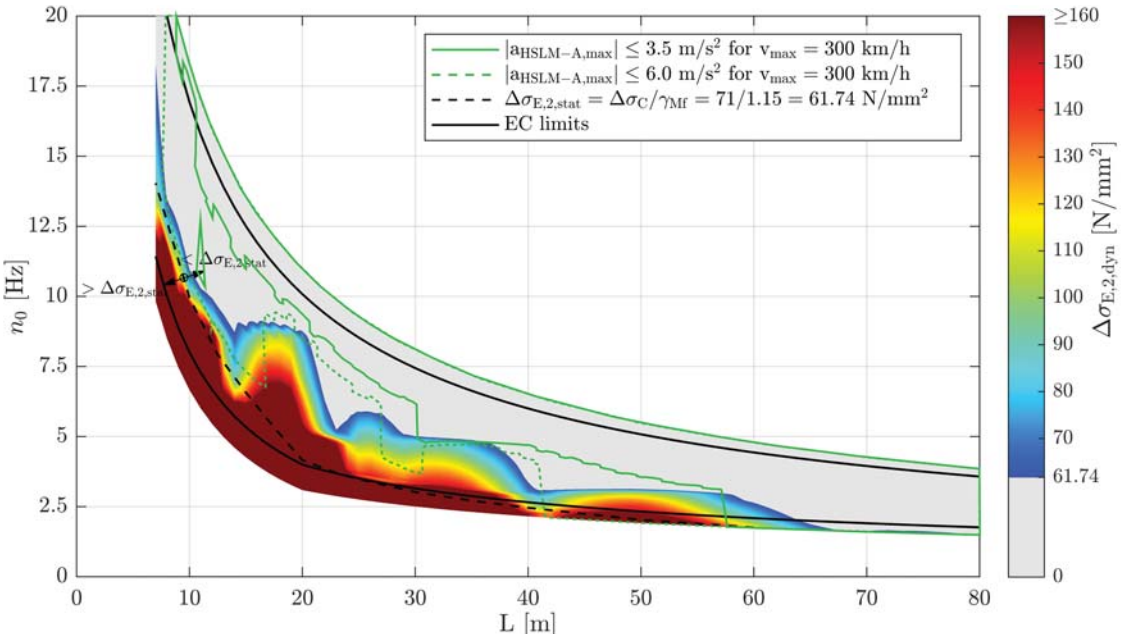

Figure C.73.: Single-span composite bridges — traffic mix TM4*** — $v_{a_{max}}$ — ζ_{V1} — Rayleigh like damping — load distribution — top view $\Delta\sigma_{E,2,dyn}$ & $|a_{HSLM-A,max}|$ & $\Delta\sigma_{E,2,stat}$

C.7. Results of single-span composite bridges due to TM5

C.7.1. Train speed v_{Train}

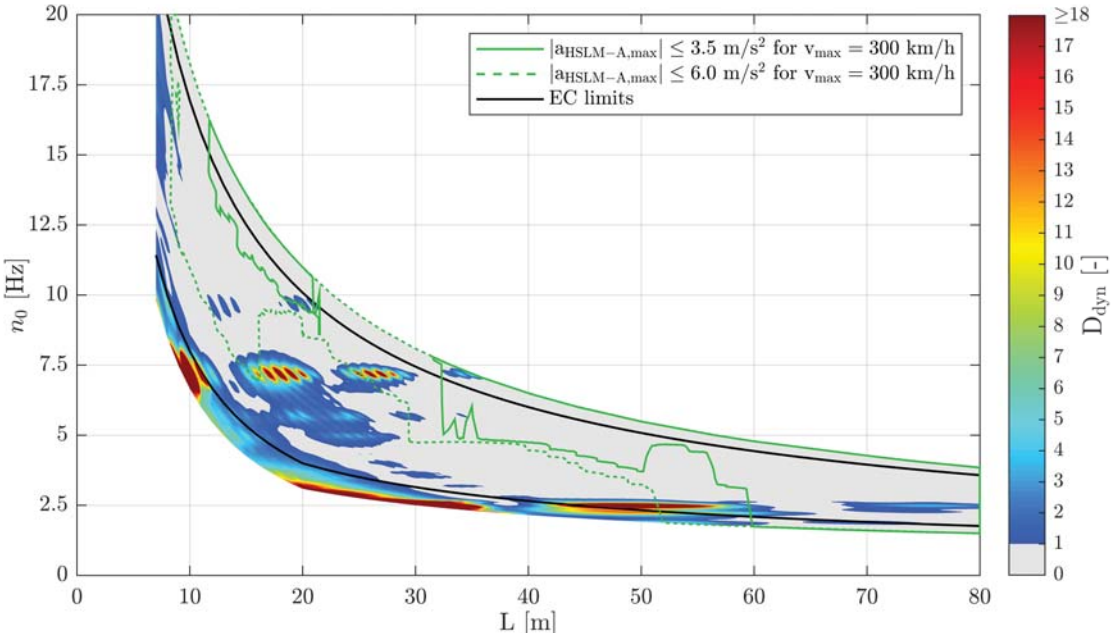

Figure C.74.: Single-span composite bridges — traffic mix TM5* — v_{Train} — ζ_{EC} — Rayleigh like damping — no load distribution — top view D_{dyn} & $|a_{HSLM-A,max}|$

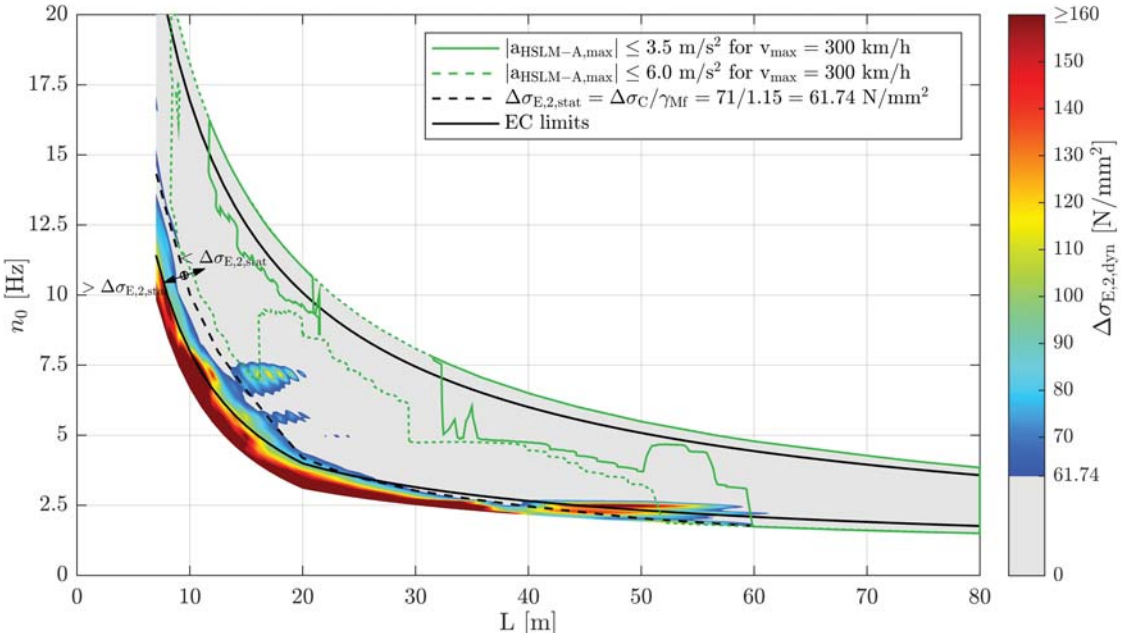

Figure C.75.: Single-span composite bridges — traffic mix TM5* — v_{Train} — ζ_{EC} — Rayleigh like damping — no load distribution — top view $\Delta\sigma_{E,2,dyn}$ & $|a_{HSLM-A,max}|$ & $\Delta\sigma_{E,2,stat}$

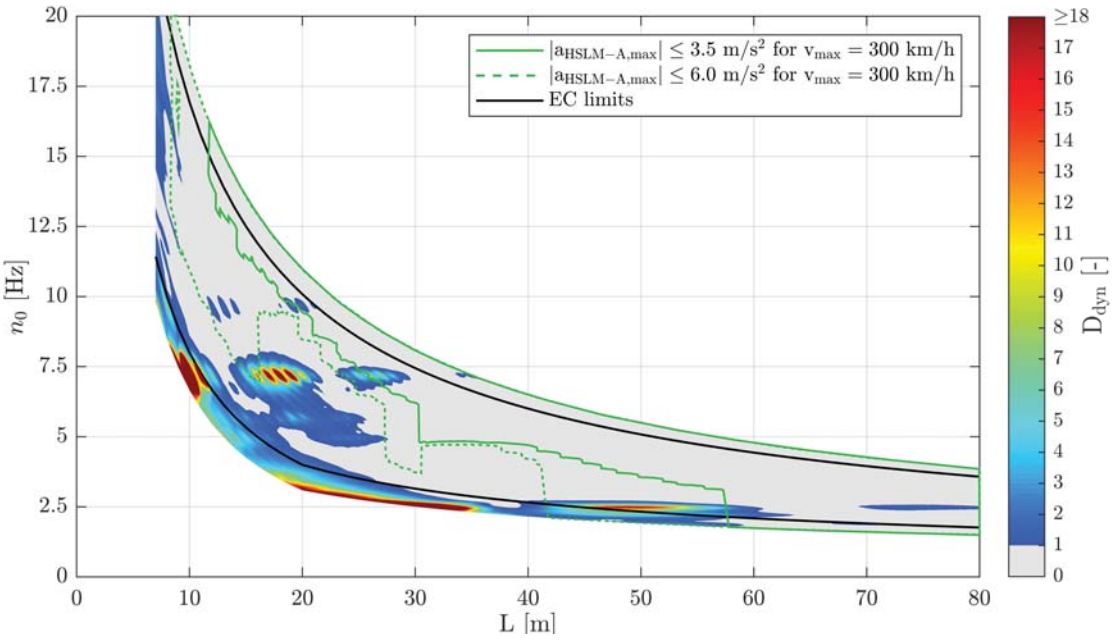

Figure C.76.: Single-span composite bridges — traffic mix TM5* — v_{Train} — ζ_{V1} — Rayleigh like damping — no load distribution — top view D_{dyn} & $|a_{HSLM-A,max}|$

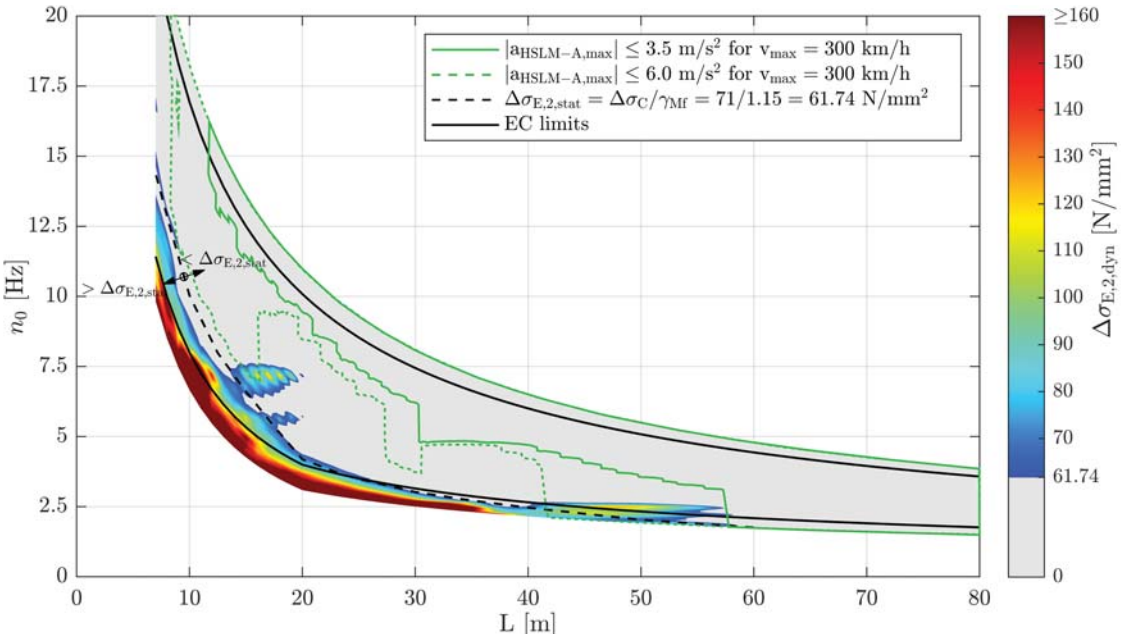

Figure C.77.: Single-span composite bridges — traffic mix TM5* — v_{Train} — ζ_{V1} — Rayleigh like damping — no load distribution — top view $\Delta\sigma_{E,2,dyn}$ & $|a_{HSLM-A,max}|$ & $\Delta\sigma_{E,2,stat}$

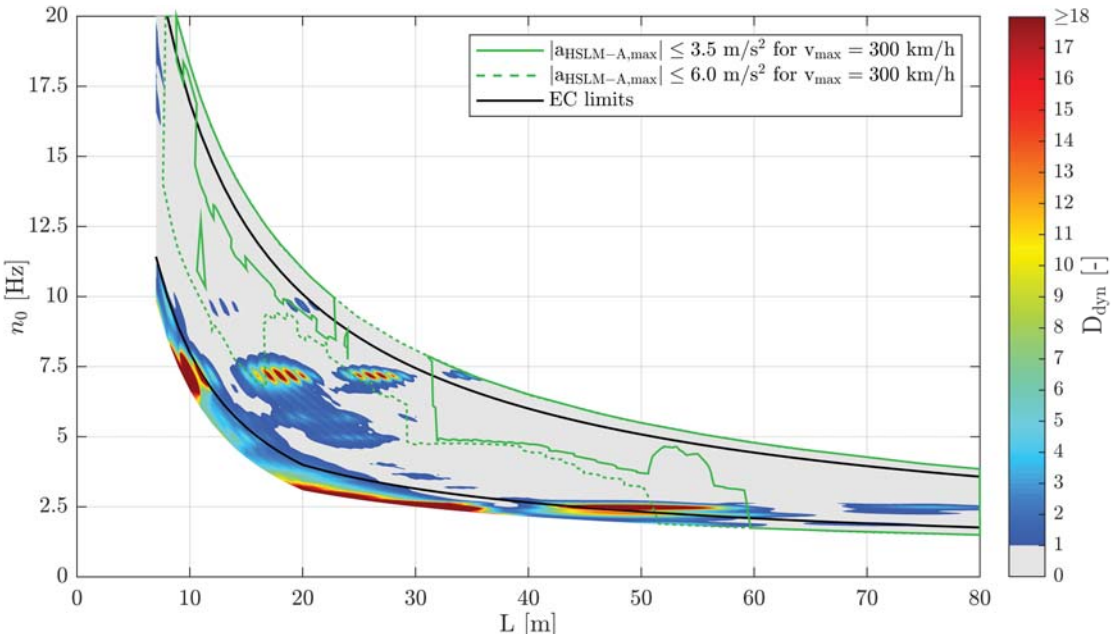

Figure C.78.: Single-span composite bridges — traffic mix TM5* — v_{Train} — ζ_{EC} — Rayleigh like damping — load distribution — top view D_{dyn} & $|a_{HSLM-A,max}|$

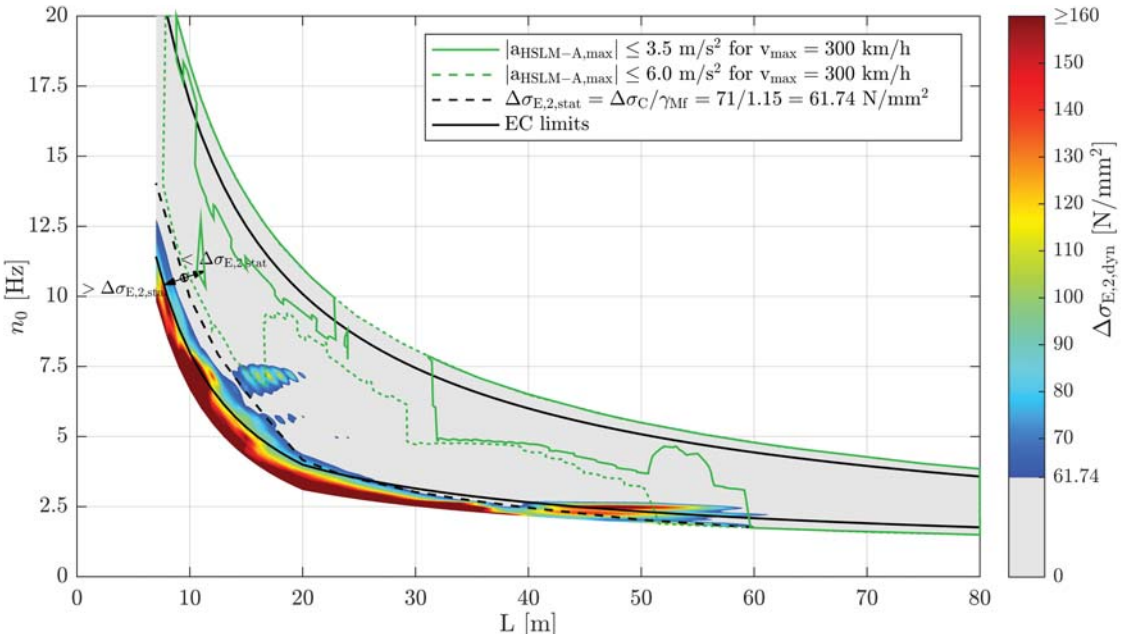

Figure C.79.: Single-span composite bridges — traffic mix TM5* — v_{Train} — ζ_{EC} — Rayleigh like damping — load distribution — top view $\Delta\sigma_{E,2,dyn}$ & $|a_{HSLM-A,max}|$ & $\Delta\sigma_{E,2,stat}$

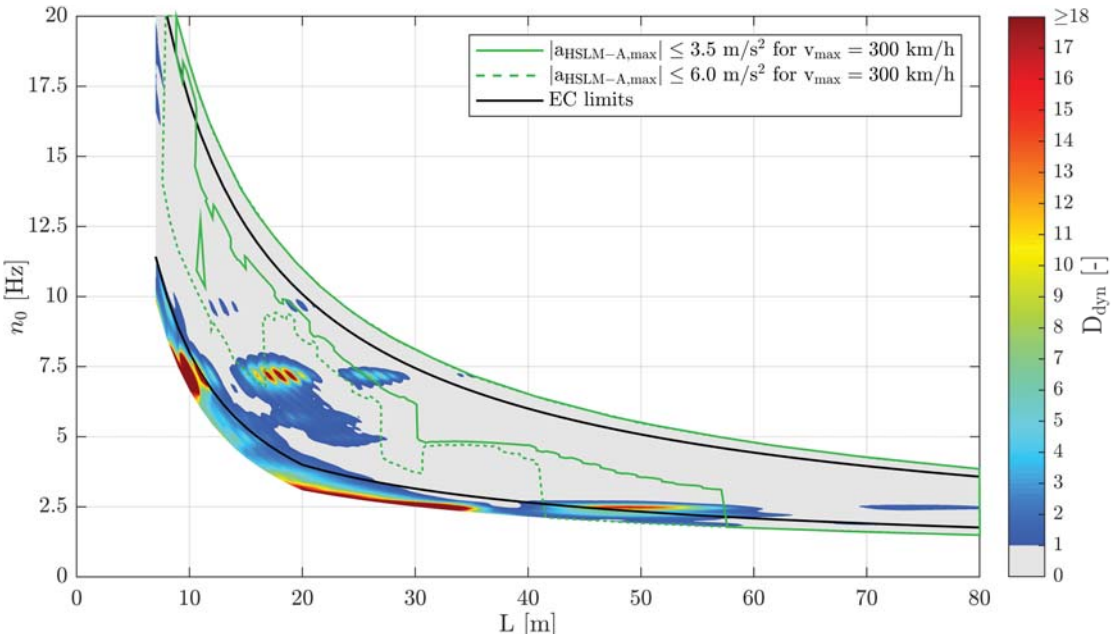

Figure C.80.: Single-span composite bridges — traffic mix TM5* — v_{Train} — ζ_{V1} — Rayleigh like damping — load distribution — top view D_{dyn} & $|a_{HSLM-A,max}|$

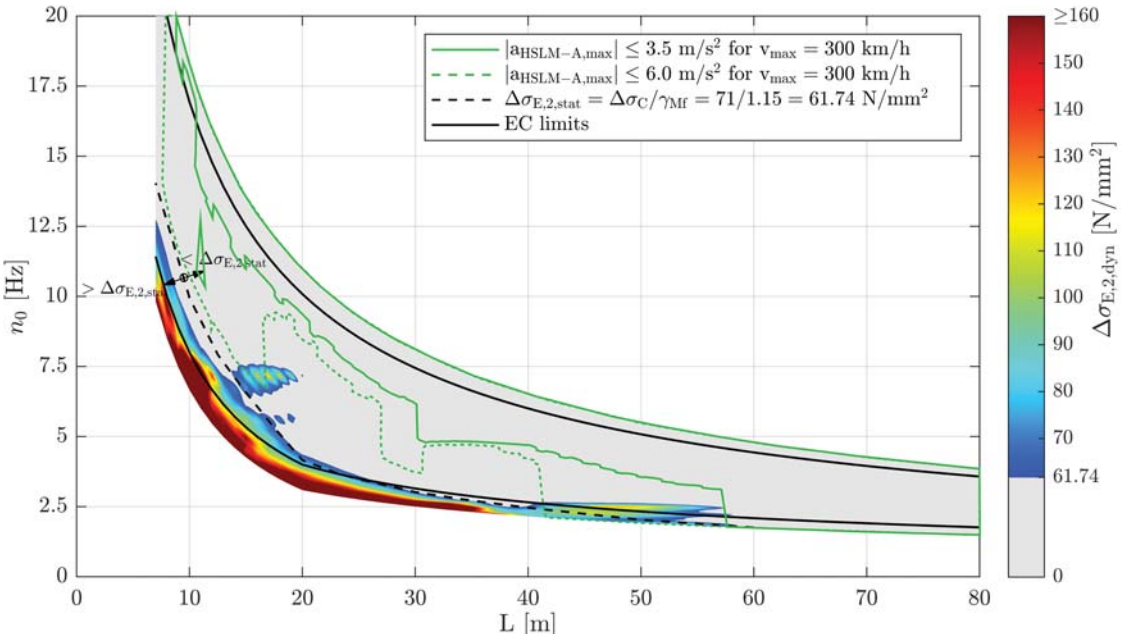

Figure C.81.: Single-span composite bridges — traffic mix TM5* — v_{Train} — ζ_{V1} — Rayleigh like damping — load distribution — top view $\Delta\sigma_{E,2,dyn}$ & $|a_{HSLM-A,max}|$ & $\Delta\sigma_{E,2,stat}$

C.7.2. Train speed $v_{D_{max}}$

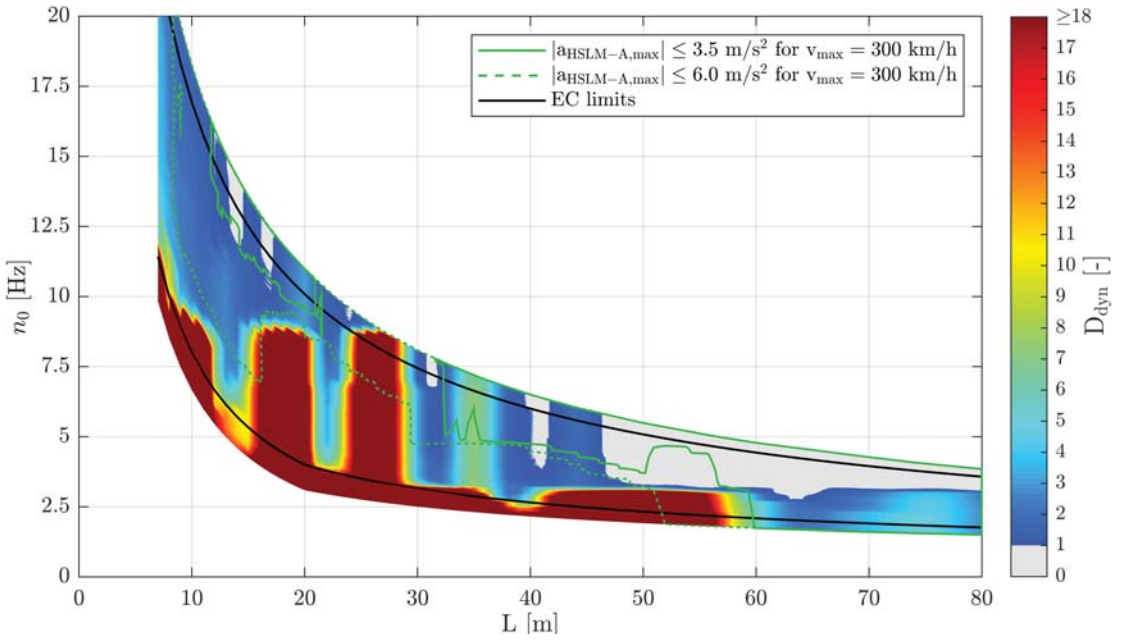

Figure C.82.: Single-span composite bridges — traffic mix TM5** — $v_{D_{max}}$ — ζ_{EC} — Rayleigh like damping — no load distribution — top view D_{dyn} & $|a_{HSLM-A,max}|$

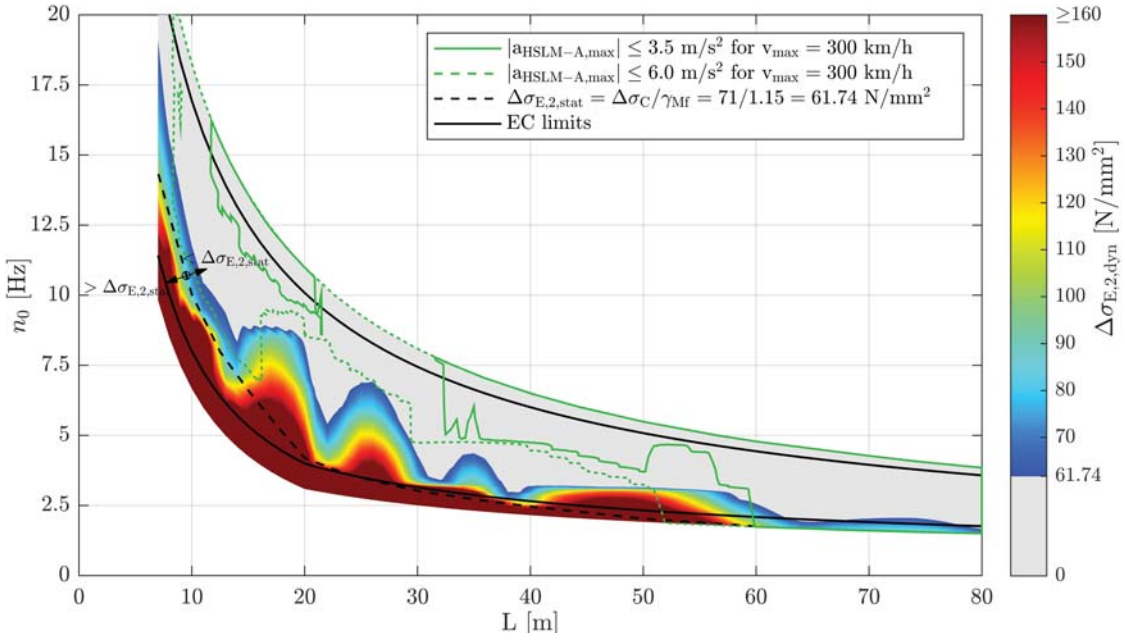

Figure C.83.: Single-span composite bridges — traffic mix TM5** — $v_{D_{max}}$ — ζ_{EC} — Rayleigh like damping — no load distribution — top view $\Delta\sigma_{E,2,dyn}$ & $|a_{HSLM-A,max}|$ & $\Delta\sigma_{E,2,stat}$

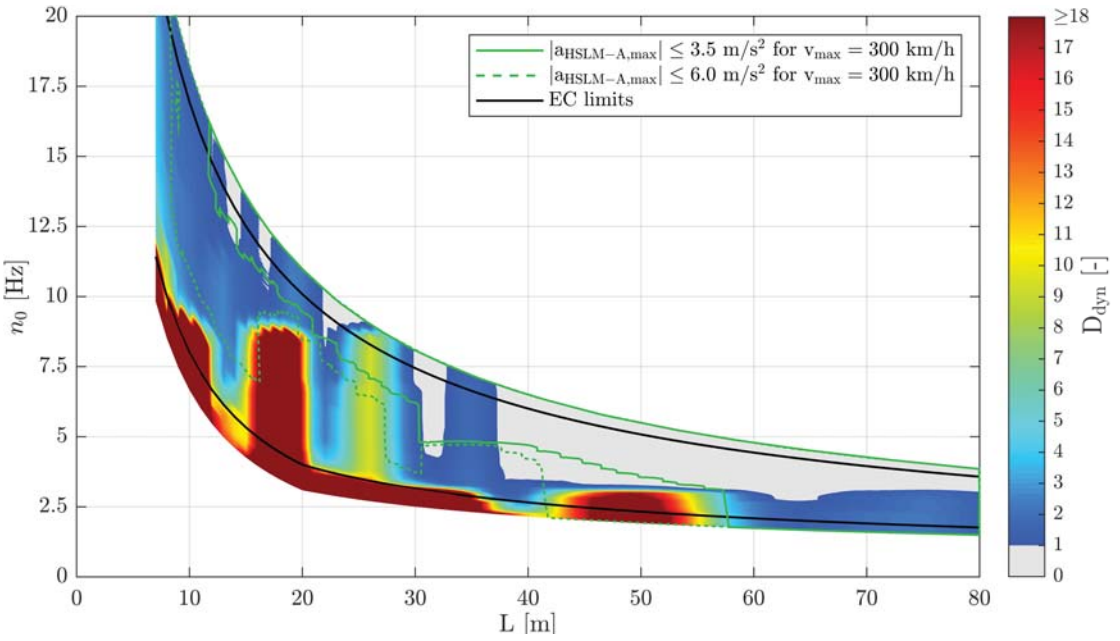

Figure C.84.: Single-span composite bridges — traffic mix TM5** — $v_{D_{max}}$ — ζ_{V1} — Rayleigh like damping — no load distribution — top view D_{dyn} & $|a_{HSLM-A,max}|$

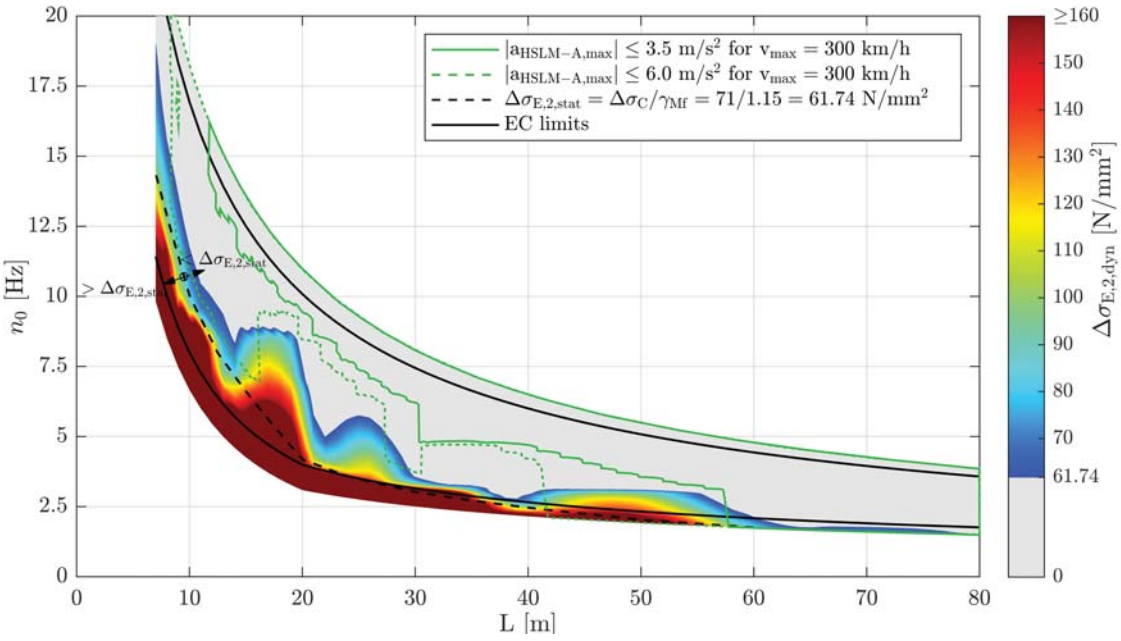

Figure C.85.: Single-span composite bridges — traffic mix TM5** — $v_{D_{max}}$ — ζ_{V1} — Rayleigh like damping — no load distribution — top view $\Delta\sigma_{E,2,dyn}$ & $|a_{HSLM-A,max}|$ & $\Delta\sigma_{E,2,stat}$

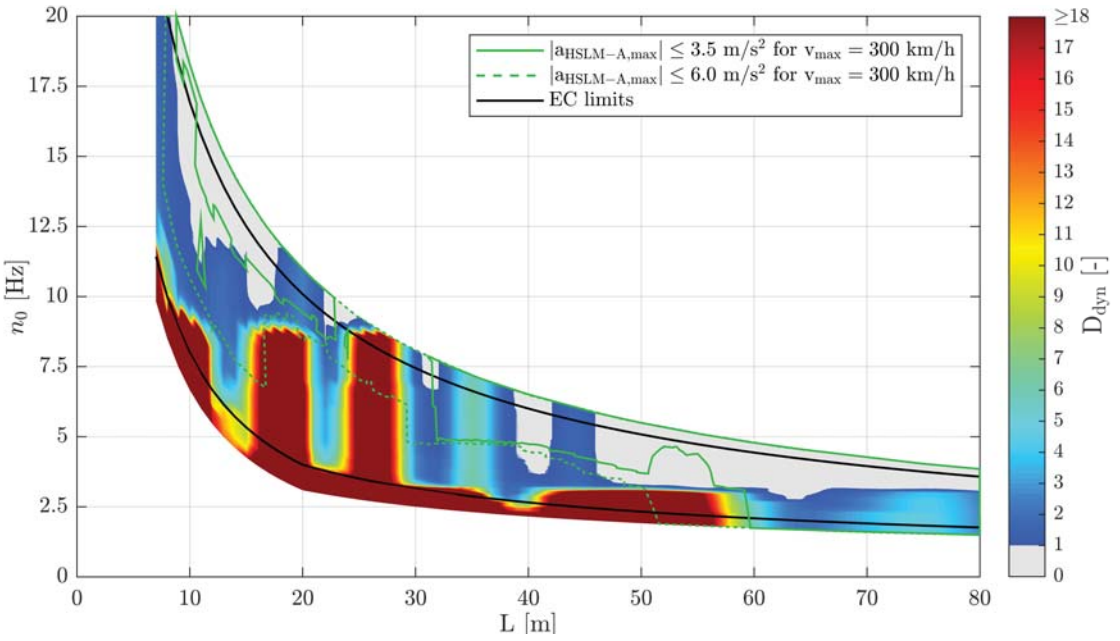

Figure C.86.: Single-span composite bridges — traffic mix TM5** — $v_{D_{max}}$ — ζ_{EC} — Rayleigh like damping — load distribution — top view D_{dyn} & $|a_{HSLM-A,max}|$

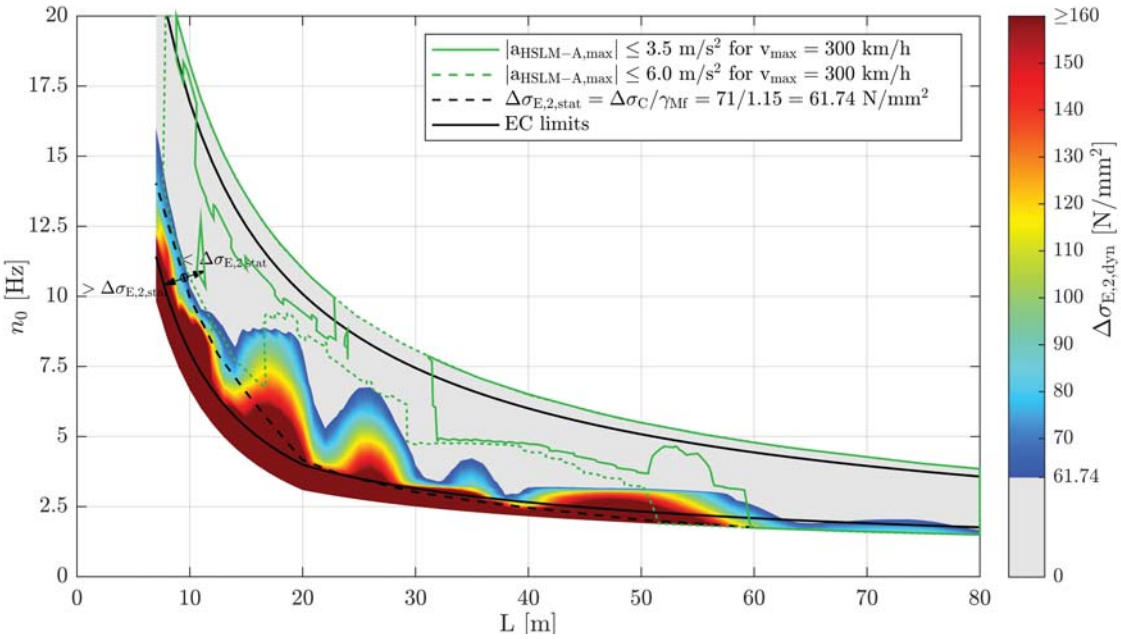

Figure C.87.: Single-span composite bridges — traffic mix TM5** — $v_{D_{max}}$ — ζ_{EC} — Rayleigh like damping — load distribution — top view $\Delta\sigma_{E,2,dyn}$ & $|a_{HSLM-A,max}|$ & $\Delta\sigma_{E,2,stat}$

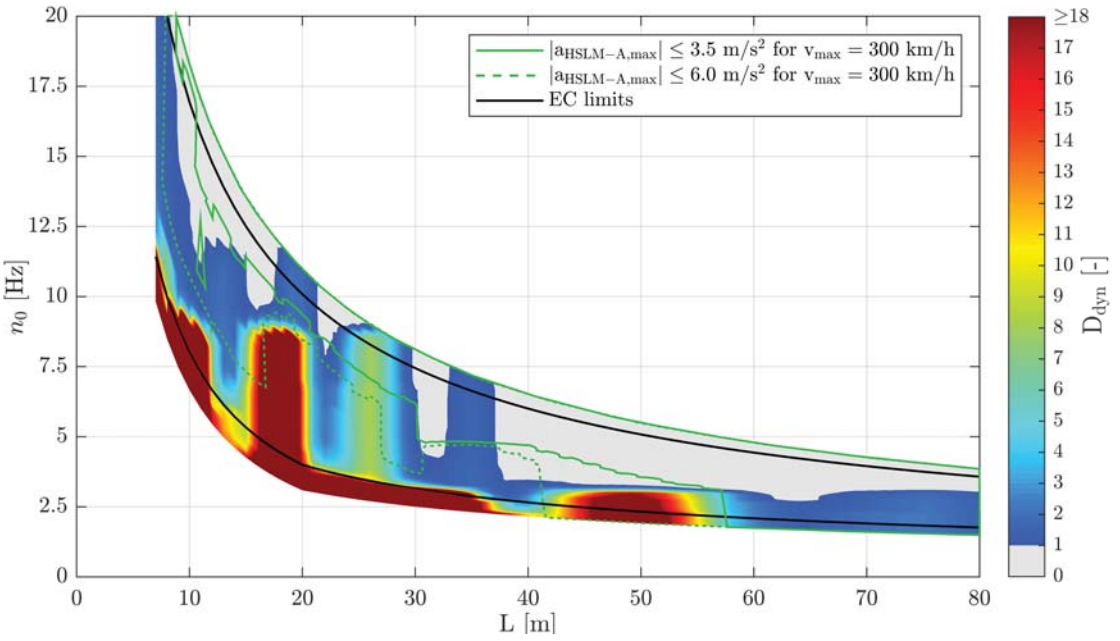

Figure C.88.: Single-span composite bridges — traffic mix TM5** — $v_{D_{max}}$ — ζ_{V1} — Rayleigh like damping — load distribution — top view D_{dyn} & $|a_{HSLM-A,max}|$

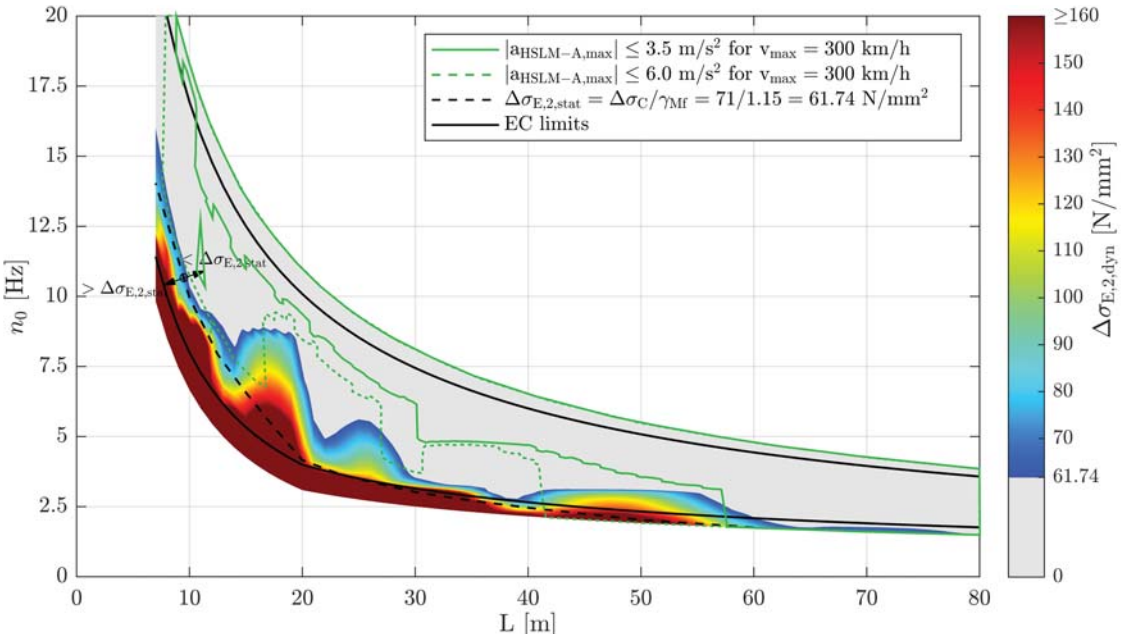

Figure C.89.: Single-span composite bridges — traffic mix TM5** — $v_{D_{max}}$ — ζ_{V1} — Rayleigh like damping — load distribution — top view $\Delta\sigma_{E,2,dyn}$ & $|a_{HSLM-A,max}|$ & $\Delta\sigma_{E,2,stat}$

C.7.3. Train speed $v_{a_{max}}$

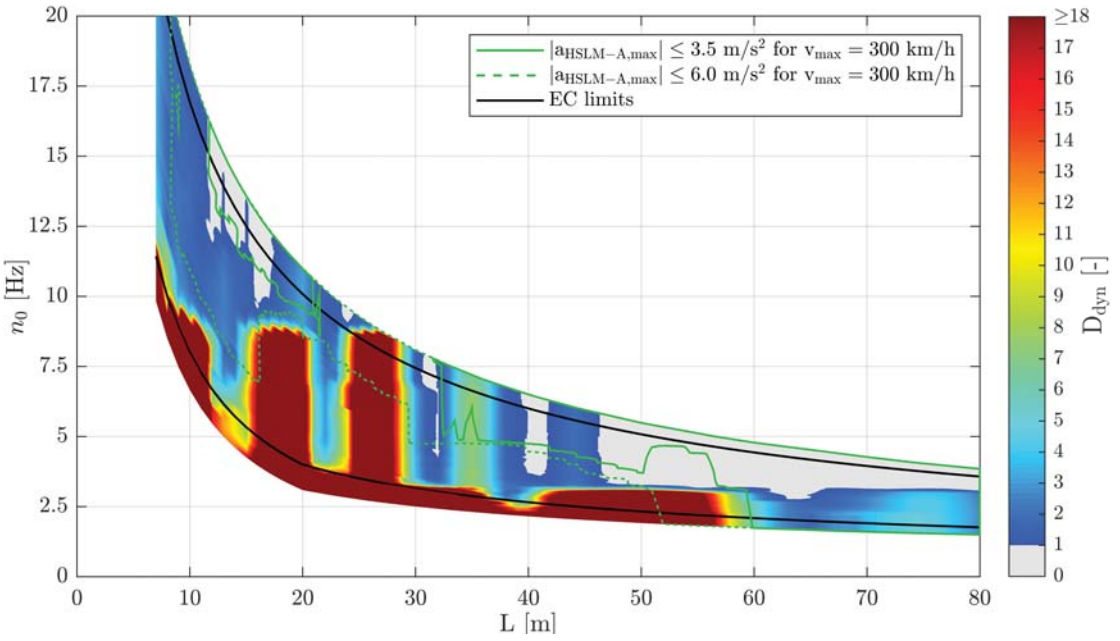

Figure C.90.: Single-span composite bridges — traffic mix TM5*** — $v_{a_{max}}$ — ζ_{EC} — Rayleigh like damping — no load distribution — top view D_{dyn} & $|a_{HSLM-A,max}|$

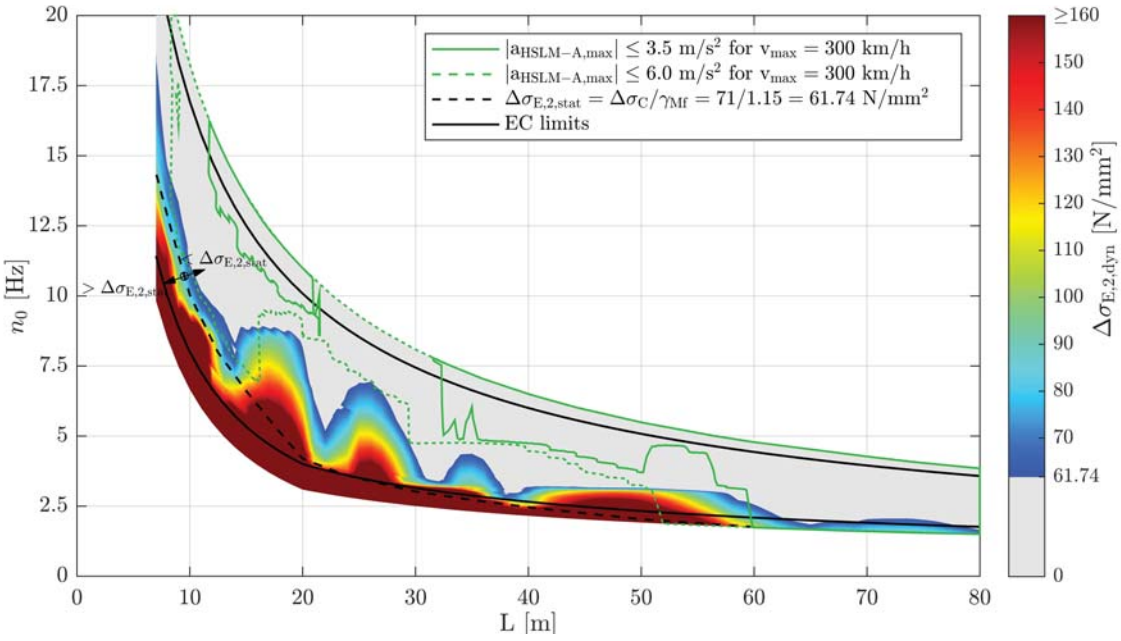

Figure C.91.: Single-span composite bridges — traffic mix TM5*** — $v_{a_{max}}$ — ζ_{EC} — Rayleigh like damping — no load distribution — top view $\Delta\sigma_{E,2,dyn}$ & $|a_{HSLM-A,max}|$ & $\Delta\sigma_{E,2,stat}$

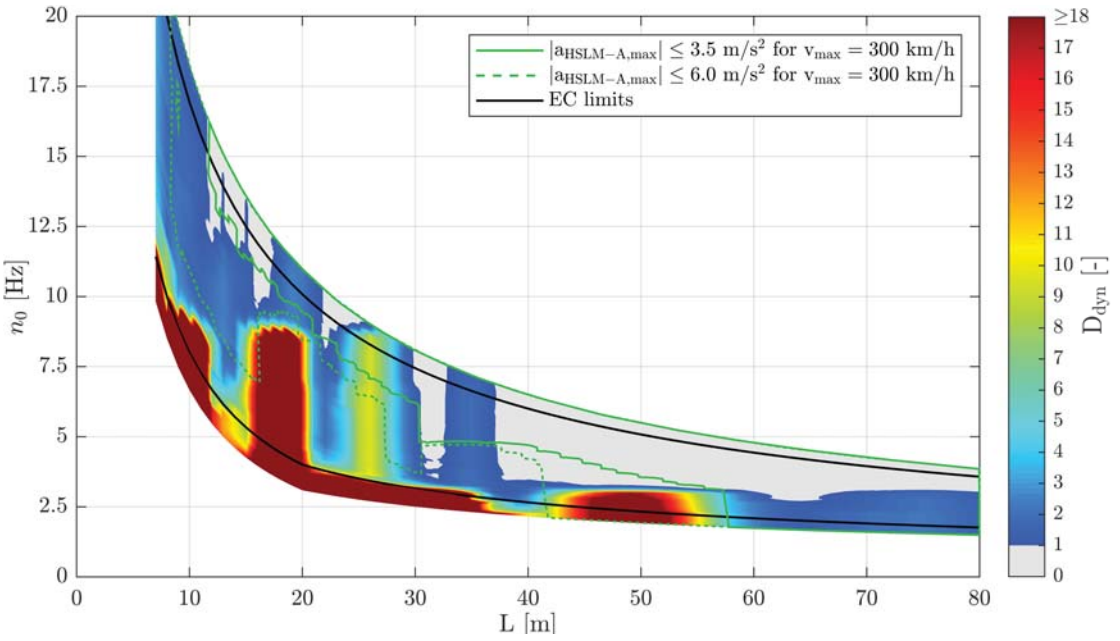

Figure C.92.: Single-span composite bridges — traffic mix TM5*** — $v_{a_{max}}$ — ζ_{V1} — Rayleigh like damping — no load distribution — top view D_{dyn} & $|a_{HSLM-A,max}|$

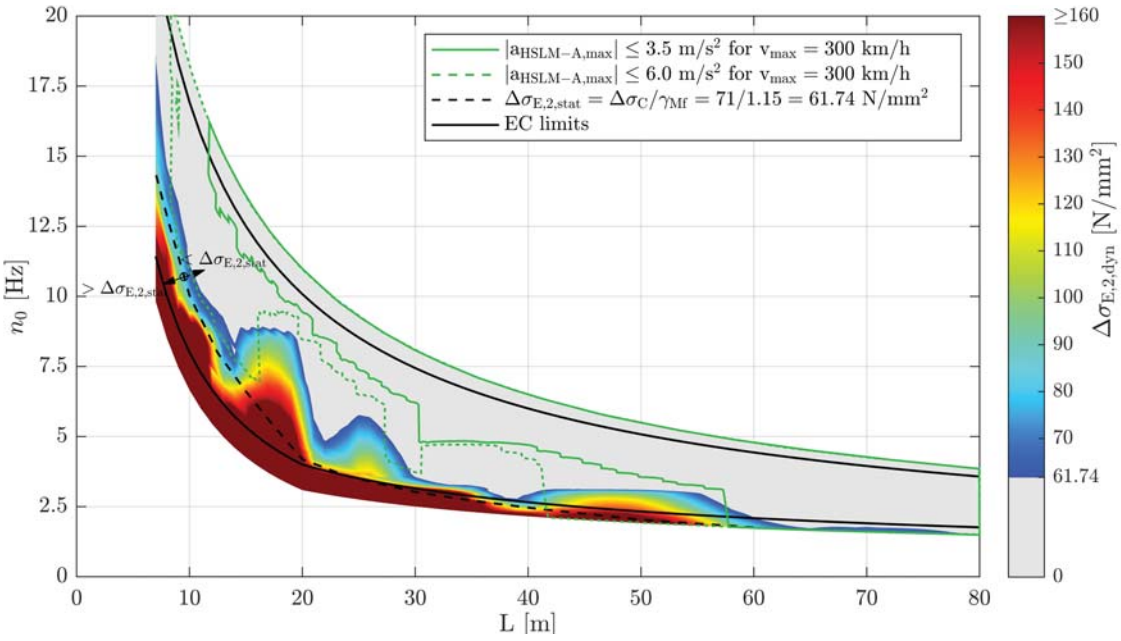

Figure C.93.: Single-span composite bridges — traffic mix TM5*** — $v_{a_{max}}$ — ζ_{V1} — Rayleigh like damping — no load distribution — top view $\Delta\sigma_{E,2,dyn}$ & $|a_{HSLM-A,max}|$ & $\Delta\sigma_{E,2,stat}$

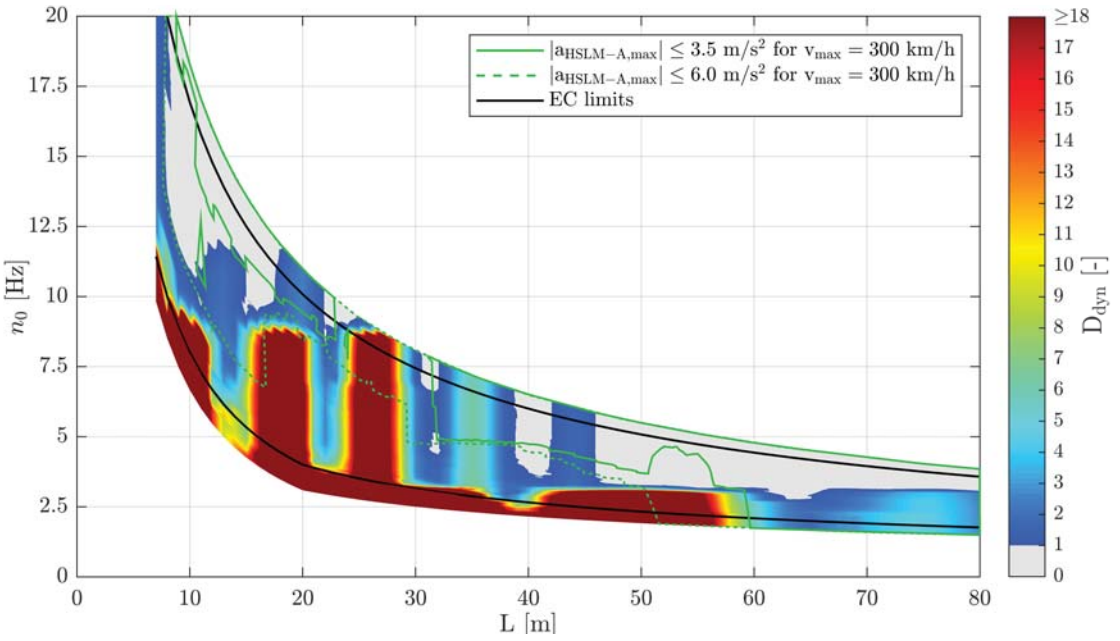

Figure C.94.: Single-span composite bridges — traffic mix TM5*** — $v_{a_{max}}$ — ζ_{EC} — Rayleigh like damping — load distribution — top view D_{dyn} & $|a_{HSLM-A,max}|$

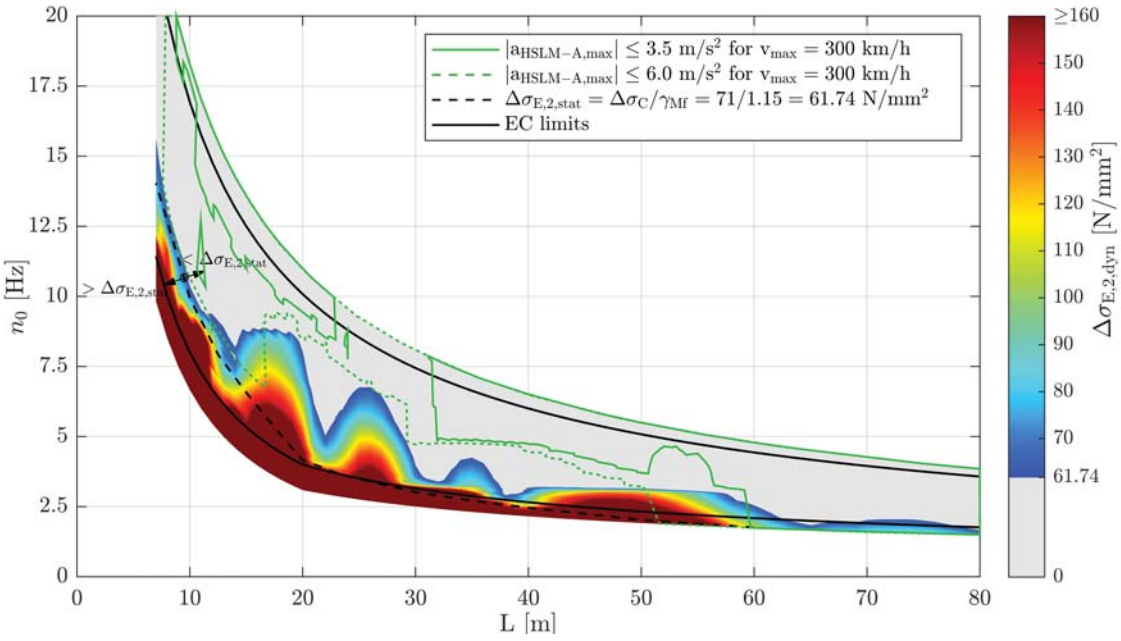

Figure C.95.: Single-span composite bridges — traffic mix TM5*** — $v_{a_{max}}$ — ζ_{EC} — Rayleigh like damping — load distribution — top view $\Delta\sigma_{E,2,dyn}$ & $|a_{HSLM-A,max}|$ & $\Delta\sigma_{E,2,stat}$

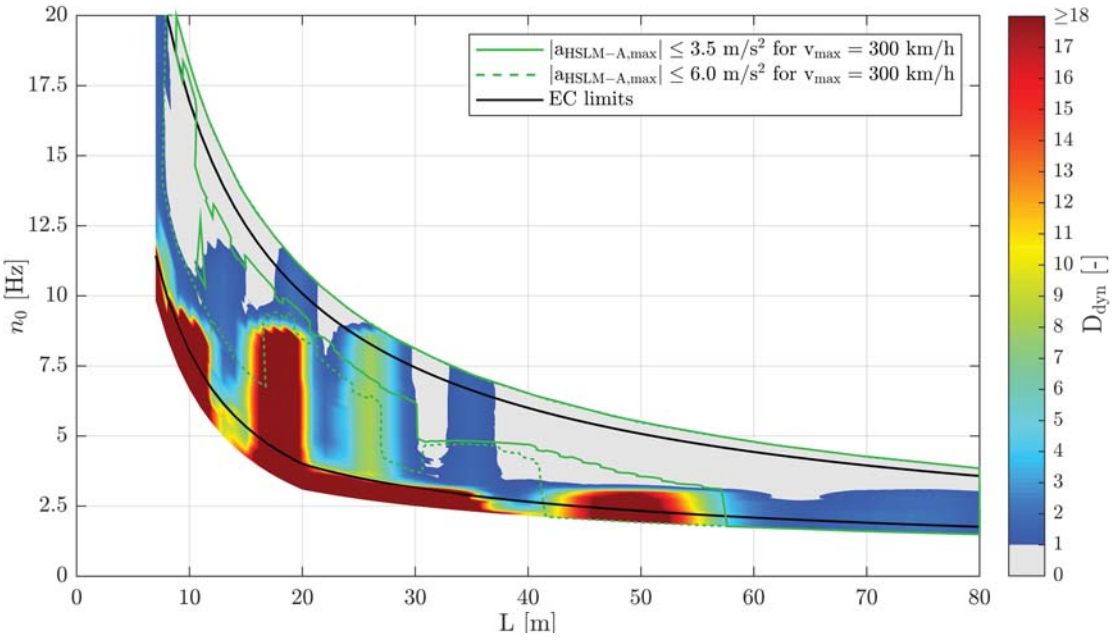

Figure C.96.: Single-span composite bridges — traffic mix TM5*** — $v_{a_{max}}$ — ζ_{V1} — Rayleigh like damping — load distribution — top view D_{dyn} & $|a_{HSLM-A,max}|$

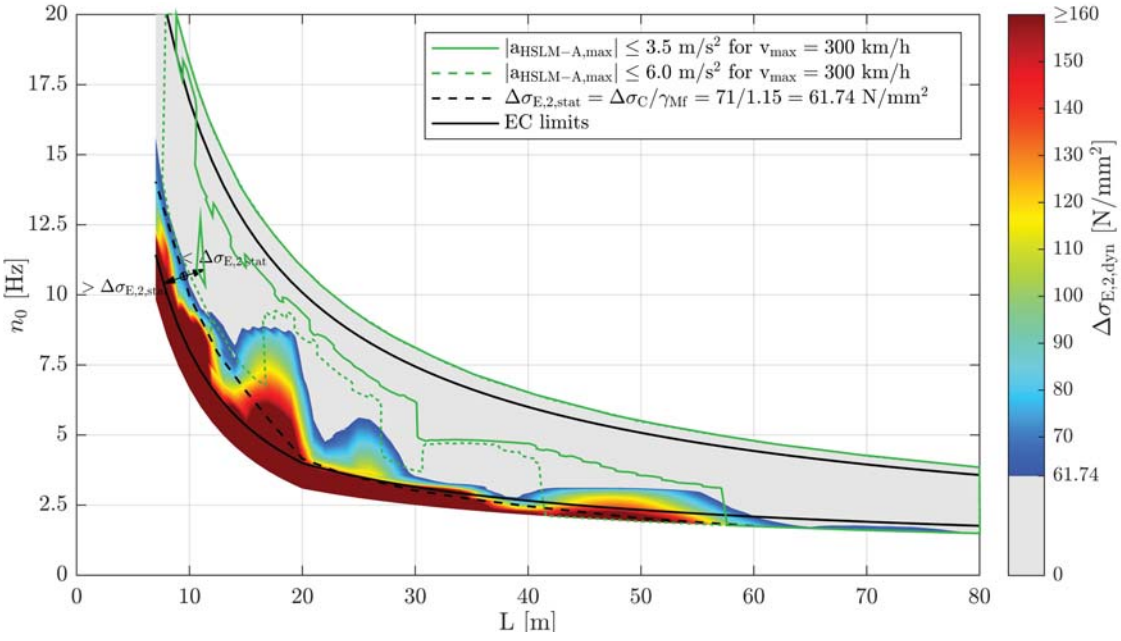

Figure C.97.: Single-span composite bridges — traffic mix TM5*** — $v_{a_{max}}$ — ζ_{ECV1} — Rayleigh like damping — load distribution — top view $\Delta\sigma_{E,2,dyn}$ & $|a_{HSLM-A,max}|$ & $\Delta\sigma_{E,2,stat}$